NANOTECHNOLOGY SCIENCE AND TECHNOLOGY

PROPERTIES AND APPLICATION OF ULTRATHIN CARBON AND SILICON FILMS

NANOTECHNOLOGY SCIENCE AND TECHNOLOGY

Additional books and e-books in this series can be found on
Nova's website under the Series tab.

NANOTECHNOLOGY SCIENCE AND TECHNOLOGY

PROPERTIES AND APPLICATION OF ULTRATHIN CARBON AND SILICON FILMS

ALEXANDER Y. GALASHEV
AND
YURI P. ZAIKOV

nova
science publishers
New York

Library of Congress Cataloging-in-Publication Data

ISBN: 978-1-53614-509-0

Published by Nova Science Publishers, Inc. † New York

CONTENTS

PREFACE

Graphene is a two-dimensional (2D) sheet structure of sp^2-bonded carbon atoms with unique electronic, chemical and mechanical properties. Graphene conducts electricity better than copper. It is 200 times stronger than steel but six times lighter. It is almost perfectly transparent since it absorbs only 2% of light. It impermeable to gases, even those as hydrogen or helium. The list of qualities that describe graphene (a sheet consisting of one layer of carbon atoms in the honeycomb lattice) is long and impressive.

Once this so-called 2D material (the first of its kind) was received in 2004. It was announced as a major breakthrough with many applications. In particular, it is expected that it could revolutionize electronics. Unfortunately, graphene has not yet fulfilled its promises in this field. This does not prevent researchers, who are now seeking to develop other 2D materials (graphene cousins) that can enter a new era in electronics.

The silicene synthesized in 2010 is the two-dimensional hexagonal honeycomb structure or, simply, a single-layer silicon. On the one hand, the cellular structures similar to graphene ones demonstrate amazing physical properties, such as the existence of the gapless fermions of Dirac at the corner of the Brillouin zone. On the other hand, this low buckled geometry provides some special properties to silicene that graphene does not have. Silicene is considered the most likely candidate to replace silicon in transistors, but now this is not the only contender.

Recently, a number of other materials have been synthesized, such as germanene, made of germanium atoms, stanene from tin, and phosphorene from phosphorus. Theoretical and experimental studies carried out are able to predict the most suitable field of application for each newly discovered two-dimensional material. The low-dimensional structures of metals, ceramics, plastics, composites, nanomaterials (extremely small substances), and other substances now have been identified as new materials that meet certain mechanical, electrical and chemical requirements. These materials can be developed and tested by computer simulation. Application of methods of the numerical experiment, such as methods of molecular dynamics and Monte Carlo, many times shortens the time of investigation of the physical properties of new materials and makes them much cheaper.

These methods give an ideal atomic representation of the structure, which cannot be achieved even with the use of scanning electron microscopy of the highest resolution.

The method of the molecular dynamics makes it possible to observe structural changes developing in time, to intervene in the course of events occurring at the atomic level, and to reproduce them repeatedly. The results of computer modeling are of great predictive value, but in no case, they should completely replace the natural experiment. The last word always remains for a physical experiment. But at any given instant, as a rule, we want to know as much as possible about the properties of the system including its characteristics, information on which cannot yet be obtained experimentally. Here, we again come to the rescue computer experiment.

This book is devoted to a computer study of the physical properties of super thin films consisting of one or two layers of graphene or silicene. The defect-free mono-layer graphene is impermeable to all gases and liquids and shows high chemical and thermal stability with little toxicity. These characteristics provide graphene with competitive advantages over the existing barrier materials. Difficulties of growing large-area defect-free graphene films interfere with the use of graphene as a protective coating. For example, graphene films grown by chemical vapor deposition possess many defects and grain boundaries and do not protect copper against oxidation, but, on the contrary, speed up its corrosion.

The simplest potential solution to this problem is the use of graphene-based multilayers. Local defects can always exist in graphene and silicene at finite temperatures. The most frequently observed defect type is the single vacancy in single layer honeycomb structures. The vacancy defects in graphene usually emerge during epitaxial growth on grain boundaries or step edges. All defects alter properties of the pristine 2D structures significantly. In this case, the resonant states arise in the material. Defects distort the pristine single layer honeycomb structure and modify the magnetic ground state.

Physical impact on two-dimensional materials by means of stress, irradiation, and sublimation can also result in a non-equilibrium concentration of such defects. The vacancy defects can be generated for various reasons. They can persist, change, or self-repair under the proper external conditions. Usually, graphene restores its defects if it is placed in a reservoir with enough host external atoms. As a result of the healing of graphene, the Stone-Wales type defects may occur. It should be noted that the Stone-Wales defects by themselves are healed by the rotation of the specific C–C bond. Structural defects play a key role in adapting the physical and chemical properties of silicene to no lesser degree than for graphene. Various types of vacancy defects on graphene and silicene have been investigated both experimentally and theoretically and can now be imaged with atomic resolution.

The knowledge and understanding of graphene and its properties have grown. So, it can be widely applied to a broad range of technologies and devices. Functionalized graphene nanoplatelets are used to prepare new printing inks. Such ink is flexible on

appropriate substrates, metal-free and 100% organic (non-tarnishing), curable at low temperatures, and environmentally friendly. Engineering graphene-based devices and applications are currently in demand in many areas such as flexible electronics and sensors, bioelectronics, nerve, muscle, and bone tissue engineering plants and devices.

The contents of this book include studies of the thermal stability of stretched thin films of metals (Cu, Al, and Ni) of monatomic thickness placed on graphene. Filters based on graphene or carbon nanotubes can help remove dyes and heavy metals by adsorption. Such a technique can be used in combination with other membrane-based processes like reverse osmosis and nanofiltration for complete and effective treatment of dye and textile industry wastewater. At the same time, it is important that the filters made on the basis of the carbon nanomaterials are renewable, *i.e.*, for them, there are effective methods of purification from heavy toxic metals. Our computer studies have shown that low-energy bombardment with noble gas clusters can be an effective method for cleaning graphene filters from copper, lead, or mercury that has settled on them.

The practical use of more extended carbon and silicene films suggests their presence on some relatively massive substrate. Influence of the substrate presence on the state of such films has been studied extremely poorly. Therefore, in this book, we focus on the investigation of the behavior of super thin carbon and silicon films placed on metallic (silver and copper) and non-metallic (pyrolytic graphite) substrates. These studies are directly related to the problem of a significant increase in the electrical capacity and the charging rate of lithium-ion batteries. Here, the weakest point is still the search for the anode material for new generation batteries.

Graphitic carbon is still considered the most reliable material for the negative electrode in lithium ion cells, mainly due to its high reversibility and low operating potential. However, the carbon anodes exhibit an average charge/discharge rate performance, which contributes to the severe structural damage to the surface. This damage is caused by the lithium transport under the prolonged cycling and limits the lifetime of the cell. The graphene-based materials are promising for use in supercapacitors and other energy storage devices due to the highly tunable surface area, outstanding electrical conductivity, good chemical stability, and excellent mechanical behavior. One of the objectives of this work is to determine the diffusion paths and lithium ion transport parameters in the graphene channel and to provide rational guidelines for design and synthesis of the high-rate graphene materials.

Silicon has not competitors in relation to the electrochemical formation of an alloy with the highest lithium content and easy recovery of its constituent components, *i.e.*, Si and Li. Therefore, silicene is considered to be an ideal candidate for the material of the anode for the lithium-ion battery. In this connection, the book deals with the interaction of lithium ions with the autonomous two-layer silicene, the behavior of the Li^+ ion in a silicene channel, whose walls are supported by graphene. Serious attention is paid to the role of substrates from the silver, copper, and pyrolytic graphite in the kinetic and mechanical

properties of the silicene channel with lithium ion moving in it under the electric field. The book also gives the results of the study of filling the silicene channel by lithium in an electric field in the presence of silver and copper substrates. Also, the process of liberation of such a channel from lithium is analyzed in detail when the direction of the electric field vector reverses.

The book is organized as follows. Introduction (Chapter 1) gives a brief description of the structure and physical properties of graphene and silicene. Chapter 2 contains a description of the models and methods for performing numerical experiments. The calculation formulas used are given in this chapter, and an example of testing the model and calculation method is also given. Transformations of the graphene into other carbon forms, as well as, the temperature dependences of its thermal conductivity are presented in Chapter 3. Chapter 4 is devoted to the study of the thermal stability of the metallic films deposited on graphene. The computer simulation of heating a mercury film on graphene is highlighted in a separate chapter (Chapter 5). Chapter 6 deals with the removal of heavy metals from graphene by low-energy bombardment with noble gas clusters. Chapter 7 describes the motion of lithium ions through graphene and silicene membranes and the passage of both perfect and defective graphene and silicene channels by a lithium ion. Moreover, here the mechanical and thermal properties of silicene are considered. The computer simulation of functioning the silicene anode on silver substrates with the determination of the stressed state of the perfect and defective silicene is discussed in Chapter 8. Fragmentary functioning and prospects for using the silicene-copper anode are described in Chapter 9. Chapter 10 presents a discussion on the stability of the two-layered silicene and thin silicon film on pyrolytic graphite, as well as, a detailed analysis of the structural changes that occur in the silicene channel when the lithium ion moves through the channel. Chapter 11 ends the book with conclusions and represents the viewpoint of the authors on the state and prospects of the studies being conducted.

This work was supported by the Russian Science Foundation, project no. 16-13-00061.

Alexander Y. Galashev
Yuri P. Zaikov
Yekaterinburg
July 2018

ABBREVIATIONS

AFM	Atomic-force microscopy
BDE	Bond-dissociation energy
CNTs	Carbon nanotubes
CVD	Chemical vapor deposition
DFT	Density functional theory
EBG	Energy-band gap
fcc	face-centered cubic
FF	Force field
GB	Grain boundary
GEA	Gradient expansion approximation
GGA	Generalized gradient approximation
HRTEM	High-resolution transmission electron microscopy
KS	Kon–Sham
LAMMPS	Large-scale Atomic/Molecular Massively Parallel Simulator
LDA	local spin density approximation
LIBs	Lithium ion batteries
LJ	Lennard–Jones
MC	Monte Carlo
MD	Molecular dynamics
MSD	Mean square of the displacement
NEMD	Non-equilibrium molecular dynamics
PBC	Periodic boundary conditions
PBE	Perdew–Burke–Ernzerhof
QM	Quantum mechanics
RDF	Radial distribution function
REBO	Reactive empirical bond order
RT	Room temperature
SC	Supercapacitor

SEI	Solid-electrolyte interphase
SG	Silver-Goldman
SIESTA	Spanish Initiative for Electronic Simulations with Thousands of Atoms
SNM	Silicene nanomesh
STM	Scanning tunneling microscopy
TEM	Transmission electron microscope
VDD	Voronoi deformation density
VGN	Vertical graphene nanosheets
VPs	Voronoi polyhedra
XC	exchange-correlation
ZBL	Ziegler–Biersack–Littmark
ZNRG	"Zig-zag" nanoribbon of graphene

Chapter 1

INTRODUCTION

In 2004 in the University of Manchester, Geim and Novoselov studied the creation of a substance obtained from graphite. In their experiments, they sought to obtain the thinnest possible slice from graphite in order to study the behavior of this new material. These scientists observed the graphene that was examined by an atomic microscope. This new material (graphene) could function as a transistor. Further, Geim and Novoselov made that material thinner and thinner, until it reached a thickness of an atom. On the other hand, they also found that this ultrafine material maintained the hexagonal bonding structure and, besides, had a peculiar symmetrical arrangement of electrons, which provided an increase of its conductivity. Six years after the discovery of graphene (in 2004), Geim and Novoselov received the Nobel Prize in Physics. Since then, research on graphene has widely begun in the world. The carbon atoms in a two-dimensional (2D) graphene (i.e., located in a plane) form a honeycomb lattice consisting of carbon atoms with the sp^2 hybrid covalent bonds. However, this honeycomb lattice is not of a conventional Bravais structure, since the atomic structures referring to two of the adjacent atoms are not equivalent [1]. The honeycomb structure lacks an atom located at the central part of the hexagon. So, this atomic structure cannot be considered as a hexagonal atomic one of a conventional Bravais lattice. The graphene unit cell can be defined as a rhombus, in which two carbon atoms are inside it. Such structure can be considered as an association of two triangular atomic structures forming a Bravais one in the honeycomb lattice of graphene.

The great development of graphene investigations is closely related to its unique electronic structure including the Dirac cones (conical singularities) where the top and bottom bands intersect at a single point. The cone, which represents linear energy dispersion at the Fermi level, gives graphene massless fermions. The latter lead to various quantum Hall effects, ultra-high carrier mobility, and many other novel phenomena and properties. The Dirac cone is responsible for many unique electronic properties of graphene and topological insulators [2]. Its band structure consisting of two conical bands touching at a single point has also appeared for photons in waveguide arrays [3], atoms in optical

lattices [4], and through accidental degeneracy [5, 6]. When a magnetic field is introduced into the wave equation, the Landau levels (energy levels of a charged particle in a magnetic field) are formed in the spectrum. The eigen states of the system congregate at discrete, highly degenerate levels. In the two-dimensional electron gas, the Landau levels are directly responsible for the presence of the discrete steps in the Hall conductivity, which is known as the quantum Hall effect. Deformation of the Dirac cone often leads to intriguing properties. The example is the quantum Hall effect where a constant magnetic field breaks the Dirac cone into isolated Landau levels. With a remarkable naturally gapless band structure, graphene can absorb light of broad spectrum extending from the ultraviolet and visible spectral region to infrared and terahertz (THz) one [7]. This property distinguishes it from other traditional semiconductors. Nevertheless, the existing natural doping of graphene leads to opening the optical band gap, which creates a deterioration in the graphene absorptivity.

Studies of the physical and chemical properties of graphene indicate the possibility of its use in batteries, nanoelectronics, fuel cells, photovoltaics, catalysis, separation, and storage, along with the gas sorption and gas sensing. Due to its unique properties, graphene finds wide application in a variety of devices. One such device is a supercapacitor (SC). The supercapacitors have higher power density and superior cycle life comparing to conventional batteries. Performance of supercapacitors is strongly dependent on the electrode material. Vertical graphene nanosheets (VGN) are ideal SC electrodes because of their distinct morphology and remarkable properties. The charge storage mechanism of VGN is based on the electric double layer formation at the electrode/electrolyte interface. They have a non-agglomerated self-supported porous structure. Each vertical sheet acts as a nanoelectrode [8]. The advantage of VGN over other electrode materials is that they do not need any binder, conductive additives, and even additional current collector [9, 10].

Defects are the most important structural properties of semiconductors since they can alter electronic and optoelectronic properties. In particular, defects can affect the local electronic structure, carrier density, thermal conductivity, and mechanical strength of 2D materials. Point defects and line defects are the most important lattice imperfections for 2D materials. They are mainly generated during the synthesis process and chemical/physical post-treatment [11]. The defects in 2D materials could be observed and characterized by the high-resolution transmission electron microscopy (HRTEM), the scanning tunneling microscopy (STM), and Raman spectroscopy. Wherein theoretical calculations are also needed to identify the formation behavior of such structure. Strain engineering can serve an effective way to tune the electronic properties of semiconductors. The energy band characteristics around the Fermi level are very sensitive to orbital coupling the neighboring atoms. Bulk materials often cannot endure the necessary large elastic strain to have sufficient changes in their electronic properties. In contrast, 2D materials have excellent elasticity and high Young modulus, i.e., properties that are necessary to be in demand for strain engineering [12].

Nowadays, researchers around the world highly immerse into detailing the electrical/optical properties related to other 2D metamaterials. Among these materials, one of the leading places is occupied by silicene, i.e., two-dimensional silicon of monatomic thickness. The term silicene was introduced by Gusman-Verry and Lew Yan Voon in 2007. The main interest in silicene is dictated due to the preservation of the silicon use in the optoelectronics industry. Besides, silicone is the second largest element in the Earth crust (28.2%), the carbon (from which graphene is obtained) is only 0.02%.

Silicene (a counterpart of graphene) has attracted tremendous attention due to its excellent electronic properties and potential applications in the silicon-based microelectronics [13]. Up to now, silicene has been epitaxially synthesized on various metal surfaces (ZrB_2(0001), ZrC(111) and Ir(111)), especially on Ag(111) [14–23]. According to the lattice match between silicene and Ag(111), several superstructures including (4 × 4), (√13 ×√13)R13.9° and (2√3 × 2√3)R30° can be formed on Ag(111) surface [14–16, 18, 20, 24]. However, the quality of the epitaxial silicene sheets is usually not satisfactory. Defects are frequently observed in the epitaxial silicene [18, 14–32], which may significantly affect the intrinsic properties of silicene [33]. Moreover, it is difficult to synthesize large-scale silicene sheet with homogeneous phase [15, 18, 20, 24]. Experiments indicate that both the temperature of the substrate and the coverage of silicon atoms have prominent effects on the stability of the silicene superstructures on the Ag(111) surface [16, 18, 20]. For three frequently observed phases of silicene, (4 × 4) and (√13 ×√13) ones always coexist [15, 18, 20, 24] implying the comparable stability of these two phases. The phase (2√3 × 2√3)R30° usually occurs at a high silicon coverage and high temperature [16, 20]. In the studies presented in this book, preference is given to a structure defined as (4 × 4) silicene/Ag, which corresponds to a (3 × 3) silicene supercell in the supercell (4 × 4) Ag.

Once again, we emphasize that most of the striking properties of graphene have been predicted to occur in silicene. Therefore, the major advantage of investigating silicene like sheets is that these can be easily incorporated into the present silicon-based microelectronics industry. It seems obvious that this will lead to the development of exotic silicene-based nanodevices. It has now been proved that interaction of the substrate with such atomically thick materials as silicene influences the properties of these materials. Therefore, experimental investigation of properties of the free-standing silicene sheets is highly desirable. Almost autonomic silicene was synthesized in the form of free-standing up to few layers like 2D silicon material [34]. This was possible due to the use of non-linear interaction of ultra-fast and ultra-short laser pulses with (111) silicon surface in aqueous ambience. The method leads to the production of partially oxidized large area silicene sheets [35]. The sheets are then separated, and hydrazine treatment allows one to remove the oxygen functional groups. Atomic-scale structural characterizations reveal the hexagonal symmetry of the lattice.

The metal substrates, on which the silicene is obtained, affect its electronic structure. The electronic structure of silicene is modified through the interface coupling. As a result

of the application of magnetic fields perpendicular to the surface of the silicene, no the Landau levels sequences were obtained [36]. The density functional theory (DFT) calculations showed that the π and π^* bands derived from the Si $3p_z$ are hybridized with the Ag electronic states. Such hybridization causes the drastic modification in the band structure, the consequence of which is the disappearance of the Dirac fermion features. Thus, the strong coupling at the interface causes the symmetry breaking for the 4×4 silicene. The electronic structures of other superstructures are also undergoing changes.

Graphite has a layered structure. This structure allows the intercalation/ deintercalation of Li ions during the charge/discharge processes in the lithium-ion batteries (LIBs). In addition, it gives rise to graphite excellent cycling stability. The number of intercalated Li ions is limited by the intercalation sites in the graphite lattice. Therefore, the theoretical specific capacity of graphite (≈ 372 mA h g^{-1}) is low. Besides graphite, which is constructed from carbon atoms, other group-IV elements (Si, Ge, and Sn) are considered as the promising alternative anode materials for LIBs. These elements can alloy with Li. In other words, there is a mechanism different from the intercalation one of Li ions that is characteristic of graphite. The specific capacities of these group-IV elements are relatively high. Their potential suitability as an anode material is due to the relatively high stoichiometric ratios of Li/IV-element in these alloys. Silicon has exceptionally the high specific capacity (4200 mA h g^{-1}). Therefore, silicene is considered to be one of the most promising anode candidate materials. Its high Li capacitance correlates with the highest equilibrium of the Li–Si alloy ($Li_{22}Si_5$). In addition to this, it should be taken into account its richness in the Earth crust, and its compatibility with current silicon-based nanotechnology [37].

Currently, the use of thin-film anodes has its pros and cons. Thin-film batteries consist of only solid materials. The electrolyte is a solid-state ionic glass or crystal, and the components are deposited via vapor deposition techniques. This design offers the highest energy density and safety in operation, but it is only applicable to small devices and involves the costliest production method.

Information about the investigated object obtained experimentally is often limited and there is a need to expand knowledge about its properties. Molecular dynamics (MD) simulation techniques are widely used in experimental procedures such as the X-ray crystallography and nuclear magnetic resonance (NMR) structure determination. The molecular dynamics simulations generate information on the microscopic level including atomic positions and velocities. Atoms interact with each other through the Van der Waals forces and electrostatic ones. When they are covalently bonded to others, strong forces hold them together as stable chemical groups. Conversion of this microscopic information to macroscopic observables such as pressure, energy, heat capacities, etc. requires statistical mechanics. The statistical mechanics provides the rigorous mathematical expressions that relate macroscopic properties to the distribution and the motion of atoms and molecules of

the *N*-body system. In turn, MD simulations provide the means to solve the equation of the motion of the particles and evaluate these mathematical formulas.

With molecular dynamics simulations, one can study both thermodynamic properties and/or time dependent (kinetic) phenomenon. The classical molecular dynamics based on the use of empirical or model interaction potentials has an equilibrium and nonequilibrium variety. If one needs to limit calculations of only the kinetic coefficients, a non-equilibrium version of the MD is usually used. When using this method, the equilibrium characteristics of the system are calculated only approximately. The use of the equilibrium version of the MD makes it possible to characterize more accurately the static structure of the material being modeled as well as to study its stressed state. If we want to calculate, for example, the thermal transport coefficients using computer simulation, we have two options. We could use equilibrium molecular dynamics to calculate the appropriate equilibrium time correlation functions. However, we could mimic experiment as closely as possible and calculate the transport coefficients from their defining constitutive relations by the non-equilibrium molecular dynamics (NEMD). Just like an equilibrium MD, the NEMD is available compatibility with the periodic boundary conditions, conservation of total energy and total linear momentum. NEMD has additional features. It can, in principle, be used to calculate non-linear as well as linear transport coefficients and the sampling of a rapidly converging quantity (temperature gradient) rather than a slowly converging one (heat flux).

Molecular modeling, which is an important part of the contemporary scientific research, constitutes the theoretical foundation for creating the "objective conceptual models". A computational model can accurately simulate a large number of different phenomena by varying parameters, configurations, initial conditions and boundary conditions. In this book, we present the results of the MD study of the physical properties of ultrathin carbon and silicon films made using both the equilibrium and non-equilibrium MD methods.

Chapter 2

MOLECULAR DYNAMIC CALCULATIONS

2.1. MOLECULAR DYNAMICS WITH CLASSICAL POTENTIALS

Classical molecular dynamics can be considered as a physical method for studying the interaction and motion of atoms and molecules in accordance with the Newton laws of motion. This method uses a force field to estimate the forces between interacting atoms and calculate the overall energy of the system. In the process of the MD calculation, integration of the Newton equations of motion generates successive configurations of the evolving system. As a result, we have the trajectories that specify positions and velocities of the particles on time. Based on the obtained MD trajectories, a variety of properties can be calculated including internal energy, kinetics coefficients, and other macroscopic quantities. These results can be compared with experimental observables. The essence of the MD simulations is studying the time-dependent behavior of microscopic systems. This is obtained by solving the Newton second-order differential equations

$$\boldsymbol{f}_i(t) = m_i \boldsymbol{a}_i(t) = \frac{\partial \Phi(\boldsymbol{r}(t))}{\partial \boldsymbol{r}_i(t)}, \tag{1}$$

where $\boldsymbol{f}_i(t)$ is the net force acting on the i^{th} atom of the system at a given point t, $\boldsymbol{a}_i(t)$ is the corresponding acceleration, and m_i is the atom mass. In equation (1), the instantaneous configuration of the system is represented by the vector $\boldsymbol{r}_i(t)$, which describes position of the N interacting atoms in the Cartesian space ($\boldsymbol{r}$ = { x_1, y_1, z_1, x_2, y_2, z_2,..., x_N, y_N, z_N,}). It should be noted that this approximation holds for rather massive particles such as nuclei, while the electron motion must be averaged out. To achieve this, an empirical potential energy function is introduced ($\Phi(\boldsymbol{r})$ in equation (1)). In this case, the model arising from this simplified representation is referred to as the force

field (FF) or molecular mechanics. Thus, the Coulomb interaction for a system of charged particles is described by the function

$$\Phi(\boldsymbol{r}) = \sum_{i,j}^{\text{pair}} \frac{q_i q_j}{4\pi\varepsilon_0\varepsilon_{\text{r}}\boldsymbol{r}_{ij}}, \tag{2}$$

where q_i and q_j are the partial charges of a pair of atoms, ε_0 stands for the permittivity of the free space, and ε_{r} is the relative permittivity (or dielectric constant), which takes the value 1 in the vacuum.

The classical molecular dynamics has advantages and disadvantages. The major advantage of FFs is that they speed up calculations considerably especially compared to the quantum mechanics (QM). The QM method is more accurate theory for processing the microscopic size systems. However, it is fundamentally difficult to solve the Schrödinger equation for many interacting particles. As a result, the QM method cannot be applied to studying very large systems of several thousand atoms. In its turn, the FFs approach have a long history of success permitting extended the MD simulations of different large systems despite some intrinsic limitations. The FFs is widely used nowadays for material science simulations (condensed-phase FFs). Moreover, calculations using widespread computer programs (including LAMMPS) have attained such a high standard of quality that the preference for one over the other is often dictated by practical considerations only that are related to their better implementation.

The total energy that is constant of the motion given by the sum of the potential and the kinetic energy $K(\boldsymbol{p})$

$$H(\boldsymbol{r}, \boldsymbol{p}) = U(\boldsymbol{r}) + K(\boldsymbol{p}), \tag{3}$$

where $H(\boldsymbol{r}, \boldsymbol{p})$ is the classical Hamiltonian of the system that depends upon the coordinates and momenta of the particles and returns the total energy *E* of the system. If the integration is carried out correctly, the MD naturally follows the motion of a microscopic isolated system where neither matter nor energy is exchanged with the surroundings. Traditional Newtonian dynamics sample is a statistical ensemble of microstates characterized by a constant number of particles (*N*), volume (*V*), and energy (*NVE* = const, for the microcanonical ensemble). However, the macroscopic behavior of the system can be reproduced more accurately by controlling the system temperature and pressure during simulation. Constant temperature in the model is maintained using computer codes that reproduce the thermostat [38] that allows fluctuations in kinetic energy as if the simulated system were immersed in a thermostatic bath (*NVT* = const, for canonical ensemble). Still, the model thermostat does not quite correspond to the real one.

More accurately, the analogy with a thermostatic bath should not be taken too literally, since heat flow is not simulated. Instead, the system temperature is forced to attain on average the desired macroscopic value. It is performed either due to proper changes in the equations of the motion or, in the simplest version, by correcting the velocities of the particles. The barostat algorithms [39], by which the pressure is controlled by opportunely scaling the system volume (N, P, T = const, for isothermal-isobaric ensemble), act in the similar way. Application of the periodic boundary conditions (PBC) makes it possible to better describe bulk properties with finite size systems in the MD model. With their help, the model system is placed in a unit cell that is replicated in all directions to form an infinite lattice of the image atoms. In this way, coordinates and velocities are stored and propagated for the unit cell only. However, evaluation of the nonbonded terms must in principle be extended to every pair of atoms in the unit cell and periodic images.

2.2. INTERACTION POTENTIALS

We performed the calculations by the classical molecular dynamics method. In the study of the "graphene-heavy metal" systems, we used three types of empirical potentials describing the carbon–carbon (in graphene), metal–metal, and metal–carbon interactions. Representations of the interactions in graphene were based on the use of the Tersoff potential [40]

$$V_{ij} = f_{\mathrm{C}}(r_{ij})\left[A\exp(-\lambda^{(1)} r_{ij}) - Bb_{ij}\exp(-\lambda^{(2)} r_{ij})\right], \tag{4}$$

$$f_{\mathrm{C}}(r_{ij}) = \begin{cases} 1, & r_{ij} < R^{(1)}, \\ \frac{1}{2} + \frac{1}{2}\cos\left[\pi\left(r_{ij} - R^{(1)}\right)/(R^{(2)} - R^{(1)})\right], & R^{(1)} < r_{ij} < R^{(2)}, \\ 0, & r_{ij} > R^{(2)}, \end{cases} \tag{5}$$

where b_{ij} is the multi-particle bond-order parameter describing in what manner the bond-formation energy (attractive part V_{ij}) is created at the local atomic arrangement because of the presence of the neighboring atoms. $R^{(1)}$ and $R^{(2)}$ are the parameters of the potential cutoff. The potential energy is a multi-particle function of atomic positions i, j, k and is determined by parameters

$$b_{ij} = (1 + \beta^n \xi_{ij}^{n_i})^{-1/(2n)}, \tag{6}$$

$$\xi_{ij} = \sum_{k \neq i,\, j} f_{\mathrm{C}}(r_{ij}) g(\theta_{ijk}), \tag{7}$$

$$g(\theta_{ijk}) = 1 + \frac{c^2}{d^2} - \frac{c^2}{\left[d^2 + (h - \cos\theta_{ijk})^2 \right]}, \tag{8}$$

where ξ_{ij} is the effective coordination number, $g(\theta_{ijk})$ is a function of the angle between r_{ij} and r_{ik}, which stabilizes the tetrahedral structure.

Table 1 shows the parameters of the Tersoff potential used to describe the interactions in graphene and silicene.

Table 1. Parameters of Tersoff potential for carbon and silicon

Parameters	Carbon	Silicon
A (eV)	1393.6	1830.8
B (eV)	346.74	471.18
λ_1 (nm)$^{-1}$	34.879	2.4799
λ_2 (nm)$^{-1}$	22.119	1.7322
n	0.72751	0.78734
c	$3.8049 \cdot 10^4$	$1.0039 \cdot 10^5$
d	4.384	16.217
$R^{(1)}$ (nm)	0.18	0.27
$R^{(2)}$ (nm)	0.23	0.30
β	$1.5724 \cdot 10^{-7}$	$1.1 \cdot 10^{-6}$
h	- 0.57058	- 0.59825

This potential was successfully tested on many single- and multi-component systems with covalent chemical bonding [41, 42]. However, the transition to the simulation of the two-dimensional systems (for example, in graphene) with covalent bonding revealed some difficulties in using this potential. The main disadvantages were as follows: the interaction was represented only by short-range covalent forces and the contributions from the interactions with neighbors of the second and higher orders were not considered. The simulation with this potential led to cracking the graphene sheet even at low temperatures. Another serious disadvantage was in existence of the net torsional moment appearing because of the lack of mutual compensation of the torsional moments determined by bonds around each atom. As a result, there occurred rotation of the graphene sheet (most frequently, counterclockwise). This effect impeded simulation of nanocomposites and made a difficult structural analysis. In the proposed model, the mentioned disadvantages were eliminated in the following way. The scale of covalent interaction in the model was

increased from 0.21 to 0.23 nm. Outside the covalent interaction, we used very weak attractive Lennard–Jones (LJ) interaction with the parameters taken from [43]. To prevent rotation of the graphene sheet, the force provided the "retardation" at each atomic site of the graphene $-dV_{ij}(\Omega_{kijl})/dr_{ij}$ was generated. Here the torsional potential $V_{ij}(\Omega_{kijl})$ is represented by expression [43]

$$V_{ij}^{tors}(\Omega_{kijl}) = \varepsilon_{kijl}\left[\frac{256}{405}\cos^{10}\left(\frac{\Omega_{kijl}}{2}\right) - \frac{1}{10}\right], \tag{9}$$

where the torsion angle Ω_{kijl} is defined as the angle between the planes, where one plane is specified by the vectors $\boldsymbol{r}_{ik}$ and $\boldsymbol{r}_{ij}$, whereas the other plane is determined by the vectors $\boldsymbol{r}_{ij}$ and $\boldsymbol{r}_{jl}$

$$\cos\Omega_{kijl} = \frac{\boldsymbol{r}_{ji}\times\boldsymbol{r}_{ik}}{\left|\boldsymbol{r}_{ji}\times\boldsymbol{r}_{ik}\right|}\cdot\frac{\boldsymbol{r}_{ij}\times\boldsymbol{r}_{jl}}{\left|\boldsymbol{r}_{ij}\times\boldsymbol{r}_{jl}\right|}. \tag{10}$$

The height of the barrier ε_{kijl} for the rotation was taken from [43].

The Sutton–Chen (SC) potential was successfully used for simulating both the bulk metals and metallic clusters [41]. The SC potential energy is written as

$$U^{SC} = \varepsilon\left[\frac{1}{2}\sum_i\sum_{j\neq i}V(r_{ij}) - c\sum_i\sqrt{\rho_i}\right], \tag{11}$$

where

$$V(r_{ij}) = (a/r_{ij})^n,\ \rho_i = \sum_{j\neq i}(a/r_{ij})^m, \tag{12}$$

where ε is the parameter having the dimensionality of energy; c is the dimensionless parameter; a is the parameter having the dimensionality of length that is commonly chosen to be the lattice parameter; and m and n are positive integers ($n > m$). The power form of the contributions makes it possible to successfully joint the short-range interactions, which are represented by *N*-particle terms with the Van der Waals "tail" that determines the long-range interaction. For copper and lead, we used the Sutton–Chen potential parameters given in Table 2 [44]. The pair potential that was used for a description of the Hg-Hg interactions was proposed in [45] in the following form

$$V_{\mathrm{Sch}}(r) = U_{\mathrm{Sch}}(\lambda r) = \sum_{j=3}^{9} a_{2j}^{*} r^{-2j}, \tag{13}$$

The authors of [42] corrected the original Schwerdtfeger (Sch) potential [43] for mercury dimer by scaling distances using the coefficient λ = 1.167. The a_{2j}^{*} scaled parameters of the Schwerdtfeger potential are shown in Table 3.

Table 2. Parameters of Sutton–Chen potential for fcc metals

Metal	m	n	ε **(meV)**	c
Cu	6	9	12.382	39.432
Ni	6	9	15.707	39.432
Al	6	7	33.147	16.399
Pb	7	10	5.5765	45.778

Table 3. Parameters for the scaled Schwerdtfeger mercury potential in equation (12)

j	a_{2j}^{*}
3	-1.036542×10^{2}
4	-1.539877×10^{3}
5	4.271609×10^{4}
6	-2.975002×10^{5}
7	9.965436×10^{5}
8	-1.633356×10^{6}
9	1.049907×10^{6}

* The units of U_{Sch} are electron volts, and the units of distance r are Angströms.

Instead of potential (11) for describing the Hg–Hg interactions, we also used the Silver-Goldman (SG) potential. The SG potential is adjusted to *ab initio* data and provides good agreement with the experimental data on spectroscopic constants [46]. The SG potential is based on the Hartree–Fock model of dispersion

$$V_{\mathrm{SG}}(r) = \exp\left(\alpha - \beta r - \gamma r^{2}\right) - f_{c}(r)\left(\sum_{n=3}^{5} \frac{C_{2n}}{r^{2n}}\right), \tag{14}$$

where

$$f_{\mathrm{c}}(r) = \exp\left[-\left(1.28\frac{r_{\mathrm{c}}}{r} - 1\right)^{2}\right], \; r < 1.28 r_{\mathrm{c}}, \tag{15}$$

$$f_c(r) = 1.0\,,\ r \geq 1.28 r_c\,.$$

The parameters of the SG potential are given in Table 4 [46].

The copper–carbon interaction was described using the Morse potential

$$V(r_{ij}) = D_0\left(\exp\left[-2\alpha(r_{ij} - r_m)\right] - 2\exp\left[-\alpha(r_{ij} - r_m)\right]\right). \quad (16)$$

The simulation was performed with the Cu-C Morse potential parameters given in Table 5 [47]. The lead–carbon, mercury–carbon, argon–argon, and xenon–xenon interactions were carried out using the Lennard-Jones potential with the parameters shown in Table 6 [48–51]. The Morse potential was used to describe the interactions between the Pb or Hg atoms and the substrate Cu ones. Parameters of this potential were calculated from data of [52, 53] and are given in Table 5 together with the corresponding parameters of other interactions. Parameters of the Lennard-Jones potential for some of the interactions of interest for this work are shown in Table 6.

Table 4. Silver-Goldman potential parameters

α	β	γ	C_6 (eV)	C_8 (eV)	C_{10} (eV)	r_c (Å)
3.71	2.26767	0.02367	6.93454	93.88854	2354.42957	5.3446

Table 5. Parameters of Morse potential describing various interactions

Interaction*	D_0 (meV)	α (nm^{-1})	r_m (nm)
Cu-C	87	17.000	0.220
Ni-C	1009.39	19.874	0.265
Al-C	809.28	18.598	0.286
Pb-C	754.26	18.693	0.307
Cu-Cu	342.9	13.590	0.287
Cu-Pb	283.74	12.713	0.327
$C^{(1)}$-$C^{(2)}$	3764.25	26.250	0.142
$Si^{(1)}$-$Si^{(2)}$	227.40	44.992	0.154
Si-C	925.20	20.820	0.253
Li-Li	420.76	7.899	0.300
Li-C	1258.51	17.074	0.206
Li-Si	309.30	36.739	0.116
Li-Ag	373.92	30.570	0.108
Ag-Si	274.89	14.540	0.374
Li-Cu	379.84	10.743	0.293
Cu-Si	279.24	14.489	0.359

* The upper indices at C and Si denote the belonging to the layer of atoms 1 or 2.

Table 6. Parameters of Lennard-Jones potential describing various interactions

Interaction*	ε **(meV)**	σ **(nm)**
Cu-C	19.99	0.3225
Ni-C	43.01	0.2830
Al-C	42.40	0.3057
Pb-C	38.00	0.3362
Hg-C	1.27	0.3321
$C^{(1)}$-$C^{(2)}$	2.84	0.3400
$Si^{(1)}$-$Si^{(2)}$	90.40	0.1851
Si-C	19.97	0.2600
Li-Li	715.97	0.1506
Li-C	4.33	0.2473
Li-Si	111.74	0.2666
Li-Ag	21.17	0.2547
Li-Cu	37.14	0.2205
Li-CH	53.27	0.2638
C-CH	45.54	0.3535
CH-CH	3.96	0.3770
Cu-CH	48.07	0.3020
Pb-CH	34.27	0.3620
Hg-CH	12.89	0.3449
Ag-Si	133.70	0.2403
Cu-Si	100.83	0.3048
Ar-Ar	10.32	0.3405
Xe-Xe	19.04	0.4100

* The upper indices at C and Si denote the belonging to the layer of atoms 1 or 2.

The interaction between the Ar atoms and the Cu or C ones was determined by purely repulsive Moliere potential [54]

$$\Phi = A\left\{0.35\exp\left(-0.3\frac{r}{a}\right)+0.55\exp\left(-1.2\frac{r}{a}\right)+0.10\exp\left(-6.0\frac{r}{a}\right)\right\}, \qquad (17)$$

where $A = Z_i Z_j \frac{e^2}{r}$, Z_i and Z_j are the atomic numbers of the i^{th} and j^{th} atoms, e is the elementary charge, r is the distance between the atoms, a is the Firsov screening length [55]

$$a = 0.885 a_0 \left(Z_i^{1/2} + Z_j^{1/2}\right)^{-2/3}. \qquad (18)$$

Here, a_0 is the Bohr radius.

The interaction between Xe atoms and target ones (Pb, Hg, and C) was defined by the purely repulsive Ziegler–Biersack–Littmark (ZBL) potential [56]

$$\Phi = Z_i Z_j \frac{e^2}{r}\left\{0.1818\exp\left(-3.2\frac{r}{a}\right)+0.5099\exp\left(-0.9423\frac{r}{a}\right)\right. \quad (19)$$
$$\left.+0.2802\exp\left(-0.4029\frac{r}{a}\right)+0.2817\exp\left(-0.2016\frac{r}{a}\right)\right\},$$

where the parameter a is determined by the expression

$$a = 0.8854\ a_0\left(Z_i^{0.23}+Z_j^{0.23}\right)^{-1}. \quad (20)$$

We disregarded the weak attraction between Xe and Hg atoms and between Xe and C ones because the primary aim of this study is the energy and angular momentum transfer rather than the chemical binding [57].

Defects substantially enhance the adhesion of metals to graphene. The most frequent defects in graphene are bi-vacancies. The sheet of graphene used for deposition of the lead had four bi-vacancies rather uniformly distributed over its surface. The hydrogenation was used for strengthening the bi-vacancy edges and boundaries. The CH groups formed at the edges and sites nearest to the bi-vacancy center were simulated in accordance with the mono-atomic diagram [58]. The C–CH and CH–CH interactions were represented by the Lennard-Jones potential [58]. The parameters of the corresponding potential are given in Table 6. The partial functionalization of graphene is the addition of the hydrogen atoms to its edges. This procedure stabilizes the structure without leading to an increase in interatomic distances and without creating roughness over the entire surface.

2.3. Calculations of Physical Characteristics

We studied the bombardment of a metal film on graphene using noble gas clusters. Here, it was assumed that the Ar (Xe) ions hit the surface as neutral atoms with the same energy as the initial ion. If the bombardment was performed with charged atoms, then the ion charge must be neutralized on the surface by the charge exchange. However, the electron moves faster than the nucleus by at least three orders of magnitude. Therefore, the dynamics of the Ar (Xe) ion is similar to that of the neutral Ar (Xe) atom within the limits of the Oppenheimer approximation [59, 60]. Under the target bombardment, the charge

cannot accumulate. Each charge carried by the ion is always neutralized impacting on the target. Numerical integration of the motion equations was carried out using the fourth-order Runge–Kutta scheme [61]. Four series of target bombardment of the Ar (Xe) clusters with the same durations (400 ps) were performed. Each cluster impact on the surface led to system heating. The heat released from the system was removed effectively in accordance with the Berendsen scheme with the bonding constant τ = 4 fs [62]. To control temperature, at each time step the velocities v were scaled in accordance with relations

$$v = \Lambda v', \ \Lambda = \left[1 + \frac{\Delta t}{\tau}\left(\frac{T_0}{T} - 1\right)\right]^{1/2}, \tag{21}$$

where v' and v are the particle velocities before and after correction, Λ is the scaling factor, T_0 is the given temperature (300 K), and T is the current temperature.

The stress at the site of the i th atom of the Cu or Pb film is defined as [44]

$$\sigma_{\alpha\beta}(i) = B\sum_{i\neq j}^{k}\left[-n\left(a / r_{ij}\right)^{n+2} + mc\left(1/\sqrt{\rho_i} + 1/\sqrt{\rho_j}\right)\left(a / r_{ij}\right)^{m+2}\right] r_{ij}^{\alpha} r_{ij}^{\beta}, \tag{22}$$

where $B = \dfrac{\varepsilon}{2a^2\Omega_i}$, the volume corresponding to an individual atom Ω_i can be associated with the volume of the Voronoi polyhedron related to the i th atom.

To calculate the stresses induced in graphene, the graphene sheet was divided into elementary areas. The atomic stresses $\sigma_J^i(l)$ in the l th elementary area for each of directions x, y and z with a current index J are determined by calculating the atomic kinetic energies in this area and projections of forces acting on the l th area from all other atoms [63]

$$\sigma_J^i(l) = \frac{1}{k}\left\langle \sum_i^k \frac{1}{\Omega_i}\left(m v_J^i v_J^i\right)\right\rangle + \frac{1}{S_l}\left\langle \sum_i^k \left(f_J^i\right)\right\rangle, \tag{23}$$

where k is the number of atoms at the l th area; Ω_i is the volume per atom; m is the atomic mass; v_J^i is the J th velocity projection of atom i; and S_l is the square of the l th area. Angular brackets indicate the averaging over time. In this case, the compressive stresses can have plus and minus signs according to directions of forces f_J^i. In this regard, the microscopic stress $\sigma_J^i(l)$ differs from the macroscopic ones $\bar{\sigma}_J < 0$.

The total stresses acting in the graphene plane were determined by adding the corresponding elementary stresses as follows:

$$\sigma_{\alpha J} = \sum_{l=1}^{N_i} \sigma_J^{\alpha}(l), \tag{24}$$

where N_l is the number of the surface elements that result from dividing the graphene sheet in a selected direction.

The radial distribution function was calculated as

$$g(r) = \left\langle \frac{1}{\rho} \sum_{i=1}^{N} \frac{n_i(r, r+\Delta r)}{4\pi r^2 \Delta r} \right\rangle, \tag{25}$$

where $n_i(r, r+\Delta r)$ is the number of atoms spaced from an atom i by the distance from r to $r+\Delta r$, ρ is the numerical density of the system. There is no division by *N* in formula (25) because the function was calculated for one (nearest to the graphene or silicene center) Me atom. The angle brackets indicate the time averaging.

The spectrum of individual atomic vibrations is found as the Fourier transform of the average autocorrelation function of velocities

$$f(\omega) = \frac{2m}{3\pi k_B T} \int_0^{\infty} \langle \boldsymbol{v}(0)\boldsymbol{v}(t) \rangle \cos(\omega t) dt, \tag{26}$$

where m is the atomic mass and k_B is the Boltzmann constant.

The self-diffusion coefficient was determined by the mean square displacement of the atoms $\left\langle \left[\Delta \boldsymbol{r}(t)\right]^2 \right\rangle$ as

$$D = D_{xy} + D_z = \lim_{t\to\infty} \frac{1}{2\Gamma} \left\langle \left[\Delta \boldsymbol{r}(t)\right]^2 \right\rangle, \tag{27}$$

where Γ = 3 is the dimension of space, D_{xy} and D_z are the horizontal and vertical components of the self-diffusion coefficient.

The density profile of the metallic film was calculated as follows:

$$\rho(z) = \frac{n(z)\sigma_{Me}^3}{\Delta h S_{xy} N_z}, \tag{28}$$

where $n(z)$ is the number of metal atoms in the layer parallel to the plane of the graphene, σ_{Me} is the effective diameter of the metal atom, Δh is the width of the layer, S_{xy} is the area of the graphene surface, and N_z is the number of tests.

We determined the contact angle θ when studied heating the liquid metal (mercury) on the surface of graphene. In order to calculate the contact angle between a droplet (film) surface and graphene, the largest horizontal cross-sectional area of a droplet was divided into three regions: (1) a circle with a constant area, which determines the region of the contact with graphene, (2) a ring comprising projections of the neighbors closest to region (1), and (3) an analogous ring used to reveal the external atoms of the droplet. Mercury atoms closest to the graphene surface were located in regions 2 and 3. Parameters of the procedure used for determining angles θ were selected empirically. The averaging was performed over the sizes of the rings and heights (or the number of selected Hg atoms), at which Hg atoms were located in regions 2 and 3. The yielded average values of the horizontal and vertical coordinates were used to find θ. Determination of the angle θ required averaging over time, as well.

The surface roughness (or the profile deviation arithmetic average) was calculated as

$$R_{\text{a}} = \frac{1}{N}\sum_{i=1}^{N}\left|z_i - \overline{z}\right|, \tag{29}$$

where N is the number of nodes (atoms) on the surface of graphene, z_i is the atomic level, $\overline{z}$ is the graphene surface level, z_i and $\overline{z}$ are the values determined at the same instant.

The total energy of free one-sheet graphene obtained at T = 300 K was – 7.02 eV. It is consistent with the result of the quantum-mechanical calculation (– 6.98 eV) [64]. The melting temperature T_m of a Pb_{201} cluster with a free surface, which was determined in a special calculation, was 417 K. This is consistent with MD calculations at T_{m} = 412 K [65], that were also performed with the Sutten-Chen potential. In both cases, T_{m} was determined based on a jump of the potential energy. The value of the isochoric heat capacity of liquid mercury at this temperature (28.4 J/(mol K) calculated in the MD model agrees with the experimental value of 26.9 J/(mol K).

The structural analysis of small objects can be carried out using the statistical geometry method based on the construction of the Voronoi polyhedra (VPs) [61]. In the case of a polyatomic system, atoms of one type may play the role of polyhedron centers, while atoms of another type may serve as their nearest neighbors determining the polyhedron faces. For example, in the case of the "Li-silicene channel" system, it is advantageous to use lithium atoms as the centers and select the nearest neighbors among Si atoms. These hybrid polyhedra are easier to construct since the number of Si atoms is greater than the Li ones. However, in this case, hybrid polyhedra are not Voronoi polyhedra, since they fail to fill completely all of the space occupied by molecules without voids and overlaps. The VP

faces determine the cyclic structures formed from Li atoms, while hybrid polyhedra faces determine rings composed of Si atoms. However, there is another way to construct the Voronoi polyhedra in a multicomponent system when the dimensions of all atoms are the same. Here, we do not take into account the difference in the sizes of Li and Si atoms in the VP construction. We construct the VP for Li atoms when the geometric neighbors are Li and Si atoms together or only Li ones.

The quantum-mechanical calculation of charge transfer was performed using the SIESTA software package. A purely geometric approach was used based on the procedure for constructing the Voronoi polyhedron to distinguish the region of space belonging to the atom. In other words, the Voronoi cell of atom A was defined as a region of space, all points of which are closer to atom A than to any other atom. The Voronoi deformation density (VDD) [66] of the atomic charge is computed as the integral of the deformation density. The presence of the latter is due to the formation of the molecule from its atoms in the volume of the Voronoi cell of the atom A

$$Q_{\mathrm{A}}^{\mathrm{VDD}} = \int\limits_{\substack{\text{Voronoi} \\ \text{cell of A}}} \left(\rho_{\mathrm{molecule}}(\boldsymbol{r}) - \sum_k \rho_k(\boldsymbol{r}) \right) d\boldsymbol{r} = \int w_{\mathrm{A}}^{\mathrm{Voronoi}}(\boldsymbol{r}) \rho_{\mathrm{def}}(\boldsymbol{r}) d\boldsymbol{r} , \qquad (30)$$

where the weight function $w_{\mathrm{A}}^{\mathrm{Voronoi}}(\boldsymbol{r}) = 1$ inside the Voronoi cell of the atom A and equal to 0 outside of it, $\rho_{\mathrm{def}} = \rho - \sum_k \rho_k$ is the deformation density or the change in density when passing from the superposition of atomic densities to the final molecular density; $\sum_k \rho_k$ is the sum over the ground states (usually with spherical averaging) of the atomic density. The $Q_{\mathrm{A}}^{\mathrm{VDD}}$ atomic charge is an addition to the main charge. Positive and negative atomic charges $Q_{\mathrm{A}}^{\mathrm{VDD}}$ correspond to the loss and acquisition of electrons, respectively. In the present version, $\rho_{\mathrm{molecule}}(\boldsymbol{r})$ acts as the electron density of all interacting atoms that contribute to the VP (faces, vertices).

The method of constructing the Voronoi polyhedra can be used not only to study the structure of the short-range order of "infinite" or finite objects. It can be used, also, to trace the short-range order in the relief of the channel when the lithium ion moves along it. To do this, it is necessary to combine the center of the ion with the center of the polyhedron being designed and to choose the Si atoms of the channel (between which the ion moves) as the geometric neighbors for the ion. Polyhedra are constructed at regular intervals until the ion leaves the channel. As a result, the ion motion along the channel under the action of a constant electric field can be represented in the form of distributions of elements of the VPs. Comparison of such distributions obtained for different channels gives an idea of the causes of the inhibitory effect produced by the channel. Therefore, we call such an

investigation the statistical-geometric method of representing the inhibitory effect in the channel.

2.4. TESTING OF METHOD AND MODEL

In this section, we present a method for testing the calculations and the model using an example of modeling the heating of an aluminum film on graphene. It was shown in a separate computation that application of the fourth-order Runge-Kutta method ensures higher accuracy in determining atomic trajectories as compared to the result obtained using the same method of the second order. In addition, the second-order algorithm is less stable and demands reduction of the time step. Application of the fourth-order algorithm ensures the optimal balance between the time step and the accuracy of computations. The computational error in the MD method is mainly determined by the systematic error depending on the integration procedure used [67]. Total computation time t_0 = 200 ps exceeded characteristic correlation one t_m for coupling functions in graphene and in the metal. The time t_m is about the ratio of the film layer thickness to the speed of sound. This time is characterized as the stabilization time of incomplete equilibrium for the quantity in question. Let us assume that the speed of sound is 5 km/s in aluminum and $u_\perp$ = 15 km/s, $u_\Updownarrow$ = 21 km/s in graphene [68]. We can estimate the sizes of atoms from the geometrical Lennard-Jones parameter. Then we find that t_m < 0.2 ps even for the doubled aluminum film on graphene. It can be expected that the computational error of the coordinates, velocities, autocorrelation functions [67], and the Fourier transform of the spectra obtained in terms of these quantities does not exceed $(t_\mathrm{m}/t_0)^{3/2} \approx 5 \times 10^{-5}$. The error in the computation of the total energy in terms of its fluctuations can be estimated as $\sqrt{\langle \Delta E^2 \rangle}/E \approx 0.1$.

The resistivity of the pure metal in the simplified approximation can be defined as [69]

$$\rho(T) = \left(\frac{m}{2}\right)^{1/2} \frac{9\pi h^2 C^2}{8n\Omega e^2 M k_\mathrm{B} \Theta \xi^{3/2}} \left(\frac{T}{\Theta}\right)^5 \times \int_0^{\Theta/T} \frac{z^5 dz}{(\exp(z)-1)(1-\exp(-z))}. \quad (31)$$

Here, *m* is the electron mass, *M* is the atom mass, *n* is the number of free electrons per unit volume, ξ is the Fermi energy level $\left(\xi = \frac{1}{2} m\bar{v}^2\right)$, Θ is the Debye temperature, Ω is the unit cell volume, *C* is the constant determining the interaction between electrons and the lattice, h is the Planck constant, and $z = \hbar\omega / k_B T$.

When the electrical conductivity (or another transport parameter) is calculated, the constant *C* can be determined from the relation [70]

$$\lambda_{tr} = 2 \int_0^{\omega_{max}} C^2 \frac{F(\omega)}{\omega} d\omega, \tag{32}$$

where $F(\omega)$ is the phonon spectrum, ω_{max} is the maximal frequency in the phonon spectrum under investigation, and λ_{tr} = 0.39 is the transport constant of the electron-phonon coupling in aluminum [70]. In the Debye model, the phonon density of states is defined as

$$F(\omega) = 9\omega^2 / \omega_D^3, \tag{33}$$

where $\omega_D = \Theta k / \hbar$ is the cutoff frequency of the Debye spectrum.

The resistivity of a single-layer aluminum film at 300 K, calculated by the formula (31) is ρ = 0.185 × 10^{-4} Ω m, and the electrical conductivity is σ = 5.4 × 10^4 Ω^{-1} m^{-1}. The electrical conductivity of a thin metal film can be written in the form [71]

$$\sigma = \sigma_0 \exp(-E_{ac} / kT), \tag{34}$$

where σ_0 is the conductivity of the bulk material and E_{ac} is the activation energy for conduction electrons. Assuming that the conductivity of bulk aluminum is σ_0 = 0.37 × 10^8 Ω^{-1} m^{-1}, we obtain from expression (34) E_{ac} = 0.098 eV. The temperature coefficient $\beta = \frac{1}{\rho}\frac{d\rho}{dT}$ of the resistance of a mono-layer Al film is found to be 4 × 10^4 K^{-1}. It is determined from the calculation of ρ at temperatures of 300 and 800 K. The electric properties of thin aluminum films with a thickness from 40 to 200 nm deposited on a glass substrate at 573 K in high vacuum were studied experimentally in [72]. The surfaces of the layers deposited one by one were subjected to the action of oxygen. Extrapolation of functions $\rho(d)$ and $\beta(d)$, where d is the film thickness, to a thickness of an atomic monolayer leads to values of 2.5 × 10^{-4} Ω m and 3 × 10^3 K^{-1}, respectively. Therefore, the values of the conductivity and activation energy of conduction electrons extrapolated from

experiments are $\sigma = 0.4 \times 10^4\ \Omega^{-1}\ m^{-1}$ and $E_{ac} = 0.168$ eV. The experimentally obtained lower conductivity and higher activation energy can be explained by oxidation and a higher temperature of the experimental sample, the extrapolation error, the roughness of calculation of ρ by formula (31), and the large temperature step in the computation of β.

The total energy of free one-sheet graphene obtained in our MD experiment at $T = 300$ K was – 7.02 eV, which is in conformity with the result of the quantum-mechanical calculation (– 6.98 eV) [64]. The aluminum–graphene interaction energy $E_{Al-C(graphene)}$ in the MD model at this temperature is – 0.225 eV. The density functional theory for the interaction between the Al (111) plane and graphene gives $E_{Al-C(graphene)} = -0.185$ eV [72]. The heat capacity c_v of the single-sheet graphene calculated in terms of kinetic energy fluctuations increases in the temperature interval 300 K $\leq T \leq$ 1300 K from 19 to 28 J/(mol K). This corresponds to the experimental values of this quantity (23.74 – 26.80 J/(mol K)) [73].

Chapter 3

MECHANICAL AND THERMAL PROPERTIES OF GRAPHENE

Owing to the ability to form sp^1, sp^2, and sp^3 bonds, carbon is an "all–round" chemical element. Under ambient pressure, carbon usually takes the form of graphite (the most stable structure) or diamond, but other sufficiently stable allotropes can exist, as well. In recent years, its numerous structures have been discovered.

The binding energy between carbon atoms is very large; for example, in diamond, the cohesion energy is 717 kJ mol. The phase transition between various stable phases of carbon requires to overcome an extremely high energy barrier. In other words, very high temperatures or pressures are required to initiate a spontaneous phase transition from one solid phase of carbon to another.

Apart from the best-known crystal forms of carbon, i.e., graphite and diamond, amorphous forms exist, such as glassy carbon and black carbon. One-dimensional carbon is the carbine with the sp hybridization. It proved to be possible to obtain amorphous carbon in the form of a film with a mixed type of hybridization [74]. A tetrahedral film of carbon can be formed upon bombardment by heavy ions. The structure of the atomic bonding in this film turns out to be extremely disordered and represents a mixture of sp^1, sp^2, and sp^3 hybridizations. Due to the high content of bonds with the sp^3 hybridization, such a film acquires diamond-like properties. The tetrahedral film is characterized by high hardness and wear-resistance, which makes it possible, in view of the optical transparency of such a film, to use it as a protective coating for optical fibers. Owing to the high cohesion energy and large activation energy, carbon polymorphism exists in a wide range of metastable states. Graphite compressed along the c-axis under a pressure of 10 to 25 GPa under the room temperature (RT) is able to retain the strongly compressed structure. However, upon heating under high pressure, graphite passes into a diamond cubic structure. The authors of [75–81] have supposed that the strong compression gives a new superhard phase of carbon. Indeed, at the pressures between 10 and 25 GPa, an increase was observed in the

resistance [75] and in the optical transparency [76, 77]. Moreover, there appear a decrease in the optical reflectance [78] and changes in the X-ray diffraction patterns [79–81]. Several hypothetical structures have been suggested to explain these features; for example, sp^2-sp^3 graphite-diamond structures [82], M-carbon [83], body-centered tetragonal (bct-C4) carbon [84], and W-carbon [85]. However, all these models have proved to be unable to represent the complete spectrum of experimental data. The problem of the existence of a superhard phase of carbon remains disputable. Apparently, a phase transformation indeed takes place, since (upon a further increase in pressure to 40 GPa or more) the compressed carbon is transformed into amorphous form. This follows from its Raman spectra (RSs) [86].

Purely carbon molecules C_{60} and C_{70} fullerenes were also discovered. Later, the carbon tubes and, finally, graphene have been obtained. The energy-band structure of ideal graphene is unique since no energy gap appears in it. In six Dirac K points, the zone with positive values of energy corresponding to the electron states touches the zone with the negative energy that characterizes the hole states. Near these points, the energy spectrum acquires a linear dependence on the wave vector. According to characteristics of the energy bands, graphene depending on the conditions and impurities can be a metal or a semiconductor. Graphene is an extremely good conductor of electricity and heat. It is the strongest of all two-dimensional media and, at the same time, the graphene is sufficiently plastic. It is almost completely impenetrable and almost completely transparent to light. Owing to these characteristics, graphene finds the very wide application.

The main experimental method for investigation of the mechanical properties of graphene or pieces of the multilayer graphene (stacks of graphene layers) is atomic-force microscopy (AFM). In [87], the AFM was used to study the elastic properties of a stack of graphene layers (fewer than five) on a substrate of silicon dioxide. The Young modulus of the graphene stack was about 0.5 TPa. An analogous experiment was performed using a graphene monolayer [88] to obtain the Young modulus of about 1 TPa.

The elastic properties of diamond have been studied experimentally much better than those of graphene, but even for diamond, the spread of the data is rather substantial (0.41–0.59 TPa). The elastic properties of diamond were apparently first measured in 1946 with the use of the ultrasonic methods [89, 90]. Later, they were also measured by the X-ray diffraction and precise acoustic methods [91–93].

The mechanical and optical properties of materials depend on their dimensions and shape. For example, the single-crystal fibers have substantially higher hardness and ultimate strength than those of loose materials in view of the absence of growth defects in such fibers. In reviews [94–97] (see, also, [98, 99]) the information on various mechanical properties of the carbon materials is given. These are nanotubes, fullerenes, and other closed carbon structures (nanotubulens: capsulens, torens, barrelens, etc.). Moreover, the data are presented on the methods of materials preparation and on the behavior of carbon during the formation of condensed phases.

In this chapter, we restrict ourselves to consideration of the mechanical properties of graphene. In addition, we partially discuss the influence of defects on its properties. The results of investigations are presented on the structure and the edges of graphene, its resistance to heating and deformations of uniaxial tension and compression. As a rule, these theoretical and calculated investigations were based (where possible) on the experimental data.

3.1. TRANSFORMATION OF GRAPHENE UNDER MECHANICAL AND CHEMICAL ACTIONS

3.1.1. Preparation of Tubes and Scrolls of Graphene

Graphene possesses a rather flexible and mobile structure and has a tendency to acquire a three-dimensional form under certain external conditions. In this case, minimization of the surface energy occurs [100]. If the ratio of the length of the graphene sample to its width is sufficiently large (narrow graphene ribbon), such a structure spontaneously begins self-folding [101]. During self-folding, the graphene ribbons can form multilayer spiral structures [102, 103] of various diameters [104, 105]. The factors that are responsible for the processes of scrolling, bending, and rotations of graphene can be low-temperature ($T < 100$ K) fluctuations [106] and the internal instability of the structure [107].

There are investigations devoted to the transformation of the graphene ribbons into nanotubes via confined polymerization of polycyclic aromatic hydrocarbons [108, 109]. Experimentally, graphene tubes are produced by scrolling a graphene ribbon located inside a carbon tube of the greater diameter [110]. In this case, the internal tubes with the desired chirality can be obtained. The theoretical model developed in [111] suggests that the graphene ribbons located inside a nanotube of a large diameter will form the spiral structures because of the external geometrical confinements. The same conclusion follows from the quantum-chemical simulations [110], according to which a graphene ribbon completely located in a nanotube will spontaneously twist into a spiral. The process of twisting is initiated by the formation of bonds between the surface of the tube and the edges of the ribbon. In this case, a torque arises. The twisting continues until the formation of a completed tube. The properties of a defect-free carbon tube obtained from graphene under the action of tension were analyzed in terms of a molecular-dynamics model [112]. As the angle of chirality increased, a monotonic increase in the tensile force and deformation of failure was observed.

Unlike nanotubes, graphene scrolls have a topologically open structure, which (along with the unique mechanical and electromechanical properties of scrolls inherited from the graphene sheet [88, 2]) opens wide opportunities for their application. The scrolls can be

used as a medium for store hydrogen [113], as water and ionic channels [114], and as nanosolenoids [115].

However, the scrolling of an isolated graphene sheet is a quite difficult problem. Its internal energy of elasticity, which is always directed towards the retention of the flat shape, creates an energy barrier to the structural transition. The scrolling becomes possible only if a nanorod, e.g., made of iron, is introduced into the system. The Van der Waals interaction between the graphene and the iron nanorod helps to overcome the energy barrier and creates a force of attraction. This leads to contact between the iron rod and the graphene ribbon in the process of scrolling. In this case, a three-dimensional core–multilayer-shell structure is formed. If the rod is initially located at the middle of the ribbon [116], the scrolling results in the formation of a nodular structure with double walls. If two nickel nanorods are placed at the different ends of the ribbon, a dumbbell-like structure is obtained. According to [100, 116], the process of scrolling the graphene on a metallic rod is irreversible. This suggests the metastability of graphene.

A scrolled graphene structure can be obtained by chemical methods [117]. The structure of carbon scrolls with various diameters and chirality was investigated experimentally, depending on the dimensions of the sheet and direction of scrolling [104, 118]. The scrolling of graphene was also studied using the MD simulation in [119, 120] where the scrolling was initiated by a carbon nanotube with the formation of a tube/scroll–core/shell composite (Figure 1). The character of this process is determined by the tube–graphene and graphene–graphene interaction energies. The success of the formation process of a scroll mainly depends on the diameter d of the tube. The tube can help graphene to overcome the energy barrier only when d is relatively large. Such a structure remains stable for at least 500 ps at $T = 300$ K. Because of the strong adhesion between the graphene and the tube, it is fairly difficult to separate such a structure into its initial components.

The controlled doping by hydrogen makes it possible to obtain graphene with easily tuned properties [121]. Via the addition of hydrogen atoms to carbon, the sp^2 structure of the graphene sheet is replaced by the sp^3 structure. In other words, the two-dimensional atomic structure of pure graphene passes into a local three-dimensional structure around each absorbed hydrogen atom [122]. Such structures can be obtained both on the macroscopic scale and on the microscale [123].

In [124], the possibility of the spontaneous scrolling of a quadratic graphene sheet (partly doped with hydrogen) has been studied using the MD calculations. Depending on the ratio between the length L_{H} of the region enriched by hydrogen atoms and its width W_{H}, three different results can be obtained: partial scrolling of the hydrogen-containing part of graphene; complete scrolling of the entire sheet; or an irregular nanostructure. The last one appears as a result of scrolling produced from three sides. A graphene sheet doped

with hydrogen forms a scroll, which is stable at T = 300 K if the following relationship is fulfilled: $0.4 \leq L_H / W_H \leq 0.6$ (Figure 2) [124].

Graphene platelets of various shapes with a significant Van der Waals interaction between the layers can also spontaneously form the large bulk structures [125, 126]. Separate platelets (graphene flakes) with a high plasticity can be twisted into nanoscrolls under the effect of certain gases and alcohols [127, 128].

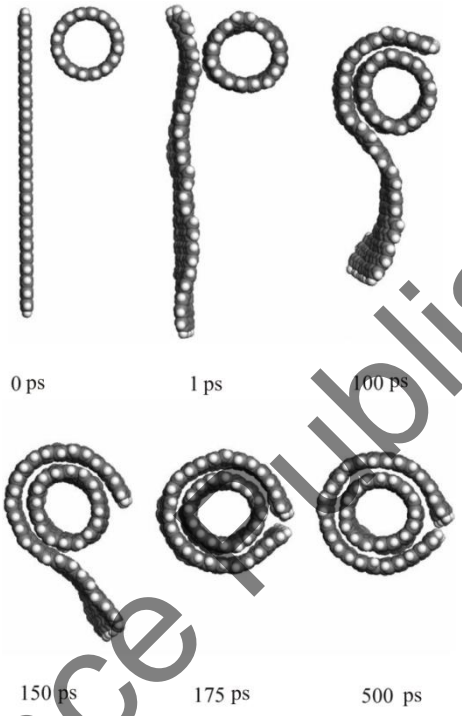

Figure 1. Spontaneous scrolling of a graphene ribbon around a carbon nanotube [119].

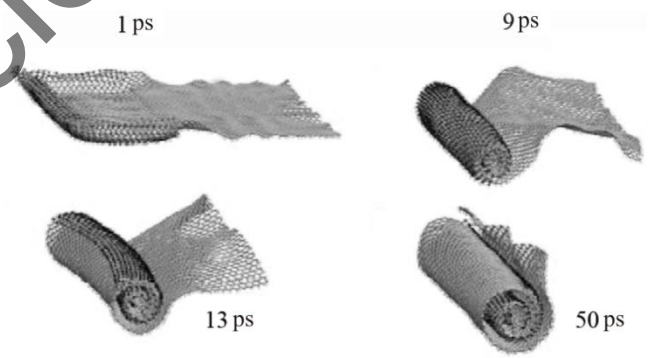

Figure 2. Complete scrolling of a graphene sheet partly doped with hydrogen (L_H/W_H = 0.4) [124].

The folding of four graphene platelets that interact with a water nanodroplet has been studied based on the MD model in [129] (Figure 3). After a certain time (50 ps), the graphene lobes closed completely. In this case, a nanocapsule containing water molecules inside was formed. The energies (determined in *ab initio* calculations [129]) of the initial (open) and final (closed) structures with water molecules inside are equal to – 150.3 and – 913.5 kJ mol^{-1}, respectively. This characterizes the water–graphene scrolls as the more stable formations than a water nanodroplets with open lobes [129]. In the presence of the SiO_2 substrate, the strong interaction between the graphene lobes and the substrate prevented the formation of a closed structure of graphene. In addition, SiO_2 is more hydrophilic than graphene. For this reason, the expanding water nanodroplet, which tends to cover the surface of SiO_2, prevents the folding of graphene. However, when there is a layer of isopropyl alcohol between the graphene and the substrate, the alcohol molecules shield the strong interaction between graphene and SiO_2. The interaction between graphene and water, in this case, is not weakened. This permits the graphene lobes to close. The governing parameters in the formation of a bulk structure, in this case, are the geometry of the flat graphene structure and the dimensions of the water nanodroplet and substrate.

The scrolling of graphene was also obtained based on the MD simulation of two rectangular plates connected by a narrow graphene ribbon, at the center of which a water nanodroplet was placed [130]. After 250 ps (at T = 300 K), the plates folded into a bulk structure with a water droplet inside. When the temperature increased to T = 400 K, the mobility of the water droplet increased, the plates contracted, and the water molecules were squeezed outside remaining on the graphene surface. The shape of the scroll could be controlled by changing the size of the droplet. When the droplet contained 10,000 molecules, the ribbon (while scrolling) formed a multilayer structure similar to a multiwall nanotube filled with water.

Thus, the computer experiment showed the ability of a water droplet to activate and guide the process of graphene folding into one of the bulk nanostructures: capsule, knot, ring, or layered [130].

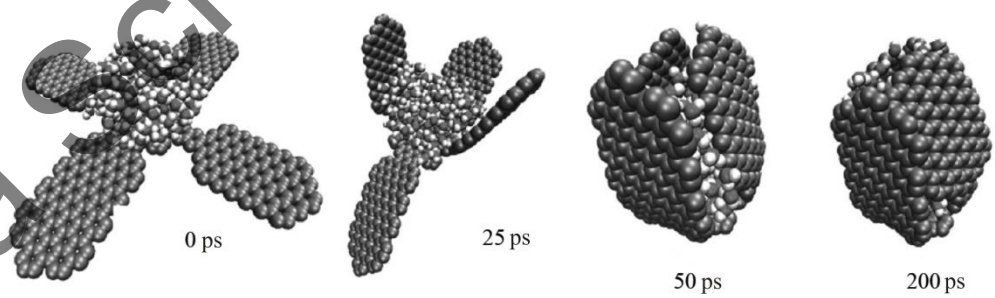

Figure 3. Scrolling dynamics of rectangular graphene sheets interacting with a nanodroplet of water [129].

3.1.2. Transformation of Graphene into Fullerene

Graphene is an ideal structure for the formation of fullerene, which consists of a finite number of sp^2 hybridized carbon atoms and does not have open edges. The graphene-fullerene transformation has been demonstrated using the MD model in [131, 132]. At temperatures of 3000 – 3500 K, the folding of the graphene film (100 – 700 atoms) into fullerene occurs in several nanoseconds. Formation of the C_{60} and C_{70} structures from graphite in a vacuum has been experimentally observed by the electron beam stimulation with the energy of 10 keV [133].

It has been shown in [134] that under the action of the electron beam with higher energy (80 keV), the graphene sheet can acquire a spherical shape. The high energy of the beam leads to fragmentation of large regions of the graphene into small flake-like structures. On the final stage, fullerenes are formed from these structures. The loss of carbon atoms from the graphene edges is a key event in the process of the fullerene formation [135, 136]. The action of the high-energy electron beam destabilizes the edge structure of graphene because of the loss of atoms from the edges and appearance of a large number of dangling bonds.

The process of transformation of the graphene into fullerene can be studied in detail using the quantum-chemical model developed in [134] (Figure 4). Formation of the pentagonal rings at the edges and the subsequent folding of the platelet are energetically favorable processes. The atoms of carbon with lacking bonds are brought to one another; thereby, the formation of new C–C bonds is initiated between them. The newly formed bonds lead to folding the edges creating a stabilizing effect (Figure 4d). Such a cap-like structure can continue folding, losing carbon atoms, and pentagons are formed in this structure. The folding continues until the final structure is formed.

Note that for the full folding of graphene into fullerene, the initial size of the graphene platelet is of large importance. If the plate is too large, significant energy should be spent on removing the edges. The etching of the edges stops only when (during the formation of the fullerene) the platelet reaches a certain size specified by the thermodynamic conditions of the chemical equilibrium. However, if the platelet is too small (less than 60 carbon atoms), then upon folding a strong tension of C–C bonds will occur. This can lead to the destruction of the pentagonal rings. The number of carbon atoms that is needed for the optimal formation of fullerene is 60–100.

Another factor that can act on graphene during the formation of fullerene is temperature [137]. The MD calculations have shown that transformation of the graphene into a fullerene under the action of the temperature of 2700 – 3500 K starts with breaking the C–C bonds located nearer to the edge of the graphene sheet. The gradual rearrangement of the edge structure continues until the planar sheet (containing 96 or 384 carbon atoms) begins transforming into a cap. In such a structure, locking the edges occurs rather rapidly with the formation of a closed structure, i.e., fullerene. The energy of activation for

this process is about 4 eV. At T = 2500 K, the average time of folding for graphene C_{384} is 3-4 times that for graphene C_{96}.

Clusters of the Ni atoms can provide a catalytic driving force for this process (Figure 5) [137]. Contemporary technology makes it possible to prepare a metallic cluster consisting of a certain number of atoms (including atoms of different elements) and to place it onto a graphene sheet of the desired size [138]. In the presence of the Ni cluster (containing 13 or 79 atoms depending on the size of the graphene sheet), the temperature of scrolling decreases to 2000 – 3000 K. The cluster moves along the edge of the graphene sheet via the diffusion transfer of carbon atoms onto the cluster and returns. This process continues until graphene is transformed into a cap-like structure and is closed around the cluster. In this case, the Ni cluster can either remain inside the fullerene shell or escape from it. The energy of activation for this process for the C_{384}+Ni_{79} system is 1.5 eV that is significantly less than that in absence of the catalyst on the graphene surface.

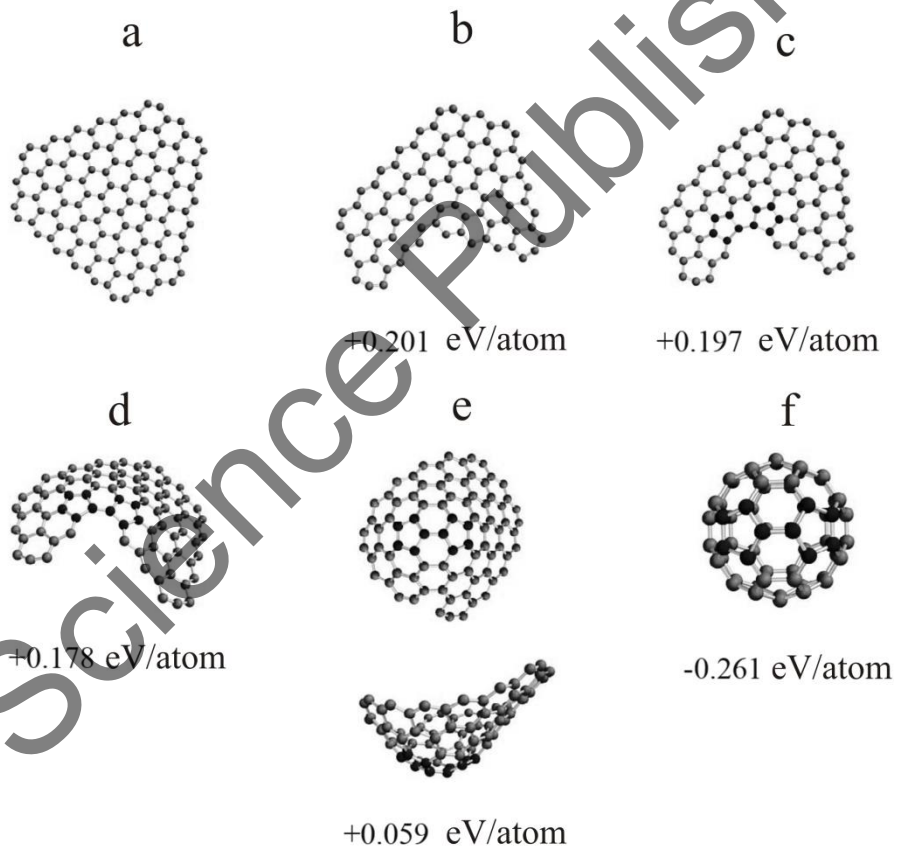

Figure 4. Stages of the formation process of fullerene from a graphene platelet [134].

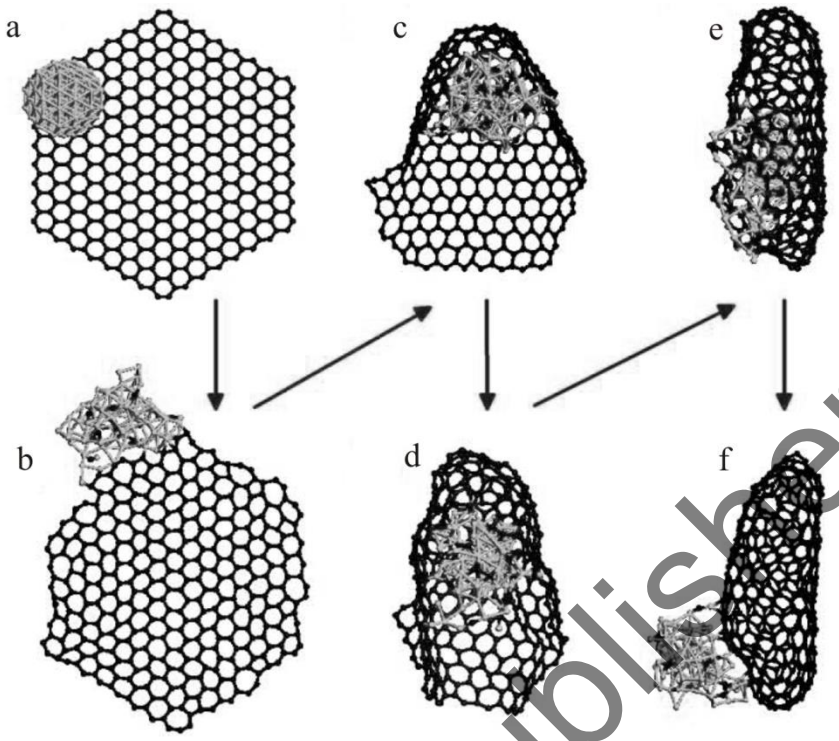

Figure 5. Structures obtained as a result of the MD simulation of the transformation of the graphene sheet C_{384} into fullerene in presence of Ni_{79} cluster under T = 2500 K at various instants: (a) 0; (b) 3; (c) 6.6; (d) 6.8; (e) 7.0; and (f) 11.5 ns [137].

3.2. Mechanical Properties of Graphene, Its Resistance to Deformation by Tension and Compression

3.2.1. Changes in Electronic Properties of Graphene upon Lattice Deformation

Graphene is a very strong and easily distensible material. Along with other mechanical properties of graphene, its resistance to elastic deformations has been studied. The creation of the elastic deformations is considered as a promising method of modifying the properties of nanomaterials [139]. A significant change appears in the interatomic spacing and in the symmetry of the crystal lattice under large elastic deformations. This can lead to appearance of unusual mechanical, thermal, optical, electrical, magnetic, and other properties of materials. For example, the thermal conductivity of graphene and carbon nanotubes decreases monotonically with increasing tensile stress [140, 141]. The optical conductivity of graphene is also very sensitive to applied stress [142, 143]. The uniaxial stress leads to a redshift of the G line (splitting it into two ones) and of the 2D line in the

spectrum of Raman scattering from graphene[1] [144]. The electronic properties of graphene depend on its two-dimensional structure and on the structure of its full symmetry. The lattice consists of two triangle sublattices. The electron spectrum of graphene is characterized by two branches, which touch each other at the so-called Dirac points, i.e., at two inequivalent points K and K_0 located at the corners of the first hexagonal Brillouin zone.[2] One of the key problems is the effect of impurities on the electronic properties of graphene [145]; comprehension of these effects is important for further technological development. Another way to modify the electronic properties is the creation of stresses in the lattice. The presence of deformations can exert a significant influence on the operation of electronic devices.

Graphene (because of its low dimensionality) has remarkable mechanical properties. In particular, *ab initio* calculations and experiments have shown that significant (up to 20%) elastic stresses can exist in the single-layer graphene [88, 146]. The uniaxial deformation initiates a modification of the electronic branches and, consequently, collective electron excitations (plasmons) [147]. The effects of the local fields make it possible to include into the consideration all processes of scattering with an arbitrarily low wavelength, i.e., to take into account the discrete nature of the crystal lattice. Contraction of the valence and conduction branch of graphene induced by the uniaxial deformation of the lattice has been considered in [147].

3.2.2. Strength of Graphene under Tension and the Mechanism of Its Fracture

In [148], the simulation of the uniaxial extension of graphene along different chiral directions was performed in the MD model with the use of the reactive empirical bond order (REBO) potential of the interatomic interaction [149]. The chiral direction was in the range of angles $0 < \alpha < 30°$; for the "zig-zag" direction $\alpha = 0$ and the step of deformation was $\Delta\varepsilon = 0.002$. The increasing dependences of the potential energy of lattice stresses under the deformation exhibit a sharp falloff corresponding to breaking the graphene sheet. With increasing angle α, the falloff of the stress is shifted towards the smaller values of ε.

Rough simulation of the graphene fracture upon uniaxial extension was performed with the use of elements of quantum-chemical calculation [150]. In this simulation the force of deformation F_i was determined as the gradient of the total energy of the system along the mechano-chemical i^{th} coordinate. A system of 88 atoms was studied with a step of deformation $\Delta\varepsilon = 0.008 - 0.009$. One of the ends of the object was fixed rigidly; the

[1] The origin of these lines is explained in Subsection 3.2.4.

[2] The Brillouin zone is defined as transform of the Wigner–Seitz cell of the crystal in the reciprocal space. Certain points of high symmetry in the Brillouin zone are denoted by special symbols.

opposite end could move. The extension was performed in both "zig-zag" and "armchair"-type directions. The final deformation was calculated with the use of a linear relation between F and ε, which was established via the Hooke law. In both cases, the same value of the fracture deformation was obtained $\varepsilon_{cr} = 0.123$ that is significantly less than the limiting values of ε determined in [88, 148]. The ratio between the values of the breaking stresses in the "zig-zag" and "armchair" directions also diverged strongly: 1.53 [150] and 1.16 [148].

Fracture of the material occurs most frequently because of formation and development of cracks. Precisely such an approach was demonstrated in [151] where the growth of cracks is considered in a discrete atomic model of graphene in the contrast to the continuum-mechanics approach. The model included 728 carbon atoms, the interaction between which is described by the Tersoff–Brenner potential [152]. The calculations were performed for the case of cracks with infinite and finite lengths. The formation of a crack was initiated by the breaking bonds between the chains of atoms. The coefficient W of the energy liberation of the elastic deformation was calculated in two ways. The first one was the method of the global energy, which is based on the determination of the total potential energy of two graphene sheets with different lengths of the central cracks ($2a$ and $2a + 2\Delta a$). So, the coefficient W was written as follows

$$W = -\frac{U_{2a+2\Delta a} - U_{2a}}{2\Delta a h}, \tag{35}$$

where U_{2a} and $U_{2a+2\Delta a}$ are the total potential energies of the graphene sheets in the deformed states obtained in the discrete atomic model; Δa is the equilibrium inter-atomic spacing in the x direction (along the crack), and h is the thickness of the graphene sheet.

In the second method (the method of local force), the virtual work, which is required to prevent crack propagation, is determined. Here, one should not calculate the total potential energy. This method is the fastest one and can be applied to large atomic systems since only neighboring atoms near the tip of the crack are taken into account in the calculations. In this case, the mechanism of fracture can be presented by two main deformation modes: I and II. The tensile mode I describes the relative displacements between the atomic pairs, whose atoms are located symmetrically with respect to the normal to the crack surface. The sliding mode II reflects sliding by making antisymmetric separation of atoms via tangential (with respect to the crack surface) displacements. In the case of modes I and II, the linear elastic solution (u_x, u_y) for the displacement fields in the vicinity of the crack tip is given in [151]. The coefficients of energy liberation W_{I} and W_{II} for modes I and II are written as follows

$$W_{\mathrm{I}} = \frac{1}{2\Delta a h} F_y (v^+ - v^-), \tag{36}$$

$$W_{\mathrm{II}} = \frac{1}{2\Delta a h}\left[F_x (u^+ - u^-) + F_y (v^+ - v^-) \right], \tag{37}$$

where F_x and F_y are the inter-atomic forces acting on the i^{th} atom in the x and y directions, respectively. These forces act from atoms located near a crack of the $2a$ length. The u^+, u^-, v^+, and v^- values are the displacements. They open the crack in the x and y directions for the i^{th} and j^{th} atoms located in the vicinity of a crack of the $2a + 2\Delta a$ length. In order to obtain the value of the virtual work, it is necessary to perform calculations with the use of two configurations. The first one restores the deformation of the crack expansion, while the second one describes the shift along the crack.

The Young modulus Y of graphene was measured using the AFM. Graphene was subjected to an external deformation and the relationship between the force and displacement was written out systematically [88]. The Young modulus measured in this experiment was equal to 1.0 ± 0.1 TPa. The usual method of measuring Y is in the determination of the dependence slope of the stress on the deformation that creates this stress [153–155]. The Young modulus of the carbon nanotubes (CNT) was also determined mainly in this way. However, in the experiments performed in [156], another approach was applied: the magnitude of Y was established from observation of the thermal vibrations near the tip of the CNT using a transmission electron microscope (TEM). For an unknown reason, this method was not employed to determine the Young modulus in graphene. The magnitude of Y for graphene was obtained by investigation of the thermal fluctuations in the MD calculation [157] with the REBO inter-atomic potential [149]. The mean square displacement (MSD) of atoms in graphene is connected with the acoustic phonon mode, which has the parabolic dispersion law $\omega = \beta k^2$.

Suppose that a graphene sheet with a square shape and a side L forms a plane xy. Then, the equation for vibrations in the *z* direction acquires the form [158]

$$\rho \frac{\partial^2 z}{\partial t^2} + \frac{Q}{h} \Delta^2 z = 0, \tag{38}$$

where $Q = {}^{1}\!/_{12} Y h^3 / (1 - \mu^2)$; Δ is the two-dimensional Laplacian; ρ is the graphene density; μ is the Poisson ratio, and h is the thickness of the graphene sheet. The solution to Eq. (38) with fixed boundary conditions in the x direction and periodic boundary conditions in the y direction has the following form

$$\omega_n = k_n^2 \sqrt{\frac{Yh^2}{12\rho(1-\mu^2)}}, \tag{39}$$

$$z_n(t,x,y) = u_n \sin(k_1 x)\cos(k_2 y)\cos(\omega_n t).$$

Here, $k_1 = \pi n_1 / L$, $k_2 = 2\pi n_2 / L$, $\boldsymbol{k} = k_1 \boldsymbol{e}_x + k_2 \boldsymbol{e}_y$, $\boldsymbol{e}_x$ and $\boldsymbol{e}_y$ are the basis unit vectors, $\boldsymbol{n}$ is the unit vector of the normal to the surface of the crack. The vectors of the normal of different crack surfaces $\boldsymbol{n}_1$ and $\boldsymbol{n}_2$ have mutually opposite directions $\boldsymbol{n}_1 = -\boldsymbol{n}_2 = \boldsymbol{n}$.

Using these eigenvalues for the MSD of the n^{th} mode of the phonon in the (x, y) plane, we obtain [159]

$$r_n^2(x,y) = 4k_B T \frac{12(1-\mu^2)}{Yh^3 L^2} \frac{1}{k_n^4} \left[\sin(k_1 x)\cos(k_2 y)\right]^2. \tag{40}$$

Under the conditions of thermal equilibrium at a temperature T, all the modes are independent and make a noncoherent contribution into the MSD. Therefore, we can obtain the following simplified expression for the MSD [157]:

$$\left\langle r^2 \right\rangle = \sum_{n=0}^{\infty} \left\langle r_n^2 \right\rangle = 0.31 \frac{(1-\mu^2)L^2}{h^3} \frac{k_B T}{Y}. \tag{41}$$

Hence, assuming that $\mu = 0.17$ for graphene [160, 161], we have

$$Y = 0.3 \frac{L^2}{h^3} \frac{k_B T}{\left\langle r^2 \right\rangle}. \tag{42}$$

Using equation (42), the authors of [157] obtained the dimension dependence of Y for a square graphene sheet. The magnitude of Y increases from 0.7 to 1.1 TPa as the edge of the graphene sheet increases from 1 to 4 nm. It is retained with small fluctuations during a further increase in the sheet dimension. In the temperature range of 100–500 K, the 15% increase in Y is observed. However, at T > 500 K, the fast decrease in Y occurs, that is related to a significant increase in the MSD in the z direction and, consequently, to an increase in the total MSD. According to the authors of [157], this method of determining Y gives correct values of the Young modulus only in the temperature range $100 \le T \le 500$ K. The authors of [157] also studied the effect of the isotopic composition of graphene on the modulus Y value. To this end, atoms of the ^{14}C isotope were introduced randomly into a pure ^{12}C system. It was shown that while the concentration of ^{14}C is not more than 5%,

the modulus Y changes in narrow limits (1.05 < Y < 1.1 TPa). However, when the concentration of ^{14}C increases to 20%, the value of Y decreases by 15%. Such a behavior of Y is opposite to the behavior of thermal conductivity of graphene upon a change in its isotopic composition. Thus, under the isotopic disorder of 5%, the thermal conductivity of graphene could decrease down to 40% [162, 163]. But a further increase in the ^{14}C concentration did not lead to substantial changes in the thermal conductivity.

3.2.3. Stability of Graphene under Effect of Compressive Deformations

A fundamentally different behavior of the graphene sheet was revealed when these deformations were present. The compression along the "zig-zag" direction weakens the edges of the sheet (that are parallel to this direction). This leads to the local destruction of the cellular hexagonal structure along the lower and upper edges of the sheet. In the final account, after implementation of 59 acts of compression through ε = 0.0058, the graphene sheet retained its integrity, losing only a small number of C atoms (Figure 6a). The defect cellular hexagonal structure was retained in the H form. Along the "armchair" direction, the graphene sheet is unable to sustain such strong stresses of compression.

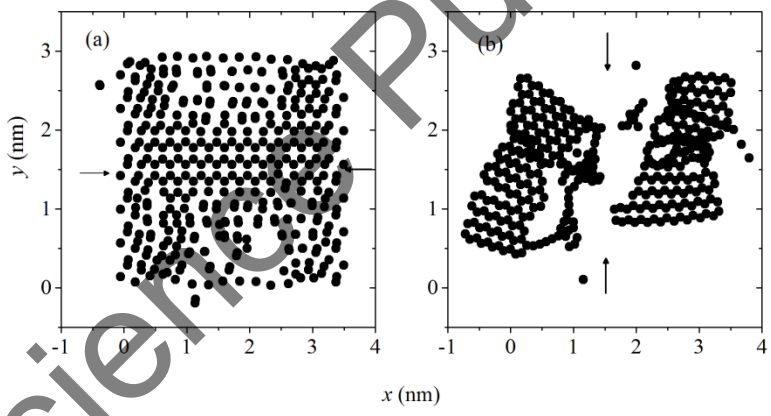

Figure 6. Projection of a graphene sheet onto the *xy* plane under its compression along the direction of (a) "zig-zag" and (b) "armchair" types at relative compressive deformations 0.3469 and 0.3929, respectively; the arrows indicate the direction of deformations.

Under the effect of compression along the "zig-zag" direction, the C atoms begin to escape from the sheet in the vertical direction (along the z-axis) already under relative deformations ε = 0.0235. Under compression along the "armchair" direction it happens at ε = 0.0266. A further compression of the sheet leads to an increase in the number of atomic displacements in the z direction. In addition, the paths passed by the atoms in this direction increase. The compression of a graphene sheet in the "armchair" direction at moderate deformations already creates cracks along the "zig-zag" direction. Then, because of these

cracks, wavy channels arise in the "armchair" direction. The separate fragments of the graphene sheet rotate and shift. In this case, some widening of one of the arising channels is observed. The rotated left-hand and right-hand parts of the sheet slide along this channel; as a result, the sheet becomes completely broken (Figure 6b). The difference in the stresses of the atomic rows of the graphene sheet, in this case, is an order of magnitude less than in the case of compression of the sheet along the "zig-zag" direction.

3.2.4. Investigation of Deformations Using the Raman Spectroscopy Method

In applications of single-layer graphene, its response to various loads is of great importance. The works in this field are mainly theoretical. Experimental investigations, as a rule, are limited to study of bending the separate graphene flakes in the air or of tensile tests until a certain deformation (≈ 1%) with the use of plastic substrates. Using a cantilever geometry, single-layer graphene can be subjected to axial compression of different degrees. The resistance of graphene flakes of different geometries to compression has been studied in [165]. In all the cases, the mechanical response was controlled by the shift of the G or 2D phonons of graphene in the spectrum of Raman scattering. The results show that graphene mounted into a plastic beam demonstrates compression on the order of 0.5 – 0.7% and sometimes more than 1%.

One of the methods (for recognizing to what extent the material is able to sustain the applied stresses or deformations) is an investigation of the material phonon frequencies under a load. The Raman spectroscopy is a very effective tool for monitoring the phonons for a wide class of materials subjected to the action of the uniaxial stress [166] or hydrostatic pressure [77]. Under the effect of a tensile load, softening of phonons is observed. Under the effects of compression, on the contrary, their hardening occurs. In general, in graphite materials (such as polycrystalline CF), the final deformation is affected not only by tensile (compressive) stresses but, also, by some mechanisms of rotation and sliding of crystallites that do not change the phonon frequency [166].

The recently developed method of obtaining graphene via the mechanical splitting of graphite [167] makes it possible to study the Raman shifts of the bands both of the G and 2D modes [168] under the tensile or compressive load on the molecular level [169–171]. This is important not only for detection of the super strength and rigidity of graphene. But it allows one to relate its behavior under mechanical deformation of other graphite structures, such as the bulk graphite, carbon nanotubes, and CFs. The G peak corresponds to the double degeneracy of the E_{2g} phonon at the center of the Brillouin zone. The D peak, which is due to the "breathing" modes of the sp^2-bonded rings, requires the presence of any defect for its activation [168, 170]. This peak is due to transverse optical phonons near the K point of the Brillouin zone [77, 172]. It is activated by the double resonance [173] and has a strong dispersion at the point K [174]. The 2D peak, which is a second-

order feature and formed from the D peak, is the only one in the mono-layer graphene. In the two-layer graphene, it is already split into four peaks reflecting thereby the evolution of the band structure [168]. Note that the 2D peak appears in the process, in which the moment is retained because of the participation of two phonons with the opposite wave vectors. So, it does not require the presence of defects for its activation and, therefore, always exists. Indeed, in the high-quality multilayer graphene, the G and 2D peaks exist but the D peak is absent [168]. A large number of studies are available, in which the behavior of these peaks was studied under application of deformations of different magnitudes to graphene [169–171, 175]. Because of the thin single-layer structure of graphene, the uniaxial deformation can strongly change its electron and optical properties. Since graphene has two carbon sublattices, which behave differently upon uniaxial deformation, it is possible to control the band gap by breaking the symmetry of the sublattices [176–178]. For example, the opening of a band gap was predicted in [178] for the growth of graphene on the hexagonal substrate of boron nitride because of the violation of the equivalency of the sublattices. In [179], graphene sheets deposited onto a flexible polyethylene substrate were subjected to the uniaxial tension (with a deformation up to ~ 0.8%). To study the effect of deformation on the single-layer and three-layer graphene, the Raman scattering has been used. Significant redshifts of the 2D peak (-27.8 cm^{-1} per percent of deformation) and the G peak (-14.2 cm^{-1} per percent of deformation) were observed for single-layer graphene under the action of the uniaxial tensile deformation. The results of a simulation based on the DFT have shown that in this case, the opening of a band gap (300 meV under 1% deformation) occurs at the K point of the Brillouin zone (Figure 7). This effect can be used to fabricate various devices based on the application of graphene properties.

3.2.5. Effect of Defects on the Mechanical Properties of Graphene

Let us now consider defects in graphene in the form of nitrogen atoms implanted into vacancies and rising above the graphene surface [180]. The initial sheet of graphene contained 588 atoms. The covalent C–C bonds were formed using the REBO potential [149]; the C–N bonds were formed using the Tersoff potential [138, 181]. The N atoms were placed into the vacancies both in a regular way and randomly. The Young moduli were determined from the slopes of the linear segments of the dependences of stresses on the tensile deformation, i.e., constructed using a step $\Delta\varepsilon = 0.004$. The stresses created by the forces applied in the "zig-zag" direction always decreased sharply when the deformation reached the critical value close to the fracture of the graphene sheet.

Calculated limiting tensile stresses and Young moduli for the cases of a regular and random placement of N atoms are given in Table 7. These characteristics change moderately with changing the nitrogen content. A decrease of the magnitudes of the

limiting deformation and ultimate strength is observed when there is a random rather than a uniform distribution of nitrogen atoms over the vacancies in graphene. The values of the Young modulus only weakly depend on the changes in the nitrogen content.

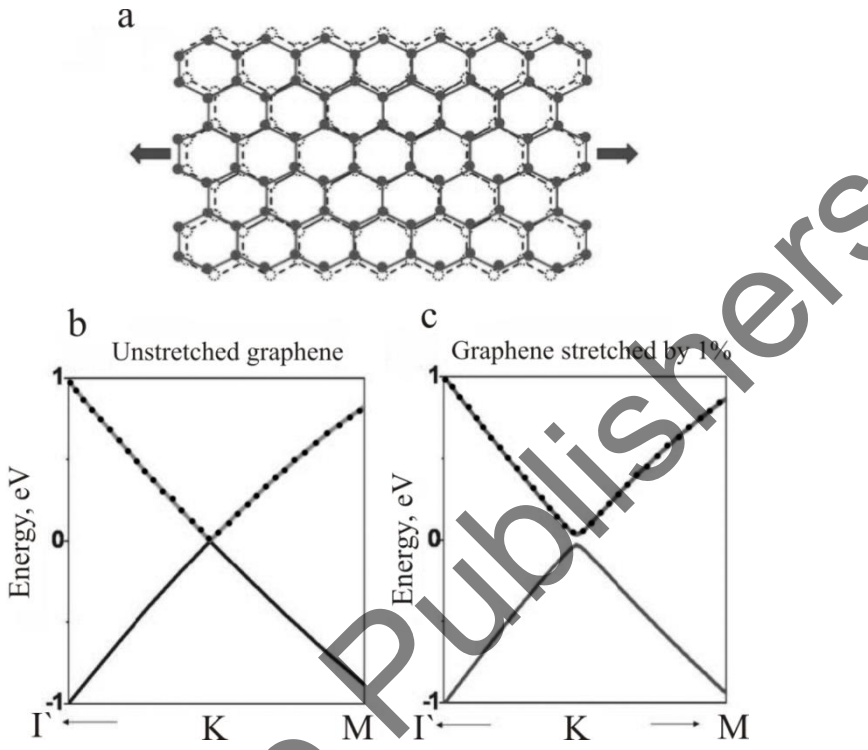

Figure 7. (a) Effect of uniaxial tensile deformation on a graphene piece (schematic); the deformed lattice is shown by solid lines; the undeformed initial lattice is marked by dashed lines; (b) the band structure of the undeformed graphene calculated along the I′–K–M direction of the Brillouin zone; (c) similarly to Figure 7b, but for graphene with 1% deformation; in the band structure of stretched graphene, the appearance of a band gap can be seen [179].

Table 7. Mechanical properties of graphene containing uniformly (regularly) and randomly distributed nitrogen atoms [180]

Nitrogen content (%)	Ultimate strength (GPa)	Young modulus (GPa)
Regular distribution of nitrogen atoms		
0	94	786
1	88	758
2	87	774
4	84	772
Random distribution of nitrogen atoms		
1	82	766
2	70	809
4	86	840

When only two nitrogen atoms have been implanted, it has been shown that the ultimate strength decreases with decreasing the spacing between them. When the spacing between N atoms was 0.176 nm, the ultimate strength decreased by 25%. The maximum stress arose near C atoms neighboring the N ones, i.e., in the vicinity of the nitrogen atoms. This is because the C–C bonds were broken, and the C–N bonds remained strong.

The experimental value of the relative deformation of the longitudinal compression for graphene ribbon on a substrate is, as a rule, 0.5 – 0.7% [165, 182]. Under such a deformation, the sinusoidal waves (buckling) are revealed on the graphene ribbon. The graphene roughness suspended in a vacuum appears at substantially lower deformations [165]. In [183], the MD method was used to study the behavior of a compressed single-layer graphene platelet on a substrate in presence of randomly distributed vacancies. In the presence of vacancies, buckling on the compressed platelet appeared under smaller deformations; the decrease in the buckling strain threshold obeyed a linear dependence. In the absence of vacancies, the nonlinearity of the stress-strain curve manifested itself under approximately the same strains as the buckling on the plate. The magnitude of the deformation corresponding to the loss of stability (~ 0.6%) agrees with the corresponding experimental characteristic.

3.3. Ion Beam Controlled Modification of Graphene

The defects of atomic scale in graphene layers change the physical and chemical properties of carbon nanostructures. The uncontrolled defects are formed spontaneously already at the stage of the graphene preparation. Defects of a certain type can be created artificially by ion bombardment [184] or by scanning probe lithography [185]. The method of scanning probe lithography makes it possible to modify the structure of graphene with high precision. However, the ion beams scan the graphene faster than the mechanical probe, and the diameter of the scanned region can be only a few nanometers. The irradiation by ions is a powerful tool for creating nanostructured surfaces. The potential for using ion beams is very large. They make it possible not only to create vacancies [186–188] and to implant ions [189]. It is also possible to tune the electronic structure [184], to change various properties of graphene [190] (including magnetic ones [191, 192]), to purify the surface of graphene [193], and to cut graphene sheets [194].

3.3.1. Creation of Defects in Graphene by Bombardment

In graphene nanostructures, various defects can be created, which affect the electrical, thermal, and mechanical properties of these nanostructures. It becomes possible to create:

(1) vacancies and vacancy complexes; (2) three-dimensional defects (humps, hills, dome-like forms); (3) embedded atoms of various metals.

1. Under the action of an ionic beam, mono-, bi-, and poly-vacancies, as well as vacancy clusters can be formed. A single vacancy at the center of graphene influences its electronic properties [186] leading to the formation of the "pentagon+dangling bond" defect, which is energetically favorable. However, because of the thermal motion of carbon atoms around the vacancy, this defect is unstable at temperatures of T = 1000 – 1500 K. Under bombardment of graphene (located on a substrate) by Xe atoms with energies of the order of several keV [195], the vacancy clusters arise, which prove to be stable at higher temperatures up to 900 K. These vacancies have the shape of a funnel propagating down to the substrate. The vacancies on the substrate, on the contrary, disappear completely at T = 700 K. All broken carbon bonds become saturated via the binding to the metallic surface forming the funnel-type vacancy structures.
   Influence of defects on the thermal properties of graphene has been studied using the MD model in [188]. The monatomic vacancies and Stone-Wales defects with different concentrations have been considered. A Stone-Wales defect represents a complex of five- and seven-atom rings that arises from two six-atom rings via the rotation of one of the C–C bonds of the graphene network [196]. In graphene located on a substrate, defects of this kind have a sufficiently large lifetime (~20 s) and disappear after the process of relaxation [197]. When there is a high concentration of the Stone-Wales defects, the scattering centers are distributed over the entire graphene, and its thermal conductivity becomes the same as that of a disordered material. In this case, the diffusion modes dominate over the processes of heat transfer, and the temperature dependence of thermal conductivity decreases sharply [188].
2. In [187], the MD method was used to study formation on the graphite surface of the three-dimensional defects containing several dozen atoms in the form of small hillocks. The hillocks regular lattice rises above the flat surface by 1–10 Å [187]. The number and location of such dome-like structures remain, as a rule, unaltered [198]. The vacancies are the main factor responsible for the formation of defects. As a result of random strikes of carbon atoms with energies of 0.1–3 keV against the surface of graphite, three types of defects can be formed: surface vacancies, inter-planar atoms located under the surface layer, and three-dimensional defects. It has been shown by *ab initio* calculations [187] that no significant change in the valence-electron density caused by an absent atom is observed in the vicinity of vacancies. However, the charge density increases near the atoms surrounding the vacancy. The single atoms located between the planes of graphite can migrate at room temperature [199]. As a result of migration, dimers and clusters are formed

between the layers, which serve as sources for the formation of the hillocks [200]. According to the results of calculations [187], the dimers and trimers form low and wide hillocks up to 1 Å high. Coarse surface defects are formed as a result of the introduction of an additional adsorbed atom (adatom) into the upper layer of graphite at a sufficiently low energy (≈ 50 eV). This adatom is incorporated into the structure of the surface layer, forming a vertical ring (Figure 8). Such a structure is stable; the binding energy is - 3.3 eV in it. In the region of the upper (rising by 2 Å) atoms, a maximum of the valence density of the electron charge is observed in the defect. The probability of formation of such structures is approximately two orders of magnitude less than that of the formation of vacancies and inter-layer clusters. However, these structures prove to be stable for at least 3 ps.

The defects significantly change the electronic states of graphene near the Fermi level, that is the important factor. Many unique properties of graphene are determined by the topology of the bands of its electronic structure in the vicinity of the Dirac point [201–203]. Experimentally obtained graphene flakes deposited onto the SiO_2 substrate were bombarded by 30-eV Ar^+ ions [184]. As a result, defects created in the form of hillocks of several angstroms high. In the vicinity of defects, large fluctuations of electron density are clearly observed; their origin is due to the interference of electrons scattered at defects. Similar density oscillations were observed in graphite [204], carbon tubes [205], and two-layer graphene [206]. The defects can also significantly affect the Fermi velocity mainly decreasing it. The possibility of tuning the electronic structure of graphene via the creation of defects opens a promising field in the application of the graphene-based electronics.

3. Mechanism of the graphene doping by single atoms of metals includes two consecutive stages: the creation of the vacancies by a high-energy beam of ions or atoms; and filling these vacancies by atoms of metals. The binding energy in the metal–vacancy complex proves to be sufficient to provide its stability. Structure of the formed vacancy depends strongly on the energy [207] and dimension [208] of the incident particles. Mono-vacancies and bi-vacancies are created with a greater probability under the effect of beams with energies of the order of 100 eV [59]. Upon irradiation of graphene, the mono-, bi-, and tri-vacancies were obtained both experimentally and by the MD simulation [209]. The type of vacancy depends on the site, which the bombarding atom hits into. If the atom hits into the C–C bond, bi-vacancies are mainly formed. The “atom-atom” collision leads to the formation of the mono-vacancy. If the bombarding atom hits the center of a hexagonal ring, then the multi-vacancies are mainly formed due to the removal of five or six C atoms. Then, Pt atoms are deposited into the formed vacancies (Figures 9a, 9b). Calculations show that the barrier to the migration of Pt atoms is 0.2 – 0.8 eV. This

is sufficient for obtaining a stable metal–vacancy structure even at room temperature. Calculations based on the DFT method yield lower energies of the Pt–vacancy complexes (~ 6 eV), which explains their stability under prolonged electron irradiation (Figure 9c).

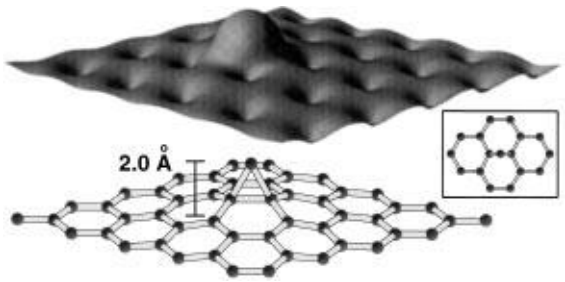

Figure 8. Atomic and electronic structures of a surface three-dimensional defect; in the inset, a top view of the defect is shown [187].

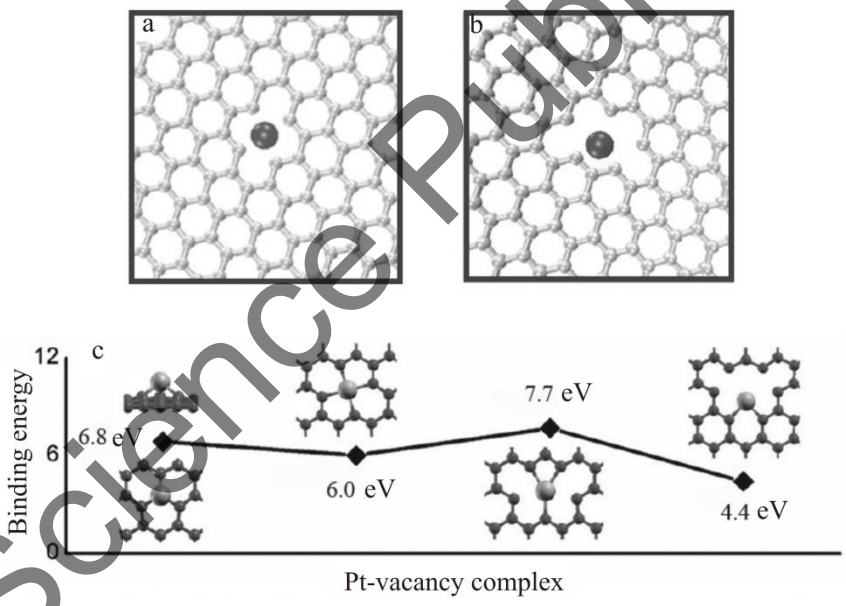

Figure 9. Diagram of implantation of a Pt atom into (a) bi-vacancy, and (b) tri-vacancy; (c) binding energy for various configurations of the Pt–vacancy complex [209].

The MD method was used to study graphene bombarded by normally incident neutral carbon atoms at various energies and T = 300 K [210]. At energies below 1 eV, the dominating process is a reflection, which is mainly caused by the repulsive interaction between the incident atoms and p electrons of the graphene sheet. The energy of the incident beam exceeding 1 eV proves to be sufficient to overcome this repulsion. As a

result, the process of absorption becomes predominant at energies of up to 100 eV. In the same energy range, defects such as adatoms, mono-vacancies, and bi-vacancies begin to arise. But these defects are reconstructed with time. At the end of the calculation, six-atom and eight-atom rings are formed.

3.3.2. Cutting the Graphene by Ion Beams

One method of cutting graphene is based on the use of a focused beam [211, 212] of helium ions with an energy of 30 keV. Such a beam stably sputters carbon atoms from the preliminarily chosen region of graphene. In this case, different mechanisms of energy transfer from the incident ion beam to the carbon structure are performed [56]. The process of cutting graphene by an incident ion beam is based on the formation of mono- and bi-vacancies or vacancy complexes.

The MD method was used to study processes of formation of the defects in graphene upon its irradiation by ions of various chemical elements (Ar, Xe, Kr, He, Ne). The angles of incidence were varied from 0 to 88°; the energies used were varied from several dozen electron-volts to 10 MeV [194]. At low energies (below 1 keV) and with a normal incident beam (zero angle of incidence), the most probable defect to be formed is a mono-vacancy. For obtaining the predominant formation of bi-vacancies, relatively small angles of incidence (less than 38°) and low energies of ions (less than 5 keV) are required. However, with increasing energy (up to 20 keV) at the same small angles of incidence, vacancy complexes begin forming. Under a further increase of the incident angle (up to 80°) and the energy of the ionic beam (up to 40 keV), mono-vacancy becomes the dominating defect again. This factor proved to be determining for the process of cutting graphene at a fixed energy. No defects are formed at very large angles of incidence (≈ 80°) and low energies of the incident beam (less than 1 keV). In the case of the glancing angle (≈ 88°), the ions interact only with the far rows of atoms. If the energies are low, then the ions are reflected from the sheet without knocking atoms from the graphene. However, when the energy increases (up to 40 keV), the ions of the glancing beam penetrate through the graphene sheet and create vacancy complexes with a large probability. At low energies (< 1 keV) when the beam energy only suffices to displace some carbon atoms, the amorphization of graphene takes place. The amorphized atoms do not lose their bonding with the sheet remaining in the form of adatoms on the surface.

Experiments in [211] confirmed that a focused beam of the He ions can be used for cutting graphene with very high precision. If the incident beam is directed normally to the sheet surface, part of the collisions leads to a sputtering of carbon atoms, and part of that leads to amorphization, which is undesirable for the process of precise cutting. The quality of cut edges can be improved by using an ion beam with the angle of incidence of ≈ 60°. Bombardment of the target at 60° angle leads to a decrease in the probability of formation

of collision cascades in the plane and of local amorphization. The obliquely incident He ions with sufficiently high energies (30 keV) create single vacancies, which makes it possible to obtain pure edges in the graphene cutting by an ion beam.

In computer experiments [194], it was established that for the normal incidence of a helium beam the fraction of scattered C atoms is ~ 6%; the other part is amorphized. However, when the angle of incidence of the ion beam is 62.5° at the energy of 30 keV, the number of scattered carbon atoms increases by a factor of three, i.e., the cutting beam acts more efficiently.

3.3.3. Magnetism Determined by Vacancy Complexes in Graphene

The perfect graphene does not have a magnetic moment in absence of an external magnetic field and, consequently, does not have ferromagnetic properties. Various defects and the topological structure (long-range ordering of paired spins) can serve as sources of ferromagnetism in graphene. The experimental hysteresis loops obtained upon magnetization [213] show that graphene sheets prepared at various temperatures exhibit a weak ferromagnetic effect at room temperature. Such magnetism in a graphene sheet is created by a certain organization of defects (vacancies) [214]. One of the important properties of graphene is the edge magnetism, which appears due to localization of the electronic states on "zig-zag" edges. It has been shown theoretically in [215] that graphene with the "zig-zag" edges and a ferromagnetic order is stable at the room temperature (with an energy of 0.3 – 0.5 eV at the Fermi level). This magnetism can be controlled by an external electrical field [216] or, for example, by using graphene islands on the SiC substrate [192]. In the process of growth of the graphene islands, energetically favorable structures incorporated into the substrate (that have no dangling bonds) are formed. The islands with "zig-zag" edges have states localized at the edges, which can lead to the magnetoelectric effects.

In this case, the carriers of magnetism are orbital interactions or spins of electrons. States with "spin-up" and "spin-down" for the mono-vacancy in graphene are asymmetric near the Fermi level. This leads to splitting and polarization of spin in the vacancy band [217]. The closely located vacancies behave independently if the spacing between them is more than 7 Å [218]. The magnetic moment depends nonmonotonically on the spacing between the vacancies. At the smallest spacing, it is equal to 1.15 μ_B; at the maximum spacing (i.e., at r ~ 7 Å), the magnetic moment is equal to 1.45 – 1.53 μ_B [219].

In the MD experiment, the polarization of the spin for mono-, tri-, and tetra-vacancies was calculated; it was found that the magnetic moment is localized near the vacancy cluster [220]. In the large vacancy complexes, the magnetic moment is concentrated at the edges of the defect. It increases with the size of the vacancy [221]. The energy band in graphene with a vacancy is absent.

Various configurations of the "graphene + vacancy cluster" system have been studied by *ab initio* simulation in [191]. The symmetrical "spin-up" and "spin-down" states have been obtained by creating a bi-vacancy in graphene, i.e., in the absence of polarization and, consequently, at a zero magnetic moment. For vacancy clusters containing from 3 to 6 defects, a nonzero magnetic moment localized near the vacancy was observed. Figure 10 displays various configurations of the "graphene + vacancy cluster" system depending on the number of carbon atoms removed from the graphene sheet. According to the MD calculations [191], the magnetic moment of the configuration V4_3 is equal to zero, since the function of the density of "spin-up" and "spin-down" states is symmetrical. The V6_2 configuration is more energetically favorable than V6_1 (the magnetic moments are 4.50 μ_B and 5.49 μ_B, respectively [217]).

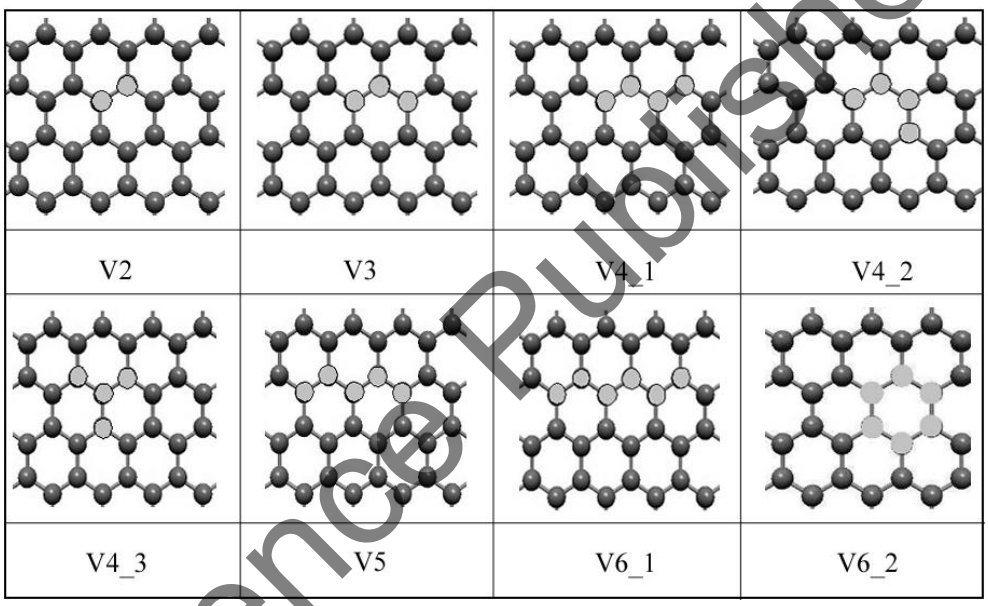

Figure 10. Various configurations of the graphene+vacancy cluster system [191].

Influence of various metallic atoms implanted into vacancies was studied in terms of the DFT [209]. According to these data, the Pt–vacancy complexes are nonmagnetic at various numbers of vacancies (1 to 4); but Co–vacancy complexes, on the contrary, have a magnetic moment. The local density of states at the Fermi level corresponds, mainly, to localized states around the Co atom. The total spin moment of the Co–mono-vacancy system is equal to 1.0 μ_B; the contribution from the Co atom, in this case, is 0.44 μ_B. However, in the Co–bi-vacancy system, the total moment of the spin equal to 1.56 μ_B contains a contribution equal to 1.50 μ_B from Co atoms (mainly due to *3d* orbitals); the other part comes from the *2d* orbitals of carbon.

3.4. PHYSICS-CHEMICAL PROPERTIES OF GRAPHENE EDGES

3.4.1. Reactive Ability of "Zig-Zag" Edges of Graphene

At the boundary determined by the edge of graphene, a complete delocalization of *p* electrons occurs. The electronic structure of a nanoribbon depends on the geometry of the edges [222, 223]. The localized state established at the "zig-zag" edge leads to interesting chemical properties.

Calculations based on the DFT (with the use of the generalized gradient approximation (GGA) for exchange correlations of electrons) made it possible to study the magnetic, electronic, and chemical properties of the graphene nanoribbons with the "zig-zag" edges saturated with hydrogen [224]. Owing to the unbound character of the localized state and the proximity of the flat branch of the electronic spectrum to the Fermi level, the "zig-zag" edges can play the role of radicals. In graphene ribbon with the "zig-zag" edges, the unpaired *p* electrons distributed over the "zig-zag" edges bring the average charge of - 0.14 e to each atom belonging to the edge. Thus, the edges of the ribbon acquire a "radical-like" character, i.e., acquire reactive ability.

Calculation of the bond-dissociation energy (BDE) has shown that the strength of the C–H bond formed at the "zig-zag" edge reaches only 60% of the strength of the analogous molecular bond between the carbon radical and hydrogen. Calculation of the BDE between carbon atoms belonging to the edge and common radicals have shown that the BDE of C–X (where X can be OH, CH_3, F, Cl, Br, or I) systems is equal to 40 – 80% of the experimental $C(sp^3)$–X energy. In addition, the "zig-zag" edges of the "zig-zag" nanoribbon of graphene (ZNRG) have a greater BDE than that of nanotubes and nanoribbons with "armchair"-type edges.

The low electron density at the edge of the ribbon is because of the collective character of the interaction of the C atom belonging to the edge with other (not "outer") atoms of graphene and, also, because of the interaction between the radicals. The ground state of a nanoribbon with "zig-zag" edges is antiferromagnetic; its energy is only insignificantly lower than that of the ferromagnetic state. In the antiferromagnetic phase, the C atoms at the edges have the magnetic moment of ~ 0.14 μ_B, and the local density of states is characterized by a sharp peak below the Fermi level for one of the spins and above it for the other spin.

3.4.2. Adsorption of Transition Metals by "Zig-Zag" Nanoribbon

The electronic properties of a nanoribbon can be changed by adsorption or doping with foreign atoms or molecules [225, 226]. The electronic and transport properties of graphene

nanoribbons doped with nickel have been studied in [227], and the structure of graphene sheets with trapped nickel was investigated in [228].

The structure and electronic properties of the ZNRG with adsorbed atoms of transition metals (Co and Ni) have been studied by the DFT method in [229], where the exchange-correlation potential was represented in the generalized gradient approximation [230]. A rectangular piece of the ZNRG was considered, containing 48 carbon atoms and one or two adsorbed atoms. The edges were decorated with hydrogen atoms; this led to neutralization of the valency of carbon atoms.

Five configurations with adsorbed atoms of transition metals have been investigated: (a) with one Ni atom adsorbed at the edge; (b) with two adsorbed Ni atoms, one at each edge of the graphene ribbon; (c) and (d) that are analogous to configurations (a) and (b), respectively, but Ni atom is replaced by Co atom; and configuration (e), in which Ni atom is adsorbed at one edge, and a Co atom at the other edge. In each case, after adsorption of a transition metal atom, six Ni(Co)–C bonds were formed. Table 8 contains the bond lengths for these five configurations after complete relaxation. In the case of configurations (b), (d), and (e), data are given for each of the adatoms Ni or Co. The shortest bond corresponds to the strongest interactions between the adatoms of the transition metal and carbon atom. In the case of adsorption of two metal atoms, all lengths of the metal-carbon bonds change because of the interaction between metal atoms. The short bonds for Co are smaller than in the case of Ni because of the greater atomic radius of the Ni atom. In configuration (e), the length of the Ni–C bond is greater than the length of the Co–C bond for the same reason. The interaction between two Co atoms is weaker than that between two Ni atoms. The changes in the structure are caused by relaxation affect the electronic properties of the configurations. The appearance of each metal atom leads to appearance of an additional subbranch in the electronic spectrum, which is related to the hybridization between the impurity states (Ni or Co) and *p* orbitals of the nanoribbon. In configuration (e), two new subbranches also appear in the conduction branch. The Fermi level of configurations (a)–(e) shifts up compared to the analogous characteristic of the ZNRG free of metal. This shift can be explained by a change in the effective Coulomb potential stipulated by the charge transfer.

The calculated portions of the transferred charges are presented in Table 9. An increase in the number of metal atoms in the ZNRG leads to a decrease in the magnitude of the charge transferred from the metal atom to the ribbon. The charge transferred from the Co atom is always less than that transferred from the Ni atom. This is related to a stronger interaction between the Ni atom and the graphene ribbon. The energy-band gap (EBG) that was determined in [229] for two (α and β) spins is given in Table 10. The largest EBG corresponds to a nanoribbon without metal atoms. Addition of the second metal atom leads to leveling of the EBG for the α and β spins. In the case of Ni adsorption, the EBG is greater than upon the capture of the Co atom by the graphene ribbon. A comparison with

configurations (b) and (d) shows that the EBG of two spins in configuration (e) reflects the hybrid interaction between the Ni (Co) atoms and the nanoribbon. Thus, the ZNRG with an adsorbed Co atom is closer in its electronic properties to semimetals than the graphene ribbon with a deposited Ni atom.

Table 8. Lengths of Co–C and Ni–C bonds for different atoms adsorbed on "zig-zag" graphene ribbon [229]

Configuration	Bond length (Ni – C or Co – C), Å					
(a) Ni atom	2.065	1.992	2.071	2.091	2.078	2.085
(b) 1st Ni atom	2.080	1.987	2.081	2.067	2.081	2.066
(b) 2nd Ni atom	2.105	1.997	2.107	2.065	2.058	2.063
(c) Co atom	2.071	1.937	2.083	2.045	2.046	2.032
(d) 1st Co atom	2.089	1.949	2.098	2.028	2.024	2.023
(d) 2nd Co atom	2.085	1.946	2.076	2.025	2.032	2.030
(e) Ni atom	2.077	1.943	2.081	2.028	2.028	2.026
(e) Co atom	2.083	1.989	2.087	2.069	2.081	2.065

Table 9. Charge* transferred from adatom to "zig-zag" graphene ribbon in the case of different configurations [229]

Configuration	Charge (e)	
	Atom 1	Atom 2
(a)	0.239	
(b)	0.222	0.224
(c)	0.196	
(d)	0.18	0.175
(e)	0.179	0.221

* Here *e* is the elementary electrical charge.

Table 10. Energy-band gap for two spins for configurations in absence of metal and for different configurations in presence of adsorbed metal atoms [229]

Configuration	α -spin (eV)	β - spin (eV)
Without Ni and Co	0.56	0.56
(a)	0.31	0.44
(b)	0.39	0.39
(c)	0.26	0.44
(d)	0.26	0.26
(e)	0.29	0.37

3.4.3. Changes in the Transport Properties, Passivation, and Reconstruction of Graphene Edges

Let us now consider the effect of other atoms and atomic groups on the electronic properties of the ZNRG. In [231], structures of the branches of the electronic spectra of ZNRG have been calculated in terms of the local DFT. Neutralization of the dangling bonds by hydrogen, oxygen, hydroxyl, and imine (nitrous analog of aldehydes) groups has been considered. Compensation of the sp^2-s orbitals by hydrogen atoms and by hydroxyl groups led to the appearance of two separated stable spin-polarized states. In this case, *s* branches are formed in the electronic spectrum that lays far from the Fermi level. On the contrary, the oxygen atoms and imine groups yield spin-unpolarized equilibrium states with a complex structure of the branches in the electronic spectrum. In this case, one of the *s* branches intersected the Fermi level, and the excessive electron per unit cell prevented the formation of the spin-polarized state. Here, just as in the case where the atoms of hydrogen and the hydroxyl groups are fixed at the edges, a transfer of a charge to the ribbon occurs, since the oxygen and imine group are more electronegative than carbon. The obtained structure of the branches of the spectrum indicates a strong change in the electron transport properties.

In the absence of control over the state of the ZNRG edges, a problem arises of reproduction of the desired transport properties. On the other hand, the possibility of controlling these properties makes it possible to use the ZNRG for various applications. For example, the attachment of the hydrogen atoms and hydroxyl groups to the edges of the ZNRG makes an opportunity to carry out some control in spintronic devices [232]. Similarly, addition of the oxygen or an imine group to the edges provides to use the ribbon as a metallic or quasi-metallic connection. It is known that strong correlations lead to new phenomena, which can appear because of the modification of the quasi-one-dimensional edges of graphene [233]. In [234], an original reconstruction of the most important edges of graphene was suggested. As a result of a rearrangement (in which two hexagons are replaced by a pentagon and a heptagon) of a “zig-zag” edge, the zz(57)-type edge was obtained, as shown in Figure 11a. The reconstruction of the “armchair”-type edge was investigated. It was shown that two separated hexagons (armrests) are transformed into contacting heptagons via the Stone-Wales mechanism. The reconstruction gives an ac(677)-type edge shown in Figure 11c. The pentagonal reconstruction of the “armchair”-type edge ac(56) differs from ac(677) only a little since it is based on the removal of carbon atoms from “far” armrests (Figure 11e). The unreconstructed edges of the “armchair” and “zig-zag” types are shown in Figures 11b and 11d, respectively.

The total energy E of a graphene nanoribbon is written as follows

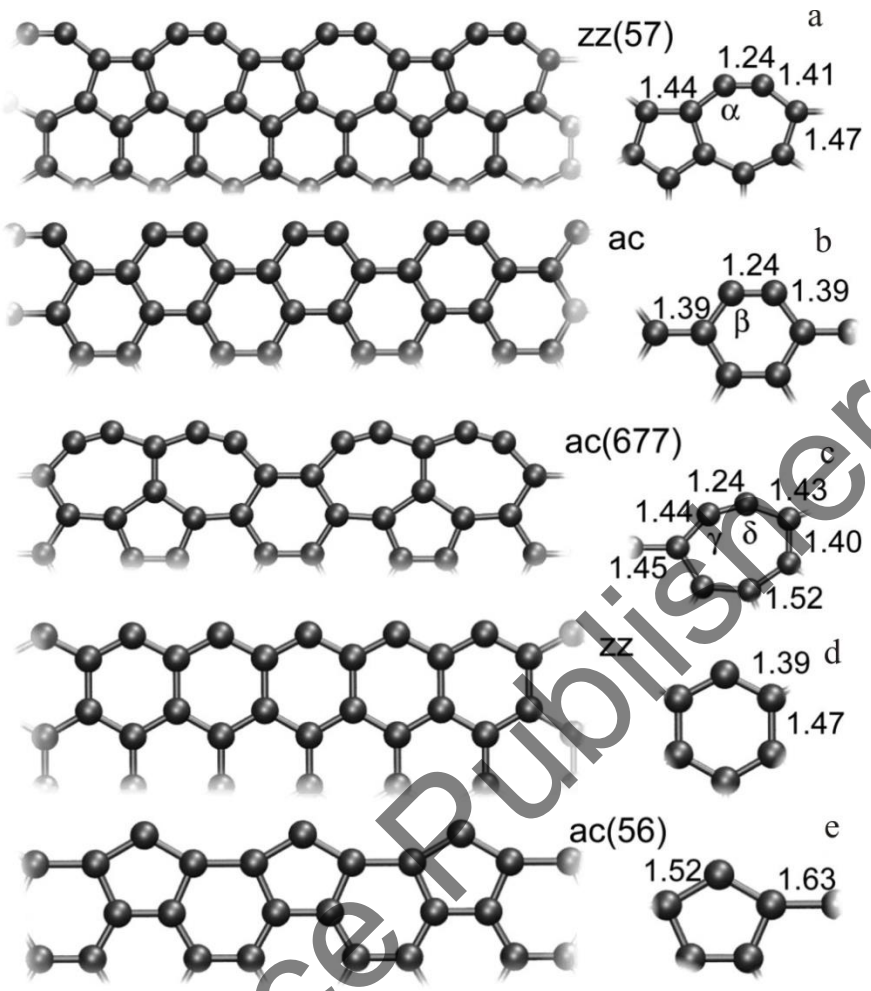

Figure 11. Geometry of graphene edges: (a) reconstructed "zig-zag" edge zz(57); (b) "armchair"-type edge ac; (c) reconstructed "armchair" edge ac(677); (d) "zig-zag" edge zz; (e) edge of a pentagonal "armchair"-type ac(56); the numbers in parentheses indicate the number of vertices in the polygons composing the edge; all geometrical figures are located strictly in the plane [234].

$$E = -NE_{\text{gr}} + LE_{\text{edge}}, \tag{43}$$

where N is the number of carbon atoms; L is the total length of edges; E_{gr} is the cohesion energy of graphene, and E_{edge} is the energy of the edges. The energy of an "armchair"-type edge calculated in terms of the DFT is lower than that of the "zig-zag" edge, just as in the case of nanotubes [235]. However, reconstruction of a "zig-zag" edge gives a lower energy and, consequently, this edge is more favorable for graphene than any of the reconstructions of the "armchair"-type edges. The energy of the ac(677) edge only insignificantly exceeds the energy of the "armchair"-type edge, whereas the ac(56) edge has the greatest energy.

The ac(56) edge is subjected to the effect of dangling bonds, just as in the case of the "zig-zag" edge. Nevertheless, the ac(56) edges can appear during the growth of graphene [235].

It is of interest to study the effect of hydrogen adsorbed on the reconstructed edges. The weaker adsorption (in the case of the "armchair" edges (4.36 eV) as compared to that for the "zig-zag" ones (5.36 eV)) is due to the presence of triple bonds in the "armchair" edges. In a similar way, the lower adsorption for the zz(57) (3.82 eV) and ac(677) (3.64 eV) indicates the weakness of the unsaturated bonds. The adsorption at the ac(56) edge (5.58 eV) is stronger. More complete data on the energy properties of the edges are given in Table 11. The "best" edges for the hydrogen adsorption are the common "armchair"-type and "zig-zag"-type edges because of the existence of the unsaturated bonds in them. On the contrary, the weak unsaturated bonds and low energy of adsorption cause high values of the energy $E_{\text{edge+ads}}$ for the zz(57) and ac(677) edges. The ac(56) edge, in spite of the high energy of adsorption for it, is not favorable for hydrogen adsorption either, since it has a large energy of deformation.

Table 11. Energy characteristics* of graphene edges upon hydrogen adsorption [235]

Edge Energy	zz(57)	"Armchair" ac	ac(677)	"Zig-zag" zz	ac(56)
E_{edge} (eV/Å)	0.96	0.98	1.11	1.31	1.51
E^{*}_{edge} (eV/Å)	2.36	2.09	2.30	3.22	6.43
E_{ads} (eV)	3.82	4.36	3.64	5.36	5.58
$E_{\text{edge+ads}}$ (eV/Å)	0.34	0.01	0.45	0.06	0.74

* E^{*}_{edge} is the energy of an edge (in eV per atom), E_{ads} is the energy of hydrogen adsorption, $E_{\text{edge+ads}}$ is the energy of an edge in the presence of hydrogen.

The reconstructions of edges discussed in [234] are expected at the terraces of graphene in view of the weak interaction (5.6 meV per atom) between the basal planes [236]. The images obtained using the scanning tunneling microscope frequently demonstrate irregular and diffuse edges (they are mainly passivated "armchair"-type edges). Probably, it is because of the reconstruction rather than the insufficient atomic resolution [237]. The zz(57) edge creates a branch in the electronic spectrum that is near the Fermi level. Thereby, this edge (unlike the convenient edges of graphene) causes enhanced conductivity. The stable chemical reconstruction plays an important role in the formation of the angular junctions in nanotubes [238] and in the closing of nanotubes after cutting [239], as well as in other systems obtained by joining the graphene sheets.

3.5. THERMAL PROPERTIES OF GRAPHENE

3.5.1. Determination of the Melting Temperature of Graphene

In many applications, graphene is used in the form of ribbons. In [240], melting the graphene ribbon in the form of the rectangle 2 nm × 3.5 nm in size was studied. The C atoms that form the rectangle perimeter were assumed to be immobile during the entire calculation. Thus, the weakest sites of graphene were artificially protected from the thermal fluctuations. The investigation was performed with the temperature step equal to 100 K. At T = 3400 K, the C atoms nearest to the immobile ones left their sites and together with the fixed atoms formed the boundary of the graphene ribbon. Therefore, at one of the rectangle corners, a cavity was formed, and the hexagonal shape of separate hexagons was distorted at its boundaries. The temperature in the model was maintained via the Nose-Hoover thermostat [241, 242]. Application of this algorithm led to strong continuous fluctuations of the temperature around its average value of 3400 K.

Taking into account the entire set of the above changes in the model, the authors of [238] interpreted the temperature equal to 3400 K as the melting temperature T_{m} of the nanoribbon. This is the lowest estimate of T_{m} for graphene. This value is even lower than that for graphite (≈ 4000 K) [243]. Most probably, the changes observed in [243] refer to melting the graphene boundaries (and, by no means, to all of them), whereas no liquid phase was actually observed outside the boundaries region. Thus, the effect observed at 3400 K is, in fact, the thermal instability of graphene edges rather than its melting.

In [244], the melting temperature of graphene was determined under periodic boundary conditions by the Monte-Carlo (MC) method in the process of simulation of melting the graphite system consisting of 16, 128 atoms (systems of a smaller size were also considered). According to the estimation in [244], the upper limit for the temperature T_{m} for graphene should be equal to 4900 K, which is higher than that for fullerenes (4000 K) [245] and nanotubes (4800 K) [246].

The MC simulation of the graphite melting process [247] with the long-range carbon bond-order potential [248] has shown that at T = 3000 K a layer-by-layer splitting of graphite with the formation of the graphene layers starts. The melting of graphene that was studied in [244] can be considered as the following step in the thermal decomposition of graphite. In this case, the two-dimensional (2D) graphene layers were melted into the three-dimensional (3D) liquid network and one-dimensional (1D) chains. The short-range order in graphene was destroyed because of the formation of the pentagon-heptagon pairs, which in this system represent dislocations (Stone-Wales defects) arising as a result of the carbon bonds rotation.

The Stone-Wales defects create regions of the local symmetry of the fifth and seventh order in a two-dimensional crystal; i.e., a symmetry that is incompatible with an infinite regular packing of atoms. According to [244], there are precisely such defects that initiate melting in graphene. Then, octagons are formed, which can serve as precursors of the spontaneous melting. Under melting, an entangled 3D network is formed consisting of chains that tightly connect the three-coordinated atoms. This structure, which has a low density, is a polymeric gel rather than a simple liquid. The simulation indeed made it possible to observe a state, in which both the solid and liquid phases exist simultaneously. However, the periodic boundary conditions eliminate the boundaries of the 2D crystal, i.e., namely those regions, in which melting should start. The simulation of melting the various three-dimensional systems, in this case, leads to overestimated values of T_m [249]. Note that T_m of small graphene flakes is lower than T_m of extended graphene sheets or nanoribbons. Defects existing in the graphene flakes decrease T_m. The hydrogen passivation of the flakes, on the contrary, increases it.

3.5.2. Thermal Conductivity of Graphene

Thermal properties of graphene (specific heat, thermal expansion coefficient, and the coefficient of thermal conductivity) significantly depend on phonon characteristics. Characteristics of the phonon spectrum are determined by the 2D structure of graphene. Graphene has extremely high values of thermal conductivity [250] and electron mobility [251]. These properties make graphene a promising material for the heat-removal applications and in electronics. The ultra-high values of the room temperature (RT) thermal conductivity $\lambda \sim 3000 - 5000$ W/m K were obtained for the rectangular graphene flakes with dimensions 5 μm × 10 μm [250]. These values are by an order of magnitude higher than the thermal conductivity of copper or gold and by a factor of 2–3 higher than λ of the bulk diamond or highly oriented pyrolytic graphite.

Graphene has a hexagonal structure with two carbon atoms in each cell. Such a structure of graphene causes the appearance of the six phonon branches in the dispersion spectrum: three acoustics (LA, TA, and ZA) and three optical (LO, TO, and ZO). The LA and TA modes correspond to longitudinal and transversal phonon oscillations in a graphene plane. The mode ZA characterizes oscillations of phonons in the direction normal to the direction of oscillation modes LA and TA. The LA and TA modes are determined by a linear dispersion law [252]: $\omega = vq$, with the velocities: v_{LA} = 18.4 km/s and v_{TA} = 16.5 km/s. There is no agreement related to the dispersion law for the mode ZA. The velocity $\omega_{ZA} = vq^{3/2}$ (instead of usually used $\omega_{ZA} = vq^2$) is calculated under the dispersion law, which better corresponds to the experimentally observable law [252]; thus,

the ZA velocity is v_{ZA} = 9.2 km/s [253]. To calculate the thermal conductivity of graphene, the γ_{LA}, γ_{TA}, γ_{ZA} Grüneisen parameters are also used, as well as, a measure of surface roughness parameter p_a and the smallest dimension in the plane of the sheet L_x. In addition, the A_d, M, and ω_D parameters are also used in these calculations. The parameter A_d is defined as $A_d = c_d \Delta M / M$, where c_d is a concentration of defects and $\Delta M / M$ is the ratio of elementary cell atomic mass change and an atomic mass of a cell; ω_D is the Debye frequency. We collected all the parameters used to calculate the thermal conductivity of graphene in Table 12.

The thermal conductivity of graphene created by the phonons of polarization *s* is determined by the expression [254]

$$\lambda = \frac{1}{4\pi L_z k_B T^2} \sum_s \int_0^{q_{max}} \left\{ \left[\hbar \omega_s(q) \frac{d\omega_s}{dq} \right]^2 \tau_{tot}(s,q) \times \frac{\exp\left[\hbar\omega_s(q)/(k_B T)\right]}{\left(\exp\left[\hbar\omega_s(q)/(k_B T)\right]-1\right)^2} q \right\}, \quad (44)$$

where L_z = 0.335 nm is the graphene layer thickness, and the summation is performed over all acoustic phonon branches s = LA, TA, or ZA, ω_s is the phonon frequency of the s^{th} phonon branch, q is the phonon wave number, $\tau_{tot}(s,q)$ is the total phonon relaxation time, T is the absolute temperature, $\hbar$ and k_B are Plank and Boltzmann constants, respectively. In determining $\tau_{tot}(s,q)$, we can distinguish three main phonon relaxation processes: phonon – phonon Umklapp scattering, phonon – rough-edge scattering, and phonon – point-defect scattering.

Table 12. Relevant parameters of thermal conductivity

L_x (μm)	v_{LA} (km/s)	v_{TA} (km/s)	v_{ZA} (km/s)	γ_{LA}	γ_{TA}	γ_{ZA}
100	18.4	16.5	9.2	1.8	1.6	- 1.2
L_z (μm)	M (kg)	A_d	p_a	$\omega_{D,LA}$ (Hz)	$\omega_{D,TA}$ (Hz)	$\omega_{D,ZA}$ (Hz)
0.35	$2 \cdot 10^{-26}$	$4.5 \cdot 10^{-4}$	0.9	$2.66 \cdot 10^{14}$	$2.38 \cdot 10^{14}$	$1.32 \cdot 10^{14}$

The thermal conductivity of graphene has a strong dependence on temperature, flake size and shape, strain, edge quality, and crystal lattice defects [255]. The phonon estimated the mean free path in the high-quality suspended graphene is about 800 nm at RT [250]. Consequently, the thermal conductivity is very sensitive to both intrinsic and extrinsic phonon scatterings. It should be emphasized that the latter circumstance is crucial for the engineering applications of the phonon and thermal properties of graphene. The dependence of thermal conductivity in the single-layer graphene on temperature and flake width d is shown in Figure 12. The theoretical curves were calculated in the framework of the Boltzmann-transport equation approach [255]. Three-phonon "umklapp" and edge roughness scatterings were taken into account. The thermal conductivity decreases as the temperature rise due to an increase of the three-phonon "umklapp" scattering. However, even at T = 400 K, the influence of flake width on λ is significant. Decreasing d from 9 μm to 3 μm results in a two-fold reduction of the thermal conductivity.

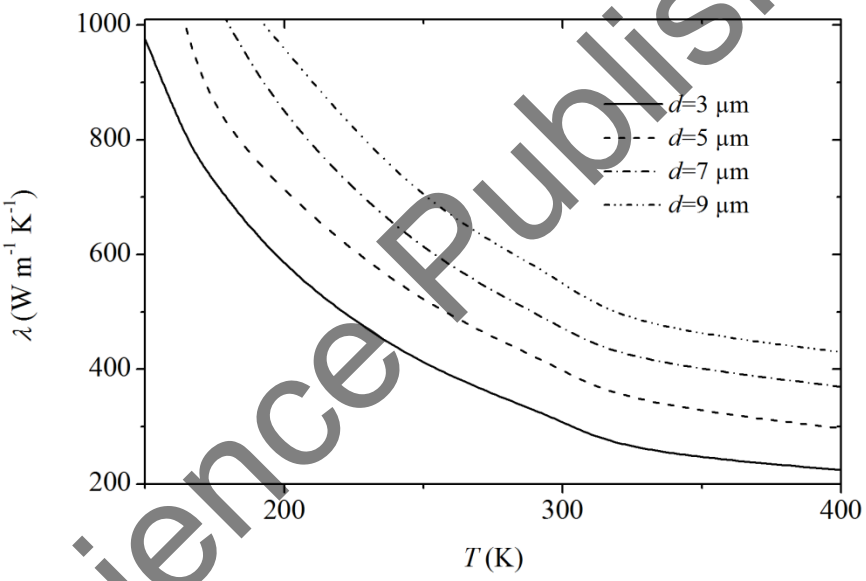

Figure 12. The thermal conductivity of graphene as a function of temperature shown for different graphene flake widths [256].

Particular attention should be paid to the low-temperature range, in which the largest contribution to thermal conductivity provides just the ZA phonon branch (Figure 13) [256]. As it is seen from Figure 13, the thermal conductivity for the ZA branch fastest drops to zero, i.e., it has the steepest decline. At the temperature T* (slightly lower than 50 K) all three phonon branches give an equal contribution to the thermal conductivity of graphene. Up to this temperature, the contribution to the thermal conductivity of the TA phonon branch is larger than that of the LA branch. For the values greater than T*, the significance of these contributions is directly opposite.

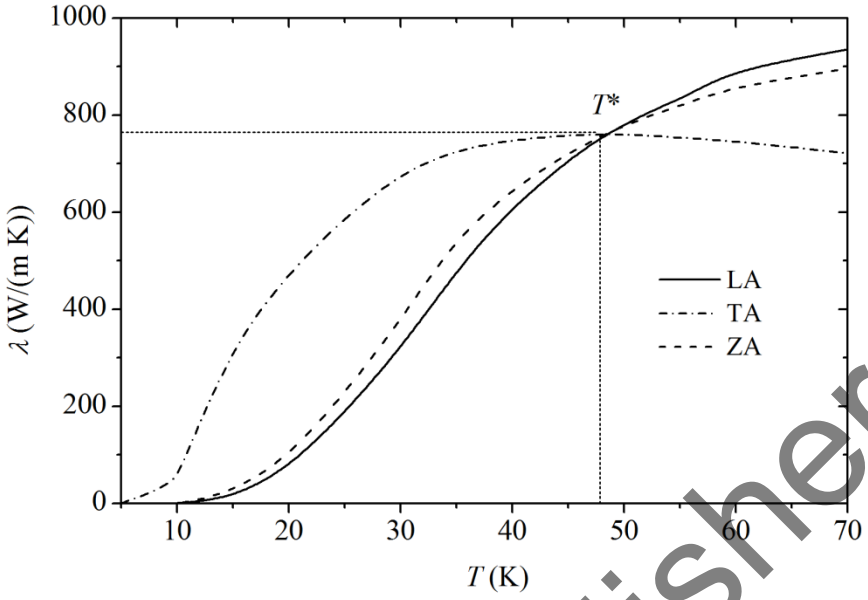

Figure 13. Low-temperature dependence of thermal conductivity for different phonon branches [257].

All carbon structures, such as diamond, graphene, and nanotubes, should have the high thermal conductivity primarily to phonons. In the layered graphite systems, the phonon thermal conductivity λ can be expressed as

$$\lambda = \left(1/2\right) c_{\mathrm{V}} v_{\mathrm{s}} \langle l \rangle , \tag{45}$$

where c_{V} is the specific heat per volume, v_{s} is the speed of sound, and $\langle l \rangle$ is the phonon mean free path.

The NEMD method introduces a small driving force characterized by the parameter F_{e}, which induces a heat flux J_z along a specific z direction [258]. The thermal conductivity λ can then be determined from

$$\lambda = \lim_{F_{\mathrm{e}} \to 0} \lim_{t \leftarrow \infty} \frac{\langle J_z(F_{\mathrm{e}}, t) \rangle_t}{F_{\mathrm{e}} T V} , \tag{46}$$

where V is the volume of the unit cell and T is the temperature. In calculations carried out in [257], the inter-atomic interactions are described by the Tersoff potential [40]. In this study, the pure carbon systems (free of isotopes) based on ^{12}C were only considered. It should be noted that simulations of the extended systems have been performed using the periodic boundary conditions in order to eliminate finite-size effects. To study the effect of the isolated Stone-Wells defects on the temperature-dependent thermal conductivity of

graphene, the rectangular graphene sheet of size 2.28 nm in the "zig-zag" direction and 2.14 nm in the "armchair" direction was modeled [257]. Behavior of the $\lambda(T)$ function shown in Figure 14 can be explained by the temperature dependence of the specific heat c_V and the phonon mean free path $\langle l \rangle$ in Eq. (45). The decrease in λ at high temperatures is due to a decrease in $\langle l \rangle$. Naturally, the thermal conductivity decreases at very low temperatures and eventually disappears at $T = 0$ because of the corresponding trend in c_V. The competition between $\langle l \rangle(T)$ and $c_V(T)$ causes a maximum in $\lambda(T)$, which was observed [259] at $T \approx 100$ K. However, the classical MD simulation does not correctly reproduce the low-temperature behavior of c_V. The maxima in the lines shown in Figure 14 represent only an extrapolation of the expected behavior. Calculations of the thermal conductivity of graphene without defects carried out using the same method [256, 260] show very large values of λ, in particular, $\lambda_{max} \approx 50\ 000$ W m^{-1} K^{-1} near 100 K. A quantitative comparison of these results suggests that even isolated Stone-Wales defects can extinguish the thermal conductivity by one or two orders of magnitude depending on the temperature T. However, this type of defective graphene is a better conductor of heat than metal thermal conductors with a typical thermal conductivity of several hundred W/(m K) at RT. The results obtained in [256, 260] show that even isolated Stone-Wales defects can significantly reduce the thermal conductivity.

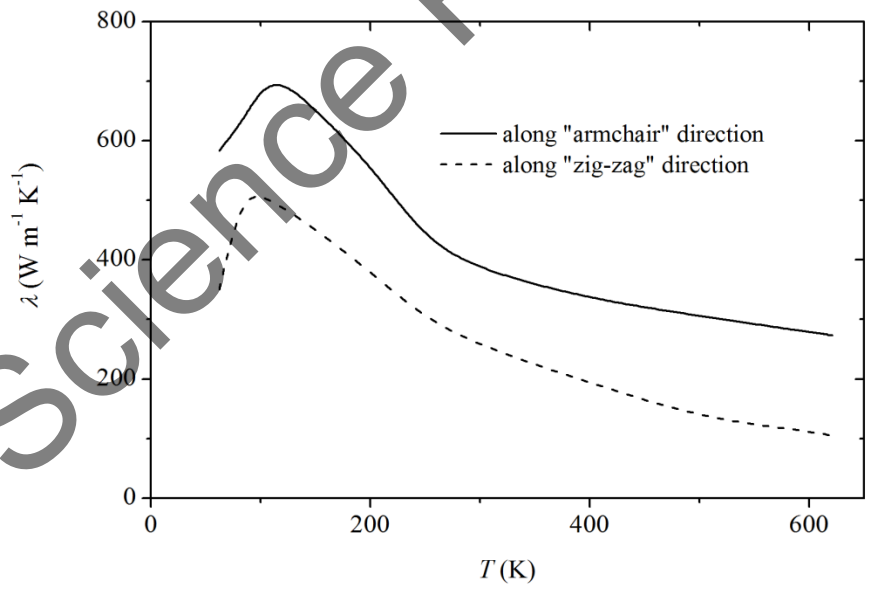

Figure 14. The thermal conductivity λ as a function of temperature T for thermal transport along the "zig-zag" and "armchair" directions [257].

The high value of thermal conductivity is one of the important characteristics of graphene and has record levels of all known materials. The thermal conductivity of graphene is essentially phonon-based. Dimensions of the analyzed graphene samples exceeded the average free path of phonons (about 800 nm). Otherwise, the so-called ballistic transport would appear with the phonons spreading through the sample without scattering. The obtained results have been achieved with the simplifying assumption that the Grüneisen parameters and group and phase velocity of phonons are of constant values. These parameters generally depend on the phonons frequency. Different measurements of the graphene thermal conductivity, as well as, different theoretical investigations give different results. Moreover, the absolute value of λ increases as the graphene sheet dimensions increase. This is associated with an increase in the number of phonon modes that occur in the sample. However, it is obvious that there are several physical mechanisms that limit the increase of λ as dimensions increase. One such mechanism is the scattering of the phonons on the defects.

Chapter 4

THERMAL STABILITY OF METAL FILMS ON ONE- AND TWO-LAYER GRAPHENE

Graphene is a layer of carbon atoms linked by sp^2 bonds into a two-dimensional hexagonal crystal lattice. The unique properties of graphene are explained by its crystalline and electronic structures. At temperature ($T > 0$) even in absence of external action, the graphene sheets have corrugation characterized by small wavelengths. The loss of stability in the normal direction to the lattice plane is explained by the instability of 2D crystals. It appears in effectively suppressing the long-wave phonons, which could otherwise melt the lattice at any temperature $T > 0$ [261]. This instability was predicted theoretically in the pioneering works of Peierls and Landau [262, 263]. The morphological corrugations can strongly affect the transport properties of graphene.

Study of the interaction of copper with graphene is of interest due to circumstances related to production and application of graphene. The methods of graphene production can be divided into three main groups. The mechanical methods that using the mechanical peeling belong to the first group. The second group includes chemical methods, and the third one includes epitaxial methods and the method of thermal decomposition of a SiC substrate. In the method of chemical gas cooling, graphene is synthesized by decomposition of a carbon-containing gas (e.g., methane) into carbon and hydrogen at the temperature about 1300 K under the presence of a metallic foil. Further cooling of the metallic substrate initiates pressing-out of diffused carbon atoms from the metal and formation of the graphene film on the substrate surface. The advantages of a copper substrate as compared to a nickel one, are the formation of graphene on the copper occurs without carbon diffusion to the metal bulk, i.e., it takes place just on the copper foil surface [264]. This makes it easy to produce single-layer graphene. The graphene layer grown on a copper-foil substrate can be introduced into transparent electrodes of sensor displays [265]. First, a two-dimensional carbon crystal is separated from the metal using a polymer adhesive and then transported onto the substrate of a sensor polyethylene terephthalate

display. Application of the copper–graphene composite is thought to be promising for fabricating a self-cooling system of transistors, which cardinally solves the problem of cooling computer devices [266]. The copper–graphene composite prepared by electrochemical deposition of copper on graphene nanoplates has a thermal conductivity of 460 W/m K, while that of copper is 380 W/m K. Application of this material to electronic systems with high heat generation provides economy of their resources due to a smaller expenditure of copper. Deposition of copper on graphene is of significant interest in relation to producing the nanomaterials with unusual magnetic properties [267]. The magnetism of complexes formed by Cu atoms appears from *s*- and *p*-states (to 30%) and since surrounding the Cu atoms by the C ones. Point defects influence the magnetism of copper–carbon complexes. The mechanism of the defects formation in graphene at high temperatures can be studied by a computer experiment. Such a simulation also makes it possible to observe the behavior of the metallic atoms introduced into the defects.

The aim of this work is to study the changes in the mechanical and kinetic characteristics of a single-layer copper film adsorbed on single-layer and two-layer graphene under increasing temperature.

4.1. Formation of a Copper Film on Graphene Surface

4.1.1. Molecular Dynamic Model

Preparation of a stable metal film on graphene primarily suggests a high degree of metal adhesion to the (graphene) substrate. This can be reached when the metal atoms closely approach the C atoms occupying the energetically favorable sites on the graphene surface. These sites are the hexagonal cells formed by the carbon atoms. An energetically favorable position of the metal atoms is centrally symmetric over the hexagonal cells. The distance from the metal atom to the graphene plane is determined either experimentally or by the quantum-chemical calculations. The problem in the covering of graphene with the metal atoms is incompatibility of the crystal lattice periods of the metal and graphene. Since the lattice period of graphene is much smaller than that of the metal, the hexagonal cells should be skipped in both dimensions when covering graphene with the metal. For copper, one cell can be skipped in both dimensions. With this coverage, a graphene sheet of 406 C atoms accommodates only 49 Cu ones. The non-adjacent cells of graphene are filled during the metal deposition at times that can hardly be achieved in a molecular dynamics calculation. Therefore, the first stage of deposition was forced accommodation of 49 Cu atoms at the energetically most favorable positions on the graphene sheet. As a result of the long-range character of interactions between the copper atoms, they have been deposited on the graphene surface. Then they serve as a basis for further growth of the metal film by the next deposition of copper atoms. The second stage of deposition was

randomly scattering 51 Cu atoms over the graphene sheet with 49 metal atoms deposited on it. The atoms were scattered in a rectangular parallelepiped with a base that reproduced the graphene sheet and with the height of $2\sigma_{Cu-C}$, where σ_{Cu-C} = 0.3225 nm [268] is the parameter of the Lennard-Jones potential that describes Cu–C interactions. The distance from the lower base of the parallelepiped to the plane through the centers of mass of the C atoms was $3\sigma_{Cu-C}$. A downward vertical component of velocity $v_{mp} = \sqrt{2kT/m}$ (the most probable velocity in the Maxwell distribution) was added at the initial instant to the randomly scattered Cu atoms in addition to the usual thermal velocities (corresponding to 300 K). With this velocity, the Cu atom could cover the σ_{Cu-C} distance in a vacuum within 11.5 ps. Once the Cu atom approached the C atoms or the preliminarily deposited Cu atoms at a distance smaller than $1.1\ \sigma_{Cu-C}$, the additional vertical component was subtracted from its velocity. Therefore, a stable copper film forms on graphene within the time of $10^6 \Delta t$ (or 200 ps). The equations of motion were integrated by the Runge–Kutta fourth order method with a time step of Δt = 0.2 fs. The calculations were performed at a temperature of 300 K. The temperature in the model was maintained with the Berendsen thermostat [62]. The total energy of free one-layer graphene obtained at T = 300 K is – 7.02 eV that agrees with the quantum mechanical calculations results (– 6.98 eV) [64].

4.1.2. Creation of Copper Film

The configurations of the graphene–Cu_{100} system corresponding to the moments of time 20 and 200 ps are shown in Figure 15. The Cu atoms deposited at the first stage formed an extended (111) plane of the fcc lattice of the copper crystal. At the instant 20 ps (Figure 15a), however, this planar lattice was severely distorted forming small atomic groups. Some atoms (especially those in the middle part of the metal film) went out of the lattice plane and approached the upper Cu atoms, which initially occupied random positions. The uniform distribution of the upper atoms was also violated and they formed small clusters. The boundary between the regularly and randomly distributed atoms started to diffuse. At the instant 200 ps (Figure 15b), the metal film looks as the single bonded irregular formation extended parallel to the graphene surface. In the central region, the density of the metal film is higher than on the periphery with voids in the film structure. We can say that in the central part the film consists of two and sometimes three layers and is monolayer on the periphery. The system continuously gradually moves to the equilibrium state; the Cu–Cu interaction energy decreases in the course of the calculation. The structure of graphene did not noticeably change during the calculation.

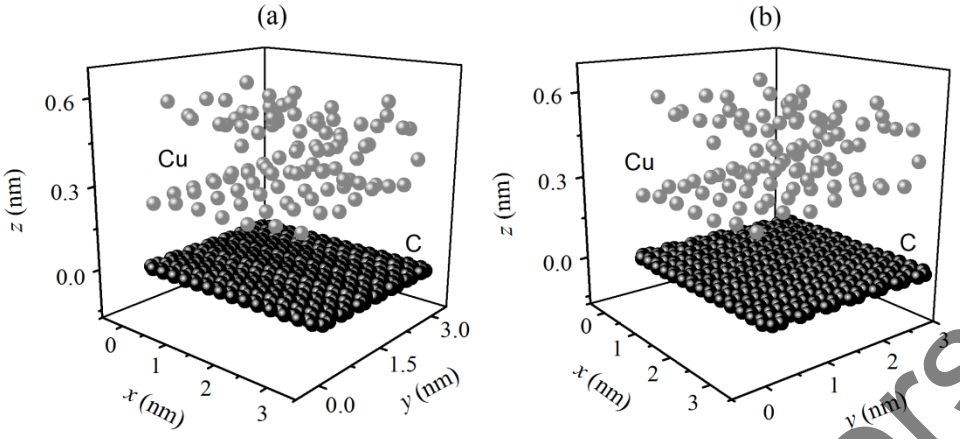

Figure 15. Configurations of the copper film on graphene obtained at the instants (a) 20 and (b) 200 ps.

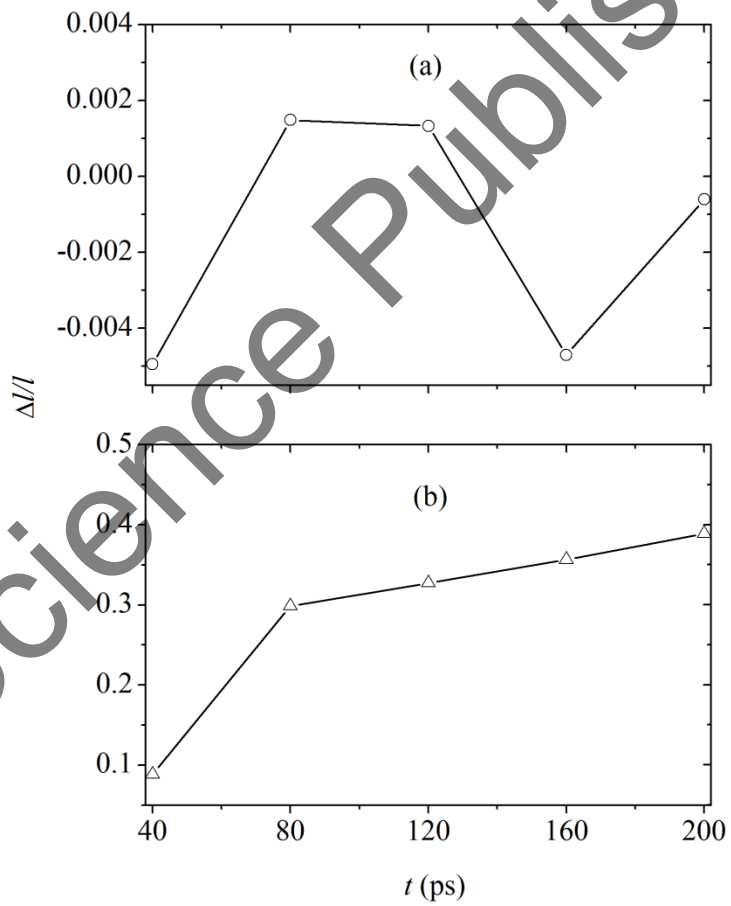

Figure 16. Relative elongation of the copper film deposited on graphene in the (a) longitudinal (*x*) and (b) transverse (*y*) directions.

The film size was determined from three time-averaged values for each size value. For example, the x coordinates of three atoms were used to determine the minimum value $x_{\min}$, and the same number of atoms were used to determine the maximum value $x_{\max}$ (x is the coordinate of the film, whose longitudinal size was determined as $l_x = x_{\max} - x_{\min}$). The transverse size of the film was calculated in a similar way. The minimum time interval (or the micro step), at which the time-averaged values were determined for the calculated characteristics, was 40 ps.

The change in the geometrical size of the Cu film is shown in Figure 16. The initial fast growth of the film size (in the range 40 – 80 ps) in both longitudinal and transverse directions is caused by the diffusion of the upper randomly ordered atomic groups having weak bonding to graphene. The distances between the Cu atoms (on the periphery of the film) and the graphene surface are shortened with time. These atoms bond increasingly with graphene, and, the film size growth is either retarded (in the transverse direction) or terminates (in the longitudinal direction). The slower growth of the transverse size of the metal film may be explained by the shift of the Cu atoms of the lower (initially regular) part of the film to the periphery. The shift develops in the direction of the "armchair" of the graphene sheet. This is associated with the lower film rigidity in this direction due to the specifics of the hexagonal packing. The higher rigidity of the (111) plane of the metal in the longitudinal direction prevents the Cu atoms from running in this direction. Under strong long-range interaction between the upper and lower groups of the metal, the atoms of these groups are mutually held, and as a result, the film size in the longitudinal direction can decrease.

The kinetic properties of the system are considered separately in the horizontal and vertical directions because of its geometrical peculiarities. As the Cu atoms are deposited on the graphene sheet, the horizontal component of the film self-diffusion coefficient D_{xy} gradually decreases (Figure 17a). This behavior of D_{xy} coefficient is caused by the approach of the Cu atoms (deposited on the metal film or directly on graphene) to other atoms. The vertical component D_z of the film self-diffusion coefficient also decreases, but the behavior of its time dependence differs considerably from that of $D_{xy}(t)$ (Figure 17b). The D_z coefficient decreased drastically at the start of the deposition. Thus, within the time period 40 – 80 ps, it decreased by a factor of 24.4. Further decrease in D_z was considerably slower. The fast decrease of D_z at the start of the calculation was facilitated by the artificial decrease of the vertical component of the velocity of Cu atoms that approached the metal atoms or graphene to a definite distance.

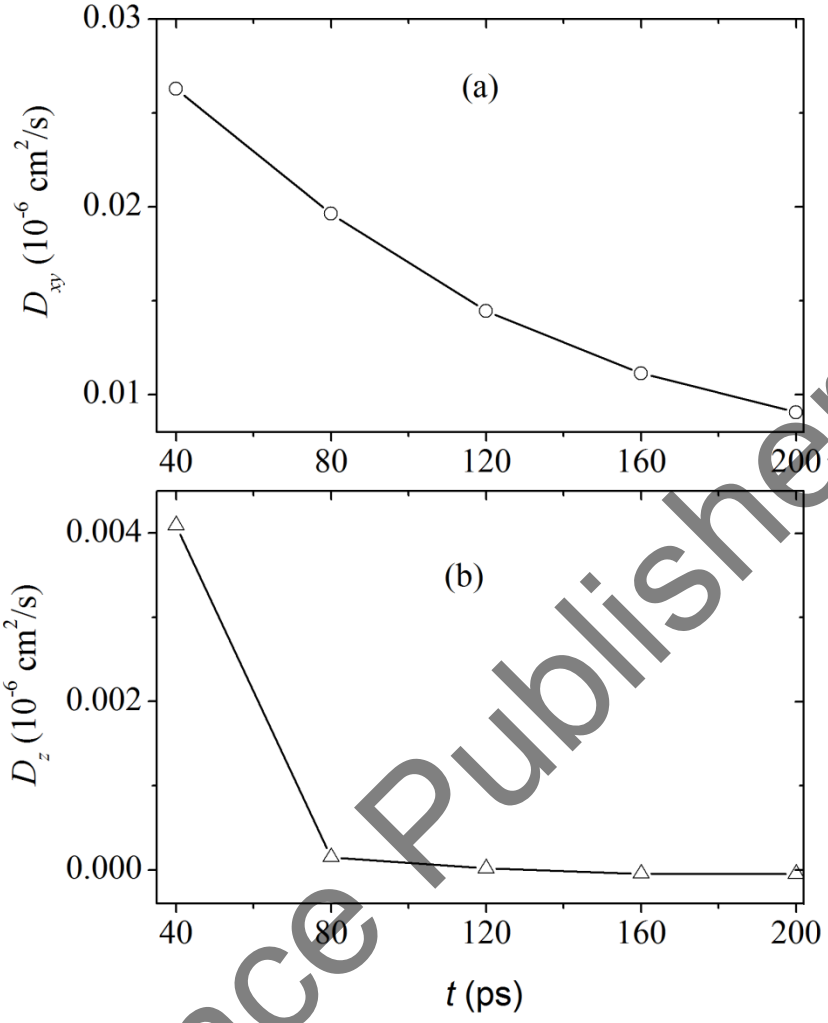

Figure 17. (a) Horizontal and (b) vertical components of the self-diffusion coefficient of the copper film on graphene.

The stresses in the deposited metal film are shown in Figure 18. Since the metal film is not fixed on the opposite graphene sides, the sign of the stress component is determined only by the dominant direction of the internal forces that the forces refer to this component. Thus, the component sign does not determine the character of the stress (e.g., compression or extension). Here, the stressed state is characterized by the absolute value of the internal stresses. The most significant changes in the behavior of the functions take place within the initial time period (below 80 ps) of the deposition of the metal atoms. The metal atoms have the maximum mobility at this time (both the horizontal and vertical components of the self-diffusion coefficients are maximum). At the instant 40 ps, the stresses σ_{zz} caused by the vertical forces become critical; they exceed σ_{zx} more than threefold and σ_{zy} more than tenfold. The stresses in the metal film are mainly caused by the stronger metal–metal

interactions. The metal–carbon interactions make a small contribution to this characteristic. After the fast decrease in the absolute values of $\sigma_{\alpha\beta}$ until the instant 80 ps, this characteristic continues to decrease, but at the significantly slower rate. At the instant 200 ps, the absolute values of σ_{zx} and σ_{zy} are minimal, while the minimum absolute value of σ_{zz} appears at 160 ps.

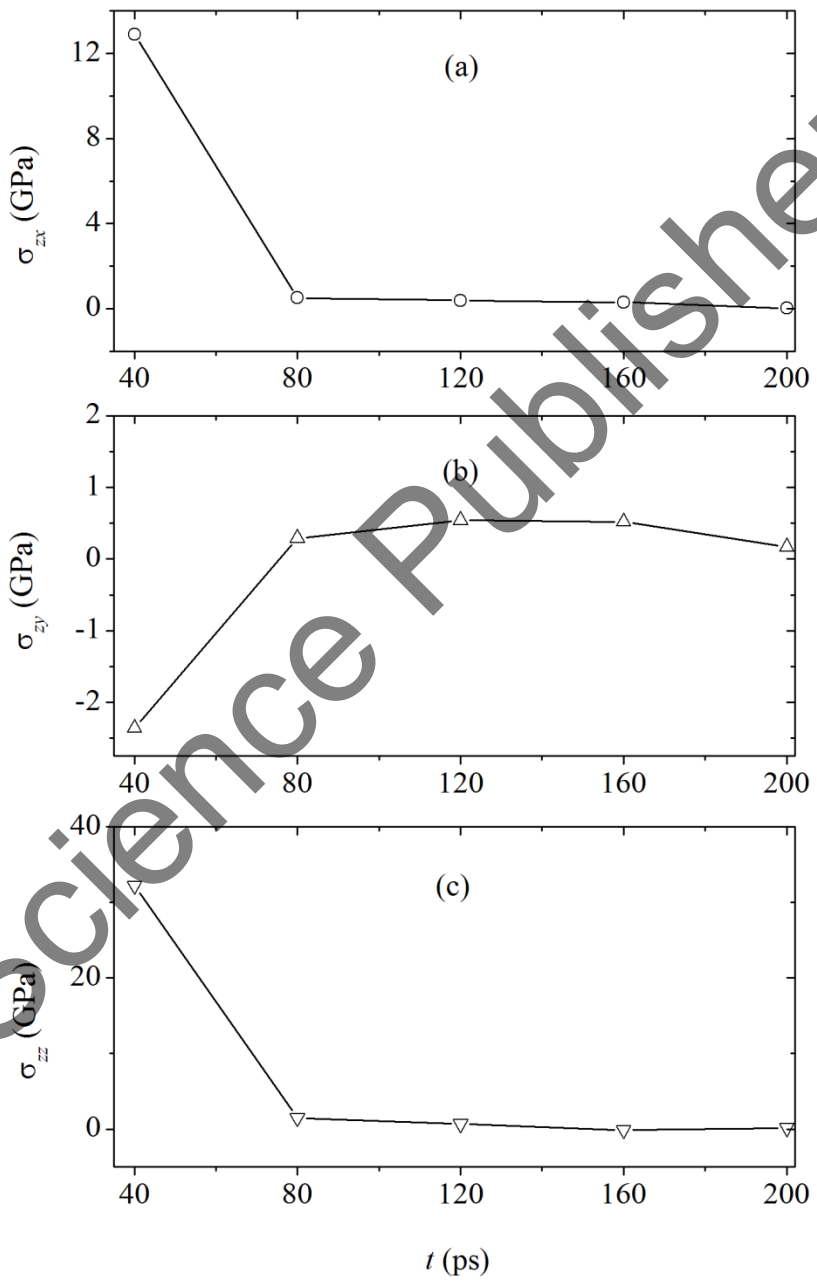

Figure 18. Stresses in the *xy* plane of the copper film adsorbed on graphene: (a) σ_{zx}, (b) σ_{zy}, and (c) σ_{zz}.

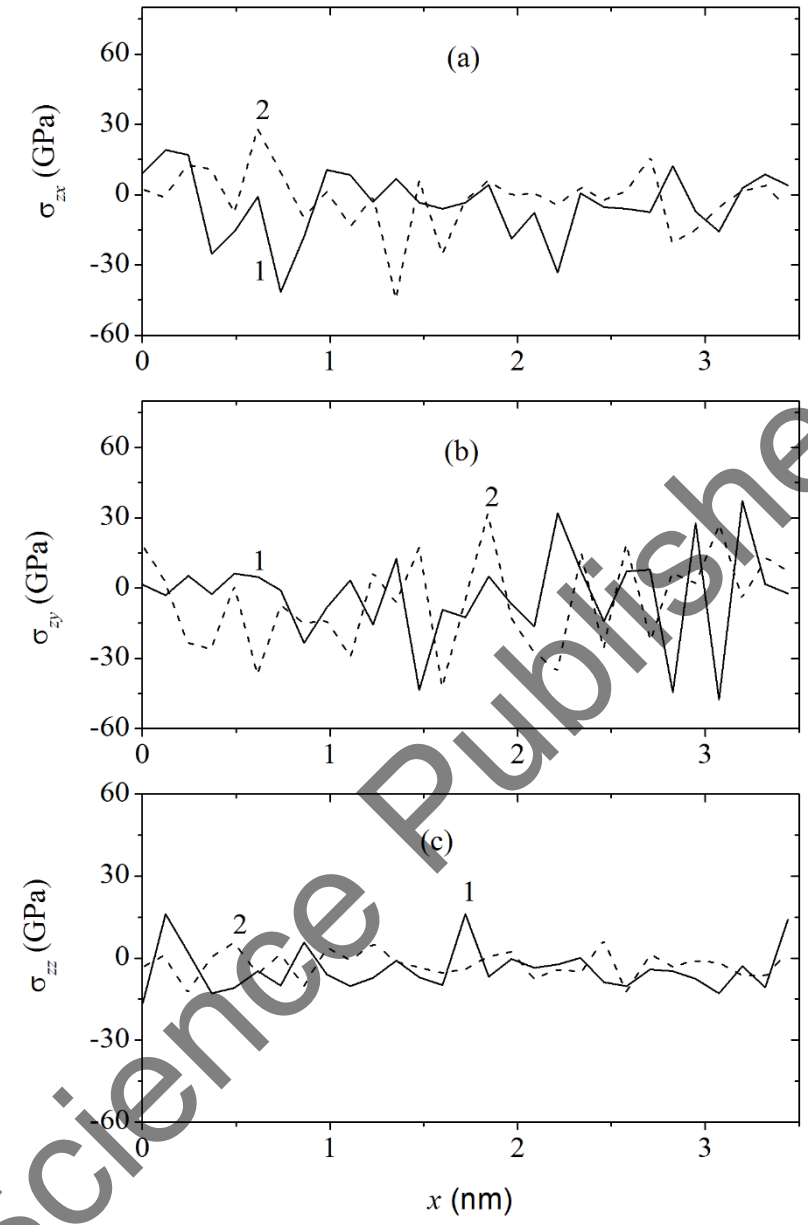

Figure 19. Distribution of stresses along the "zig-zag" direction in graphene: (a) σ_{zx}, (b) σ_{zy}, and (c) σ_{zz}; (1) graphene sheet with the copper film deposited on it and (2) free-metal graphene sheet; the distributions correspond to the instant 200 ps.

It was interesting to compare the distribution of stresses in the pure graphene sheet (free from the metal) with that in the graphene sheet with the copper film. The distribution of σ_{zx}, σ_{zy}, and σ_{zz} in the plane of the graphene sheet created by the rows of atoms in the *y* direction ("armchair" one) for the motion in the *x* direction ("zig-zag" one) is shown in Figure 19. It is seen that the copper film enhances the stress created by the forces in the

plane of the graphene sheet insignificantly (σ_{zy}), or even decreases (σ_{zx}). The maximum absolute value of σ_{zx} decreased by 6.2% with respect to the corresponding values for metal-free graphene for the forces that acted in the "zig-zag" direction. However, simultaneously the similar value of σ_{zy} increased by 12.5% for the forces that acted in the "armchair" direction. Note that due to the presence of the metal film, the number of high-stress (with $|\sigma_{zy}| > 30$ GPa) zones in graphene increased from three to five. The appearance of the metal film affected most significantly the stress σ_{zz} created by the forces perpendicular to the plane of the graphene sheet. Presence of the Cu film increased the maximum amplitude of σ_{zz} by 35.9%. However, the σ_{zz} stresses were 2.8-fold lower than the most significant stresses σ_{zy} .

The radial distribution functions show changes in the structure of the formed copper film (Figure 20). This spherically symmetric function was constructed for one Cu atom, which was the closest to the center of mass of the metal film. The function obtained at the instant 40 ps reflects the loose planar random atomic packing. The first peak of the function is doubly split and localized at 0.33 nm. This value exceeds the distance between the closest neighbors (0.255 nm) in the copper crystal. The second peak of this function is divided into three subpeaks, the most intense of which lies at the distance of 0.57 nm. At the instant 120 ps, a copper film with a denser structure forms on graphene. The single split first peak of the function $g(r)$ is increased by 31% in intensity and shifted toward the smaller distances (to 0.25 nm). The copper film with irregular dense structure finally formed on graphene at the instant 200 ps. The first peak of the function was not split and its intensity increased 2.4-fold compared to that at 40 ps. The position of this peak corresponds to the distance of 0.25 nm, which is in good agreement with the shortest distance in the copper crystal. The intensity of the second peak of this function also increased by the large amount (1.8-fold) with respect to the height of the second peak of the function at 40 ps. At t = 200 ps, the second peak of the function still remained doubly split, but the ratio of intensities of the subpeaks changed. The peak was recorded at 0.48 nm; i.e., it considerably shifted toward the short distances. All the structural features suggest a dense cluster-like atomic packing in the film with the retained medium-range order (at distances $r \leq 1$ nm).

Formation of the stable copper film on graphene was studied by the molecular dynamics method. The film grew in two stages. At the first stage, the Cu atoms occupied advantageous sites over non-adjacent hexagonal cells of graphene. At the second stage a cloud of randomly distributed metal atoms was deposited on the graphene surface partially occupied by copper ones. The addition of copper atoms to the film led to an insignificant decrease in its size in the "zig-zag" direction of graphene and to the expansion of the film in the "armchair" direction. The horizontal component of the self-diffusion coefficient gradually decreased with time. The vertical component exhibited a crucial reduction at the

first stage of film formation and further slowly decreased with time. The stresses in the plane of the Cu film parallel to the graphene sheet fast decreased at the start of film formation and slowly changed thereafter. The distribution of the similar stresses in graphene shows that the formed metal film has an insignificant effect on the mechanical properties of graphene. The stress regions were especially strengthened by the forces that acted along the normal to the surface. The radial distribution function reflects the presence of the medium-range ordering in the copper film formed on graphene.

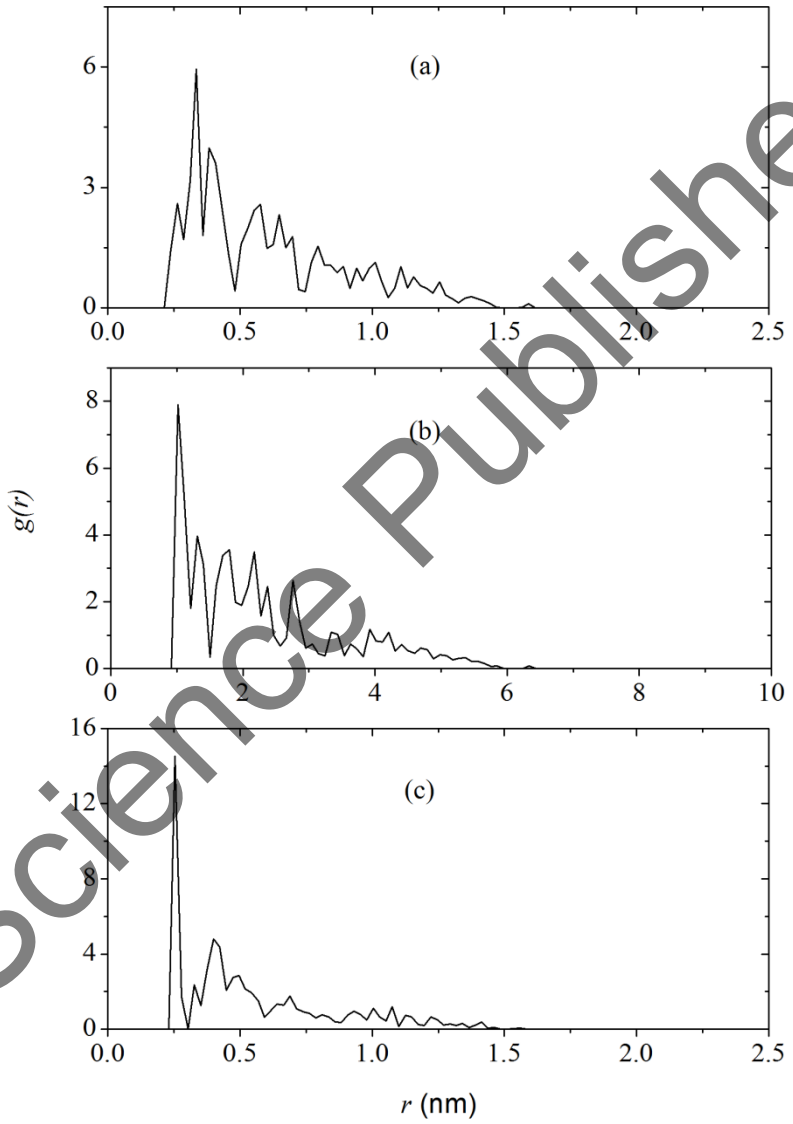

Figure 20. The radial distribution function of the copper film on graphene corresponding to the instants (a) 40, (b) 120, and (c) 200 ps.

4.2. COMPUTER ANALYSIS OF COPPER FILMS STABILITY ON GRAPHENE

The stability of three types of copper films on graphene (having dimensions 3.4 × 4.0 nm and 406 C atoms) was studied in [269]. The first copper film was the (111) plane of the fcc copper crystal and was formed of 208 Cu atoms. The film was initially placed at the middle of a graphene sheet at the equal small (of the order of the Cu atom diameter) distances from the opposite edges of the sheet. The structure of the second film corresponded to the (100) plane of the copper crystal and had only 49 atoms. It was also placed at the middle of the graphene sheet. Its size was chosen such that the number of metal atoms corresponded to the number of Cu atoms in the third film (49 as maximum). The arrangement of Cu atoms in the first two films was not correlated with the structure of graphene. The initial arrangement of Cu atoms in the third film was a monolayer in the form of a loose (111) plane of the fcc lattice (parallel to the graphene plane) with the distance between the nearest atoms $r_{\mathrm{Cu-Cu}} = 0.6507$ nm. The Cu atoms were right opposite to the centers of the non-adjacent hexagonal cells formed by the carbon atoms. The shortest distance between the C and Cu atoms $r_{\mathrm{C-Cu}} = 0.2243$nm corresponded to the distance $r_{\mathrm{C-Cu}}$ calculated in terms of the density functional theory [270]. In a bulk copper crystal, $r_{\mathrm{Cu-Cu}} = 0.2556$ nm. Consequently, the Cu film was initially stretched because of the incompatibility of the lattice constants of graphene and copper. The shortest distance between the C atoms in graphene was $r_{\mathrm{C-C}} = 0.142$ nm. The equations of motion were integrated by the fourth order Runge–Kutta method with a time step of $\Delta t = 0.2$ fs. The calculation time was $10^6 \Delta t$ or 200 ps for each temperature. The calculations were started at 300 K. After every million time steps, the temperature of the system was raised by 500 K, and the next calculation was performed with the same duration. The last calculation corresponded to the temperature 3300 K. The temperature in the model was maintained with the Berendsen thermostat [62].

The close-packed copper monolayer was placed on the surface of graphene in such a way that none of the atoms characterized by the size $r_0^{\mathrm{Cu}} = 0.2277$ nm [271] (r_0^{Cu} is the Lennard-Jones parameter) went beyond the limits of the graphene sheet. The arbitrary arrangement of the copper film with respect to the carbon atoms was justified by the fact that the lattice constants of the metal film and graphene were incompatible. As a result, the coordinates of the centers of all 208 Cu atoms that formed the (111) plane were within the area of the graphene sheet that contained 406 C atoms. However, the Cu (111) plane (that was stable in a bulk copper crystal and had the shortest interatomic distance of 0.256 nm) proved to be unstable when placed on the graphene sheet. The atoms of this plane initially started to move in horizontal directions in parallel to the graphene plane.

As a result, the Cu (111) plane expanded. The terminal Cu atoms that went beyond the limits of the graphene plane lost support from graphene and abandoned the sheet (Figure 21). At the instant of 200 ps, the Cu atoms lying over graphene did not form a regular packing any longer. The majority of these atoms rose over the graphene sheet and only the insignificant number of them remained in the plane parallel to the graphene sheet. Thus, the close-packed copper film proved to be unstable on the graphene sheet already at 300 K.

The arrangement of the 49 Cu atoms of the (100) facet of the copper crystal in the central part of the graphene sheet did not lead to deviation of the metal atoms from the sheet at the instant 200 ps. However, the nearly horizontal metal film was no longer the (100) facet of the copper crystal; it had a loose structure, which was more likely to be disordered. The film proved to be unstable against heating; nearly half of all Cu atoms quit it already at 1800 K. Thus, the lack of coordination between the Cu atoms packing in the film and the graphene structure led to instability of the film; i.e., the effect of graphene on the state of the metal film was rather significant. The energy of the copper–graphene interaction $E_{\mathrm{C-Cu}}$ for this film at T = 300 K was 22.2% of the energy of the copper–copper interaction $E_{\mathrm{Cu-Cu}}$ (– 0.28 eV, while the starting energy was $E^{\mathrm{init}}_{\mathrm{Cu-Cu}} = -2.4$ eV); for the first film, it was 0.3% of the corresponding $E_{\mathrm{Cu-Cu}}$ (– 2.8 eV) energy.

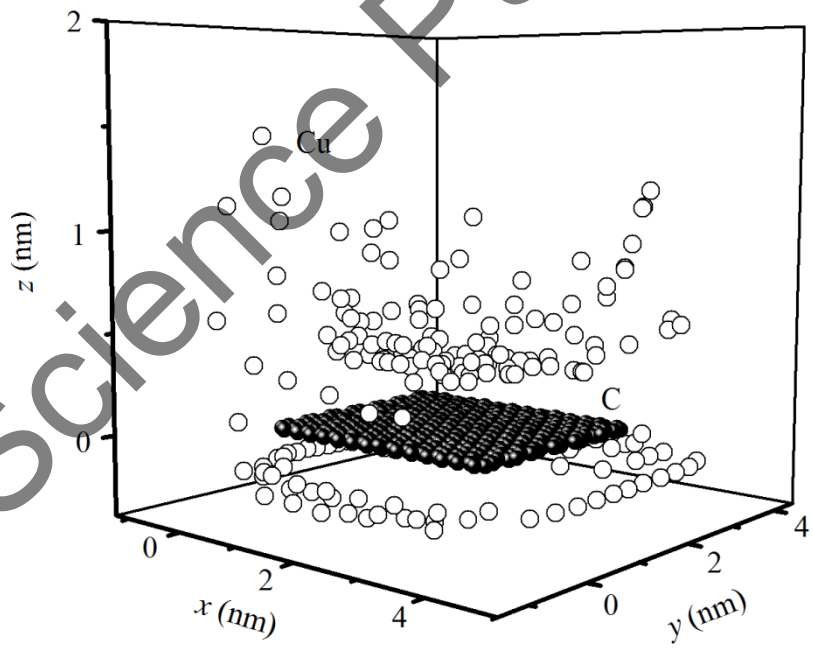

Figure 21. Configuration of the system of a copper film on graphene where the film is a close-packed (111) plane of Cu crystal at the instant 200 ps.

The structure of the Cu film formed from 49 atoms (initially placed opposite to the centers of the non-adjacent honeycombs of the 406-atomic graphene sheet) was also loose, but slightly less planar form. At the instant 200 ps at 300 K, the Cu atoms assembled into three similarly orientated serpentine lines in the middle part of the graphene sheet. At 3300 K, the Cu atoms formed an elongated dense drop whose acute apex was "closed" by a serpentine line of 10 atoms. At the instant 200 ps under this temperature, six atoms in the metal film rose above the other atoms to a distance of the order of the distance from the drop to graphene. At 300 K, the energy E_{C-Cu} was 3.3% of the energy E_{Cu-Cu} (– 1.96 eV) for this film. Thus, the Cu film formed in accordance with the graphene structure showed the highest thermal stability among the films under study.

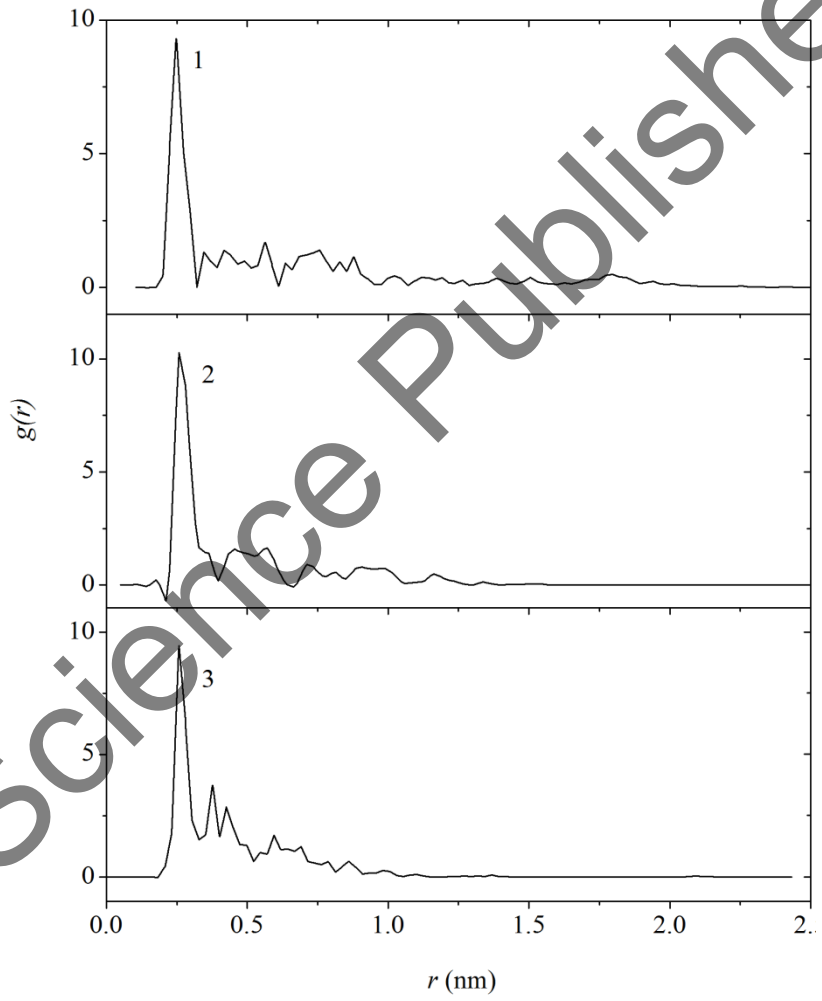

Figure 22. Radial distribution functions (calculated for the central atom) of various Cu films on graphene: (1) close-packed (111) plane of copper, (2) (100) plane of copper, and (3) elongated (111) plane of copper, whose atoms occupy non-adjacent cells of the graphene lattice.

The radial distribution functions $g(r)$ of three above-described types of the copper film on graphene are presented in Figure 22. All these functions have the high first peak. It reflects the presence of the short-range ordering in the films or, more exactly, shows that the Cu atoms in the films tend to lie at approximately the same shortest distance from one another. With a good accuracy this distance agrees with the distance between the nearest neighbors in the copper crystal. The other peaks of the function $g(r)$ reflect the structure with the medium-range ordering. In other words, they show how the neighbors are located around the central atom at distances of up to ~ 1 nm. At distances r > 1 nm, the functions $g(r)$ for the films damped almost completely; i.e., there is no long-range ordering here. According to the shape of the functions $g(r)$ shown in Figure 22, the model films differ in the medium-range order. The third film exhibits the highest stability against heating; even at 3300 K, approximately ~ 2/3 of all of its Cu atoms remained in the film forming the bound structure.

The kinetic and mechanical properties of the third Cu film (formed under the allowance for the graphene structure) were studied in the form of the components $D_{\leftrightarrow}$ and $D_{\updownarrow}$ of the self-diffusion coefficient and nine components of the stress tensor $\sigma_{\alpha\beta}$. The horizontal component $D_{\leftrightarrow}$ (curve 1) of the self-diffusion coefficient of Cu atoms tends to decrease as the temperature increases, while the vertical component $D_{\updownarrow}$ (curve 2) tends to increase (Figure 23). The decrease in the values is caused by the gradual approach of Cu atoms, i.e., by the densification of the film because its initial packing density did not correspond to the stable state at the given temperatures. The increase in $D_{\updownarrow}$ at elevated temperatures is explained by the increased mobility of atoms in a direction that is open for their motion. The increase in $D_{\leftrightarrow}$ at T = 1300 K may be interpreted as reaching the melting point in the Cu film because the melting temperature of the bulk copper is 1357 K. The decrease in $D_{\leftrightarrow}$ at 800 and 2800 K may be regarded as fluctuations caused by the adjustment of the film structure to the graphene one.

The film formed by Cu atoms and arranged in a honeycomb structure experiences considerable stresses, the greatest of which at 300 K are σ_{xx}, σ_{xy}, and σ_{yy} (Figure 24). These components of the stress stay longer in the metal film as the stress temperature increases. As the temperature increases, all stresses dissipate. The interaction of Cu atoms with graphene affects the film structure; i.e., the film becomes structured in accordance with the crystal directions in graphene. If the stresses in the film are considered with respect to the directions of the graphene sheet, then we can conclude that the long-living stresses are those in the regions perpendicular to the “zig-zag” and “armchair” directions, including the “zig-zag”– “armchair” and “armchair”– “zig-zag” variants.

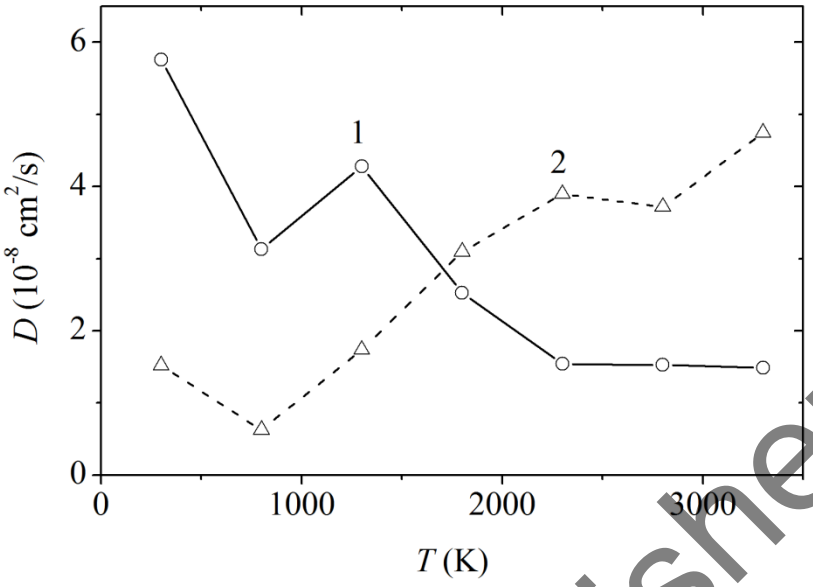

Figure 23. The (1) *xy* and (2) *z* components of the self-diffusion coefficient of the elongated copper film on graphene whose atoms initially occupy non-adjacent cells in the graphene.

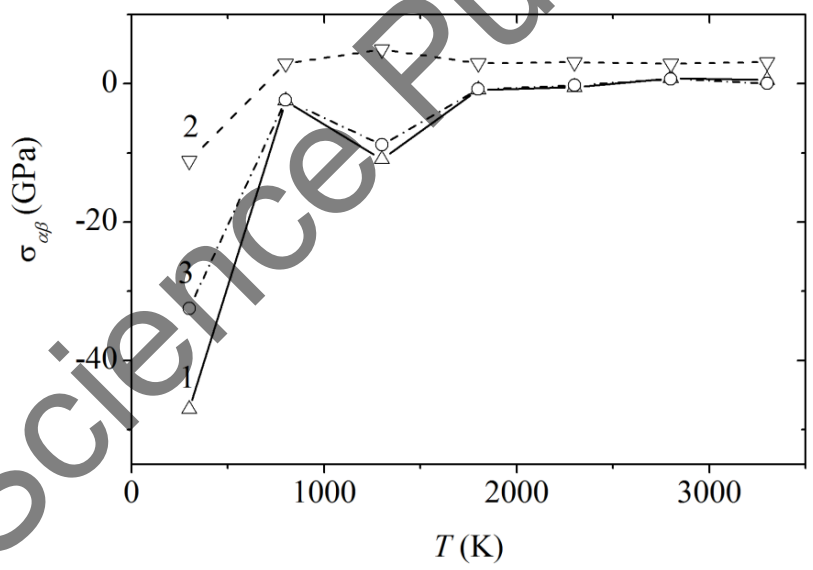

Figure 24. Most significant stresses in the elongated copper film on graphene: (1) σ_{xx}, (2) σ_{yy}, and (3) σ_{xy}.

Thus, the thermal stability of the monolayer copper film on graphene is considerably affected by the agreement between the arrangement of Cu atoms and ones of the graphene structure. In addition, the stresses in the metal film are determined by the crystallographic directions of graphene.

4.3. COPPER FILM ON A HEATED GRAPHENE SURFACE

Let us first consider some experimental results of the interaction of graphene with the copper substrate. The tensile strength and strain to failure of the chemical vapor deposition (CVD) graphene are 2 − 3 GPa and 0.2 − 0.3% of strain, respectively [272]. Such brittle fracture may also occur in the roll-to-roll (R2R) processing of the CVD graphene. Effects resulting in graphene cracking may be modulated by the behavior of the interface between the graphene and copper and the degree for sliding. For example, when a polymer film with graphene transferred, it was experienced to small strains (< 0.5%), the deformation through the thickness of the bi-layer was uniform [182, 273−276]. However, at larger strains, there was slippage between two films [273−275]. It was also observed that tiny graphene delamination was induced when the stretched film was released [274]. In [277], a method was developed to study the tensile response of graphene grown on the copper foil. *In situ*, the scanning electron microscope tensile testing established that graphene cracked at relatively low levels of applied strain(~ 0.44%) and formed new wrinkles parallel to the loading direction. The graphene began to develop the channel cracking at the applied strain level of almost 0.5% and doubles the yield strength of the annealed seed copper. The crack spacing decreased with increasing the applied strain until saturation occurred at the level about 6%. In addition, pre-existing wrinkles tended to arrest channel cracks. One of the reasons for this was that the adhesion interaction between graphene and copper foil is stronger than that of the interlayer graphene.

Graphene synthesized with chemical vapor deposition is polycrystalline. Note that a grain boundary (GB) is the interface between crystalline regions of different lattice orientations. A triple junction (TJ) is the intersection of three such interfaces. In the graphene, the GBs and TJs are typically composed of the pentagon-heptagon defects. As a rule, pairs of such defects are called the five to seven defects [11]. Defects of this type involve significant residual stresses and act like stress concentrators. Preliminary (before applying the metal film to graphene), we created four paired defects of 5 – 7 types along the "zig-zag" direction of the graphene sheet. Thus, we crossed the entire graphene sheet with the inter-grain boundary. After heating a graphene sheet coated with a copper film, a crack is formed just along the grain boundary.

In the initial state, Cu atoms were disposed above the centers of hexagonal cells formed by the C atoms; in this case, each of the adjacent carbon cells was missed in both the longitudinal and transverse directions. The geometric parameters of the model and the calculation procedure were identical to those described in Section 4.2. Similar calculations were performed for two-layer graphene. The graphene sheets were arranged according to the Bernal packing (ABAB…) exactly in the same manner as is the case in the bulk graphite. The distance between the graphene sheets was taken to be the value predicted in the density functional approximation (0.3347 nm) [278]. The interaction between the C atoms belonging to the layers A and B was considered to be based on the

application of the LJ potential with the parameters [279] given in Table 6. A graphene sheet containing 210 atoms was expanded in horizontal *x* and *y* directions due to applying the periodic boundary conditions. The action of the periodic boundary conditions was also applied to the metallic film. In the vertical *z* direction, the boundary conditions were free. At T = 300 K, the calculated energy of the copper–graphene interaction is – 1.4 eV. In the temperature range 300 K $\leq T \leq$1300 K, the heat capacity c_v of the single layer graphene (calculated from the fluctuations of the kinetic energy) increases from 19 to 28 J/(mol K). This corresponds to the experimental values of this quantity (23.74 – 26.80) J/(mol K) [280].

The initial arrangement of Cu atoms on the graphene sheet is optimal from the standpoint of their interaction with the substrate. It is not an equilibrium for the metallic system with a regular atomic packing at the temperature of 300 K [281]. So, even at this temperature, the atoms significantly approach each other. As a result, the metallic film size decreases, and this reduction is more substantial in the transverse ("armchair") direction as compared to the longitudinal ("zig-zag") one (Figure 25). Determination of the film size is related to the determination of the average *x* and *y* coordinates of three edge non-evaporated Cu atoms. We consider atoms to be evaporated if they are spaced at more than 0.3 nm from all other atoms. As the temperature increases, there are some oscillations in the size reduction in the "zig-zag" direction. However, the film size almost monotonically decreases in the "armchair" direction. At any temperature, the size decrease in the "armchair" direction exceeds the decrease of the film length in the "zig-zag" direction. At temperatures of 1300 K and higher, the film size decreases due to both approaching metallic atoms in the *xy* plane and their evaporation (displacements in the *z* direction). The longitudinal film size of two-layer graphene decreases more smoothly as the temperature increases. The transverse size decreases not so fast as in the case of the single-layer graphene. As a result, at T = 3300 K, the length of the metallic film more significant decreases in the "zig-zag" direction for the two-layer graphene and in the "armchair" direction for the single-layer graphene. In [240], the molecular dynamics model of a two-dimensional hexagonal lattice (using the Brenner potential [152]) was used to study the melting of a graphene nanoribbon. The removal of atoms from the ribbon (continuing with increasing the calculation time and the formation of voids at T = 3400 K) was interpreted as the melting of the graphene. However, the MC method using the LCBOPII potential [248] and the two-dimensional Lindeman criterion gives the significantly higher (4900 K) melting temperature of graphene.

The transition of the metallic film to the liquid state is accompanied by the concentration of the majority of Cu atoms predominantly in the central region of the graphene sheet (Figure 26). In this case, the main part of atoms is assembled as a flat droplet of rounded form. Such a pattern is observed at the lower temperature (1300 K) as compared to the melting temperature of the bulk copper crystal (1356 K). In this state, two longitudinal cracks (from the center to the edges) formed in the graphene sheet. These

cracks formed at the grain boundary of polycrystalline graphene. At T = 1300 K, the Cu atoms are no longer arranged in the *xy* plane, but they have displacements in the *z* direction (both up and down). The displacements do not lead to appearing the significant distances of the Cu atoms from the main material of the metallic film or graphene sheet. It is the state, in which the penetration of a Cu atom to another side of the graphene sheet is observed for the first time. At the temperature of 1800 K, individual Cu atoms begin to evaporate up. The boiling temperature of the massive liquid copper is more than 1000 K higher than this temperature (2840 K). The evaporation (along with the penetration of Cu atoms to another side of the graphene sheet) becomes crucially more intense at the temperature of 2300 K. However, at T = 2800 K, Cu atoms approach closely to each other and are forced against the graphene sheet. But at T = 3300 K, the evaporation and the penetration of the Cu atoms to another side of the graphene sheet become more intense once again. Presence of another graphene layer changes the behavior of the Cu atoms deposited on the first layer as the temperature increases. In this case, the cracks in the graphene sheet sufficient for the Cu atoms to penetrate are formed even at T = 800 K. The atoms penetrated are attracted by the second graphene layer and remote from the first layer to larger distances than in the case of the single-layer graphene. However, in none of the cases, even at T = 3300 K, the Cu atoms do not penetrate through the second graphene layer. More likely, the Cu atoms penetrating through the first graphene layer are merely accumulated in the gap between the graphene layers because both the layers equally attract them.

The existence of the second graphene layer significantly increases the Cu atom mobility in the *xy* plane and, at high temperatures, decreases it in the *z* direction (Figure 27). The mobility of Cu atoms in the vertical direction in the case of the two-layer graphene is higher than in the case of the single-layer graphene only to the temperature T = 1300 K. In the case of the single-layer graphene, the maximum of the self-diffusion coefficient D is at the temperature of 2300 K in both the *xy* displacements and the motion in the *z* direction. For the two-layer graphene, the maximum of D_{xy} corresponds to the temperature of 2800 K, and the maximum of D_z corresponds to a temperature of 1300 K.

Because the temperature of 1300 K is close to the melting temperature of copper, we should expect the extrema in the dependence $D_{xy}(T)$. During collecting Cu atoms into a droplet on the single-level graphene, the coefficient D_{xy} first increased (Cu atoms were accelerated due to the forces of mutual attraction) and then decreased (at T = 1300 K). The atomic mobility decreases due to the increase in the density of the two-dimensional liquid metallic droplet. Further increase in the temperature leads once again to increase in the horizontal mobility of atoms because of their motion beyond the *x* and *y* boundaries of the sheet and in the vertical direction. Up to T = 2300 K, the larger contribution to the value

of D (for both directions) is that of atoms moving up and moving away from the sheet surface; another smaller part of atoms moves to the sheet surface.

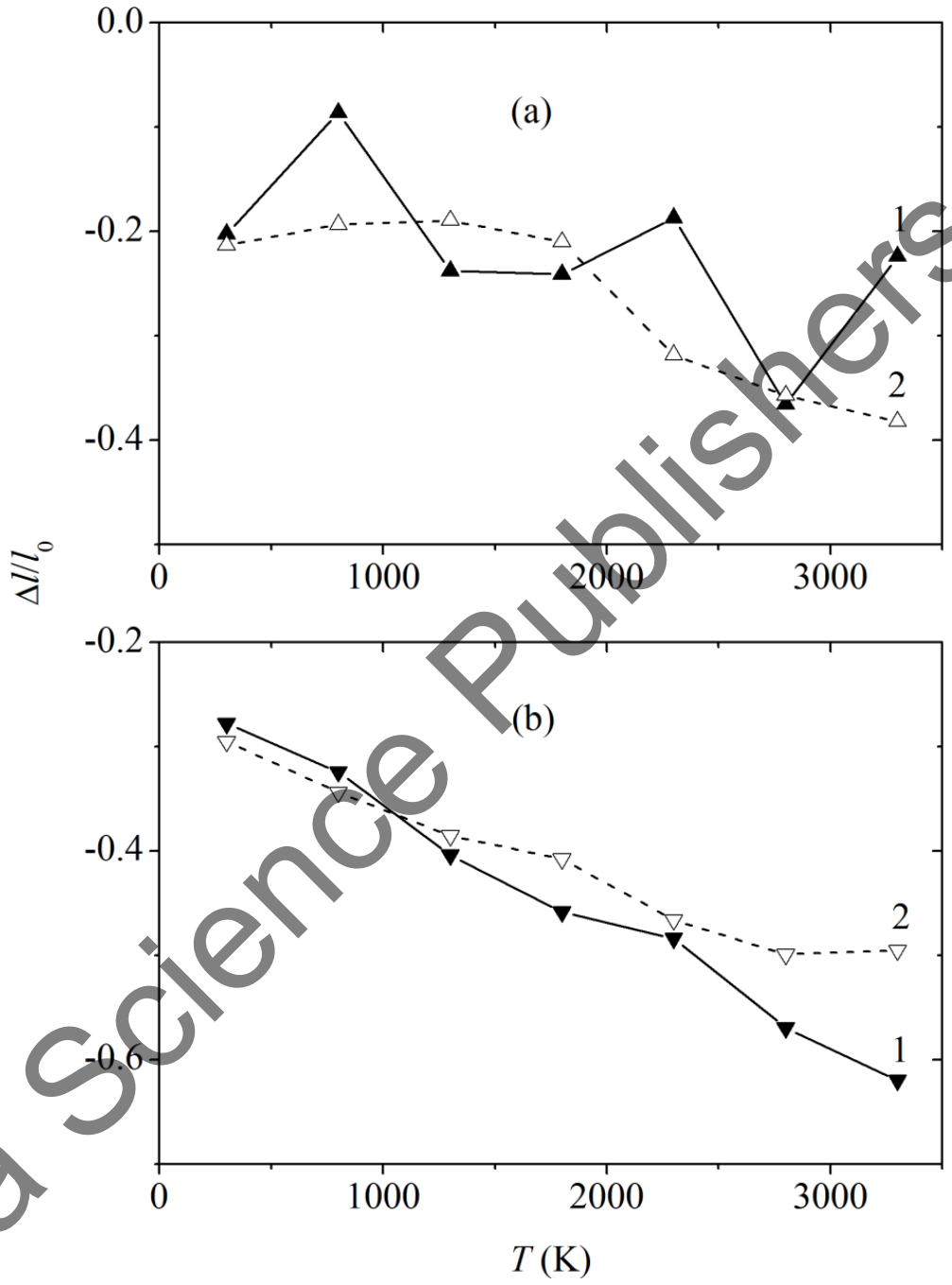

Figure 25. Relative change in the copper film size in (a) the longitudinal and (b) transverse directions vs. temperature for the cases of (1) single-layer and (2) two-layer graphene.

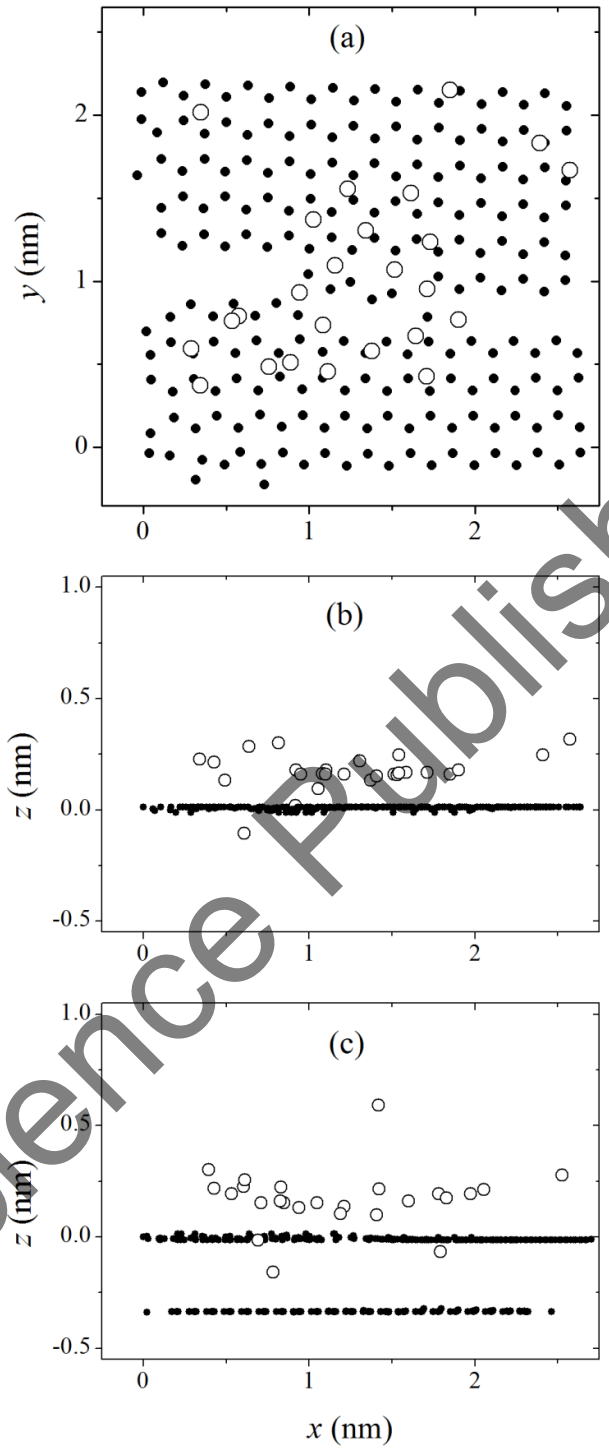

Figure 26. (a) *xy* and (b) *xz* projections of the copper film on single-layer graphene calculated for the temperature 1300 K corresponding to the instant 100 ps; (c) *xz* projection of the configurations of the copper film deposited on the two-layer graphene corresponding to the same temperature and instant; the open circles are the copper atoms, and closed circles are the carbon ones.

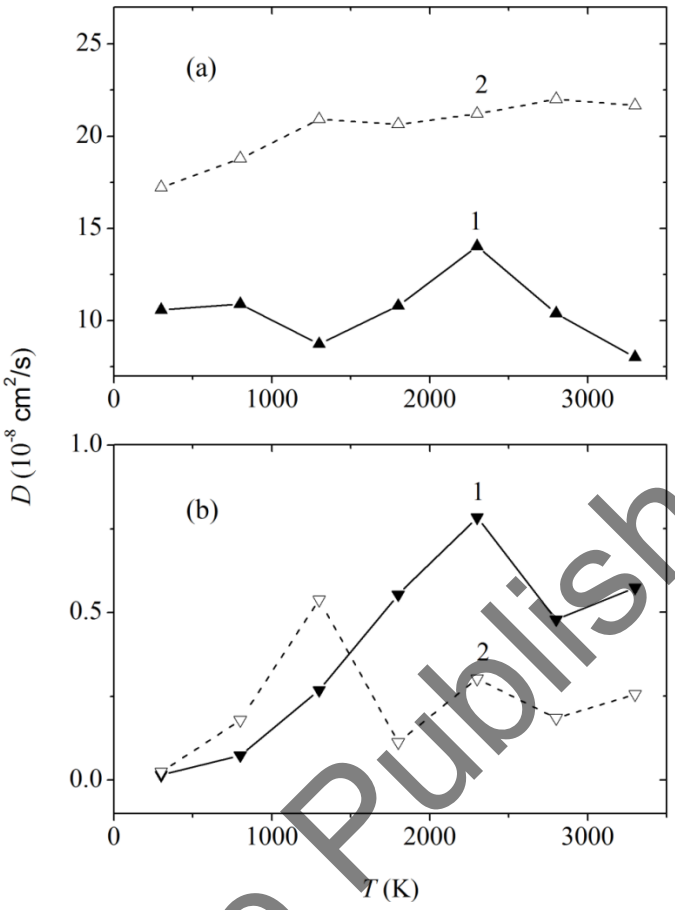

Figure 27. Self-diffusion coefficient of copper atoms in (a) the horizontal plane and (b) the vertical direction: (1) on single-layer graphene and (2) on two-layer graphene.

First, their contribution to the coefficient D is relatively small. When the temperature becomes higher than 2300 K, Cu atoms begin to be significantly slowed down by the carbon atoms meeting with them. As a result, the coefficients D_{xy} and D_z decrease, and the main maximum appear in the dependences 1 depicted in Figures 27a and 27b.

The coefficient D_{xy} of Cu atoms disposed above the two-layer graphene has slightly observed maxima at T = 1300 and 2800 K. On the one hand, these extrema are due to approaching the atoms to each other and their collection into a liquid droplet which is damaged as the temperature increases. On the other hand, it is stipulated by the variation of the proportion of the contributions of the vertical atomic displacements in the opposite directions. This variation is clearly observed in dependence 2 (Figure 27b) that demonstrates the oscillating behavior with the maxima at 1300 and 2300 K. The minimal value observed in the dependence $D_z(T)$ at T = 2800 K (Figure 27b) can be explained by the passage through the boiling point in the model followed by increase in the Cu atom mobility with temperature.

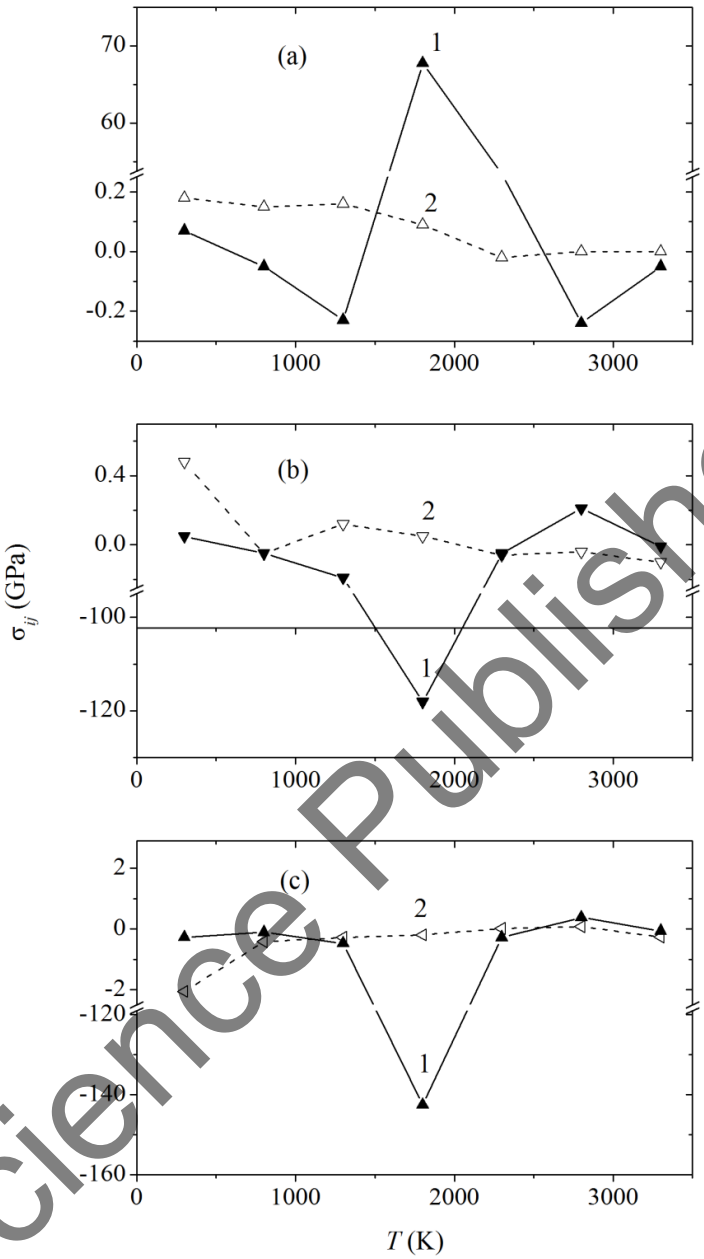

Figure 28. Stress tensor components (a) σ_{zx}, (b) σ_{zy}, and (c) σ_{zz} of the copper film deposited on (1) single-layer graphene and (2) two-layer graphene.

Stress tensor components σ_{zx}, σ_{zy}, and σ_{zz} characterize the action of the coordinate components of the force in the *xy* plane for the Cu film on the single-layer and two-layer graphene. These components undergo substantially different changes with variations in the temperature (Figure 28). In the case of the single-layer graphene, the temperature dependences of these parameters are complex.

However, all the temperature dependences of the components have a general feature; namely, a sharp extremum at T = 1800 K. At this temperature, the copper atoms form dense aggregates in the central part of the graphene sheet at places of disposing the bridges between the cracks. Therefore, the high stresses can be transmitted to the metallic film from the crack of the graphene sheet.

At all other temperatures, these stress components for the single- and two-layer graphene have commensurate values. At the highest temperature (T = 3300 K), the difference in the values of corresponding components (for the cases of the single- and two-layer graphene) is noticeably smaller than that at the lowest temperature (T = 300 K).

Thus, the copper atoms (initially regularly arranged in the interstitial sites of the single- and two-layer graphene) form the instable metallic film, which tends to decrease its size. The Cu film size decreases most significantly in the transverse ("armchair") direction in both the single- and two-layer graphene. Heating the film stimulates the decrease in its initial sizes. At high temperatures, the film is contracted due to approaching the Cu atoms to each other and due to the evaporation of Cu atoms from the substrate.

The graphene cracking in the model was caused by the strong adhesion between the copper film and graphene and the contraction of the initially non-equilibrium metal film. The increase in temperature accelerated the process of graphene cracking. At all temperatures, the copper atoms mobility in the horizontal direction is higher in the case of their deposition on the two-layer graphene. On the other hand, the mobility of the copper atoms deposited on the single-layer graphene in the vertical direction becomes higher from a temperature of ~1500 K. The stress tensor components of the copper film reflecting the action of forces in the horizontal area behave differently in the cases of the film deposition on the single- or two-layer graphene.

4.4. Computer Simulation of Thin Nickel Films on Single-Layer Graphene

The interface between the graphene and metallic substrate is of great importance for the use of graphene in integrated electronics (as heat-insulating materials) and in electromechanical devices including those that need for protecting their microscopic units from aggressive environmental factors. A promising method for producing large graphene areas [146, 282, 283] is the catalytic decomposition of the hydrocarbons on a hot metallic surface. The possibility of the chemical dissolution of the metallic substrate (after the growth of graphene has been completed) provides means for producing the free graphene sheets. Subsequently, the sheets can be transferred to any other substrate.

Nickel is a typical catalyst for the growth of nanotubes and materials used in the formation of the graphene [284]. Carbon atoms are easily dissolved in nickel with the formation of the ordered metastable phase of nickel carbide Ni_2C on the surface [285, 286].

The formation of this coating (Ni_2C) with the thickness of one atomic layer competes with the growth of graphene. In the fabrication of the electronic circuits, it is particularly important to obtain graphene directly on the working surface. The Ni_2C coating is formed by the thermal decomposition of the hydrocarbons at low temperatures. Graphene is predominantly formed at higher temperatures between 750 and 980 K. At still higher temperatures, carbon diffuses deep into the coating.

It is known that transition metal (nickel) has been used for the preparation of the graphene by means of evaporation and subsequent precipitation of the carbon atoms. A method for producing graphene (that does not require heating of the material components to temperatures ~ 1300 K) was proposed in [287]. Therefore, the synthesis of graphene can be performed on a substrate of the material that is not capable of withstanding the intense heating. The essence of this technique is the follows: after drying a nickel–graphite film, a part of carbon atoms diffuses through the natural channels under the nickel component of the film and form the monoatomic layer, i.e., graphene. Then, the upper layers are removed by the chemical method.

The computer model of the nickel film on graphene and the method of calculation was identical to the corresponding model and method for a copper film. The initial packing of the Ni atoms was represented by a mono-layer in the form of a loose (111) plane of the fcc lattice (parallel to the graphene plane) with the distance between the nearest neighbor atoms $r_{\mathrm{Ni-Ni}}$ = 0.6336 nm [288]. In this case, the Ni atoms were arranged directly against the centers of the hexagonal cells formed by carbon atoms. The shortest distance between the C and Ni atoms $r_{\mathrm{C-Ni}}$ = 0.2018 nm corresponds to the distance $r_{\mathrm{C-Ni}}$ calculated in terms of the density functional theory [269]. In the bulk nickel crystal, $r_{\mathrm{Ni-Ni}}$ = 0.2489 nm. Therefore, the Ni film was initially in a stretched state due to the lattice mismatch between graphene and nickel. The temperature in the model was increased by 500 K on every million time steps and was maintained at a predetermined level using the Berendsen thermostat [62].

Here, we consider two systems. We denote by the index I the system where the nickel film was located above the graphene sheet. We also consider system II with two identical symmetrically arranged nickel films with respect to the graphene sheet.

The configuration of graphene at the temperature of 1300 K covered from the top and bottom with nickel is shown in Figure 29. Ni atoms in the upper layer are arranged in the form of a dense drop. The metal atoms located below the graphene sheet are spread such that one part of them adheres to the graphene sheet and the other part is substantially distanced from it. Some of the lower Ni atoms are outside the *xy* boundaries determined by the graphene sheet. A part of these atoms moves upward passing the graphene sheet on the sides.

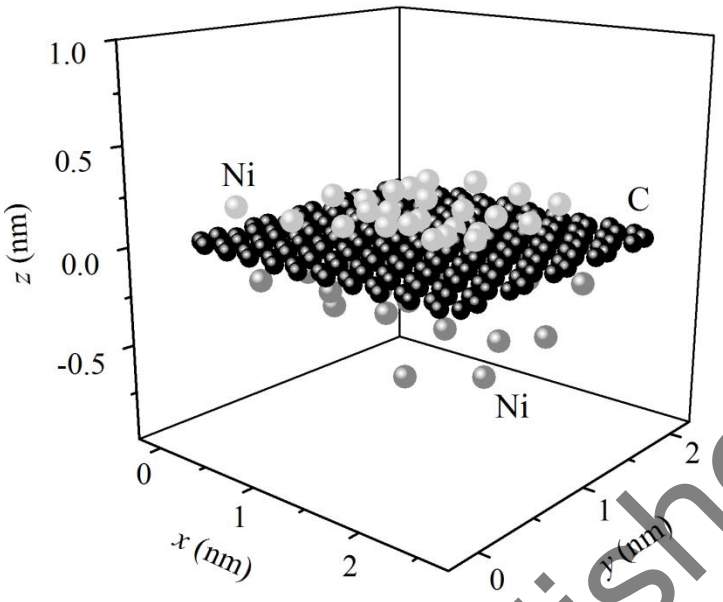

Figure 29. The configuration of the graphene–nickel system with a two-sided arrangement of Ni atoms on the graphene sheet at the instant 200 ps and at the temperature of 1300 K.

The potential energies of the interactions nickel–nickel $U_{\mathrm{Ni-Ni}}$, nickel–carbon $U_{\mathrm{C-Ni}}$, and carbon–carbon $U_{\mathrm{C-C}}$ for systems I and II are shown in Figure 30. The initial arrangement of the metal atoms on graphene does not correspond to the stable crystalline state, because the Ni atoms are located at a considerable distance from each other. The increase of the temperature and the associated enhancement in the mobility of the Ni atoms lead to the structural relaxation of the metallic film. Consequently, we should expect a decrease in the potential energy for the nickel–nickel interactions with the initial increase in the temperature. That was actually observed in both cases. The potential energy $U_{\mathrm{Ni-Ni}}$ decreased already at the temperature of 800 K in the presence of one metallic film on graphene. In the presence of two metallic films, the value of $U_{\mathrm{Ni-Ni}}$ decreased later at T = 1300 K. That was caused by a greater adhesion of the metal to the substrate.

The volume energy of the metal corresponds to the binding energy of the considered element. The experimental value of this energy at T = 300 K for nickel is equal to –4.44 eV/atom [289]. The close value of $U_{\mathrm{Ni-Ni}}$ (− 4.39 eV/atom) for the nickel fcc crystal was obtained from the molecular dynamics calculation in an NPT ensemble [290]. The energy $U_{\mathrm{Ni-Ni}}$ (– 3.70 eV/atom) was also calculated for the Ni_{23} cluster by the molecular dynamics method using the Sutton–Chen potential [291]. This characteristic for a highly stretched nickel film at the considered temperatures has even higher values.

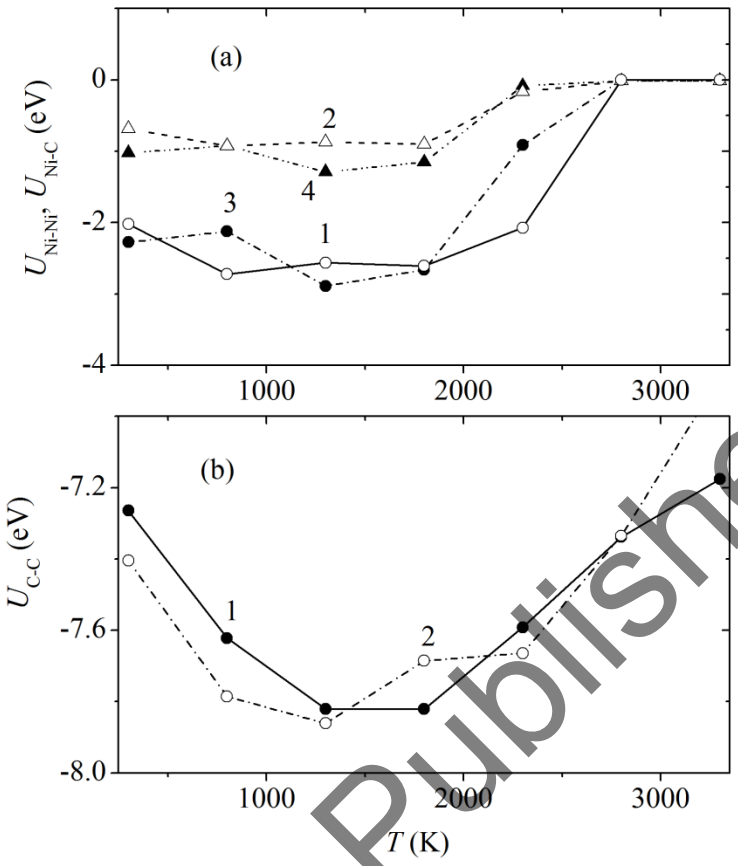

Figure 30. (a) Partial potential energies (1, 3) $U_{Ni–Ni}$ and (2, 4) U_{C-Ni} for different systems: (1, 2) Ni film on one side of the graphene sheet and (3, 4) Ni film on both sides of the graphene sheet; (b) potential energy $U_{C–C}$ for (1) free graphene sheet and (2) graphene sheet covered by the Ni film on one side or on both sides.

A further heating leads to the increase in the energy $U_{Ni–Ni}$ for both systems. This increase is especially evident after the temperature of 2300 K for system I and after the temperature of 1800 K for system II. The dependence $U_{C–Ni}(T)$ for both systems exhibits the similar behavior. However, there is no decrease in the value of $U_{C–Ni}$ under the initial heating of system I and there is a rapid increase in the energy $U_{C–Ni}$ for both systems after reaching the temperature of 1800 K.

The potential energy for the free graphene sheet (in the absence of the metallic film) has the minimum at the temperature of 1800 K (curve 1 in Figure 30b). The temperature dependences $U_{C–C}(T)$ for graphene in the presence of one and two films of the Ni atoms are almost identical (curve 2 in Figure 30b). At lower temperatures ($T \leq 1300$ K), the presence of a transition metal in the system stabilizes the graphene sheet. The energy

U_{C-C} becomes lower than that of the free graphene sheet. This result is consistent with the data reported in [256] where it was shown that the stresses in graphene decrease after the graphene sheet is coated with nickel.

The observed decrease in the energies U_{Ni-Ni} and U_{C-C} after contacting the graphene sheet and the nickel surface (including the nickel cluster) was explained in [292] by a significant attractive interaction between them. Increase in the temperature eventually leads to the increase in the potential energy. Increase in the graphene energy with increasing temperature in the presence of metal atoms occurs more rapidly (after 1300 K) than in their absence. The energies U_{C-C} at T = 3300 K for systems I and II are 4% higher than that for the free graphene sheet.

The temperature relaxation of stresses in the nickel films is illustrated in Figure 31. It is seen that each of the stresses σ_{zx}, σ_{zy}, and σ_{zz} decreases as the temperature increases. In the case where the graphene sheet is covered by one metallic film, it experiences very weak stresses, among which the stress σ_{zz} has the highest value. The strong interaction of nickel films with graphene in system II leads to the development of the significant stresses in the film plane.

The absolute values of the stresses acting in the *xy* plane are always higher in the lower film than in the upper one. This is caused by the smaller thermal stability of the lower film because of the rise of the atoms in the upper film. There is the long-range interaction between atoms in the metal. The Ni atoms of the upper film lift with increasing temperature and "drag" the Ni atoms of the lower film. These atoms change their motion direction encountering the impermeable graphene, and finally acquire the higher velocities. Their further interaction with the lower lying atoms destroys the film.

The initial minimum distance between the Ni atoms in different layers is almost 2.7 times longer than the distance between the nearest neighbors in the bulk metal. Already at the initial temperature (300 K), the stresses σ_{zz} in both the upper and lower metallic films have negative values. This is associated with a significant convergence of the metal atoms with the graphene that separates two nickel films. The positive value of σ_{zz} at T = 300 K for the system I (in the presence of one Ni film on graphene) indicates that, in this case, there is no strong attraction of the Ni atoms to the graphene sheet; i.e., the Ni atoms have a looser packing.

The degree of divergence of the Ni atoms in the horizontal direction can be estimated from the temperature dependence of the elongation (per unit length) of the film in the directions of the *x* and *y* axes (Figure 32). At temperatures below 1800 K, the small effective decrease in the sizes of the films (in the cases of the one and two films on graphene) is observed in both directions. This is caused by the instability of the stretched metallic structures.

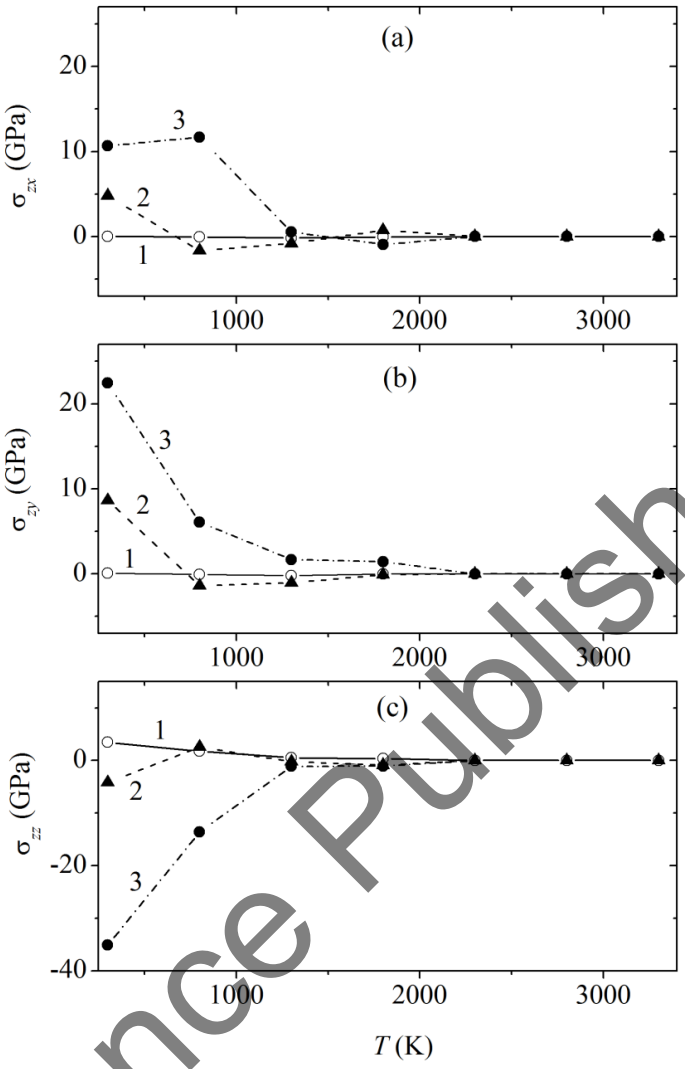

Figure 31. Thermal relaxation of the stresses (a) σ_{zx}, (b) σ_{zy}, and (c) σ_{zz} in the plane of nickel films: (1) Ni film on one side of the graphene sheet, (2) upper Ni film on the graphene sheet with the two-sided coverage, and (3) lower Ni film on the graphene sheet with the two-sided coverage.

Consequently, during the heating, the Ni atoms are pulled together into more compact planar structures. At the higher temperatures, the horizontal lengths of the films increase. The value of $\Delta l/l$ for a single film increases more slowly than that for each of the films in the case of the two-sided coating of the graphene. The increase in the elongation $\Delta l/l$ is caused not only by the thermal expansion but, also, by the melting of the films. Recall that the melting temperature of the bulk solid nickel is equal to 1726 K. According to the molecular dynamics calculation (using the Sutton–Chen potential), the melting temperature of the fcc Ni_{336} cluster is equal to 980 K, whereas the Ni_{8007} cluster melts already at 1380 K [293].

In all the considered cases, the Ni films are most strongly expanded along the *x* axis, which coincides with the "zig-zag" direction in graphene. For example, in the case of the single-sided coating of graphene, the quantity $\Delta l / l$ increases noticeably along this direction. This increase is 4 times larger than that in the y direction as the temperature increases from 1800 to 3300 K. In the same temperature range, the value of $\Delta l / l$ for the lower Ni film of the two-sided coating of graphene in the *y* direction increases in the average twice as fast as the corresponding characteristic for the upper film or the Ni film of the single-sided coating.

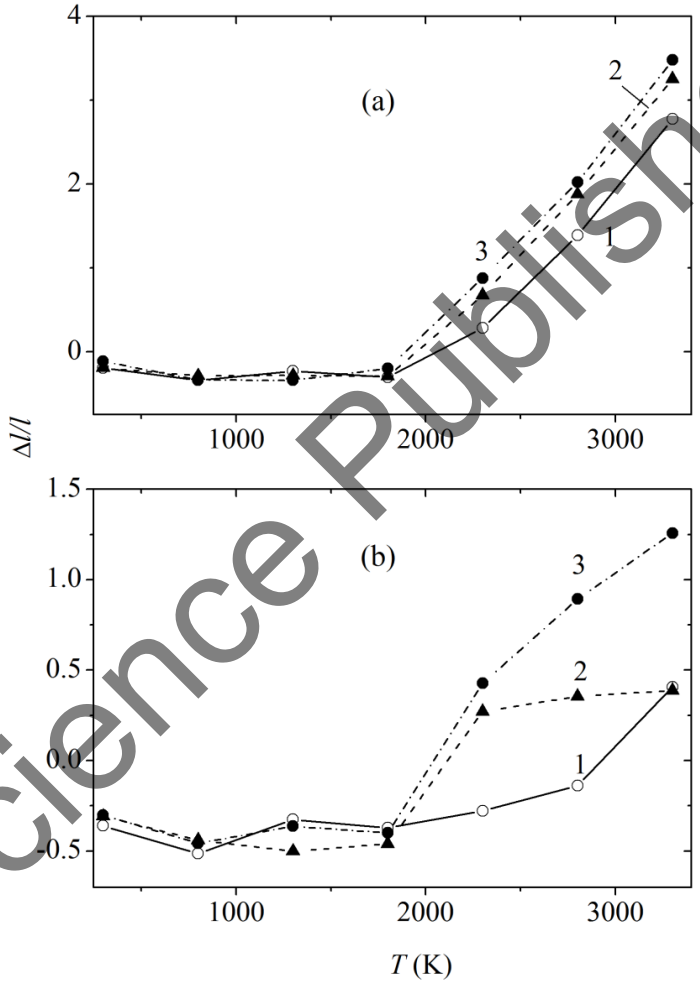

Figure 32. Temperature dependences of the elongation per unit length of the nickel films on the graphene surface (a) in the "zig-zag" direction and (b) in the "armchair" direction for (1) Ni film on one side of the graphene sheet, (2) upper Ni film on the graphene sheet with the two-sided coverage, and (3) lower Ni film on the graphene sheet with the two-sided coverage.

The self-diffusion coefficients D_{xy} and D_z of the Ni films for both the horizontal and vertical directions vary slightly to the temperature of 1800 K. This is associated with the conservation of the connectivity of atoms in the films, as well as, with the densification of the structure at moderate temperatures. However, the coefficients of mobility of the atoms in different directions significantly increase after the temperature of 1800 K (Figure 33).

It is worth to note that the most significant increase in the coefficient D_{xy} is observed for the Ni film covering the graphene sheet on one side. This is associated with the weak influence exerted by graphene on the Ni atoms of the single-sided coating at high temperatures. The metal atoms, which interact through the graphene sheet, mutually inhibit their own horizontal displacements. The increase in the coefficient D_{xy} of the Ni atoms for the system I in the average exceeds the corresponding characteristic for the upper and lower metallic films of system II by the factor of 5.7.

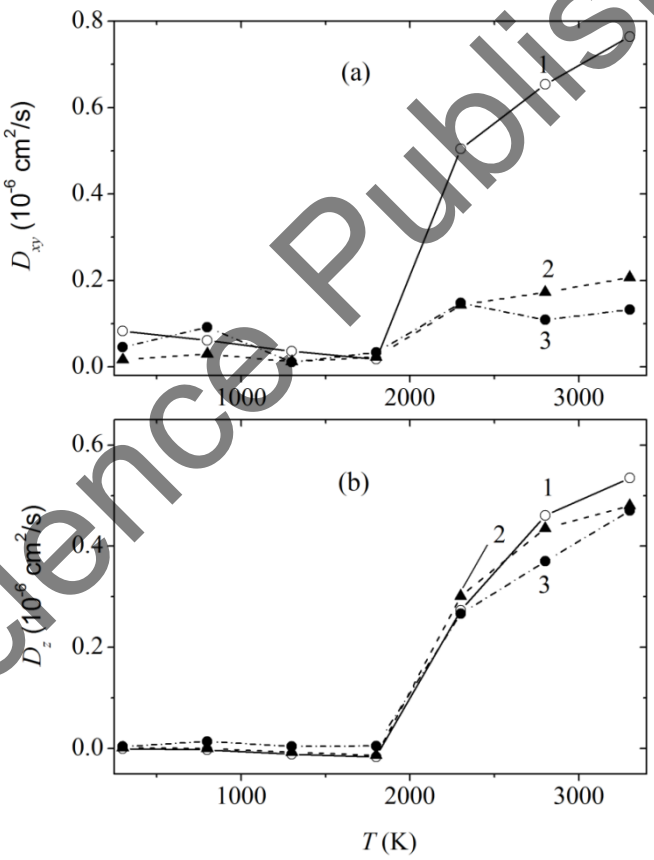

Figure 33. Temperature dependences of the self-diffusion coefficients of nickel films on the graphene surface during the displacement of the Ni atoms in the (a) horizontal directions and (b) vertical direction for (1) Ni film on one side of the graphene sheet, (2) upper Ni film on the graphene sheet with the two-sided coverage, and (3) lower Ni film on the graphene sheet with the two-sided coverage.

The similar behavior is observed in more degree for the self-diffusion coefficient D_z in the vertical directions for the Ni films in the single-sided and two-sided coatings of the graphene sheet. At the highest temperature (3300 K), the displacements of atoms in the vertical direction are still more preferred in the case of the single-sided coating. In each case, the graphene offers resistance to the motion of the Ni atoms from only one side. The metal atoms that interact through the graphene sheet weakly hold each other from the removal from the sheet in the vertical direction.

Thus, the presence of one metallic film on the single-layer graphene has the same effect on the energy state of the graphene sheet as the presence of two metallic films on it. Moreover, the change (in the energy of graphene covered by a metallic film with respect to the energy of a free graphene sheet) has an alternating character. The maximum difference between these energies is observed at the temperature of 3300 K. The stresses generated in the Ni films for the system with the two-sided coverage of the graphene sheet are substantially higher than those for the single-sided coverage of the graphene. These stresses decrease as the temperature increases and reach the minimum even at the temperature of 1800 K. A significant increase in the elongation per unit length of the films in the "zig-zag" and "armchair" directions of the graphene sheet at $T > 1800$ K begins to occur with a substantially stronger effect in presence of metallic films on both sides of the sheet. The self-diffusion coefficients, which characterize the displacement of the Ni atoms in the horizontal and vertical directions, also increase at the temperatures above 1800 K. Furthermore, in the horizontal directions, the steepest increase in the coefficient of mobility of the Ni atoms is observed for the single-sided metallic film.

4.5. Computer Simulation of the Thermal Stability of Nickel Films on Two-Layer Graphene

Deposition of the single- and multi-layer graphite films on the bulk transition metals has been known for a long time and is widespread [294, 295]. This deposition process can be implemented due to the temperature dependence of the carbon solubility in transition metals. Carbon can be introduced into thin (up to 500 nm) nickel film by decomposing strongly diluted gaseous methane CH_4 [296]. Graphene films containing only a few layers were grown by heating (in argon) polystyrene films deposited on a polycrystalline Ni substrate [297]. There is no need to use any reactive gas in this method. Instead, the necessary thickness of the graphene film is determined by the initial thickness of the polystyrene film. This method of growing the graphene films is safer and simpler than the chemical vapor deposition.

The number of graphite layers in multilayer graphene affects its mechanical, photomechanical, and thermophysical properties [298–300]. Therefore, an analysis of these layered thin films is of technological interest. It was shown in [301] that such formed

layered graphene structures have a high stability and the edges of individual layers serve as potential barriers for the electron flux. It was established that the photocurrent is affected by the temperature gradients induced by the laser excitation.

The electronic properties of a stack of graphene layers differ strongly from those of a single-layer structure due to the interlayer interaction. In the case of even two layers, the unique graphene property disappears: electrons cease to act as massless particles. It is energetically efficient for the transition metal atoms to be agglomerated into clusters on the surface of the nanotubes or fullerenes [302]. However, it was not shown whether or not this tendency remains when passing to a flat thin carbon structure (graphene). It would be useful to understand the processes occurring at the graphene–metal interface for forming reliable contacts between carbon nanostructures and metal electrodes in nanoelectronics [303].

The edges of graphene generally determine its physical properties. Graphene nanoribbons with a "zig-zag" atomic arrangement at the edge have no band gap (i.e., they are metallic). If atoms have the "armchair" arrangement, the band gap can be formed under certain conditions and, correspondingly, the graphene nanoribbon exhibits the semiconductor properties. The term "armchair" indicating the grapheme-edge configuration is generally accepted in the scientific literature.

We investigate two systems: the system I is the nickel film on the two-layer graphene, while system II is the two-layer graphene coated with identical Ni films from both sides. The modeling method was similar to the method used in the previous section to study the nickel film on a single-layered graphene.

The configurations of the nickel two-layer graphene system (graphene is coated with metal from one side) at the instant 200 ps and temperatures of 300 and 3300 K are shown in Figure 34. It is seen that Ni atoms are agglomerated into a dense two-dimensional "drop" located in one of the graphene sheet corners even at 300 K. However, the structural connectivity in the "drop" is violated. There are both a detached chain of four atoms and, at least, one removed atom. Both graphene sheets retain the correct hexagonal cell structure at this temperature. Graphene sheets become deformed as the temperature increases, compressing at the middle in the "armchair" direction. At 3300 K, this leads to bulging the sheet vertices. In the vicinity of sheet edges of the "armchair" direction, C atoms are somewhat disordered; however, none of these atoms detached from its sheet at T = 3300 K.

On the whole, the graphene sheets, as previously, retain the cell structure, and no global melting is observed (although there is slight melting at the "armchair" edge in the metal-atomic position). At 3300 K, more than half of the Ni atoms have been evaporated. The metal atoms that remained on the graphene are mainly arranged along the sheet edges, and only one Ni atom is in the central region.

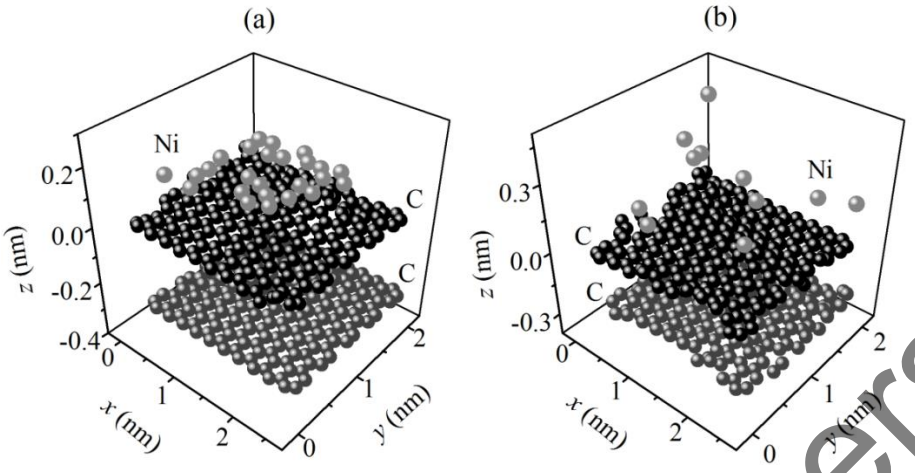

Figure 34. Structure of two-layer graphene with a nickel film at the instant 200 ps at the temperatures (a) 300 and (b) 3300 K.

When the Ni atoms are located on the external sides of the upper and lower graphene sheets, the structures of the lower and upper metal films differ significantly even at the temperature of 300 K. But their initial structures were identical. The difference in the structures of metal films for one- and two-sided coatings is partially due to the vertical film stratification in the latter case [304, 305].

Figure 35 shows the radial distribution functions $g(r)_{\mathrm{Ni-Ni}}$ plotted for one Ni atom, which is closest to the graphene-sheet center, for both upper and lower coating layers at T = 300 K. On the upper sheet, the Ni atoms are arranged in a more compact group, which is indicated by the strong first and (partly) second peaks, whereas other peaks have low intensity. The Ni atoms are arranged much more uniformly on the lower graphene sheet. In this case, four peaks (with subpeaks) are seen; however, the first peak intensity is much lower (by a factor of 2.5).

On the whole, the shape of these functions indicates different arrangements of the metal atoms with respect to the small central regions of the upper and lower sheets. This is mainly due to the fact that vertical displacements of the Ni atoms (lying on different sides of two-layer graphene upwards along the axis) are inequivalent. The reason is that the upper metal atoms can move unlimitedly in this direction, whereas the lower atoms cannot because their displacement is limited by the lower graphene sheet.

Counter motion of the upper and lower Ni atoms is due to their long-range interaction of the attractive type. After interaction with graphene, the upper Ni atoms having acquired a vertical velocity component may easily be evaporated. The lower atoms remain near the graphene surface for some time colliding with other Ni atoms, and then move away in different directions of the lower half-space. Increase in the system temperature accelerates this process. So, at T = 3300 K there are hardly any Ni atoms remaining on the surface of the lower graphene sheet.

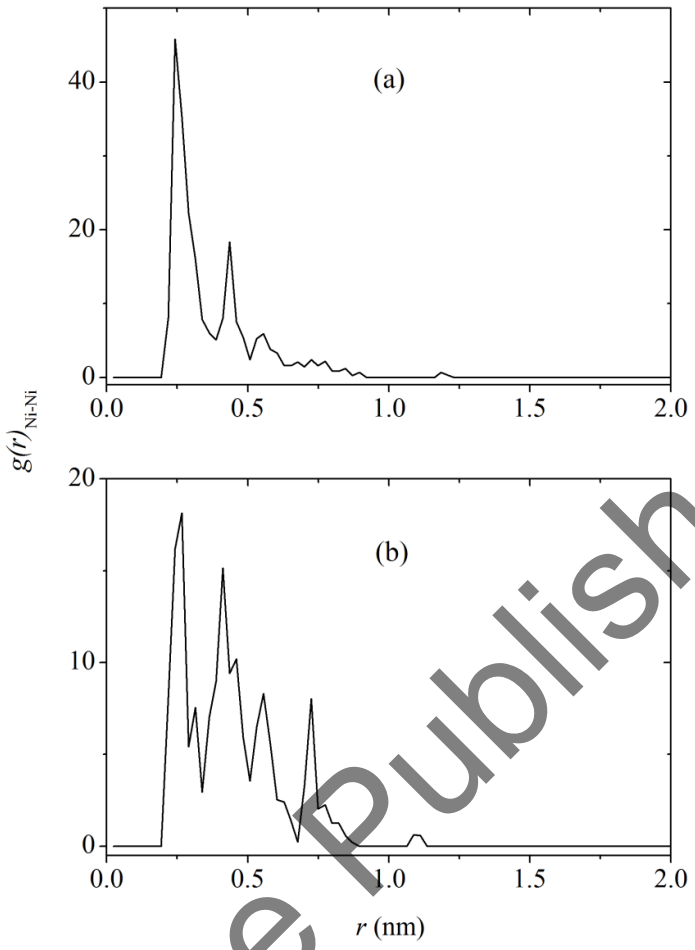

Figure 35. The radial distribution function for the (a) upper and (b) lower nickel films on the two-layer graphene at T = 300 K.

Presence of the lower metal-atomic layer also affects the graphene structure. At 3300 K, detaching the C atoms can be observed near one of the vertices of both upper and lower sheets. In this case, the type of deformation of the graphene sheets at high temperatures is basically identical to the case of coating the two-layer graphene with nickel from one side. The scale of damages in the upper graphene sheet at T = 3300 K is larger than that for the lower one. This is due to the stronger bending of the front "zig-zag" edge and more extended fracture of the left "armchair" edge. The lower sheet underwent strong local fracture only near one of the corners.

Kinetics of the Ni atoms on the surface of two-layer graphene is shown in Figure 36. Here, the temperature dependence of the self-diffusion coefficient of this metal is presented for the cases of one- and two-sided coatings of graphene with nickel. It is seen that the mobility coefficient D_{xy} of Ni atoms in the horizontal direction (Figure 36a) for the system I first decreases up to the temperature of 1800 K and then sharply increases.

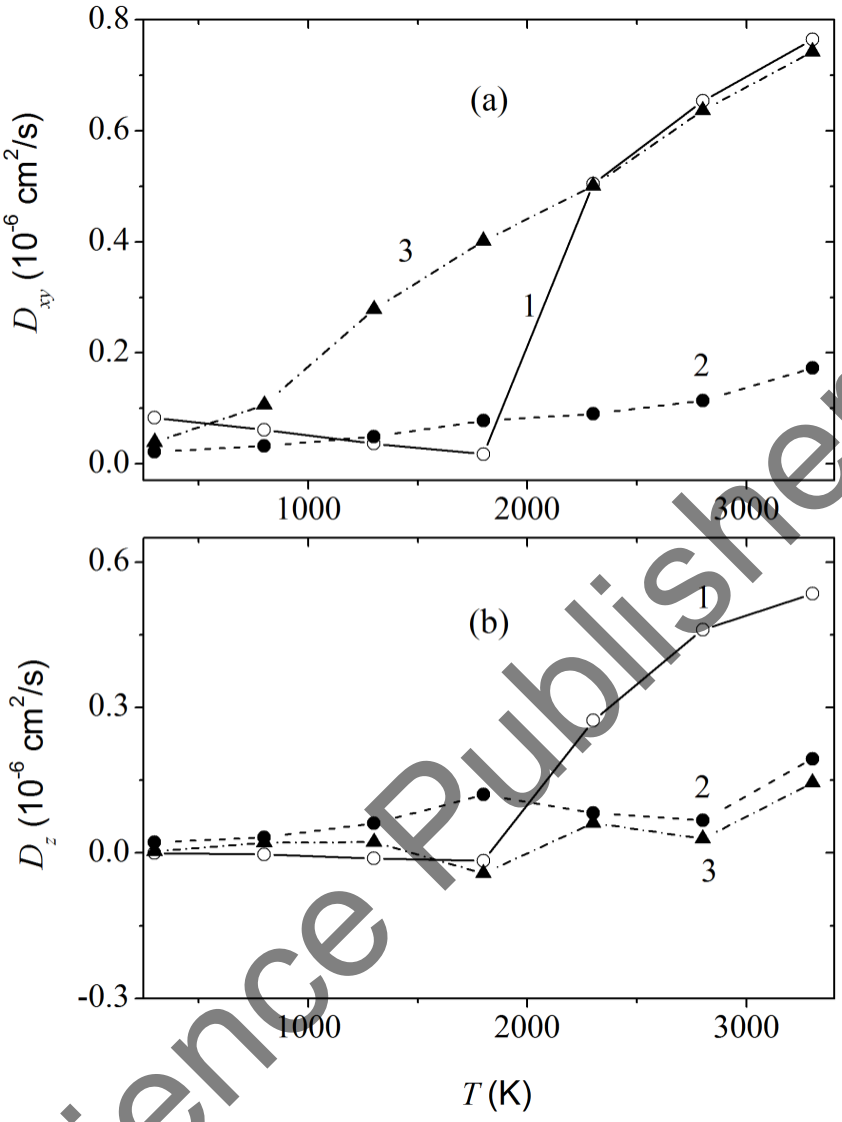

Figure 36. Self-diffusion coefficient of nickel atoms in (a) the horizontal plane and (b) in the vertical direction for (1) one Ni film, (2) the upper Ni film, and (3) the lower Ni film.

The amplification of adhesion between Ni atoms and the graphene substrate causes the initial decrease in the coefficient D_{xy} until a certain threshold temperature. The second reason is in compacting the nickel film on graphene. This is caused by the mismatch between the initial density of Ni and its density in the condensed state. The experimental nickel melting temperature T_{m} is 1726 K. Therefore, a further increase in the temperature (above 1800 K) will most likely cause film melting and the related increase in the mobility coefficient D_{xy}. Note that the melting temperature of the monoatomic Ni film on graphene may differ from the T_{m} value of a crystalline nickel. At $T > 2300$ K, the D_{xy} value of the

one-sided Ni film continues to increase as the temperature increases, but with a more moderate rate.

The situation is quite different for the nickel films of system II. In this case, the coefficient D_{xy} almost monotonically increases as the temperature increases, and this is typical of both the upper and lower Ni films. The monotonic behavior of the temperature dependence of D_{xy} can be explained by the dominance of stronger Ni–Ni interactions. These interactions occur in the same film in comparison with interactions between the Ni atoms belonging to different films, as well as, by the Ni–C interactions. Note that the mobility coefficient for the upper Ni film is much smaller than that for the lower one at all temperatures under study. For example, at 3300 K, the latter value may exceed the former by the factor of 4.3. This fact indicates the tendency of Ni atoms to leave the lower graphene sheet.

The components D_z of the vertical-mobility coefficient of Ni atoms also behave differently for systems I and II as the temperature increases (Figure 36b). The coefficient D_z in the system I remains constant and small up to 1800 K. However, with further increase of temperature, the D_z value for Ni atoms of this system increases fast.

System II exhibits no such very fast increase in the D_z value. In this case, the coefficient D_z for Ni atoms first slightly increases (up to T = 1800 K for the upper Ni film and 1300 K for the lower film) and then its behavior becomes oscillating. As a result, it is only slightly increased when the temperature of 3300 K is achieved. The significant increase in the coefficient D_z in the system I at T > 1800 K is due to evaporation (directed mainly upwards) of a part of the Ni atoms from the grapheme-sheet surface. The interaction between Ni atoms belonging to different films hinders this process in system II. In this case, the Ni atoms leaving the graphene surface have larger horizontal velocity components.

Let us now consider what dynamic properties graphene acquires at high temperatures. There is the tooth shape of the $f_{xy}(\omega)$ spectrum of individual horizontal vibrations of C atoms in the upper and lower graphene sheets at T = 3300 K. This indicates that the directions of the carbon atoms motion change fast (Figure 37a). Non-zero values of the $f_{xy}(\omega)$ spectra at a zero frequency indicate that C atoms acquired translational mobility in these directions. Overall, the $f_{xy}(\omega)$ spectra are similar for the upper and lower graphene sheets and, accordingly, the behaviors of horizontal displacements of C atoms, belonging to different sheets, are also similar.

A somewhat different situation occurs for vertical displacements of C atoms of the upper and lower graphene sheets at T = 3300 K (Figure 37b). In this case, the $f_z(\omega)$ spectra also have non-zero values at zero frequency. This indicates the presence of the

vertical translational motion of C atoms for both sheets. However, the $f_z(\omega)$ spectrum for the lower sheet is characterized by the higher intensity of other peaks and better peak resolution at high frequencies. This means that the lower sheet is characterized by not only the vertical translational displacements of the C atoms. It is also characterized by the vibrational atomic motions in the vertical direction, which are less developed for the C atoms of the upper sheet.

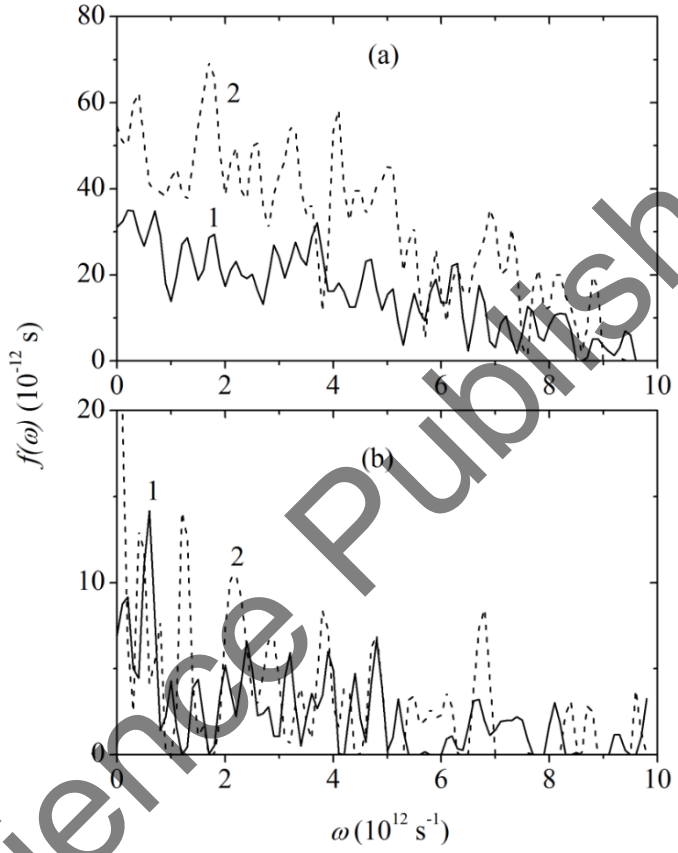

Figure 37. Spectra of individual (a) horizontal and (b) vertical carbon atomic vibrations in the two-layer graphene coated with two Ni films: (1) upper and (2) lower layer.

It is reasonable to consider the main stresses in the temperature range $300 \le T \le 1800$ K when there are still sufficient number of metal atoms remaining on the graphene surface (Figure 38). The film on one side of two-layer graphene is characterized by the lowest stresses. The highest stresses of a particular sign acting in the metal-film plane manifest themselves at temperatures of 300 or 800 K. The stresses σ_{zx} and σ_{zy} caused by the horizontal forces are somewhat increased in the film of the system I as the temperature increases, whereas the σ_{zz} stresses (caused by the vertical force) become weaker.

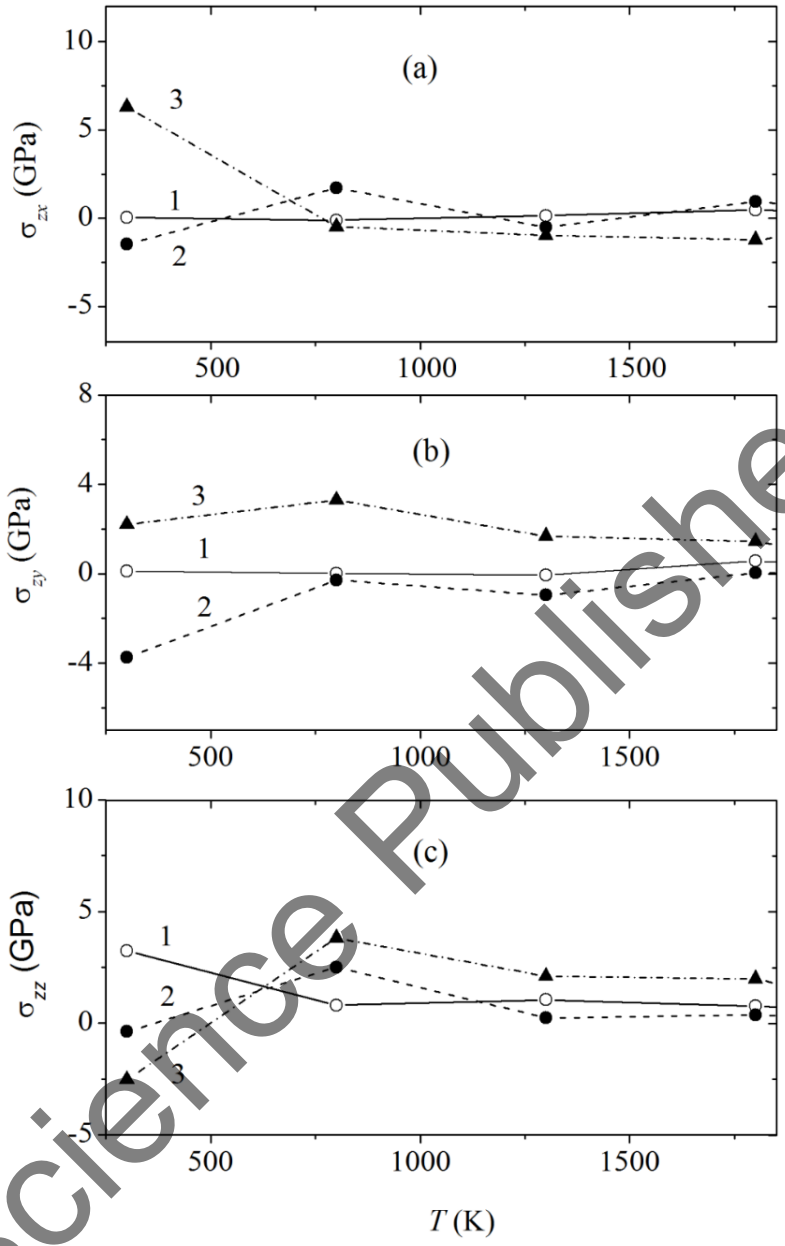

Figure 38. The stress tensor components: (a) σ_{zx}, (b) σ_{zy}, and (c) σ_{zz} in nickel films on the two-layer graphene: (1) one Ni film, (2) upper Ni film, and (3) lower Ni film.

When two metal films are deposited on the two-layer graphene, they have much higher horizontal stresses as compared with the case of one deposited Ni film. These stresses relax to some extent upon heating. The magnitudes of the stresses σ_{zx} and σ_{zy} in the metal films of system II at 1800 K are always smaller than those at T = 300 K. In principle, the situation for the σ_{zz} stress is similar but not expressed so evidentially. For example, in the

case of the upper Ni film, the σ_{zz} stress at T = 1800 K is lower than that at T = 300 K by only 2.6%. Since the major part of Ni atoms of the lower metal film is weakly coupled with graphene at 1800 K, all three stresses (σ_{zx} , σ_{zy} , and σ_{zz}) in the upper film are close to the corresponding stresses in the system I.

The cell hexagonal structure in the two-layer graphene has high thermal stability. The two-layer graphene coated with the Ni mono-layer retains the honeycomb structure even at high temperatures. For example, only individual atoms located in the sheet corners are detached from graphene at 3300 K. The perfect structure remains in the rest of the sheet. When the Ni films are deposited on the two-layer graphene, the horizontal dynamics of Ni atoms in the upper metal layer is significantly decelerated. This is due to the Ni–Ni interlayer interactions. The stresses in the metal films on the two-layer graphene mainly cease to relax at T = 800 K.

Thus, it was shown that the presence of the second graphene sheet increases significantly the stability of the flat hexagonal cell structure with respect to heating. It was found that even at T = 300 K the Ni atoms (deposited on the upper and lower graphene sheets) form films with the different structures (metal atoms on the upper substrate are closer packed). The nickel films are destroyed under heating the system. However, even at T = 3300 K a part of the Ni atoms remains on the upper graphene sheet irrespective of whether or not the lower sheet was previously coated with the metal.

The lower graphene sheet loses all Ni atoms when the temperature of 3300 K is achieved. The spectrum of the individual horizontal vibrations of the C atoms has a shape that differs significantly from the shape of the vertical-vibration spectrum. The horizontal-vibration spectra of the upper and lower graphene sheets are basically identical, whereas the corresponding spectra of vertical vibrations differ. The temperature dependences of the horizontal and vertical components of the self-diffusion coefficient of the Ni atoms have the sharp kink at T = 1800 K. In this case the two-layer graphene is coated with the metal film from one side.

However, when the metal coating is two-sided, the dependence $D_{xy}(T)$ monotonically increases for each coating. Here, the D_{xy} values for the lower Ni film are much larger than those for the upper one. The dependences $D(T)$ for the upper and lower nickel films have only the slight kink at T = 1800 K. The stresses acting in the metal-film plane (σ_{zx} and σ_{zy}) are much higher in the case of the two-sided coating of graphene with nickel than those for the one-sided coating. These stresses are caused by the horizontal components of interatomic forces. The σ_{zz} stresses are comparable in these cases. However, the σ_{zz} stresses for the metal film deposited on graphene from only one side disappear faster under the heating.

4.6. COMPUTER STABILITY TEST FOR ALUMINUM FILMS HEATED ON GRAPHENE SHEET

Interest in experimental investigations of ultrathin aluminum films on graphene has considerably increased in recent years [306–308]. At the same time, these objects have not been sufficiently investigated theoretically. Coating the graphene oxide by the thin aluminum film makes it possible to generate a high acoustic-optical pressure. This is due to the optimization of the thermal elasticity produced by the metal film, as well as, by the thermal conductivity exhibited by graphene oxide [306]. Ultrathin films obtained by deposition of the aluminum oxide on graphene are characterized by a very high strength [307]. Such films can be used as thin film coatings, membranes, and in flexible electronics. The dielectric properties of a naturally oxidized aluminum film on graphene make it possible to use it for preparing electric shutters [308].

In actual experiments, it is difficult to control the nanoscratches and nanodents. Such difficulties can easily be eliminated using the molecular dynamics simulation. This method is widely used for studying the friction and cracks in thin films [309, 310]. On the basis of the MD simulation, the elastoplastic deformation on the surface of a nickel single crystal was considered as the nucleation of dislocations [311].

Initially, Al atoms were on the graphene sheet in the form of a loose (111) plane in the fcc lattice (parallel to the graphene plane) with distance $r_{\mathrm{Al-Al}}$ = 0.6336 nm between the nearest atoms. The Al atoms were located strictly against the centers of the hexagonal cells formed by carbon atoms. Here, the shortest distance between C and Al atoms $r_{\mathrm{C-Al}}$ = 0.248 nm corresponded to the value calculated within the density functional theory [72]. In the bulk aluminum crystal, $r_{\mathrm{Al-Al}}$ = 0.2857 nm. Therefore, the Al films were initially stretched due to the lattice mismatch between graphene and aluminum.

The simulation was performed in accordance with the methods used to theoretically study of the heating of the thin Cu and Ni films on graphene. Here, we analyze two systems. The system I is the aluminum film on the mono-layer graphene, while system II corresponds to a graphene mono-layer coated on both sides with identical Al films [312].

The Al atoms of system II leave the graphene sheet at the temperature of 1800 K, while all atoms of system I remain in the vicinity of the graphene sheet even at 3300 K. The relative elongation of the Al films in the longitudinal (x) and transverse (y) directions is shown in Figure 39. The direction of the x axis corresponds to the "zig-zag" one of the graphene sheet. The direction of the y axis coincides with the "armchair" direction.

The longitudinal and transverse sizes of the films were determined by averaging the atomic positions of the corresponding opposite edges of the films. In both systems, the Al films exhibited contractions in the longitudinal and transverse directions up to 1300 K (the values of $\Delta l/l$ were negative). The only exception was the longitudinal size of the lower film in system II at T = 300 K, where $\Delta l/l > 0$. The positive values of $\Delta l/l$ for the Al film

in system I were observed only at 2300 and 2800 K exclusively in the longitudinal direction.

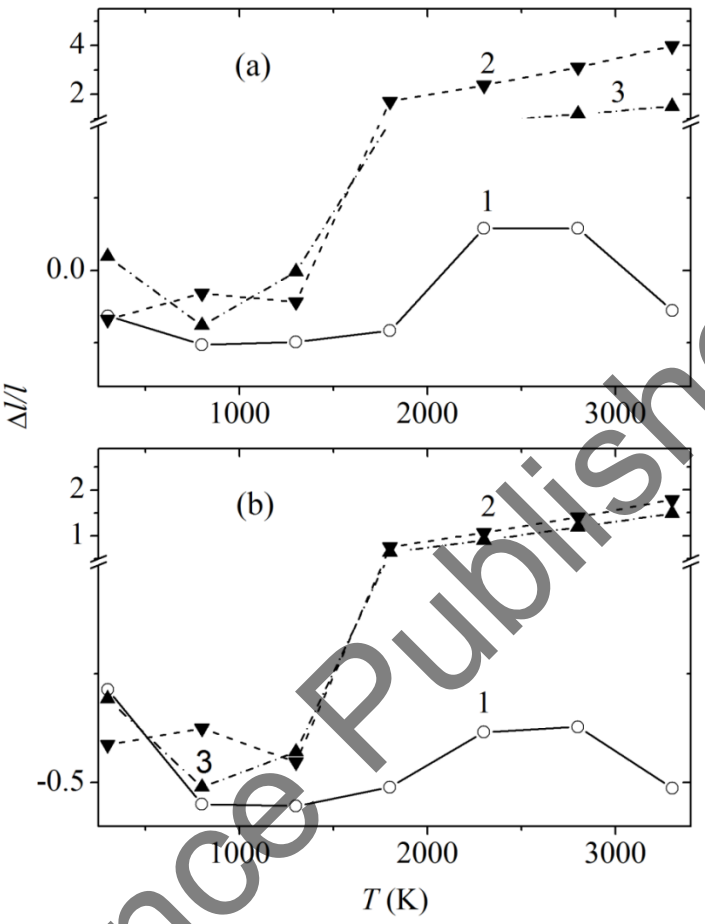

Figure 39. Relative elongation of Al films in (a) longitudinal (*x*) and (b) transverse (*y*) directions for systems comprising of a single Al film on a graphene sheet (1), top (2), and bottom (3) Al films on the graphene sheet with the double-sided coating.

Thus, the double-sided coating of the graphene sheet by the stretched monolayer Al films considerably reduces the thermal stability of these films with respect to the corresponding single-sided coating. This is due to the strong repulsive interaction between the Al atoms in the vicinity of T = 1800 K in the case of insufficiently strong binding of aluminum with graphene.

Figure 40 shows the temperature dependences of horizontal D_{xy} and vertical D_z components of the self-diffusion coefficient of the metal films under investigation. For the Al film coating one side of the graphene sheet, the value of D_{xy} first decreases as the temperature increases up to T = 1300 K. Then the $D_{xy}(T)$ dependence passes through a

small peak (at T = 2300 K). Finally, the values of D_{xy} sharply increase when the temperature of 3300 K is approached. The decrease in D_{xy} is associated with compaction of the Al atoms on the substrate.

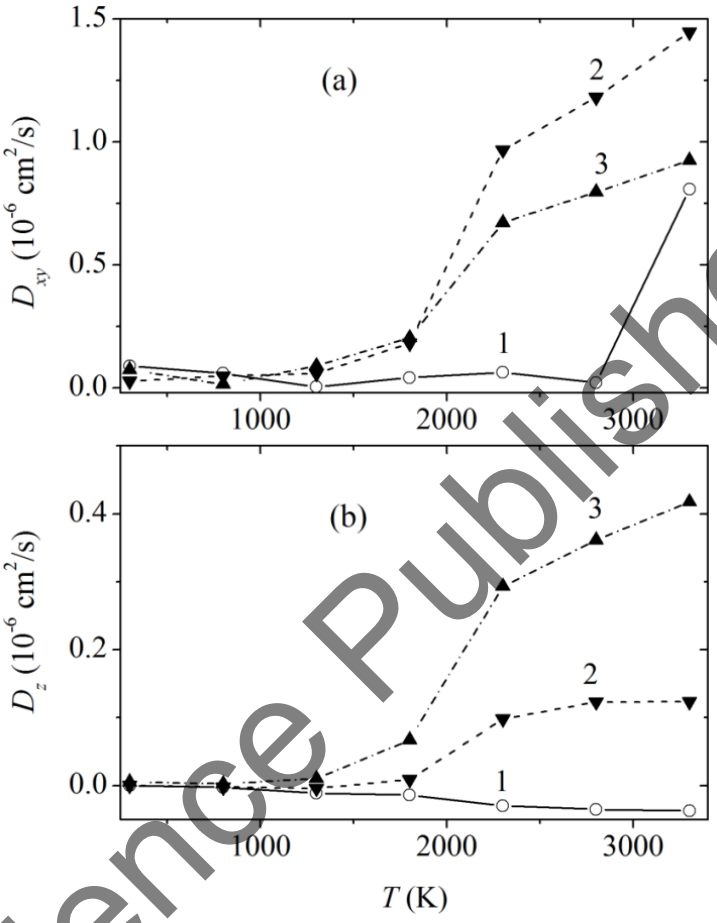

Figure 40. (a) Horizontal D_{xy} and (b) vertical D_z components of the self-diffusion coefficient of the Al films: single Al film on the graphene sheet (1), top (2), and bottom (3) Al films on the graphene sheet with the double-sided coating.

The melting point of the bulk aluminum obtained in the actual experiments is 933 K, and its experimental boiling point corresponds to 2773 K. The Al film passes to the liquid state at T = 1300 K. The large variety of structures in the liquid state leads to the emergence of the peak on the $D_{xy}(T)$ curve. At the temperature of 2800 K, the Al film passes to the state, in which the metal atoms begin to evaporate. As a result, the D_{xy} component of this film increases significantly.

The behavior of D_{xy} value for Al films coating both sides of the graphene sheet is different. Such films exhibit an insignificant increase in the D_{xy} component under heating from 800 to 1800 K. The sharp increase in D_{xy} is observed near 2300 K, which is followed by the significant increase in the horizontal mobility at higher temperatures. The D_z component for the system I decreases under heating. This is due to formation of the dense flat Al droplet on the surface of the graphene sheet.

Collective adhesion of the Al atoms with the sheet surface reduces the vertical component of the self-diffusion coefficient. The analogous adhesion is also observed for the Al films in system II, but only up to the temperature 1300 K. The attraction of Al atoms belonging to different films at high temperatures leads to strong collisions of the metal atoms with the substrate. As a result, the Al atoms acquire large vertical velocity components, and the D_z component increases fast.

Let us now consider the change in the vibrational motion of the Al atoms after addition of the second (bottom) metal film to the graphene sheet. The frequency spectra of the Al atoms vibrations in the *xy* plane for the film in system II at 1300 K are shown in Figure 41. At this temperature, most Al atoms in system II are still in the vicinity of the graphene sheet. The frequency spectrum for Al atoms of the top film has four intense peaks in the frequency interval $(5.0 \le \omega \le 6.5) \times 10^{12}$ s^{-1}. At the lower frequencies, the intensity of the peaks decreases. Conversely, the intensity of the peaks for the bottom film in this frequency interval is minimal, while the peaks localized at the lowest frequencies (1.3×10^{12} and 1.7×10^{12} s^{-1}) have the maximal intensity. Thus, as a result of the separation of a small amount of aluminum by the graphene sheet, the Al atoms in each film perform natural vibrations. But they are often mismatched for the top and bottom films. At a certain temperature, vibrations of the carbon atoms in the graphene sheet (which are chaotic for both films) produce a repulsive effect. As a result, the Al atoms leave the surface of the sheet.

Temperature variations of the stresses acting in the plane of the films are illustrated in Figure 42. The strongest temperature oscillations of the stresses are observed for the Al film in the system I. As the temperature increases, the stresses in the films decrease and ultimately vanish. The extremely low values of stresses for the Al film in the system I are attained at 2300 K, and the film itself can exist even at $T = 3300$ K.

The Al films in the system II are preserved on the graphene up to 1300 K, and at 1800 K, only their remains are observed. The non-zero stresses are observed in such films up to 1800 K. The stresses σ_{zx} and σ_{zy} produced by the horizontal forces in the Al films can be considerably lower (by an order of magnitude) than the stresses σ_{zz} produced by the vertical forces due to small distances between C and Al atoms.

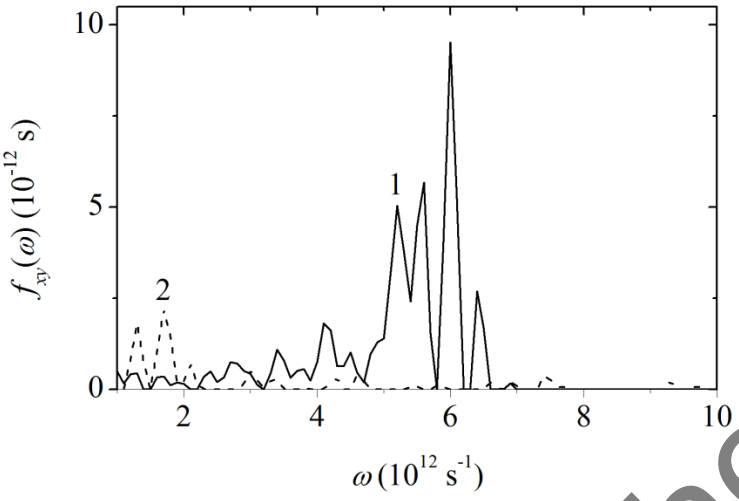

Figure 41. Frequency spectra of individual vibrations of Al atoms in the *xy* plane: top (1) and bottom (2) films at 1300 K.

Let us now see how the presence of the metal film affects the graphene stressed state. In the case of the single-side coating of the graphene sheet by the metal film, stresses σ_{zx} (Figure 43a) exhibit a much smaller amplitude spread as compared to the stresses σ_{zy} (Figure 43b). Consequently, the interatomic forces acting in the "armchair" direction exceed the forces oriented in the "zig-zag" direction. The middle part of the graphene sheet experiences higher stresses than the edges in the "zig-zag" direction. As the temperature increases, the amplitude of the stress oscillation decreases, and the amplitude excursion of quantity σ_{zy} remains larger than the analogous characteristic of the stress σ_{zx}. At the temperature 3300 K the stresses at the middle of the sheet generally become even lower than at the edges in the case of the motion in the *x* direction.

Due to the vertical forces, the stress σ_{zz} acting in the plane of the graphene sheet exhibits slightly different temperature behavior as compared to σ_{zx} and σ_{zy} produced by the horizontal forces (Figure 43c). The maximal absolute values of the stress σ_{zz} at T = 300 K are observed not in the middle part of the sheet, but at the edges for small values of *x*. At the temperature 1300 K, the high peak of the stress σ_{zz} appears in the middle part of the sheet, while lower peaks of the stresses σ_{zz} are located closer to the sheet edges. The high peak is due to vertical displacements of the closely packed Al atoms. Because of such displacements, the stress σ_{zx} in the metal film also decreases sharply.

Stresses σ_{zz} in the graphene sheet dissipate under further heating. However, even at 3300 K, the amplitude of fluctuations in the value of σ_{zz} exceeds the corresponding characteristics of σ_{zx} and σ_{zy} at this temperature.

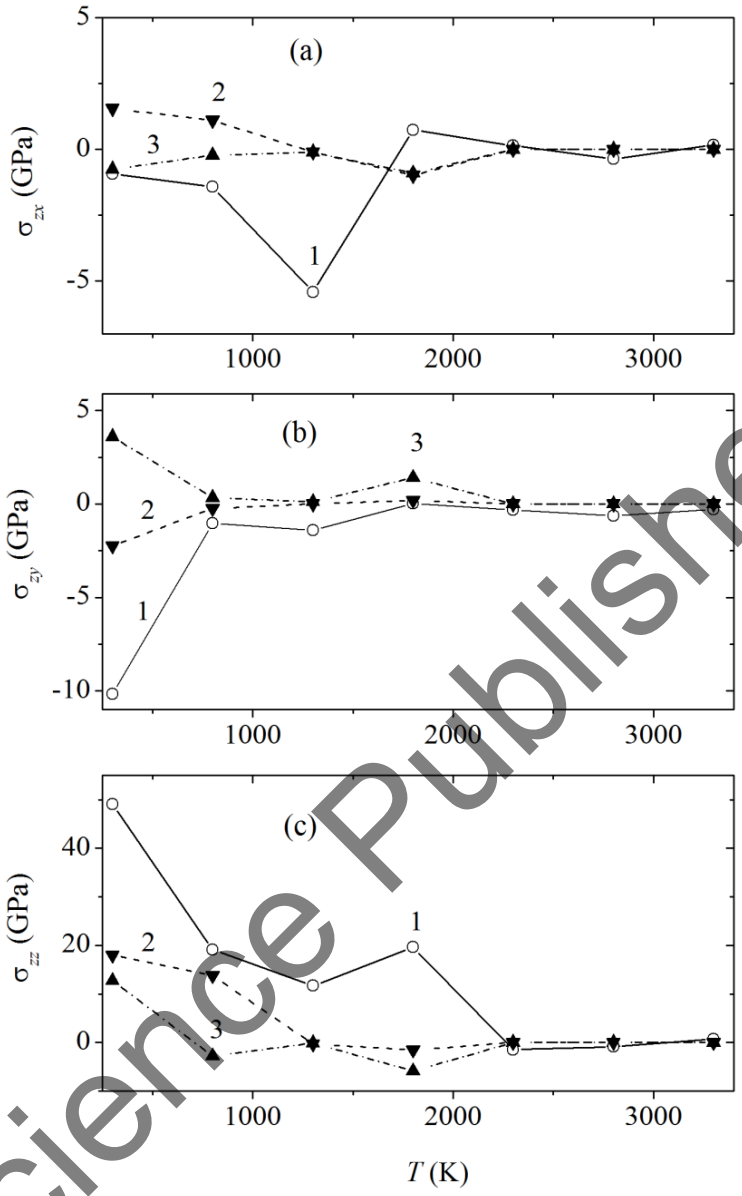

Figure 42. Stresses (a) σ_{zx}, (b) σ_{zy}, and (c) σ_{zz} in the *xy* plane of the metal film for systems with the single Al film on the graphene sheet (1), top (2), and bottom (3) Al films on the graphene sheet with the double-sided coating.

Thus, the stability of the Al films on graphene depends on their number. In the case of the single-side coating of the graphene sheet by aluminum, the metal atoms are preserved on the graphene surface even at 3300 K. The doubled coating leads to evaporation of all Al atoms at the temperature of 1800 K. On the first stage (up to T < 1300 K), the Al atoms are gathered into a dense flat droplet, reducing the film size predominantly in the "armchair" direction. The self-diffusion coefficients of Al atoms in the horizontal

and vertical directions considerably increase at $T > 1800$ K in the case of the double-sided coating of graphene with aluminum. The low values at the top side of the graphene sheet up to 2800 K in the case of the single-side coating are preserved.

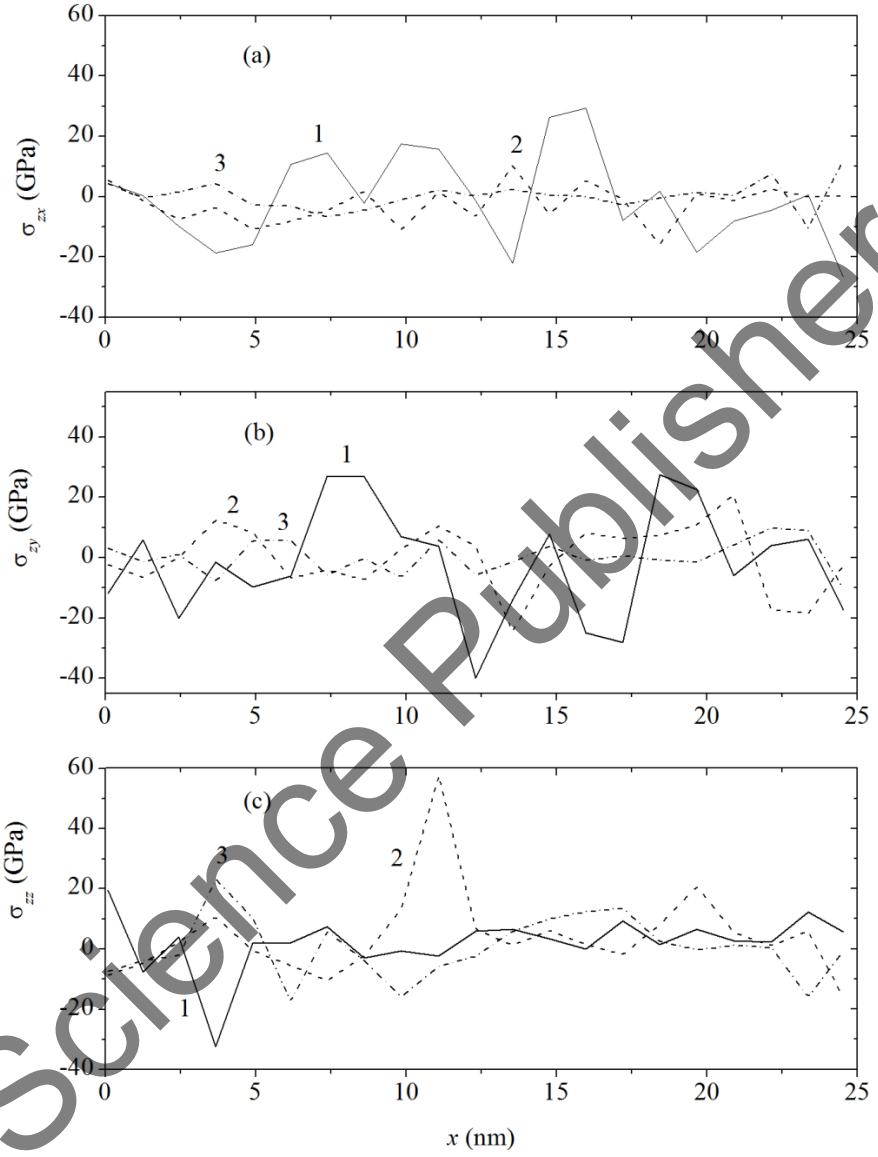

Figure 43. Distributions of stresses (a) σ_{zx}, (b) σ_{zy}, and (c) σ_{zz} in the graphene sheet over rows of the C atoms passing in the "armchair" direction at 300 (1), 1300 (2), and 3300 K (3).

The Al atoms are preserved for a longer time on the top side of the graphene sheet, that is reflected in the richer and more intense spectrum of individual vibrations of atoms in the horizontal direction at $T = 1300$ K. The initial predominant contraction of the metal films in the "armchair" direction is due to the prevailing the magnitude of the interatomic forces

in this direction. For the same reason, the absolute values of stresses σ_{zy} in the Al films at T = 300 K exceed the corresponding characteristics of stresses σ_{zx}.

However, the highest stresses in metal films are primarily caused by the vertical forces emerging not only due to mutual attraction of the Al atoms belonging to different films but, also, due to the interaction between graphene and aluminum. The importance of this interaction follows from the high initial stress σ_{zz} for the Al film coating graphene sheet only from one side. With such a coating of the graphene sheet, the stresses from the horizontal forces are mainly concentrated in its middle part.

The magnitude of the stresses caused by the forces acting in the "armchair" direction is noticeably larger than the corresponding characteristic for the "zig-zag" direction. Heating leads to relaxation of the stresses σ_{zx} and σ_{zy}; however, the stresses σ_{zz} can be locally enhanced as the temperature increases due to the strong convergence of the C and Al atoms.

4.7. Numerical Simulation of Heating an Aluminum Film on Two-Layer Graphene

The general tendency in the production of the crystalline silicon solar cells implies the use of wafers that are as thin as possible. The efficiency of the solar batteries depends strongly on the rear cell surface. The rear surface in silicon solar cells is often improved by inducing the rear-surface field. This field is mainly formed due to sintering (in the temperature range from 1073 to 1273 K) thin (about 10 μm and even 2 μm thick) aluminum films with silicon [313]. The two-layer graphene has unique electronic properties. They differ from those of the single-layer graphene and bulk graphite due to the parabolic dispersion of its particles [314–316].

It was shown experimentally [317] that the two-layer graphene is rippled in the same way as the single-layer one. However, its structure has not been investigated systematically. This ripple may lead to charge inhomogeneity (electron and hole puddles) [318]. Mechanical properties of the two-layer graphene are also important because they are representatives of the crystalline membranes formed by two atomic layers. Let us consider the behavior of a single-layer stretched aluminum film on the bilayer graphene with heating up to 3300 K. The results presented here were obtained [319] on the basis of the model and calculation method corresponding to the technique used for aluminum films on the single-layer graphene.

The relative change in the aluminum-film sizes is shown in Figure 44. The film begins to be contracted both in the "zig-zag" (Figure 44a) and "armchair" (Figure 44b) directions even at the initial temperature (i.e., at T = 300 K). This contraction becomes more intense when the temperature reaches 800 K. The decrease in the distance between Al atoms at

these temperatures is due to the discrepancy between their initial loose packing and the metal density corresponding to the condensed state.

In our model, a solid aluminum film containing defects is formed on the graphene surface at low temperatures. Influence of the defects can be estimated in the simplest way from the temperature change in the specific heat. It becomes possible since the latter is easier to measure (in comparison with other properties) when the temperature changes fast [320]. The isochoric specific heat of the Al film does not increase under heating; i.e., the influence of defects on the caloric properties was not manifested.

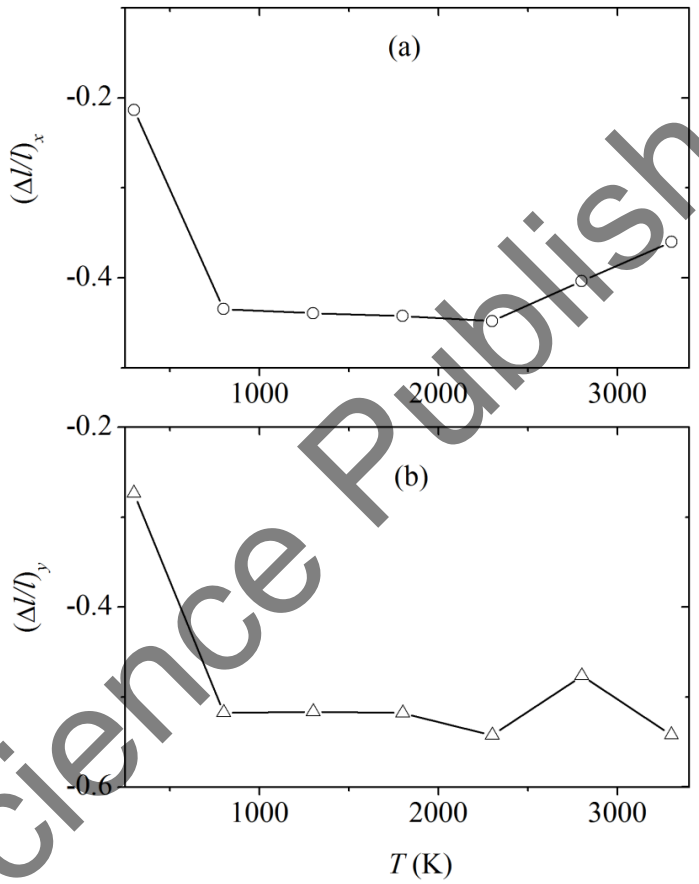

Figure 44. Relative change in the length of Al films in the (a) longitudinal (x) and (b) transverse (y) directions.

The sizes of the metal film in both directions are stabilized in the temperature range $800 \le T \le 2300$ K. Further heating leads to the stable increase in the film size in the "zig-zag" direction and to the oscillating change in the film size in the "armchair" direction.

The temperature changes in the radial distribution function in the Al film (constructed for the atom located most closely to the center of the graphene sheet) are illustrated in Figure 45. Presence of a symmetry center is a necessary condition for the correct

construction of this function. It is seen that at T = 300 K the function $g(r)_{\mathrm{Al-Al}}$ has a number of peaks at $r \leq 1$ nm (Figure 45a). The peak intensity generally decreases as r increases.

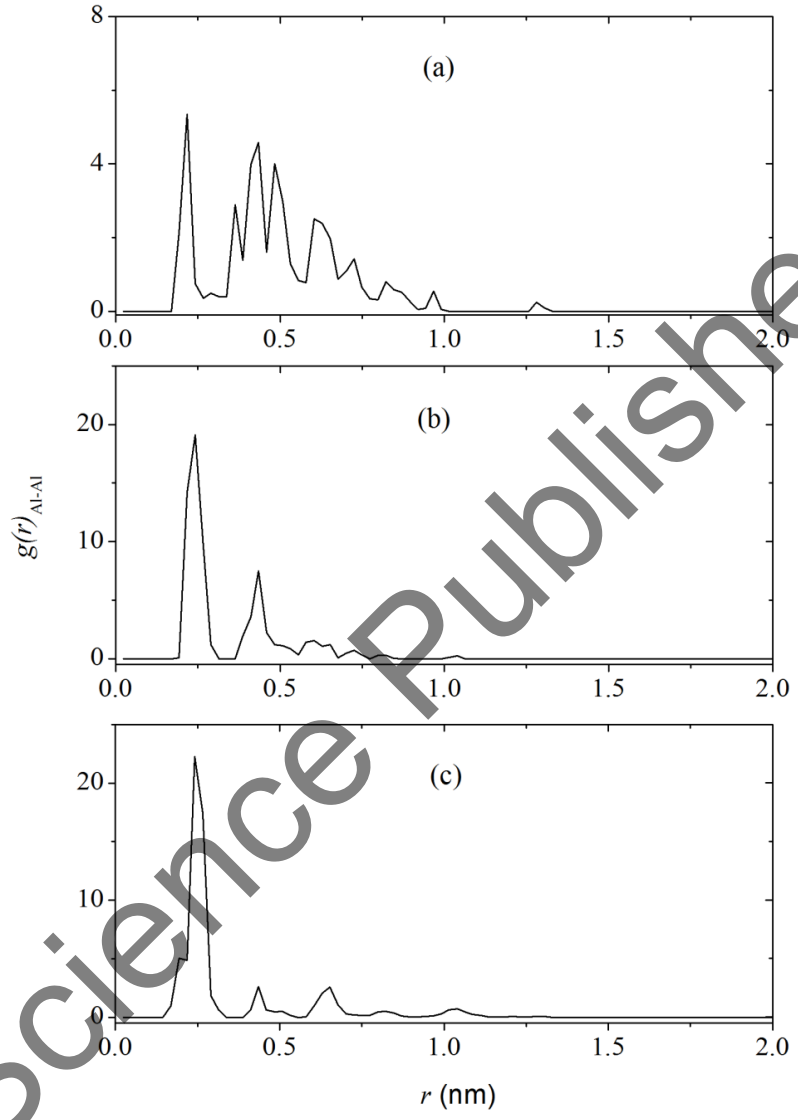

Figure 45. Radial distribution functions of the aluminum film corresponding to temperatures of (a) 300, (b) 1300, and (c) 3300 K.

The film structure in the region of stable film sizes is described by the function $g(r)_{\mathrm{Al-Al}}$ at T = 1300 K (Figure 45b). Here, the function $g(r)_{\mathrm{Al-Al}}$ exhibits two pronounced peaks at 0.24 and 0.43 nm. The first-peak position is close to the distance between the neighboring atoms in the bulk aluminum crystal (0.2489 nm). At 3300 K, the function $g(r)_{\mathrm{Al-Al}}$ retains only one evident peak (Figure 45c). The peaks at 0.43 and 0.65

nm are weak. Thus, the increase in temperature reduces the number of well-resolved peaks of the function $g(r)_{\mathrm{Al-Al}}$ and increases the intensity of its first peak.

The behavior of the mobility of Al atoms on graphene becomes atypical as the temperature increases (Figure 46). The horizontal and vertical components of the self-diffusion coefficient D were calculated from the corresponding squared atomic displacements. The horizontal component D_{xy} of the self-diffusion coefficient decreases as the temperature increases up to 1800 K. The component D_z, which describes the vertical atomic displacements, also decreases until the temperature reaches 1300 K. This behavior of the temperature dependence of components D_{xy} and D_z is due to the decrease in the distance between Al atoms as well as the hindrance caused by graphene. At T > 1800 K, the component D_{xy} of the aluminum film increases, whereas the value of the component D_z fluctuates.

At these temperatures, the kinetic factor is dominant in comparison with the residual influence of the substrate in the horizontal direction. The vertical displacements of Al atoms are still hindered due to the attraction by the two-layer graphene. The horizontal component D_{xy} of the self-diffusion coefficient increases significantly when approaching the experimental value of the Al boiling temperature (2773 K). The vertical component D_z increases only after reaching this temperature.

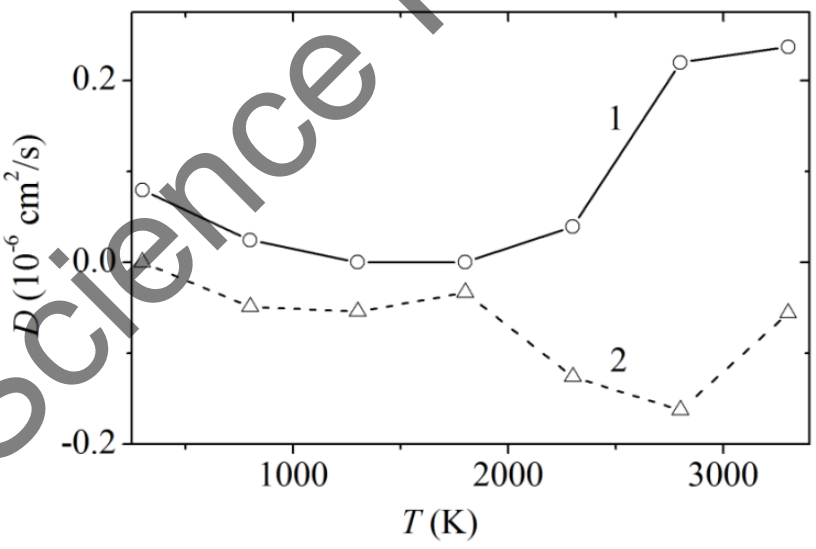

Figure 46. (1) Horizontal (D_{xy}) and (2) vertical (D_z) components of the self-diffusion coefficient of Al film.

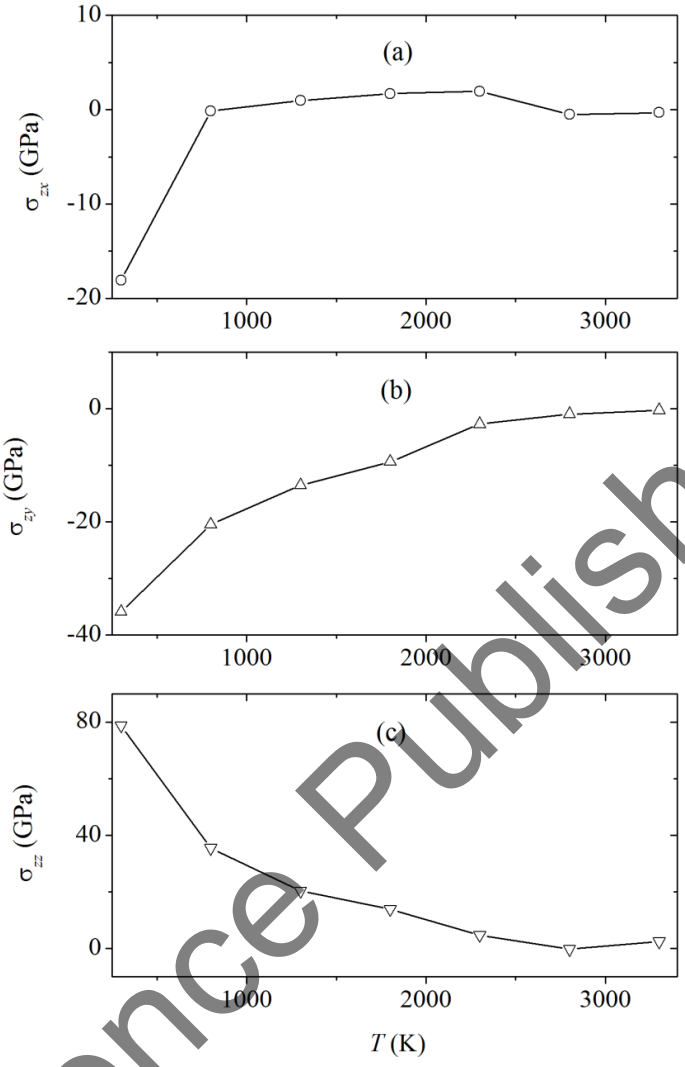

Figure 47. Stresses in the *xy* plane of Al film: (a) σ_{zx}, (b) σ_{zy}, and (c) σ_{zz}.

The inequivalence of the directions in graphene leads to the anisotropy of stresses in the Al-film plane, i.e., the stresses σ_{zx} and σ_{zy} differ significantly (Figure 47a, b). When the forces causing stresses in the film act in the "zig-zag" direction of the graphene sheet, the initial stresses σ_{zx} are the lowest ones and have the shortest relaxation time. The initial stresses in the film increase by the factor of almost 2 in the case where the forces inducing the stress σ_{zy} are oriented parallel to the "armchair" direction of the graphene sheet. These stresses relax slowly. The forces acting in the vertical direction induce the highest stresses σ_{zz} in the Al film. These stresses decrease as the temperature increases as slowly as the stresses σ_{zy}.

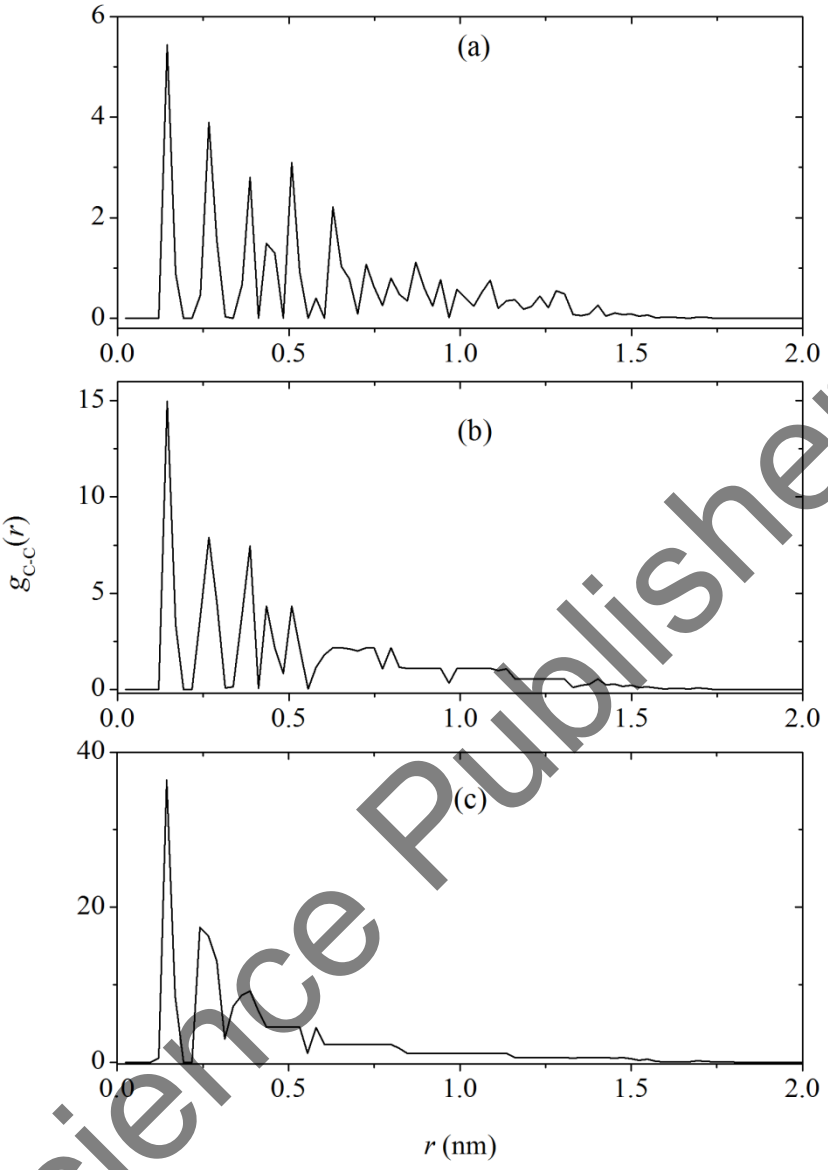

Figure 48. Radial distribution functions of the upper graphene sheet at temperatures (a) 300, (b) 1300, and (c) 3300 K.

The temperature changes in the graphene structure are illustrated in Figure 48. The radial distribution functions of the C atoms for the upper graphene sheet are presented at three temperatures. Similarly, to the case of the Al film, the functions $g(r)_{\mathrm{C-C}}$ were constructed for the single atom located most closely to the sheet center. Many well-resolved peaks of this function at 300 K indicate the presence of an ideal two-dimensional crystal structure. Such structure becomes more distorted as the temperature increases. This is indicated by the disappearance of the furthest peaks of the function $g(r)_{\mathrm{C-C}}$. For

example, almost all remote peaks disappear at T = 1300 K. Only three peaks remain at the temperature of 3300 K. These peaks are shifted to smaller distances with respect to their position at lower temperatures. This indicates the presence of very dense atomic packings in the graphene sheet. The long-range order in heated graphene gradually disappears.

The mobility of the C atoms in the plane of the lower graphene sheet fluctuates at T = 2300 K (Figure 49a, curve 2). This behavior of the dependence $D_{xy}(T)$ can be due to detachment of the single C atoms from the sheet corners. However, even at T = 2800 K, the D_{xy} value for this sheet becomes low again. The D_{xy} value increases simultaneously for both graphene sheets only at 3300 K. It is related to the beginning of fracture of the edges of both sheets. The function $D_z(T)$ increases with the temperature for both sheets more gradually although this increase fluctuates.

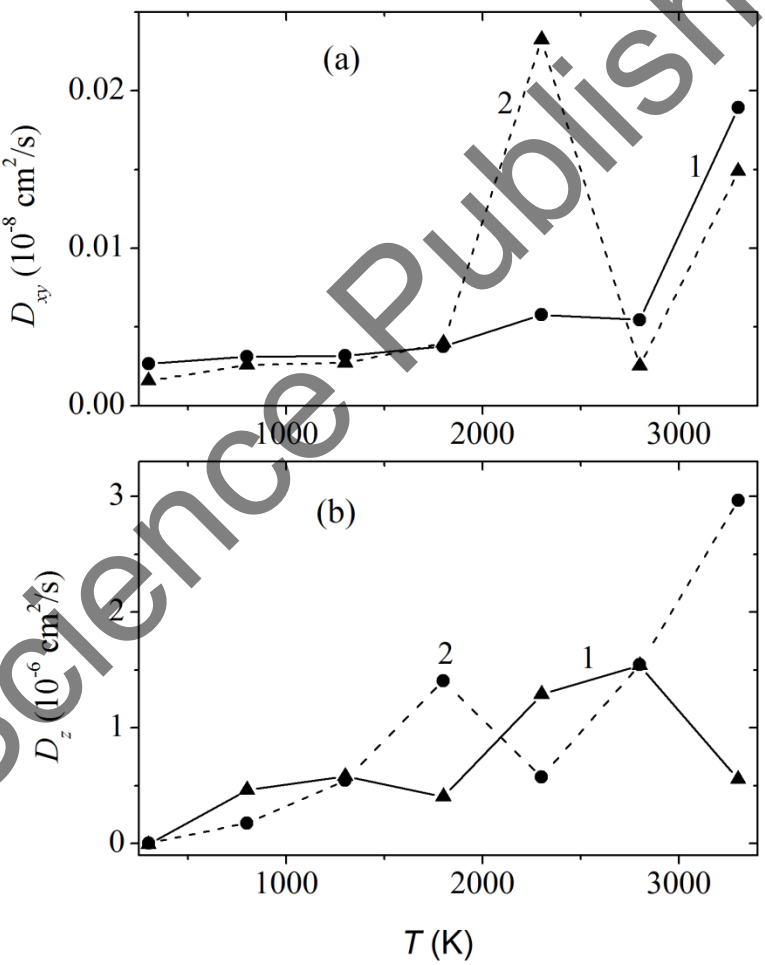

Figure 49. (a) Horizontal (D_{xy}) and (b) vertical (D_z) components of the self-diffusion coefficient of the (1) upper and (2) lower graphene sheets.

At T = 3300 K, the vertical mobility coefficient of the C atoms in the lower sheet increases faster. Although the fluctuations of components D_{xy} and D_z for the upper sheet are weaker than those for the lower one, the former, overall, appears to be more distorted than the latter.

We will consider how the stresses σ_{zx} and σ_{zy} (formed by atomic rows in the "zig-zag" direction) are distributed in the upper graphene sheet (Figure 50). Even at 300 K (curve 1), the stresses in the sheet plane caused by the forces in the "zig-zag" direction are distributed more non-uniformly than the stresses caused by the forces in the "armchair" direction. In addition, the stress σ_{zx} has the larger maximum values as compared with the stress σ_{zy}.

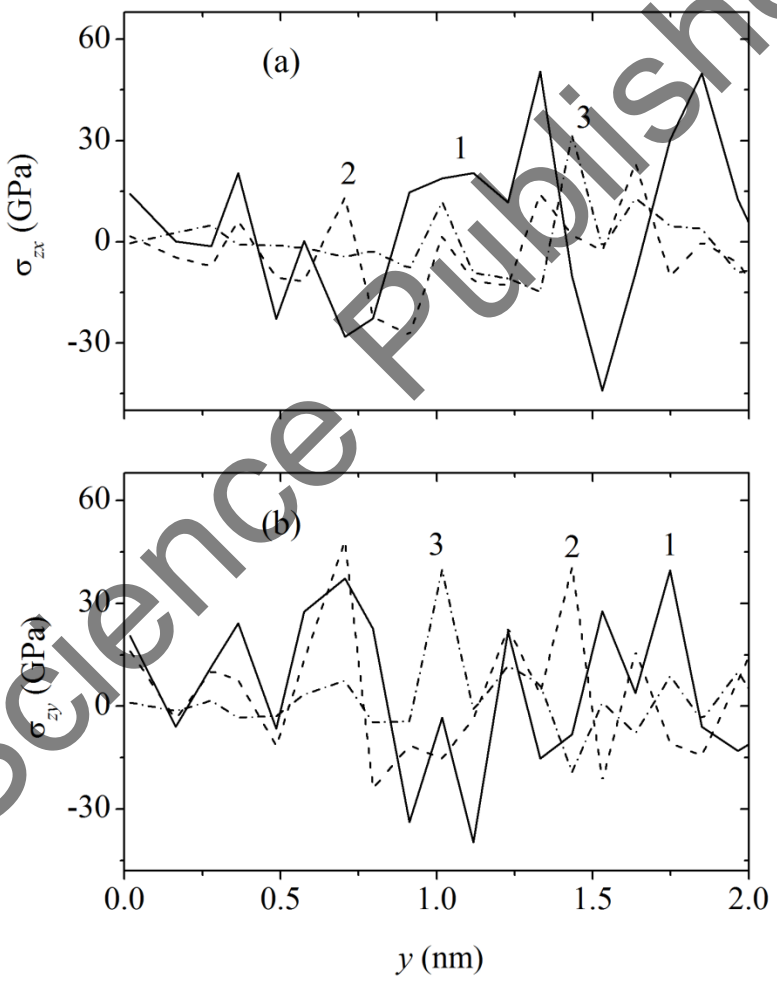

Figure 50. Distribution of stresses (a) σ_{zx} and (b) σ_{zy} in the upper graphene sheet over rows of the C atoms oriented in the "zig-zag" direction at (1) 300, (2) 1300, and (3) 3300 K.

Since we use the free boundary conditions, the value of the change in stresses σ_{zx} and σ_{zy} (when passing from one atomic row to another) decreases as the temperature increases. However, the decrease in the value of this change is more significant for the stresses σ_{zx} (i.e., when the forces act along atomic rows in the "zig-zag" direction).

Our simulation showed that a monoatomic aluminum film on the two-layer graphene has the high thermal stability. It is provided by the high-temperature stability of the graphene structure and high absorption properties of graphene. The Al atoms freely move over the substrate surface to form a close-packed mono-layer island. The size of the metal film decreases more significantly in the transverse direction (i.e., the "armchair" direction with respect to graphene). Below some temperature, the decrease in the distance (between the metal atoms that are bonded with the substrate) reduces both the horizontal and vertical components of the self-diffusion coefficient of the Al atoms. However, when the film temperature is near the experimental value of the Al boiling temperature, both components of the self-diffusion coefficient increase. The stress caused by the longitudinal forces (in the "zig-zag" direction) relaxes in the Al film with the highest rate.

The stresses induced by the forces acting in the vertical and "armchair" directions undergo slow temperature relaxation. There is no explicit correlation between the kinetic properties of the aluminum film and graphene sheets. The horizontal mobility of the C atoms sharply increases at T = 3300 K (which is in agreement with the behavior of the function $D_{xy}(T)$ for aluminum). The vertical mobility of the C atoms is rather ambiguous.

The stress in the plane of the upper graphene sheet caused by the forces acting in the "zig-zag" direction changes (decreases) as the temperature increases more significantly than the corresponding stress caused by the forces acting in the "armchair" direction.

Chapter 5

HEATING OF MERCURY ON GRAPHENE

Mercury is emitted not only by natural processes but, also, by human activities such as burning the fossil fuels. Nowadays, we have not technology that can uniformly control mercury from flue gas emissions by a cost-effective criterion. The cost of the 90% mercury removal by applying a carbon bed adsorption is very high. The carbon is impregnated with sulfur at the concentration about 10 to 15 wt%, and mercury reacts with sulfur as the gas goes through the sulfur-impregnated carbon bed to form the mercuric sulfide (HgS). Activated carbon cannot be used to collect mercury at high temperatures, because it is destroyed at 130°C. For this purpose, application of the Pd-based sorbents, which are resistant up to the temperature of 400°C is proposed [321]. The mechanisms of mercury removal by the gold sorbents and synthetic sorbents based on MnO_x, as well as, across vanadia-titania SCR catalyst are considered in [322–324].

The above factors make to use the activated carbon for removing mercury from the industrial plants heavy smoke to be problematic. Mercury is often present in natural gas, petrochemical, and some refinery feed streams. The mercury level in natural gas can reach about 1.2×10^4 ppt by volume. Mercury can be removed from the regeneration gas by condensation when the mercury level in the feed gas is high. Various, methods (including energy consuming) of purification from mercury have been proposed. There is a method of reducing the mercury levels in the mercury-contaminated material using microwave energy. Graphene oxide effectively removes the radionuclides (including uranium, europium, strontium, and technetium) in water even at the concentration of < 0.1 g/L.

Graphene is inexpensive, but it is very delicate because of its thinness and difficultly to transfer. It is expected that graphene may be put to work in the large-scale desalination. Mercury in water has been found in groundwater and wells where it is present in mineral deposits or where a volcano has been active. Adsorption holds great promise for mercury

removal due to the simplicity and relatively low-cost of the method, as well as, its effectiveness to purify water. Now a better way to remove mercury in drinking water is filtration using activated carbon that allows removing 95 − 97% of mercury in water.

The molecular dynamics simulation method was used to investigate the removal ability of the Hg ions from aqueous solution using the functionalized graphene membrane [325]. It turned out that the Hg^{2+} ions met a relatively small energy barrier and under using an external electrical field, they could pass through the F-pore graphene. It was found that graphene is an ultrafast water purifier [326]. Filters swell in water, but they retain the ability to allow water molecules to pass through quickly. It is possible to perforate the graphene sheet with holes only 1 nm wide. The holes allow water molecules to pass through but block the salt. A graphene filtration system could reduce costs while shorting the filtration time to get drinkable water directly from the ocean.

On the other hand, graphite and glassy carbon electrodes are widely used as a substrate for the mercury film electrodes. Such a combination is possible due to the inertia of graphite and glassy carbon toward mercury. This minimizes contamination of mercury film on the substrate. There are opinions that the mercury film deposited on the graphite substrate does not consist of a uniformly arranged layer of mercury, but it consists of an aggregate of very small mercury droplets [327]. This hypothesis needs to be thoroughly checked. On the other hand, it is known that the first mono-layer of a deposited metal on a various solid substrates (electrodes) can have a considerably larger bonding energy with a different substrate than the normal bonding or lattice energy of this metal [328]. Therefore, the potentials that are more positive should be used to oxidize the first mono-layer. In this context, it is of interest to investigate graphene wetting by mercury.

Liquid mercury does not wet graphite. Indeed, on highly ordered pyrolytic graphite, the fresh mercury droplets have a contact angle of 152.5° [329]. As any other liquid metals (with surface tensions γ higher than 0.18 N/m) do the mercury does not wet carbon nanotubes [330]. The surface tension of mercury is 0.46 N/m. Nevertheless, wetting and filling of the internal cavities of carbon nanotubes with mercury take place due to the electrowetting [331]. The effect of electrostatic interactions on the sorption of hydrocarbons by water droplets (γ_{H_2O} = 0.0729 N/m) was investigated in [332]. The mercury contact angle linearly increases with the curvature of carbon nanotube walls. Therefore, the internal surface of a nanotube has a higher persistence with respect to mercury than that of the graphene planar surface [333]. Graphene wetting with mercury has not been studied.

5.1. COMPUTER MODELING OF STRUCTURE AND PROPERTIES OF MERCURY FILMS ON GRAPHENE

Environmental pollution with heavy metals is a global problem [334, 335] due to its detrimental consequences for health [336]. Composite membranes based on graphene for the accumulation of mercury have been proposed in [337]. The structure and physical properties of the liquid mercury–graphene interfaces remain unstudied; meanwhile, the prospect of using graphene as a filter demands study. Liquids with isotropic pair interactions encounter vibrational interface structures at temperatures close to melting point T_m, providing that the T_m / T_c ratio (where T_c is the critical temperature) is low. The melting point of the bulk mercury is T_m = 234 K.

Cold liquid metals such as Hg and Ga have low ratio T_m / T_c = 0.13 and 0.15, respectively. The MD modeling reveals their non-monotonous density profiles near the liquid mercury/vapor interface [338]. On the other hand, the interface range has a non-zero thickness that depends on temperature. Calculation of the properties was performed for the liquid/vapor interface with clear allowance for the dependence of the density potential. However, it did not result in satisfactory agreement with the experimental data on ionic and electron density distributions orthogonal to the surface or on the reflection coefficient [339].

Theoretical study of liquids of this type requires knowledge of the effective atomic potential, which allows one to correct predictions of the liquid/vapor phase diagram in the temperature–density coordinates. Out of all the proposed potential functions for mercury, it is difficult to choose one, on whose basis the structure of liquid mercury on graphene can be reproduced satisfactorily. The structure of solid metals in contact with graphene (e.g., deposited copper films) has been studied more thoroughly [269].

On a graphene sheet containing 406 atoms, 50 atoms were deposited in a random manner. The resulting system was then set to equilibrium in the MD calculations with the period of 200000 time steps (Δt = 0.2 fs). Interatomic interactions in graphene were represented by the modified Tersoff many-particle potential [40]. This potential is based on the concept of bond order and its modification is described in Chapter 2. The Schwerdtfeger (Sch) and Silver–Goldman (SG) pair potentials were used to describe the interaction of Hg-Hg (see formulas (13) and (14) in Chapter 2). The graphene–mercury interaction was represented by the LJ potential with the parameters from [45]. Bi-vacancies are one of the most widespread defects in graphene. The presence of such defects remarkably enhances the coupling of graphene with a deposited metal. In the present model, nine bi-vacancies were formed nearly uniformly on the 3.4 × 2.8 nm graphene sheet [340]. The hydrogenation of graphene results in slight surface ribbing, which also increases the linkage between the metal and graphene. Preliminary partial hydrogenation strengthened the graphene edges and stabilized bi-vacancies. A hydrogen atom was

effectively added to each boundary atom (including those in the vicinities of bi-vacancies). More specifically, an entire CH group was considered in considering interactions rather than the individual H atoms. This group interacted with C atoms [341], other CH groups [58], and Hg atoms [342] through the LJ potential. Fourteen CH groups were arranged along the perimeter of each bi-vacancy. Each CH group was described according to the monoatomic scheme in [341].

The energy $U_{\mathrm{Hg-Hg}}$ of Hg–Hg interaction in the film (which was set after equilibrating the system with the potential) was one-third of the bond energy in the $\mathrm{Hg_2}$ dimer determined with the same potential [342]. The analogous energies $U_{\mathrm{Hg-Hg}}$ for two other potentials and energies of the mercury–graphene interaction $U_{\mathrm{Hg-C}}$ are given in Table 13. It is seen, that the highest absolute values of the energy $U_{\mathrm{Hg-Hg}}$ were obtained for the Sch potential. The lowest ones correspond to the SG potential. On the other hand, the best cohesion between mercury and graphene was provided by the LJ potential. The worst was obtained by the Sch potential.

Application of the LJ, Sch, and SG potentials for mercury yielded metal films of various structures on graphene. The LJ potential yields a denser packing of atoms, while the SG potential yields more loose and uniform packing. There is a tendency toward the vaporization of atoms at temperatures as low as 300 K for the SG potential. The configuration of the H–graphene–Hg-film system obtained with the Sch potential is given in Figure 51 at the instant 200 ps. At this instant, the graphene had a slight ribbing that could be detected from the deviation of the boundary of the C atoms from the even row of H atoms. Note that the latter were built along the initial coordinates of the CH-groups. In this case, the Hg film was quite uniform. However, it did not spread over the entire graphene surface; rather, it gathered into an elongated drop that was flattened to graphene. None of the Hg atoms got onto the other side of graphene through a bi-vacancy, though, several metal atoms did get stuck in defects. The motion of the Hg atoms to the other side of the graphene was observed for two other potentials, though, these penetrations were less than 0.08 nm long. The Sch potential was the one that was best from the viewpoint of retaining the Hg atoms on graphene.

Table 13. Energies $U_{\mathrm{Hg-Hg}}$ and $U_{\mathrm{Hg-C}}$ of a liquid mercury film on graphene for three potentials

Energy	Potentials		
	LJ	Sch	SG
$U_{\mathrm{Hg-Hg}}$ (eV)	- 0.0236	- 0.0280	- 0.0011
$U_{\mathrm{Hg-C}}$ (eV)	- 0.0154	- 0.0121	- 0.0148

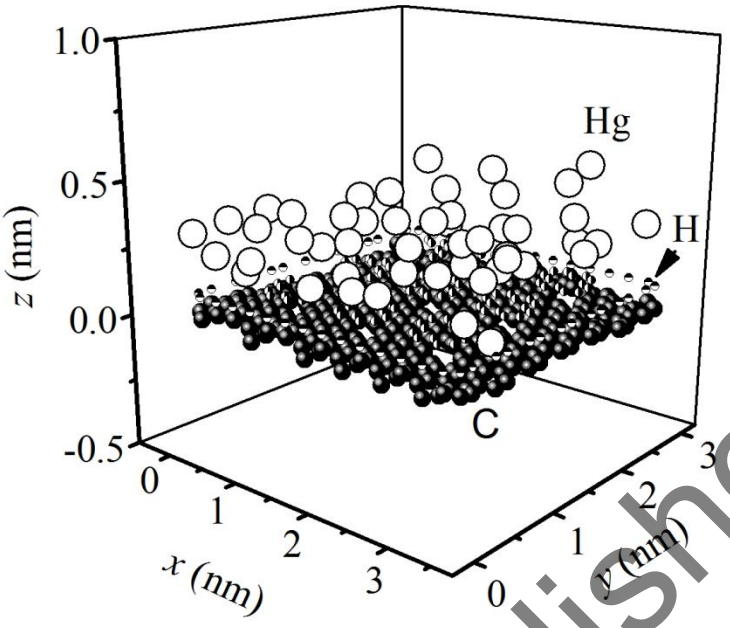

Figure 51. The configuration of mercury film on the modified graphene system obtained at the instant 200 ps; the positions of H atoms correspond to the coordinates of CH-groups reduced to one point at the initial instant.

Due to the thinness of the film, its density profile was determined quite roughly and revealed no oscillations for the mentioned three types of potentials. However, distribution of the Hg atoms over the graphene surface was neither homogeneous nor uniform in the considered cases. The greatest tendency toward the formation of dense clusters in a film was characteristic for the system created using the LJ potential for mercury (Figure 52). There the first three peaks of the function $g(r)$ were the highest and well resolved. A tighter and more compact structure was characteristic of the film obtained using the Sch potential: only the first four peaks of the function $g(r)$ were clearly resolved. However, in this case, the Hg film was also shown to be very loose. We see that the first peak of the function $g(r)$ shifted ~ 0.07 nm away from the position of the corresponding peak of the function $g(r)_{\text{liquid}}$ for the bulk liquid mercury [338]. The four first peaks of this film were distributed between the positions of the first and third peaks of the function $g(r)$ for liquid mercury.

The radial distribution function for the film obtained with the SG potential had the greatest (~ 0.17 nm with respect to the position of $g(r)_{\text{liquid}}$ peak) shift of the first peak. The emergence of the second peak $g(r)$ of this film only slightly anticipated the position of the third peak of this function for the film formed using the Sch potential.

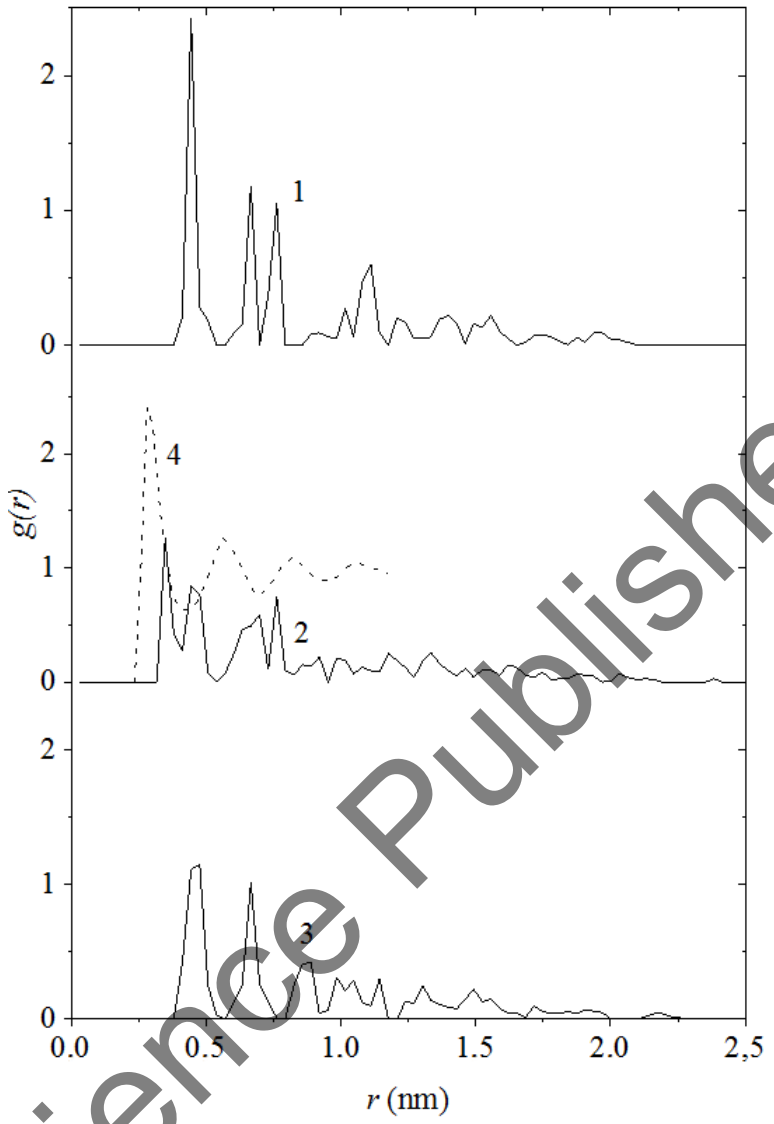

Figure 52. Radial distribution functions of mercury films on graphene obtained with the atomic interaction potentials (1) LJ, (*2*) Sch, (3) SG; (4) *g(r)* of the bulk liquid mercury (the MD calculations) [338].

The specificity of the system geometry requires individual consideration of the horizontal and vertical mobility of Hg atoms. The behavior of the horizontal D_{xy} and vertical D_z components of the self-diffusion coefficient of the Hg atoms is shown in Figure 53. These components were calculated at the time intervals of 40 ps with different atomic interaction potentials for mercury. The component D_{xy} grows only up to $n = 2$. At subsequent time intervals, the D_{xy} usually stabilized or fell inconsiderably. This behavior

of D_{xy} is due mainly to the initial sealing of the film and the subsequent retention of its density. The highest values of D_{xy} were obtained using the SG potential while the lowest values were obtained with the LJ potential. The Sch potential produced the most stable values of D_{xy} at $n \geq 2$. In addition, these values did not differ essentially from the D_{xy} value obtained with the LJ potential. The vertical component of the atoms mobility behaved differently for all considered potentials. In all cases, the D_z value grew non-monotonously. Finally, the maximum value of D_z was reached with the LJ potential. The minimum value was achieved with the SG potential.

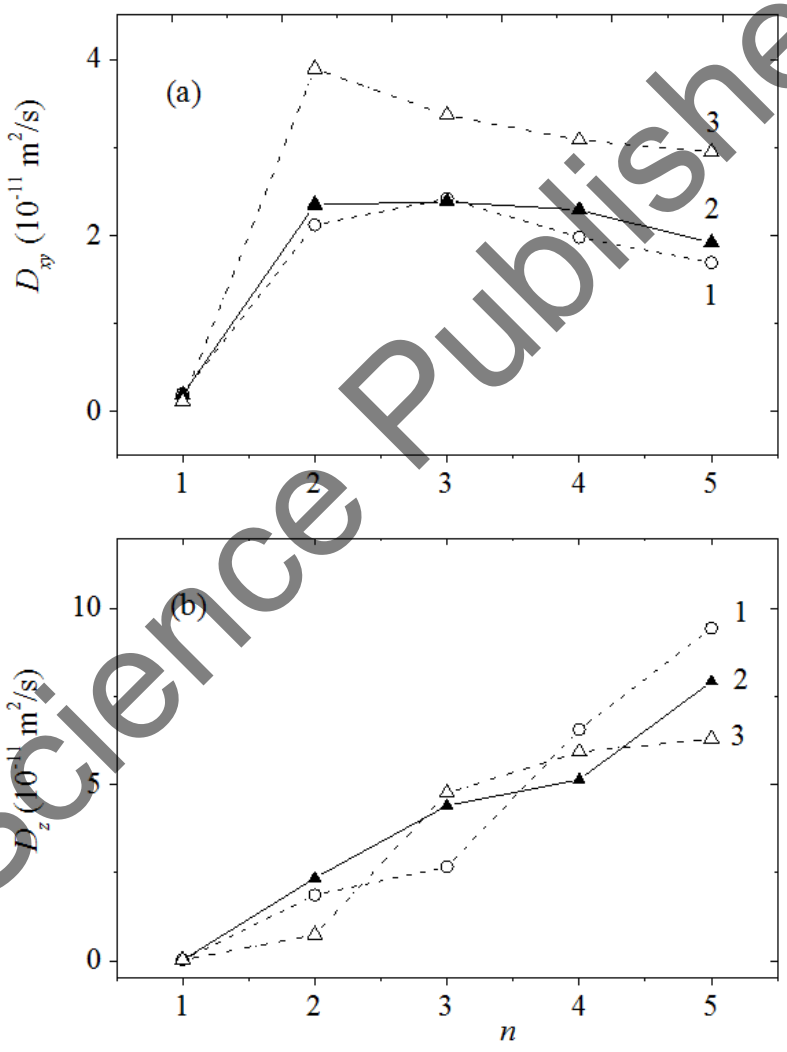

Figure 53. (a) Horizontal and (b) vertical components of the mobility coefficients of the Hg atoms in mercury films on graphene obtained using the atomic potentials (1) LJ, (2) Sch, (3) SG; *n* is the number of the intervals, in which coefficients D_{xy} and D_z were determined.

In this context, the situation is inverse to the behavior of the component D_{xy} at high n. Another feature of the $D_z(n)$ dependence was determined by the tendency toward vaporization from the film of atoms for each potential. For all three our model potentials, the self-diffusion coefficients were obtained to be lower than the experimental value of D (15.9×10^{-11} m^2/s at T = 298 K) for the liquid mercury [343]. Somewhat better agreement with the calculated values of $D = D_{xy} + D_z$ was achieved when D was determined via non-elastic neutron scattering on the liquid mercury (14.3×10^{-11} m^2/s at T = 297 K) [344].

Similarly, to the hydrogenation, a mercury film (that forms on graphene) affects its 3D structure (i.e., its roughness R_a). In calculations, the R_a value increases for the Hg films that form for all three potentials (Figure 54). The highest R_a values are characteristic of graphene with a metal film obtained via the Lennard-Jones interaction. The Hg films created with the Sch and SG potentials have the similar R_a values throughout all calculations. However, at the final step of calculation the R_a value for the Hg film (formed as the result of using the SG potential) becomes lower.

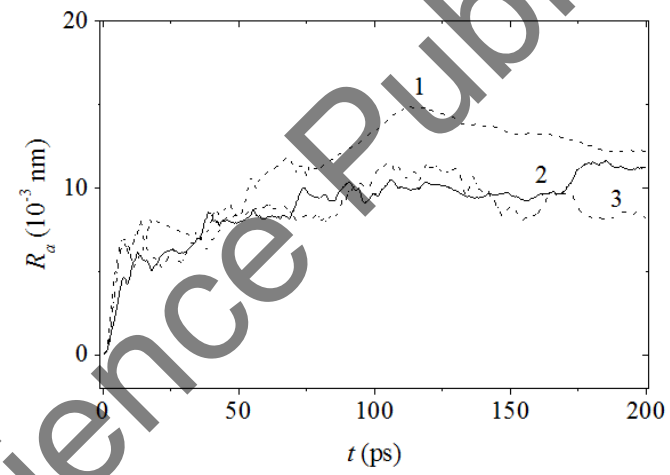

Figure 54. Evolution of the graphene roughness coated by the mercury films obtained using the atomic potentials (1) LJ, (2) Sch, and (3) SG.

The forces of cohesion between the mercury and graphene atoms are weak compared to ones between the mercury atoms. Mercury tends toward its natural boundary angle, wetting is terminated, and mercury gradually consolidates into individual drops. This phenomenon is largely reproduced using the Sch potential. A tendency toward drop formation is also observed for the LJ and SG potentials. However, in these cases, there are considerably more individual atoms on the graphene surface, and each drop has a less distinct profile. For real mercury, the vaporization proceeds at temperatures above 291 K. Cohesion with the modified graphene does not allow the Hg atoms to detach from the film

at distances much greater than atomic one at 300 K. However, the tendency toward the vaporization of Hg atoms is still observed in model systems and is clearer when using the SG potential.

5.2. Mercury Droplet Formation on Graphene Surface

Modeling the mercury adsorption on the surface requires exact potentials of the Hg−Hg and Hg−substrate interaction. Potentials presented as pair interactions are usually used to describe adsorption. The Lennard−Jones potential is one of the simplest of these. The parameters of this potential were chosen according to the data on the viscosity of gaseous mercury [345]. In this section, we consider the behavior of the mercury film on graphene when the Hg−Hg interaction is based on the Schwerdtfeger interaction potential. All potentials used are described in the previous section.

A graphene sheet is placed on a copper substrate, which does not allow C atoms to move vertically downward [346]. Therefore, the motion of the sheet under the influence of cluster impacts was completely excluded. The copper substrate was the slice of five atomic layers of the fcc lattice, and the lattice (100) plane served as a surface of the slice. This surface has a square shape, 10 Cu atoms are located along the edge of this square, and the entire slice contains 1000 Cu atoms. The graphene sheet of size 3.4 × 2.8 nm containing 406 atoms of C is placed on the substrate and fully fitted into this square. In the chosen coordinate system, the graphene sheet had "zig-zag" edges along the x axis and the "armchair" edges, in the direction of the y axis. Initially, all the C atoms have coordinates $z = 0$. The substrate atoms were fixed but could interact with the C atoms of the graphene and the Hg atoms of the film [347]. Boundary conditions at the edges of graphene were free. This allows investigating the stability of edges to external dynamic loads. At the initial state, mercury was present on graphene in the form of a thin film. The film of mercury on graphene was formed in a separate molecular dynamic calculation in two stages. At the first stage, the Hg atoms were placed above the centers of nonadjacent cells of the graphene. Their locations were such that the nearest inter-atomic distance between Hg and C atoms was equal to 2.30 Å. This distance was calculated according to the density-functional method [337]. On top of this loose film consisting of 49 mercury atoms, 51 additional Hg atoms were deposited randomly. Then the system, which consists of 100 atoms of Hg and 406 atoms of C, was brought to equilibrium in the MD calculation with a duration of 1 million time steps (Δt = 0.2 fs). The graphene contained bi-vacancies or Stone–Wales defects. The graphene edges were hydrogenated, i.e., the model representing mercury on graphene was almost similar to the one described in the previous section. Each Stone-Wales defect is a combination of two contiguous five- and seven-membered rings. When heating was investigated, the graphene sheet that was used to deposit Hg had six such defects approximately uniformly distributed over its surface [348].

It is easy to show that the average rate of the system heating is ~ 10^{11} K/s taking into account the value of the time step, the calculation time, and the addend for the increase in the temperature [349]. Under these conditions of incomplete structural relaxation of the system, it may be superheated. In the case of metals, the superheating is aggravated by the effect of the electron subsystem, which stabilizes the condensed state. Variations accompanying the heating of the mercury film on graphene are illustrated in Figure 55. The liquid metal film begins to partially separate out of graphene already at T = 300 K. This is reflected in the rise of the film edges over graphene and film thickening (Figure 55a). The atoms of the central region of the bent Hg film are more strongly bonded to the substrate and have average minimum distance (created by 12−18 Hg atoms) $\overline{r}_{\mathrm{C-Hg}}^{\mathrm{min}}$ = 0.28 nm.

At 600 K, the Hg film is completely transformed into a droplet contacting with graphene (Figure 55b). In this case, the average distance $\overline{r}_{\mathrm{C-Hg}}^{\mathrm{min}}$ increases to 0.34 nm. Further increase in the temperature leads to a higher rise of the majority of the droplet mass over the graphene surface; for example, at 1100 K, $\overline{r}_{\mathrm{C-Hg}}^{\mathrm{min}}$ = 0.47 nm. As the Hg film contracts into the droplet, the horizontal component D_{xy} of the mobility coefficient of mercury atoms decreases, while the vertical component D_z passes through the minimum at 600 K (Figure 56). The smooth decrease in D_{xy} characterizes the rolling of the film into a dense droplet. The behavior of the component D_z indicates that the process of droplet formation ends at T = 600 K. The vertical mobility of Hg atoms is somewhat enhanced under a further increase in the temperature and a slight increase in the distance between the droplet and the graphene surface appears.

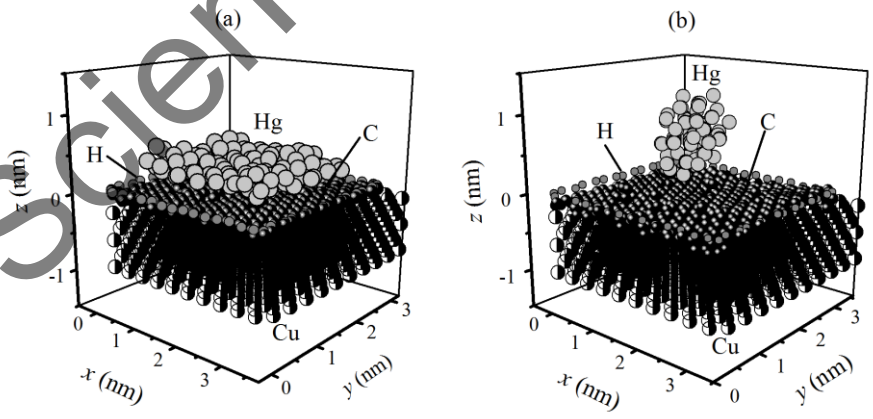

Figure 55. Configurations of the “Hg film on partly hydrogenated defective graphene” system resulting from the stepwise heating at temperatures (a) 300 and (b) 1100 K.

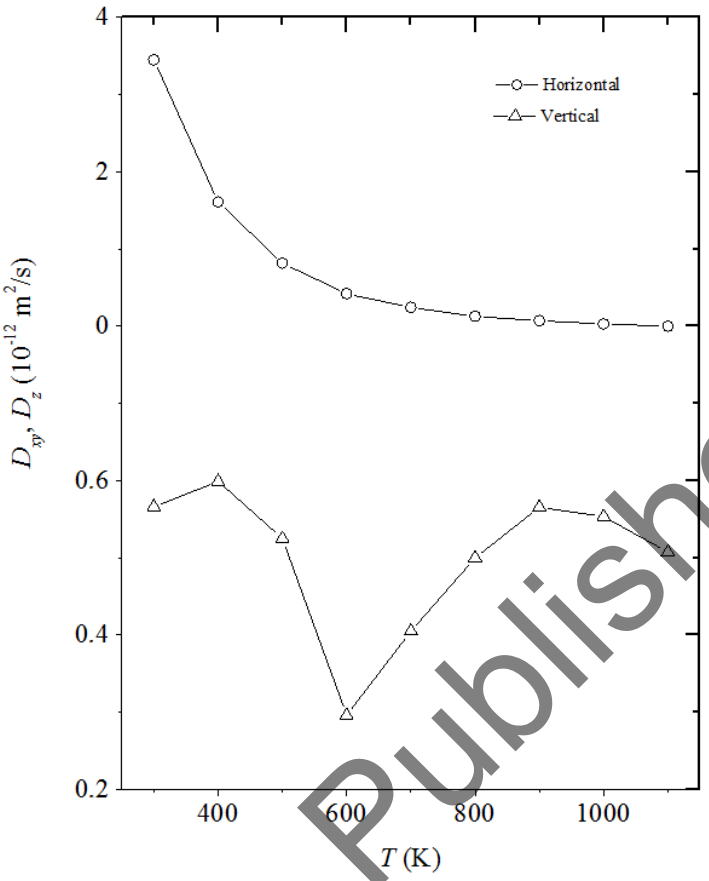

Figure 56. Temperature dependences of the horizontal and vertical components of the mobility coefficient for the Hg atoms.

Vertical (scanned along the z axis) density profiles $\rho(z)$ of mercury at 300, 600, and 1100 K are presented in Figure 57. The narrow $\rho(z)$ profile measured at T = 300 K has two sharp peaks, which suggest a predominantly two-layer arrangement of the Hg atoms on graphene. However, at T = 600 K, the density profile widens and shifts upward. The low intensity of the $\rho(z)$ spectrum at the edges and the higher density of the intense peaks in the middle of the spectrum characterize the appearance of a sphere-like formation, i.e., a droplet with a layered structure. This is evident from a large number of narrow peaks in the $\rho(z)$ spectrum. The very close location of a number of these peaks indicates the irregularity of the formed structure.

At 1100 K the profile $\rho(z)$ has a length close to the length of the corresponding profile at T = 600 K that indicates the formation of a dense droplet of mercury already at the temperature of 600 K. Because of the uneven peak intensities of $\rho(z)$ at T = 1100 K, one can conclude that the upper part of the drop is denser than the bottom one.

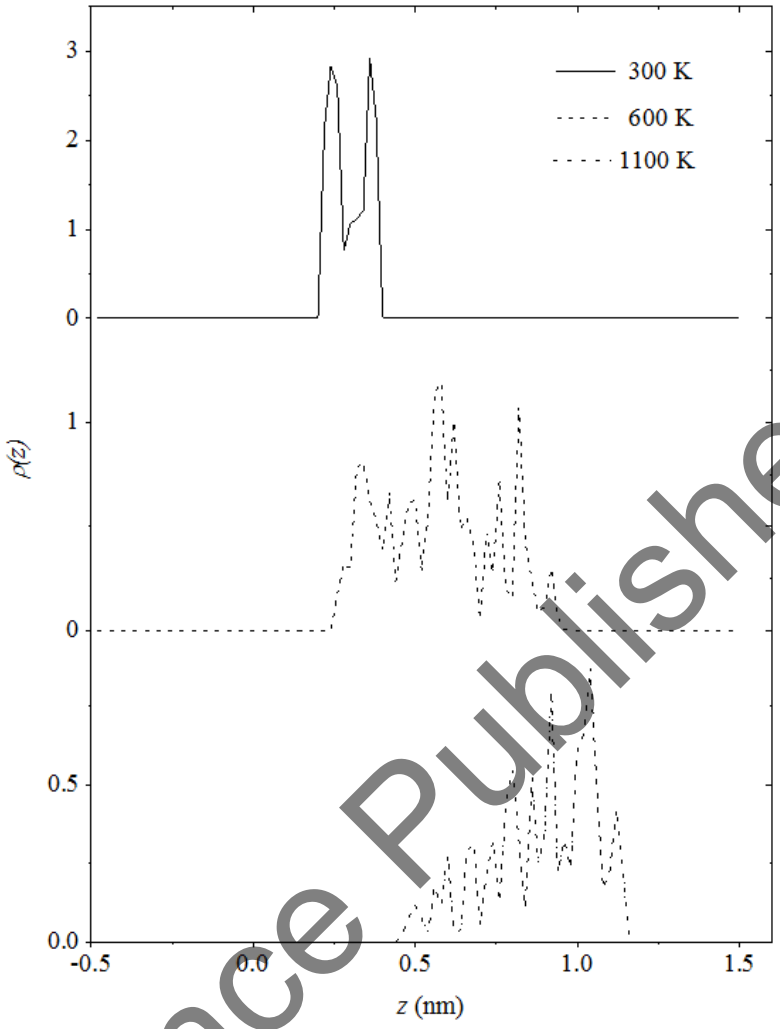

Figure 57. Vertical density profiles for the liquid mercury on graphene at different temperatures.

The $g(r)$ radial distribution functions (Figure 58) (plotted for the Hg atom nearest to the center of mass of liquid mercury) also indicate the formation of a more compact structure at T = 1100 K than that at the initial temperature 300 K. The $g(r)$ function reflects the spherically averaged structure of liquid mercury including that in the horizontal plane, while the $\rho(z)$ function does not do so. Reduction in the number of peaks in the $g(r)$ function at T = 1100 K suggests the formation of an irregular compact structure. Here, the distances to the first and second-order neighbors are estimated to be r_1 = 0.29 nm and r_2 = 0.48 − 0.57 nm, respectively. The experimental values of these parameters for the liquid mercury at 300 K are r_1 = 0.31 nm and r_2 = 0.59 nm [347].

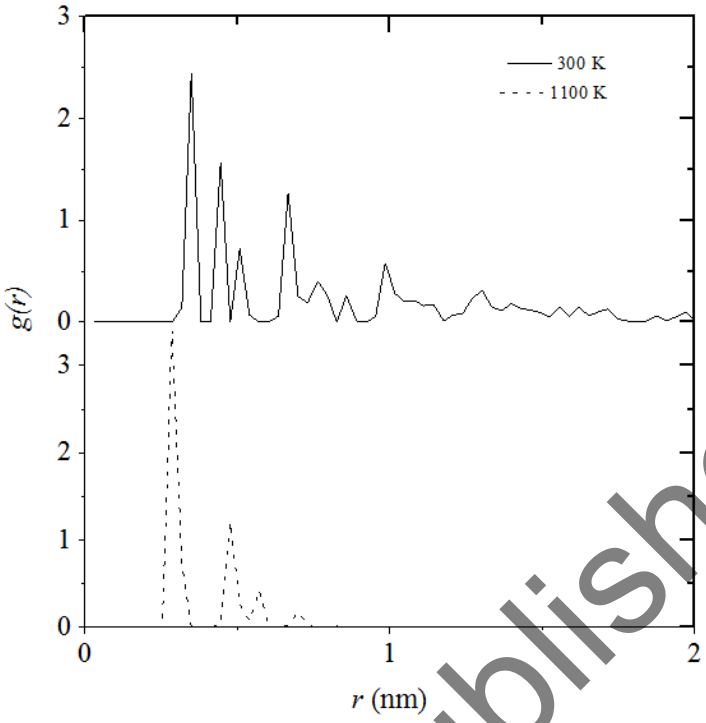

Figure 58. Radial distribution functions calculated for the liquid mercury on graphene at different temperatures.

Variations in the wettability that accompany mercury film rolling into a droplet are evident from the temperature dependence of the calculated contact angle θ (Figure 59). The initial increase in the $\theta(T)$ function (up to T = 500 K) is due to the predominance of the influence of film heating over the effect relevant to variations in its morphology. It is known that, as the temperature increases, the blunt contact angle of a droplet becomes closer to the flat angle. Despite a noticeable rise of the droplet over the graphene, which begins at 600 K, its separation from the substrate may only be related to the temperature 800 K.

The calculation at 600 K ends when seven Hg atoms are still located at distances r from graphene shorter than distance $r_{\min}$ = 0.3727 nm. The latter corresponds to the minimum of the LJ potential describing the Hg−C interactions. At 700 K, two such cases are observed, while at T = 800 and 900 K, they are absent. However, one and two Hg atoms with $r < r_{\min}$ arise at T = 1000 and 1100 K, respectively. The average angle $\bar{\theta}$ = 127.1°, which corresponds to temperatures 900 − 1100 K, may be considered to be the contact angle of the Hg 100-atom cluster on graphene. This angle is noticeably smaller than the contact angle for a macroscopic droplet of mercury on pyrolytic graphite (straight line in Figure 59) [329]. This agrees with the common ideas of reduction in the angle θ with a decrease in the droplet radius.

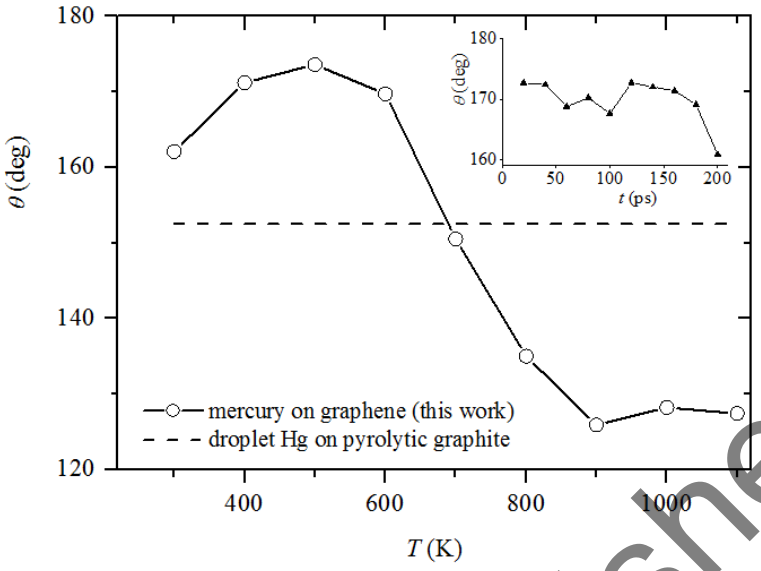

Figure 59. Temperature dependences of the contact angles for mercury on graphene and macroscopic mercury droplet on pyrolytic graphite; the inset shows the time dependence of the contact angle θ for mercury droplet on graphene at T = 600 K.

The Young−Laplace equation gives the relationship between the interfacial pressure (the pressure across the interface) and these radii of curvature

$$\Delta P = \gamma\left(1/R_1 + 1/R_2\right), \tag{47}$$

where ΔP is the inter-facial pressure difference, γ is the interfacial tension, and R_1 and R_2 are the radii of curvature.

The surface tension varies greatly from substance to substance, and with temperature for a given substance. In general, the surface tension of a liquid decreases with temperature and becomes zero at the critical point. The effect of pressure on the surface tension is usually negligible. The shape of a drop is determined by its radii of curvature R_1 and R_2. In the case of a spherical drop, those are equal. The droplet radius decreases as the temperature increases. A drop disappears at the critical point because there is no distinct liquid-vapor interface at temperatures above the critical point. When we have a high internal pressure at small values of R_1 and R_2, then a decrease in the compression of the drop under its own weight is observed. This decreases the contact angle θ. This behavior of the function $\theta(R_1, R_2)$ is not always observed, but it is confirmed for mercury droplets on the carbon substrate. The inset of Figure 59 shows the time dependence of θ at 600 K. It is seen that the angle θ has begun to decrease noticeably by the end of the calculation at this temperature.

The peak at 120°, which indicates the presence of the main elements of the two-dimensional structure, i.e., the hexagonal honeycombs, dominates in the angular distribution of the nearest neighbors in graphene at T = 300 K (Figure 60). Additional peaks arise in this distribution due to the high density of the Stone-Wales defects (penta- and heptagonal cells). Despite the fact that 1100 K is not a high temperature for graphene (its melting temperature is T_{m} = 4900 K), its structure has already suffered from obvious changes. The peak at 120° has become significantly wider. Moreover, the intensities of peaks at 30°, 90°, and 148° have substantially increased.

These changes indicate the growth of the defects in the graphene structure at T = 1100 K. The stresses σ_{zx} and σ_{zy} (that characterize the action of the internal horizontal forces in the graphene plane) have close values that weakly vary with increase in the temperature (Figure 61). A noticeable difference between these stresses, which is observed at T = 300 K, disappears while approaching the temperature 500 K. The values of stress σ_{zz}, which characterizes the action of the vertically directed forces, have the same order of magnitude as the stresses σ_{zx} and σ_{zy}. The function $\sigma_{zz}(T)$ comprises two regions of the fastest variations, i.e., a decrease upon heating to 400 K and an increase under heating over 1000 K. The weakest changes of $\sigma_{zz}(T)$ are observed in the temperature range 600 − 800 K, in which the majority of the droplet mass rises over graphene.

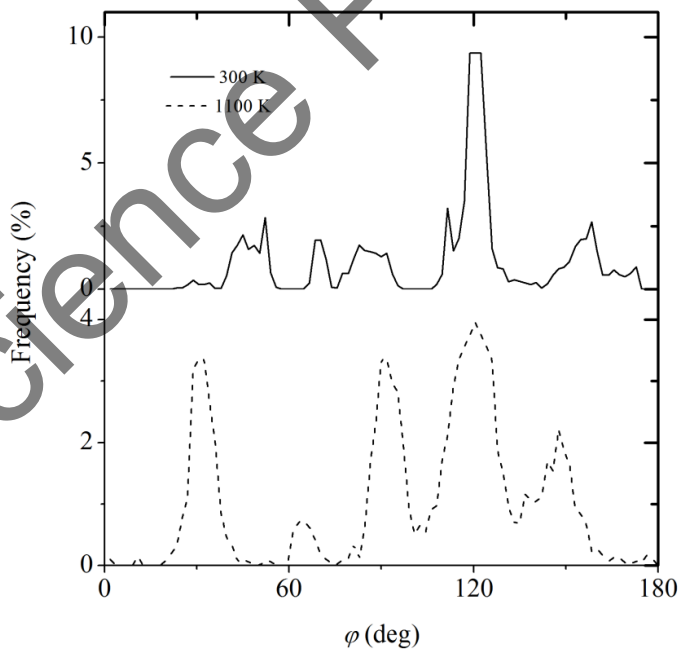

Figure 60. Angular distributions for the nearest neighbors in graphene at a high concentration of the Stone-Wales defects and different temperatures.

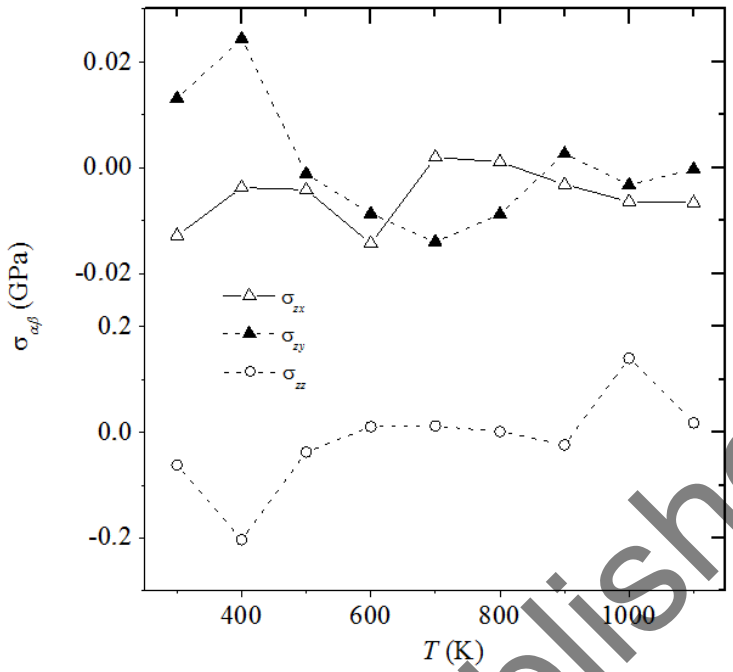

Figure 61. Temperature dependences of the components of the stress tensor in the plane of a mercury-coated defective graphene sheet.

The roughness R_a of the graphene saturated with the Stone-Wales defects increases fast with temperature (Figure 62). Because of vertical bombardment by the Xe_{13} clusters with the energy 30 eV, the graphene containing vacancies and coated with a mercury film acquires a roughness. It is close to R_a at 400 K without the bombardment [40]. The strong bond between the carbon atoms in graphene is better preserved at a high temperature ($T \geq$ 1000 K) when the simulation is performed in terms of the Sch potential than within the framework of the SG potential.

For mercury located on glass, quartz, or sapphire, the prewetting transition is distinctly observed. The existence of the metal−non-metal transition noticeably affects the thermodynamic, structural, interfacial, and dynamic properties of metals. The conductivity–density dependence for bi-valent mercury may be divided into three regions.

Mercury is a polyvalent metal, which is available for study in the liquid state at low temperatures. The critical point of its vapor is characterized by the following parameters: T_c = 1751 K, P_c = 167.3 MPa, and ρ_c = 5.8 g/cm^3. Mercury has the lowest critical temperature of those known for all liquid metals. This fact is of importance from the point of view of the precise measurement of the physical properties at high temperatures and pressures.

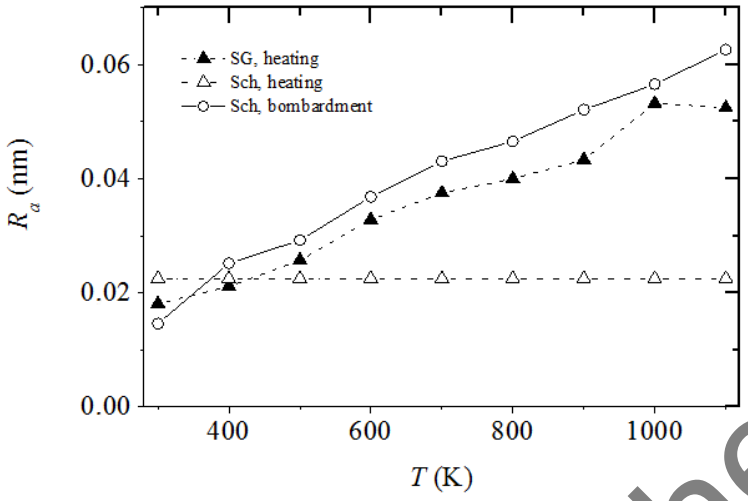

Figure 62. Temperature dependences of the roughness coefficient for mercury-coated graphene with respect to Hg−Hg interactions plotted with the use of different models: SG potential and Sch potential; temperature is varied by means of heating and vertical bombardment by the Xe_{13} clusters with the energy of 30 eV.

The experimental data on droplet evaporation on a hot surface indicate the existence of a discontinuity in the dependence of temperature difference $\Delta T = T^i_{\text{vap}} - T^i_{\text{liq}}$ (i denotes the interface) for the vapor pressure P^i_{vap} [350, 351]. At a liquid−vapor interface, the temperature is always higher on the side of the vapor. This is explained by the fact that the high-energy molecules are primarily evaporated, while molecules with lower energies remain in the droplet. Reduction in the flux of molecules into the vapor phase is mainly observed at high temperatures, for example, for water at $T / T_c \approx 0.84$ [352]. The value of the temperature discontinuity for water may be higher than 1400 K [56]. Mercury atoms are 11 times heavier than the water molecules. Another type of interaction characterizes mercury. It may be thought that a mercury droplet remains stable at high temperatures, because of a reduction in the flux of Hg atoms into the vapor phase; however, the characteristic features of this process differ from the behavior of water.

The high stability of a model mercury droplet may also be explained as follows. The interaction potential between two mercury atoms is, as a rule, considered to be a potential between the highly polarizable closed shells. This permits very low migration of electron density from one partner to another. Thus, this potential is, to some extent, similar to a potential function that describes the interaction between atoms of the noble gases. We have proven (using the Sch potential) the formation of a mercury droplet on graphene under fast heating using a calculation similar to that described above but performed in terms of the SG potential.

It was noted that the model approximations that use the pair interaction potentials to describe the liquid−gas transition for mercury are rough [353]. Experimental gas−liquid coexistence curves may be precisely reproduced. This proves that the two-atom curves obtained for the potential energy from the former principles are supplemented with the many-body potential. Note that such a potential describes the associative interaction of an atom with neighboring atoms that altogether form a virtual cluster. The liquid−gas transition for mercury is distinguished by the fact that the local electronic state changes from the metal to non-metal ones, because of the weakened many-particle interactions and decreased average coordination numbers.

According to the calculation in terms of the Sch potential, the Hg film rolls into a droplet under heating. By the end of the calculation at 600 K, an almost spherical droplet is formed on graphene, and this droplet remains near the graphene surface even at 1100 K. When the SG potential function is used, the distance between the droplet and graphene fast increases up to the temperature 1000 K. No significant separation of the Hg atoms from the droplet takes place in this case. Most likely, the Sch and SG potentials give an overestimated indirect effect of the electron component on the Hg−Hg interaction. That leads to the high stability of the liquid mercury with respect to its vapor.

The forces of cohesion between mercury and graphene atoms are weak compared to the ones between the mercury atoms. Increase in temperature has been shown to cause gradual rolling of the film into a droplet and a slow motion of the droplet away from the graphene. This phenomenon is largely reproduced using the Sch potential. The horizontal component of the mobility coefficient of Hg atoms smoothly decreases in the course of this process, while the vertical component nonmonotonically increases after the reduction reached at the temperature 600 K.

The vertical profile of mercury density shifts upward and widens to a size that corresponds to the diameter of the formed liquid metal droplet. Formation of the mercury droplet is accompanied by a reduction in the domain of the radial distribution function and a decrease in the number and intensity of the mentioned peaks of the $g(r)$ dependence. Increase in the temperature accelerates the formation of the droplet and decreases the contact angle. In the angular distribution of the nearest neighbors, the intensity of the main peak at 120° (which reflects the hexagonal cells) decreases. The intense peaks corresponding to the angles 30°, 90°, and 148° arise. The stresses in the graphene plane that are caused by the horizontal and vertical forces have close magnitudes in the considered temperature range. The graphene roughness grows fast with the temperature and reaches the maximum value at 1000 K. The hydrogenated graphene edges are not damaged significantly under heating to the high temperatures. Thus, under fast heating, the mercury film on graphene is transformed into a droplet with substantial changes in atomic packing and physical properties.

Chapter 6

REMOVAL OF HEAVY METALS FROM GRAPHENE

Graphene has unique physical properties and energy-band structures. It is possible now to receive graphene of a small size with the help of various technologies. However, there is a new technology for graphene film production of the size up to 70 cm [354]. Graphene can be used in different membranes due to its highest flexibility and mechanical strength. As an absorbing material, graphene is an effective one only in the case of multiple using. Consequently, the question arises of graphene cleaning from deposited substances. In addition, there was a need to develop an effective method for releasing copper from a scrap of copper-graphene electrodes used in electrochemical devices operating in aggressive environments. Graphene coating on copper significantly (by one and a half orders of magnitude) increases the metal resistance to electrochemical degradation. The copper has a significant practical interest.

The surface pollutions on graphene are removed by ion beam [355]. The bombardment with the cluster beam can be an effective method of graphene cleaning. However, it is important to find the correct bombardment energy to avoid the damage of the graphene membrane. Molecular dynamics simulation of plasma interaction on a graphite surface has shown that the graphite surface absorbs the most part of hydrogen atoms when the energy of the incident beam is 5 eV [356]. At the same time, almost all hydrogen atoms are reflected from the surface at the beam energy 15 eV. Vertical bombardment by the Ar_{10} clusters with kinetic energy $E_k < 30$ eV executed in the MD model does not result in the break of graphene sheet during 100 runs [357]. Graphene is broken at $E_k = 40$ eV.

The ion track lithographic method uses the passage of energetic ions through nanoholes in the mask and subsequent bombing of the graphene sheet only within a limited nanoregion. It is important to investigate in detail the entire lithographic process to predict how nanostructures can be produced in the suspended graphene sheet using this method. The present study will contribute to achieving this goal. Controlled ion parameters obtained in our simulation will be used to obtain desirable defective structures. No experimental

studies have been performed so far to produce such cluster ions by irradiating the target containing graphene. Furthermore, it has been shown that the theory of irradiation effects for bulk targets does not always lead to satisfactory results for the low-dimensional materials, such as graphene [358, 359]. It is obvious that an atomically thin target of graphene requires explicit consideration of the atomic structure [281, 360].

The trace amounts of metals always occur in the natural biosphere. Their presence even in a low concentration requires rapid oxidation. It is since metals in higher concentrations and products in low oxidation states can be toxic and dangerous. Unfortunately, the difference between the admissible and dangerous concentration levels is small [361, 362]. Such, PbS belongs to the most frequently occurring trace compounds in nature. It is used in electrical batteries, small arms, X-ray units, and as a pigment in domestic metallic mixtures. Detection of industrial lead in the environment is of considerable importance. Until now, lead has been determined by various methods such as spectrophotometry [363, 364], liquid–liquid extraction [365, 366], turbidimetry [367, 368], and electrochemical measurements [369]. Some of these methods are inaccurate because of the low limits of detection and harmful solvents. In recent years, the solid-phase extraction has been used for determination of the Pb traces. The trace amounts of Pb in aqueous media are detected with the aid of a surfactant covered with modified f-OH graphene.

The negligibly small amounts of heavy metals can be removed from air and water using filters with graphene membranes. However, in this case, the filters should be subsequently cleaned for removal of a metal deposit. Lead has a low energy of adhesion with perfect graphene (0.2 eV) [370]; however, the binding energy of Pb atoms with graphene at a bi-vacancy boundary is very considerable (3.4 eV) [371]. A heavy metal film can be removed from graphene by bombarding of the latter with noble gas clusters [193, 372–374]. Simulation of a cluster bombardment process showed that the energy transferred upon the impact should be entirely released in a critical region near the surface in order to obtain the maximum effect [375–377]. The experiment was implemented with the incidence of a beam of Xe atoms onto the surface of graphite at an incidence angle of 55°. It was found that the energy transferred to the phonon modes of the surface is approximately 20% smaller than that in the case of a vertically directed beam [378]. In this case, the Xe atoms are scattered on the smooth surface of graphite even at energies of several tens of eV. Energies of the cluster beams used were much lower than the energies of beams in the experiments oriented to sputtering of a bombarded substance.

Mercury is the only metal among the most abundant ones that remains liquid at the room temperature. Study of the mercury adsorption on activated carbon was, as a rule, carried out experimentally. There is a limited number of theoretical studies concerning this theme. Steckel [379] investigated the interaction between elemental mercury and a single benzene ring in order to explain the mechanism, through which the elemental mercury is bound with carbon. Padak et al. [380] investigated the effect of different surface functional groups and halogens (that were presented on the surface of activated carbon) on the

adsorption of the elemental mercury. It has been established that the addition of halogen atoms intensified the mercury adsorption.

In [381], Padak and Wilcox have demonstrated a thermodynamic approach to the examination of the mechanism of binding the mercury and its capture in the form of HgCl and $HgCl_2$ on the surface of activated carbon. The energies of different possible surface complexes have been determined. In the presence of chlorine, the mercury atoms strongly cohere to the surface. In the case of dissociative adsorption, Hg can undergo desorption, while HgCl remains on the surface. The compound $HgCl_2$ was not found on the stable carbon surface [382]. Understanding the mechanism of the mercury adsorption on the activated carbon is important for the development of the efficient technologies for capturing mercury.

Mercury is one of the most toxic heavy metals, and its presence is due to a combination of natural processes (volcanic activity, erosion of the mercury-containing sediments, etc.) and anthropogenic activity (extraction of minerals, pollution from the leather-dressing production, and metallization of objects). Adsorption is considered to be one of the most efficient and economical methods of removing mercury from wastewater and air. Recently, graphene membranes began to be used for capturing super small amounts of substances [383]. The repeated application of graphene in the filters requires its non-destructive cleaning from the adsorbates.

The removal of metals from graphene can be produced by its irradiation by a beam of rare–gas clusters [193, 346, 372, 373, 384, 385]. The use of cluster beams for the surface cleaning is more efficient than the application of ion beams to this purpose. In this case, the energy of a cluster grows in proportion to the number of atoms in the cluster at the same velocity of the projectile and, thus, it is possible to avoid large optical aberrations in the focusing systems. Bombardment using cluster projectiles proves to be much more sparing in comparison with the ionic bombardment. It is since the cluster projectile cannot penetrate the target so deeply as an atomic analog. In the prospect, application of the cluster beams will make it possible to create a number of fundamentally new technologies of the surface cleaning and to develop a new generation of ionic sources.

In this chapter, we present the investigation on the thin metal (Cu, Pb, Hg) film stability on graphene under the noble gas (Ar_{13} or Xe_{13}) clusters bombardment with the kinetic energies 5, 10, 20, and 30 eV and incident angles of the cluster beam 90°, 75°, 60°, 45°, and 0°.

6.1. METHODS AND CALCULATIONS

Below, we present a computer model of a copper film on graphene and the used scheme of its bombardment by clusters Ar_{13}. The models of Pb and Hg films on a graphene

substrate were created in a similar way. The bombardment of these targets was carried out by the Xe_{13} clusters. The graphene sheet is placed on a copper substrate, which contained 1000 Cu atoms. The bombing target was built as the model described in Section 5.2. The target obtained in this manner was subsequently bombarded with icosahedral Ar_{13} or Xe_{13} clusters during 1 ns. A schematic diagram of the inclined bombardment of the target with Xe_{13} (Ar_{13}) clusters is shown in Figure 63. The figure reflects the cluster bombardment of the mercury film on graphene. A similar bombing scheme was used to remove Cu and Pb atoms from graphene.

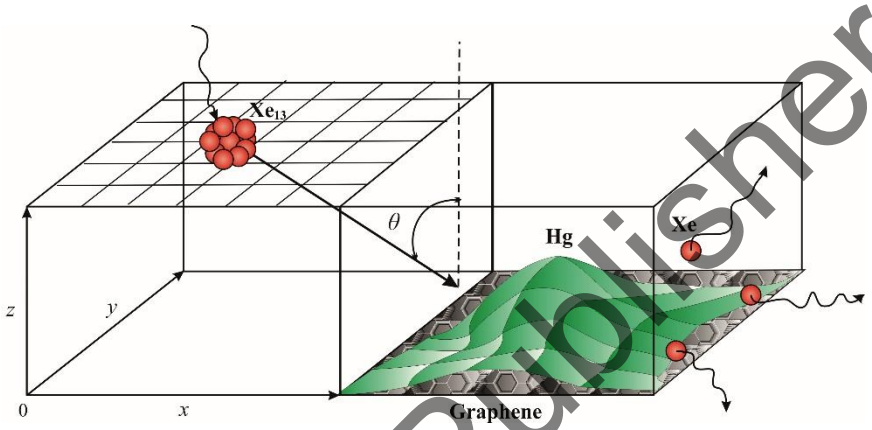

Figure 63. A schematic diagram of the inclined bombardment of the target with Xe_{13} clusters; mesh nodes define the starting location of inert gas clusters; at regular intervals, Xe atoms of the destroyed cluster are removed from the system, and a new cluster Xe_{13} appears in the next node of the grid.

In the case of vertical bombardment ($\theta = 0^{\circ}$) the virtual rectangular two-dimensional 5 × 5 grid covers the graphene sheet. The virtual grid is lifted over the graphene sheet at a distance of 1.5 nm. Every grid node gives the initial position for Ar_{13} cluster living 8 ps. The lifetime includes time of flight and time of interaction with the target. After this time, the Ar atoms of the decayed cluster were excluded from consideration and a new cluster Ar_{13} was launched from a different point cluster sources.

In the case of inclined bombardment, five starting points for placing the centers of the Ar_{13} clusters were uniformly spaced apart on a line parallel to the *y* axis ("armchair" direction). This line was displaced to the left (along the *x* axis) from the left edge of graphene by a distance of 1.5 nm and raised to such a height (in the direction of the *z* axis) to provide an effective impact to the copper film. Interval equal to the L_x length of the graphene sheet in the axial direction (the "zig-zag" direction) was divided into 25 equal segments of length $L_i = L_x / 25$. Five-point cluster sources moved horizontally forward at a distance L_i at the beginning of each cycle (except for the first). As a result, the graphene sheet was covered with 125 evenly spaced points for the target cluster impacts.

The calculations were performed by the classical molecular dynamics method. In this study, we used three types of empirical potentials describing the carbon–carbon (in graphene), metal–metal, and metal–carbon interactions. Representations of the interactions in graphene were based on the use of the Tersoff potential [40]. The Sutton–Chen potential was successfully used for simulating metallic (Cu, Pb) films on graphene [44]. The Schwerdtfeger pair potential was utilized for the description of Hg–Hg interactions [45]. The simulation was performed with the Cu–C Morse potential [47]. The lead–carbon, mercury–carbon, argon–argon, and xenon–xenon interactions were given by the Lennard-Jones potential [48–51]. The Morse potential was used to describe the interactions between the Pb or Hg atoms and the substrate Cu atoms [52, 53]. The interaction between the noble gas atoms and the atoms Cu and C was determined by purely repulsive Moliere potential [54]. A similar repulsive ZBL potential was used to describe interactions between Pb, Hg, C atoms with Xe ones [56].

Defects substantially enhance the adhesion of metals to graphene. The most frequent defects in graphene are bi-vacancies. The sheet of graphene used for the deposition of lead had four bi-vacancies rather uniformly distributed over its surface. Graphene sheets with copper and mercury films did not contain the point defects. Hydrogenation was used for strengthening the bi-vacancy edges and boundaries. The CH groups formed at the edges and sites nearest to the bi-vacancy center were simulated in accordance with the mono-atomic diagram [58]. The C–CH and CH–CH interactions were represented by the Lennard-Jones potential. The partial functionalization of graphene in the form of the addition of the hydrogen atoms to its edges stabilizes the structure without leading to an increase in interatomic distances and without creating roughness over the entire surface. The parameters of all the potentials used are given in Tables 1–6.

6.2. COPPER

There is no graphene surface cleaning after vertical bombardment at energy 5 – 20 eV. Bombardment with the 10 and 20 eV energies gives significant damage of graphene edges up to knocking out carbon atoms. The copper film becomes looser, and Cu atoms form a column. The graphene sheet is partially cleaned of copper atoms after bombardment with the energy 20 eV at the incident angle $\theta = 75°$. Graphene is almost cleaned of Cu atoms at the angles $\theta = 45°$ and $\theta = 60°$. In every case after finishing of inclined bombardment, the graphene sheet together with the substrate is removed in parallel or perpendicular (down) direction with respect to its initial position. It allowed one to remove copper from graphene totally only after bombardment at 45º. In the case of bombardment by the method of the "nap of the earth" flight (incident angle 0°), a big amount of metal atoms is still on the graphene surface when the emitted cluster energy is 10 eV. However, the number of copper atoms is reduced at the energy 20 eV (Figure 64).

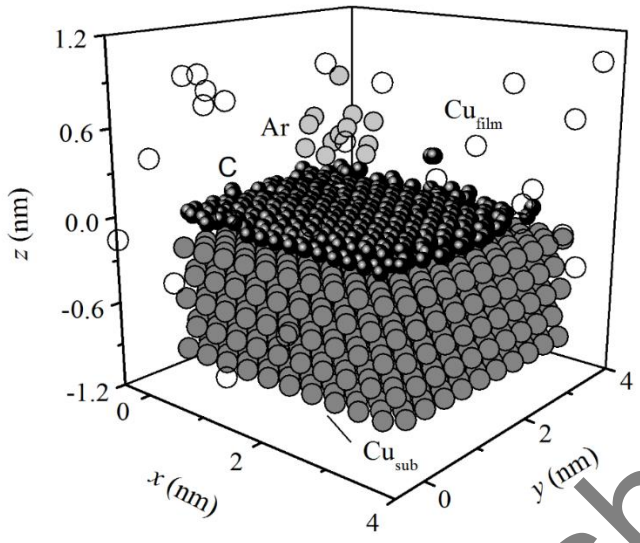

Figure 64. The configuration of a system "copper film on the graphene sheet with the copper substrate" bombarded by Ar_{13} cluster with energy 20 eV during final impacts cycle at the incident angle $\theta = 90°$.

At any cluster incident angle, the mobility of Cu atoms in the horizontal plane exceeds considerably (in order) the mobility of ones in the vertical direction. After the first cycles of cluster impacts, there are high values of D_{xy} components, especially, at the incident angle $\theta = 60°$ (Figure 65a). It seems reasonable because the copper film has not yet adapted to the bombardment. The more intensive fluctuations and significantly higher D_{xy} values testify continuous fast destruction of the copper film during the clusters impacts at the incident angle 45°. The vertical components D_z of the self-diffusion coefficient of the copper film have mostly the same behavior as $D_{xy}(n)$ function (Figure 65b).

Stresses in xy plane of copper film at every bombardment have extensive fluctuations, which become weaker during the last impact series. At all incident angles excluding $\theta = 90^o$, the σ_{zz} stresses are considerably higher than σ_{zx} and σ_{zy} ones. At $\theta = 90^o$ and energy of 10 eV, the stress components σ_{zx}, σ_{zy}, and σ_{zz} for metal film in the horizontal plane have comparably low values during the whole run (Figure 66a, σ_{zz} is only shown). For the energy 20 eV at the initial target bombardment ($n \leq 10$), there are significant fluctuations of all stress components in the horizontal plane. The σ_{zz} component has the most intensive fluctuations. Such fluctuations at the 20 and 30 eV energy of the bombarding clusters are connected with impacts of the Ar atoms compressing the film and knocking out Cu atoms. The fluctuation size of σ_{zz} value is further decreased because of metal film loosening in the vertical direction.

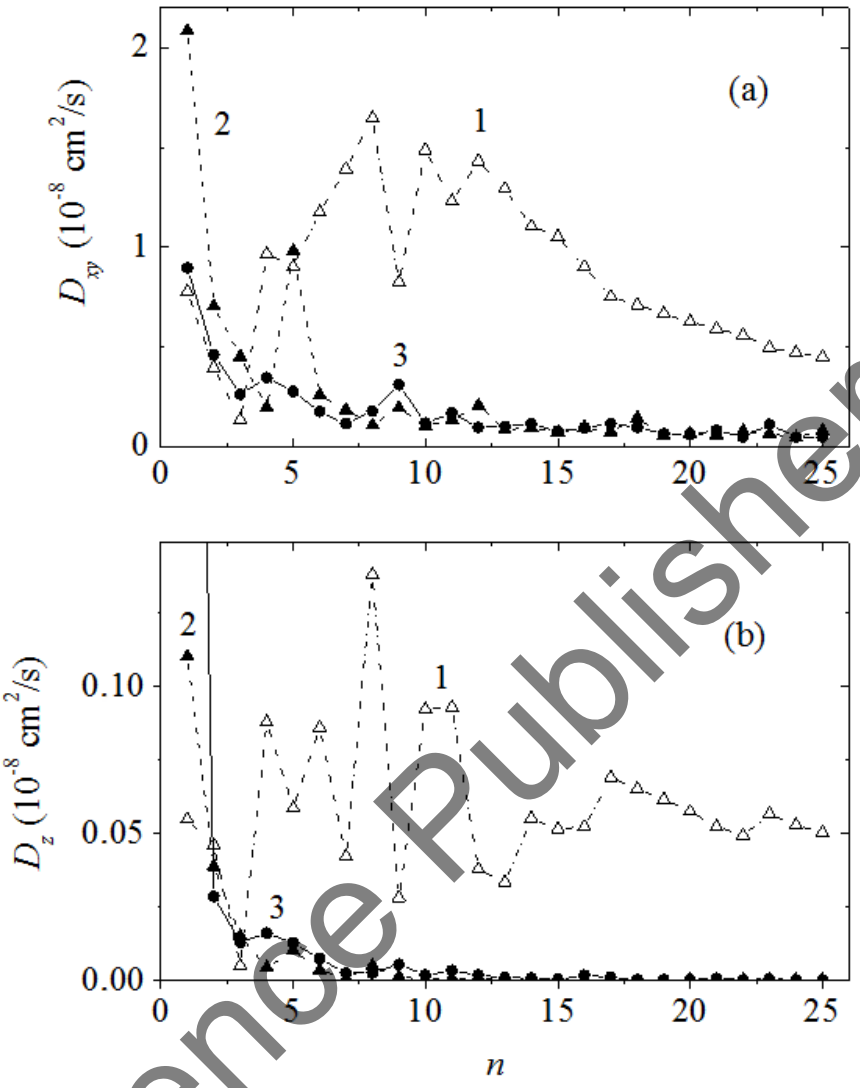

Figure 65. (a) Horizontal D_{xy} and (b) vertical D_z components of self-diffusion coefficient of Cu film for series of bombardments by Ar_{13} clusters at kinetic energy 20 eV and different incident angles: 1) 45°, 2) 60°, 3) 75°; n is the cycles each of 5 impacts.

On the contrary, stress distribution in the graphene sheet does not almost depend on the direction of the incident cluster beam. The copper film mainly weakens cluster impacts. Figure 66b shows the stresses distribution in graphene between the rows in the "armchair" direction under the Ar_{13} cluster bombardment with energies 10 and 20 eV at θ = 90º. Because of strong shot-interacting bonds in graphene, there are no essential differences between stresses values of σ_{zx}, σ_{zy} and σ_{zz} for series of cluster bombardment with energies 10 and 20 eV. The stresses σ_{zx} and σ_{zy} are uniformly distributed in the plane of

the graphene sheet. For both energies, the maximum σ_{zz} stress in this area of graphene sheet exceeds by 4–7 times the maximum values of σ_{zx} and σ_{zy} stresses. It is connected with impulses transmitted to graphene from the Cu atoms, which they get because of interactions with the Ar ones.

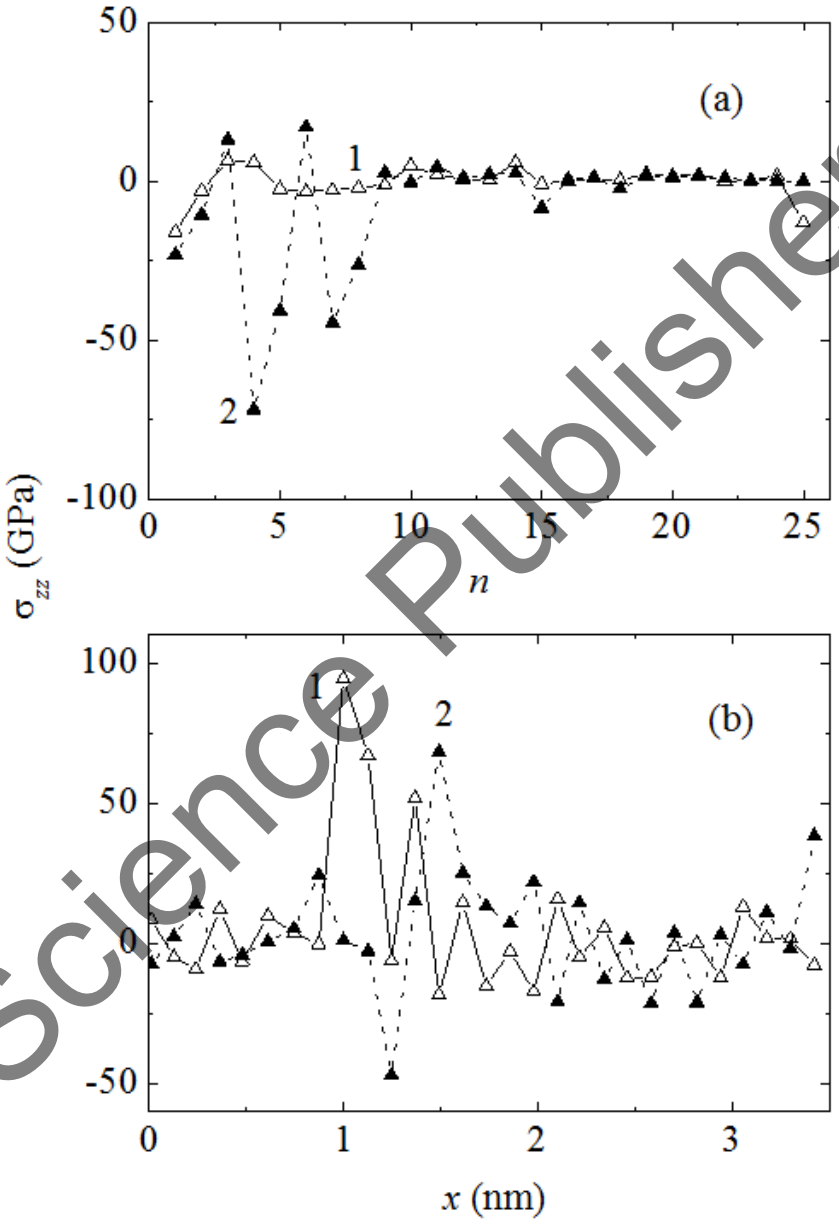

Figure 66. (a) σ_{zz} stress in *xy* plane of the metal film and (b) σ_{zz} stresses distribution in the graphene sheet by the rows of C atoms along the "armchair" direction for bombardment series by Ar_{13} clusters at the incident angle θ = 90º with energies: 1) 10 eV, 2) 20 eV.

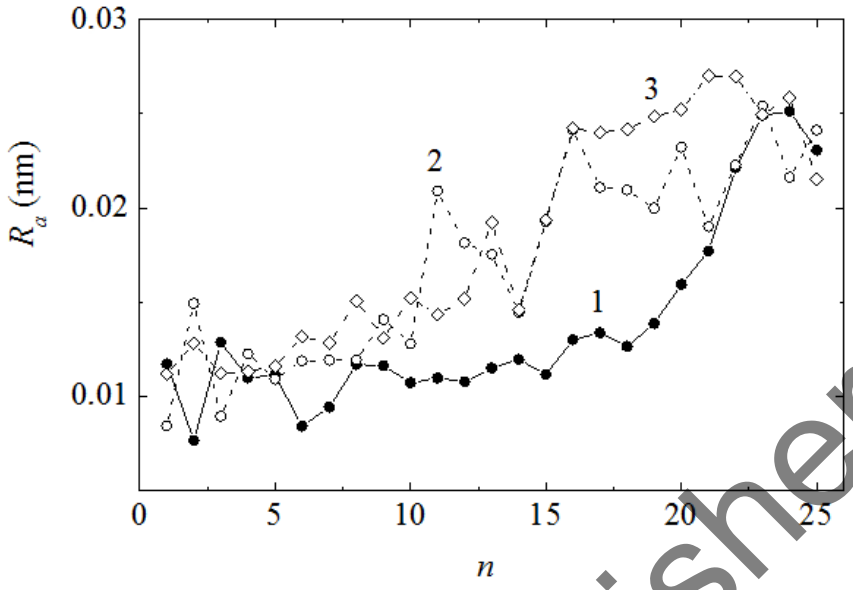

Figure 67. The roughness of the graphene surface at the bombardment of "metal film on the graphene sheet with the copper substrate" system by Ar_{13} clusters at the incident angle θ = 90º with energies: 1) 10 eV, 2) 20 eV, 3) 30 eV.

The graphene roughness increases significantly at the end of bombardment. It does not depend on the incident angle and energy of Ar_{13} clusters' beam. Rigid bonds in graphene limit significant growth of roughness. The roughness R_a of the graphene sheet rises non-monotonically during bombardment (Figure 67). When the clusters energy is 10 eV, the increase of R_a is slow with low values. There are considerable fluctuations of $R_a(n)$ function especially in the values range of $10 \le n \le 25$ when energies are 20 and 30 eV. The decrease of the initial growth of roughness in the case of energy 20 eV is connected with the reduction of final R_a value because of the smoothing effect. At the final bombardment step, the Ar_{13} cluster flies rather low over graphene surface and "polishes" it not meeting the Cu atoms.

6.3. LEAD

Investigation of the influence of the incidence angle of clusters Xe_{13} on the result of the bombardment of a lead film on graphene showed that the best degree of purification of graphene is achieved at the angle θ = 60° [386–388]. This case is considered in this section. As a result of bombardment with the 5 eV clusters, the film of Pb remained on the graphene. In this case, a small part of metal atoms was knocked out from the film, and the film itself was bent to keep contact with graphene only in its middle part; that is, the film edges

became raised. Bombardment with the beam energy of 10 eV led to the complete separation of a Pb film from the graphene. Only an insignificant part of the Pb atoms was knocked out from the film, and the major portion went away in the form of a dense cluster.

In general, the similar behavior was also observed in the bombardment with a beam energy of 15 eV (Figure 68). However, in this case, the major portion of the film was immediately detached away from graphene to a small distance. Since it was conically shaped and expanded upwards, it was forced to remain in this position until the end of the Xe_{13} clusters bombardment.

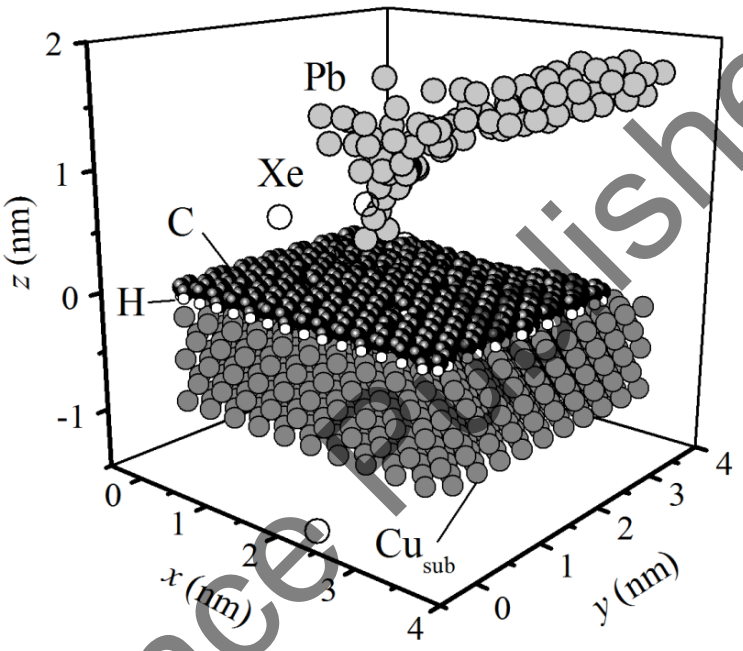

Figure 68. Configuration of the lead film–partially hydrogenated graphene system after bombardments at the incidence angle of 60° with Xe_{13} cluster energy 15 eV.

We found that the further increase in the cluster beam energy did not facilitate the removal of the Pb film from graphene. Thus, as a result of bombardment with the energy of 20 eV, the film was not separated from graphene with the loss of a portion of individual knocked-off atoms. Two atoms were stuck in bi-vacancies, and they helped to retain the film on graphene by attracting other Pb atoms. The film had close contact with graphene at the center. The film edges were elevated. Using the 30 eV Xe_{13} clusters crushed the film of lead and pushed several Pb atoms through bi-vacancies. A small lead cluster was arranged at the front edge of graphene without loss in binding with the base layer. Since the hydrogenation, the graphene edges remained intact even after bombardment with the energy of 30 eV.

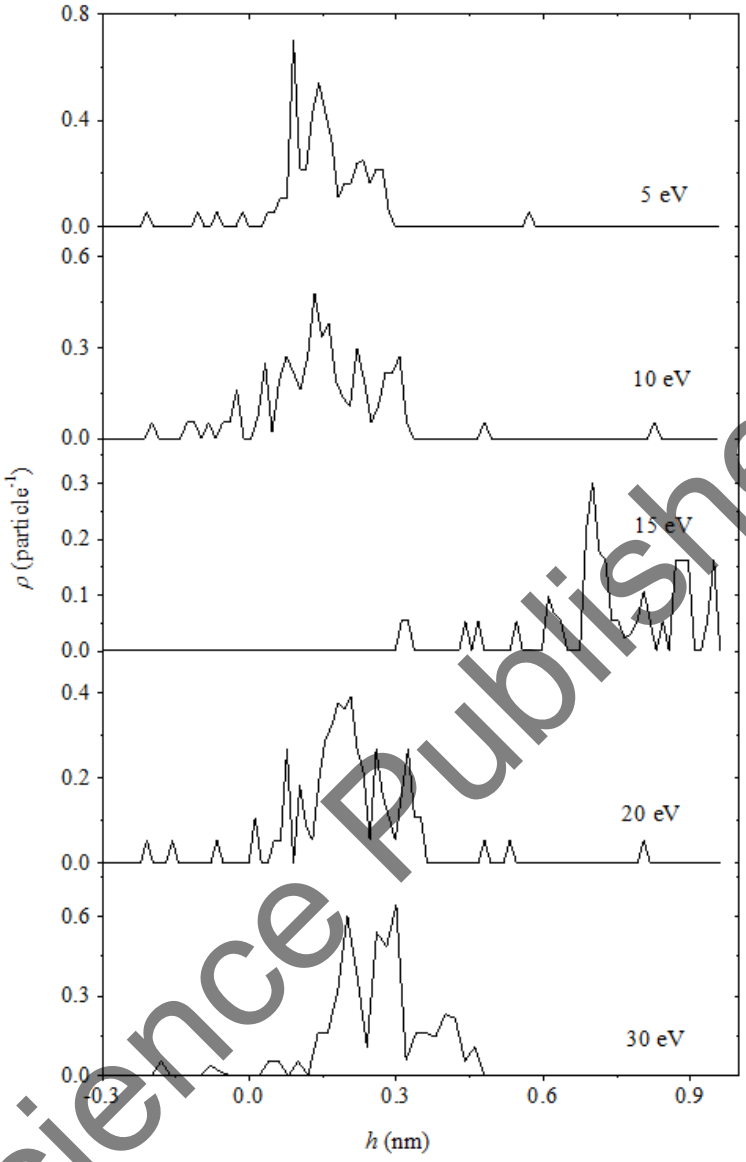

Figure 69. Lead film density profiles obtained in the course of the cluster bombardments of a target with different energies; the Level $h = 0$ corresponds to the vertical mark of the presence of the C atoms in graphene.

Figure 69 demonstrates the vertical profiles of density. Bombardment with the cluster energy of 5 eV left a sufficiently monolithic film on graphene. Moreover, in the course of bombardment, the Pb atoms (located in the lattice dimples of the honeycomb type formed by the C atoms) retained their positions as it is evidenced by the sharp peak at 0.237 nm. A small number of single atoms descended into bi-vacancies or moved away from the film as confirmed by the presence of separate low peaks.

Approximately the same pattern of the arrangement of Pb atoms was observed at 10 eV energy of the Xe_{13} clusters. The film thickness increased due to swelling under the impacts of the clusters, and the number of separated Pb atoms increased. At the end of the bombardment, the film separated from graphene and fast moved away to the distance greater than 1 nm. The new film position is not reflected in the $\rho(z)$ profile.

The fast rise of the entire film at the distance $r > 0.3$ nm over graphene occurred at the energy 15 eV of the clusters bombardment. The density profile in the whole was shifted to the right. At the cluster beam energies $E_{Xe} > 15$ eV, the film was either unseparated from the graphene (20 eV) or broken into separate pieces (30 eV). At the energy of 20 eV, a noticeable number of the Pb atoms were pushed through bi-vacancies, and single scattered Pb atoms were present too. Penetration of the lead atoms to the reverse side of graphene was insignificant at energies of 30 eV. In this case, the knocked-out film pieces moved away to the distances greater than 1 nm, and they are not seen in the $\rho(z)$ profile.

The horizontal component D_{xy} of the Pb atoms mobility tends to decrease as the energy of bombarding clusters is increased up to 20 eV (Figure 70). However, the value of D_{xy} sharply increases under cluster energy 30 eV. This fact shows to change in the nature of deformation in the film of lead under the action of the cluster beam. The vertical component D_z of mobility of the Pb atoms does not exhibit significant lift at a beam energy 30 eV, but it manifests a sharp burst at the energy 10 eV. This burst is caused by the detachment and fast removal of the major portion of the film from the graphene. In general, the vertical component of mobility of the Pb atoms is lower by almost an order of magnitude than of the horizontal mobility.

The curves of $D_{xy}(E_{Xe})$ and $D_z(E_{Xe})$ for the C atoms in graphene (Figure 71) are mainly consistent in shape with analogous curves for the Pb atoms (Figure 70). The presence of the local minimum under $E_{Xe} = 15$ eV at the place of the local maximum in the curve $D_{xy}(E_{Xe})$ for graphene is the exception. Furthermore, at low energies ($E_{Xe} \leq 10$ eV), the values of D_{xy} are even higher than those at the energy $E_{Xe} = 30$ eV when the Pb atoms injected into dimples produce local pressing and decrease mobility of the C atoms in the horizontal directions. The burst in the function $D_z(E_{Xe})$ at $E_{Xe} = 10$ eV for graphene is impressive the same as that is in the analogous function for lead. This is most likely indicative of the fact that the impacts of Xe_{13} clusters, which caused the detachment and fast withdrawal of the film, arrived directly on the graphene surface. The Xe_{13} atoms were scattered upward. The loosely lying Pb film was pushed in the opposite direction and removed from graphene. An insignificant increase in the value of D_z for the C atoms at the energy $E_{Xe} = 30$ eV is related to the presence of the rigid C–C bonds and absence of the graphene integrity damage.

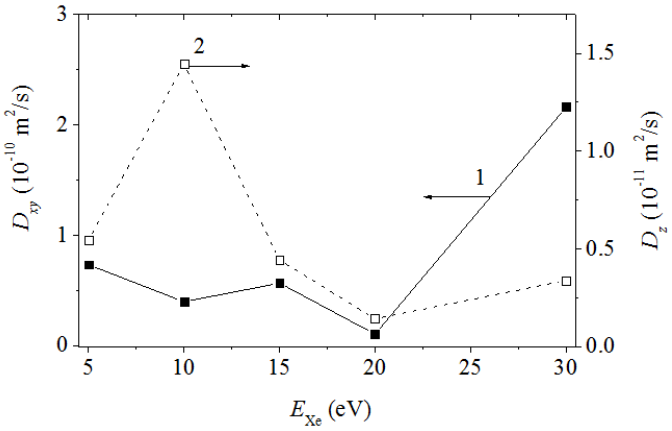

Figure 70. Horizontal D_{xy} and vertical D_z components of the coefficient of mobility of Pb atoms obtained as a result of the entire bombardment as functions of the energy of bombarding Xe_{13} clusters.

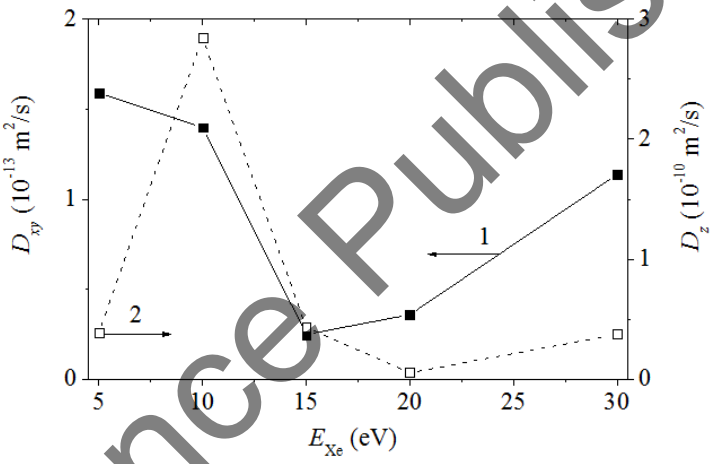

Figure 71. Horizontal D_{xy} and vertical D_z components of the coefficient of mobility of the C atoms of graphene as functions of the energy of bombarding Xe_{13} clusters.

The study of the evolution of the stresses σ_{zx}, σ_{zy}, and σ_{zz} in the cases of removal of the Pb film from graphene (E_{Xe} = 10 and 15 eV) showed that their smooth relaxation occurred only during the first series of impacts. Already in the course of the fifteen cycles of impacts, strong changes in the stresses created by horizontal forces (σ_{zx} and σ_{zy}) were observed, especially, at the final stage. In this case, the stress created by vertical forces (σ_{zz}) increased much more intensively. After 100 cycles of bombardment, the stresses σ_{zx} and σ_{zy} became even more significant. Over the course of this series, the stresses σ_{zz}

strengthened almost continuously. In general, the stresses σ_{zx} , σ_{zy} , and σ_{zz} in graphene obtained after 100 cycles of impacts were no higher than the stresses resulting from the five cycles of bombardment. In other words, in the course of the entire bombardment, increase in the local stresses in graphene was not observed. Note that the value of the stresses σ_{zz} created by vertical forces was much greater (by the factor of ~ 2) than the stresses σ_{zx} and σ_{zy}, which appeared due to the application of horizontal forces.

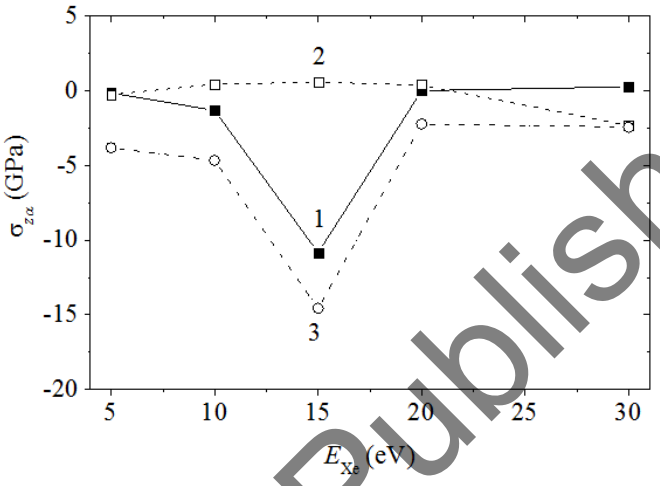

Figure 72. Basic stresses (1) σ_{zx} (2) σ_{zy} and (3) σ_{zz} in the Pb film obtained as a result of the complete bombardment as functions of the energy of bombarding Xe_{13} clusters.

In view of a specific shape taken by the film of lead after bombardment with an energy 15 eV, the final stresses σ_{zx} and σ_{zz} in the film were considerably different from analogous ones obtained after bombardments with other energies of the Xe_{13} clusters (Figure 72). At the same time, the function $\sigma_{zy}(E_{Xe})$ has a smooth shape; that is, the value of σ_{zy} at E_{Xe} = 15 eV is not strongly different from the values of this stress obtained at other E_{Xe}. All these three stresses have values of the same order of magnitude (in the majority of cases, the absolute value of σ_{zz} is somewhat greater) with the exception of the value of σ_{zy} at E_{Xe} = 15 eV.

Dependence of the resulting stresses σ_{zx} , σ_{zy} , and σ_{zz} in graphene on the energy E_{Xe} only partially correlates with the behavior of analogous characteristics in the Pb film (Figure 73). Only the behavior of the quantity σ_{zz} is similar in many respects to that of the corresponding stress in the metallic film. Here, the dip of the curve of $\sigma_{zz}(E_{Xe})$ into the region of negative values was also observed at E_{Xe} = 15 eV. However, the σ_{zz} value did

not reach positive values at E_{Xe} = 20 eV, as was the case in the lead film. The function $\sigma_{zx}(E_{Xe})$ was characterized by a smoother behavior, whereas the function $\sigma_{zy}(E_{Xe})$ for the Pb film exhibited this property. The function $\sigma_{zy}(E_{Xe})$ for graphene exhibited a maximum at E_{Xe} = 15 eV. The largest negative stress (σ_{zy}) caused by the horizontal forces in the direction of the *y* axis appeared at E_{Xe} = 5 eV, and stress of the same sign from the vertical forces (σ_{zz}) appeared at E_{Xe} = 15 eV.

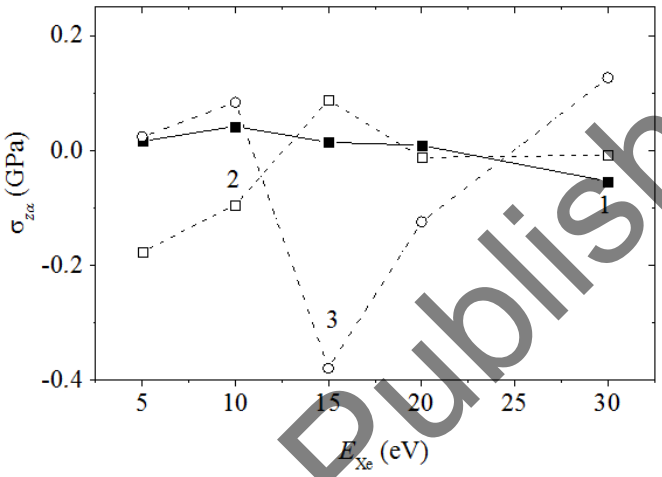

Figure 73. Basic stresses (1) σ_{zx} (2) σ_{zy} and (3) σ_{zz} in graphene obtained as a result of the complete bombardment as functions of the energy of bombarding Xe_{13} clusters.

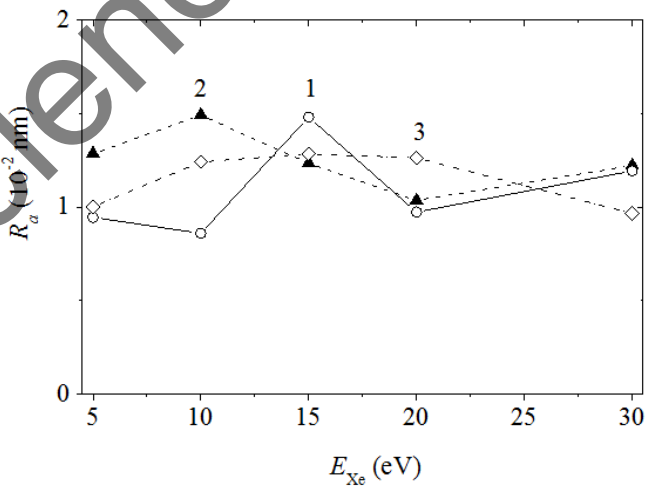

Figure 74. Dependence of the roughness of the graphene on the energy of bombarding Xe_{13} clusters at the incidence angles of (1) 0°, (2) 60°, and (3) 90°.

As a rule, the roughness of graphene R_a almost does not increase with the energy E_{Xe} of the bombardment of a target at the angle of incidence $\theta = 60°$ (Figure 74). The maximum roughness reached at $E_{Xe} = 10$ eV was caused by the early detachment of the Pb film from graphene. As a result, graphene directly took a great number of the impacts of Xe_{13} clusters. Figure 74 compares the function $R_a(E_{Xe})$ at $\theta = 60°$ with analogous functions obtained at incident angles of 0° and 90°, i.e., with the vertical and horizontal directions of bombardment. The difference in the roughness of graphene subjected to the uniform (in terms of Xe_{13} cluster energy and intensity) bombardment with different angles of incidence can be greater than 40% (at $E_{Xe} = 10$ eV). The smooth function $R_a(E_{Xe})$ was obtained under low-level bombardment. In this case, the roughness maximum was reached at $E_{Xe} = 15$ eV.

6.4. MERCURY

At the temperature of 300 K, mercury is in the liquid state (melting point $T_m = 234$ K). If the attraction forces between the Hg atoms exceed the forces of cohesion of the mercury film with graphene, the film contracts into a droplet. In order to investigate the opportunity rolling the film into the droplet, we carried out the MD calculation of the Hg film on graphene at $T = 300$ K using 10 million time steps in the absence of the cluster bombardment. As a result of this calculation, a drop of mercury on the graphene sheet close to a spherical shape was obtained. In this case, a substantial part of the lower surface of the drop (that is in contact with graphene) was flat. Thus, the film of mercury (that was simulated based on the Schwerdtfeger interaction potential) has a tendency to roll into a drop. The cluster bombardment using 125 impacts with the angle of incidence 0° did not lead to any significant removal of mercury from graphene at all energies of Xe_{13} clusters in the range of 5 – 30 eV. As a rule, more than half of the Hg atoms after the completion of the bombardment retained near the graphene, as before it.

The bombardment at the angle of incidence 45° was considerably more successful [63, 389–391]. In this case, the beginning with the energy of the beam equal to 15 eV, graphene was almost completely cleaned off the mercury. Only single atoms could remain connected with the graphene sheet; moreover, the majority of these atoms were retained at the edges of the sheet. The remaining atoms of Hg were scattered far beyond the limits of the graphene sheet predominantly in two directions (in the horizontal direction at a sharp angle to the axis *ox*, and upward). As a rule, the Hg atoms were knocked out from the film one by one and less frequently in the form of dimers and trimers. However, at the energies of the cluster beam $E_{Xe} \geq 15$ eV, there was always a drop of mercury separated from the

graphene. Increase in the angle of incidence of the Xe_{13} clusters to 60° led to the removal of mercury from graphene at the energy of the beam of 10 eV (Figure 75). A subsequent increase in the energy of the cluster beam at $\theta = 60°$ did not give the desired result: graphene was not cleaned off the mercury.

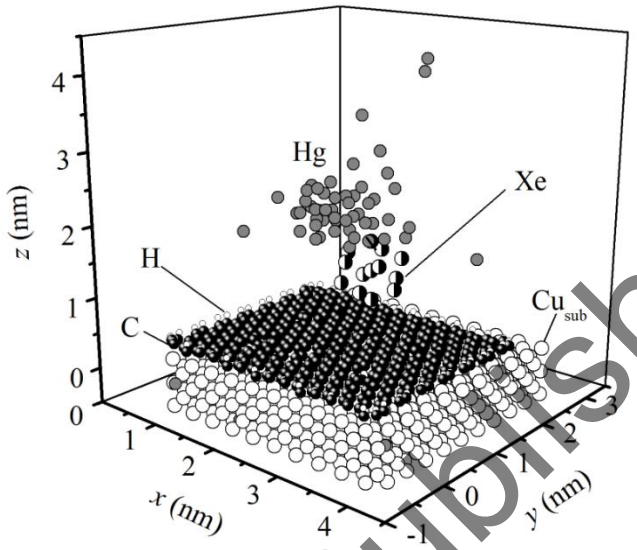

Figure 75. The configuration of a system consisting of the mercury film on a partially hydrogenated imperfect graphene sheet after bombardment by a beam of Xe_{13} clusters at the angle of incidence 60° and the energy 10 eV.

Figure 76 shows the dependencies of the mercury internal energy U_{Hg} and the energy of mercury-graphene interaction $U_{C\text{-}Hg}$ on the energy of the incident cluster beam at angles θ = 0°, 45°, and 60°. As it is seen from the figure, from 3% (in the case of E_{Xe} = 5 eV) to 1% ($E_{Xe} \geq 15$ eV) of the energy of the cluster beam is transferred to mercury. Hence, from 97% to 99% of the beam energy is scattered in the graphene and substrate. This result agrees with the data of [392]. Rebound velocity demonstrates that graphene absorbs a considerable amount (up to 97%) of the energy of the impacting particle.

The idea of using graphene for the energy dissipation of indenter was proposed in [393]. The mercury film on graphene has the highest U_{Hg} value, i.e., it has the lowest stability when the bombardment is carried out at the angle θ of 0°. However, in this case the energy $U_{C\text{-}Hg}$ has the smallest value, i.e., the Hg film is more strongly bound to graphene than at the angles of incidence θ = 45° and 60°. Attenuation of the bond between the Hg film and graphene (when the energy of the cluster beam increases at the angle of incidence θ = 0°) begins at E_{Xe} = 15 eV. The bond of the Hg film to graphene disappears for almost all energy values at the angles θ of 45° and 60°.

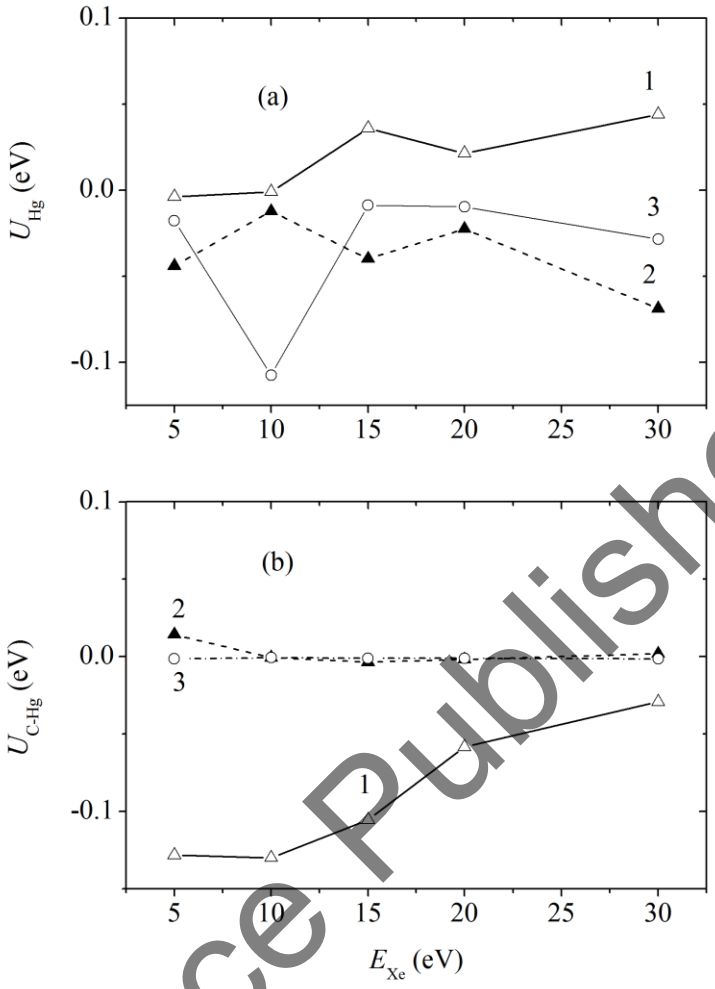

Figure 76. Dependence of the interaction energy (a) Hg–Hg and (b) C–Hg of mercury film laying on graphene on the energy of the cluster beam at various incidence angles of the Xe_{13} clusters: (1) θ = 0°, (2) θ = 45° and (3) θ = 60°.

As the angle of incidence of the xenon clusters increases, there occurs an increase in the self-diffusion coefficient of mercury atoms; especially, this is noticeable moving from the angle θ = 45° to the angle 60°. The lowest value of the self-diffusion coefficient of Hg atoms is observed under the vertical bombardment with the energy 5 eV of Xe_{13} clusters (Figure 77). At energies E_{Xe} >10 eV and at the angle of incidence θ = 0°, there is a very weak dependence of the self–diffusion coefficient on the energy of the falling clusters.

The similar weak dependence is manifested in the entire range of cluster energies at the angle of incidence θ = 45°. At the angle θ = 60°, the $D(E_{Xe})$ function has the deep minimum at 15 eV. The origin of this minimum is most likely connected with the fact that the bombardment with such energy of clusters provides the faster formation of a droplet

from the mercury film. The Hg atoms can be kicked out only with difficulty from this film. Except for this specific feature, no significant changes in the behavior of the coefficient of self-diffusion is observed under the variations of the energy E_{Xe} with the angle of incidence $\theta = 60°$.

Dependences of the stresses on E_{Xe} in the graphene plane caused by the horizontal (Figures 78a, 78b) and vertical (Figure 78c) forces exhibit a complex behavior, which is different for different angles of incidence. As a rule, the stresses σ_{zz} created by the vertical forces are noticeably higher than the stresses σ_{zx} and σ_{zy} that appear due to the action of the horizontal forces. At cluster energies E_{Xe} (that lead to the detachment of the majority of Hg atoms from graphene), the stress has relatively low values. Recall that this occurs at energies $E_{Xe} > 15$ eV at the angle of incidence 45° and at $E_{Xe} = 10$ eV at the angle $\theta = 60°$.

The roughness R_a of graphene increases continuously in the course of cluster bombardment. The inset in Figure 79 gives a representation of the $R_a(t)$ function variation in time in the case of bombardment with the energy of Xe_{13} clusters 15 eV at the angle of incidence 0°. The bombardment has a significant effect on the roughness of graphene. The magnitude of R_a increases by 20 – 40%, even as a result of the bombardment with the energy of clusters equal to only 5 eV; the effect is strongest at the angle of incidence 60°. The form of functions obtained under different values of the energy of the Xe clusters is shown in Figure 79. It is seen that the bombardment at the angle $\theta = 45°$ leads to the lowest R_a values. Thus, after this bombardment at the beam energy equal to 30 eV, the R_a value proves to be below the appropriate characteristics that correspond to the angles of incidence of 0° and 60° by 9.6% and 11.8%, respectively.

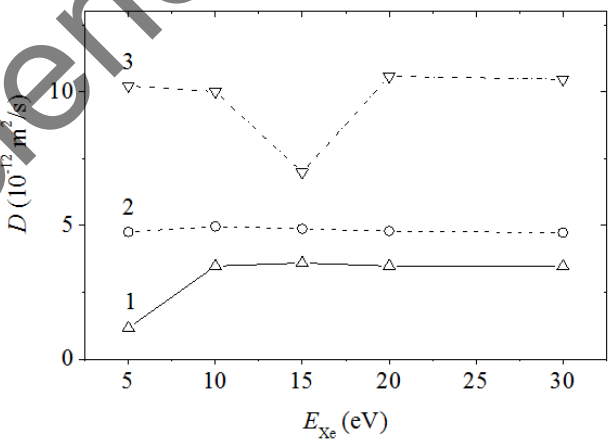

Figure 77. Self-diffusion coefficients of the Hg atoms calculated for the cases of the bombardment of the target at the angles of incidence (1) 0°, (2) 45°, and (3) 60° depending on the energies of the cluster beam E_{Xe}.

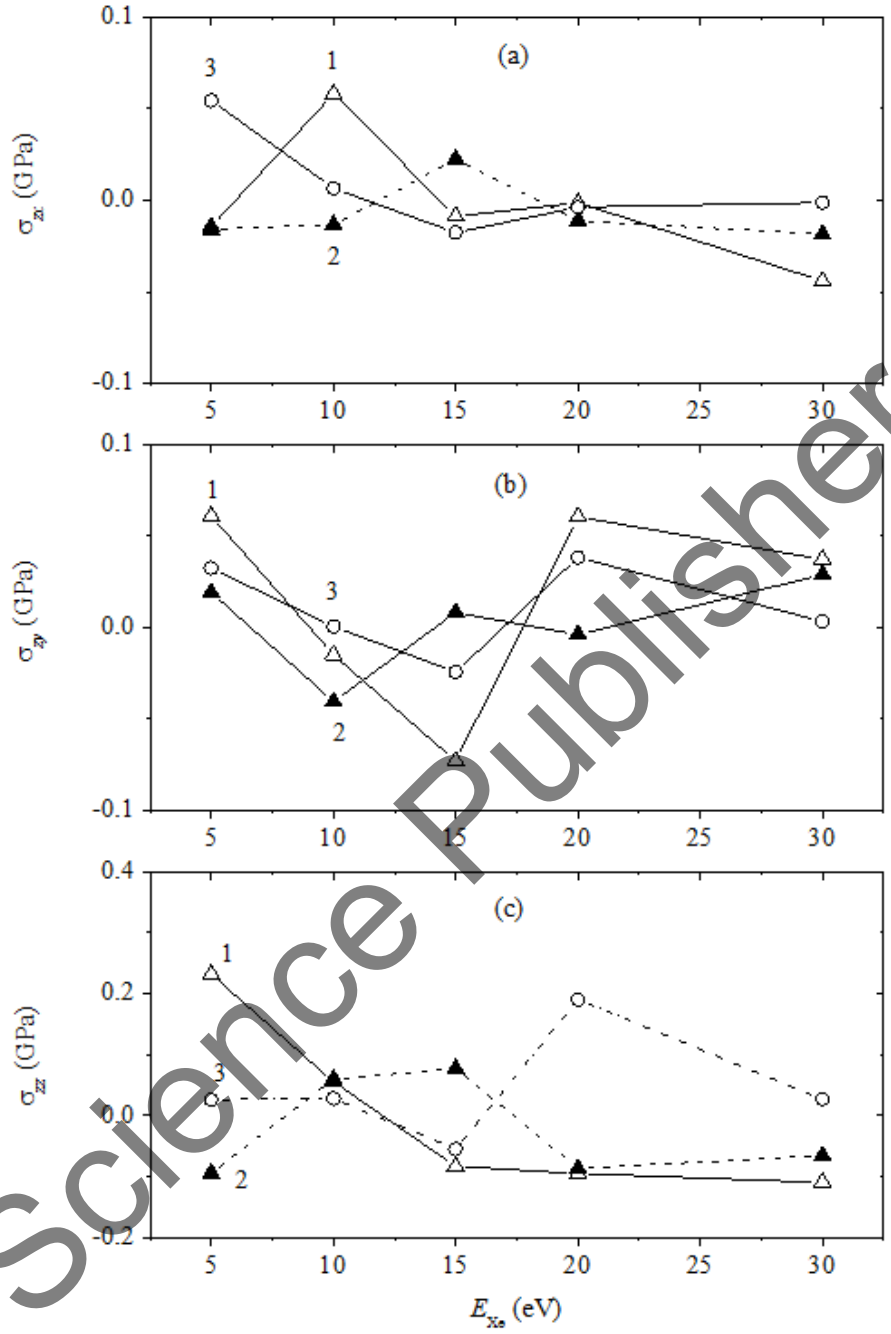

Figure 78. Components of the stress tensor in graphene ((a) σ_{zx}, (b) σ_{zy}, (c) σ_{zz}) obtained for the cases of the bombardment of targets at the angles of incidence (1) 0°, (2) 45°, and (3) 60° depending on the energies of the cluster beam E_{Xe}.

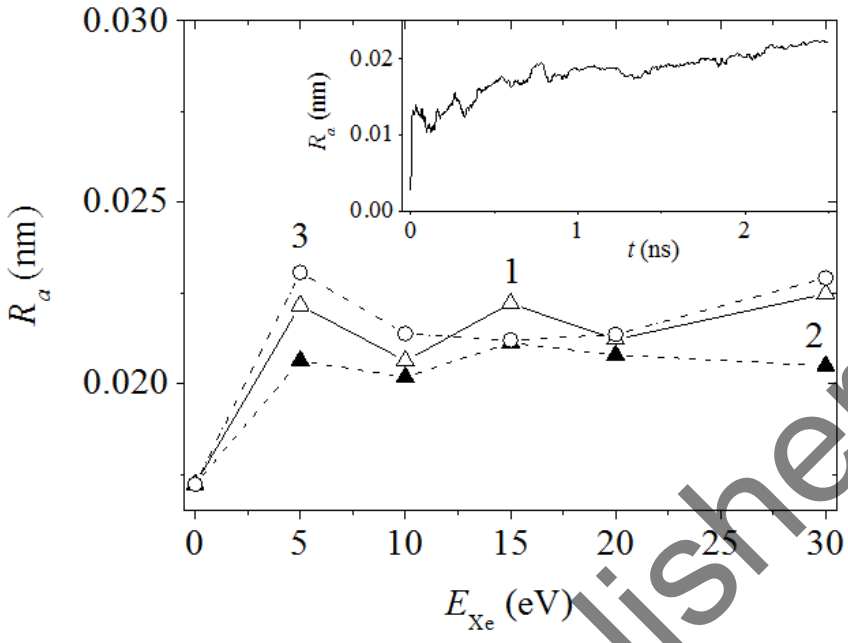

Figure 79. Roughness of graphene obtained as a result of bombardments of the target at the angles of incidence (1) 0°, (2) 45°, and (3) 60° at the energies of the cluster beam E_{Xe}; the inset shows the change in the roughness of graphene in the course of the bombardment of the target by Xe_{13} clusters at the angle of incidence 0° and at the energy of the cluster beam of 15 eV.

6.5. Effectiveness of the Cluster Bombardment Method for Removing Heavy Metals from Graphene

All graphene-based devices must unavoidably be electrically contacted to the outside world by metal contacts. Graphene films can be made by catalytically decomposing the hydrocarbon precursors over thin films of copper. Wrinkles in a graphene film have a negative impact on electronic properties by introducing strains that reduce the electron mobility. Often, the final product must be a single-layer graphene film. Graphene-based membranes could be used to capture carbon dioxide from certain industrial processes, such as coal burning, and there to reduce greenhouse emissions. Graphene could remove cheaply and easily salt from the seawater. With properly sized holes, graphene sheets may be able to serve as all-purpose filters.

The present study is expected to provide predictive design capability for controlling the surface patterns and stresses in nanotechnology products. For example, the improved understanding could help to make biocompatible surfaces for medical devices. When the argon ions hit the copper surface, they penetrate it knocking away the nearby Cu atoms like billiard balls in a process that is akin at the atomic level to melting or evaporation.

We carried out the bombardment of graphene by the argon clusters with low energy in the way not to damage the graphene when cleaning from the metal. The cluster bombardment with significantly higher energy can cause sputter of material with covalent bonds as observed when Si is bombarded with 15 keV C_{60}^{+} [394]. In this experimental work, the incident angle is increased from 0° to 60°. Hill and Blenkinsopp [394] observed a higher sputter yield of Si at 45° than at normal incidence angle. The molecular dynamics simulations [395] of the bombardment of a silicon crystal with C_{60} are used to understand and interpret the puzzling experimental results [394]. At both incident angles, all of the carbon atoms in the projectile become deposited in the substrate by forming the SiC bonds. However, for the angle of 45° the MD simulation more energy is deposited near the surface creating the larger Si yield [395]. Thus, the incident angle of 45° is, also, the most favorable at sputtering the material with a covalent bond under irradiation of the high-energy ion beam.

Because of its plasticity and due to a large loss of atoms the stresses in the copper film relax rather quickly (especially σ_{zz}). Local stresses in graphene relax in order slowly due to the presence of the hard bonds and do not disappear even after the bombardment. This indicates its crystalline nature. The presence of the local stresses even in thermodynamic equilibrium is a characteristic feature of ordinary three-dimensional crystals. Instability of two-dimensional crystals with respect to the displacement of atoms in the third dimension is well known and experimentally expressed in a rippled graphene surface. Cluster bombardment of the target greatly enhances this instability and ultimately leads to the surface topography characterized by a large (with respect to the R_a value of non-bombarded graphene) roughness.

Calculations using the density functional theory for the main crystallographic planes of a number of metals (such as Ag, Au, Cu, Pt, and Al) predict weak binding to graphene [396]. However, there is a group of metals such as Ni, Co, Pd, for which substantially stronger binding occurs due to hybridization between graphene and d-metal states. Therefore, the results obtained here for the Cu-coated graphene are also valid for the cluster bombardment of a graphene sheet with deposited noble metals or aluminum. At the same time, it is not critical how the metal is placed on the graphene sheet. However, the energy of the cluster beam necessary for graphene cleaning may require some adjustment due to significant differences in masses of the elements.

It is of interest to compare the results of the study of removing the films of copper and lead (by the bombardment with clusters of rare gases) with the present investigation of the graphene purification from mercury. The different mechanisms of the detachment of these heavy metals from graphene during the irradiation of the target by a cluster beam should be noted. In the case of the bombardment of the copper film with Ar_{13} clusters, separate Cu atoms are knocked out [193, 372, 373, 346, 384, 385]. No regime of bombardment led to the separation of rather large fragments of the Cu film from graphene.

When the lead film is bombarded, separate atoms are also knocked out, but the prevailing mechanism of the removal of the metal from graphene is the separation of islands of the Pb film from the substrate [397]. Only being detached away from graphene, the island experiences a transformation from the two-dimensional to the three-dimensional structure.

Mercury is separated from graphene in a different way. The unique behavior of mercury is due to its liquid state and poor wetting the graphene; as a result, the Hg film has a tendency to roll into a drop. For this reason, both separate atoms and droplets of significant size are separated from graphene in the course of bombardment. Let us emphasize that it is namely a drop that is torn off rather than an island with a two-dimensional morphology.

There are several other differences in processes of the removal of the film of heavy metals from graphene. Thus, the film of copper is not completely removed from graphene even under the energy of the beam 30 eV at the angles of incidence 0° and 60° [193, 373]; and the most efficient method is removal using the cluster bombardment at the angle θ = 45°. In the case of lead, the most efficient procedure can be considered as irradiation by a cluster beam at the angles of incidence 0° and 60°. In this case, graphene was completely cleaned of metal at energies of the beam 10 and 15 eV.

The complete cleaning was also achieved at the angle θ = 45°, but in this case, the energy of the cluster beam required was equal to 20 eV. The greatest effect from the bombardment of the mercury–on–graphene target is obtained at the angle of incidence of 45°. At this angle, graphene is cleaned of Hg at all energies $E_{Xe} \geq 15$ eV. A less stable cleaning effect was achieved at the angle of incidence of 60°. In the case of the angle of incidence 0°, no significant removal of mercury from graphene occurs in the range of the beam energies 5 – 30 eV. Thus, the removal of different heavy metals requires different conditions for bombardment and occurs via different mechanisms.

To check the correctness of the results, we also conducted calculations with another pair potential for mercury and another potential describing the mercury–graphene interaction. The Hg–Hg interactions were determined based on applying the potential proposed by Silver and Goldman (SG potential) with the parameters given in [46]. Here, we have obtained results close to those where the SCH potential served as the potential function for mercury. In the calculations that applied the SG potential upon bombardment, the Hg film was faster transformed into the drop and was separated from the graphene. The complete mercury removal from graphene was only achieved at the angle of incidence 45° at $E_{Xe} \geq 15$ eV. When using the Morse potential with the parameters given in [398] for the representation of Hg–C interactions, mercury under the bombardment was separated from graphene more difficulty. The complete cleaning at the angle θ = 45° was achieved at the energies $E_{Xe} \geq 20$ eV.

Incident angle θ = 45º is the most effective one for graphene cleaning of copper by bombardment with the argon clusters. Cluster beam energy should be no less than 20 eV. The stresses in the copper film relax fast due to its plasticity and due to a large loss of atoms. Local stresses in graphene relax rather slowly due to the presence of the hard bonds and do not disappear even after the bombardment; this indicates its crystalline nature.

Cluster bombardment of the target greatly enhances this instability and ultimately leads to the surface topography characterized by a large (relative to the R_a value of non-bombarded graphene) roughness. To use such a cleaning method, it is important to protect graphene edges because they can be strongly damaged. If it is possible to execute accurate bombardment, then the "nap of the earth" flight method becomes the most effective one. The total cleaning can be obtained with emitted clusters energy 20 eV and higher. The graphene edges in such a cleaning method are less damaged. The prediction model for nanopattern evolution during cluster bombardment can guide the nanomanufacturing processes.

We studied the bombardment of a Pb film on graphene by clusters with energies from 5 to 30 eV. The best cleaning effect was achieved at E_{Xe} = 10 eV. The Pb film can also be removed (on point contact) for the cluster energy 15 eV. Application of the higher beam energies is ineffective because of pushing the Pb atoms into bi-vacancies where they are firmly stuck. The hydrogenated edges of graphene do not acquire noticeable damage even after the bombardment with 30 eV clusters. Unlike copper, the prevailing mechanism in the process of lead removal is the detachment of the major portion of the film from graphene rather than the knocking out the separate Pb atoms. This is evident from the analysis of the density profiles of the system and the energy dependence of the mobility components of Pb atoms.

The bombardment of graphene after the removal of the Pb film leads to a considerable increase in the vertical component of mobility of the C atoms. As a rule, stresses in graphene were not accumulated in the course of bombardment. The highest stresses occurred in the detached film of lead (which increased its vertical size and took a torch shape) are the result of the action of both the vertical and horizontal forces. In this case, increase in the internal stress was also extended to graphene. The graphene subjected to direct bombardment with 10 eV clusters acquired the greatest roughness due to the rapid removal of the Pb film.

The behavior of the system "mercury on partially hydrogenated graphene" has been investigated under irradiation by the beam of Xe_{13} clusters with energies 5 – 30 eV at the angles of incidence 0°, 45°, and 60°. Over a wide range of energies ($E_{\mathrm{Xe}} \geq 15$ eV), the almost complete removal of mercury from graphene was only achieved at the angle of incidence of 45°. The mercury film, which has a tendency to become rolled up into a drop, is separated from the graphene in the form of single atoms, dimers, trimers, and spherical droplets. In the course of the bombardment, the mercury exhibits a weak cohesion with

graphene. The smallest change in the components of the Hg atoms mobility under variation of the cluster beam energy occurs at the incidence angle 45°. At the energies of the cluster beam under consideration, the stresses in the plane of graphene caused by the vertical forces noticeably exceed the stresses created by the horizontally directed forces regardless the angle of incidence. The roughness of graphene increases noticeably in the course of cluster bombardment. The lowest roughness is demonstrated by graphene subjected to irradiation with the beam of clusters at the angle of incidence 45°. The hydrogenated edges of graphene do not suffer from noticeable damages at all the energies investigated and at all the angles of incidence of the clusters bombardment.

Chapter 7

FORCED MOTION OF LITHIUM ION IN VICINITY OF GRAPHENE AND SILICENE MEMBRANES

In graphene, the Fermi level is localized between two symmetrical conic zones that contact the Fermi level at six spaced points called the Dirac ones. The latter are localized on the edges of the hexagonal Brillouin zone. In the vicinity of these points, the zero-excitation energy operates. Graphene has the linear energy spectrum of the Dirac type near each (of 6) singular points. The linear dispersion near these points means that the charge carriers in graphene can be considered as zero-mass relativistic particles. This gives rise to many unusual phenomena such as the Hall quantum effect [399] or the Klein paradox [400]. However, the Dirac equation describes not only the motion of an individual particle but also the time evolution of the quantum field, in which antiparticles are also present. According to calculations, the electron is completely reflected from a barrier and the electron–positron pairs are formed at the barrier [401].

In contrast to the case of zero-mass Dirac fermions for which the barrier is totally transparent in the case of normal incidence, the probability of charge transfer from non-zero-mass carriers is below unity and depends on the Brillouin zone index [402]. Thermal transition probabilities (proportional to $\exp(-k_B T / E_b)$) depend only on the E_{b} height of the barriers. The quantum tunneling probability through the same barrier depends not only on the height of the barrier, but also on its width d. The probability P of tunneling for normal incidence is approximately proportional to $\exp(-2kd)$ [403], where k is the wave vector (oriented in the direction perpendicular to the barrier). The electron energy is proportional to k: $E_{\mathrm{e}} = \hbar\omega = \hbar kc$, where c is the light velocity. Hence, the dependence $P(d, E_{\mathrm{e}})$ exponentially decreases with the potential-barrier width and height E_{b}. As applied to our model, the paradox lies in the fact that due to the small d of graphene for

all really observed k values, the value of P is close to 1 for any ion contacting with graphene. However, the physical transfer of a charge carrier does not occur under its collision with graphene and the carrier retains its electrical properties.

The functionalized graphene sheets were used in the lithium-air batteries to provide the high electrochemical capacity (~ 15000 mA·h/g) [404]. However, since preparation of graphene electrodes with 2D geometry is very difficult, these electrodes are made of hierarchical porous graphene with the 3D geometry. During the discharge, the strong large tunnels present in electrodes provided the fast access of oxygen from environmental air and the small pores in walls served as "ways out" for oxygen. Thus, the three-phase state (solid–liquid–gas) are maintained. The deposits of reaction products (such as Li_2O_2) on the carbon electrode eventually block the oxygen access and limit the capacity of the lithium-air battery. The open 2D structure of the electrode in this battery could be more efficient if there were the necessary gaps between graphene sheets that are stable during the electrode charge-discharge processes.

The presented model shows the diffusion of Li^+ ions in a planar anode of the lithium–air battery where oxygen supplied from air serves in fact as the cathode. The battery discharge produces Li_2O_2. The percentage of oxygen ions in the air is not very high. The oxidation reaction does not also produce free oxygen ions O^{2-}. Hence, the model assumes the absence of the negative ions. The cathodic processes are beyond our consideration. The interaction of carbon materials with hydrogen was considered earlier in application to hydrogen storage in solids [58]. The encouraging results were produced by functionalizing graphite basal planes (graphene) with hydrogen atoms. Hydrogen was adsorbed uniformly over the whole graphene surface, which eventually produced a stable material [405].

At present, it is known that lithium clusters represent a wonderful material for hydrogen storage [406]. The nature of hydrogen interaction with lithium clusters was studied both theoretically and experimentally; in particular, the possibility was demonstrated for hydrogenation of the lithium clusters [407]. The MD density functional simulations [406] have shown that the hydrogen atom passes from the graphene layer to the lithium cluster at 300 K and atmospheric pressure. Under this, the binding energy exceeds the corresponding energy of the hydrogen atom in the graphene layer.

In the present study, we consider the possibility of charging a planar graphene electrode in the lithium–air battery representing two functionalized graphene sheets with six different versions of pores.

The basic cell of the model represents a rectangular parallelepiped elongated along the z axis with the planes impermeable for Li^+ ions. The boundary conditions operating on the planes correspond to reflection of the elastic balls from a wall. In its middle part, the parallelepiped is divided into parts by two parallel membranes of defective graphene. The size of the graphene sheets was 3.2 × 2.8 nm. Each membrane contained 6 or 9 pores of a certain size, which were distributed approximately uniformly over the graphene sheet. Figure 80 shows the types of membranes used. The pores in the upper membrane

were shifted by a value not exceeding the graphene lattice period in order to prevent the direct vertical crossing of two membranes at once by the Li^+ ion. The upper and the lower membranes could be of either identical or different types.

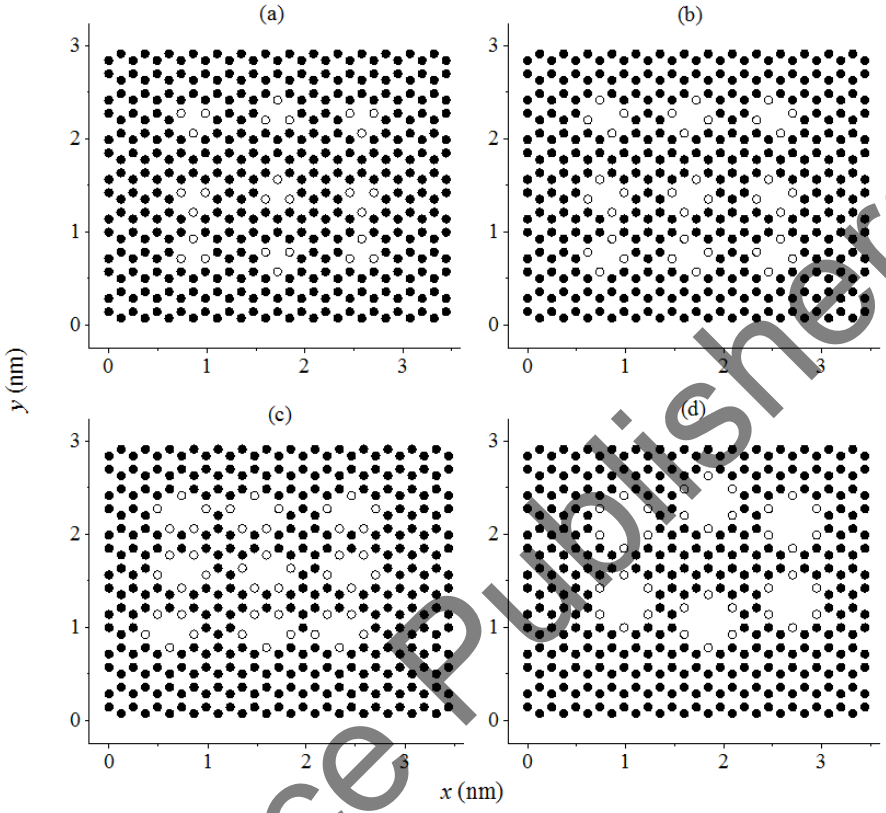

Figure 80. Modified graphene sheets with (a) mono-, (b) bi-, (c) tri-, (d) hexa-vacancies, (solid circles) C atoms, (open circles) C atoms with added H atoms.

Table 14 shows numbers of basic cells with different types of membranes. Thus, each of 6 basic cells was divided into three chambers, i.e., lower, middle (between two graphene membranes), and upper ones with the equal height of 0.6 nm. An additional calculation has shown that this gap provides the best way for rectifying the trajectory of the Li^+ ion in a flat channel under the effect of a constant electric field with the intensity of 10^3 V/m.

At the initial instant, by means of a random numbers generator, the lower part of the cell was filled with 10 Li^+ ions each with the electric charge of $+1.0e$, where e is the elementary electric charge. The directed motion of ions (upward) was provided by the positive electric charge of $+10e$ at the lower base of the cell and the negative charge of $-10e$ at its upper base. Each of these charges was created by 10 identical point charges. Such a virtual capacitor acted on the model cell during the first 4 million time steps $\Delta t = 2 \times 10^{-16}$ s. This process will be referred to as "charging."

Table 14. Versions of a membrane set in the basic cell (types and number of vacancies and number of C atoms in the lower and upper membranes) and stationary temperatures

Versions	**1**	**2**	**3**	**4**	**5**	**6**
Type and number of pores in the lower membrane	mono-vacancies 9	bi-vacancies 9	tri-vacancies 9	bi-vacancies 9	tri-vacancies 9	hexa-vacancies 6
Type and number of pores in the upper membrane	bi-vacancies 9	tri-vacancies 9	hexa-vacancies 9	bi-vacancies 9	tri-vacancies 9	hexa-vacancies 6
Number of C atoms in the lower membrane	397	388	379	388	379	370
Number of C atoms in the upper membrane	388	379	370	388	379	370
T (K)	311.5	312.5	312.8	311.6	313.9	298.8

To perform further randomize of the ion transport in the cell, we used the effect of migrating electric charges (positive at the lower base of the cell and negative at its upper base). Charge migration along the bases of the model cell was achieved by means of a random numbers generator, which changed the position of charges on each time step. After the "charging" period (4 million time steps), the Li^+ ions that reached the upper base lost their charge. Then, for the next 8 million time steps, we monitored the behavior of the system in absence of the electric charges at the ends of the cell and under the presence of a constant electric field with the intensity of 10^3 V/m that transferred the still remaining Li^+ ions into the opposite direction.

Transportation of the Li^+ ions through pores in membranes was put under special control. The membrane could be crossed by an ion only through a point (on the membrane plane) within the circle of effective radius of one or another pore. The ion could find a pore by the presence of the fractional electric charges on its perimeter. The charges were ascribed to both CH groups. The equal number of C atoms was randomly chosen among the boundary atoms of each pore. The number of CH groups corresponded to the number of its nearest neighbors (of C atoms) to the pore center. Thus, we had 3 such bonds for mono-vacancies, 4 for bi-vacancies, 5 for tri-vacancies, and 6 for hexa-vacancies. The CH group was described according to the mono-atomic scheme [58]. The positive charges of CH groups and the negative charges of C atoms free of hydrogen at the pore edges were of the fluctuating nature preset by the random numbers generator.

The maximum charge value for the CH group ($+ 0.35\,e$) created the Coulomb potential for the Li^+ ion motion. This value corresponded to the energy barrier for the diffusion of a Li atom on the graphene sheet over the vertices of the C atoms [408]. Calculations by the density functional method suggest the alternating-sign nature of fluctuations of the charge

of atoms near the graphene-sheet pores [409]. In our model, the fluctuating charge of CH groups and C atoms varied in the interval $-0.35 \le q_{CH} \le 0.35\,e$.

The Tersoff potential was used for describing the interatomic interactions in graphene [40]. The Coulomb interaction was present between all electric charges in the system, i.e., the Li^+ ions, wandering point charges on cell ends and fluctuating charges located in the pore vicinity. Furthermore, the Li atoms and ions experienced the LJ interaction with the potential parameters taken from [410]. The LJ potential (parameterized in [58, 411]) was used for describing the interactions between CH groups and, in the $Li^{(+)}$–C pairs too. The LJ interaction was also realized between the following pairs of atoms: C–CH and $Li^{(+)}$–CH. The parentheses in the superscript point to the possibility of charge disappearance.

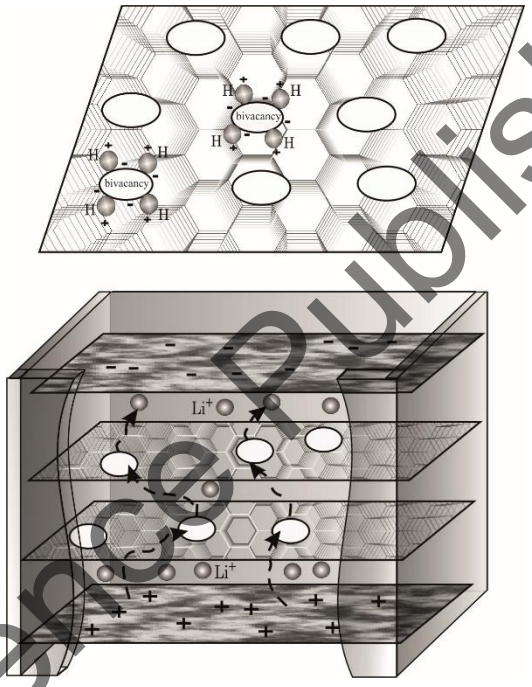

Figure 81. Schematics of the (a) membrane and (b) basic cell: (H) CH groups represented by the united atom scheme; C atoms are omitted; ellipses indicate bi-vacancies; signs "+" and "–" are positive and negative charges, and the arrows in dashes show Li^+ ion drift.

The moderate removal of liberated heat from the system was accomplished according to the Berendsen scheme with the binding constant $\tau = 4$ fs [62]. The basic-cell diagram is shown in Figure 81. One of the graphene membranes used is shown schematically with C atoms not highlighted at the top. The pores in the upper membrane are shifted by a distance no larger than the graphene lattice period to avoid direct vertical propagation of the Li^+ ion through two membranes at once. The lower and upper membranes could be of either identical or different type. Thus, each of the six basic cells was divided into three chambers

with identical heights (0.6 nm): lower, intermediate (enclosed between graphene membranes), and upper.

The best result of Li^+ ion passage through membranes was achieved in version 4 (Figure 82). In the latter case, 9 of 10 ions have reached the upper base of the cell after 4 million time steps, and only the lower membrane hindered one ion to do it. In the worst version 2, after 4 million time steps, 6 Li^+ ions found themselves immediately at the upper base and one ion has just penetrated through a pore in the second (upper) membrane, 2 ions have passed the first membrane, and one ion was still in the lower chamber of the cell. At the end of the "charging" process in other versions, 7 Li^+ ions were present in the upper chamber and the largest number of ions (two) still stayed in the lower chamber of the membrane combination (version 1). The latter fact is explained by the difficulty for Li^+ to pass through mono-vacancies.

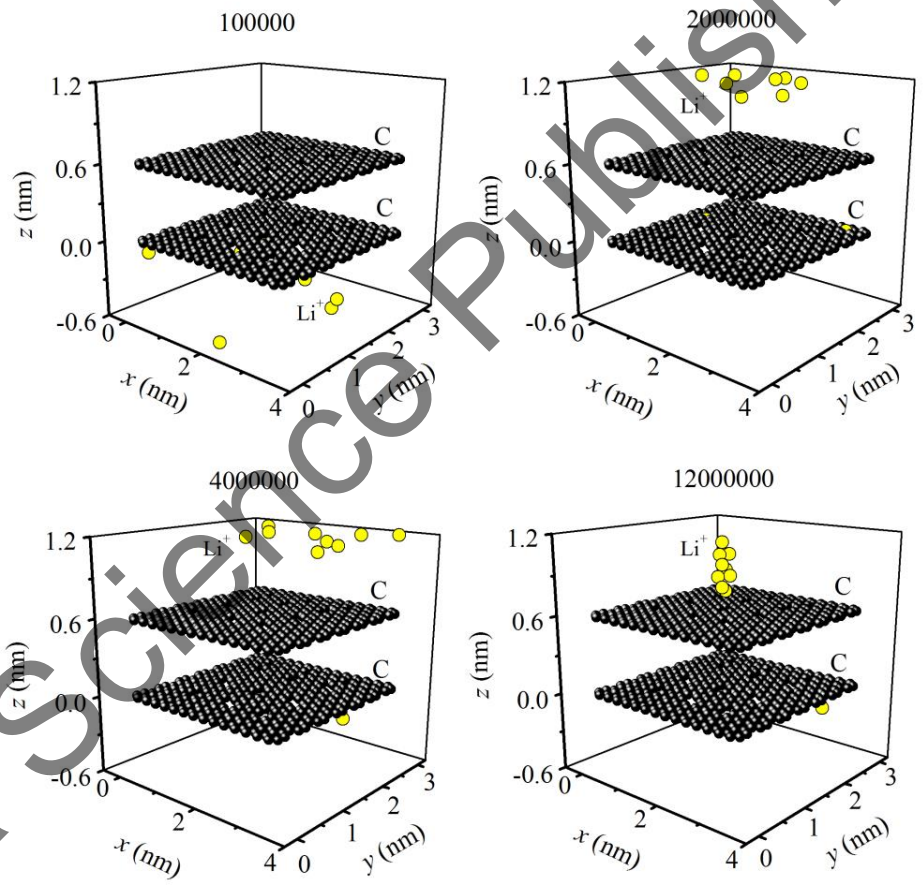

Figure 82. A basic cell with membrane combination of version 4 at different instants; numbers correspond to the number of time steps.

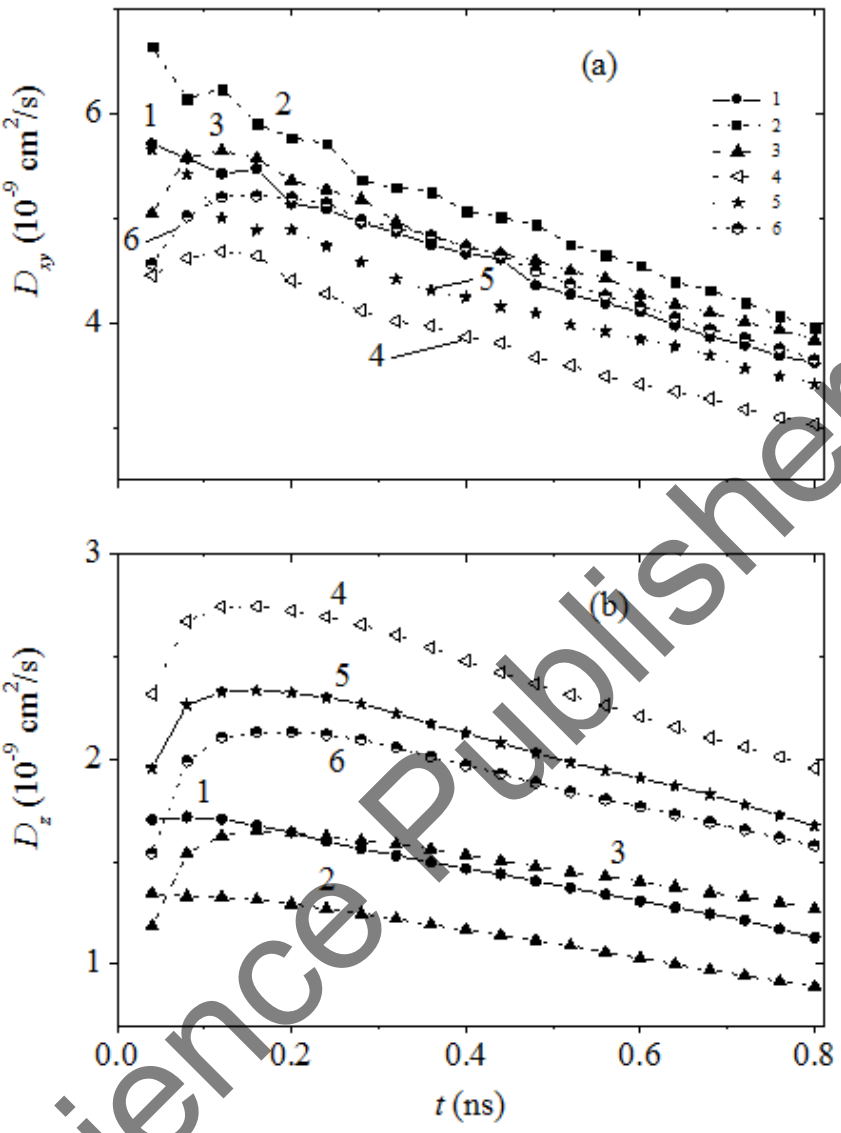

Figure 83. (a) Horizontal and (b) vertical components of the Li^+ ion mobility coefficient for versions 1–6 of the membrane sets listed in Table 14.

The mobility coefficients of Li^+ ions in both the horizontal (D_{xy}) and vertical (D_z) directions have the tendency to decrease after the first million time steps of the "charging" process or n = 5 (Figure 83). Note that the interval values of D_{xy} and D_z change at an even higher rate. However, at the initial stage of "charging," the coefficient D_{xy} can either increase or decrease for different versions of the combination of graphene membranes (Figure 83a). The coefficient D_z at this stage of "charging" increases in four of six cases [412]. Only version 2 exhibits a stable decrease in the D_z value. A weak short-term

increase of this coefficient is observed in the initial calculation stage for version 1. Obviously, the initial rise of the coefficients is related to the fact that ions acquire certain energy. It is stipulated by the mutual repulsion. In addition, the expansion of the ion migration volume takes place due to their ability to pass through the membranes.

The subsequent stable decrease in these coefficients is caused by a gradual reduction of the available-for-migration volume due to the approach of ions to the upper cell base and the low probability of their motion in the reverse direction. The largest D_{xy} values and the smallest D_z ones were revealed for the system with the membrane set of version 2. Here, the highest mobility of Li^+ ions in the horizontal directions is combined with the lowest mobility in the vertical one. The antipode of this version is version 4 where the minimum ion mobility in the horizontal directions is compensated by the highest mobility in the direction perpendicular to the membrane plane. The mutual compensation of D_{xy} and D_z values is observed for the other versions of membrane combinations too [413].

The relationship between the throughputs of the membrane sets used is also confirmed by the time dependence of the mean level $z_{\text{lev}} = \frac{1}{n_i}\sum_i^{n_i} z_i$ (where z_i is the ion coordinate and n_i is the number of ions) of the lift of Li^+ ions in the system (Figure 84). Here, the highest mean lift of ions in the cell was detected for the membranes of version 4, while the lowest one was observed for versions 1, 2, and 6. In all cases, the highest point of the ion lift is near the end of the "charging" time (i.e., 4 million time steps). Having reached the upper negatively charged plate of the external "capacitor," positively charged lithium ions should be electrically neutralized due to the charge flow. Therefore, the contact with the upper wall of the basic cell was accompanied by removal of the electric charge from the ion.

The "charging" end in the model indicated the cessation of the virtual external "capacitor." The "charging" is feasible when the external "capacitor" is used and unfeasible when the dc electric field with the strength of 10^3 and 10^4 V/m is applied. In this case, ions have remained in the lower chamber near its walls rather than move upwards through the membranes. The "discharge" process began with switching on the dc electric field E = 10^3 V/m inducing the reverse ion motion. It is worthy to note that after the ions that reached the upper cell base lost the electric charge and acquired the status of atoms. They inherited the tendency of cluster formation.

In all cases, without exception, the Li atoms in the upper chamber were agglomerated into clusters after 12 million time steps (Figure 82). As a result, this made it impossible for them to pass through the upper membrane in the reverse direction (downwards). The formed clusters always had contact with the graphene. Rather fast (within 1.8 million time steps) during the "discharging", a small decrease in the z_{lev} value was observed. Two

million steps after the end of the "charging," the dependence $z_{lev}(t)$ is shown by the horizontal lines in all the cases under consideration. This is due to cluster formation by the Li atoms in the upper cell chamber and the ion adhesion to the graphene surface.

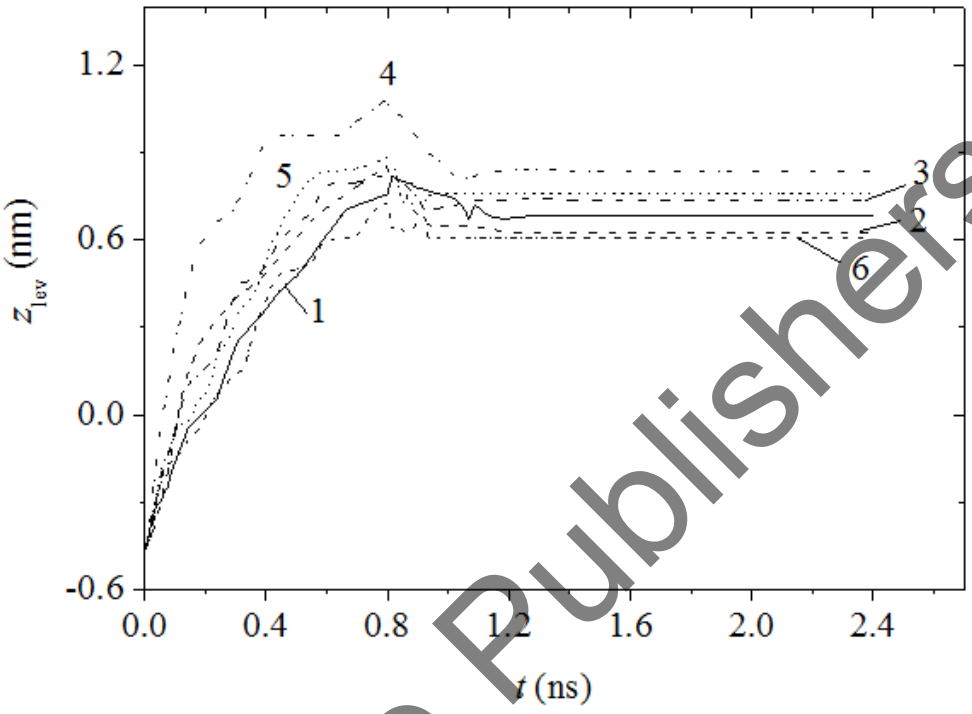

Figure 84. Mean lift level of Li^+ ions in the basic cell for versions 1–6 of the graphene membrane sets.

Among six membrane pairs under study, the most efficient was the pair of two identical graphene sheets containing bi-vacancies. Moreover, the close-to-equilibrium distribution of bi-vacancies in each sheet was shifted by ~ 0.2 nm in order to prevent ions from the straight-through crossing of two membranes at once. The loss of electric charge by Li^+ ions resulted in the formation of a lithium cluster insensitive to the electrostatic directing force. Moreover, in a constant electric field, the Li^+ ions "adhered" to membranes due to their high adhesion to graphene.

These factors complicated the "discharge" process in the device under consideration. The ions moved along very short back trajectories. In the "discharge" period for the efficiently permeable membrane pair, the Li^+ ions exhibited the lowest mobility in the horizontal directions and the highest mobility in the vertical direction. For inefficiently working membrane pairs, the inverse situation was also true. The average level of vertical travels of ions in the system can be also used in assessing the efficiency of membrane pairs. The time dependence of the latter level makes it possible to determine the extent and duration of the "charging" stage.

7.1. PASSAGE OF DEFECTIVE GRAPHENE CHANNEL BY LITHIUM ION

Electrochemical devices for energy storage include batteries, fuel cells, and supercapacitors. Graphene has high electric conductivity and strength, and supercapacitors based on it could find wide application in portable electronics. Porous graphene-based nanostructures with large surface areas could be used for their manufacture. However, the optimum pore size and distance h_g between stacked graphene sheets remain undetermined. A simple statistical estimate was found in [411] on the minimum distance h_g between two parallel graphene sheets that is favorable for the motion of the metal ions without interference from the molecular force field. For lithium ions, this value was 0.50 nm.

According to [411], the forces of attraction and repulsion acting on an ion placed between sheets of graphene compensate one another in the interplanar spacing range of 0.50 nm, and the ion moves in the gap as a free particle. In reality, however, the relief of the molecular force field of a graphene sheet is not flat. This forces the ion to perform micro vibrations during its motion and deviate from the direction of the surrounding electrostatic field. The ion is strongly inhibited in the intraplanar gaps with $h_g \approx 0.5$ nm. So, the considerable force is required to overcome the resistance of the molecular field. Such force can be created by an electric field of high strength.

The *h* value must be determined in a rigorous dynamic model for each value of the field strength. Functionalization allows us to change the physical properties of graphene. With its metallization by the lithium, the charge transfer occurs from Li to C resulting in a modified graphene that becomes able to retain hydrogen [408]. Due to the presence of the dangling bonds, hydrogen adsorption can occur near defects present on the graphene or on its edges [58].

The adsorbed hydrogen in graphene creates the electrical charge approximately of $+0.21e$ [406]. Real graphene usually contains defects, near which the electrical charges appear and retain. This can create additional obstacles for the motion of the Li^+ ions between the graphene sheets. Contact between Li^+ ions and C atoms in graphene is necessary for the functioning of the graphene anode.

Thus, the problem is posed to determine the shortest distance between sheets of perfect graphene, on which Li^+ ions would move with minimal interference in a constant electric field without losing contact with C atoms and, thus, being slowed by the graphene.

The interactions in this model were described by the same potential functions as in the previous section. Our sheets of graphene contained 406 atoms and were rectangular in shape at 3.4 × 3 nm (the sheet had 14 atoms along each edge). The high capacity of the electrode is achievable upon the fast motion of electrolyte ions. Therefore, the self-

diffusion coefficient of the ion would lay within the range of 10^{-10} to 10^{-13} cm^2/s [434]. In preliminary computer experiments with the gap of 0.50 – 0.65 nm between the graphene sheets, we showed that this effect was achieved starting from a value of electric field intensity close to 10^3 V/m. A constant electric field with the intensity of 10^3 V/m accelerated Li^+ ions along *x* axis oriented along the "zig-zag" direction of the graphene sheets. The graphene sheets were arranged in accordance with Bernal laying (ABAB…) in exactly the same manner as in the bulk graphite. The gap of value h_g was set between these two parallel sheets of graphene.

Two series of calculations were performed that corresponded to schemes 1–2 and 1–3 (Figure 85). In the first series, a Li^+ ion at the initial instant was in front of the gap that was formed by the graphene sheets. The distance σ_{Li-C}^{LJ} [414] from the front boundary of the gap (with the *yz* plane passing through the front edges of the sheets) was 0.2473 nm. The initial position of the center of the ion in the second series of calculations was at the internal point near the entrance to the channel.

Each series included four calculations with duration of 1 million time steps $\Delta t = 1 \times 10^{-16}$ s with different values of h_g. Values of h = 0.50, 0.55, 0.60, and 0.65 nm were used. For both series, the initial location of the ion corresponded to the height of $h_g / 2$. At t = 0, the ion was in front of or right near the middle of the plate channel formed by the "zig-zag" rows of atoms of the lower graphene membrane (Figure 85).

The interaction between parallel graphene sheets falls fast as the distance between them grows and almost completely disappears in the investigated range of distances (0.50–0.65 nm). Under this, the Li^+ ion was not free to move in the inter-planar gap. This was because the strong covalent bonds acting in the plane of the graphene allowed only slight warpage vibration of sheets during the motion of the Li^+ ion. Affected by the Van der Waals interaction with close-packed C atoms of graphene sheets, the Li^+ ion decelerated.

Before leaving the channel, the ion passes over the length of the graphene sheet during 100 ps when the gap is 0.60 or 0.65 nm wide. Coming out of the channel, the ion does not travel too far from it; instead, it is attracted to the lower sheet of graphene, indicating that there is a tangible interaction between C atoms and the ion (Figure 85).

Trajectories of the Li^+ ion in front of a flat graphene channel and the motion under the effect of a constant electric field with the intensity 10^3 V/m are shown in Figure 86. For detection of the transverse oscillations during the ion motion, the scale on the vertical axis (z) was stretched about 4 times. When the gap was 0.50 nm, the ion was unable to enter the channel. Its motion is described by looping trajectories directly in front of the channel. Increasing the interplanar gap to 0.55 nm drastically altered the ion motion pattern. The translational motion became dominant. With small smooth oscillations, it reached the opposite end of the channel, where the C atoms slowed it. Then it performed an oscillating translational motion in the opposite direction.

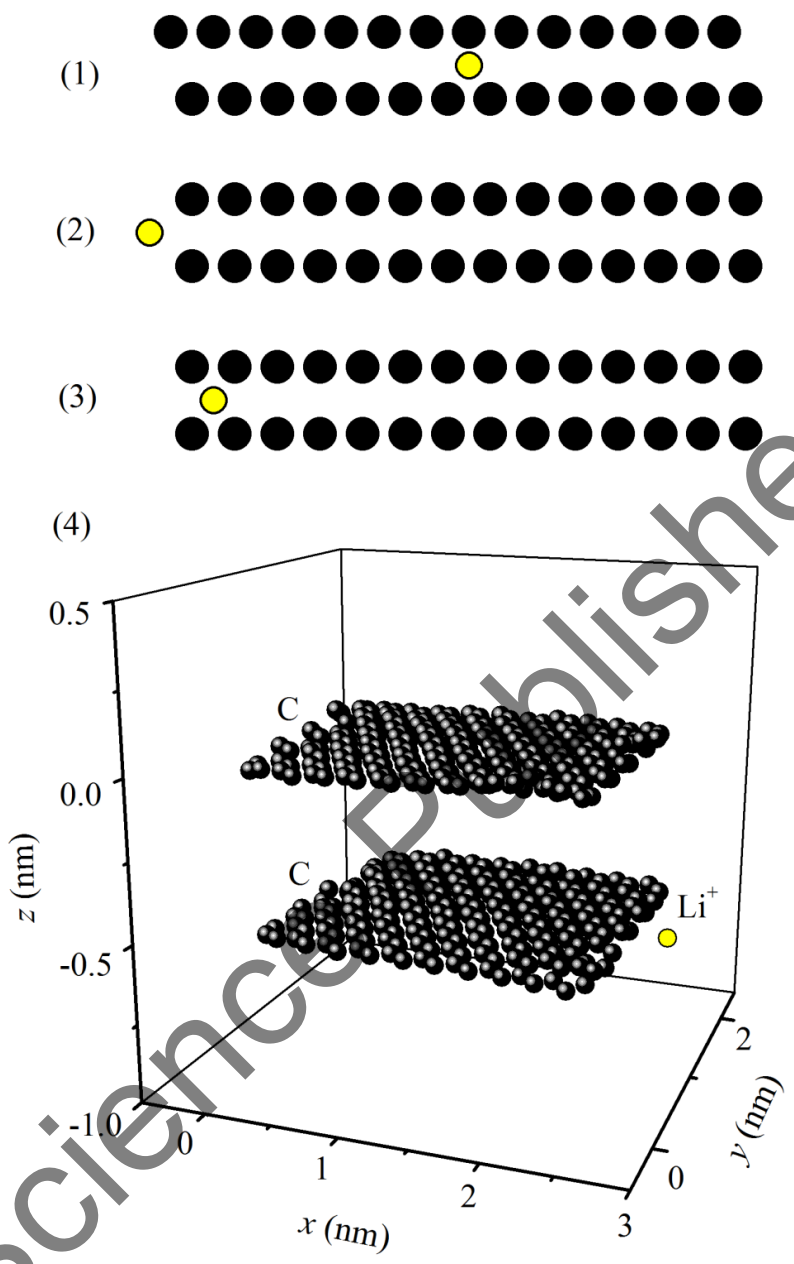

Figure 85. Scheme of the atoms arrangement at t = 0: (1) view of the frontal plane; (2, 3) side view (on xz plane) of the external and internal location of Li^+ ion in channel, respectively; (4) flat channel of graphene–lithium ion system configuration at the instant 100 ps and h_g = 0.60 nm; the electric field intensity is directed along the x axis; initially, the Li^+ ion is located at the front of the yz plane outside the channel.

The resistance from the C atoms finally exceeded that of the inertia of the decelerated ion, preventing it from leaving the channel. The motion of the Li^+ ion along the channel under the constant electric field was due to the presence of the energy barrier to inertial

motion at both the entrance and exit of the channel. Further increasing the gap (to 0.60 nm) allows the ion to travel over the length of the channel. Low-frequency quasi-periodic oscillations are superimposed on the translational motion of the ion. The magnitude of these oscillations is much larger than before. The trajectory of the ion leaving the channel is deflected downward. Further expansion of the gap (to 0.65 nm) does not appreciably alter the path of the Li^+ ion in the channel. In this case, the ion performs aperiodic oscillations and flies upward upon the channel.

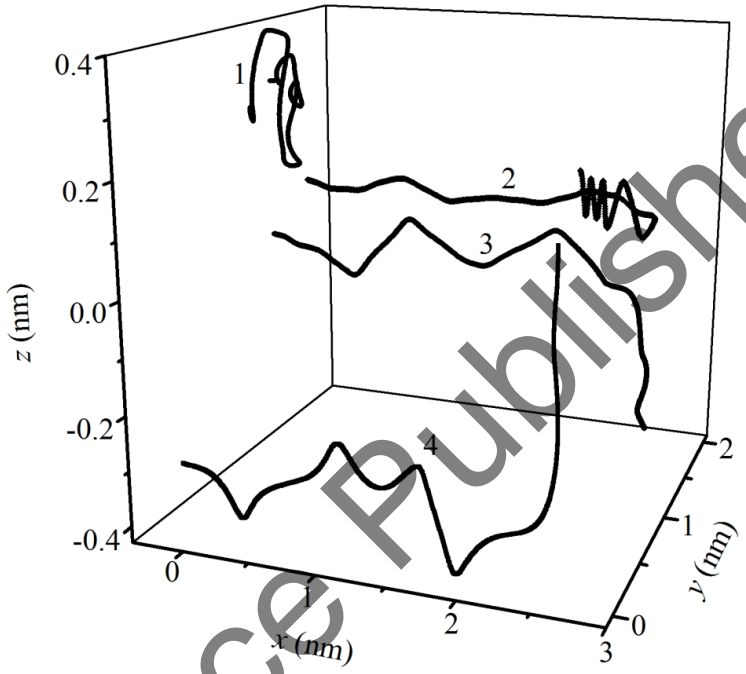

Figure 86. Trajectories of the lithium ion in a flat channel of graphene with the gap (1) 0.50, (2) 0.55, (3) 0.60, and (4) 0.65 nm.

The deceleration effect of the relief of the molecular field becomes apparent at the instant 100 ps. The Li^+ ion inside the gap traveled only 0.40 and 1.18 nm in the direction of the electric field with the intensity 10^3 V/m when the gap was 0.50 and 0.55 nm, respectively. If the starting point of the ion trajectory lies within the channel when the gap is 0.60 nm, the Li^+ ion passes through the channel for100 ps. When the gap was 0.65 nm, the ion remains in the space between the sheets and changes its path of the motion before leaving the channel. From the standpoint of effective control of the ion motion along the channel and application of the constant electric field with the intensity 10^3 V/m, it is the most expedient to use the gap of 0.60 nm between the sheets of graphene.

Let us now consider the effect the gap has on the kinetic and mechanical properties of the graphene sheets themselves when the ion is outside the flat channel at $t = 0$. The initial localization of the ion within the channel leads to the identical conclusions. Considering

the geometry of the system, it is advisable to investigate the behavior of the horizontal D_{xy} and vertical D_z components of the mobility factor of C atoms in graphene separately. The values of these components at different values of the gap are shown in Figure 87. As the gap increases, a component D_{xy} for the lower graphene sheet grows continuously (Figure 87a, curve 1), while the dependence $D_{xy}(t)$ of the top sheet (curve 2) has the minimum at h_g = 0.55 nm.

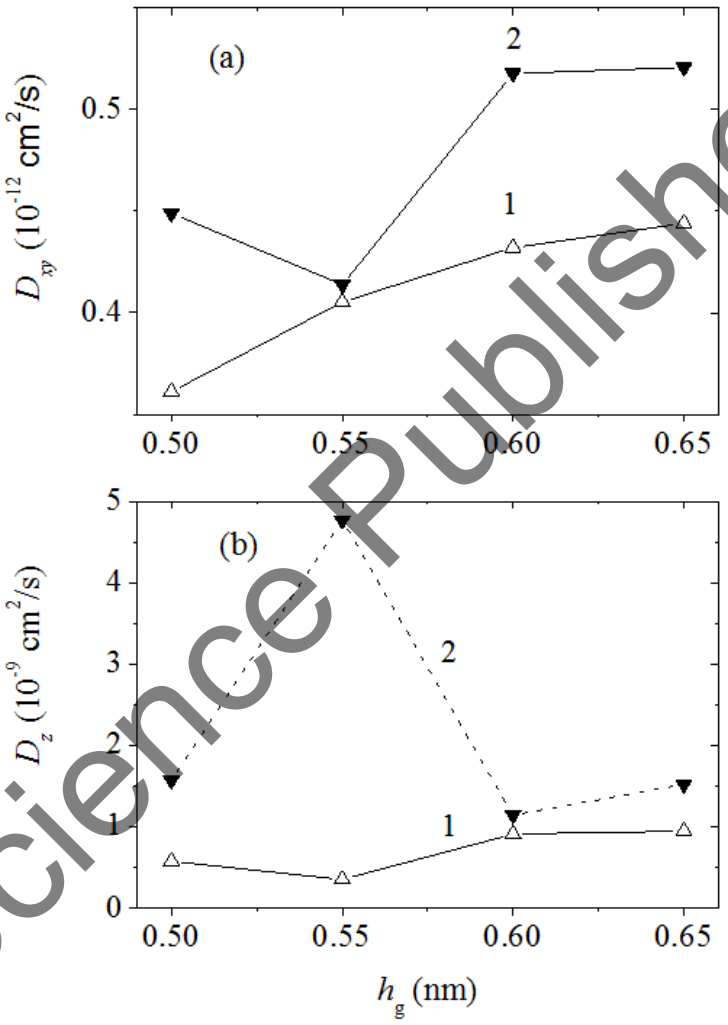

Figure 87. Coefficients of the (a) horizontal and (b) vertical mobility of graphene atoms in the (1) lower and (2) upper sheets forming a flat channel; at t = 0, the Li^+ ion was at the front of yz plane of the channel.

In general, the horizontal mobility of the atoms in the top sheet of graphene is greater than in the lower one. There is both a reduction in the horizontal mobility of the atoms in

the upper graphene sheet and the slight decrease in the vertical mobility of the atoms in the lower sheet at h_g = 0.55 nm. At this size of the gap, they are compensated by a considerable increase in the value of D_z for the upper graphene sheet. In this case, the strong fluctuations in the atoms mobility indicate that the Li^+ ion finds it difficult to move within the interplane gap. When h_g = 0.60 nm, the vertical mobility of the atoms of the lower and upper sheets of graphene approach each other most strongly.

The average values of D_{xy} and D_z for these sheets are somewhat lower than for h = 0.65 nm. The low values of D_z for both graphene sheets (at relatively high values of D_{xy}) begin at the gap size of 0.60 nm and are maintained at the gap of 0.65 nm. These conditions are favorable for the ion motion within the channel. Consequently, the gap of h_g = 0.60 nm may be considered optimal for the motion of the Li^+ ion in the flat graphene channel.

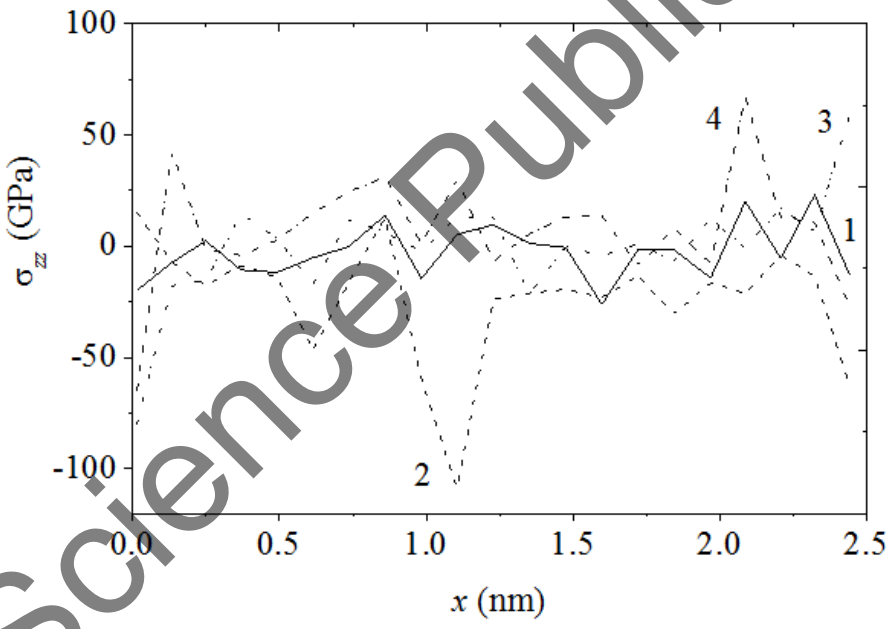

Figure 88. Distribution of strain $\sigma_{zz}(x)$ averaged over both sheets of graphene along axis x ("zig-zag" direction) coinciding with the direction of the electric field strength at the gap (1) 0.50, (2) 0.55, (3) 0.60, and (4) 0.65 nm.

Distribution of the greatest strains σ_{zz} in the graphene sheets (lower and upper combined) along the x axis (the "zig-zag" direction) is shown in Figure 88 for four values of the inter-sheet gap. Increasing the gap slows the rate, at which the Li^+ ion enters the channel (due to weakening the attraction of C atoms). The decelerated ion is deflected more

strongly by the molecular force field. This results in more enlarged fluctuations of σ_{zz} at the entrance of the channel when h_g = 0.60 and 0.65 nm. For the free two-layer graphene, the fluctuations of function $\sigma_{zz}(x)$ do not exceed ±50 GPa [304, 319, 374]. This range also fits the oscillations of function $\sigma_{zz}(x)$ when the Li^+ ion moves between the graphene sheets with the gap h_g = 0.50 nm. Increasing the gap leads to increased fluctuations. In the range of $x \approx 1.1$ nm at h_g = 0.55 nm, particularly strong fluctuations are observed due to the considerable deflection of the Li^+ ion upward. The ion is decelerated near the exit of the channel further strengthening the $\sigma_{zz}(x)$ fluctuations. The optimum size of the gap between the planes does not prevent moderate stains from arising in the graphene sheets.

Let us note the main differences associated with changes in the location of the initial point of the Li^+ ion trajectory. The vertical mobility of the carbon atoms is almost identical for both ways of introducing the ion. The horizontal mobility of C atoms differs appreciably only at the smallest value of the gap, i.e., when h_g = 0.50 nm. Both mobilities have lower values for both the lower and upper graphene sheet when the Li^+ ion is outside the channel at the initial instant. Strains that arise in the graphene sheets are generally not strongly dependent on the location of the Li^+ ion at $t = 0$. The exception is when h_g = 0.50 nm where stronger positive strains emerge at the entrance and negative strains (as strong as the first ones) arise at the exit when the Li^+ ion is introduced into the channel.

7.2. MECHANICAL AND THERMAL PROPERTIES OF SILICENE

It is obvious that the mechanical properties of 2D materials are harder to compare to their three-dimensional (3D) forms. This is because there are fundamental differences in the definition of the various quantities. For example, there are only two elastic constants for 2D materials instead of three ones for the bulk Si. Two-dimensional materials are expected to have much higher mechanical strengths than the bulk ones [415]. It was established in [416] that free-standing silicene would be unstable under a compressive bi-axial strain larger than 5%. When the strain is larger than 17% [417], the strain energy decreases sharply with the strain increases, and this corresponds to the yield point. Mechanical response under a uniaxial strain has also been computed [416, 418–421].

The strain created in the autonomous silicene along directions “zig-zag” and “armchair” directions could lead to different responses. Moreover, the Poisson ratio is isotropic and constant for the low strain (below 2%), but further decreases (increases) for the “armchair” (“zig-zag”) strain [419, 420]. The molecular dynamics method was used to calculate the elastic stiffness (50.44 N/m for “zig-zag” direction, and 62.31 N/m for the “armchair” one) and the ultimate strength (about 5.85 N/m) and the ultimate strain (about

18%) of mono-layer silicene [422]. Additionally, the effective bending stiffness of silicene (38.63 eV per unit width) was calculated indicating that its corrugated-like structure increases the bending rigidity compared to the similar system of graphene.

Molecular dynamics finite element methods (sometimes known as atomic-scale finite element methods) were used to determine the mechanical properties of silicene [423]. The silicene sheet contains 4 032 atoms and has approximately a squared shape. The sheet lengths are 16.116 and 16.316 nm in the "armchair" and "zig-zag" directions, respectively. Figure 89 shows that the tensile response in the "armchair" and "zig-zag" directions of the pristine sheet is rather different up to the fracture points. The magnitudes $\sigma_{z\alpha}$ and ε_{α} in the figure denote the nominal axial stress (engineering stress) and nominal axial strain (engineering strain), respectively.

Silicene exhibits brittle fracture with a fast destruction process and a drop in its stress–strain curve as shown in Figure 89. The process of destruction of the silicene sheet is accelerated in the presence of the bi-vacancy in it. In this case, the destruction of the sheet occurs somewhat faster when uniaxial deformation is carried out in the "armchair" direction. The Young modulus is determined from the first derivative of the stress–strain curve at $\varepsilon_{\alpha} = 0$. At a given axial strain, the axial stress in the "zig-zag" direction is slightly higher than that in the "armchair" one. The 2D Young modulus is estimated as 60.0 and 59.7 N/m in the "zig-zag" and "armchair" directions, respectively.

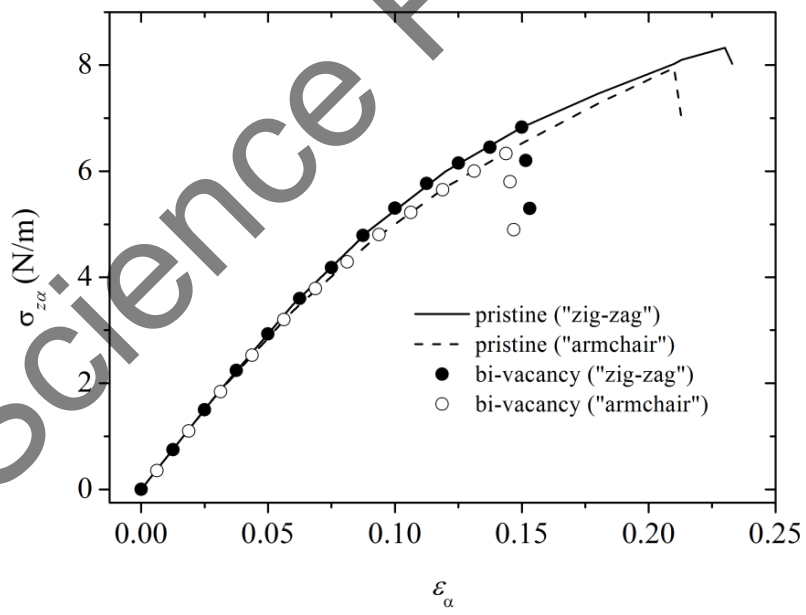

Figure 89. Stress–strain curves of the pristine silicene sheet under the uniaxial tension in the "armchair" and "zig-zag" directions, as well as, defective silicene sheets under the "zig-zag" and "armchair" direction [423].

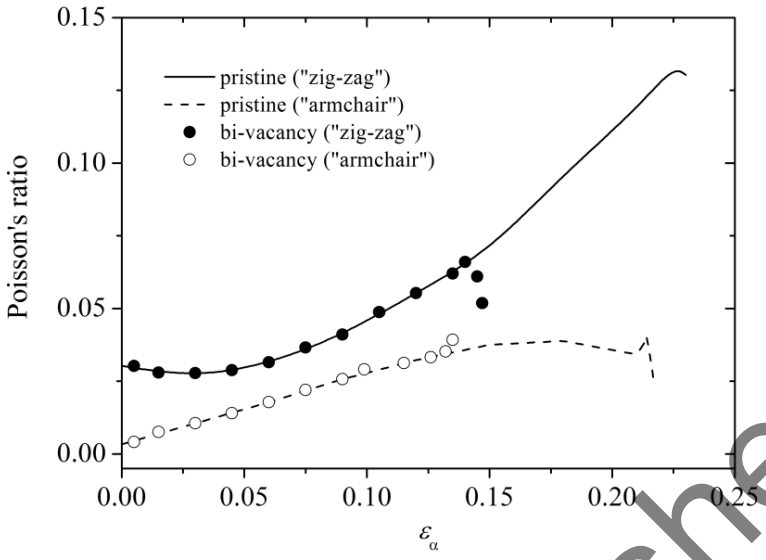

Figure 90. Variations of the Poisson ratio versus axial strain for the pristine and defective silicene sheets under uniaxial tension in the “armchair” and “zig-zag” directions [423].

It follows from Figure 90 that at a given axial strain prior to the fracture, the Poisson ratio of the defective silicene sheets is almost equal to that of the pristine one. Note also that the Poisson ratio in the “zig-zag” direction is always higher than that in the “armchair” one. This means that under tension in the “zig-zag” direction the decrease in the sheet length in the transverse direction is higher than that under tension in the “armchair” one.

The main results can be presented as follows. The fracture strength is significantly reduced by a single defect. One bi-vacancy in the sheet center reduces by 18 – 20% the fracture stress and 33 – 35% the fracture strain. Uniaxial stress–strain curves of pristine and weakly defective silicene sheets are almost identical up to the fracture points. This leads to the almost unchanged Young modulus. At a given axial strain prior to the fracture, the Poisson ratio of the defective sheet is almost equal to that of the pristine one.

The thermal conductivities λ of the free-standing silicene and silicene supported on amorphous SiO_2 substrates were predicted in [424] in the temperature range from 300 to 900K using the NEMD simulations. After obtaining the temperature gradient and heat flux q, the thermal conductivity was calculated according to the Fourier law as $\lambda = -q/(\partial T/\partial x)$. Dependences $\lambda/\lambda_0(T)$ are shown in Figure 91. It is seen that the thermal conductivities of the free-standing and supported silicene both decrease as the temperature increases, but that of the supported silicene has a weaker temperature dependence. The presence of the SiO_2 substrate results in a large reduction up to 78.3% at 300 K of the λ coefficient of silicene. Thus, the free-standing silicene and that on the substrate exhibit completely different thermophysical properties. The estimated value of the silicene melting point is 1500 K [388].

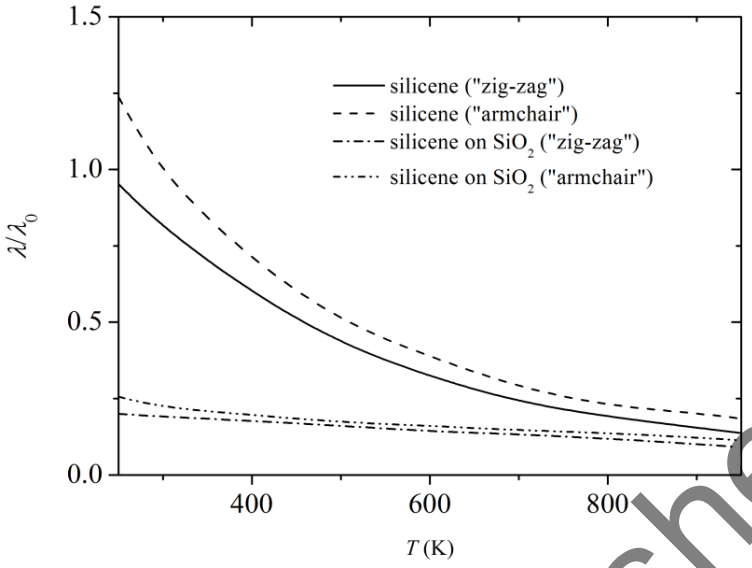

Figure 91. Variation of the thermal conductivities of the free-standing and supported silicene in the "zig-zag" and "armchair" directions with temperature; the thermal conductivities are normalized against λ_0 = 48.1W/m K, which represents the thermal conductivity of free standing silicene in the "armchair" direction at 300 K [424].

Since silicene cannot be separated from the substrate, on which it was obtained, it is expedient to investigate the possibility of using silicene together with the substrate. In this connection, it is not necessary to consider in detail the physical properties of the free-standing silicene as is done in a large number of papers devoted to the study of the silicene properties. Of course, the mechanical stability of silicene is important for its use as the anode material. Nevertheless, it is reasonable to investigate the silicene on the substrates on which it is obtained. Since namely in this combination, the silicene can find use in the very near future. Therefore, here, we do not consider in detail the mechanical properties of the autonomous silicene, as it was done for graphene.

7.3. Forced Motion of Lithium Ion through Flat Channel of Perfect Silicene

Electric fields on the atomic scale are characterized by much higher values of field strength than the usually applied fields. Inter-atomic forces used in molecular dynamics simulations are ultimately determined by the properties of electrons, according to which the atomic units are chosen. The atomic unit of electric field strength is the E_h / ea_0 = 5.14220652 × 10^{11} V/m, where E_h = 4.35974417 × 10^{-18} J, the Hartree unit, e is the elementary electric charge, a_0 is the Bohr radius. Studying multiple electron scattering as

well as the electron momentum transfer was implemented in the $SrTiO_3$ ceramic. It results in determining the quantitative characteristics of the atomic electric field [425]. The maximum field strength near the oxygen atoms as measured by a probe was 4×10^{11} V/m and that near Ti and Sr atoms was 10^{12} V/m. The measurement accuracy is determined by the microscope resolution.

Similarly, to the case with graphene, it is natural to consider silicene as a potential material for application in the lithium-ion batteries. The almost 4-fold swelling in the bulk of a crystalline silicon anode ultimately results in its degradation during the lithium ion intercalation–deintercalation cycles. Analysis showed that a change in the volume of the mono-layer and bi-layer silicene (because of full lithiation) increased by 13 and 24%, respectively. Besides, silicene is restored to the initial state after delithiation unlike the crystalline Si [426].

Mobilities of Si atoms and distributions of the main stresses in silicene appearing in the course of the lithium ion motion along the silicene channel were calculated in [427]. Interactions in silicene were represented using the Tersoff potential [428]. The Morse potential was used to describe interactions between the Si atoms belonging to different silicene sheets [429], as well as, to represent interactions between the Li^+ ion and Si atoms [425, 429–431]. Here, we consider the case of reconstruction of 4×4 surface area. A unit cell in this silicene structure (contained in the rhombus in Figure 92) includes 18 Si atoms. Six Si atoms in the unit cell are shifted to the distance of 0.074 nm normally to the surface while other Si atoms are located on a common (initial) plane. Such a silicene sheet structure is close to the silicene surface observed on the Ag(111) support [432].

While atoms bulging from the initial surface in the upper bi-layer silicene sheet are shifted upwards, the atoms in the lower sheet are projecting downwards. We used 6 values of distances between the silicene sheets: 0.50, 0.55, 0.60, 0.65, 0.70, and 0.75 nm. These distances essentially exceed the distance of 0.2481 nm between the sheets of bi-layer silicene with the AB packing obtained in calculations using the density functional theory [433]. However, such a set of distances covers the range of clearances used for studying the motion of the Li^+ ion in the electric field between the graphene sheets [414] and through the porous graphene membranes [412].

Here, the silicene sheets containing 406 atoms are rectangular of size 5.5×4.7 nm (14 atoms along each sheet edge). High electrode capacity is attainable when electrolyte ions move fast. Therefore, the self-diffusion coefficient of the ion would be in the range of 10^{-10} to 10^{-13} cm^2/s [434]. In the computer experiments [414] with the clearance of 0.50 – 0.65 nm between the graphene sheets, we showed that such an effect is obtained starting with the electric field strength of about 10^3 V/m. The initial location of the ion corresponded to the height of $h_g / 2$. At $t = 0$, the ion was located across from the hollow formed by rows of the Si atoms of the lower silicene membrane closest to the sheet middle (Scheme 1, Figure 92). Despite the fact that interaction between the parallel silicene sheets

decreases fast (as the distance between them increases) and becomes weak in the distance range under consideration (0.50 – 0.75 nm). However, under this, the Li^+ ion motion in such interplanar clearance is not free. This is related to the fact that strong covalent bonds acting in the silicene plane adopt only insignificant corrugation of the sheets when the Li^+ ion moves. When the Li^+ ion is affected by the Van der Waals forces from close-packed Si atoms of silicene sheets, its motion becomes slower.

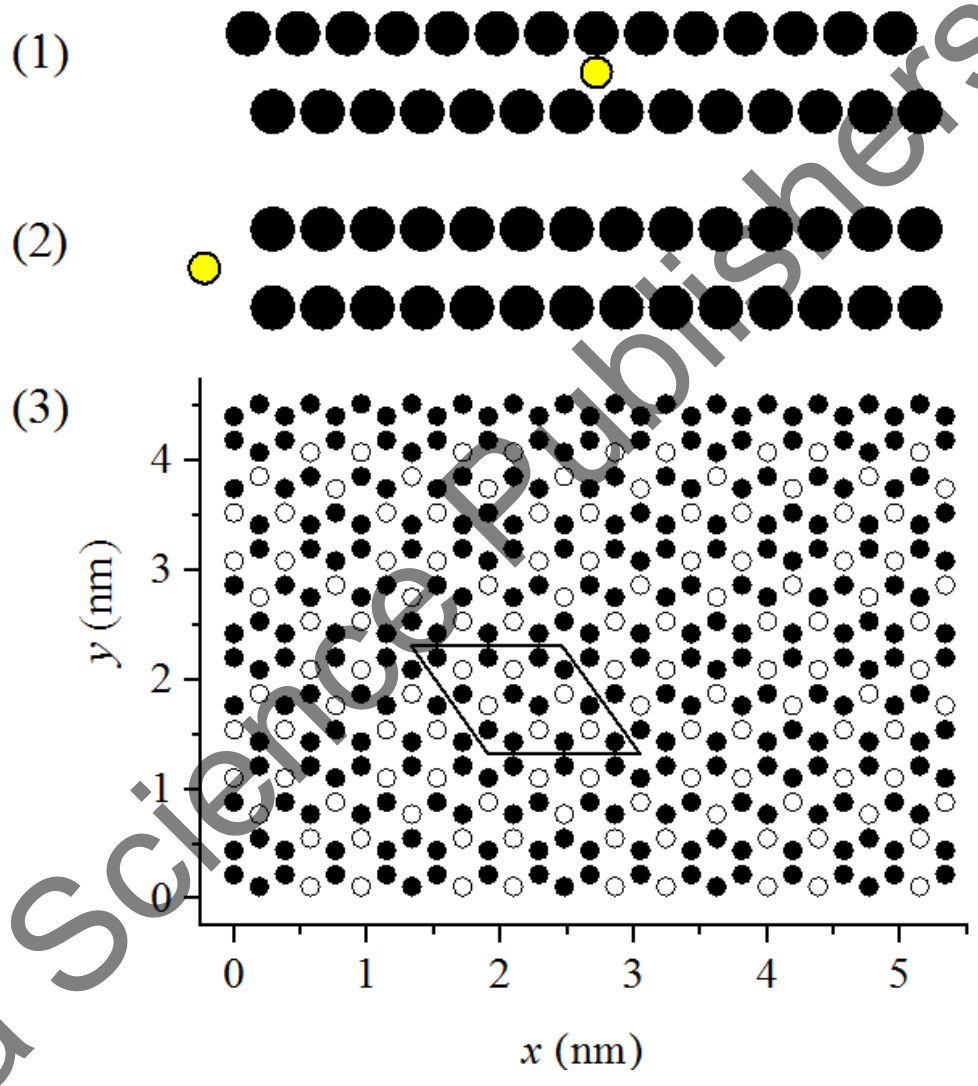

Figure 92. Schemes of arrangement of atoms at $t = 0$: (1) frontal view of plane, (2) side view of plane with the Li^+ ion before the channel; (3) top view of the 4 × 4 silicene structure at the initial instant; open circuits are Si atoms displaced normally to the surface, solid circles are Si atoms in the initial plane; an outline shows a unit surface cell of the silicene sheet; electric field strength is directed along the *x* axis; at the initial instant, the Li^+ ion was located before the *yz* plane outside the channel.

The electric field strength of 10^3 V/m proved to be insufficient for the Li^+ ion to enter the planar channel formed by silicene sheets with the clearance of 0.50 nm. In this case, the ion having walked for some time in front of the channel entrance descended and passed on the outer side of the channel to its exit in the direction of the field (axis *x*) interacting with the Si atoms of the lower sheet. Then it leaves the exit behind and went forward and upward. After long walking around the entrance, the Li^+ ion finally entered the channel at h_g = 0.50 nm and at the field strength 10^4 V/m. However, its slow motion inside the channel was limited at reaching coordinate x = 0.8 nm, near which the ion remained at t = 100 ps. When the field strength was increased to 10^5 V/m, the ion spent half the assigned time searching for the possibility to enter the channel. Entering the channel, the ion advanced to almost the same distance (0.8 nm) along the *x* axis, changed its direction while walking, and having passed along the *y* axis, and exited the channel.

The Li^+ ion could not pass the whole channel in the field direction and exit on the channel opposite side at h_g from 0.50 to 0.75 nm, when the field strength was from 10^3 to 10^4 V/m. Almost the same pattern was observed at E = 10^5 V/m except for h_g = 0.70 nm. The trajectory of the Li^+ ion corresponding to this phenomenon is shown in Figure 93. In this case, when the ion reaches the exit at the opposite side of the channel, it leaves the channel moving along a straight line forward and downwards. Increase in the clearance to 0.75 nm under the same field strength (10^5 V/m) has not yielded such effect: the ion walked in the channel during the whole period of 100 ps.

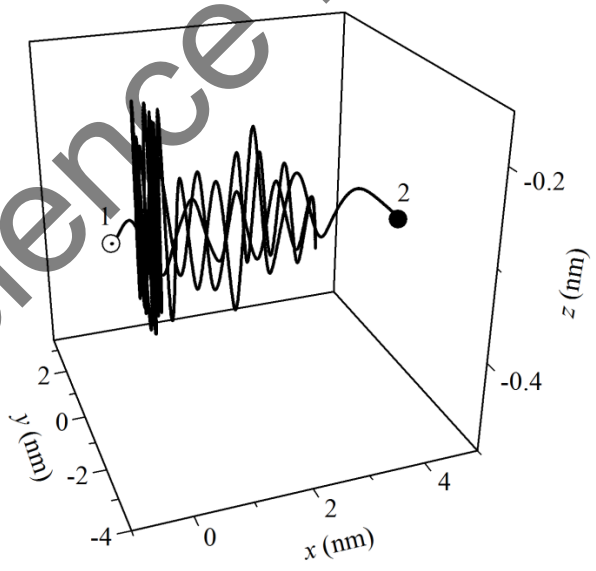

Figure 93. The trajectory of the Li^+ ion motion in a planar channel formed by silicene sheets at the clearance 0.70 nm and electric field strength 10^5 V/m: (1) the initial point of the trajectory, (2) the final point.

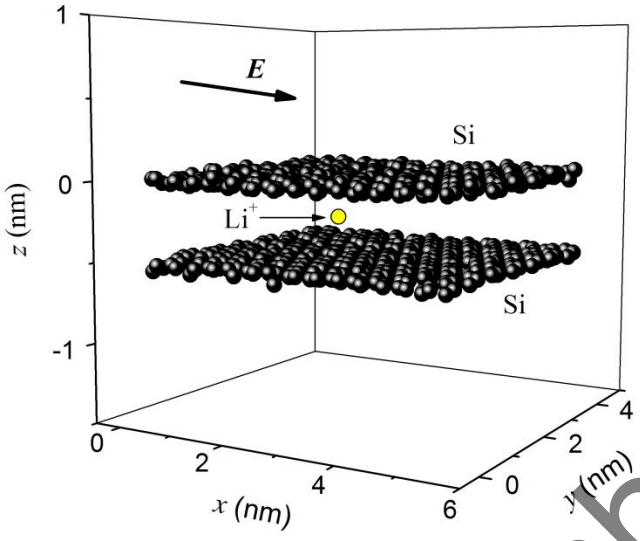

Figure 94. The configuration of the system of "the lithium ion in bi-layer silicene" obtained at the instant 100 ps under the electric field strength of 10^5 V/m with the clearance between the sheets of 0.55 nm.

As a rule, the ion remains within the channel in the period under consideration. A typical configuration of the system "Li^+ ion in bi-layer silicene" obtained at the instant 100 ps is shown in Figure 94. The Li^+ ion forms a much stronger bond with silicene than with the graphene. The predicted behavior of the lithium ion is to pass the whole sheet in the direction of the applied electric field and leave the channel on the opposite side from the entrance. In this case, this occurs at much higher field strength (10^5 V/m against 10^3 V/m) and greater clearance (0.70 nm against 0.60 nm) comparing with the intercalation of an ion into the bi-layer graphene. Thus, the field strength of 10^5 V/m and clearance of 0.70 nm are determined as the optimum values for the lithium ion motion in a planar silicene anode.

Energy U of the interaction of the Li^+ ion with silicene depends directly on the position of the ion in the silicene channel or beyond it. Therefore, the value of U indirectly depends on the electric field strength determining the motion of the ion in the channel. Figure 95 shows the function $U(t)$ for the case of $E = 10^5$ V/m for clearances between Si layers h_g = 0.5, 0.6, and 0.7 nm. At such field strength, the Li^+ ion can enter the channel even at h_g = 0.5.

However, the motion in a narrow channel proves to be very constrained and occurs at sufficiently high interaction energy U. Having overcome not more than a quarter of the channel length in the x direction and experiencing significant fluctuation in energy, the ion leaves the channel up to the instant 80 ps. From this instant, the potential energy of the ion becomes zero. Considerably lower values of the ion energy U are obtained for the channel clearances of 0.6 and 0.7 nm. In the case of h_g = 0.6 nm, the low energy values are

preserved during the whole time of observation of the system, since the ion does not leave the channel for 100 ps. At h_g = 0.7 nm, the Li^+ ion remains in the channel only for 40 ps. During this time, it passes the whole channel length. Its potential energy becomes zero when t > 40 ps.

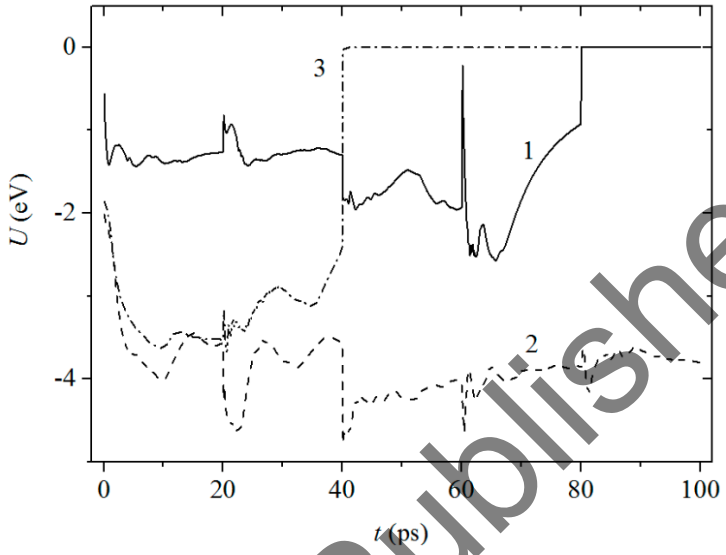

Figure 95. Interaction energy of the lithium ion with silicene at the electric field strength of 10^5 V/m and clearance h_g between the layers: (1) 0.5 nm, (2) 0.6 nm, and (3) 0.7 nm.

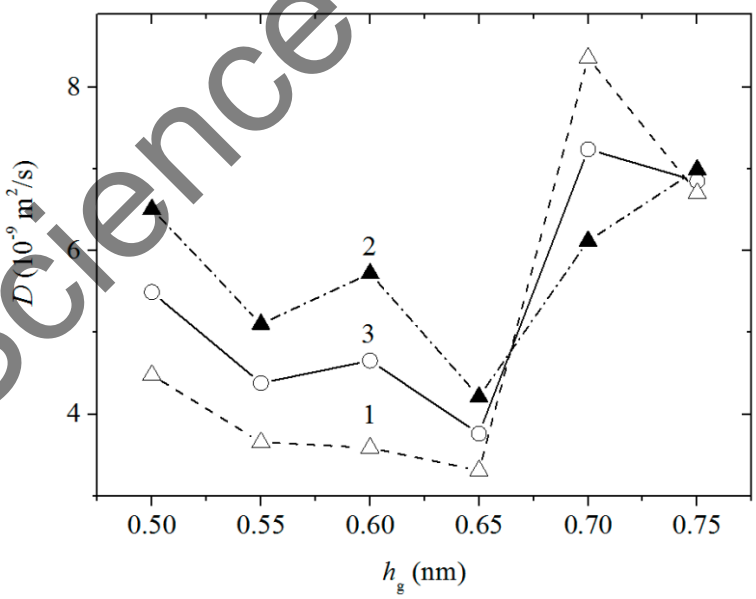

Figure 96. Self-diffusion coefficient of the Si atoms in bi-layer silicene: (1) in the top layer, (2) in the bottom layer, (3) average for both layers.

The self-diffusion coefficients D of Si atoms do not depend on the Li^+ ion velocity or field strength $\boldsymbol{E}$. Mobility of Si atoms in the bottom silicene layer almost at all h_g is higher than that in the top layer (Figure 96). Decreasing the Si atoms mobility as the clearance increases from 0.50 to 0.65 nm is due to the slackening of the mutual influence of the silicene sheets with the h_g rise. The sharp increase of D value under the rise of h_g from 0.65 to 0.70 nm is due to sufficient enhancement of the channel ability by Li^+ ion, and, therefore, due to an increase of the intensity of the ion interaction with Si atoms. Since the Li^+ ion does not leave the flat channel with h_g = 0.75 nm during its motion for the observation time, the ion covers more than half of the silicene area and decelerates the Si atoms. Therefore, the average mobility of Si atoms decreases but insufficiently.

As it is seen in Figure 97, behavior of the horizontal components of Si atoms mobility is analogous to one described above. According to quantitative values of D and its components, it is precisely the horizontal mobility of atoms is the factor determining the behavior of Si atoms. This fact can be explained by the existence of the oriented covalent bond between silicon atoms.

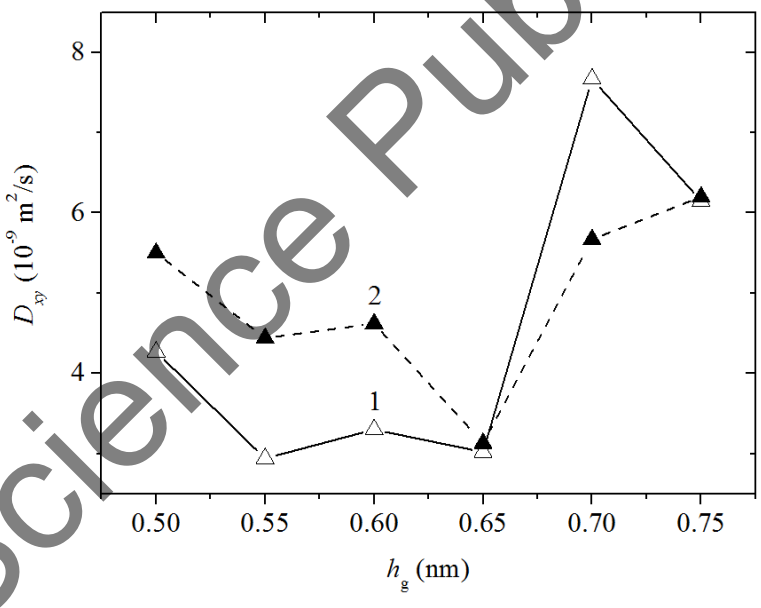

Figure 97. Horizontal components of the self-diffusion coefficient of the Si atoms in bi-layer silicene: (1) in the top layer, (2) in the bottom layer.

The presence of the Li^+ ion creates additional stress in the silicene. This is mainly reflected in the considerable enhancement of the stress component σ_{zz} that grows by tens of times. In the silicene free of the Li^+ ion, components σ_{zx}, σ_{zy}, and σ_{zz} are of about the same order of magnitude. Figure 98 shows the distribution of the analyzed stresses over

elementary areas elongated along the *y* axis in the case of intercalation of the Li^+ ion in bi-layer silicene with the clearance of 0.7 nm. As seen from distributions in the figure, the direction of growth of stresses is strongly reoriented towards vertically directed forces *z*. It is seen that the big stress surges σ_{zz} correspond to the middle part of the sheets. The peak stresses σ_{zz} are still lower than similar surges of the corresponding stress appearing during the motion of the Li^+ ion through the channel formed by the graphene sheets [412].

Dependence of the character of stresses σ_{zz} in silicene along the *y* axis on the clearance (in the case of the motion of the Li^+ ion at the field strength of 10^5 V/m) can be seen in Figure 99. The stress peaks σ_{zz} can appear on both edges of the silicene sheets in the direction *y* normal to the field strength. These oscillations are significant at the low clearances (h_g = 0.50 and 0.60 nm) and undergo a decrease by half at h_g = 0.70 nm.

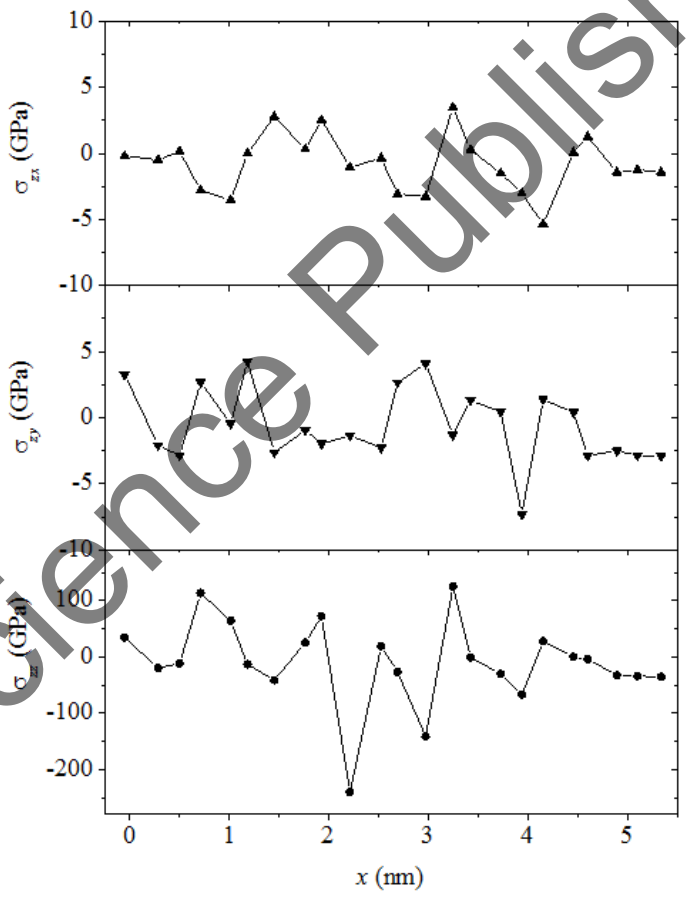

Figure 98. Distribution of stresses (σ_{xz}, σ_{yz}, and σ_{zz}) in the silicene plane in the case of intercalation of the Li^+ ion at the field strength of 10^5 V/m into the planar channel with the clearance of 0.70 nm; elementary areas are elongated along the *y* axis.

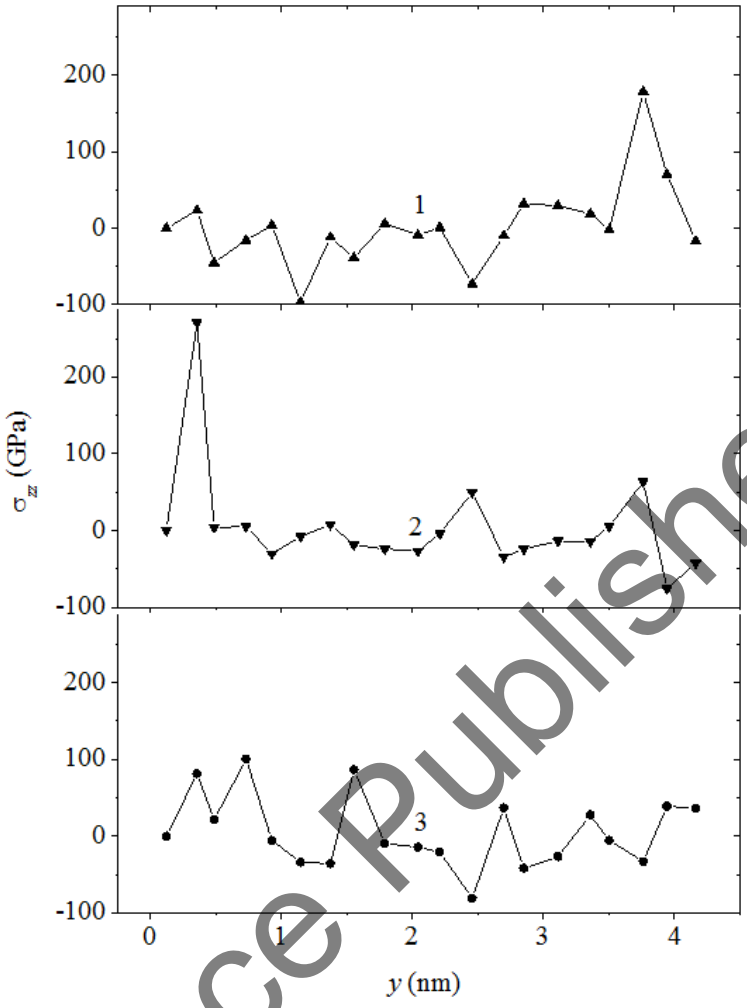

Figure 99. Average distribution of stress σ_{zz} in the silicene plane at the field strength of 10^5 V/m at clearances between the top and bottom layers (1) 0.5 nm, (2) 0.6 nm, and (3) 0.7 nm; elementary areas are elongated along the *x* axis.

The initial roughness R_a (corresponding to the profile formed by the bi-layer silicene on the Ag support) decreases fast almost to the zero values (Figure 100). The silicene sheets flatten before the Li^+ ion enters the planar channel. In other words, the experimentally observed [432] profile of the bi-layer silicene on a silver support proves to be unstable, as soon as the silicene leaves the support. As the Li^+ ion moves inside the planar channel, R_a grows fast and reaches relatively stable values already for approximately 20 ps. However, these values are lower than the initial roughness characteristic for the silicene formed on the Ag support. Further, at 40 ps, R_a somewhat decreases (up to 11%) in the case of small clearances (h_g = 0.50 nm) and increases (by ~ 3%) for the larger clearances (h_g = 0.70 nm).

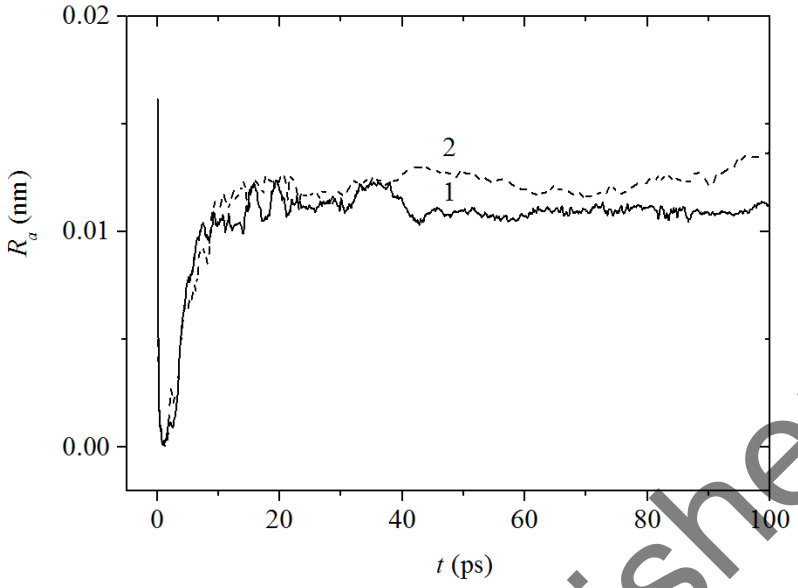

Figure 100. The roughness of the bi-layer silicene for intercalation of the Li^+ ion at the field strength of 10^5 V/m and clearances between the layer (1) 0.5 nm, and (2) 0.7 nm.

The silicene sheets were exposed to the constant electric field with the strength of 10^3 – 10^5 V/m. The clearance from 0.50 to 0.75 nm was formed between the silicene sheets. The ion completely passes through the planar channel in the field direction at the field strength of 10^5 V/m during100 ps, if the clearance is 0.70 nm. In other cases, the ion either passed around the channel or left the inter sheet space in the direction differing from the direction of the field or were stuck in the channel. The roughness of silicene (corresponding to the case of the Ag support) completely disappeared even before the ion enters the channel. When the ion moves along the channel, the R_a magnitude assumes a new value lower than the initial one. This value changes in time and depends on the clearance between the silicene sheets.

The ion entering the channel corresponds to the periods of negative values of the silicene-Li interaction energy. The mobility of the Si atoms tended to decrease as the clearance increases to 0.65 nm and then grew drastically under the further clearance increase. The similar behavior was characteristic of the horizontal mobility components of Si atoms in the silicene sheets. When the ion moves along the channel, significant fluctuation in the stresses σ_{zz} (exceeding by tens of times fluctuation of stresses σ_{zx} and σ_{zy}) appear in the distributions along the length and width of the silicene sheets. The location and range of the strong fluctuations of σ_{zz} depend on the clearance between the graphene sheets.

7.4. NANOSCALE SIMULATION OF PENETRATION OF LITHIUM ION INTO DEFECTIVE SILICENE

The use of silicene as an anode material implies its separation from the substrate. This operation will inevitably lead to the appearance of the different types of defects in silicene. In this connection, it is important to know how the mechanical stability of defective silicene will change and how the presence of a defect will affect the interaction of silicene with the lithium ion. These issues have not yet been considered. This problem can be solved by the method of classical molecular dynamics, which (unlike the *ab initio* calculations) makes it possible to trace the motion of lithium ion through the two-layer silicene both horizontally and vertically during the essential time interval. The surface area and porosity of the material are two important physical quantities, which significantly affect the efficiency of future devices. It is expected that in the two-layer silicene the structural defects such as poly-vacancies possibly create additional ways for the lithium passage through planes and its mobility will be increased. Intercalation of the lithium ion into the two-layer silicene usually causes deformation, which extent does not exceed 3 – 4 nm. The deformation extends to the same distance when the lithium ion is stuck between the silicene sheets.

Therefore, it is of interest when the Li ion can pass a path of approximately this length in the silicene. The electric field (10^5 V/m) used in this study was chosen empirically. This field cannot have a significant impact on the parameters of the electron orbits of atoms and, consequently, cannot make changes to the widely used inter-atomic interaction potentials. We investigated the diffusion of lithium in the two-layer silicene with the AB stacking, which has a lower binding energy (– 5.32 eV) than silicene with AA laying (– 5.25 eV) or a monolayer silicene (– 5.13 eV) [435].

These calculations were performed by the classical molecular dynamics method [436]. The Tersoff potential with the parameters [428] is taken for representation of the interactions in silicene. The interaction between the Si belonging to different sheets of silicene is described by the Morse potential [429]. The interactions between the Li^+ ion and Si atoms are presented by the Morse potential, also [430, 431]. Various periodic structures are observed for silicene on Ag(111) such as 4 × 4, (2√3 × 2√3)R30°, (√7 × √7)R19.1°, and (√13 × √13)R13.9° [15, 437, 438]. Almost all experimental studies confirm that Si atoms in the silicene form a buckled honeycomb lattice.

We apply the 4 × 4 model of silicene since its validity was confirmed by various experimental methods including the non-contact atomic force microscopy, scanning tunneling microscopy, angle resolved photoelectron spectroscopy, and low energy electron diffraction [432]. In addition, the atomic structure of the mono-layer 4 × 4 silicene occupies the largest part of the surface of the epitaxial silicene on the substrate Ag(111) [439]. During the entire calculation, the average height of the protrusions produced by the Si atoms in the model was kept with a good degree of accuracy. A slight difference (< 0.005 nm) in the height of the buckles, as well as, the horizontal dimensions of the reconstruction

(determined by different silicene models) obviously cannot greatly affect the result of the simulation. According to that, the h_g gap between the silicene sheets exerts the main influence on the result. It is the value of h_g and the electric field strength that determine the channel capacity.

The estimated concentrations of mono- and bi-vacancies in silicene obtained on Ag(111) can be quite high such as 4.4×10^{13} cm^{-2} and 5.0×10^{13} cm^{-2}, respectively [32]. It means that there would be one defect in every 2 nm^2 area. The large concentration of the point defects (together with easy diffusion and coalescence of the vacancy defects) correctly explains a low stability of silicene in the experiments.

Study of the Li^+ ion permeation through the pores of the Si-membranes is performed in the presence of the gap between the silicene sheets h_g = 0.2481 nm. In the case of the Li^+ ion motion in the flat channel under the action of the longitudinal electric field, the gap was h_g = 0.75 nm wide. Perfect silicene sheet had the size of 4.8 × 4.1nm (taking into account the size of Si atoms) and contained 300 atoms. Nine similar defects were created approximately evenly with the displacement of 0.1 – 0.2 nm in each (*x* and *y*) direction for different sheets of the silicene with the mono-, bi-, tri-, and hexa-vacancies. The silicene sheet contained 291, 282, 273, and 246 atoms in each of these cases.

Study of the vertical (perpendicular to the plane of the membrane) Li^+ ion transport through silicene sheets was performed by 20 tests for each set of membranes. Twenty points for the initial arrangement of ions were placed almost evenly over the silicene top sheet (Figure 101). Each test was carried out for the new location of the ion and had a duration of 1 million time steps. In most cases, during this time, the ion successfully overcame the double-barrier in the form of silicene membranes containing mono- or poly-vacancies. The average time for an ion to overcome silicene obstacles was determined based on these tests. Only successful tests were taken into account.

In the case of the horizontal ion motion, two sheets of silicene contained the same set of defects, and the ion was similarly moved by the longitudinal electric field with the intensity of 10^5 V/m. Initially (at t = 0), the Li^+ ion was located at coordinates x = 0.198 nm, y = 2.245 nm, i.e., it was slightly pushed into the silicene channel. In this case, each run had a duration of 1 million time steps. Necessary conditions for preserving the morphology of porous silicene were created by securing its sheet edges.

Consider first the situation where the direction of the electric field vector is perpendicular to the plane of the silicene membrane. Suppose that in this case, the pores appear in the form of single vacancies. The lithium ion initially moves in the direction of the field. Figure 102 shows the ion passage through the pores of the two-layer silicene. Here, the open circles marked with numbers 1 and 2 refer to the original location of the ion and the location immediately after its overcoming the two-layer membrane, respectively. The top layer of the membrane is shown in the figure by dark beads and the lighter beads

present the bottom layer. Note that the ion overcomes a considerable distance in the space between the layers from the entrance place being on the upper layer to the exit point on the lower layer. The residence time in the inter-layer space, in this case, can be a few picoseconds. The first ion diffuses over the surface of silicene until it finds a position to enter the flat channel. Then, the ion leaves the channel when it finds a vacancy in the lower layer. It has a complex trajectory that ends with an exit from the channel. Replacement of the defects leads to shortening the path, which the ion overcomes inside the two-layer silicene, and the time of overcoming these obstacles reduces.

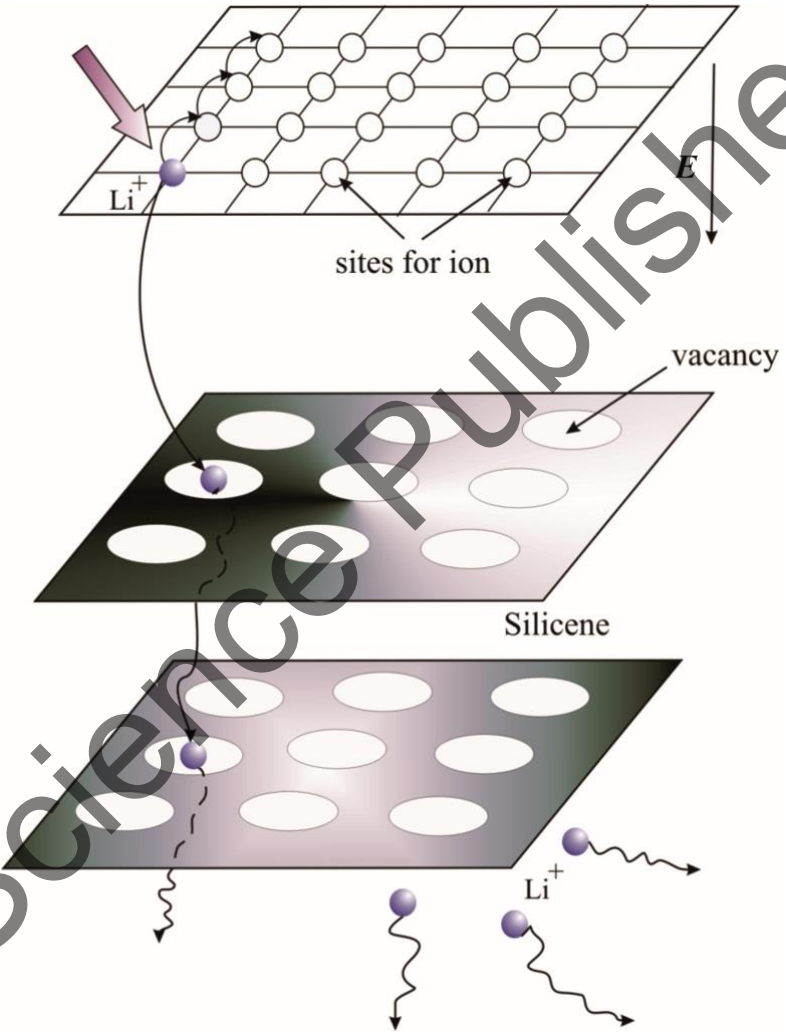

Figure 101. The scheme of the successive passage of Li^+ ions through the silicene membranes in a constant electric field; initially, the ion is placed in the next adjacent site, which is in the plane over membranes and starts moving due to existence of the field strength ***E***; the ions that have passed both membranes are removed from the system, as well as, the ions that cannot pass through the upper membrane during 100 ps.

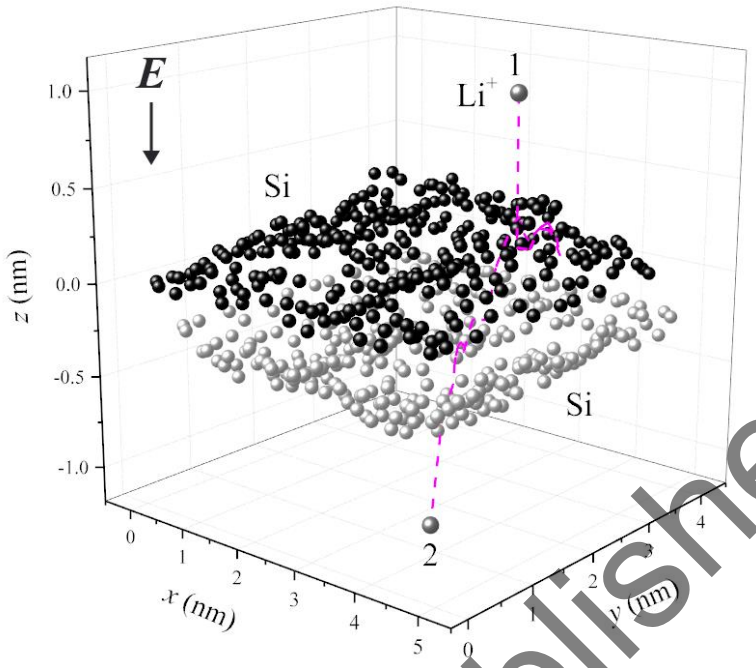

Figure 102. Drift of the lithium ion through the bi-layer silicene membrane with single vacancies; circle 1 shows the original location of the ion, circle 2 reflects the ion location immediately after the passage through the membrane; the arrow shows the strength vector of the applied electric field.

Constructions created by nature are sometimes used in engineering. In fact, the model we use is similar to the crude model of the cell membrane. Some channels open or close in the neurons and muscle cells are in response to changes in the charge passage across the plasma membrane. The active transport is also possible, for example, to pump molecules or ions through a membrane against their concentration gradient.

Starting the motion from one of the 20 points evenly distributed over the silicene surface, the Li^+ ion is not always able to pass through the bi-layer silicene membrane. In some cases, throughout the timing (mainly for the membranes with single vacancies), the ion was moving along the surface of the top sheet of silicene and non-penetrating through it. An example of such a trajectory is shown by the curve "b" in Figure 103. The curve "a" shows the trajectory when the Li^+ ion after a short motion passes through the bi-layer silicene membrane. The arrow shows the direction of the electric field intensity.

The mean time $\langle t \rangle$, which the Li^+ ion needs to overcome each of the silicene layers, is shown in Figure 104. It is seen that the mean time $\langle t \rangle$ for passage of the first (upper) layer has a substantially larger value only in the case where the silicene sheets contain mono-vacancies. The similar trend is observed in the second (bottom) layer. The ion passage of the second layer of silicene in the presence of bi-and tri-vacancies requires a much longer time than that in the presence of hexa-vacancies. At the same time, the $\langle t \rangle$

value of the inter-layer ion drift in the presence of the bi-vacancies in layers is only slightly higher than that in the case of tri-vacancies presence in silicene sheets.

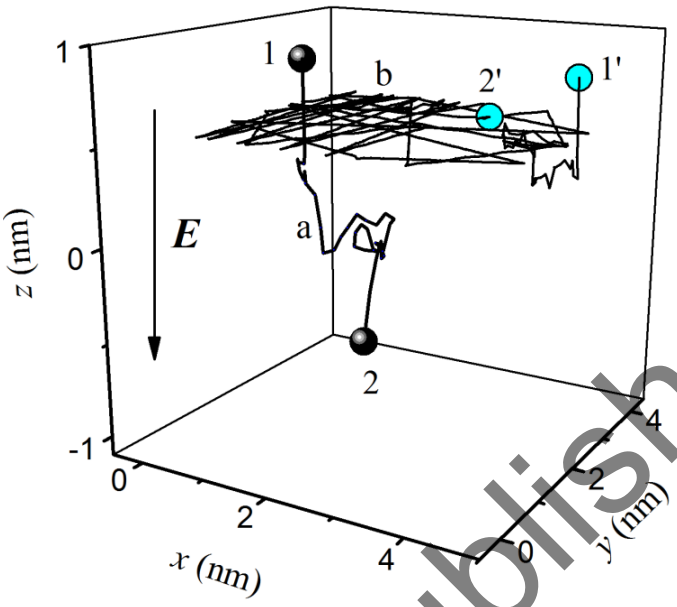

Figure 103. Two trajectories (a, b) of lithium ion moving under the influence of the electric field ***E***; 1, $1'$ are the ion motion start points; 2, $2'$ reflect points of ion location after 100 ps; points 1, 2 refer to the "a" trajectory, $1'$, $2'$ correspond to the "b" path.

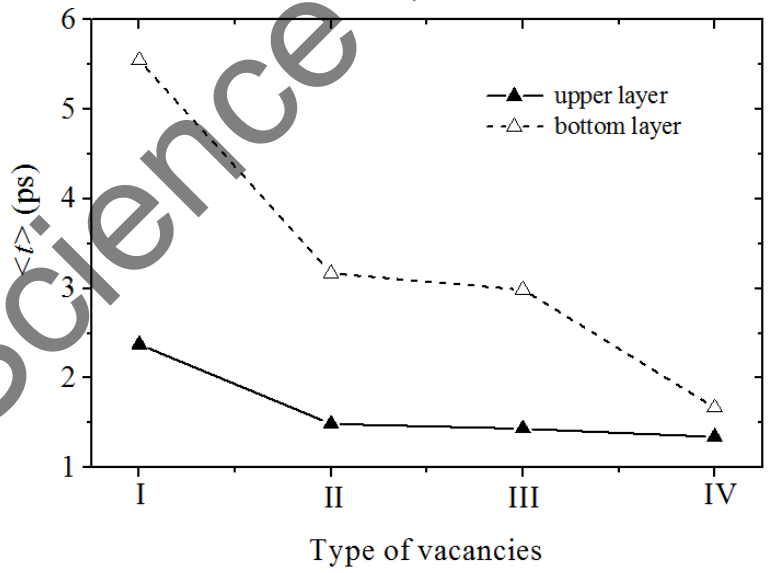

Figure 104. The mean time of the lithium ions passage through the first and the second layer of the two-layered silicene; the numbers on the *x* axis denote the type of defects in the membranes: I mono-, II bi-, III tri-, IV hexa-vacancies.

When the Li^+ ion moves along the channel, it "clings" to silicene sheets and slows down in the channel. Moreover, the Li^+ ion in the silicene channel easily moves in the opposite direction with respect to the applied electric field. The Li^+ ion passes through the entire length of the channel and leaves it when the gap h_g = 0.80 nm and when the silicene is perfect or has mono- or bi-vacancies. The ratios of roughness and potential energies are shown in Figure 105 where the corresponding characteristics with the upper indexes "vac" and "per" designate the defective and perfect silicene, respectively. These characteristics are determined at the longitudinal motion of the lithium ion between the silicene sheets with the gap of 0.75 nm.

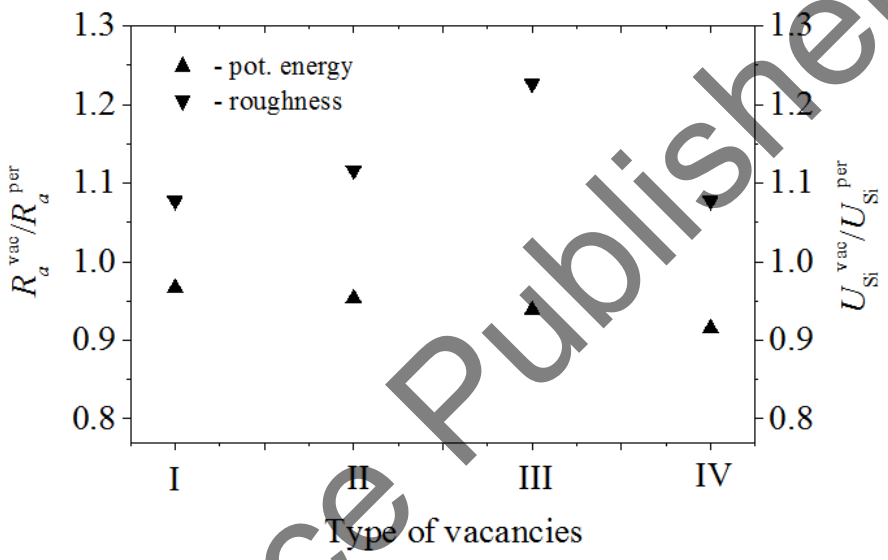

Figure 105. The ratio of roughness and potential energy of porous silicene to the values of perfect silicene during the lithium longitudinal motion in the channel; the numerical designation is similar to that in Figure 103.

With increasing the pore size, the potential energy of the system increases while the average roughness passes through the maximum, which falls on the system III. Thus, borders with tri-vacancies are the most vulnerable to displacements perpendicular to the plane of each membrane.

Figure 106 presents the similar relative characteristic for the self-diffusion coefficient of Si atoms in two identical silicene sheets with the gap between the sheets of 0.75 nm. In almost all cases, the ratio D^{vac}/D^{per} is larger 1, i.e., the mobility of the Si atoms in the membranes with pores is greater than that in the perfect silicene sheets. It is true with exception of the lower membrane with single vacancies. In this case, the mobility of Si atoms decreases due to changes in its relief and the reduction of the force of interaction with Li^+ ion drifting in the space between silicene sheets.

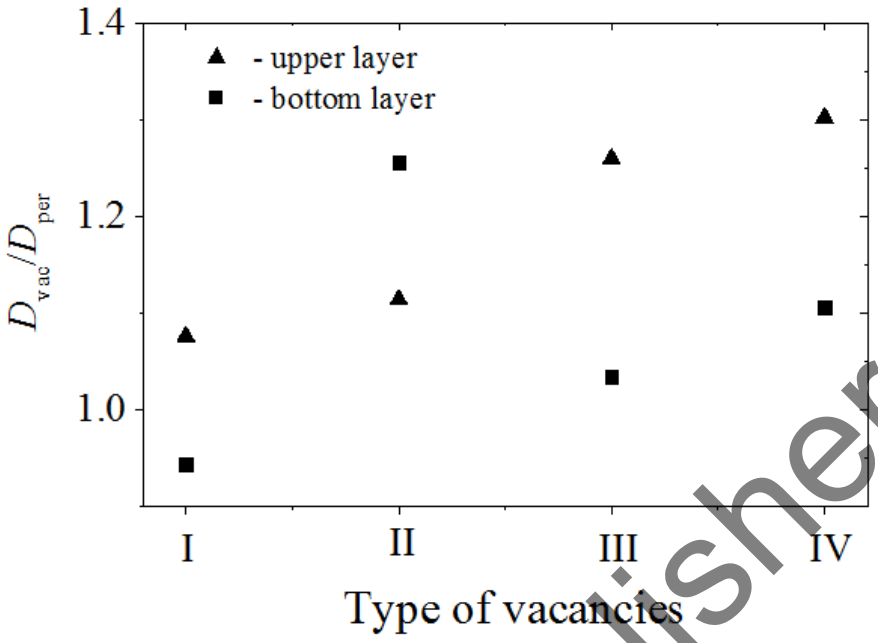

Figure 106. Ratio of the self-diffusion coefficients of Si atoms in the sheets of porous silicene to the corresponding characteristics of the perfect silicene with lithium longitudinal motion in the channel; the numerical designation is similar to that in Figure 103.

The peak mobility for the lower sheet of silicene corresponds to the membrane with bi-vacancies. In this case, the ion passing along the lower membrane transmits to the Si atoms more energy due to frequent collisions with atomic boundaries of bi-vacancy compared to other cases under consideration. The ion "glides" along the surface of this membrane for much shorter time.

In connection with the questions considered here, it is important to know the stresses appearing in the sheets of silicene, between which the lithium ion moves. The average stresses appearing in this process in the plane of the perfect silicene sheets are: σ_{zx}^{per} = 0.22 GPa, σ_{zy}^{per} = 2.38 GPa, and σ_{zz}^{per} = 0.75 GPa. The strongest stress (σ_{zy}^{per}) appears because of the action of the force directed perpendicularly to the electric field strength vector. Figure 107 shows the relative average stresses acting in the defective silicene sheets when lithium ion moves between them. It is seen that, as a rule, the weakest stress (σ_{zx}) in the defective silicene is amplified, but more significant stresses (σ_{zy} and σ_{zz}) are weakened. Such particularly strong decrease is observed for the σ_{zz} stress that is associated with the increase in the freedom of the ion motion in the *z* direction due to the presence of the poly-vacancies.

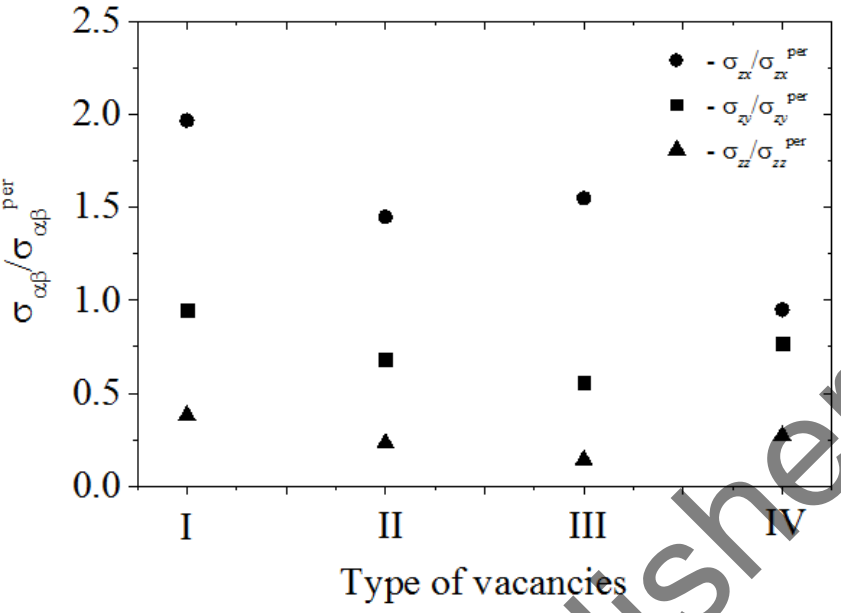

Figure 107. Change of stresses acting in the plane of silicene sheets in the cases of appearance of mono- and poly-vacancies in them; the numerical designation is similar to that in Figure 103.

Silicene is a much less durable material than graphene [412]. Its stability is not high, especially, when silicene has a large number of defects with respect to friction and the lithium ions motion around it under the influence of the electric field. The Li^+ ion motion between the sheets of silicene requires the application of a much stronger electric field 10^5 V/m than the field 10^3 V/m. The latter is needed to move the ion along a flat channel formed by the sheets of graphene [427]. The lithium ions motion is more controlled when they move along the graphene channel than the silicene one, where the ion trajectory covers a large area of the silicene sheet [414]. In the case of silicene, the Li^+ ion inputs easier in a flat channel. However, the ion usually is stuck in the silicene channel even when the channel has a sufficiently large value of h_g and significantly, higher values of the applied electric field are used.

The average stress of the "zig-zag" direction (0.22 GPa) appearing in the perfect silicene does not exceed 5% of the stress limit, which is installed in silicene under uniaxial tension [423]. However, in the presence of the mono-vacancies, this stress achieves 13% of the corresponding stress σ_{zx}. We cannot make such a comparison if there are larger poly-vacancies in silicene because of the lack of data on the ultimate stretching. Note that the σ_{zx} calculated value has some decrease for silicene with poly-vacancies. Stresses σ_{zy} and σ_{zz} initially decrease as defect size increases, but for silicene with hexa-vacancy, they increase. At the same time, the σ_{zx} stress (in the case of the hexa-vacancies presence in silicene) decreases substantially compensating for the increase in the values of σ_{zy} and

σ_{zz}. Redistribution of stresses in silicene containing hexa-vacancies is associated with increasing the symmetry of defects and the change in the role of various Si–Si bonds. The σ_{zy} stress (caused by the action of forces directed parallel to the plane of silicene and perpendicular to the electric field strength vector) is the most significant among the other stress components acting in the plane of the silicene sheet. As expected, the creation of the vacancy defects leads to the strongest decrease in the stress caused by the action of the vertical forces. For all types of defects, the stress in silicene is more than 2 times lower than that for the pristine silicene. Thus, a change in the mechanical properties of the defective silicene is not critical for its use as an anode material.

The passage of lithium ion through a two-layer porous silicene membrane in an electric field was studied. Moreover, the ion forced motion was studied along a flat channel formed by sheets of porous silicene. Mean transit time of the ion through the silicene membrane in the transverse electric field is reduced under increase of the pore size of silicene. Under influence of the longitudinal electric field, the Li^+ ion performs a complicated oscillating motion in the space between silicene membranes and is experiencing difficulty to exit from the gap bounded by the silicene sheets. The simulation showed that bi-vacancies in the silicene are more stable than tri- and hexa-vacancies. They retain their shape under frequent ion strikes onto the boundaries of the pores at much higher values of the *D* coefficient than other poly-vacancies.

The presence of a sufficiently large number of the mono- and bi-vacancies in silicene allows monitoring the charging/discharging process of the electrode. However, coarsening the size of defects, i.e., replacement of the mono- and bi-vacancies by the tri- and hexa-vacancies makes corresponding processes uncontrollable. The σ_{zx} stress caused by the electrostatic force $e\boldsymbol{E}$ is greatly enhanced when the lithium ion moves in the flat channel formed by the defective silicene sheets. There is a redistribution of the stresses existing during the motion of the lithium ion in silicene when the defect symmetry coincides with the symmetry of the two-dimensional structure. The most significant stress is produced by the transverse forces acting parallel to the plane of silicene and perpendicular to the electric field strength vector. The results of the present study may be useful in the development of the silicene anode design for the lithium-ion batteries.

Chapter 8

APPLICATION OF SILICENE ON AG(111) SUBSTRATE AS ANODE OF LITHIUM-ION BATTERIES

8.1. STRUCTURE AND STABILITY OF DEFECTIVE SILICENE ON AG(001) AND AG(111) SUBSTRATES

Defects have often been a dominant factor in the use of two-dimensional materials. Laser radiation or an electron beam can easily create some types of defects, such as vacancies. Their formation is almost inevitable in the manufacturing and processing the mono-layer materials. Sometimes, small defects can be purposefully introduced into materials for specific applications [11, 440]. For example, the creation and elimination of the point defects provide a means to tune the local structure, to change the thermal stability, and to control the band gap of low-dimensional materials [312, 374, 441–442]. It is also well known that two-dimensional materials with defects are excellent membranes for separation of gases [443, 444].

The structure and energetics of point defects in the free-standing silicene was investigated in [25, 374, 442–445]. For example, Ozcelik et al. [442] investigated the atomistic mechanisms of self-healing the vacancy defects and found that in silicene the energy gained during formation of new Si–Si bonds becomes the driving force for the reconstruction. Gao et al. [441] systemically investigated the structure, energy of formation, behavior during the migration, as well as, the electronic and magnetic properties of typical point defects in silicene including single and double vacancies. Vacancy defects formed during local structural changes significantly decrease the silicene thermal stability [445].

Previously performed studies provided a deeper insight into the diffusion of the vacancies in silicene. As a rule, they were focused on the analysis of the mechanisms of formation of the single-, double-, and triple-site defects. Recent experimental studies have revealed that a large number of defects in the form of clusters with more than three missing

silicon atoms are observed in scanning tunneling microscopy images [25]. Although the investigation of many-atomic vacancies is of fundamental importance for understanding the formation and operation of layered materials, the mechanisms of their nucleation are far from being fully understood. This problem was solved by Li et al. [446] using the method of calculation within the framework of the density functional theory with emphasis on studying the reconstruction, coalescence, and diffusion of vacancy defects in the free-standing silicene. These authors also investigated the adsorption and diffusion of silicon atoms on the silicene layers and found that such adsorption process can enhance the stability of the system and open a significant part of band gaps in silicene. Until now, there have been no studies carried out on the stability of the defective silicene on substrates. Nevertheless, namely those substrates, on which silicene can be obtained experimentally, are of particular interest.

It seems to be promising to change the electronic structure of silicene by the creation of defects in it. Vacancies or multi-vacancies can be created in silicene by means of the ion bombardment. The uncompensated bonds of silicon atoms located at the edges of vacancies (multi-vacancies) attract electric charges; thereby change the electronic properties of silicene. Negative charges retained at the edges of vacancies lead to the formation of the *n*-type regions, whereas positive charges near these defects form the *p*-type regions. It is possible to form the *p*- and *n*- type transitions on the same silicene sheet, having both negative and positive charges at the edges of vacancies. The number of electric charges on each defect can be controlled by varying the size of multi-vacancies, for example, by changing over from the mono-, bi-, and tri-vacancies to hexa-vacancies.

If the silicene cannot exist as an independent phase, application of this material in practice is possible only together with the substrate supporting it. One of the most important directions in the practical application of silicene is that it has been used as an anode for the lithium-ion batteries. This is associated with the high theoretical lithium capacity of silicon (6 lithium atoms per silicon atom), the relatively small change of the volume (13% and 24% for the single- and two-layer silicene sheets, respectively) during the lithiation of silicene, and the complete reconstruction of its structure because of delithiation [447].

Here, we consider the stability of a two-layer silicene saturated with mono-, bi-, tri-, or hexa-vacancies on the Ag(001) and Ag(111) substrates in absence of electric charges at the vacancy edges [448]. We also investigate the Li^+ ion motion between the silicene sheets with this type of defects in the direct-current electric field.

The model and the main interactions in the system were similar to those described in Section 7.5. The Morse potential was used to describe the interaction between the silicon and silver atoms [429, 449], and the interaction between the Li^+ ion and Ag atoms [52, 431]. The Morse potential used for the representation of these interactions is shown in Figure 108. We used the single cutoff radius of interactions r_{cut} = 0.5 nm. Taking into account the cutoff radius of interactions, each silicon atom could interact with silver atoms

from no more than two surface layers with the distance between the silicene sheet and the substrate $r_{\text{Ag-Si}}$ = 0.27 nm [432].

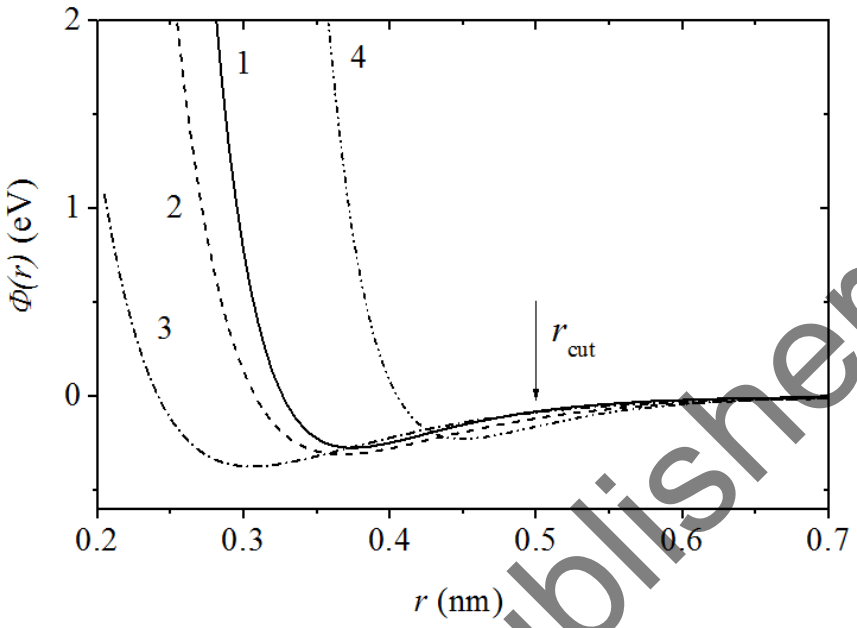

Figure 108. The Morse potential describing the interactions (1) Ag–Si, (2) Li–Si, (3) Li–Ag, and (4) Si–Si between the silicene layers.

The model under consideration implies the 4 × 4 surface reconstruction. The unit cell of this rhomb-shaped silicene structure contains 18 Si atoms. Six Si atoms of the unit cell are displaced by 0.074 nm normally to the surface. Other Si atoms are on the same (initial) plane. The initial structure of the silicene sheet was close to the silicene surface observed on the Ag(111) substrate [432]. If the Si atoms protruding above the initial surface in the upper sheet of the bi-layer silicene are displaced upward, such atoms in the lower sheet are displaced downward. We performed a number of calculations for choosing the optimum distance h_g between the silicene sheets. According to calculations within the framework of the density functional theory, the gap h_g between the two-layer silicene sheets with the AB packing amounts to 0.2481 nm [433]. In the case of the longitudinal displacement of the Li^+ ion, we used the values of h_g = 0.75, 0.80, and 0.85 nm.

Nine defects of the same type were created approximately uniformly. Wherein for different sheets in silicone a displacement by 1 – 2 nm in each direction (x and y) was performed. The two-layer silicene was located on the unreconstructed Ag(001) and Ag(111) surfaces of the fcc silver crystals. The silver atoms were 3.84 times heavier than the silicon ones. Consequently, the velocities acquired by silver atoms in collisions with silicon atoms had to be lower by the factor of 3.84.

Therefore, with good accuracy in calculations, we restricted ourselves to an approximation of the interaction, but not the motion of the silver atoms. In a number of molecular dynamics calculations, the minimum value of the electric field strength was chosen. Therefore, starting from this value, the lithium ion could pass through the entire graphene channel in the direction of the applied electric field and leave it through the imaginary back surface. This condition is satisfied under the electric field strength 10^6 V/m. Such an electric field cannot have a significant effect on the parameters of the electron orbits of atoms and, consequently, cannot introduce changes in the widely used potentials of the inter-atomic interaction.

In the case of the gaps h_g = 0.75 and 0.80 nm, the Li^+ ion was always stuck in the channel formed by the defective silicene. The Li^+ ion did not leave the silicene channels containing bi-vacancies for the gap h_g = 0.85 nm during the entire calculation. In the other cases with this gap, the lithium ion passed through the silicene channels located on the substrates of both types for the time interval 7 – 38 ps. During this motion, the absolute velocity of the lithium ion u_{abs} was, on the average, equal to 3.59×10^{-4} cm^2 V^{-1} s^{-1} on the Ag(001) substrate and 3.51×10^{-4} cm^2 V^{-1} s^{-1} on the Ag(111) one. In an aqueous solution at the temperature of 298 K, the Li^+ ion has, on the average, the absolute velocity u_{abs} = 3.88×10^{-4} cm^2 V^{-1} s^{-1}. In all the cases under consideration, the lithium ion motion had a diffusive character. The ballistic character of this ion motion could be observed for the gaps h_g > 1 nm.

The general view of the system "two-layer silicene with bi-vacancies on the Ag(001) substrate" after 4 000 000 time steps (400 ps) is shown in Figure 109. It is seen that, during the calculation, the significant vertical displacements of silicon atoms occur both in the top and bottom silicene sheets. It is worthy to note that, under changing from silicene with mono-vacancies to silicene with hexa-vacancies, the magnitude of the displacements increases. The similar picture is observed for the system with the Ag(111) substrate. For both substrates, there are rearrangements of silicon atoms in the planes of the top and bottom silicene sheets.

A schematic of the trajectory of the Li^+ ion motion through the channel [450] is shown in Figure 110 for (a) ideal silicene and (b) silicene filled with mono-vacancies. The gap value is 0.75 nm. Points 1 and 2 correspond to the places where the Li^+ ion enters the channel and exits it. When the silicene sheets forming the channel are perfect, the transportation of the ion moving horizontally under the action of a field occurs almost rectilinearly, and the Li^+ ion easily passes through the channel (Figure 110a). With mono-vacancies in the silicene, the trajectory of the ion in the channel is crooked, and the Li^+ tends to exit the channel through the vacancies (Figure 110b).

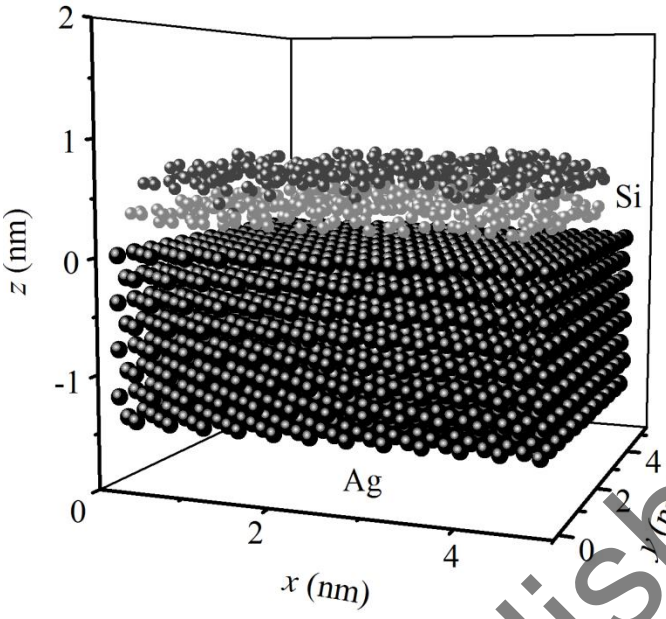

Figure 109. The configuration of the "two-layer silicene on the Ag(001) substrate" system obtained at the instant 400 ps.

Two coordination spheres limited determination region of the radial distribution function. The radial distribution function (RDF) of each defective silicene sheet (irrespective to the substrate type) has a lower intensity of the peaks reflecting the presence of the nearest neighbors and next-to-nearest neighbors as compared to the corresponding RDF for perfect silicene (Figure 111). The calculated RDFs were obtained by averaging over the last four-time intervals with the duration of 100 ps, i.e., over the period accounting for 1/4 of the total molecular dynamics calculation. For comparison with the RDF of the perfect silicene on the Ag(001) substrate, Figure 111a shows the function $g(r)_{\mathrm{Si-Si}}$ obtained for the planar model of the free-standing silicene [451]. The Lennard-Jones potential parameters were fitted from the molecular dynamics simulation data with the Stillinger–Weber potential function [452].

The density of the "planar" silicene is 24% higher than the density of the perfect silicene simulated on the Ag(001) substrate in our study. The molecular dynamics simulation has demonstrated that the positions of the first peaks of these functions are very close to each other. But the position of the second peak of the radial distribution function of the planar silicene is shifted by 2.5% toward the short distances. Figure 111b shows the RDF of the bottom silicene sheet with tri-vacancies on the Ag(001) substrate. The second peak of function $g(r)$ of the perfect silicene has a "shoulder" on the right, which is smeared for the RDF of the defective silicene. Formation of the shoulder and a significant broadening of the peaks indicate substantial vertical displacements of silicon atoms in the model.

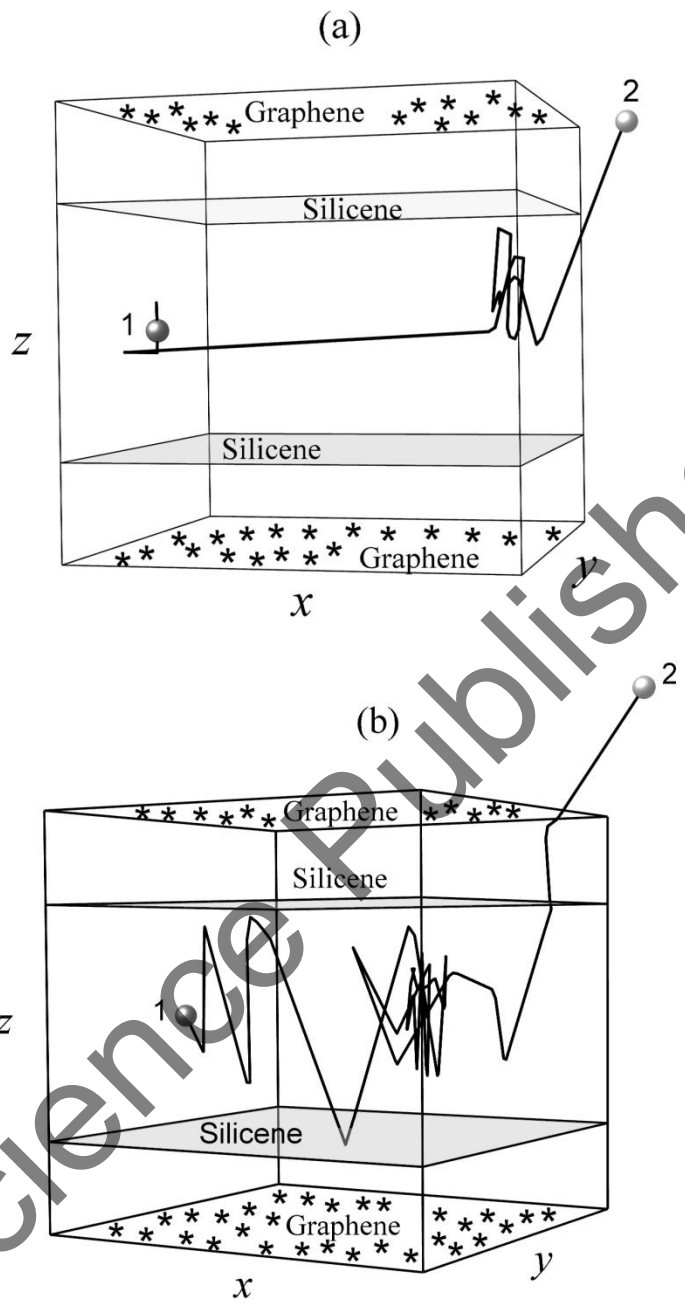

Figure 110. Trajectory of the Li^+ ion motion in the graphene–silicene channel: (a) defect-free silicene, (b) silicene sheets filled with mono-vacancies; the gap value is 0.75 nm.

We introduce the following notation for the systems under investigation: I defect-free silicene, II silicene with mono-vacancies, III silicene with bi-vacancies, IV silicene with tri-vacancies, and V silicene with hexa-vacancies. The relative decrease in intensity of the first peak of RDF $\delta_g = \left(g_1^{\mathrm{I}} - g_1^{j}\right) / g_1^{\mathrm{I}}$ (where 1 is the number of the peak and *j* denotes the

system) increases slowly under changing over from the silicene with mono-vacancies to silicene with bi-vacancies and tri-vacancies and increases fast for the silicene sheets with hexa-vacancies (see insert in Figure 111b). The similar characteristic for the intensity of the second peak of this function behaves in the opposite way: it decreases monotonically upon changing over from the systems with mono-vacancies to silicene with hexa-vacancies.

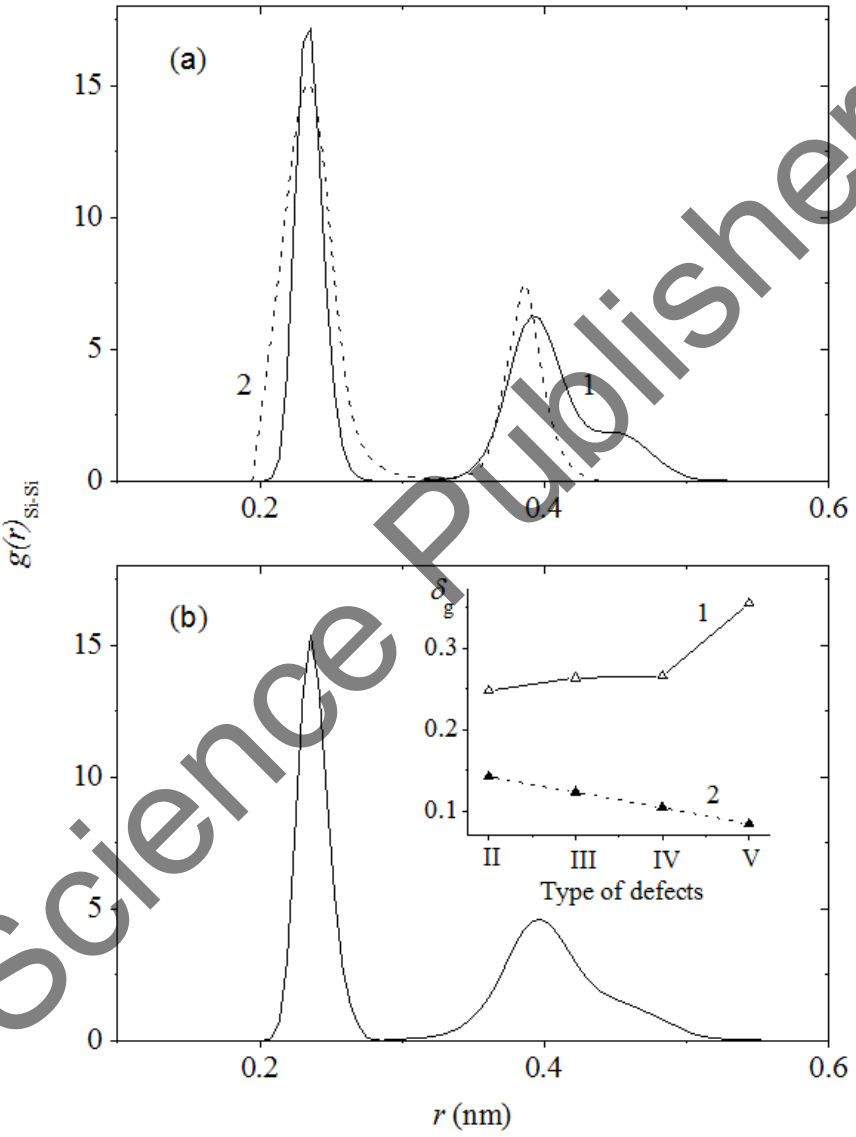

Figure 111. The radial distribution functions: (a) (1) perfect silicene on the Ag(001) substrate (averaged over the silicone sheets), (2) free-standing planar silicene [451], and (b) silicene with tri-vacancies on the Ag(001) substrate; the inset shows the characteristics of decreasing intensity of (1) the first peak and (2) the second peak of the radial distribution function.

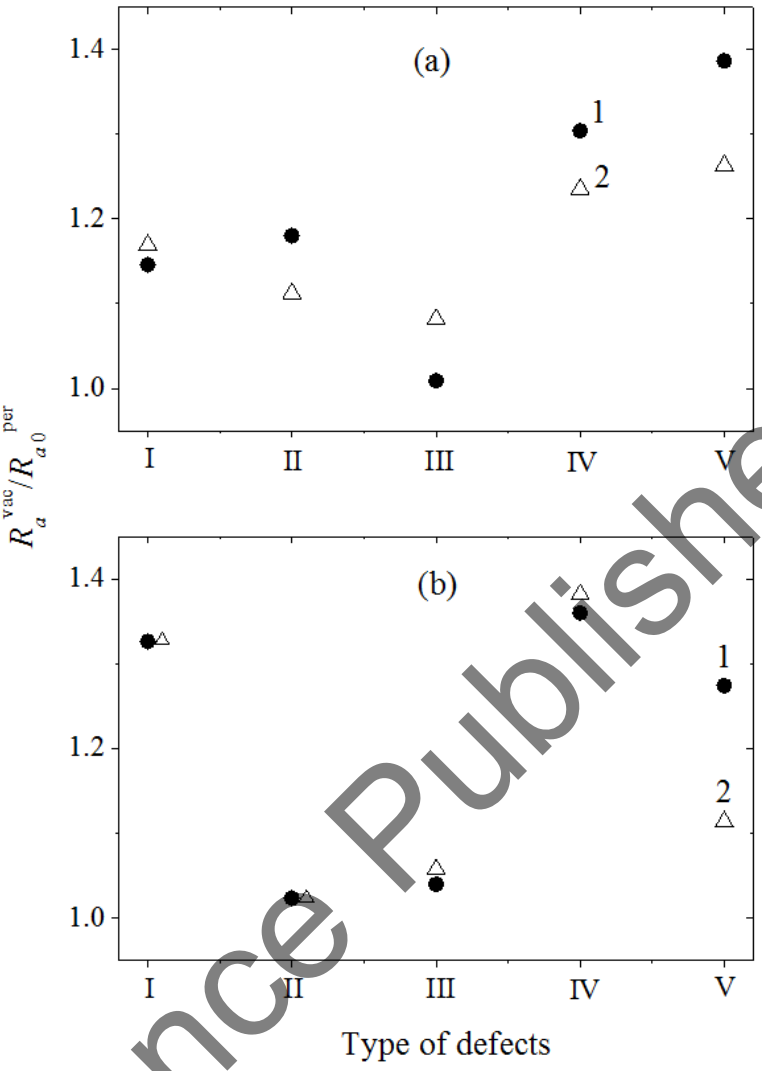

Figure 112. Relative roughnesses of (1) bottom defective silicene sheet, and (2) top defective silicene sheet on the (a) Ag(001) and (b) Ag(111) substrates.

The relative roughness R_a^{vac} / R_{a0}^{per} of the defective silicene sheets with different types of vacancies is shown in Figure 112. The roughness of the defect-free silicene at the initial state is denoted by R_{a0}^{per}. The data obtained for the systems with the Ag(001) substrate are presented in Figure 112a, and the results for the systems with the Ag(111) substrate are demonstrated in Figure 112b. It is seen from the figures that in all the cases under consideration, the roughness of the defective silicene rises above the level of the initial roughness of the perfect silicene ($R_a^{vac} / R_{a0}^{per} > 1$). It should be noted that due to the atomic interactions and appearance of corrugation, the roughness of the perfect graphene also

increases slightly. Moreover, the roughness of the perfect silicene on the Ag(001) substrate is lower than that on the Ag(111) one.

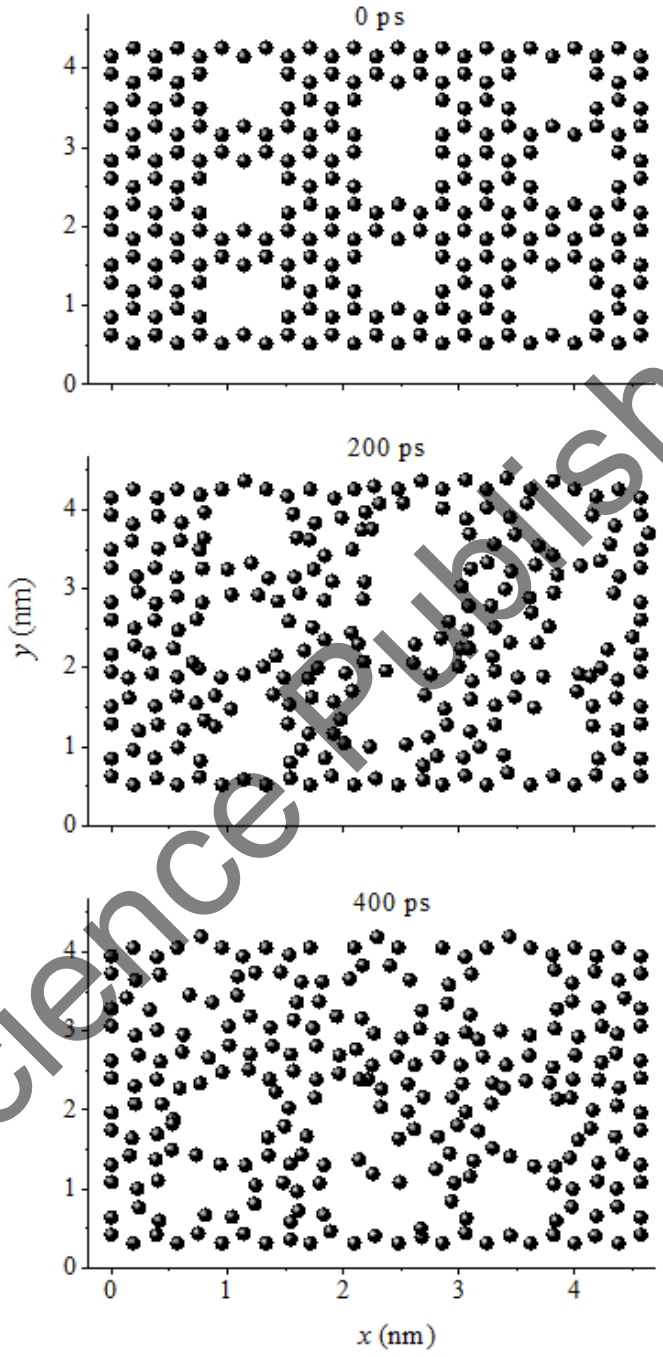

Figure 113. Dynamics of the hexa-vacancies collapse in the bottom silicene sheet supported by the Ag(111) substrate.

In the tests with the Ag(001) substrate, the roughness of the top silicene sheet, as a rule, is lower than the roughness R_a of the bottom silicene sheet, except for the silicene sheet with bi-vacancies. In the case of the Ag(111) substrate, the roughness of the defective silicene sheets are approximately equal to each other, and only for defective silicene with hexa-vacancies, the bottom sheet is characterized by a higher value of R_a. Thus, on each of the silicene sheets regardless of the type of silver substrate, the tri-vacancies and hexa-vacancies lead to a larger roughness as compared to mono-vacancies and bi-vacancies.

Dynamics of distraction the hexa-vacancies in the bottom silicene sheet is illustrated in Figure 113. At the initial instant, this bottom sheet of silicene contained seven single hexa-vacancies and two bound vacancies of the same type. For 200 ps on this sheet of silicene, two doubled multi-vacancies and seven single vacancies of different types were formed. For 400 ps two vacancy clusters were formed on the top and bottom parts of the sheet under consideration. Each of the clusters combined eight large and small vacancies of different types. The similar structural rearrangements occurred in both the bottom and top silicene sheets in the presence of vacancies of different types. Generally, we observed the fragmentation of multi-vacancies into smaller ones and their subsequent coalescence into vacancy clusters.

The average internal energies $U_{\text{Si-Si}}$ obtained for silicene sheets in each of the systems are shown in Figure 114. Figure 114a presents the results obtained for the systems with the Ag(001) substrate, and Figure 114b illustrates the systems energies with the Ag(111) substrate. In both cases, there is the tendency toward an increase in the internal energy $U_{\text{Si-Si}}$ as the vacancies size increases in the silicene sheets. The main difference in the behavior of the energies $U_{\text{Si-Si}}$ of the systems with substrates of different types lies in the fact that this characteristic for the silicene with bi-vacancies on the Ag(001) substrate has a very low value. This value is even less than the internal energy $U_{\text{Si-Si}}$ of silicene with mono-vacancies on the identical substrate. The energies of the perfect silicene and the silicene with mono- and bi-vacancies on the Ag(001) substrate are lower than the corresponding value for silicene on the Ag(111) substrate.

However, in the presence of the tri- and hexa-vacancies in the silicene sheet, the ratio between the energies changes to the opposite one. For comparison, Figure 114b shows the estimated value of the cohesion energy of an endless silicene band that does not have a substrate [448]. This value is significantly higher than the internal energies $U_{\text{Si-Si}}$ obtained in our study for the perfect silicene on both the Ag(001) and the Ag(111) substrates. It should also be noted that the values of $U_{\text{Si-Si}}$ considered here for silicene are substantially higher than the experimental value of the energy obtained for diamond-like silicon (– 4.63 eV/atom).

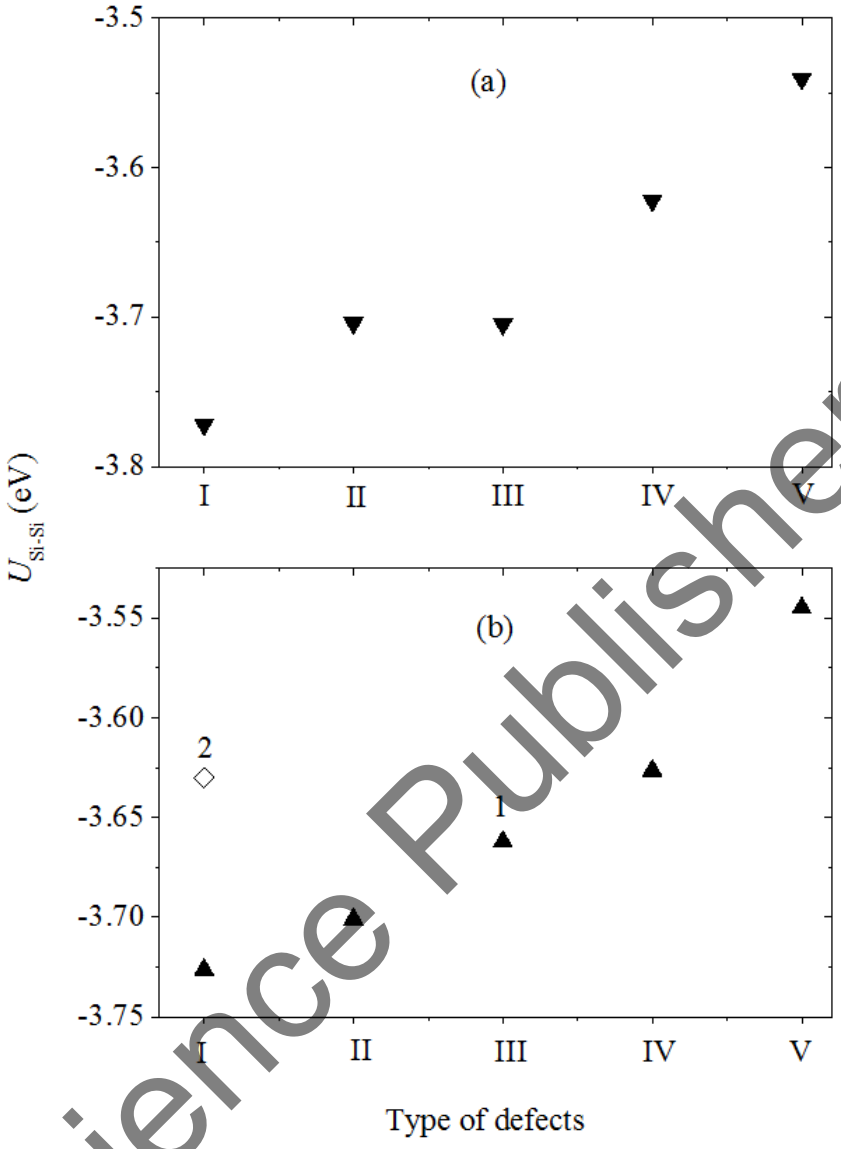

Figure 114. Average internal energy *E* of silicene sheets on the (a) Ag(001), and (b) Ag(111) substrates in the absence of defect for systems (I): (1) silicene and (2) silicene band, and in the presence of the defects: (II) mono-, (III) bi-, (IV) tri-, and (V) hexa-vacancies.

The presence of the Li^+ ion in the silicene channel leads to a gradual destruction of the silicene honeycomb structure. This especially occurs in the silicene with multi-vacancies. Figure 115 shows the distribution of stresses along the length of the channel with the gap of 0.75 nm in the bottom silicene sheet containing hexa-vacancies and located on the Ag(111) surface. The patterns of stress distributions in the top and bottom sheets of silicene in all the cases under consideration are similar to each other. It is in the presence of hexa-

vacancies in the silicene sheets where the strongest local stress σ_{zy} was obtained in calculations with the gap of 0.75 nm.

The observed surges of the stress closer to the middle part of the length of the silicene sheets are caused by the presence of the lithium ions in these regions of the channel. It is worthy to note that the stresses σ_{zz} caused by the vertical forces, as a rule, are considerably less than the stresses σ_{zx} and σ_{zy} induced by the horizontal forces.

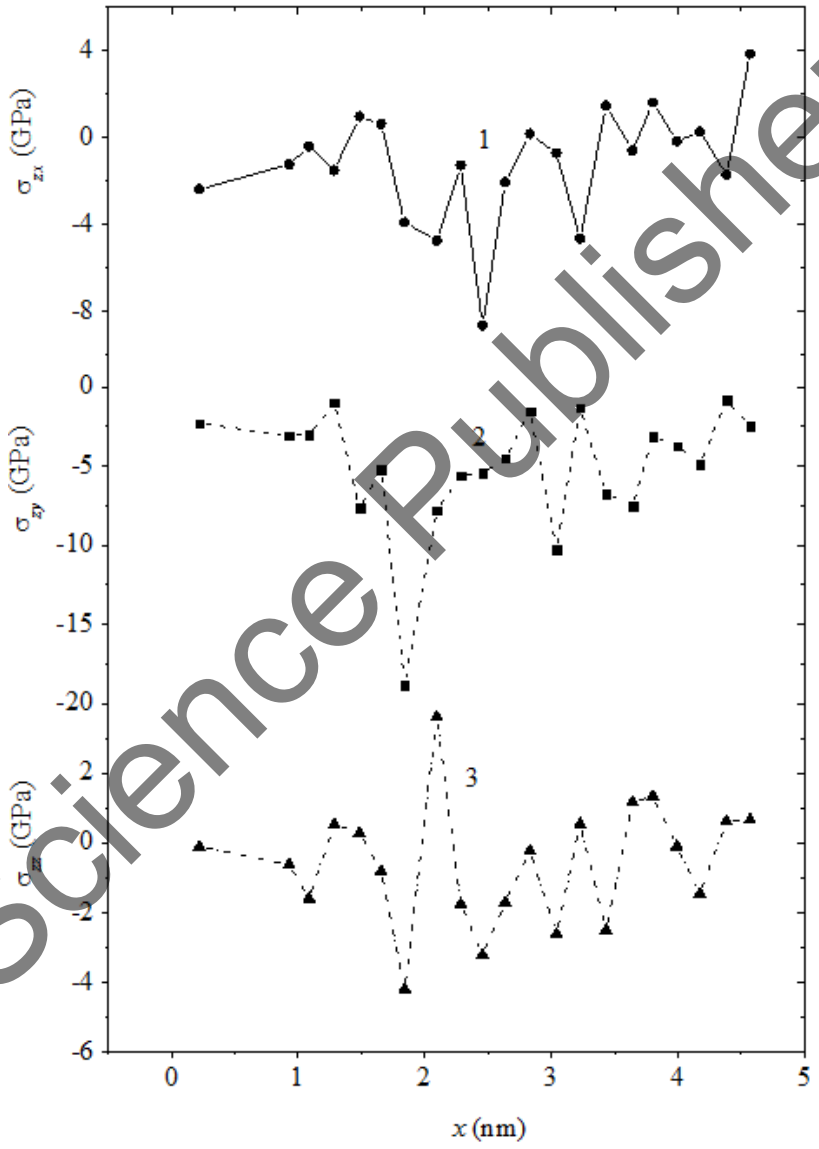

Figure 115. Distribution of stresses (1) σ_{zx}, (2) σ_{zy}, and (3) σ_{zz} acting in the plane of the bottom silicene sheet containing hexa-vacancies and located on the Ag(111) substrate when the Li^+ ion moves in a planar silicene channel under the influence of the electrostatic field.

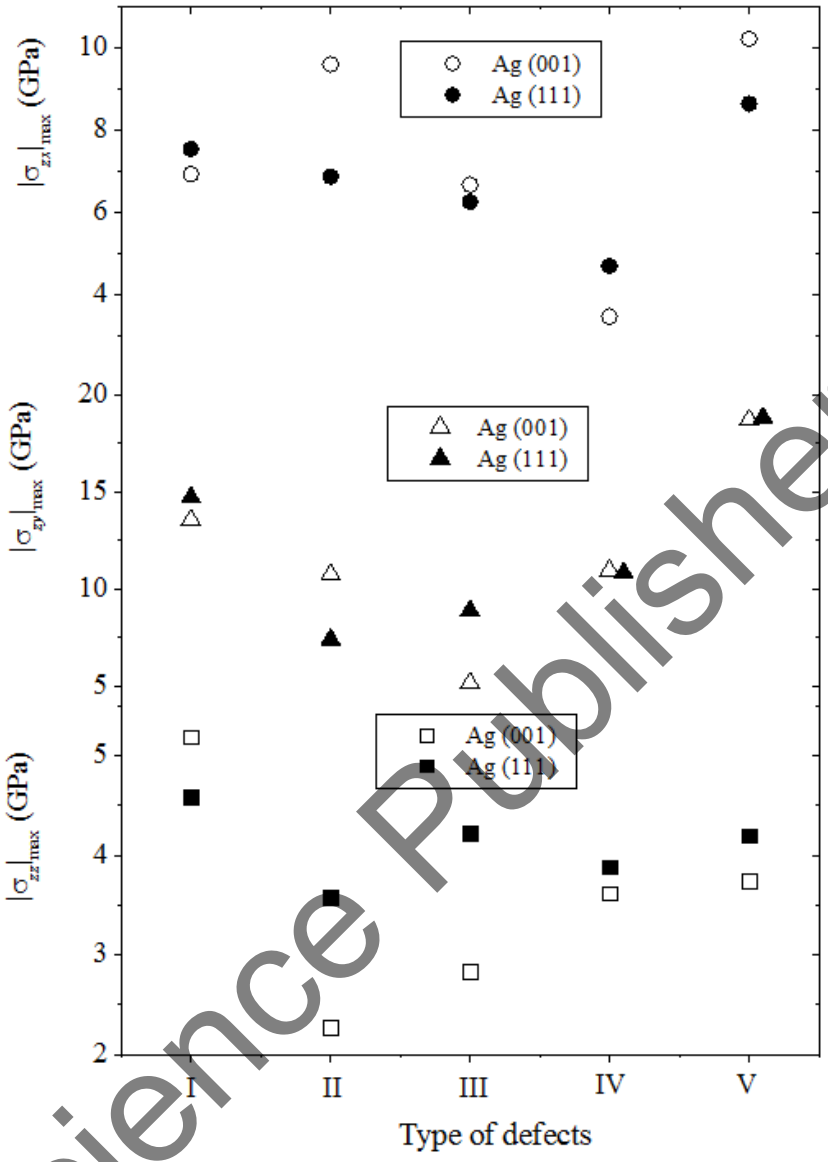

Figure 116. Maximum absolute values of the local stresses in the bottom silicene sheets located on the Ag(001) and Ag(111) substrates when the Li^+ ion moves in the planar silicene channel under the influence of the electrostatic field: (I) defect-free silicene sheets and (II–V) silicene sheets with (II) mono-, (III) bi-, (IV) tri-, and (V) hexa-vacancies.

The maximum absolute values of the stresses are shown in Figure 116. The values are obtained as averages over the time macro step (10 ps) for all the silicene channels under investigation. It is seen that the orientation of the substrate surface has a more expressed influence on the value of $|\sigma_{zz}|_{max}$, especially, in the presence of the mono- and bi-vacancies in the silicene sheets. The highest value of $|\sigma_{zz}|_{max}$ is reached in the perfect silicene on the

Ag(001) substrate. The maximum absolute value of $|\sigma_{zx}|$ is also reached on the same substrate in the presence of the hexa-vacancies in silicene sheets. Moreover, the presence of hexa-vacancies in the silicene sheets is characterized by the maximum value of $|\sigma_{zy}|$ (which is approximately the same for both substrates). The external action is transmitted by the Li^+ ion to the silicene sheet when the electrostatic force acts along the *x* axis. However, the maximum stresses appear in the silicene sheet due to the forces acting in the perpendicular direction (along the *y* axis) and leading to its compression. The strained two-layer silicene has the positive Poisson ratio.

The VDD method is necessary to compute the atomic charge distribution of a molecule. There is no need to measure the amount of charge Q_A associated with a particular atom A, because Q_A directly monitors how much charge flows due to chemical interactions out of ($Q_A > 0$) or into ($Q_A < 0$) the Voronoi cell of the atom A. The lithium ion location in the flat channel formed by silicene sheets is associated with the transfer of part of the charge from the ion to the surrounding Si atoms. Figure 117 shows the local configuration of the system "perfect silicene on the substrate Ag (001)", which is separated by the sphere of radius 0.65 nm centered around the Li^+ ion location at the instant when the ion is near the middle of the silicene sheets. In addition to the Li^+ ion, 16 Si atoms entered the sphere. Moreover, 14 of them belong to the lower sheet of silicene, to which the lithium ion was attracted, and 2 atoms were caught from the top sheet.

The numbers in Figure 117 point to the charges assigned to particles in absence of the ion (Figure 117a) and in its presence (Figure 117b). At the instant, for which the figure is calculated, the lithium ion lost 8.3% of its charge that passed to the surrounding Si atoms. In this case, the charge redistribution touched all the atoms in the selected region. Under the influence of the ion, the charges of most of the Si atoms have become more positive, but there are also atoms, whose charge has become more negative. Atoms of the upper sheet weakly bound to the atoms of the lower sheet of silicene reduced their negative charge under influence of the Li^+ ion. The presence of defects in the silicene sheets, as a rule, leads to an increase in the number of Si atoms near the Li^+ ion. For example, when defects are hexa-vacancies, the number of Si atoms entering the sphere of radius 0.65 nm around the ion increases to 27. Increasing the number of Si atoms in the sphere is due to the attraction of the regions of both sheets nearest to the ion. This is caused by weakening the bonds between atoms Si in the defective silicene. The approach of the Si atoms to the ion leads to an increase in the transfer of the ion charge to the Si atoms. In the presence of the hexa-vacancies in the silicene sheets, the lithium ion transfers for Si atoms 81.5% of its original charge at the given time. The residual charge of the lithium ion becomes comparable with the charge of the individual Si atoms. The nature of charge redistribution (caused by the presence of the lithium ion in both cases of defective and perfect silicene) is the same type.

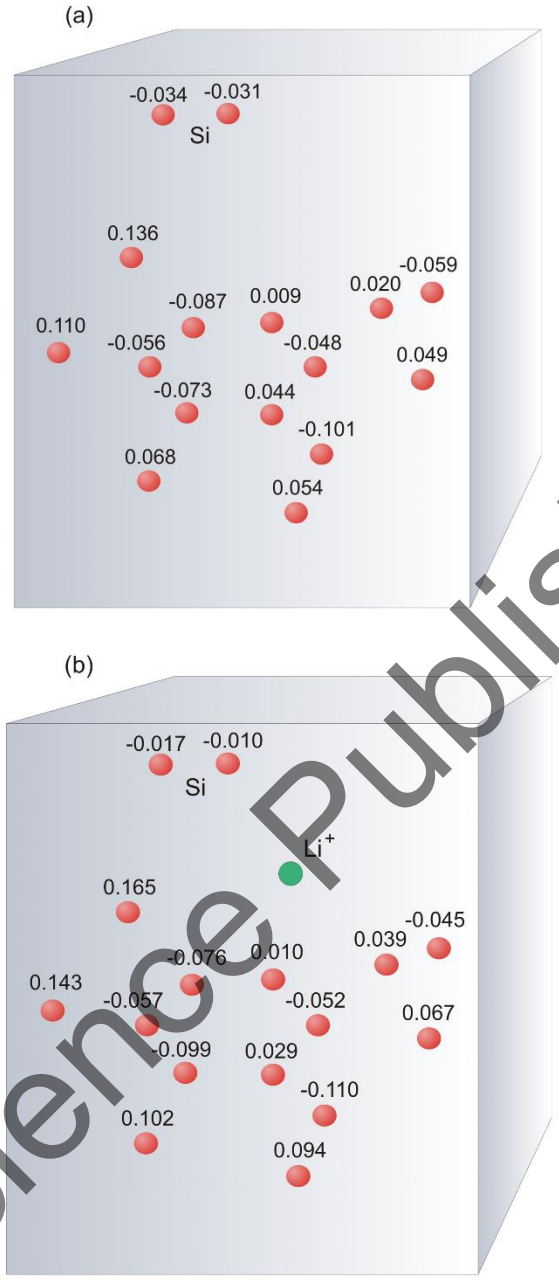

Figure 117. The VDD charge distribution in the spherical neighborhood (R = 0.65 nm) of the lithium ion location point under: (a) absence and (b) presence of the Li^+ ion at this point; the point is closest to the midpoint of both perfect silicene sheets; the numbers near the depicted atoms indicate the magnitude of their charges.

The silver substrate has a significant effect on the stability of the two-layer silicene sheets, especially, in the cases where the silicene contains vacancies and multi-vacancies. It is of interest to compare the behavior of silicene contacting the metal with the

corresponding behavior of graphene. It is obvious that, as in the interaction of graphene with a metallic surface (for example, copper), the influence of a close contact between the materials should be mutual. In the case of the copper/graphene contact, the metal film is subjected to considerable stresses, the greatest of which are σ_{xx}, σ_{xy}, and σ_{yy} [269]. In graphene, relaxation of the stresses is much slower than in the metal [312]. The components of the stress tensor of the copper film (that reflect the action of forces on the horizontal pad) have a fundamentally different behavior in the cases where the film is located on the single- or two-layer graphene [281].

If you want to remove the copper film from graphene, then, for this purpose, it is advisable to use a cluster argon beam directed parallel to the plane of the graphene sheet [193]. In this case, the destructive effect on graphene will be minimal. Depending on the field of application, it is necessary to choose one or another technology for the production of nanomaterials [453]. The identification of structural defects becomes more reliable with increasing density of free bonds [454]. The diffusion considered as the processes of formation, interaction, and migration of defects can occur according to the type of relay-race transfer of the free bonds.

Stability of the system, in which there is no chemisorption of silicon atoms on the silver surface, is very low. The tendency toward the sp^3-hybridization creates a prerequisite for displacement of the silicon atoms of multilayer silicene in the direction perpendicular to the plane of the material. The results obtained in this study have demonstrated that the silicene sheets weakened by the presence of the vacancy-type defects initially are deformed due to the vertical displacements of the silicon atoms. This is facilitated by the Li^+ ion interaction with the silicon atoms. Moreover, the Si–Si bonds are further weakened, and a gradual destruction of point defects begins to occur. Small defects, namely, mono-vacancies can be healed with the formation of new rings consisting of silicon atoms, as a rule, with an odd number of links. Large multi-vacancies change in their shape and size, thus, provoking a change in the structure of the entire graphene sheet where the honeycomb structure transforms into an amorphous one.

The perfect two-layer silicene on the Ag(001) substrate has a lower energy as compared to its analogue on the Ag(111) one. The creation of a large number of tri- or hexa-vacancies in the silicene can lead to the inverse relationship between the energies of silicene on these substrates. The structural rearrangements occurring in the two-dimensional system do not substantially affect the form of the radial distribution function of the silicene. The influence of substrates primarily manifests itself in the enhancement of the vertical displacements of the silicon atoms. However, expansion of the gap between the silicene sheets and the motion of a Li^+ ion between them in the presence of an external electric field also significantly change the horizontal projection of the two-dimensional structure of silicene.

The energy characteristics of silicene on the Ag(001) and Ag(111) substrates differ only slightly from each other with the exception of the system with bi-vacancies, for which

the Ag(001) substrate is more preferable. The Li^+ ion motion between the silicene sheets is associated with the strong local fluctuations of the stresses acting in the plane of the silicene sheets. Moreover, in the majority of cases, the stresses generated in the perfect silicene dominate over the corresponding stresses in a defective silicene. The main exception in this pattern is the defective silicene with hexa-vacancies, which is characterized by the most significant stresses σ_{zy} on both types of substrates. Investigation of the charge transfer from the Li^+ ion to Si atoms showed that the larger the size of the poly-vacancies, the more charge can be transmitted to Si atoms during the ion motion along the channel.

It is easier to control the Li^+ ion motion under the influence of an electric field in the planar channel formed from a free-standing silicene than in a two-layer silicene sheet located on the Ag(001) or Ag(111) substrates. In this case, the vacancy-type defects are also better preserved in the silicene.

8.2. Computer Study of Atomic Mechanisms of Intercalation/Deintercalation of Li Ions in a Silicene Anode on Ag(111) Substrate

Silicene anodes can be constructed only in the presence of a substrate. The simplest way is to make an anode on the same substrate, on which the silicene was obtained. The main substrates for production of the silicene are still silver ones, and the silicene sheets are obtained on the Ag(111) substrate. Thus, as the object of investigation, we chose a two-layer silicene, which is located on the Ag(111) substrate.

The silicon enables long life and high-energy storage resulting in a significantly longer lasting battery. If in the anode structure under consideration during charging the lithium ions fit into the gaps between the silicene sheets, the process known as intercalation. Penetrating into the anode, the Li^+ ion quickly acquires an electron and becomes a neutral atom. In the course of the reverse process (deintercalation), the Li atoms discharge electrons and in the form of ions rush to the cathode.

The vast majority of available lithium-ion batteries consist of two electrodes connected by a liquid electrolyte. This electrolyte makes it difficult to reduce the size and weight of the battery. Additionally, the electrolyte is subjected to leakage; so, the lithium in the exposed electrodes then encounters with oxygen in the air and undergoes self-ignition. Optimization of the liquid electrolyte composition to extend the LIB life remains challenging. The LiPON (lithium phosphorus oxynitride) is an amorphous glassy material that can be used as an electrolyte material in thin film lithium-ion batteries.

In this section, we present results of the study of processes of intercalation and deintercalation of lithium ions occurring in a plane silicene channel. Moreover, we describe the determination of the kinetic properties of Li ions and atoms in the channel and

investigation of the effect of the defects on the stress distribution in the lithiated silicene sheets on the Ag(111) substrate.

Lithium ions are efficiently transferred and electronically isolated in a lithium-ion battery. The scheme of a typical lithium-ion battery with liquid electrolyte is shown in Figure 118. To improve the battery, the liquid solvent and polymer separator should be replaced by the solid electrolyte. When using silicene on the metal substrate as an anode material, the metal part of this structure should not directly connect to an external electrical circuit. The contact with the circuit must be carried out only through the silicene. In addition, the metal substrate must be isolated from the electrolyte. Metal (in this case, Ag) is present only because silicene cannot be separated from it. Although the presence of the Ag substrate can increase the electron transfer rate to Li^+ from the silicene. In the lithium-ion batteries, capacity fade occurs over thousands of cycles limited by slow electrochemical processes, such as the formation of the solid-electrolyte interphase (SEI) in the negative electrode, which compete with reversible lithium intercalation. The fast degradation is often the limiting factor in developing new electrode materials but practical Li-ion batteries necessarily exhibit slow degradation over hundreds or thousands of cycles.

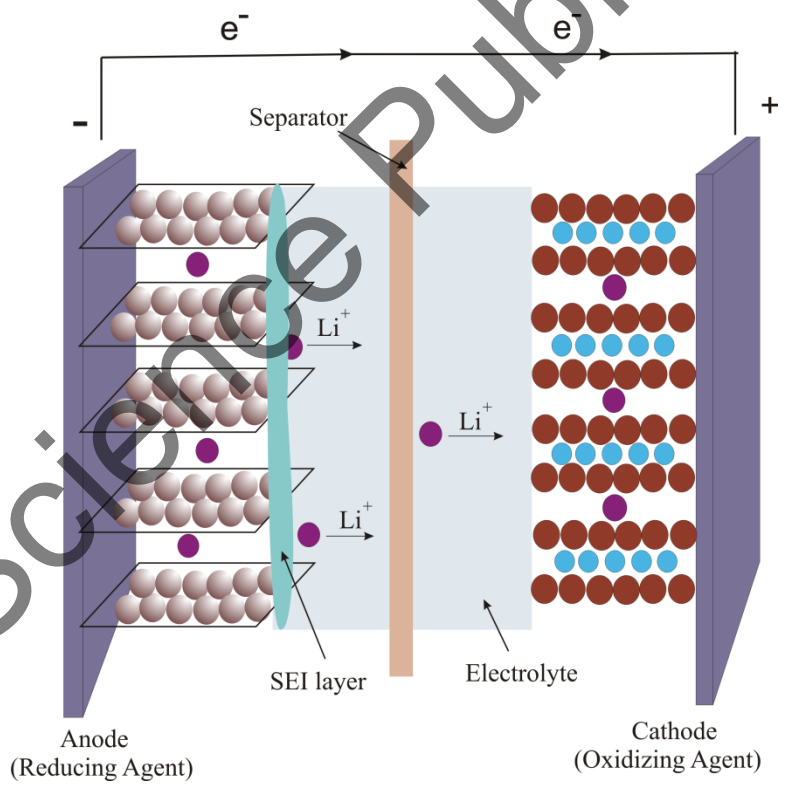

Figure 118. Schematic of a typical state-of-art of the lithium-ion battery.

Such slow capacity fading usually arises from irreversible electrochemical processes. Initially, the SEI formation protects the electrode against solvent decomposition at large negative voltage, but over time, it leads to a gradual capacity fade as the SEI layer thickens. However, the formation of the SEI is not the only problem when finding new anode materials for LIB. It is very important to know how thin-film silicon materials on substrates will behave themselves when intercalating with lithium. Theoretical understanding of the processes occurring at the anode will assist the design of high-performance batteries. The model used in the theoretical analysis should be as simple as it can be without neglecting important effects.

The interaction potentials and overall dimensions of the system, as well as, number and type of defects are described in Section 8.1. Atoms of the substrate were immobile. The Ag-Ag interaction was not considered in the model. The electric field acted only on the Li^+ ions that have the electric charge $1e$, where e is the elementary electric charge. The Coulomb interaction acted between two lithium ions when they were introduced into the channel or were removed from it by pairs. When two ions are introduced into the channel simultaneously, the distance between them was not less than 1 nm. In this case, the interaction energy between two-point elementary charges was not more than 1.44 eV.

The work on moving an elementary point charge over the distance of 1 nm along the field force line exceeded this value by more than 2.5 times and was equal to 3.69 eV. The binding energy of lithium with the silicene is ~ 2.2 eV per Li atom and shows small variation with respect to the Li content, while the barriers for Li diffusion are relatively low typically less than 0.6 eV [427]. The results of the molecular dynamics simulation performed with the selected potentials indicate the adequacy of the model used [427, 436, 448]. The height of the silicene buckle Δh and the Si−Si bond-length $\bar{L}$ can vary for various reasons. For example, the reasons may be: the interaction with the substrate, the presence of the defects (especially large ones) in silicene, the silicene interaction with adatoms and metal ions, etc. In the present simulation of lithium adsorption on silicene, the value of Δh increases from 0.64 (for perfect silicene) to 1.44 Å (for silicene with tri-vacancies) and the value of $\bar{L}$ changes from 2.30 to 2.44 Å. These values of $\bar{L}$ agree well with the values of the average Si-Si bond length for Si_{400} nanoparticles in the vitrified (0.242 nm) and an amorphous state (0.236 nm) [453]. The calculated adsorption energy for the lithiated silicene ranges from 2.27 to 2.52 eV/Li (depending on the location of the Li atom). The average length of the Si–Li bond is 0.265 nm, which agrees well with the data from [455].

The electric field strength directed along the *x* axis during intercalation of Li^+ ions was 10^3 V/m. About such electric field strength is achieved by using the LiPON film with the thickness of ~ 30 microns as a solid electrolyte to create the working voltage of 1.5 V in the LIB [456]. To observe the similar effect in a silicene channel having the length 4.7 nm, it was necessary to increase the gap width to 0.75 nm and the electric field to 10^4 V/m

[448]. The lithium ion migrates along such a channel and at the electric field strength 10^3 V/m, but in this case, the ion cannot overcome the energy barrier to exit the channel.

Simulation of the intercalation process consisted in the periodic single or double emission of the Li^+ ions from points with the random y coordinates on the line having constant coordinates x = 0.198 nm, z = 0.375 nm. In other words, the line of initial points was near the channel entrance with a slight shift inward at the height $h_g / 2$. The endpoints of the line were inside the channel at the distance of 0.2 nm from the coordinates of the extreme silicene atoms, which limit the extent of the sheets along the y direction. The ion moved under the action of the constant electric field with the strength 10^3 V/m during 100 000 time steps. In the case of the uniform lifetime (10 ps), the ion succeeds in finding the advantageous location on the surface of the silicene and staying there until the end of the time allotted to it. Ion would not have this opportunity if the lifetime were a stochastic variable.

Until the maximum filling of the channel with lithium, the ion remained in the channel during the entire lifetime (10 ps), mainly, because it could not overcome the barrier created by the attracting interaction of other atoms. When the lithium ion is converted to a Li atom (after a set time of 10 ps), the nature of its interaction with other atoms (Si and Li) does not change, but the electric field no longer had any influence on it. In other words, the Li^+ ion transition to an atom means a change in its electric charge from +1 to 0 (every 10 ps) that does not affect its interactions that are not related to the presence of the electric charge.

After every 10 ps, a new Li^+ ion is launched into the channel. This procedure is repeated until the ions could find a place in the channel. The limiting number of intercalated lithium atoms turned out to be 39 in the case of a channel from the perfect silicene. All attempts to increase the number of Li atoms above this value were unsuccessful since the Li^+ ion eventually either left the channel outward or did not enter the channel at all. For the channels formed by the defective silicene, intercalation and deintercalation were carried out by inserting ion pairs into the channel and removing them from it, respectively. At the end of the intercalation, we obtained a system, in which the electrically charged particles (ions) are completely absent.

During deintercalation, the charged particles were again in the system: one ion in the case of a channel formed by the perfect silicene and two ions in a channel with the defective silicene walls. The process of lithium deintercalation was carried out when the direction of the electric field was reversed and the modulus of its magnitude was increased to 10^4 V/m. The order of appearance of ions in the system also has the inverse order, i.e., the last Li^+ ion that has been got into the channel became the first one, etc. The lifetime of the ion remained the same, i.e., was 10 ps.

The ion always left the channel during its lifetime without the accompaniment of lithium atoms. In a separate series of calculations, it was established, that such a character of the inverse process is not related with the order in the sequence of the atoms conversion into the ions. It was shown that a change in the order of exit of the ions from the channel did not lead to any new result. Therefore, when the choice of the outgoing ions was made randomly, each ion came out from the channel alone without the accompaniment of other atoms.

Figure 119 shows the configuration of the "Ag-Si-Li" system referring to the instant 390 ps at the final filling by lithium the channel formed by sheets of perfect silicene. During this time, 39 lithium ions were introduced into the channel. All intercalated Li atoms are visible in the figure because the silicene sheets are shown as transparent. It is seen that not all Li atoms are adsorbed by the silicene. Four Li atoms were found outside the channel, one of which is found at a considerable distance from the lower sheet of the silicene. It is clear that in the process of deintercalation, each of these atoms turning into an ion freely leaves the system. At the same time, the external Li atoms will not affect the location of other lithium atoms in the channel. In addition, the arrangement of these four atoms is such that they cannot interfere with the escape of other ions from the channel during deintercalation. Therefore, these four Li atoms located outside the channel were removed from the system before the deintercalation process began.

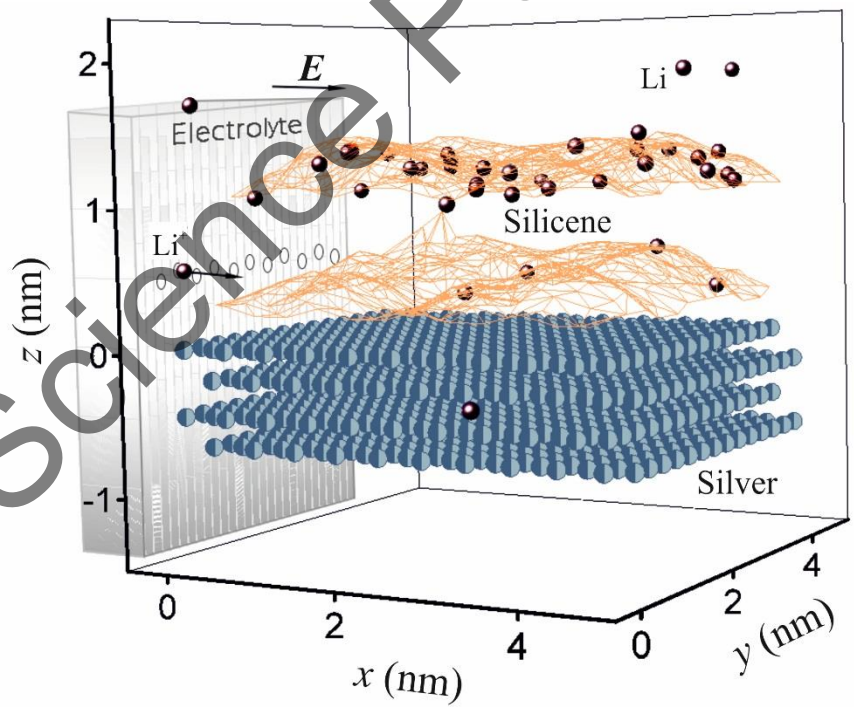

Figure 119. The channel formed by perfect silicene sheets on the Ag(111) substrate after the intercalation process of lithium.

The procedure for liberation from the "extra" Li atoms was also carried out for the silicene channels containing the mono- and bi-vacancies. In these cases, prior to deintercalation, 5 and 15 Li atoms were removed from the system for channels with the mono- and bi-vacancies, respectively. It is seen from Figure 119 that the top sheet of the silicene adsorbs the overwhelming majority of Li atoms. This is the result of the influence of the metal substrate since in absence of a substrate the number of adsorbed Li atoms by each silicene sheet is approximately equal.

The complete filling of the channel with lithium led to the highest height of the dome formed by the upper sheet of silicene. The highest dome was formed for sheets of the perfect silicene. Deformation of the silicene sheets leads to the increase of space available for filling the channel with lithium, which in the case of perfect silicene reached 45%. Strong deformations of the silicene sheets on the Ag(111) substrate contribute to the structural rearrangement of the vacancy-type defects in silicene. For the sheets of silicene with defects, magnitude of the vertical deformation was reduced, as well as, the volume of the inter-sheet space decreased. The horizontal (along the x axis) and vertical (along the z axis) profiles of lithium density in the silicene channel are usually of the same type for both the perfect silicene sheets and ones with various vacancy-type defects. For example, Figure 120 shows the corresponding profiles of numerical density in the case of the presence of the bi-vacancies in silicene.

The values of x and z are calculated from the entrance of the channel ($x = 0$) and from the level of the lower sheet of silicene ($z = 0$). In this case, 64% of all Li atoms are more "tied" to the upper sheet and only 36% to the lower one. Depending on the size of the defects, from 15 to 40% of Li atoms "adjoin" to the lower sheet of silicene lying on the Ag(111) substrate, and from 60 to 85% atoms "adjoint" to the upper one. The range of distribution of the Li atoms along the z coordinate is much larger than the initially specified interval between the silicene sheets (0.75 nm). This is due not only to the strong deformation of the silicene sheets but, also, to the escape of the individual Li atoms through the bi-vacancies beyond the sheets boundary. The region at the half-width level of the channel is free.

The use of the Cu(111) substrates changed the lithium density profiles. In this case, the silicene channel is filled with lithium more homogeneously. The horizontal density profile indicates a significant fraction of the Li atoms concentrated near the entrance and exit of the channel. The shape of the vertical density profile indicates that the middle part of the channel is not free but is most densely filled with the Li atoms. The Li atoms are not densely "adjacent" to the upper sheet of the silicene but leaving a small free gap near it. This is because there is a stronger attraction between the Cu and Li atoms than between the Ag and Li ones. The results of MD simulations show that the vacancy defects are better preserved during lithiation in the silicene located on the Cu(111) substrate than on the Ag(111) one.

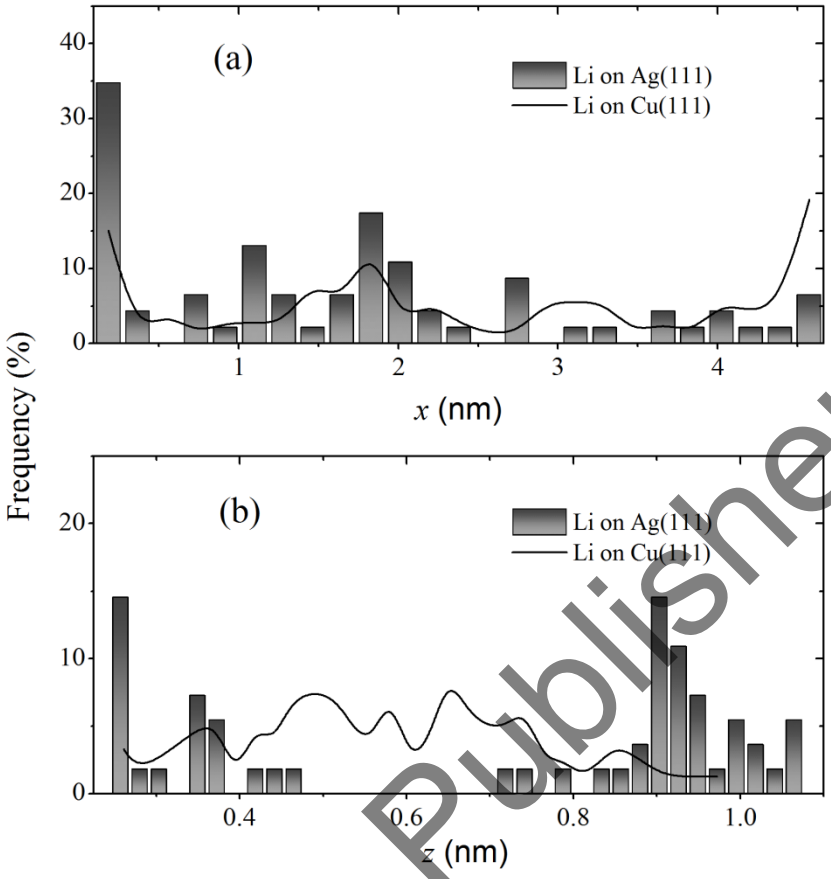

Figure 120. Horizontal (longitudinal) and vertical profiles of lithium density in the silicene channel with bi-vacancies on the Ag(111) and Cu(111) substrates.

Let us consider in more detail behavior of the defects and attachment of the Li atoms to silicene sheets by the example of a silicene channel having mono-vacancies and being fully filled with lithium. The investigated configurations refer to the instant 0.51 ns (or 5.1 × 10^6 Δt). The *xy* projections of the upper and lower layers of the channel cut by the mean ($z = h_g^* / 2$) plane are shown in Figure 121. The view is from the side of the plane $z = h_g^* / 2$, where h_g^* is the vertical channel size after lithium intercalation. There are 8 cavities in each silicene sheet. Their sizes exceed the size of any cavity formed by the six-link rings.

The bottom sheet contains two largest cavities, which boundary is formed from 23 and 15 Si atoms. 13 and 10 Si atoms bond two largest cavities of the top sheet. Their size is significantly inferior to the size of the largest cavities of the bottom sheet. That is due to the interaction of this sheet with the substrate. There are 8 rings in each sheet. The number of links in them exceeds 6 and 12 five-link rings. The upper and lower parts of the channel have equal volumes, but the number of Li atoms in them is different: 27 Li atoms are in the upper part and 20 Li atoms are present in the lower part. Four Li atoms are

outside the gap (formed by silicene sheets) and are not included in the *xy* channel projections.

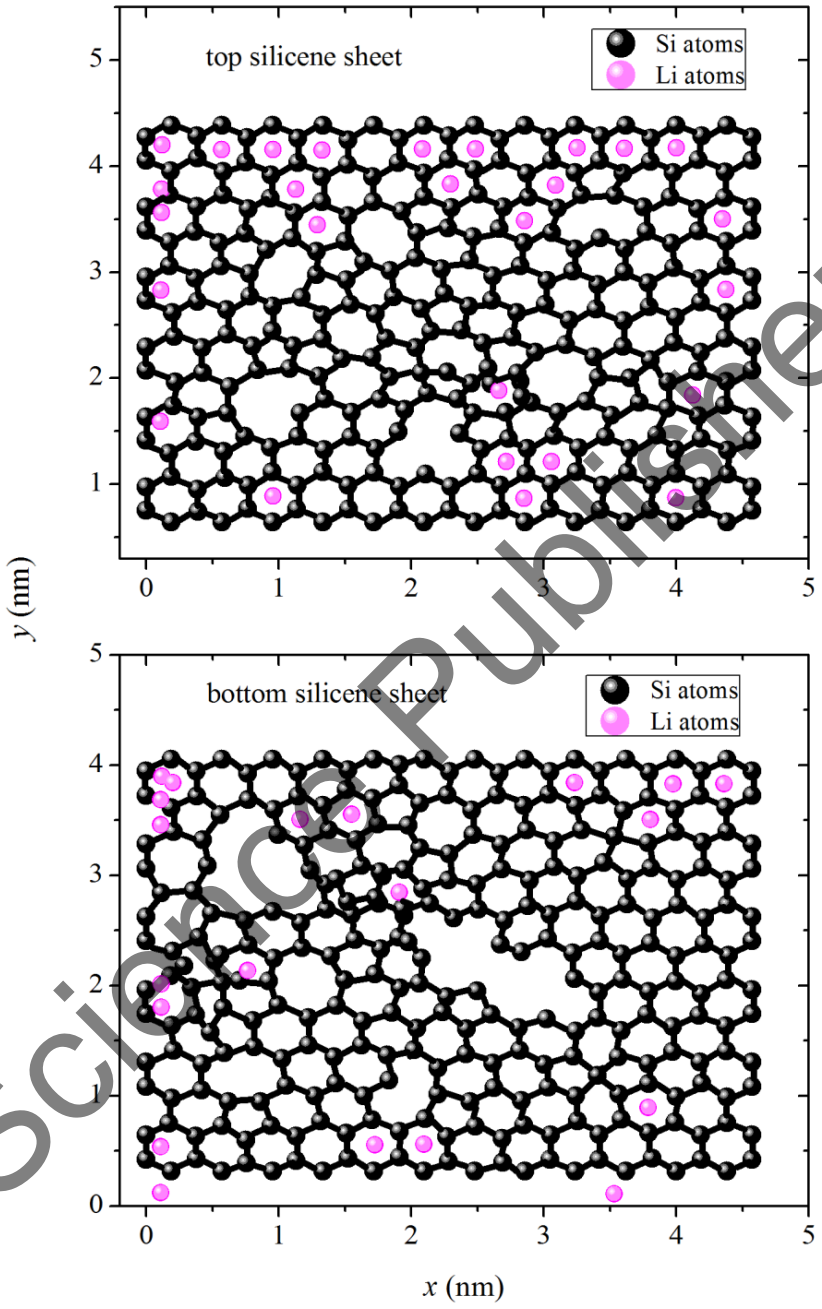

Figure 121. The *xy* projections of the upper and lower sheets of silicene with mono-vacancies on the Ag(111) substrate, at the instant of complete lithiation (51 lithium atoms were adsorbed on the silicene surface).

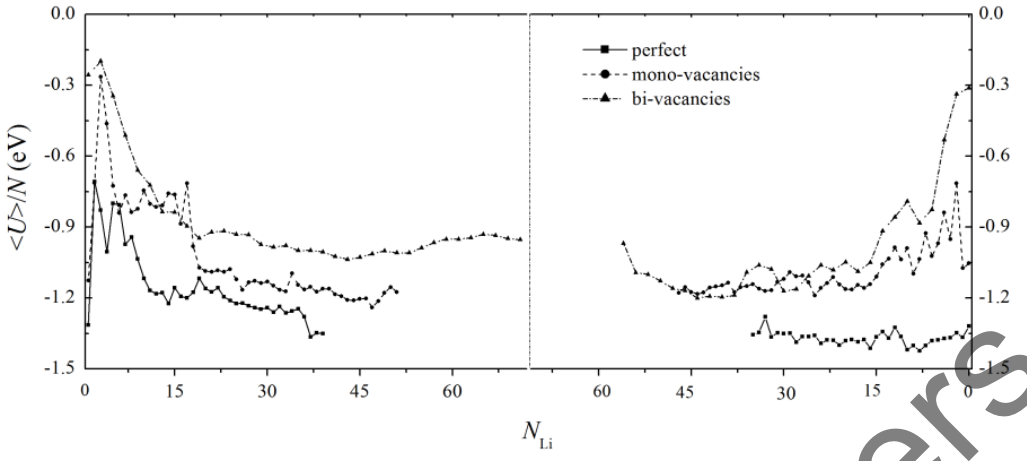

Figure 122. The internal energy of lithium atoms in the process of intercalation (left) and deintercalation (right) in various flat silicene channels; N_{Li} is the number of lithium atoms in the channel.

The change in the specific internal energy $\langle U \rangle$ of lithium during filling the silicene channel with Li atoms is shown in Figure 122. The figure is divided into two parts by a dashed line. The left part of the figure shows the lithium intercalation into the gap between the silicene sheets, and the right side of the figure reflects the reverse process of the lithium deintercalation. In each part of the figure, three graphs are presented related to the silicene channels formed by the defect-free silicene sheets: ones with the mono- and bi-vacancies. The abscissa is the number of Li atoms in the channel. The limiting number of Li atoms intercalated into the channel increases in the sequence "defect less silicene → silicene with mono-vacancies → silicene with bi-vacancies".

In all the cases considered, the intercalations of the first 1–3 lithium atoms give rise to the energy $\langle U \rangle$ burst. This is due to the structural perturbations produced by the high-energy lithium ions (atoms) freely moving through the channel. Under further increase of the Li atoms in the channel, the growth of the $\langle U \rangle$ value is replaced by its decrease. This is due to Li atoms binding to the Si ones of the upper and lower sheets of silicene.

Deformation of the silicene sheets and their binding to lithium are factors acting on the $\langle U \rangle$ magnitude in different directions. Since the fast change in these events, the $\langle U \rangle$ magnitude undergoes strong fluctuations, which are manifested to be especially long when there are mono-vacancies in the silicene sheets. It is obvious that it is easier to deform the sheets of defective silicene than that of the perfect one. However, when the silicene sheets contain bi-vacancies, the Li atoms bind to these defects more easily and are held by them. As a result, the $\langle U \rangle$ fluctuations, in this case, turn out to be minimal, but the "Si-Li" system as the whole proves to be more strongly disordered in comparison with the cases of the

perfect silicene and silicene with mono-vacancies. The minimum value $\langle U \rangle$ for saturation of the channel with lithium is observed for paired sheets of the perfect silicene, and the maximum value for the silicene sheets with bi-vacancies.

The deintercalation process is also accompanied by jumps of $\langle U \rangle$, but not as strong and fast as during intercalation. These oscillations are mainly associated with the destruction of the Li structure in the silicene channel during deintercalation. In the case of the perfect silicene, the $\langle U \rangle$ energy retained its low value after the channel became completely free from lithium. However, when the silicene sheets have defects, the $\langle U \rangle$ value begins to increase after approximately 30 lithium ions are removed from the system because the residence time of the ion in the channel increases. This makes it possible to disperse lithium ions in the channel by the applied electric field. The collision of a fast lithium ion with Li and Si atoms is even stronger than that in a period of the unchanged energy $\langle U \rangle$. Such collisions destroy the structure of the "Si-Li" system and lead to an increase of the $\langle U \rangle$ magnitude.

The behavior of the *D* self-diffusion coefficient of Li atoms during intercalation and deintercalation of lithium ions into silicene channels is shown in Figure 123. Dependencies $D(N_{\mathrm{Li}})$, where N_{Li} is the number of atoms Li in the channel, are presented for: (a) the flat perfect silicene channel; (b) the channel formed by silicene sheets with mono-vacancies; (c) the channel constructed from silicene sheets with bi-vacancies. The vertical line divides each of the figures (a)–(c) into the left and right parts. The left-hand parts of the figures represent the process of the lithium ions intercalation into the flat silicene channel. The right-hand parts of these figures reflect the Li^+ ion deintercalation process. In the case of the channel formed by sheets of the perfect silicene, the limiting number of Li atoms filling the channel was 39. The silicene channel with mono-vacancies was able to hold a maximum of 51 Li atoms, and the channel with bi-vacancies could contain no more than 71 Li atoms. In cases (a) and (b), the lithium ions were intercalated and deintercalated one by one sequentially, while in the case (c), sequential pair intercalation and deintercalation were simulated. In other words, in the case (c), simultaneously two Li^+ ions entered the channel and emerged from it.

In each of the cases (a)–(c), the self-diffusion coefficient of Li atoms decreases as the channel is filled with these atoms. The strongest fluctuations of *D* magnitudes are observed at the initial part of the channel filling with Li atoms. It is since the Li^+ ion has a higher velocity, which is lost when the ion collides with the Si and Li atoms. We note that the *D* value increases by an order of magnitude in both processes when passing from the channel formed by the perfect silicene to the channel formed by silicene sheets with the mono-

or bi-vacancies. This is due not only to achieving the greater freedom of motion in the presence of the defects in the silicene sheets but, also, to weakening the interaction of the Li^+ ion with Si atoms in the presence of the mono- or bi-vacancies. The smoother attenuation of the coefficient fluctuations during the lithium ions intercalation in the case (c) is due to the simultaneous action of two ions on the channel walls and on its contents.

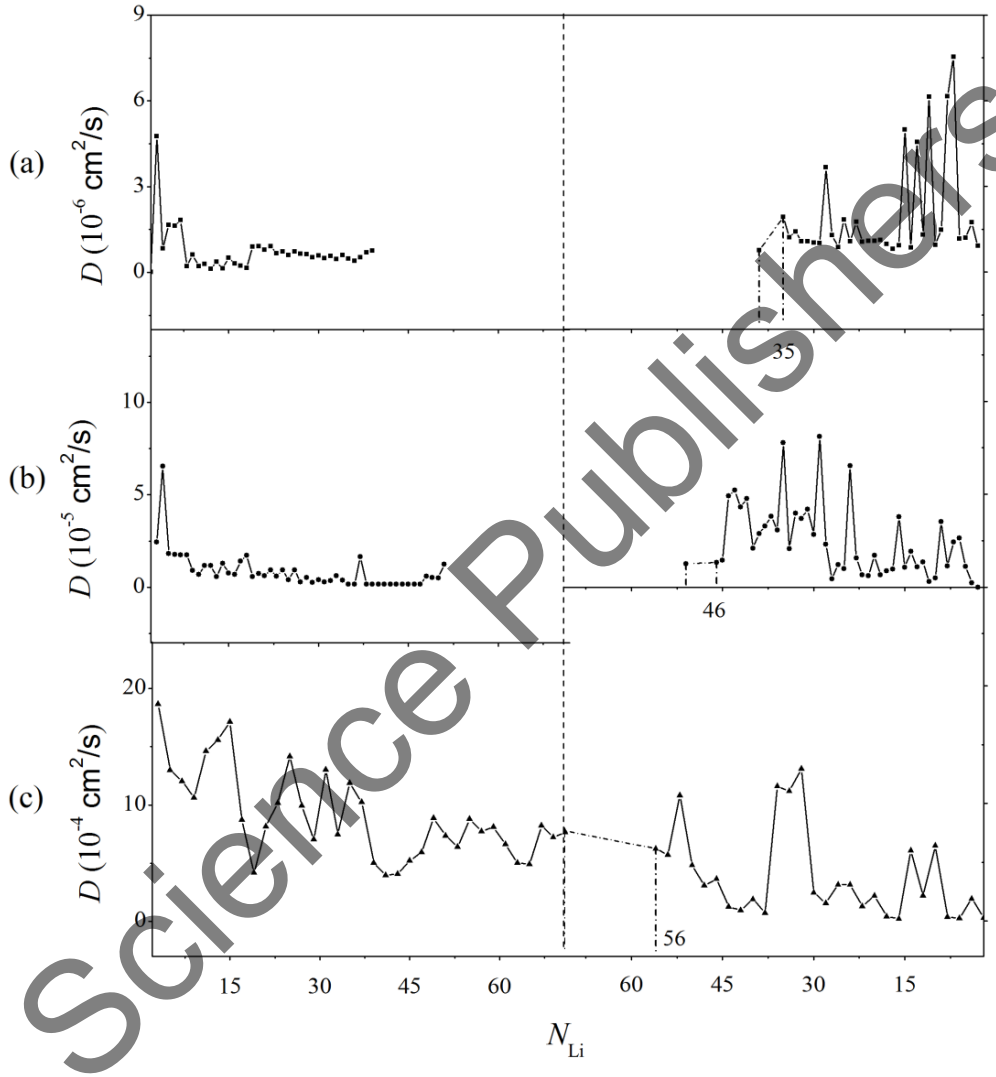

Figure 123. The coefficient of self-diffusion of lithium atoms in the process of intercalation (left) and deintercalation (right) in silicene channels characterized as: (a) perfect, (b) with mono-vacancies, (c) with bi-vacancies; removal of the lithium atoms that are outside the channel before the start of deintercalation is marked in the figure by dashed lines and dot-dash lines.

At the initial stage in the cases (a) and (b), the Li^+ ion deintercalation occurs without large changes in the D coefficient of lithium atoms. However, when about a dozen or two dozen Li atoms leave the channel, fluctuations in the D magnitude become large. This is

due to increase of the Li^+ ion velocity in the freer channel, and, consequently, also, by the ion stronger collisions with Si and Li atoms. The paired exit of Li^+ ions from the channel in the case (c) occurs without amplification of the coefficient fluctuations D at the final stage of deintercalation. This is due to the effect of a paired and smoother action of the Li^+ ions on the Si and Li atoms.

The following comparison gives an idea on the magnitude of the ion lifetime (10 ps). Helium is the nearest chemical element to lithium in the atomic mass. Helium is a monoatomic gas at T = 300 K. If we consider the motion of the He atom in the identical channel as the thermal motion of an atom in a gas, then its average arithmetic velocity is $\bar{v} = \sqrt{\frac{8RT}{\pi\mu}}$, where R is the gas constant, T is the absolute temperature, μ is the mass of 1 helium mole that at the temperature 300 K will be 1260 m/s. The He atom can travel at this velocity for the time of 10 ps the distance 12.6 nm, which is approximately 2.7 of the channel length. If we assume that $D = \frac{1}{3}\bar{v}\bar{\lambda} = 10^{-4}$ cm^2/s, then the mean free path $\bar{\lambda}$ of the He atom is 0.024 nm.

The method of statistical geometry based on the construction of the Voronoi polytopes has found wide application to analyzing the structure of irregular systems, for example, a simple fluid [457]. In our case, we use this method to analyze the structure of the region filled with lithium atoms embedded in the silicene channel. We calculated two types of the VP distributions using the statistical geometry method. In both cases, the VP were constructed for Li atoms. However, in the first case, only Li atoms could be neighbors of Li atoms, and in the second case, both Li atoms and Si ones forming the silicene sheets could be neighbors of Li atoms. These distributions are shown in Figure 124 in the case of complete filling of the channel by Li atoms. The channel was constructed using the perfect silicene sheets. In the case of channels formed from sheets of the defective silicene, the distinguishing features for these distributions remain the same.

The first type of neighbor formation (only from Li atoms) leads to the appearance of the large number of polyhedra with 4 – 6 faces (about 44%), and the maximum of this distribution corresponds to n = 5. The number of the VP faces (n) increases being in addition to Li atoms; the Si atoms are also regarded as neighbors. The maximum of the n-distribution is shifted to n = 9. The distribution of faces by the number of sides (m-spectrum) also turns out to be different in the presence of neighbors of the first and second types. In the m-spectrum obtained in the analysis of the first type VP, the faces with m = 4 (31%) dominate. The main maximum of the m-spectrum for the second type VP still remains at m = 4, but the share of quadrilateral faces decreased to 25%. The inclusion of the Si atoms into the geometric neighbors slightly affects the shape of the θ-distribution.

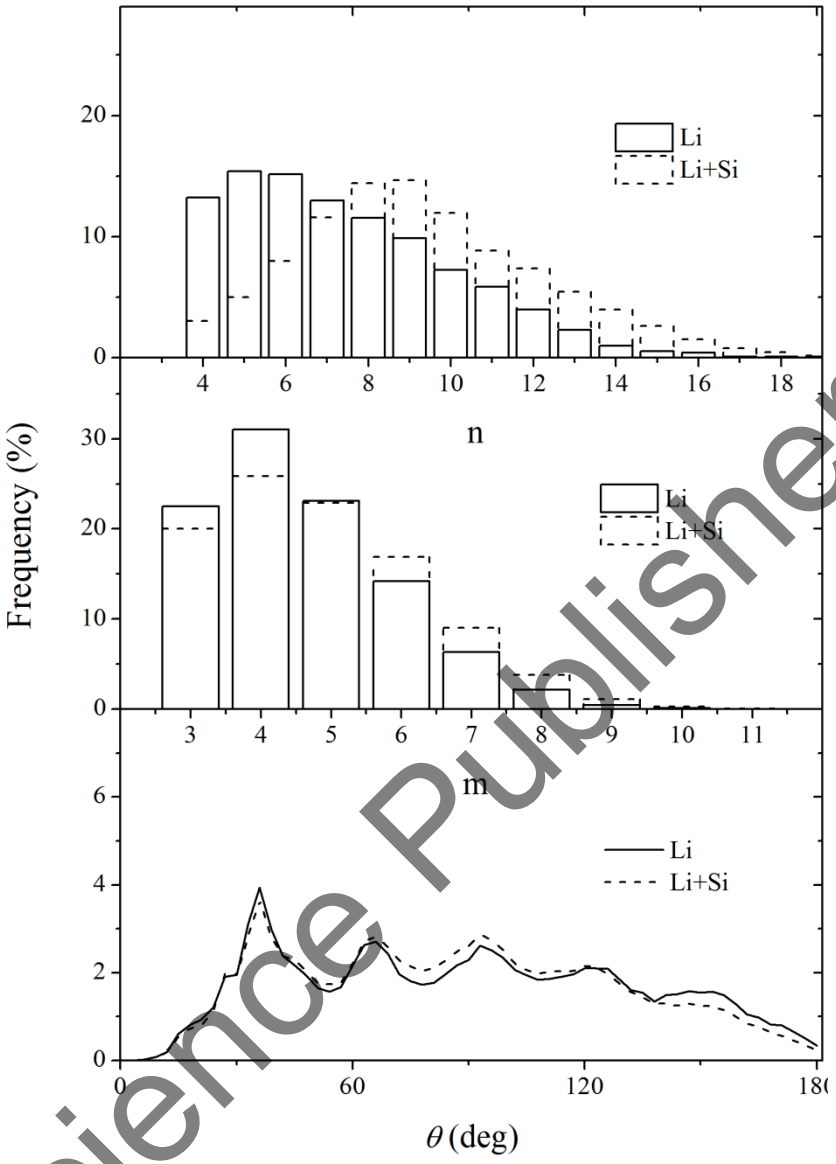

Figure 124. Distribution of the VP with respect to the number of faces (n), distribution of faces by the number of sides (m) and distribution of angles (θ) formed by the nearest geometric neighbors; the VP are constructed for Li atoms in the case when they completely fill a flat silicene channel formed by the perfect silicene sheets on the Ag(111) substrate; the neighbors were created either by Li atoms or by together Li and Si atoms forming channel walls.

The σ_{zz} component is the most significant and reflects the stresses acting in the plane of the silicene sheets due to forces directed along the *z* axis. Here, in the calculation of the σ_{zz} stress, the elementary areas stretched along the *y* direction ("armchair") are considered. Consequently, the stresses are investigated along the *x* direction ("zig-zag"). Filling the channel with lithium does not lead to significant increase of the stresses in the

sheets of silicene. Quite the contrary, the principal stresses in the sheets even slightly decrease. Here, we will consider the stresses averaged over both sheets of silicene. Stresses σ_{zz} arising at different stages of the process of the lithium intercalation in flat channels from the perfect silicene and silicene with vacancy-type defects are shown in Figure 125.

The strongest bursts of the σ_{zz} stresses are observed for the perfect silicene sheets. These stresses slowly decrease over time. However, at the time when the channel is filled with the limiting number of Li atoms, the maximum value of σ_{zz} approaches to the corresponding value of σ_{zz} for silicene with mono- and bi-vacancies. At the initial stage of filling the channel with lithium, the σ_{zz} stress for silicene with bi-vacancies has the lowest values. The weakening of the oscillation intensity of σ_{zz} is caused by dissipation of the kinetic energy of Li^+ ions as the channel is filled with Li atoms.

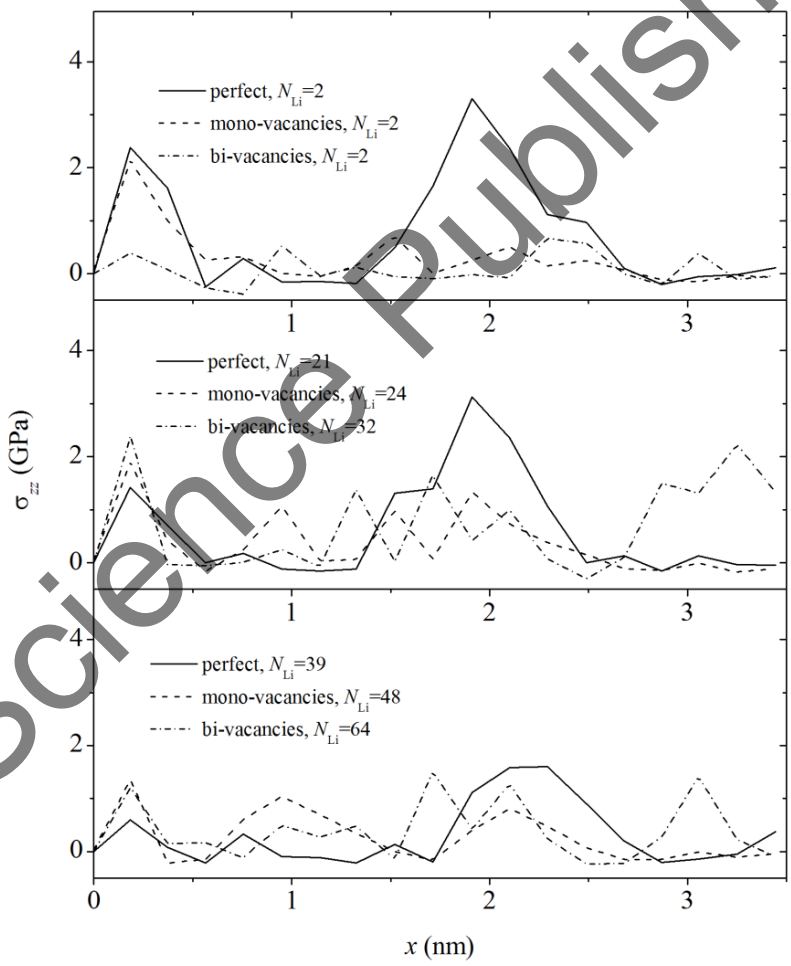

Figure 125. Distribution of σ_{zz} stresses in sheets of the perfect and defective silicene forming a flat channel on the Ag(111) substrate at the initial, intermediate, and final stages of intercalation.

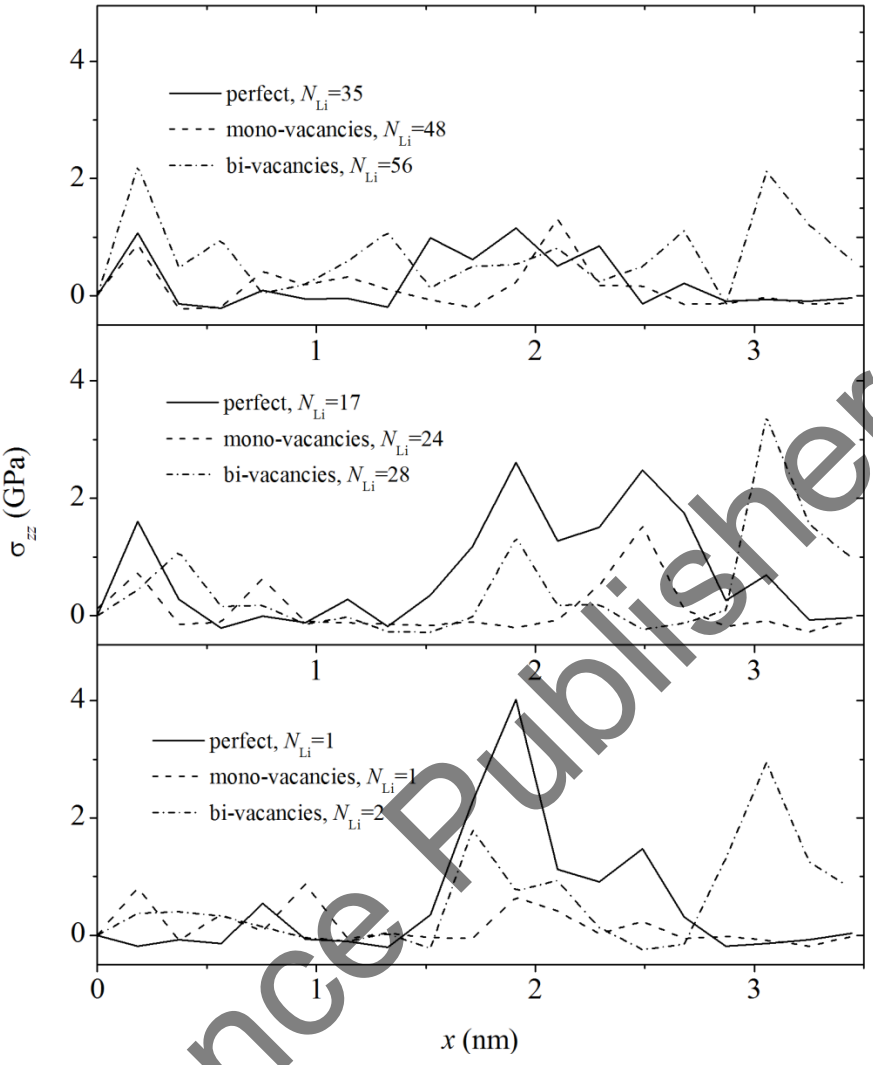

Figure 126. Distribution of σ_{zz} stresses in sheets of the perfect and defective silicene forming a flat channel on the Ag(111) substrate at the initial, intermediate, and final stages of deintercalation.

At the initial stage of lithium deintercalation in the channels under consideration, the strongest local stresses appear in silicene sheets with bi-vacancies (Figure 126). As a rule, when the lithium deintercalation passes through, the bursts of the σ_{zz} stress are amplified. The strongest local stress σ_{zz} is observed for the perfect silicene at the final stage of lithium deintercalation. This peak falls on the middle part of the length of the channel, where the ion stays for most of its lifetime. Increase in the stresses in the channel walls during the deintercalation process is caused by an increase in the kinetic energy of Li^+ ions when the channel is free from Li atoms.

Here, we have investigated the effect of the vacancy type defects on the lithium fill ability of the channel formed by silicene sheets, as well as, on the structural and kinetic

properties of lithium. It was found that the defective silicene on the Ag(111) substrate is rather stable when the channel is filled with lithium. The peculiarity of silicene is that when the temperature rises, the vacancy defects result in local structural changes of the silicene lattice reducing the number of dangling bonds near the defects [458]. They reduce the thermal stability of silicene considerably. We also observed a rearrangement of the defective structure of silicene, which, as a rule, ended at 100 ps. Instead of the vacancy defects, the five-link rings and rings of eight or more links were formed that created defects in the form of a hole. Such structural rearrangements were observed even when only one Li^+ ion moves along the graphene-silicene channel [450].

The initial distance z_s between the lower sheet of silicene in the channel and the Ag(111) substrate was 0.27 nm. During the lithium intercalation, this distance increased by 59%, 43%, and 50% for the perfect silicene and one with the mono- and bi-vacancies, respectively. In the case of the Cu(111) substrates, the similar increase in the distance z_s was 20%, 19%, and 11%. Thus, silicene is much more distanced from the Ag(111) substrate than from the Cu(111) one. In this case, the interaction of Ag-Si becomes even weaker. The attraction between Li and Si atoms became decisive. As a result, the "adhesion" of Li atoms to the silicene sheets occurred, and free space in the middle of the channel appeared. The copper substrate has the attractive effect the silicene atoms. Therefore, the channel is filled with the Li atoms more evenly, but a small gap appears near the top silicene sheet.

A wide set of VP types classified by the number of faces and a wide range of faces differing by the number of sides indicates, in general, the irregular packing of Li atoms in the silicene channel. Regardless whether Si atoms are included in the number of the nearest neighbors, the θ-distribution is characterized by the presence of several big peaks. Moreover, in the case of the first type of VP construction, the number of peaks (5 ones) in the θ-distribution is even greater than in the second case (4 ones).

If the number of peaks in the θ-distribution is greater of two, then the structure in question has features of crystallinity [346]. A certain crystalline order in the packing of Li atoms is created since some of the Li atoms occupy locations above the centers of the hexagonal cells formed by Si atoms. Thus, in both ways of considering the geometric neighbors, the Li atoms packing in the channel is represented as quasi-crystalline, i.e., irregular, but with elements of local regular placement of atoms.

When the channel is slightly filled with lithium, the stress σ_{zz} in sheets with the mono- and, especially, bi-vacancies is even lower than in the case when the channel is formed by the perfect silicene. This decrease can be almost twofold for the silicene sheets with bi-vacancies. However, when the channel is almost densely packed with lithium atoms, the difference in stress σ_{zz} for sheets of the perfect silicene and one with defects is erased. Stresses σ_{zz} observed in silicene sheets during the lithium intercalation and

deintercalation have the similar values. However, if the lithium intercalation decreases stresses with time, in the case of the deintercalation, on the contrary, they increase.

As a rule, the creation of the vacancy-type defects (mono- and bi-vacancies) in a two-layered silicene reduces the stress appearing during the lithiation/delithiation of the silicene channel and increases the limiting number of intercalated lithium atoms. However, when the strength of the two-layered silicene decreases, the magnitude of vertical displacements of Si atoms increases, which leads to a decrease in the velocity of lithium ions along the channel. Deformations of the silicene sheets caused by the presence of a silver substrate substantially reduce the capacity of Li atoms in the channel, and, consequently, reduce the capacitance of this electrode. It possible to improve this situation by at least two ways: 1) to use a substrate of another material better non-metal, for example, graphite, 2) to use an expanded multilayer silicene as an anode design when the layers of silicene are periodically reinforced with a material stronger than silicene, for example, graphene.

The stresses caused by the lithium ions motion in the channel and the deposition of Li atoms are much lower than the tensile strength of silicene. The maximum local stress σ_{zz} appears in the perfect silicene upon delithiation of lithium (4.1 GPa). It is much less than the ultimate stress (38.7 GPa), which is installed in silicene under the uniaxial tension [459]. The number of lithium atoms obtained at the maximum filling of the channel constructed from silicene having the mono- and bi-vacancies increases in comparison with the case of intercalation of lithium in the channel of the perfect silicene by 1.2 and 1.8 times, respectively.

Analysis of the detailed structure (revealed based on the construction of Voronoi polyhedra) indicates the presence of some general regularities in the arrangement of the Li atoms in the perfect and defective silicene channels. Similar structures are formed when lithium is deposited on silicene regardless of the type of defects present in the silicene sheets. These structures are partially ordered, since, some Li atoms "settle" opposite the centers of the hexagonal Si-cells. Thus, the nature of the inter-atomic interaction of Li–Si, and Li–Li is decisive for the location of lithium atoms in the channels.

We have shown that the main stresses arising in the intercalation and deintercalation processes of lithium are serious enough to produce strong structural rearrangement of atoms in the defective silicene. Therefore, the two-layer silicene on the Ag(111) substrate is not very suitable for use as the anode of a lithium-ion battery. Instability of defects in the silicene on a silver substrate is the main problem for the use of such a structure as the anode of a lithium-ion battery. Solving this problem can give impetus to the creation of new generation of LIB.

From a practical point of view, it is important that the vacancy-type defects in silicene sheets are stable. They increase the adsorption capacity of the flat channel and, consequently, lead to an increase in the charge capacity of the silicene anode. However, the Ag(111) substrate does not prevent strong deformation of the silicene sheets and, thus,

has a destabilizing effect on the stability of the vacancy-type defects in silicene during the lithium intercalation and deintercalation.

In further studies, it is necessary to investigate the behavior of the two-layer silicene on other substrates under the operational conditions of the lithium-ion batteries anode. Since the energy barrier for lithium atoms is not large, they can easily penetrate into the bi-layer or multi-layer silicene. Silicene is a good anode material for the lithium-ion batteries with a large capacity and low lithium migration energy barriers. However, the free-standing form of silicene is unstable virtually requiring the substrate support. The theoretical estimate of Li adsorption performed in our investigations will be important for comparison with the results of future experiments. It seems natural to obtain experimentally quantitative characteristics of the lithium electrochemical deposition on silicene located on the metal substrate. The maximum value of the ratio of Li/Si atoms and the optimum gap between the silicene surfaces are of the greatest interest if the anode is constructed in the form of parallel plates coated with silicene.

Chapter 9

PROSPECTS FOR THE USE OF SILICENE-COPPER ANODE FOR LITHIUM-ION BATTERIES

The silicone nanocomposite provides much higher specific capacity (~3500 $mA \cdot h \cdot g^{-1}$) than graphite (372 $mA \cdot h \cdot g^{-1}$) [427]. Ion transport is possible through the structure enhanced by diffusion channels and in-plane silicon vacancies in the silicene sheets [448, 450]. This creates conditions for silicene successful application as an electrode. Superior electrical conductivity and packing density, as well as, excellent structural integrity (due to the high flexibility of the silicene sheets) allow one to create the large volume changes of lithiated silicon compounds [436, 460].

Nowadays, silicene has not yet been obtained on a copper substrate. However, the copper films on various silicon substrates have been investigated many times [461]. For example, a quantitative analysis of the hardness results shown that the copper films have much higher hardness than that of the bulk Cu. The maximum hardness observed with Cu on Si (110) is 2.5 GPa [462]. The film thickness on different Si substrates depends on the hardness, texture, and state of the grain boundary. In general, finer microstructures attribute partly in the mechanical properties of the thin film. Dislocation density, grain size, and film thickness itself can be a huge factor contributing in the hardness.

The difficulty of obtaining thin copper films on silicon is due to the high penetrating power of copper atoms in silicon. To prevent copper diffusion, barriers are necessary. Polycrystalline tantalum and amorphous tantalum nitride films can act as such barriers [463]. The stability of such barriers against copper diffusion is very good, since, according to the equilibrium phase diagrams, no Ta–Cu compounds are expected. It is well known that placing chemically different atoms in close proximity results in the migration of atoms in order to reduce the total free energy and establish equilibrium [374]. As a rule, the atomic migration is due to the presence of the differences in concentration, the presence of the negative free energy of the reaction, the use of an electric field, the presence of the thermal energy, generation of a strain gradient, or combination of some or all of these factors.

Meanwhile, carbon analog of silicene-graphene can be grown on a copper substrate. It was found that diffusion of the single copper adatoms on the surface of graphene oxide occurs extremely intensively as a result of spatial and energetic disorder inherent in the substrate [464]. Growing the graphene by CVD on metals (notably copper and nickel [465]) is currently the most promising way to achieve low-cost scalable graphene synthesis. The substrate preparation quality and other process parameters affect properties of the carbon films obtained at different pressures and temperatures on the copper foil and copper films. Large single-crystal domains of graphene can be produced on a copper substrate. Dissolving metallic foils after CVD growth is commonly employed to transfer graphene sheets from metals to other substrates [465] producing the long structurally well-defined graphene. Adhesion of the graphene in combination with the copper film, as well as, the thermal and dynamic stabilities of this system was investigated in [193, 269, 281].

At present, the most of lithium-ion batteries use graphite powder as an anode material. Graphite anodes meet the voltage requirements of the most common Li-ion cathodes and are relatively affordable, extremely light, porous, and durable. However, silicene has great promise as a novel anode material for high-performance LIBs [449]. Battery packs can contain several series or parallel strings of many individual cells. It is necessary to understand completely the lithium adsorption, diffusion, and capacity on the inner surface of a bi-layer silicene and, therefore, the prospects of silicene as an anode material for high-performance LIBs. To do this we carried out the molecular dynamics calculations and studied the lithium adsorption, diffusion mobility, intercalation and deintercalation. The lithium intercalation and its deintercalation in a flat silicene channel were studied by considering various $LiSi_p$ combinations including using perfect silicene, as well as, one with defects in the form of mono-, bi-, tri-, and hexa-vacancies. These studies fully take into account the dynamics of the diffusion processes that occur when the silicene channel is filled with lithium, which is almost always excluded in studies based on the first-principles calculations of the DFT.

The Tersoff potential with the parameters from [428] was taken for representation of interactions in silicene. The copper substrate atoms interacted through the embedded atom potential [466]. The interaction between Si atoms belonging to different sheets of silicene is described by the Morse potential [429]. The Li–Li, Li–Si, Li–Cu, and Si-Cu interactions were presented by the Morse potential as well [430, 431]. The copper substrate was formed by four (111) planes of the corresponding crystal and contained 1536 atoms. Atoms of the substrate were immobile; so, the Cu–Cu interaction was not considered in the model. The electric field acted only on the Li^+ ion having the electric charge $1e$ where e is an elementary electric charge. The model and method of filling the channel with lithium corresponded to those described in Section 8.2. In particular, the gap h_g between the silicene sheets was equal to 0.75 nm. The electric field during intercalation was 10^3 V/m. The process of deintercalation of lithium was carried out when the direction of the electric field was reversed and the modulus of this magnitude was increased to 10^5 V/m.

Structural analysis of small objects can be carried out using the statistical geometry method [467] based on the construction of the VPs. We construct VPs for Li atoms, and geometric neighbors are chosen only of the Li atoms.

To define the intercalation potential of lithium into silicene, whose computational cell contains *p* silicon atoms (Si_p), we take into account the following two electrochemical reactions of silicene and lithium:

$$\text{Silicene: } \mathrm{Si}_p + \mathrm{Li}^+ + e^- \Leftrightarrow \mathrm{LiSi}_p, \tag{48}$$

$$\text{Lithium: } \mathrm{Li} \Leftrightarrow \mathrm{Li}^+ + e^-. \tag{49}$$

By introducing the equilibrium potential of silicene (Φ_{Si}) and lithium (Φ_{Li}), we obtain the following equations:

$$\text{Silicene: } p\mu(\mathrm{Si}) + \mu(\mathrm{Li}^+) - e^-\Phi(\mathrm{Si}) = \mu(\mathrm{LiSi}_p), \tag{50}$$

$$\text{Lithium: } \mu(\mathrm{Li}) = \mu(\mathrm{Li}^+) - e^-\Phi_{\mathrm{Li}}, \tag{51}$$

where $\mu(\mathrm{X})$ is the chemical potential of species X. As a result, we receive the intercalation potential measured from the redox potential of metallic Li

$$\Phi[\mathrm{Si}_p \rightarrow \mathrm{LiSi}_p] = \Phi_{\mathrm{Si}} - \Phi_{\mathrm{Li}} = [p\mu(\mathrm{Si}) + \mu(\mathrm{Li}) - \mu(\mathrm{LiSi}_p)]/e. \tag{52}$$

The calculations of $\Phi[\mathrm{Si}_p \rightarrow \mathrm{LiSi}_p]$ were performed based on the SIESTA program using the *ab initio* pseudopotential on the basis of density functional theory (DFT) [468, 469].

The silicene channel on the Cu(111) substrate after complete intercalation with lithium is depicted in Figure 127 as a thin web to show all the Li atoms deposited on the channel walls. It is seen that the arrangement of Li atoms in the channel is not uniform. The first half of the channel along the direction of the *x* axis is filled with Li atoms much more densely than the second half: 33 Li atoms have a coordinate $x \leq 2.6$ nm and only 15 Li atoms are located in space with the coordinate $x > 2.6$ nm. In the middle part of the lower sheet of silicene, convexity is observed with respect to the substrate, and the concavity is in the same part of the top sheet. A significant narrowing of the channel in the middle part makes it difficult for Li^+ ions to pass the channel and limits the channel filling with lithium.

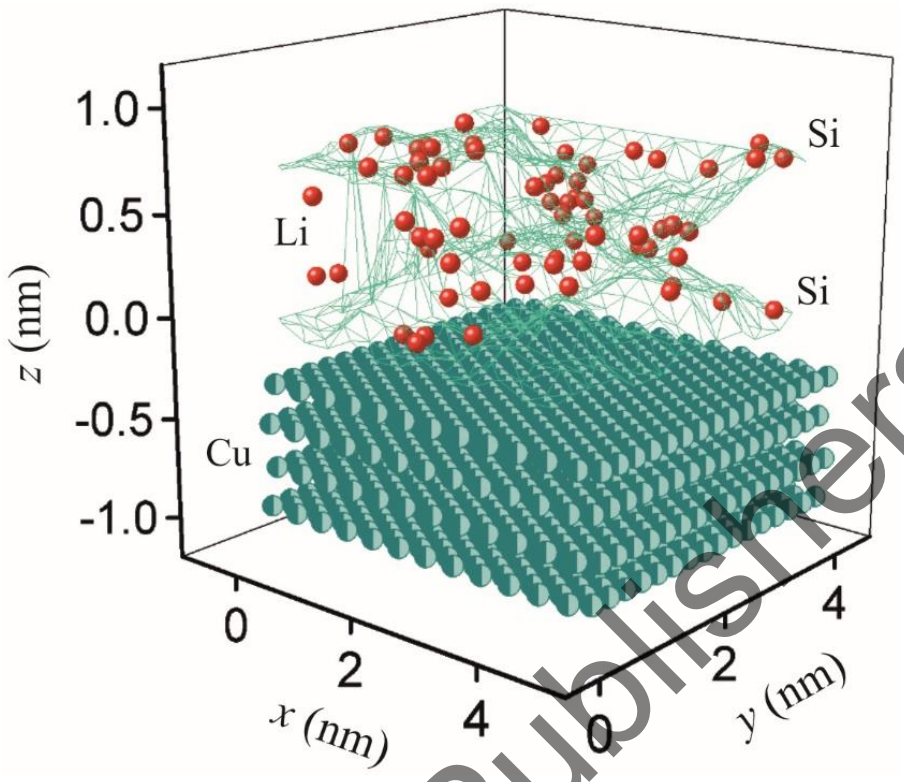

Figure 127. Channel formed by silicene sheets with mono-vacancies, on the Cu(111) substrate after the intercalation process of lithium.

The horizontal and vertical profiles of lithium density in the silicene channels are rather inhomogeneous (Figure 128). In the case of perfect silicene, a high value of the lithium density is reached at the entrance to the silicene channel (Figure 128a). This is due to a strong deterioration of the channel patency as it is filled with lithium. The value of the lithium density at the channel inlet decreases when defects of the vacancy type are present in the silicene sheets. The middle part of the channel (under the Li ions motion along the *x* direction) turns out to be much more populated when there are defects in the silicene. Moreover, in the silicene channel with bi-vacancies, the increased lithium content is observed at the channel exit. The vertical density profile in the perfect silicene channel is divided into the lower and upper parts (Figure 128b) separated by the gap 0.15 nm. Here, the effect of the substrate proves to be stronger than in the channel with defects. In the lower part of the channel, 58% of the total amount of precipitated Li atoms is concentrated. However, in the channel with defects, the gap disappears. In the presence of the bi-vacancies in the silicene sheets, the density of lithium in the middle part of the channel is even higher than near the walls. The number of Li atoms in the lower part of the channel decreases to 53%.

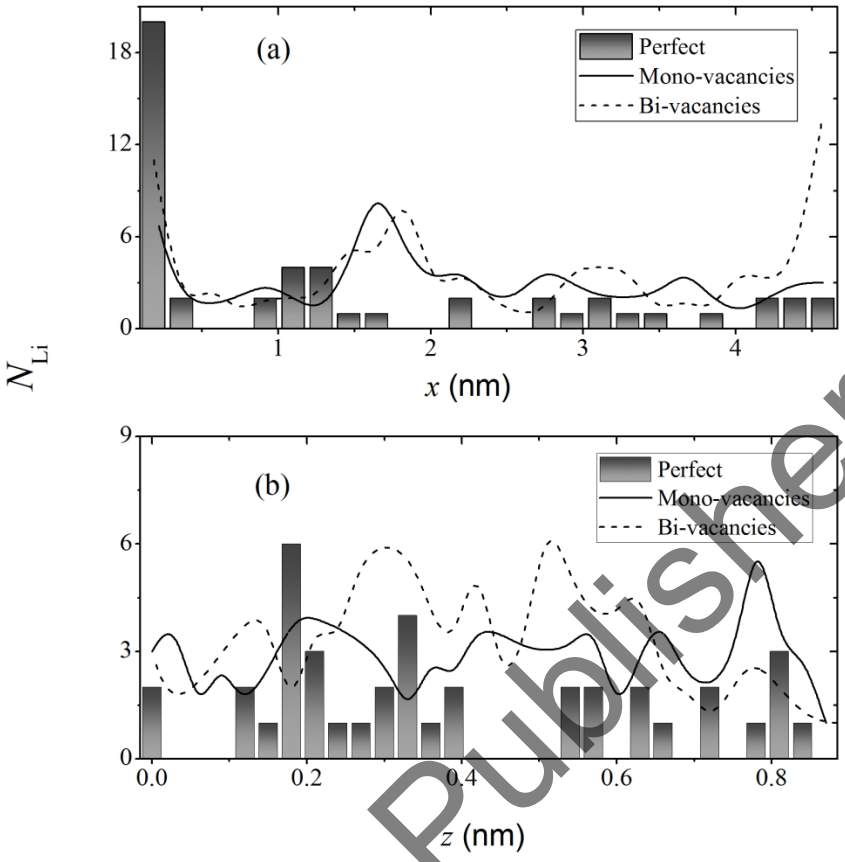

Figure 128. Horizontal (longitudinal) and vertical profiles of lithium density in silicene channels on the Cu (111) substrates.

Table 15. The maximum number of lithium atoms intercalated in a silicene channel on silver and copper substrates for various types of vacancies in silicene

Type of vacancies in silicene sheets	Substrate type	
	Ag(111)	Cu(111)
Perfect	39	48
Mono-vacancies	51	67
Bi-vacancies	71	86
Tri-vacancies	79	60
Hexa-vacancies	42	23

The maximum number of Li atoms embedded in the silicene channels with different types of vacancy defects is given in Table 15. Here, we also compare the results of lithium intercalation in the cases of the silicene channel on the Ag(111) and Cu(111) substrates. It is seen that in variants suitable for the real use, (i.e., for the perfect silicene and silicene with mono- and bi-vacancies) the number of Li atoms embedded in the channel is significantly larger when the silicene sheets lie on the copper substrate. Calculations for

channels with tri- and hexa-vacancy showed non-viability of these structures due to the significant structural rearrangements in the silicene and beginning of the destruction of its sheets.

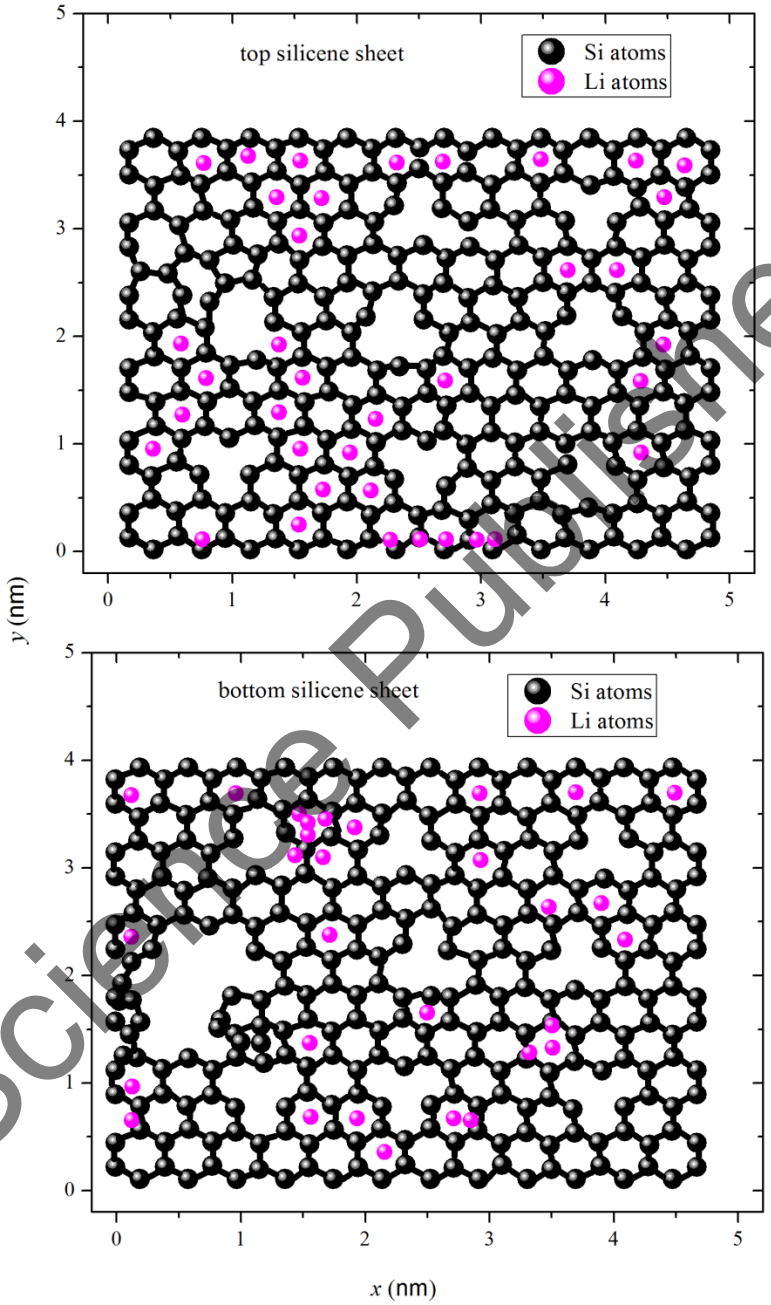

Figure 129. The *xy* projections of the upper and lower sheets of silicene with mono-vacancies on the Cu(111) substrate at the instant of complete lithiation (67 lithium atoms are in the channel).

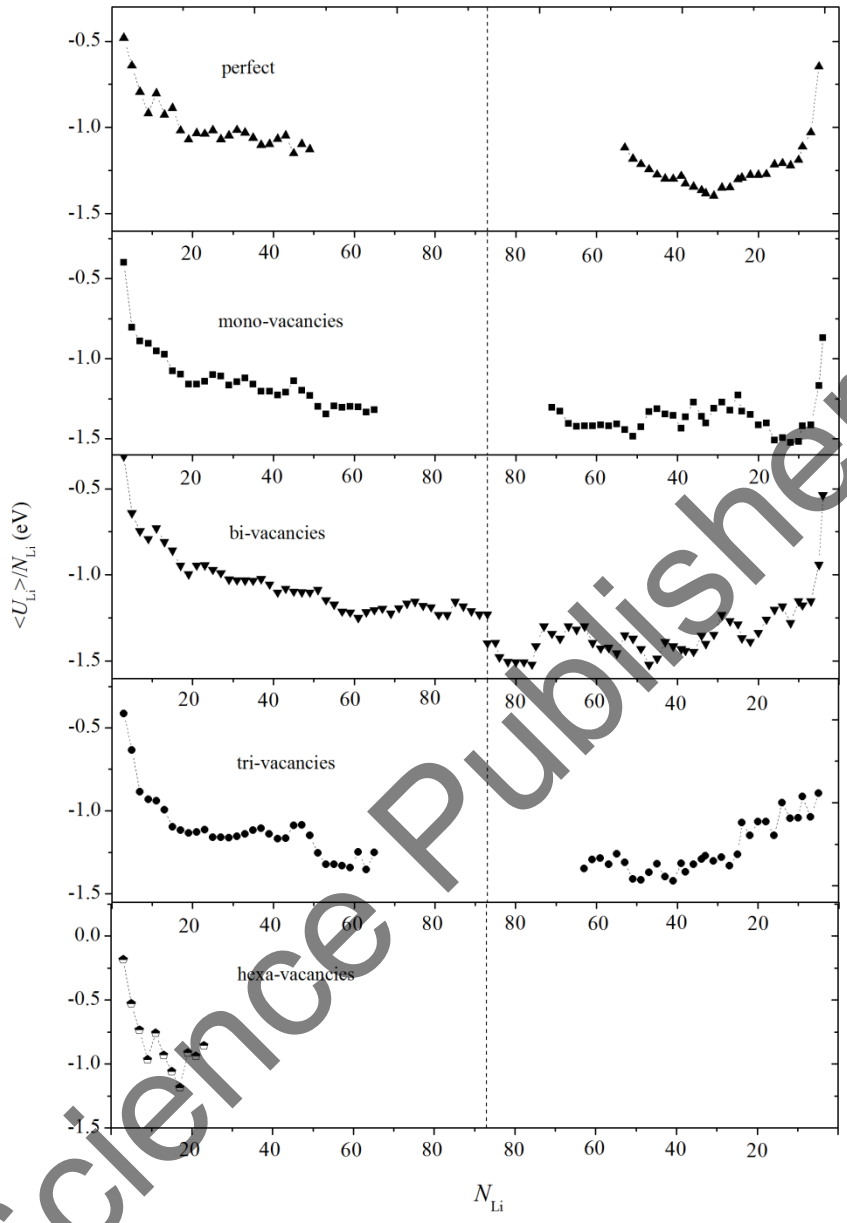

Figure 130. The total energy of lithium atoms in the process of intercalation (left) and deintercalation (right) in silicene channels with the perfect silicene and silicene having mono-, bi-, tri- and hexa-vacancies.

Let us consider in more detail behavior of the defects and attribution of the Li atoms to the silicene sheets by the example of a silicene channel having mono-vacancies and fully filled with lithium. The investigated configurations refer to the instant 0.75 ns (or 7.5×10^6 Δt). The *xy* projections of the upper and lower layers of the channel cut by the mean ($z = h_g^* / 2$) plane are shown in Figure 129. The view is given from the side of the plane $z =$

$h_g^*/2$. Here, h_g^* is the vertical channel size after intercalation of lithium. One of the mono-vacancies of the lower sheet was transformed into a large hole, which, apparently, is manifestation of the destructive effect of the copper substrate on silicene. There is transformation of some mono-vacancies into cyclic formations of the oval form containing from 7 to 9 Si atoms in the upper sheet. Eight mono-vacancies of the bottom sheet and seven mono-vacancies of the top sheet though were deformed, but as the whole have kept the initial form. The upper and lower parts of the channel have equal volumes, but the number of Li atoms in them is different: 37 Li atoms are in the upper part and 30 Li atoms are present in the lower part.

During the intercalation, the total energy U_{Li} of the resulting packing of the lithium atoms decreases (Figure 130). In addition, a particularly fast decrease in the value U_{Li} occurs before the introduction of approximately 20 lithium ions. Subsequently, there was a gradual decrease in the value of U_{Li} with increasing number of lithium atoms N_{Li} in the channel both in the case of the perfect silicene and silicene with mono- and bi-vacancies. Transition to a smoother change in energy is associated with an increase in the number of N_{Li}. Consequently, it is associated with a smaller fraction of the ion energy received by one atom and more favorable arrangement of the Li atoms in the channel. However, in the presence of the tri-vacancies in the silicene, it is possible to observe horizontal sections in the dependence $U_{\mathrm{Li}}(N_{\mathrm{Li}})$ during intercalation. In the presence of the hexa-vacancy in the silicene, the intercalation process provided only the number of ions N_{Li} = 23, and further increase in the number of N_{Li} led to the destruction of the silicene sheets.

The initial stage of deintercalation is not associated with the increase in the energy U_{Li}. On the contrary, in most cases (with exception of the system with tri-vacancies in silicene), the energy continues to decrease. The longest period of U_{Li} decline is observed for a system with the perfect silicene, and the shortest period is when there are bi-vacancies in silicene. In the presence of tri-vacancies in silicene at the initial period of deintercalation, the energy U_{Li} retains the values acquired during intercalation. Deintercalation has always been associated with the yield of Li^+ ions rather than Li atoms from the channel. After remaining about 20 Li atoms in the channel, there was a fast increase in the value of U_{Li} under deintercalation. The fast growth of U_{Li} is due to increase in the deceleration energy of ions per atom with a decrease in the number of atoms in the channel. The system with tri-vacancies in silicene behaves somewhat differently. In this case, an increase in the value of U_{Li} in the final stage of deintercalation occurs much more slowly than in the cases with the perfect silicene. The similar increase is observed in the silicone having mono- and

bi-vacancies. This circumstance is associated with the formation of a less ordered structure of Li atoms in the channel when the tri-vacancies are present in the silicene.

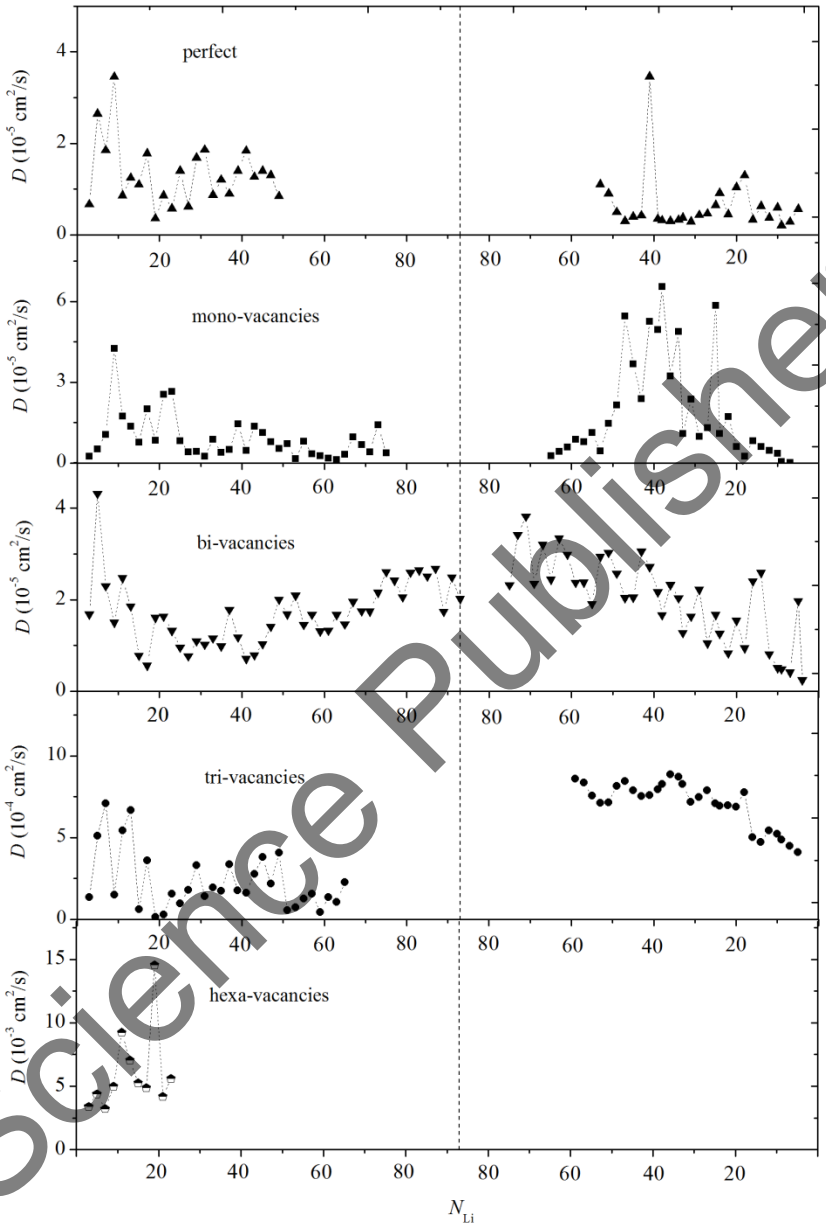

Figure 131. The coefficient of self-diffusion of lithium atoms in the process of intercalation (left) and deintercalation (right) in silicene channels with perfect silicene and silicene having mono-, bi-, tri- and hexa-vacancies.

Behavior of the self-diffusion coefficient *D* of Li atoms in the channel in the processes of intercalation and deintercalation proves to be more unpredictable than the behavior of

the total energy U_{Li} in these processes (Figure 131). Common to the behavior of *D* in all considered cases is its high value in the initial stage of intercalation. This is natural because for a small number of Li atoms in the channel, a larger specific impulse value is transferred from the Li^+ ions that leads to the increase in the value of *D*. However, when the number of Li atoms in the channel becomes larger than 20, the relief of the channel walls begins to exert a strong influence on the mobility of the Li atoms. In this connection, the value of *D* can both decrease (in the presence of mono-vacancies) and increase (in the case of bi-vacancies). The value of *D* also behaves quite unpredictably in the case of deintercalation. This value is subject to narrow (for the perfect silicene) and wide (for silicene with mono-vacancies) bursts during deintercalation. The coefficient *D* can also decrease its values during deintercalation by means of fluctuation changes (as it takes place in the presence of bi-vacancies in silicene) or almost continuously (when there are tri-vacancies in the silicene).

In the case of silicene with tri-vacancies, a sufficiently strong rearrangement of the structure in both sheets of silicene is observed. In the upper sheet, some of the defects retain their shape. The vertical distortion of the sheets after the lithiation/delithiation process is insignificant. Neither one atom of lithium leaves the channel, being trapped between the Si-rings stabilizing structure in the center of the silicene channel.

The local structure of simple substances is best reflected by constructing the Voronoi polyhedra with the subsequent statistical analysis of various elements of the polyhedra. Figure 132 shows the angular distribution of the nearest geometric neighbors for lithium packings in the silicene channels on the Cu(111) substrate at the maximum number of N_{Li}. In all cases, except for the presence of hexa-vacancies in silicene, five peaks can be distinguished in the θ-distribution in the presence of intense background. The presence of more than two peaks in this distribution indicates the existence of a crystalline order in the system [457]. Indeed, a significant number of Li atoms find a stable position in the channel locating above the centers of the Si hexagonal rings. This arrangement of Li atoms creates a certain crystalline order in the metallic phase formed between the silicene sheets. In the turn, when lithium is introduced into the silicene channel that contains the hexa-vacancies, the preferred sites for fixing the metal atoms disappear because of the instability of such large defects at their high concentration.

In general, a wide set of the VP types classified by the number of faces (*n*-distribution) and a wide range of faces differing in the number of sides indicate the irregular packing of Li atoms in the silicene channels. As it is seen from Figure 133, 5 – 7 polyhedra dominate in the VP distributions over the number of faces. Moreover, the pentahedra prevail for Li structures formed in the perfect silicene and in the silicene with mono- and hexa-vacancy. In all cases (with the exception of the *n*-distribution for packing of Li atoms in the perfect silicene) a relatively small number of Li-neighbors for Li atoms is observed. In other words, the packing of atoms is not as dense as, for example, in a simple liquid. A certain

crystalline order in the Li atoms packing is created due to the fact that some Li atoms occupy locations above the centers of the hexagonal cells formed by the Si atoms. Thus, the Li atoms packing in the channels is represented as quasi-crystalline, i.e., irregular, but with elements of the regular placement of atoms. The long tail of the *n*-distribution (extending up to $n = 19$ for Li-packing in the case of the perfect silicene) is absent in the silicene channel with defects. The shortening of the *n*-spectrum in the case of the defective silicene channel is associated with the Li atoms absence in the voids that are present in the silicene.

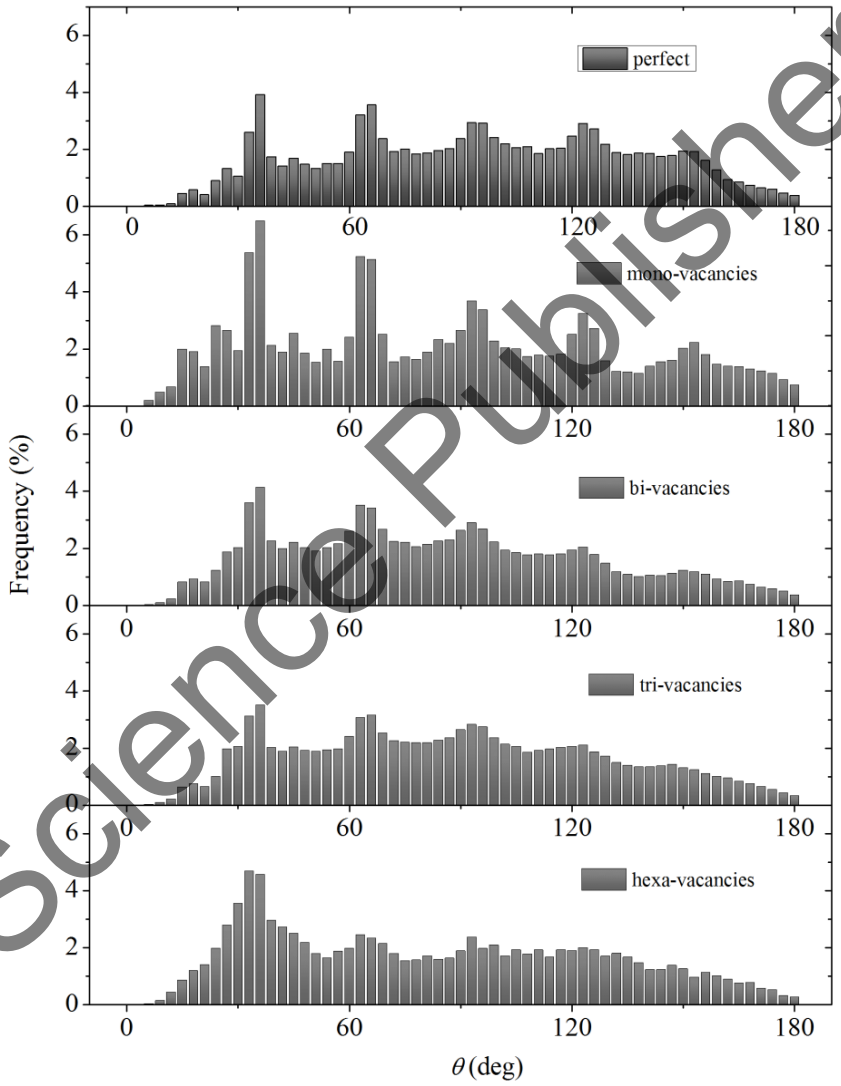

Figure 132. The angular distribution of the nearest geometric neighbors for metal structures obtained as a result of intercalation of lithium in the perfect and defective silicene channels on the Cu(111) substrate.

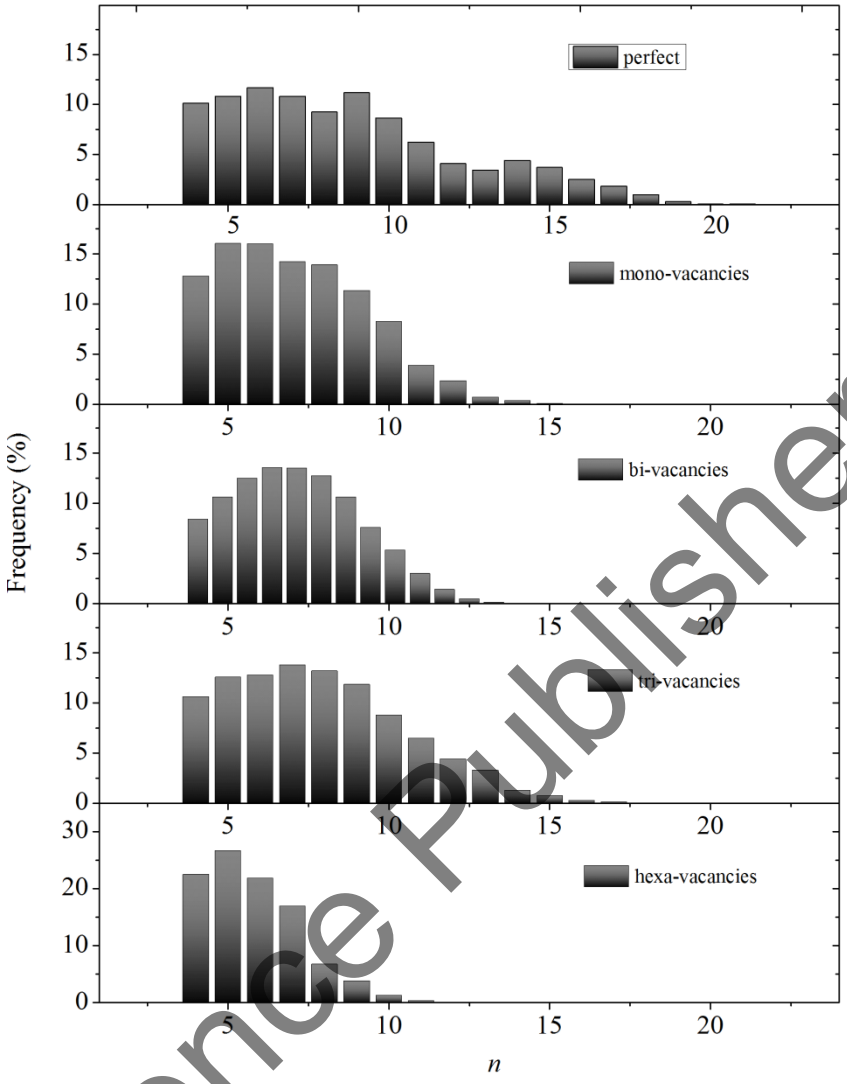

Figure 133. Distribution of the VP types on the number of faces contained therein for metal structures obtained as a result of intercalation of lithium in the perfect and defective silicene channels on the Cu(111) substrate.

The most significant stresses appearing in silicene sheets (when the lithium ions introduce into the channel) are σ_{zz} ones. Both in the lower and upper sheet of the silicene, there are observed bursts of the σ_{zz} stress with approximately the same intensity (Figure 134). The frequency of the bursts is usually increased for the defective silicene sheets. The greatest value of the local stress σ_{zz} for the top sheet of silicene appears when there are tri-vacancies in it under 1.57 GPa. The corresponding value for the lower sheet (σ_{zz} = 1.60 GPa) is found when silicene contains the hexa-vacancies. These values are approximately 7.8% of the ultimate strength (20.45 GPa) [422] and are not critical.

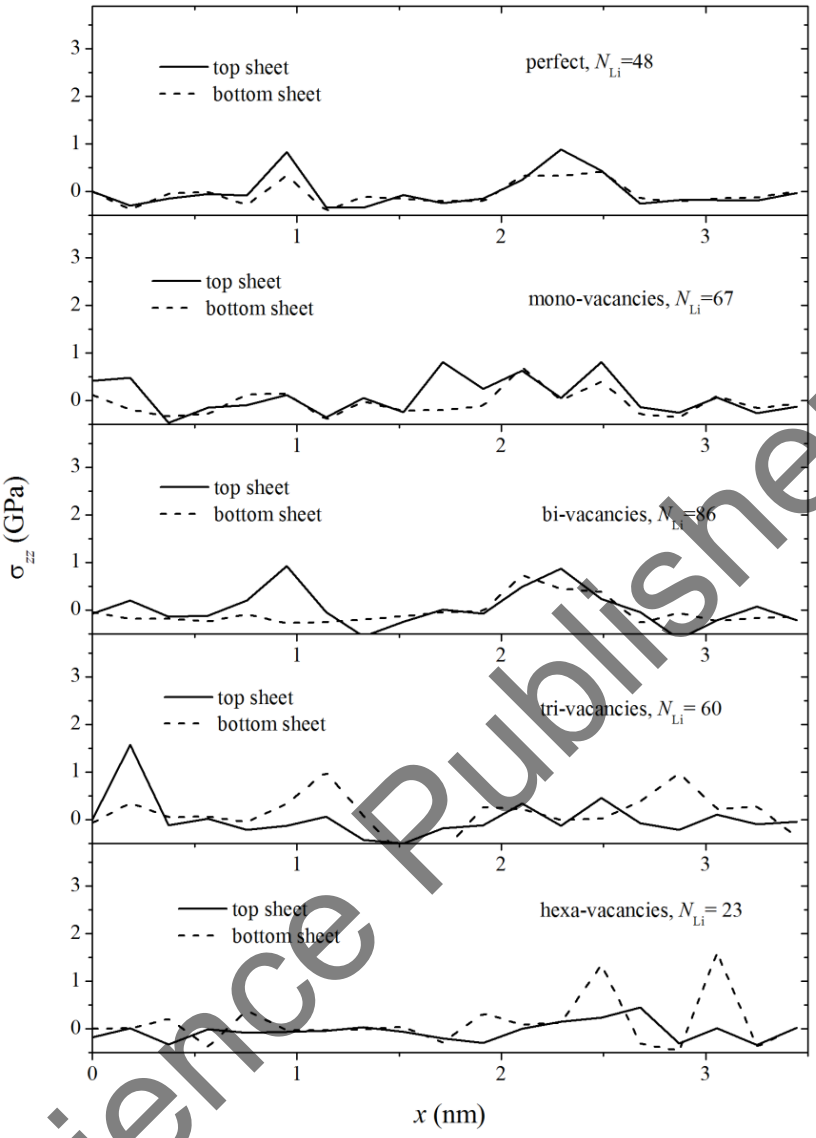

Figure 134. Distribution of the σ_{zz} stresses in silicene sheets forming the flat channel on the Cu(111) substrate when the channel is filled with lithium to the limit depending on the type of defects.

As it is known, the local density approximation severely overestimates the Li–Si binding, which impacts both the relative phase stability between the staged compounds and the Li migration barriers. We are more interested in obtaining the correct order of magnitude for the binding energetics in the high Li concentration range. Therefore, we use the generalized gradient approximation method (GGA). The GGA method (with the improvements described in the Appendix) allows one to establish qualitatively the voltage profile of the Li intercalation into silicene. Figure 135 shows a voltage profile of Li intercalation that consist of the intercalation potentials of Li-undoped silicene to stage Φ[Si→LiSi].

Three thermodynamically favorable phases corresponding to stages I, II, and III (dash-dotted lines in Figure 135) with atomic concentrations of Li $0 \le c < 0.31$, $0.56 \le c < 0.81$, and $0.81 \le c \le 1.00$ can be distinguished in the obtained profile, respectively. The two-phase region, stage I + stage II with $0.31 \le c < 0.56$ is unstable, since has a concentration gradient. The voltage profile is represented by a step function (dotted line in Figure 135), which decreases as the Li intercalation progresses. It occurs without introducing an *ad hoc* empirical parameter characterizing the dispersion energy. In other words, the interaction of mutually polarized electron distributions for Li and silicene is not explicitly considered here. The curve "a" shows an approximation of the $\Phi(c)$ function by a polynomial of degree 5 in the entire domain of $0 \le c \le 1$ definition. It shows the level of decrease in the intercalation potential as silicene is filled with lithium. The points "b" and "d" are joint with the lithium concentrations $c = 0.08$ and 0.16 that correspond to the ratio of the number of intercalated Li atoms into the perfect silicene channel to the number of Si atoms in two and one silicene sheets, respectively.

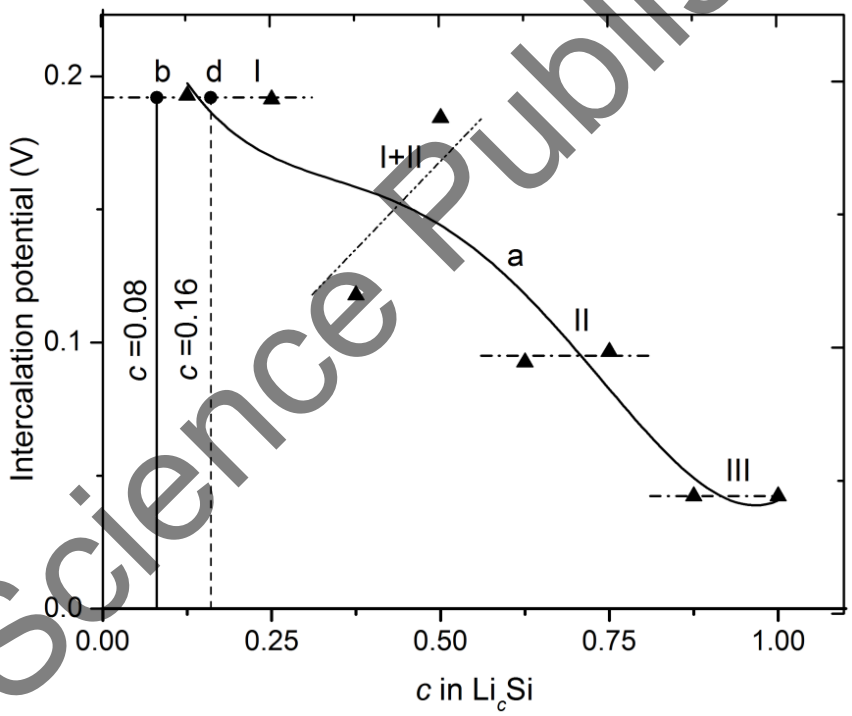

Figure 135. Voltage profile of Li intercalation into silicene; three thermodynamically favorable phases correspond to stages I, II and III; the two-phase region (stage I + stage II) is unstable; the curve "a" reflects approximation of the $\Phi(c)$ function by a polynomial of degree 5 in the entire domain of definition $0 \le c \le 1$; the points "b" and "d" correspond to the lithium concentrations $c = 0.08$ and 0.16, respectively.

Calculations show that silicene used in lithium-ion batteries should have defects only in the form of mono- and bi-vacancies. The use of the perfect silicene and silicene with such defects increases the number of adsorbed Li atoms by 20% (in average) compared to using a silver substrate to support the silicene. The use of silicene with defects (in the form of tri- and hexa-vacancies on the copper substrate as an anode material) not only leads to reduction in the number of adsorbed Li atoms, but, also, to destruction of the anode material. The lithium ions and atoms intercalated into the perfect silicene channel (as well as, into a channel with the mono- or bi-vacancies on the copper substrate) have approximately the same diffusion rate. This diffusion rate increases by more than order of magnitude when using silicene with tri- and hexa-vacancy. However, instability of such a silicene does not allow us to take into account mentioned advantage.

The preferred location of the Li atom in the silicene channel is the site located above the center of the hexagonal Si-ring. However, at the edges of the silicene, the Li atoms tend to be above (or under) the Si ones. This arrangement of Li atoms in the silicene channel creates five peaks in the angular distribution of the nearest geometric neighbors. Defects in silicene reduce the number of nearest geometric neighbors in the lithium atoms packing in the channel. However, the density packing is increased if the silicene has defects in the form of mono- or bi-vacancies. The σ_{zz} stresses acting in the plane of the silicene sheets (caused by the forces of interatomic interaction directed perpendicular to these planes) are dominant in the lithium intercalation into the silicene channel. The stress state of the walls of the silicene channel is not homogeneous. As a result of the lithium atoms and ions motion, the stress bursts appear in the channel. Its magnitude does not exceed 8% of the ultimate tensile stress of silicene.

Now, very incomplete information is available on the chemical and physical properties of silicene. These properties could be controlled by several different methods for the surface or compositional modification. The use of graphene along with silicene in the layered structure will allow strengthening the electrode to counteract the mechanical expansion associated with lithium intercalation. Silicene nanocomposites must create reliability. Defects such as copper cracking and delamination in these structures will be minimized using a barrier/adhesion metal layer. This will also reduce the copper dendrite formation. Particle cracking and lithium plating will also be reduced by using the silicon-based nanocomposite.

The voltage profile is divided into 3 sections corresponding to different stages of the lithium presence in silicene. Our MD studies indicate that each of these stages can be associated with the formation of a certain group of the lithium clusters. The first stage has the boundary value c = 0.31. This value is close to the obtained limiting number of Li atoms attributed to the number of Si atoms in the silicene sheet with bi-vacancies (c_2 = 0.305). This value agrees with the greatest value c achieved in our investigation. This supports the fact that the stages created by the lithium content are determined not by the

structural features of the silicene, but by the kinetic properties of the Li atoms. Until now, silicene has been grown on a metal surface, and it was impossible to separate it from the substrate to create a free-standing material that could then be incorporated into electronic devices. The task of separating the defective silicene from the substrate is even more complicated. This problem has to be solved when it is desirable to use the defective or porous silicene as the anode material.

The performed studies showed that in contrast to crystalline silicon the two-layer silicene does not lead to the irreversible destructive effect caused by the lithium intercalation. The abundance of Si, the high Li capacity of silicene, the flexibility of its atomic layers, and the small energy barrier for Li diffusion are the decisive factors. They allow one to consider silicene as a candidate to be used as the anode material of LIBs. Computer experiment shows that for this purpose it is preferable to use silicene containing mono- and bi-vacancies. It is the presence of these defects in the silicene sheets that contribute to the significant increase in the capacitance of the electrode. Application of nanomaterials based on layered silicon for Li-ion storage can indeed become a practical technology. Nevertheless, our results show that it is difficult to obtain the capacitance values close to the theoretical value for the silicene electrode. It is necessary to pay serious attention to the substrate material, which will be used together with silicene. The absorption properties of silicene (including binding energy with lithium and stability of the silicene to cycling) depend on the substrate material. In particular, copper can be considered as a relatively good material for use as such a substrate. This allows obtaining a good silicene electrode capacity. In this regard, we believe that our findings describe necessary but not sufficient conditions for the design of a high-performance electrode material based on silicene. We emphasize, that in this respect, it is much more important to obtain silicene on a suitable substrate for use in LIBs than to strive to create a free-standing silicene. In addition, more rigid construction of silicene should be created. This construction should provide much less deformation of the silicene sheets during the lithium intercalation and its deintercalation.

Chapter 10

APPLICATION OF CARBON MATERIALS TO SILICENE STABILIZATION

10.1. GRAPHENE SUPPORT FOR SILICENE STABILIZATION

A graphene-silicene-graphene heterostructure was investigated for possible application to Li-ion batteries [470]. The effectiveness of the graphene supports for silicene channels was studied by simulating a lithium ion motion along the channel in an electric field. This motion was studied completely for the gap h_g = 0.75 nm between the silicene sheets. Fixation of the edges of silicene sheets preserves the gap h_g constant along the perimeter of the channel. It is made to avoid the rotation of the sheets due to resultant torque occurring as a result of using the Tersoff potential for modelig the dynamic two-dimensional systems [281, 414].

The model included perfect rectangular silicene sheets of 300 atoms of dimensions 4.7 × 4.0 nm (12 atoms along each edge of the sheet). Nine mono- or poly-vacancies were distributed approximately uniformly over the area of the silicene sheet. Therefore, the number of Si atoms in each sheet was 291, 282, 273, and 246 for the sheets with mono-, bi-, tri-, and hexa-vacancies, respectively. A constant electric field of 10^5 V/m was directed along the *x* axis oriented in the "zig-zag" direction of graphene sheets. Such an external action to the Li^+ ion could ensure the ion passage of the entire channel in the direction of the *x* axis. The graphene sheets were placed in parallel to the silicene sheets outside the channel. The front edges of graphene and silicene sheets were aligned with each other. The rectangular graphene sheet contained 820 atoms (20 atoms along each edge). The initial position of the ion corresponded to the channel height $h_g/2$. The ion was located near the middle of the sheet along the coordinate *y* and slightly shifted (*x* = 0.198 nm) inside the silicene channel.

Figure 136 shows the trajectory of a lithium ion in a constant electric field *E* inside the silicene-graphene channel when each silicene sheet contains 9 mono-vacancies. After

starting from point 1, the ion makes several vertical oscillations in the course of the translational motion. Then it approaches the exit and, after a short delay accompanied by fast increased vibrations, leaves the channel (point 2). Both graphene sheets are buckled outwards.

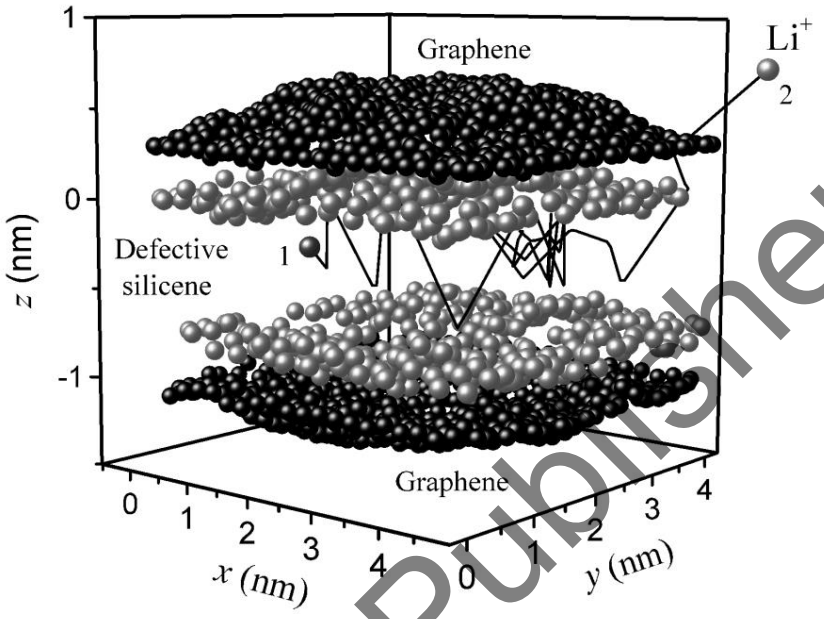

Figure 136. The trajectory of the lithium ion inside the silicene channel supported from both sides by graphene sheets; the gap between the sheets is h_g = 0.75 nm, the motion occurs in a constant electric field ***E***; each silicene sheet contains 9 mono-vacancies; 1 and 2 are the initial and the final trajectory points, respectively.

The radial distribution functions averaged over both silicene sheets are shown in Figure 137. The RDF of the perfect silicene (curve 1) has two distinct first peaks localized at 0.239 and 0.399 nm, respectively. The distance of 0.239 nm between the nearest neighbors was found in the complete relaxation of the structure of the two-layer silicene [30]. At the second peak, the left and weakly expressed right shoulder is found. All other peaks in the RDF are of much less intense. The RDF of silicene changes after the introduction of defects into it. Thus, the first two peaks of the function $g(r)$ for silicene with hexa-vacancy (curve 2) are symmetrical and characterized by a lower intensity than the corresponding peaks of the RDF of the defect-free silicene. Their location is determined by the values of 0.256 and 0.409 nm, i.e., both peaks are shifted to the right with respect to their location in the perfect silicene. The third peak of the RDF represented by curve 2 is bifurcated and its intensity decreased. However, the total number of peaks remained unchanged. Changes in the silicene RDF (with the defects created in it) indicate the process of structural relaxation, possibly, associated with the destruction of defects.

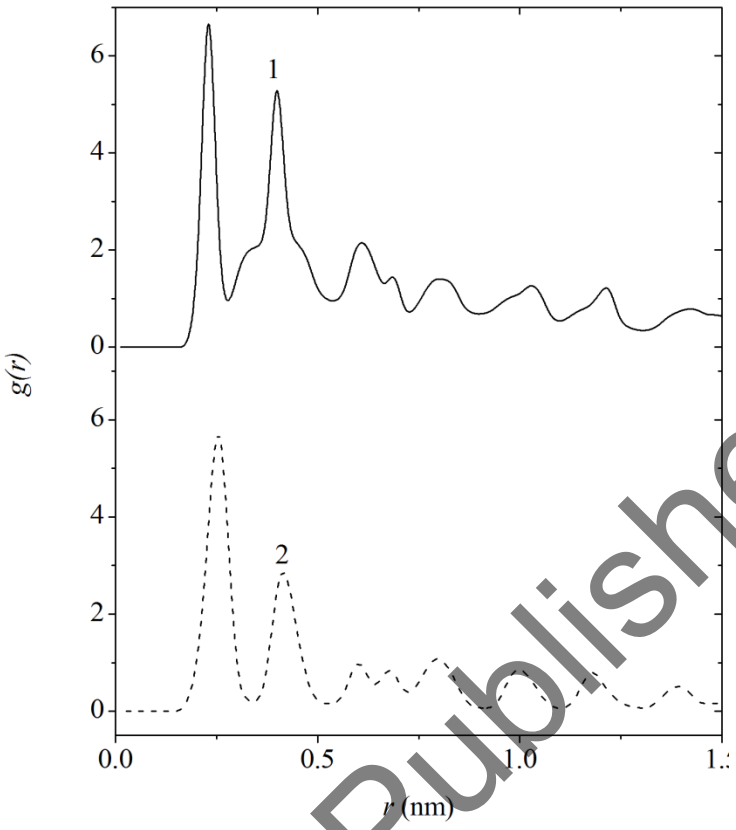

Figure 137. The function of radial distribution of silicene (common for the upper and lower sheets) in presence of the Li^+ ion in the planar channel: 1 perfect silicene, 2 silicene with hexa-vacancies.

Figure 138 shows the *xy* projections of the top sheets of the defective silicene with different types of vacancies obtained at the instant 150 ps. It is seen that at this instant a part of the vacancy defects did not retain its shape. Moreover, some of them completely collapsed or disappeared altogether or completely lost the semblance of their initial contour. So, three of the 9 mono-vacancies disappeared (Figure 138a) forming a junction of two five-membered rings marked with circles in the figure. Two bi-vacancies turned into cavities of a significantly smaller size by forming the five-membered rings. The rings were woven with the eight-membered formations using their common atoms (Figure 138b). All atomic formations are marked in the figure with circles and ovals. The five-membered rings (marked with circles) also actively participate in the transformation of tri-vacancies leaving cavities of different sizes (outlined by ovals). As a rule, these cavities have sinuous boundaries (Figure 138c). The boundaries of some hexa-vacancies are partially rounded, but in the whole, these defects retain their individuality and are still easily recognizable (Figure 138d). Thus, despite the stabilizing influence of graphene sheets, the gradual destruction of the vacancy defects in silicene is observed. In this case, the size of most pores decreases and the atomic structure becomes more disordered. The large defects

formed by the removal of 6 atoms retain better than the small ones. Probably, the increased stability of hexa-vacancies is associated with the absence of the need for rebuilding bonds in silicene when the entire hexagonal cell is removed during the formation of this defect.

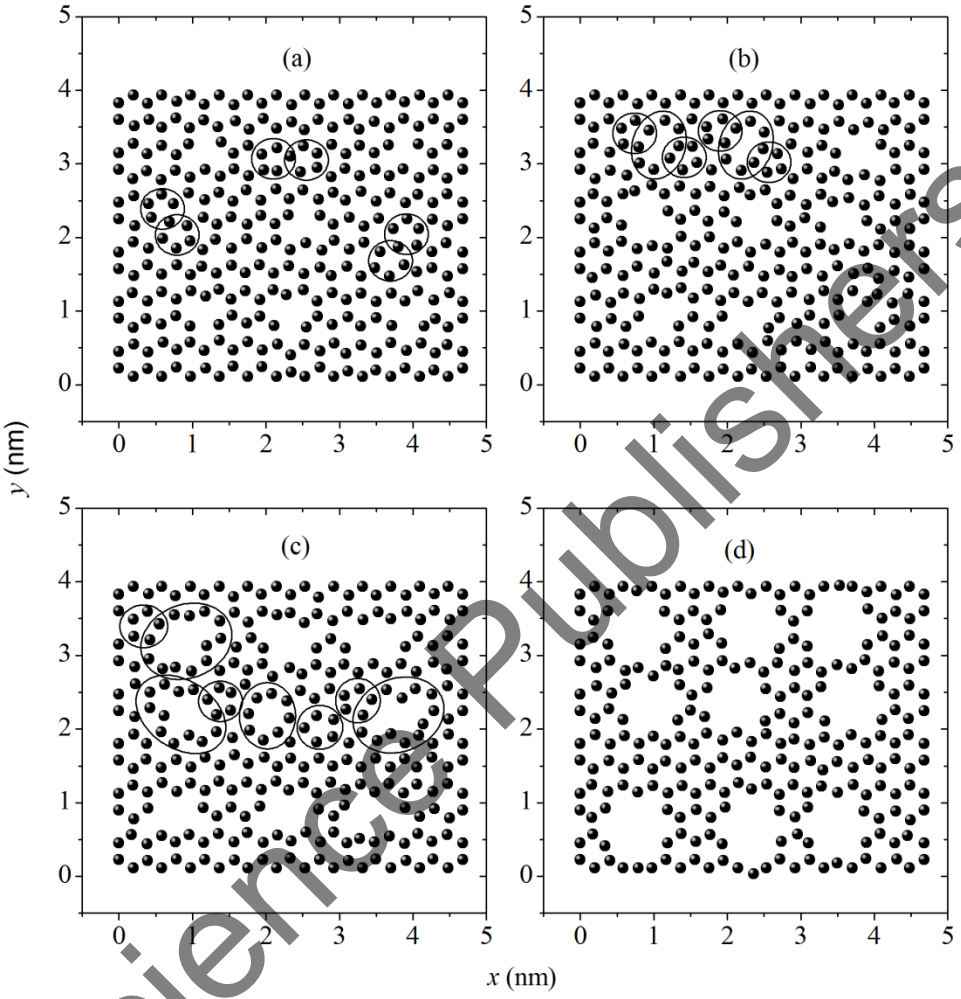

Figure 138. The *xy* projections of the top sheet of silicene containing: (a) mono-, (b) bi-, (c) tri-, (d) hexa-vacancies, referring to the instant 150 ps; circles show the five-membered rings, and ellipses present the multi-link cyclic formations.

Despite the presence of the graphene support, the motion of the ion along the channel increased the roughness R_a of both sheets of the perfect silicene and silicene with mono- and bi-vacancies (Figure 139) with respect to the roughness of the perfect silicene sheets at the initial instant R_{a0}^{per}. However, R_a decreases and becomes even smaller than R_{a0}^{per} in the presence of the larger vacancies in silicene. Roughness in the lower silicene sheet is much higher than R_a of the upper sheet only for the case of silicene sheets with

bi-vacancies. There is not enough free space (in the plane of silicene sheets formed by mono- and bi-vacancies) to change the preferential displacement of atoms from the vertical to the horizontal direction. However, the presence of the tri-vacancies in silicene sheets makes such a transition possible, and it retains in the case of hexa-vacancies.

The inset in Figure 139 shows the time dependencies of the $R_a^{\text{vac}} / R_{a0}^{\text{per}}$ ratio for the upper and the lower silicene sheets in the case of bi-vacancies. The greatest relative error in determining the ratio obtained for the upper sheet of silicene does not exceed 8%.

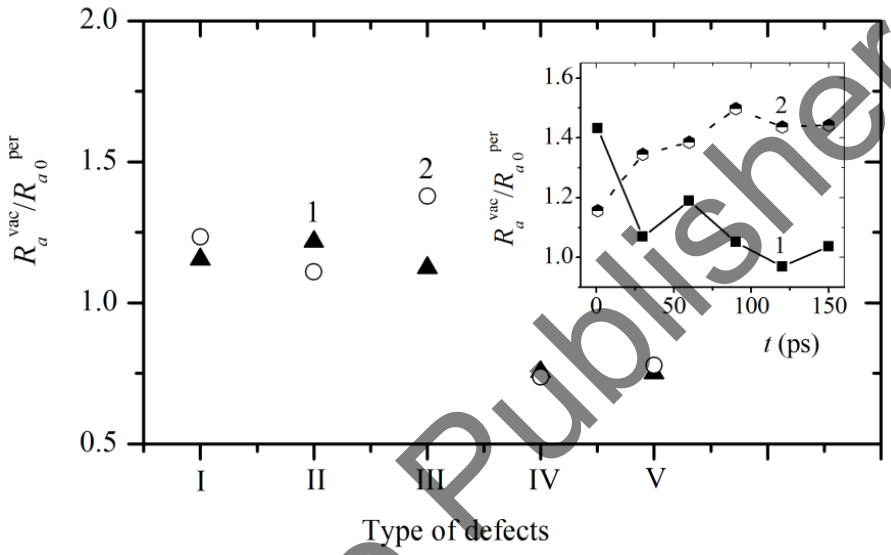

Figure 139. Relative roughness of the silicene sheets, depending on the type of their defects obtained during motion of the Li^+ ion inside the channel: 1 is the top sheet, 2 is the bottom sheet; the inset shows time dependences of relative roughness for the upper (1) and the lower (2) silicene sheets.

It is interesting to consider how the self-diffusion coefficient D_{Si} of Si atoms changes as a result of changing the relief of channel walls from the defect-free to one containing various types of vacancy defects. Figure 140 shows the mobility characteristics of atoms D_{Si} of the lower and upper silicene sheets as well as the change of their mean values (dashed line). In general, the mobility of the Si atoms increases non-monotonically with the size of defects. However, the average atomic mobility even decreases in the case of mono-vacancies and remains almost at the same level as in the defect-free silicene in the case of tri-vacancies. It is worthy to note that there is a large difference between D_{Si} values of the lower and the upper silicene sheets with bi-vacancies and very close values of this quantity for the corresponding sheets with hexa-vacancies. The large difference between

D_{Si} can be explained by the different effect of the Li^+ ion on the mobility of the atoms in the sheets with bi-vacancies, while close D_{Si} values for the sheets with hexa-vacancies are more likely due to the sufficiently high stability of such structures.

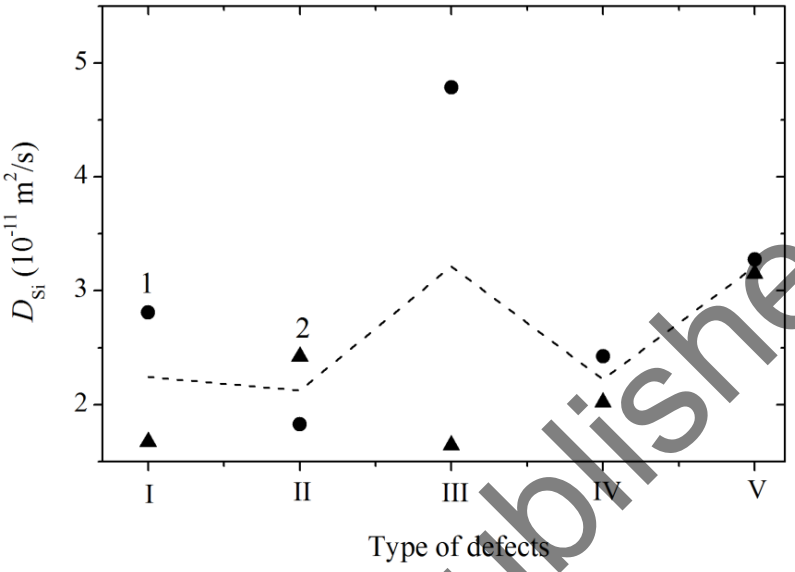

Figure 140. Self-diffusion coefficient of Si atoms in the lower (1) and the upper (2) silicene sheet: I is the perfect silicene, II, III, IV, and V is the silicene with mono-, bi-, tri-, and hexa-vacancies, respectively; dashed line shows the average mobility for the case of two silicene sheets.

Figure 141 shows the values averaged over the top and bottom sheets of the distribution of the principal stresses acting in the plane of the perfect silicene sheets during the motion of the Li^+ ion through the channel. Attention is attracted to the low values of the stresses σ_{zz} caused by the action of forces normal to the plane of the sheets. However, these stresses are still 2.2 times higher than the σ_{zz} stress appearing in the similar system in the absence of any ion. We also note significantly higher values of the stress σ_{zy} (with respect to σ_{zx} and σ_{zz} stresses) which is also caused by the motion of the Li^+ ion through the channel. Moreover, the maximum value of the stress σ_{zy} under the presence of the ion exceeds the corresponding characteristic under its absence by 8.4 times. The analogous increase for the stress σ_{zx} is only 2.2 times.

The total stresses σ_{zx}, σ_{zy}, and σ_{zz} (determined by equation (23)) under the influence of the moving ion increased in 6.6, 8.6, and 2 times for the bottom sheet and 3.2, 10.3, and 2.2 times for the top sheet of silicene, respectively. Thus, the displacement of the Li^+ ion through the channel significantly enhances the stress state of the silicene sheets.

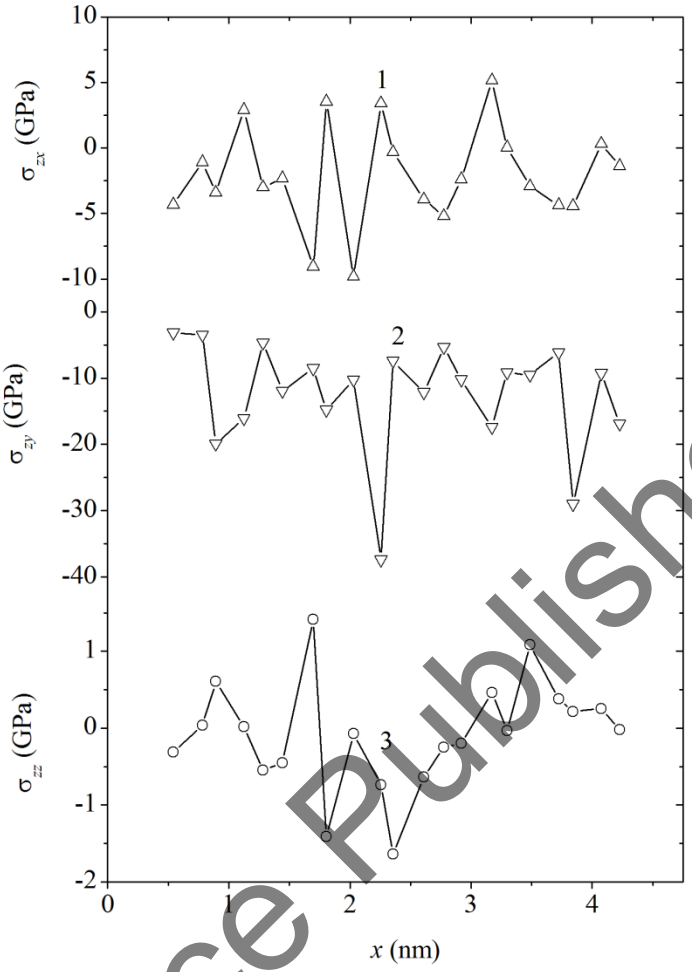

Figure 141. Distribution of the average stresses in the plane of silicene sheets: 1 σ_{zx}, 2 σ_{zy}, 3 σ_{zz}; elementary areas are elongated along the *y* axis.

Figure 142 shows the absolute value of the total stress $|\sigma_{zy}|$ in silicene sheets as a function of the size of the defects. This characteristic of stress is the largest for almost all considered silicene sheets with rare exceptions for the $|\sigma_{zx}|$ value. It is seen that the magnitude of the stress in the lower silicene sheet (data 2) is always much larger than the corresponding characteristic of the upper sheet (data 1). Both the upper and lower perfect silicene sheets possess much larger $|\sigma_{zy}|$ values than any corresponding sheet of the defective silicene. The magnitude of stress σ_{zy} in the lower sheet decreases in silicene with mono- and bi-vacancies with respect to its value in the defect-free silicone. Then the value σ_{zy} increases for the cases of tri- and hexa-vacancies. Thus, starting with the tri-vacancies, the dimensional effect of defects works in the opposite direction to increase the internal stress in silicene.

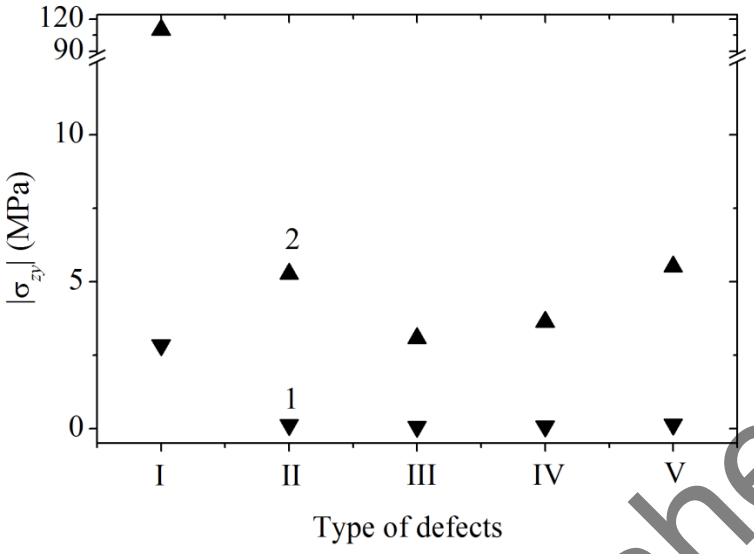

Figure 142. Magnitude of total stress σ_{zy} in the lower (1) and the upper (2) sheet of the perfect silicene (I) and silicene with mono-(II), bi- (III), tri- (IV), and hexa-vacancies (V).

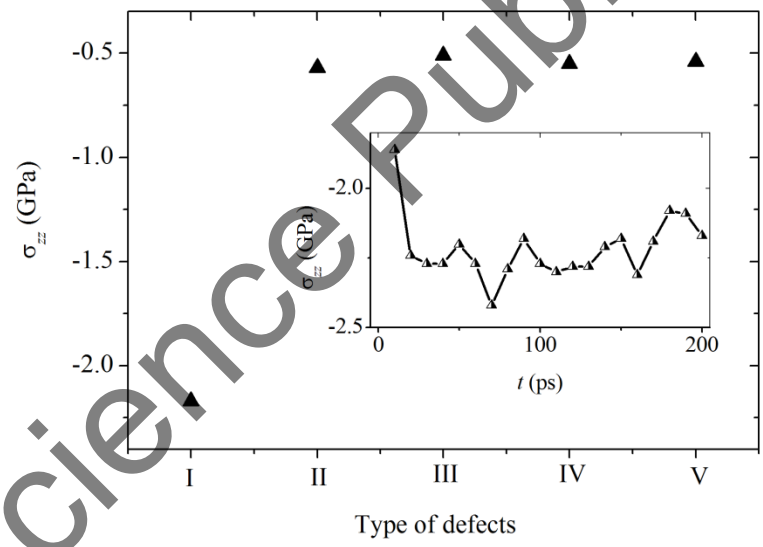

Figure 143. Dependence of the average stress σ_{zz} in sheets of graphene on the type of defects in the silicene channel with the Li^+ ion moving in an electric field: I is the perfect silicene, II, III, IV and V is the silicene with mono-, bi-. tri- and hexa-vacancies, respectively; in the inset, the time dependence of the average stress in graphene sheets is shown.

Moving along the silicene channel, the lithium ion creates a stress state in the graphene sheets supporting this channel. The stress component σ_{zz} is dominant in this case. Moreover, when sheets of the perfect silicene form the inner flat channel, the average value of the component σ_{zz} for graphene sheets takes on the largest absolute value. In all the

cases, the values considered are negative. It shows the compression deformation due to the action of forces normal to the plane of the sheets. The stresses σ_{zz} in sheets of graphene supporting the walls of a flat channel from defective silicene have the similar values. These values are significantly (4 times) less than the corresponding stress characterizing the support of graphene for the perfect silicene (Figure 143). The inset in this figure shows the time dependence of the σ_{zz} value for the case of graphene supporting the perfect silicene sheets. There is a fast convergence in determining this characteristic. The relative error in the calculation does not exceed 8%.

The natural buckling of silicene leads to the loss of the sp^2-hybridization and decreases the stiffness of the base plane. The linear chains of atoms are formed when the buckled silicene is ruptured [442]. It is assumed that any state of silicene has a certain level of stability loss, i.e., the flat structure of this material is metastable. The calculated Young modulus for silicene (62 N/m) [471] is significantly inferior to the corresponding characteristic of graphene (342 N/m) [472]. It is assumed that the presence of the silicene between graphene sheets can increase its stability level. The analysis of scanning tunneling microscopy images indicates the formation of the defects with more than three missing silicon atoms [446]. Undoubtedly, the presence of polyatomic vacancies has a great influence on functioning the ultrathin materials with monoatomic thickness and limits their stability.

Hexa-vacancies in the functioning silicene-graphene channel turned out to be the most stable defects, which throughout the calculation retained their size and shape. The perpendicular electric field $E_{\perp}$ opens a band gap in silicene. The method to open the band gap in silicene is to make a periodic array of holes in it, i.e., to fabricate the silicene nanomesh (SNM) [473]. It is suggested to use the SNM model built by digging a simple triangular array of the hexagonal holes in a silicene sheet to create a transistor. Let us denote the width of the wall between nearest-neighbor holes as N_{SNM} integer determined by the number of hexagonal honeycombs located between the holes. Theoretical calculations show that the SNM behaves semi metallically like the pristine silicene when N_{SNM} is odd. When N_{SNM} is even, the band gap of silicene hexagonal nanomeshes is opened at the Γ point of the Brillouin zone. There is a linear relationship between the width of the band gap E_{g} and the field strength $E_{\perp}$: $E_{\mathrm{g}} = (e\Delta)E_{\perp}$, where e is the elementary electric charge, Δ is the buckle height in the silicene layer. The maximum band gap of about 0.68 eV is observed.

The largest of the stresses (σ_{zy}) that appear in the perfect silicene sheet under the Li^+ ion motion along the flat channel is at least 10 times inferior to the experimentally established limiting stress for the tension of polysilicon. This material is widely used in the contemporary electronics [474]. The stress created in the supporting sheet of graphene is more than 40 times less than the limiting stress observed in computer models when

graphene is tested for a break [374]. Thus, the motion of the Li^+ ion along the silicene-graphene channel does not create any threats to the destruction of the channel material.

Vacancy defects reduce the total stress state of the silicene created when the ion moves along a flat channel. If there are defects in the silicene, the much lower stress is created in the graphene supporting the silicene sheets. Graphene support allows one to make the silicene channel more passable for the lithium ion.

In the study of the Li^+ ion passage through the graphene channel, the optimum gap (h_g = 0.60 nm) between graphene sheets was found. With this gap, the ion passes the entire channel in the direction specified by the electric field strength 10^3 V/m without losing contact with graphene [427]. The similar characteristic was determined in the present work when a Li^+ ion passes through a silicene-graphene channel. The transit time under the constant electric field of 10^5 V/m in the defect-free silicene-graphene channel having the gap of 0.75 nm was 12.8 ps. This time increased by 2.2 and 4.8 times for the ion drift in the channel with mono- and bi-vacancies, respectively. The Li^+ ion does not pass through the entire channel with the similar gap and electric field strength if the tri- or hexa-vacancies are present on the silicene walls. It is worthy to note that controllability of the ion motion can be lost even with a larger gap. For example, at the gap of 0.80 nm and E = 10^5 V/m the Li^+ ion is present in the similar channel during 31.2 ps and eventually, it exits through its imaginary frontal surface. Thus, it should be assumed that the optimal gap for the Li^+ ion passage through the silicene-graphene channel is 0.75 nm.

The mechanical test of silicene is difficult because of the rather small thickness of the material. The present study of the passage of lithium ion through the silicene-graphene channel made it possible to obtain a numerical characteristic of the emerging stressed state in the channel. Large local stress fluctuations in silicene are due to the action of the forces lying in the plane of the silicene sheets and perpendicular to the intensity vector of the applied electric field. The optimal parameters for the Li^+ ion motion through the channel are established by the electric field strength and the gap between the silicene sheets forming the channel. Vacancy defects filling silicene walls of the channel significantly reduce stresses both in the silicene and graphene walls of the channel. The passage through the channel decreases with a consistent increase in the size of defects. Unlike mono- and bi-vacancies, the tri-, and hexa-vacancy do not cause any increase in roughness of the silicene walls of the channel. Mono-, bi-, and tri-vacancies in the silicene walls of a channel with a moving Li^+ ion are prone to failure due to the formation of the five-membered rings of silicon atoms. The hexa-vacancies in silicene demonstrate greater resistance to degradation than other defects when the graphene support occurs in the silicene channel. The shape of the radial distribution function confirms the crystalline nature of the atoms ordering in such a system. Thus, the mechanical properties of silicene (including the defected one with a graphene coating) allow this material to be used as an anode of the lithium-ion batteries.

10.2. COMPUTATIONAL STUDY OF PROPERTIES OF SILICON THIN FILMS ON GRAPHITE

Thin film silicon solar elements are frequently produced by deposition in vacuum using carbon as a substrate. Pyrolytic graphite, extruded graphite, and glassy carbon are among the carbon materials that serve as substrates. Auger spectroscopy of the interface region reveals the formation of the silicon carbide, while the carbon diffuses deeply into the silicon [475]. Silicon also diffuses deeply into carbon except in the case of glassy carbon. Thin films of silicon on graphite can potentially be used for solar elements due to their low cost. Silicon films are deposited on graphite substrates via sputtering or the pyrolytic deposition of silane crystallize from the liquid phase [476]. A melted zone can be created on a graphite substrate by an electron beam irradiating at a constant rate. Gas inclusions in the silicon ensure the formation of the silicon carbide during crystallization. As a result, a silicon/graphite interface with the high ohmic resistance is formed.

The super-thin silicon films of mono-atomic thickness (silicene) have already obtained on some substrates. Hexagonal rings are the basis of the silicene structure, as well as, that of graphene. However, there is a slight deviation from the ideal plane in a silicene sheet. Experiments show that the shift of some Si atoms out of the plane ranges from 0.06 to 0.08 nm [477]. For silicene, π and π^* branches in the Brillouin zone intersect linearly on the Fermi level forming a so-called Dirac cone [478, 479]. This means that the charge carriers in silicene behave like the Dirac massless fermions moving with the ultra-fast Fermi velocities of ~ 10^5 – 10^6 m/s [17]. Until now, it was possible to obtain silicene only on some types of substrates and among them, silver ones were most common: Ag(111), Ag(110), and Ag(100). The advantage of silver substrates is explained by passivation of the unsaturated edges from Si atoms and *p–d* hybridization between the internal Si atoms and the Ag substrate [480]. In addition, calculations based on the density theory indicated that the local difference between the energies of silicon atoms on the surface could be the key factor. Moreover, this factor determines the suitability of a substrate for the epitaxial growth of silicene on a metallic surface. This difference is minimal for the silver substrates [17]. Therefore, there is a high probability of chemical interaction between the Si atoms of a thin film and the material supporting it when dealing with both carbon and metallic substrates. Such interaction explains why silicene still cannot be separated from a substrate. At the same time, obtaining free-standing silicene is very important to both fundamental research and applications.

Graphite formed by 3775 carbon atoms was represented by five graphene layers (755 atoms in each layer) arranged according to the scheme ABAB… with the inter-layer distance h_g = 0.371 nm. The inter-atomic distance within the layers was 0.142 nm. The layers of the system were parallel to the *xy* plane. Here, we will study two types of Si films on graphite. The first type is a film made up of ten Si(100) layers with a diamond-like

silicon lattice and interatomic distance $r_{\text{Si-Si}}$ = 0.234 nm. The second type is bi-layer silicene with the inter-planar distance 0.2481 nm obtained from the density functional theory calculations [432]. These both silicene sheets possess the reconstructed 4×4 surface. The Si(001) film contained 1280 atoms, while the bi-layer silicene was formed by 600 Si atoms. The distance between silicene sheets and graphene (graphite sheet) was the same as in [432], i.e., 0.222 nm. The free boundary conditions were applied to the entire system in three directions of coordinate axes. The simulation was performed at the temperature of 300 K in the NVT ensemble. The first stage concerned with modeling the films and the substrate separated from each other in a vacuum. Duration of these calculations was 50 ps that was enough for each system to come into equilibrium by establishing the Maxwell distribution of atomic velocities. Then, the film and substrate were brought into contact, and the main calculation was carried out with the duration 200 ps. In this study, the Si–C interactions, also, as the Si–Si and the C–C ones were described by the many-body Tersoff potential [40, 428, 481], and all the atoms participated in the motion. The free boundary conditions were used.

Figure 144 shows configurations of the films on graphite substrates obtained as a result of the main MD calculation (200 ps). It is seen that each subsystem preserves its integrity both in the case of Si(001) film on graphene and in the case of bi-layer silicene. All surfaces of the Si(001) film including the lateral ones are subjected to considerable structural relaxation. In general, the upper surface of the film remains horizontal. Three graphite sheets closest to the film are substantially deformed. Both films have strong contact with the top graphite sheet. The lower silicene sheet undergoes strong structural changes, while the upper sheet (with exception of individual edges) preserves the honeycomb structure and horizontal surface. Only two upper graphite layers adjacent to silicene undergo substantial changes in their shape. The average distance between the silicon and graphite surfaces is preserved in both cases. The final value of cross-coupling energy $E_{\text{Si–C}}$ for the system with silicene (– 1.45 eV/atom) is lower than for the system with the Si(001) film (– 1.07 eV).

In general, the two-dimensional crystalline structure (though not completely perfect) is preserved in silicene on graphite. The radial distribution function for the Si atom closest to the center of the sheet adjacent to graphite in both cases demonstrates numerous peaks corresponding to the regular structure (Figure 145). When constructing this function, we considered the coordinates of Si atoms in the lower silicene sheet or in two lower (already mixed) crystalline layers of the Si(001) film. Remember that one crystalline layer of the silicon film contains 128 atoms. Therefore, the combined film layer contains 256 Si atoms, which is closer to the number of atoms (N = 300) in the silicene sheet. The positions of the first two maxima of $g(r)$ in the combined lower film layer are close to those in the lower silicene sheet: r_{m1} = 0.24 nm, r_{m2} = 0.39 nm (in the film) and r_{m1} = 0.23 nm, r_{m2} = 0.40

nm (in silicene). The third peak (at 0.46 nm) exhibited by $g(r)$ for the lower layer of the Si(001) film is absent in the RDF of the lower silicene sheet. The following maxima appear at 0.57 nm for the Si(001) film and at 0.59 nm for silicene.

An important characteristic feature of the RDF for silicene is the higher intensity of the first peak $g(r)$ with respect to other peaks. Therefore, the intensity ratios of the first four $g(r)$ peaks for the lower silicene sheet (1:0.46:0.30:0.23) are very different from those of the corresponding Si(100) film layer (1:0.75:0.54:0.37). In other words, the short-range order or preservation of the honeycomb structure in silicene is the characteristic feature of the silicene structure.

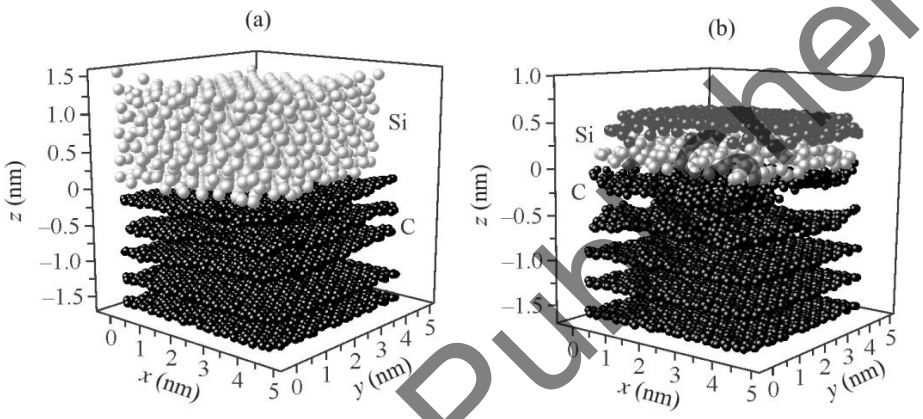

Figure 144. System configuration: Si(001) film on graphite (a) and bi-layer silicene on graphite (b) at the instance 200 ps.

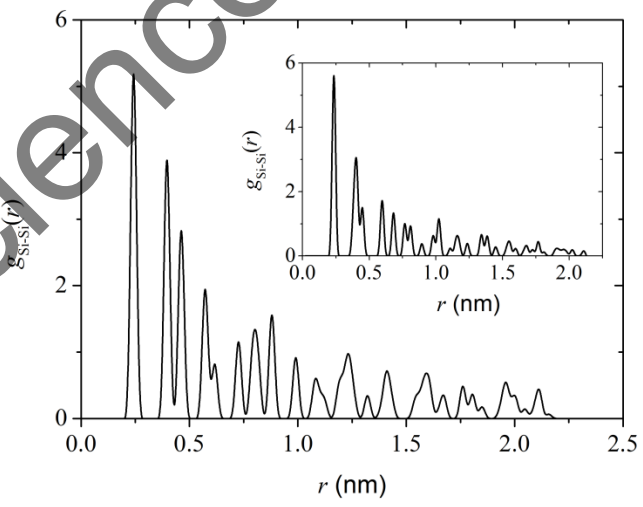

Figure 145. Radial distribution function for the central atom of the lower (256 atomic) Si(001) film on graphite; the inset shows RDF for the silicene sheet on graphite.

The lithium ion motion along the silicene channel was investigated in the constant electric field of 10^5 V/m. Here, the gap between the channel-forming sheets has the width of 0.70, 0.75, 0.80, and 0.85 nm. The channel was located on a graphite substrate. Sheets of the perfect silicene, as well as, silicene containing vacancy defects were used for the creation of the channel. On each sheet of silicene with the area of ~ 20 nm^2, there were 9 mono-, bi-, tri-, or hexa-vacancies. The time of each test was 100 ps or 1 million time steps of computation. The model and test method corresponded to these calculations described in Section 8.1. Here, the simulation was also performed under the free boundary conditions, the graphite atoms were immobile, the Si–Si interactions were described by the Tersoff potential [281, 414], and the Si–C interactions were represented by the Morse potential [431, 482].

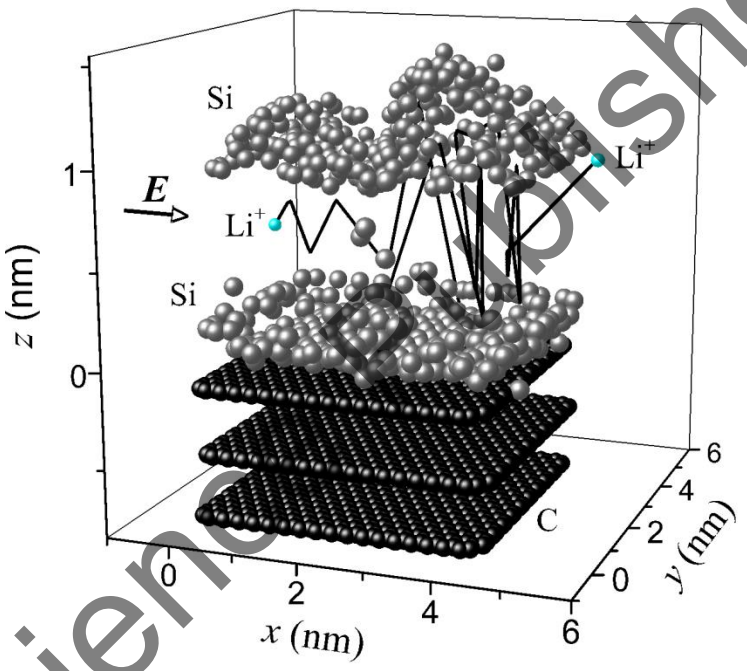

Figure 146. Configuration of the system "coupled sheets of silicene with bi-vacancies on graphite" with the initial gap between sheets with h_g = 0.80 nm is shown together with the trajectory of the lithium ion motion along the channel during the time 32.5 ps; the constant electric field ***E*** acts along the *x* axis.

The general view of the system "coupled sheets of silicene with bi-vacancies on graphite" is shown in Figure 146 after 32.5 ps from the start of the Li^+ motion in the channel. The channel has the initial gap h_g = 0.80 nm. The Li^+ ion enters the channel from the left side (Figure 146) and has both the horizontal and vertical displacements. It moves in the electric field. The intensity vector is directed along the *x* axis. It is seen that in the course of the calculation noticeable vertical displacements of the Si atoms occur both in the upper and lower sheets of the silicene. Moreover, in passage from silicene with mono-

vacancies to one with hexa-vacancies, the magnitude of the displacements increases. The similar picture is observed for systems with Ag(001) and Ag(111) substrates [448]. In the presence of both silver and graphite substrates, the Si atoms are rearranged in the plane of the lower sheet of silicene. On the silver substrates, in the presence of defects in the upper sheet of silicene, significant structural rearrangements are also observed.

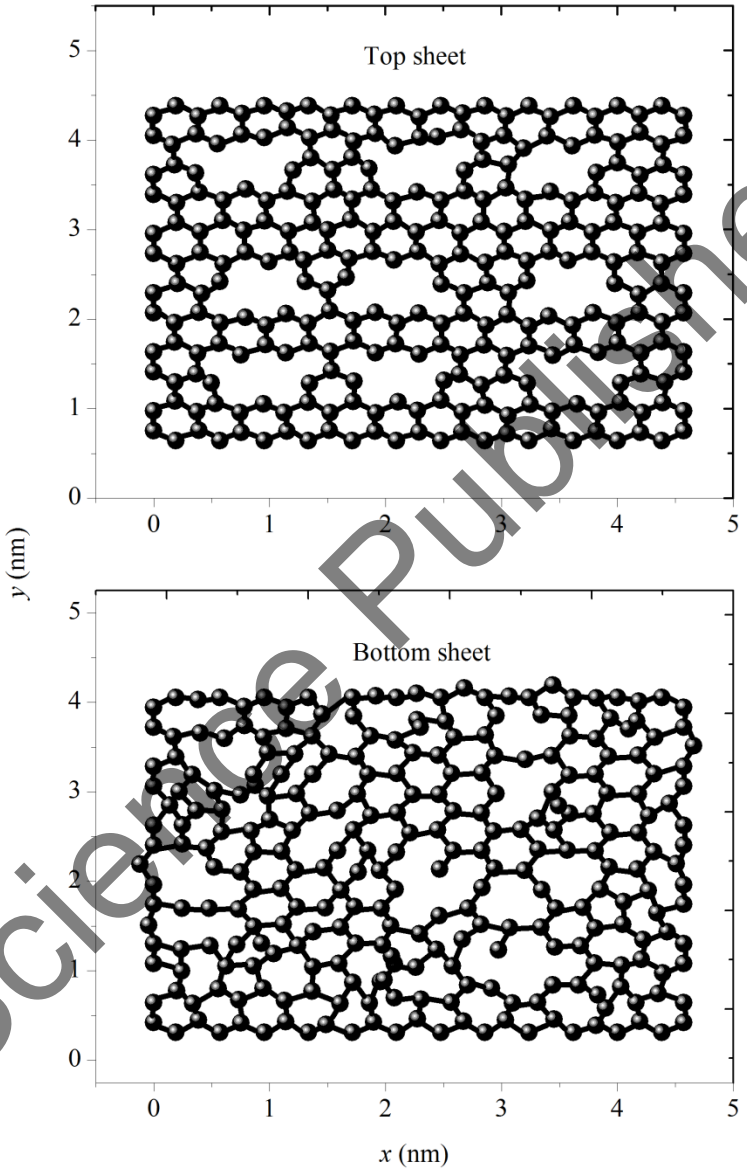

Figure 147. *xy* projections of the upper and lower sheets of silicene with tri-vacancies on the graphite substrate, with the inter-layer gap of 0.75 nm and at the instant 100 ps.

Figure 147 shows the *xy* projections of the upper and lower sheets of silicene with tri-vacancies obtained at the instant 100 ps. The silicene was placed on a graphite substrate. It is seen that the substrate has a strong influence on the structure of the lower sheet of silicene, whose snapshot at the end of the calculation has changed greatly. At the same time, the top sheet has retained not only all nine defects, but with their size and shape extended significantly.

The number of pores in the underlying lower sheet of silicene increased, but the size of most pores became smaller than the size of the original tri-vacancy. Most of the pores formed in the lower silicene have meandering boundaries, but there are also pores with smooth boundaries. It is worthy to note that atoms with two dangling bonds appeared in the strongly rearranged structure of the bottom sheet. Thus, the incompatibility of periods of the silicene and graphene lattices (on the graphite surface) exerts a strong influence on the structure of the defective silicene after the lithium ion passage through the entire channel.

The statistical-geometric method of representing the inhibitory effect in the channel was carried out by constructing the Voronoi polyhedra for the ion every 1000 time steps. Thus, during the time of the ion passage through the channel, there were built from 600 to 1000 of the VPs. Figure 148 shows the angular distributions of geometric neighbors encountered in the ion path in channels with the perfect silicene walls, as well as, with silicene sheets containing bi- and hexa-vacancies. The vertices of the corners are places of localization of the ion. The sides of the angle are the rays drawn from the center of the ion to its nearest geometric neighbors. It is seen from the figure that these characteristics change significantly not only when the defectiveness of the channel walls changes, but, also, when its gap changes.

As a rule, the intensity of the peaks lying near angles of 30° and 45° increases as the size of the gap increases. However, the growth of these peaks slows down as the size of the defects increases. These peaks are formed due to the most distant geometric neighbors. The number of such neighbors increases with expansion of the channel and decreases because of the increase in the size of the defects. The behavior of the peaks mentioned is mainly due to these factors. In the angular range $120° \le \theta \le 180°$, the angular spectra show greater stability as the channel gap increases. The expansion of the channel has a weak effect on the number of the nearest geometric neighbors of the ion.

Figure 149 shows the faces number distributions of VPs (*n*-distributions) formed around the Li^+ ion moving along the channel. These distributions also characterize the number of all Si atoms entering the nearest environment of the Li^+ ion. In the case of a channel with walls of the perfect silicene, 9 Si atoms most often surround the Li+ ion if the gap is $h_g \le 0.75$ nm. However, as the gap increases, the certainty in determining the most preferable number of Si atoms surrounding the ion decreases. Thus, for $h_g = 0.80$ nm, the 13- and 15-atom Si environment of the Li^+ ion occurs most often, but for $h_g = 0.85$ nm the

4-atom Si environment dominates. The appearance of vacancy defects in the channel walls makes the Si environment of the ion even more unpredictable. Only in the channel formed by silicene sheets with mono-vacancies and h_g = 0.70 nm, preference is given to the 15-atom Si environment. In other cases, as a rule, there is great uncertainty in establishing this characteristic.

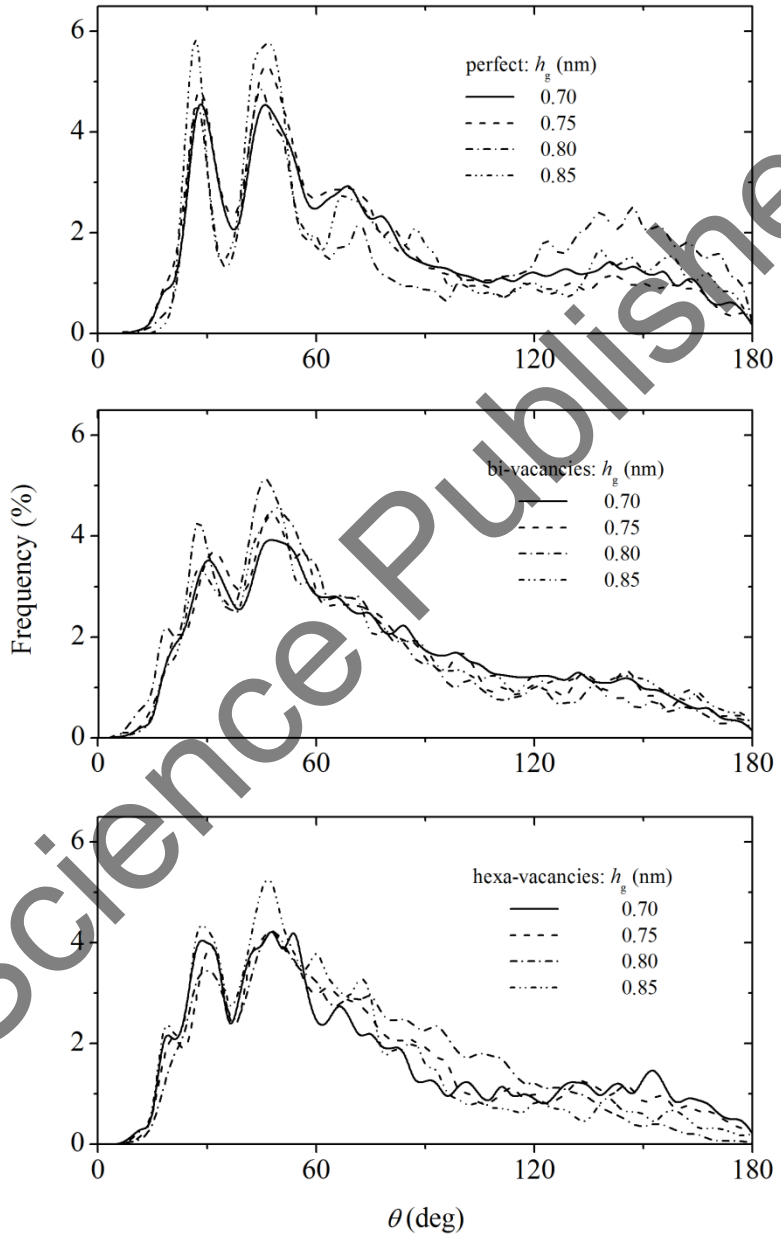

Figure 148. Angular distributions for the geometric neighbors of the lithium ion during its motion along various silicene channels.

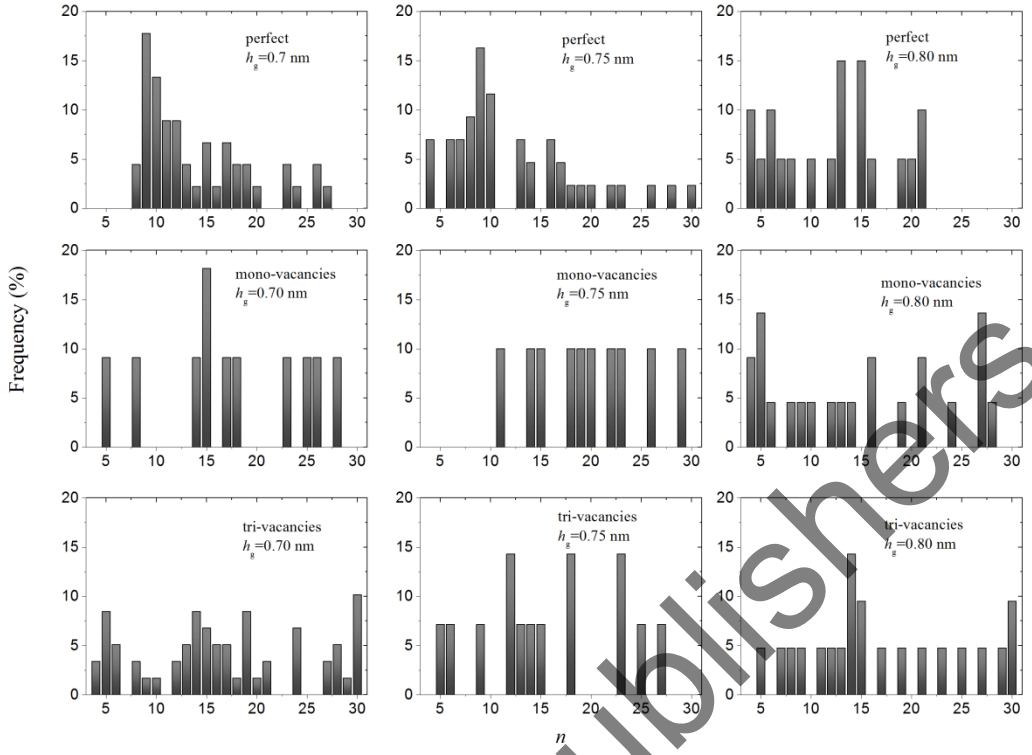

Figure 149. The frequency of occurrence of the number *n* of Si atoms included in the nearest geometric neighbors of the Li^+ ion during its motion along the perfect silicene channel and the channel, whose walls contain different vacancy defects; h_g is the width of the gap of the silicene channel.

Exclusion of small geometric elements in the Voronoi polyhedra allows one to proceed to an analysis of the more probable geometric neighbors found in the environment of the Li^+ ion. Truncated polyhedra have *n*-distributions that are more compact because they have not small faces. In this case, the value of *n* does not exceed 25 (Figure 150). However, even in this case, it is difficult to find regularity in dependences of the number of the most probable faces on the value of the h_g gap of the silicene channel and on the size of the defects in the silicene sheets. It is seen from Figure 150 that the peaks with an intensity greater than 15% exist only in the *n*-distributions for the channel with perfect walls and with walls having mono-vacancies.

Figure 151 presents the distribution of the rings (*m*-distribution) formed by Si atoms around the Li^+ ion moving along the channel with walls from the perfect and defective silicene at different gaps h_g. For the gap h_g = 0.70 nm, the peak of the *m*-distribution is shifted from the value $m = 10$ to the values $m = 5$ and 4 when the channel with the perfect silicene walls changes to the channel with walls containing bi- and hexa-vacancies, respectively. The maximum of the *m*-distribution lies in the range of values $3 \le m \le 6$ in

the remaining cases shown in Figure 151. Influence of the bi-and hexa-vacancies on the formation of the short-range order around the moving Li^+ ion proves to be most noticeable in the narrowest channel considered here (for h_g = 0.70 nm).

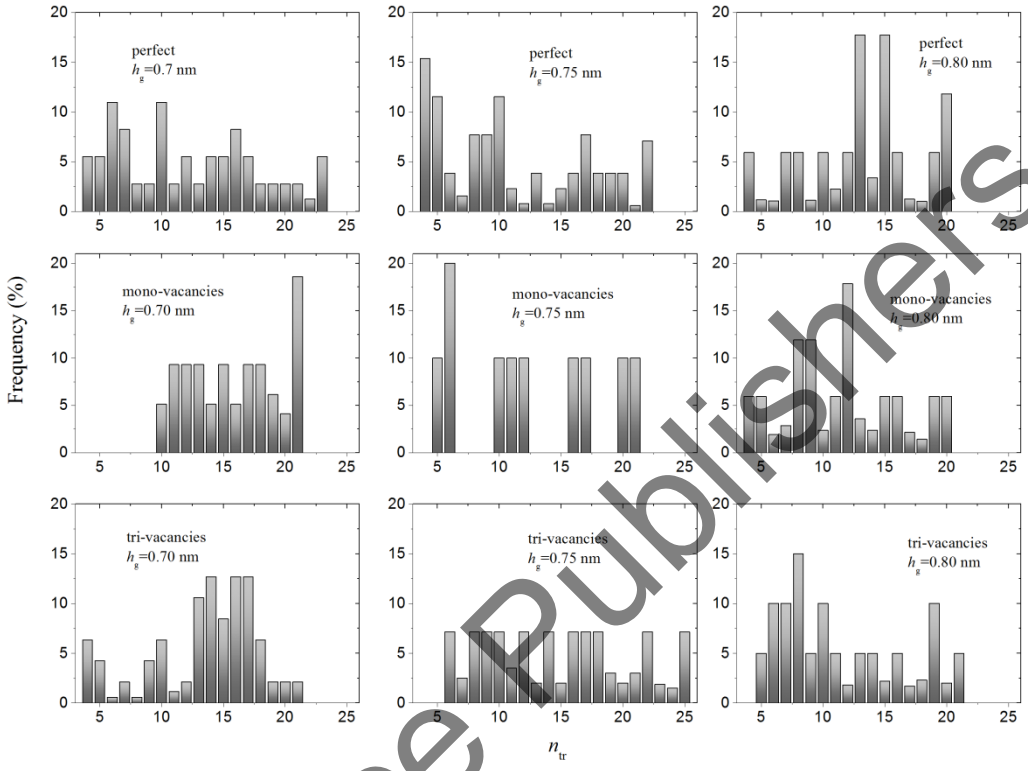

Figure 150. The frequency of occurrence of the number n_{tr} of Si atoms included in the more probable geometric neighbors of the Li^+ ion during its motion along the perfect silicene channel and the channel, whose walls contain different vacancy defects; h_g is the width of the gap of the silicene channel.

Statistics of the *m*-membered rings existing around the moving Li^+ ion is significantly clarified in the case of passage from the Voronoi polytopes to truncated polyhedra. Figure 152 shows the distributions for the truncated polyhedra faces (m_{tr}-distribution) characterizing the motion of the ion Li^+ in silicene channels with different gaps h_g. Here, sheets of the perfect and defective silicene form the walls. In this case, the four-membered rings predominate in the narrowest considered channels (with h_g = 0.70 nm) regardless whether its walls contain any defects. The four- and five-membered rings are the most representative in the remaining cases shown in Figure 152. Moreover, the channel expansion more often leads to the appearance of the main peak of the m_{tr} distribution at m_{tr} = 5.

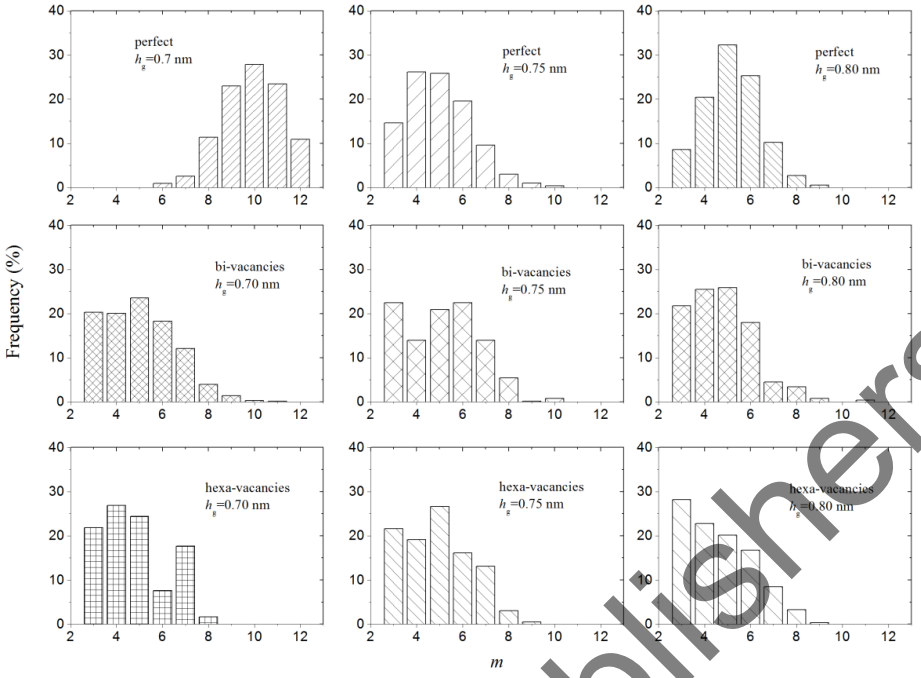

Figure 151. The number of Si atoms forming rings around the Li^+ ion in channels with different gaps with the walls having various defects.

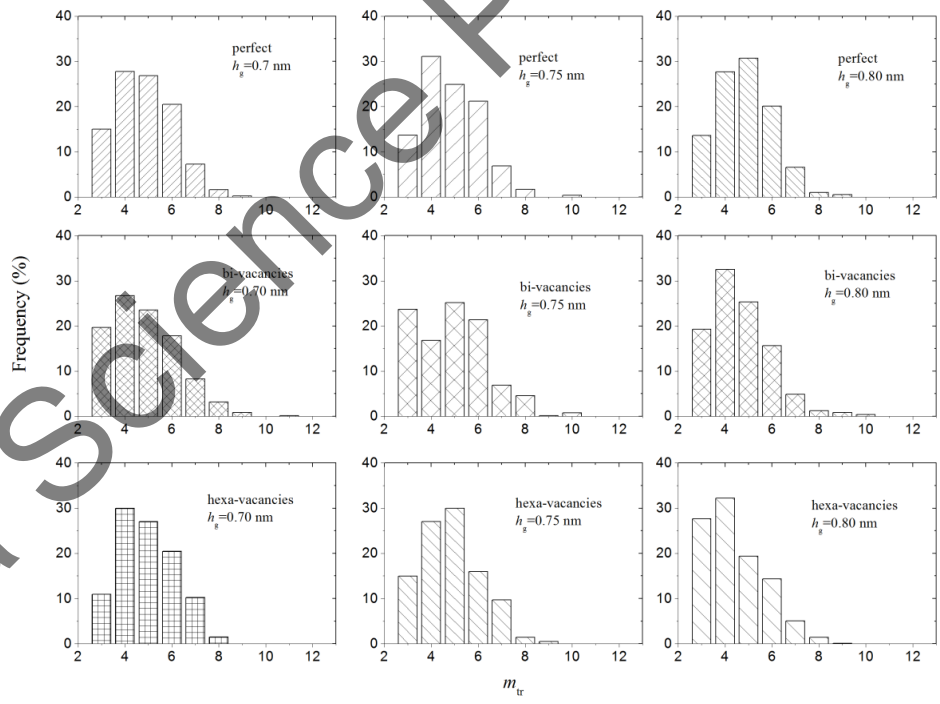

Figure 152. The number of Si atoms that form the averaged rings around the Li^+ ion in channels with different gaps with the walls having various defects.

Figure 153 presents the distribution of distances (*r*-distribution) to the nearest geometric neighbors of the Li^+ ion in different channel types and at different gaps. The appearance of defects in the channel walls leads to a decrease in the standard deviation of the *r*-distribution. On the average, a reduction in the standard deviation (for the channels constructed from the defective silicene with respect to the channel formed by the perfect silicene) was 19%. Change in the channel gap leads to an ambiguous change in the distance r_{mp} from the ion to the most probable geometric neighbor. Averaged over the channel gap, the value of r_{mp} is 0.588, 0.542, and 0.546 nm for the perfect silicene channel and the channels with mono- and hexa-vacancies, respectively.

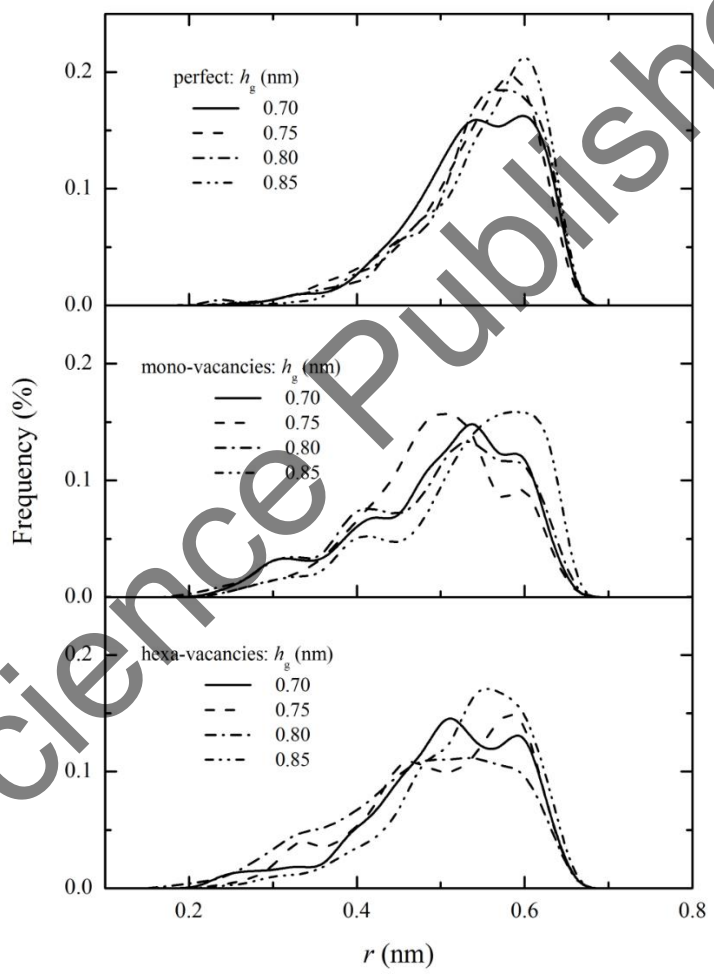

Figure 153. Distribution of distances to the nearest geometric neighbors of the Li^+ ion in the channel with walls of perfect and defective silicene at various gaps h_g.

Figure 154 shows the distribution of the most significant stresses σ_{zz} acting in the plane of the silicene sheets during the the Li^+ ion motion through the channel. The elementary areas are elongated along the *y* axis. The electric field of intensity 10^5 V/m is directed along the *x* axis. Here, the explicit dependence of the intensity of the σ_{zz} stress fluctuations on the value of the channel gap and on the type of defects present in the silicene is not traced. Since the force creating the stress σ_{zz} is usually directed downward (due to the attraction of the silicene to the graphite substrate), the stress values σ_{zz} are usually negative. The strongest local stresses appearing when the Li^+ ion moves through the channel in absolute value are not more than 1.65 GPa or 0.693 N/m. This value is 8.4 times lower than the tensile strength for silicene obtained in [422]. Thus, when the Li^+ ion moves through the channel formed by sheets of a perfect or defective silicene, there are no dangerous local stresses capable to cause the destruction of silicene.

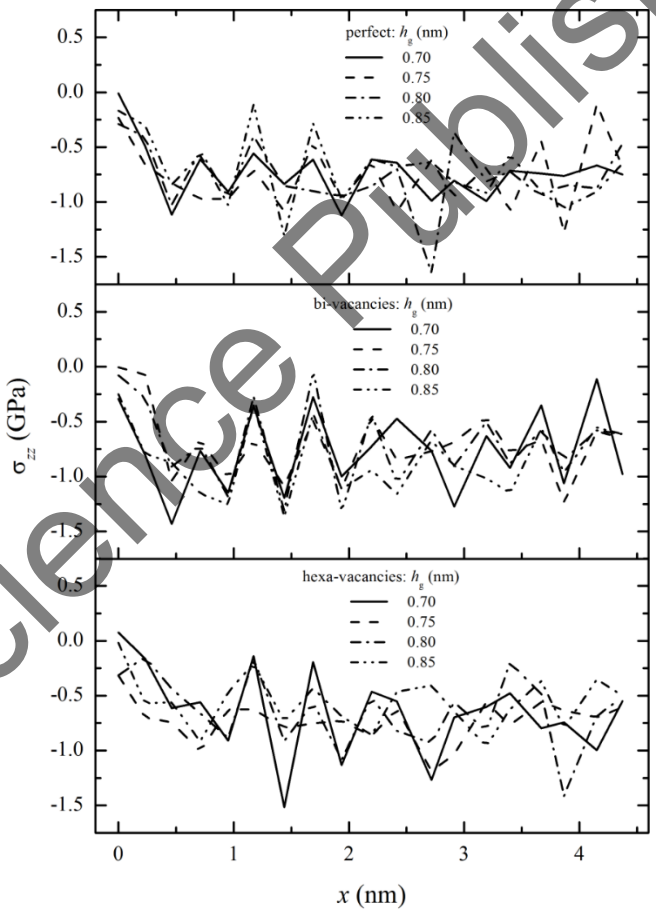

Figure 154. Distribution of the stress $\sigma_{zz}(x)$ averaged over both sheets of the perfect and defective silicene along the *x* axis ("zig-zag" direction) coinciding with the direction of the electric field strength for different gaps.

The motion of the Li^+ ion in the flat silicene channel is much more complicated than in the similar graphene channel. Thus, under the gap of h_g = 0.60 nm the electric field strength $E = 10^3$ V/m and the gap between the sheets with is sufficient for the Li^+ ion passage through the perfect graphene channel of length 4 nm and without substrate [414]. The lithium ion completely passes the perfect silicene channel (without substrate) of the same length at $E = 10^5$ V/m beginning with the gap h_g = 0.75 nm between the channel walls [427].

The Li^+ ion motion through the silicene channel becomes even more complicated in the presence of the vacancy-type defects in the channel walls. So, with the gap of 0.80 nm and the field strength of $E = 10^5$ V/m, the ion passes through the channel for less than 35 ps if the channel walls contain mono- and bi-vacancies. However, the ion cannot leave the channel if there are tri- and hexa-vacancies in its walls even for 100 ps [436].

In the case when the defective silicene on both sides was supported by the single-layer perfect graphene, the lithium ion managed to completely pass (during < 0.65 ps) the narrower channel (h_g = 0.75 nm) with walls including mono- and bi-vacancies. However, such a channel with walls that have tri- and hexa-vacancies cannot be passed by the Li^+ ion for 100 ps [449]. Thus, the use of silicene instead of graphene as the anode material requires expansion of the gap between adjacent sheets and a significant increase of the electric field strength.

In the present study, we found that with the electric field strength of 10^5 V/m, even narrower silicene channel with the gap of h_g = 0.70 nm ensures passage of the lithium ion if the channel is supported by the graphite substrate. In this case, the patency of the channel is preserved not only in the presence of the mono- and bi-vacancies in its walls but, also, in the presence of tri- and hexa-vacancies in them.

Table 16. Time of passage of the lithium ion through a silicene channel located on a graphite substrate (ps)

Type of vacancies in silicene	**Gap size (nm)**			
	0.7	0.75	0.8	0.85
Perfect	45.4	42.2	20.4	73.6
Mono-vacancies	10.3	12.2	24.3	16.5
Bi-vacancies	74.5	Ion does not leave the channel	35.2	16.8
Tri-vacancies	64.0	13.8	21.2	25.9
Hexa-vacancies	16.7	18.2	Ion does not leave the channel	19.4

For the lithium ion, the transit times are shown in Table 16 for the silicene channel located on the graphite substrate. The greatest passage time of the channel (74.5 ps) at the gap of 0.70 nm is fixed when the walls contain bi-vacancies. The Li^+ ion remains during 100 ps in the silicene channel with the gap of h_g = 0.75 nm and walls containing bi-vacancies. Nevertheless, the ion passes this channel rather quickly (faster than 36 ps) in the presence of the tri- and hexa-vacancies in its walls. The tri-vacancies in the channel walls do not interfere with the Li^+ ion for its complete passage through it. This was observed for all considered gaps (0.70 – 0.85 nm) and for the time not exceeding 64 ps. In the case of hexa-vacancies, the channel obstruction for 100 ps appears only at the gap of 0.80 nm.

Strong interaction with the substrate destroys the lower and upper sheets of both the perfect and defective silicene on the Ag(001) and Ag(111) substrates. Therefore, this material is unsuitable for designing the anode of the lithium-ion battery [448]. Thus, the use of the graphite substrate to support the silicene channel creates a better channel for the lithium ion passage than the use of the silver substrate or bi-layer support of the silicene channel with graphene sheets.

In all the cases considered, the Li^+ ion motion along the silicene channel cannot be regarded as the motion of a particle in a disordered medium. This is indicated by the appearance of two peaks with locations lower 50° in the angular distribution of the nearest geometric neighbors. For disordered systems, there is only one peak in this region [483].

The calculated polyhedron distributions over the number of faces extend to a wide range of values reaching n = 30 in some cases. This behavior of the n-distribution cannot be a characteristic for disordered systems. In addition, many of the calculated n-distributions have a large number of equiprobably distributed types of faces. The last feature is likely to be a specificity of 2D systems, which is also preserved when we move to consideration of the statistical distributions for truncated polyhedra. The type of distribution of the VP faces on the number of sides is largely determined by both the size h_g of the gap and the type of defects contained in the walls of the channel. Both these characteristics also influence the form of m-distributions constructed for the truncated polyhedra. The similar assertion is valid as a whole for distributions of distances from the ion to the nearest geometric Si neighbors.

Location of the silicene channel on graphite significantly reduces the maximum local stresses $|\sigma_{zy}|_{max}$ appearing in the walls of the channel when the Li^+ ion moves along it. Thus, the $|\sigma_{zy}|_{max}$ average value (for the silicene channel placed on the graphite) is approximately in 2.4 times less than that found on the Ag(001) and Ag(111) substrates. It is also 5.3 times less than the $|\sigma_{zy}|_{max}$ value obtained when graphene is used to support the channel [448, 449]. Attenuation of the $|\sigma_{zy}|_{max}$ stress under transition to a nonmetallic substrate is associated with much weaker Si–C interactions than in Si–Ag interactions.

A sharp decrease in the $|\sigma_{zy}|_{\max}$ value (when the silicene channel is on the graphite) can be explained by the removal of its second wall from the substrate on a distance exceeding the distance between the silicene and the supporting graphene by at least 4.4 times. In addition, the initial distance $r_{\text{Si}-\text{C}} = 0.286$ nm between the lower layer of silicene and graphite was greater than the distance (0.222 nm) between silicene and graphene in the hybrid channel. There is a very weak influence of the graphite substrate on the top sheet of silicene. The structure of this sheet can persist throughout the simulation even there are large defects in the sheet such as tri- and hexa-vacancies.

Scanning the sheets of the perfect silicene and silicene containing vacancy-type defects by the lithium ion motion in the channel was considered. It showed that the channel formed by the sheets has a specific structure that is not similar to the structure of the 3D the ordered or disordered materials. The structure of layered 2D materials is characterized by the presence of two distinct peaks in the angular distribution of the nearest geometric neighbors. The locations of these peaks are limited by the condition $\theta_1, \theta_2 < 50°$. The structure of 2D silicon is described by a very wide set of nearest geometric neighbors determined for the moving center.

Regardless of the presence of defects of one or another type in silicene sheets, the number of geometric neighbors for the lithium ion lies in the range of 4 – 30. A noticeable presence of an equal probable distribution of various geometric neighbors is a common characteristic for the 2D silicon spectra. Depending on the width of the gap in the channel and the type of defects contained in its walls, the most probable rings of Si atoms (formed around the ion) can have from 3 to 10 links. Elimination of small-scale fluctuations accompanying the ion motion reduces the range of variation in the number of links (leading to a value of 4 – 5) in the most frequently encountered rings. Moreover, the four-link rings from geometric neighbors occur more frequently than the five-link ones. The most probable distances from the ion to the nearest geometric neighbors can vary noticeably depending on the size of the gap in the channel and the type of defects contained in its walls. The stresses (acting in the plane of the silicene sheets and caused by the forces directed perpendicular to this plane) are most significant when the Li^+ ion moves along the silicene channel. The local stress surges are noticeably inferior to the value of the ultimate strength of silicene under the uniaxial tension.

Thus, the paired silicene sheets on a graphite substrate are applicable to the construction of the anode of a lithium-ion battery. In this case, the presence of the vacancy-type defects in silicene does not introduce any significant restrictions in its use for this purpose.

Chapter 11

CONCLUDING REMARKS

Concrete conclusions for each of the topics discussed in this book are made at the end of each section or chapter. But here, we should like to make some general remarks in order to take a broader look at such new two-dimensional materials as graphene and silicene. We see the prospect in the widest possible use of these materials in the near future.

The deep theoretical studies performed in recent years show the great opportunities for a breakthrough in both nanoelectronics and in developing the new generation of the lithium-ion batteries based on the use of these materials. Research in this direction will continue. It is necessary to study the properties of not only individual 2D materials but, also, the characteristics of composite materials obtained on their basis. Graphene has already become quite cheap material, and silicene has to become much cheaper because of the wide prevalence of chemical elements C and Si in the Earth crust. The long cycle of life and good rate performance of Si-based anodes are usually more often observed with composites made from nanostructured Si. Carbon is most widely adopted in the construction of Si-based composites. Now the main task is to create cheap technologies for obtaining high-quality materials based on graphene and, especially, silicene. Below, we shall try to disclose in more detail some important areas of current and future research.

Graphene has exotic mechanical, thermal, electronic, optical, and chemical properties. These are the high carrier mobility, a weak dependence of mobility on carrier concentration and temperature, unusual quantum Hall effect. Its hardness is 100 times greater that of the strongest steel of the same thickness. Graphene is characterized by flexibility. It can sustain strains more than 20% without breaking. Graphene is brittle at certain strain limit. Its high thermal conductivity comparable to that of diamond and 10 times greater than that of copper. Graphene has a negative coefficient of thermal expansion over a wide range of temperature. It has potentials for many novel applications [484–488]. It was shown experimentally [489] that free-standing graphene sheets have spontaneous ripples owing to the thermal fluctuations, and, therefore, real graphene is not perfectly flat.

The fast development of graphene research has been stimulating by the great interest in producing all kinds of the two-dimensional (2D) layered materials. Silicene (the two-dimensional honeycomb allotrope of silicon) has attracted considerable interest due to its unique properties [490, 491]. Charge carriers in silicene behave like massless Dirac Fermions, whose velocity near the Fermi level is estimated to be on the order of magnitude of 10^6 m/s. Thus, the Fermi velocity in silicene is comparable to that of graphene [492, 493]. The sp^2–sp^3 hybridization of Si atoms in this 2D material leads to a buckled structure of silicene distinguishing it from the planar graphene. Such a specific structure of silicene makes its properties different from those of graphene. At the same time, new opportunities are created for manipulating the dispersion of electrons and enabling the tuning of the electronic and magnetic properties of silicene by external fields [494, 495].

It has been shown theoretically that the silicene has a strong spin-orbit coupling. For the practical use of this material, the opening and controlling of the band gap of silicene are critical [496]. Silicene has a reactive surface, which allows one to use chemical modification for tuning the band structure of silicene [497]. The procedure necessary to achieve this goal can be carried out by using an inorganic surface modification [498], organic surface modification [499], oxidation [500], doping [501], and the formation of 2D hybrids [502]. A theoretical study of the chemical modification of silicene is carried out intensively and has considerable success, while the modification of experimental investigation is still at the preliminary stage [503].

Using the first-principles calculations and *ab initio* molecular dynamics simulations, the electronic and structural properties and thermal stability of a silicene layer between graphene layers were investigated. A silicene layer obtained in the model between graphene layers forms a buckled honeycomb structure resembling very closely the properties of standalone silicene. The electronic and atomic structure of silicene intercalated by graphene layers is almost identical to the one of standalone buckled silicene. Therefore, graphene layers are an almost ideal template for the formation of silicene. This is in contrast with previously synthesized silicene on top of metallic surfaces where hybridization modifies the electronic and structural properties of silicene.

Graphene and silicene are perfect materials that possess an even better performance than silicon in the semiconductor devices. It is expected that novel devices developed with them will be much faster and smaller in size than their contemporary counterparts. Although graphene and silicene display different behavior of the electrical conductivity, their carrier concentration has the similar one. By now, the characteristics of silicene/graphene field effect transistors have already been tested. The model was suggested for a gas sensor based on graphene that shows higher electrical conductivity compared to silicene.

The first silicene transistors were recently reported [504], and, unlike graphene, this material does have a bandgap. Another potential advantage for silicene is that the semiconductor industry has invested the past sixty years in understanding every aspect of

silicon, not carbon. In theory at least, when introducing into the electronic technique of silicene, this should mean that the required process changes are less drastic.

Although silicene has very attractive properties, it is difficult in producing and handling compared to graphene. Silicene is extremely unstable in air, which creates a very serious problem. The only experimental transistor produced so far degraded in minutes. When working with this material, the manageability can be achieved if the silicene can be sandwiched between layers of some other two-dimensional materials to help protect it. However, this would require the development of the production processes for the whole range of new materials. Other new 2D materials such as germanene also face the similar problems.

Graphene can make the Li-ion batteries that are light, durable, and suitable for high capacity energy storage, as well as, shorten charging times. It will extend the battery life-time. Graphene adds conductivity without requiring the amounts of carbon that are used in conventional batteries. Graphene can improve such battery attributes as energy density and form in various ways. The Li-ion batteries can be enhanced by introducing graphene to the battery anode, capitalizing on the material conductivity, and large surface area traits. These allows one to achieve the morphological optimization and performance.

Laboratory tests of new LIBs have shown that graphene has demonstrated a good capability in reversibly storing Li [505], as well as, improving the performance of both cathode and anode materials [506]. With an excellent electrical conductivity and superb mechanical properties, graphene is also able to greatly reduce the negative phenomena associated with the use of the Si anodes.

Silicone has received great attention as an anode material because of several advantages. First, Si creates a capacity of about 4200 $mA \cdot h \cdot g^{-1}$ under the full lithiation with the formation of $Li_{22}Si_5$. Second, the Si anodes have a relatively low discharge potential plateau ~0.4 V versus Li^+/Li. This can contribute to high working voltage when connected to the cathode that leads to a high energy density. Third, there is a high abundance of Si element in the Earth crust. So, the cost to obtain both single crystalline and polycrystalline Si comes to a level that can be adopted for use them in electrodes. In addition, Si has good environmental compatibility, low toxicity, and relatively stable chemical property. All these properties make Si a very promising candidate for the next-generation Li-ion battery anodes.

The next step in mastering silicene for technical applications is to combine this substance with insulating materials to verify their benefits in electronic devices. To approve further verification in the laboratory of silicene properties in association with insulating compounds, it is necessary to agree with the theory and rely on it as our most accurate source of knowledge on the material. One of the most striking applications is related to silicene use in lithium ion batteries, which are currently most common in the electronics industry.

Silicene has a very high charge storage capacity much larger than that in graphene. This makes a good performance in the anodes of the lithium-ion batteries. This feature alleviates volume changes (that occur during charging) approaching the margins offered by graphite, the material that is currently used. However, silicene offers twice the capacity for the anode and its mechanical properties also prevent its suffering changes during charging and discharging. It can be expected that the silicene anode will have a long service life, i.e., it will be sufficiently stable when the charge/discharge cycles are completed.

However, all these conclusions were obtained from investigations with silicon nanostructures (such as nanowires), but not with silicene. Thus, they are only theoretical. Commercial usage is still far off. First, experiments must be conducted with the new material and then assessments should be made to determine whether this really takes place. Then, a sustainable production model must be found on that. Obviously, it will take not a little time.

Here, it is appropriate to pay attention to the use of silicene for rechargeable batteries based on the lithium metal anodes [507]. They have high capacity and energy density, but the implementation of the lithium metal anode still faces many challenges, such as low Coulombic efficiency and dendrites growth.

According to the computation results, the introduction of the defect, the increase of bond length, and proximity effect have positive effects on the conductivity of Li^+ ion, which can induce lower diffusion barrier and higher diffusion rate. Conversely, the factors named here can have a negative influence on the hardness or stiffness of the materials. That is unfavorable for the suppression of the lithium dendrites. The latter circumstance makes it difficult to optimize simultaneously both the diffusion and mechanical properties. Therefore, a balance should be struck between the considerations of ion conductivity and the stiffness in relation to the growth of the lithium dendrites.

Discovery of the graphene and its remarkable and exotic properties have aroused interest to other elements and molecules that form 2D atomic layers, such as metal chalcogenides, transition metal oxides, boron nitride, silicon, and germanium. Silicene and germanene (the Si and Ge counterparts of graphene) have interesting fundamental physical properties with potential applications to technologies. The symmetric buckling in each of the six-membered rings of silicene differentiates it from graphene and stipulates a variety of interesting properties with potential technological applications. In graphene, two sublattice structures are equivalent that does not allow one to open the band gap by an external electric field. However, in silicene the neighboring Si atoms are displaced alternatively perpendicular to the plane. So, the intrinsic buckling permits a band gap opening in silicene under the presence of an external electric field.

In silicene the spin-orbit coupling is stronger than in graphene. So, silicene has far reaching applications in the spintronic devices. Because silicon prefers sp^3-hybridization over sp^2, the hydrogenation is much easier in silicene. The hydrogenation of silicene with forming the silicane opens the band gap. Lithiation can flatten the silicene structure while

opening the band gap. Silicene sheets and nanoribbons over various substrates such as silver, diboride thin films, and iridium have been successfully produced recently. The supporting substrate crucially controls the electronic properties of silicene, and the match of the appropriate support and its use is critical in applications of silicene.

Thermal conductivity and mechanical stiffness of graphene sheets may rival the remarkable in-plane values of graphite. Their fracture strength can be comparable to that of carbon nanotubes for the similar types of defects. Besides, individual graphene sheets have extraordinary electronic transport properties. One possible route to harnessing these properties for applications would be to incorporate graphene sheets in a composite material. The manufacturing of such composites requires that graphene sheets be produced on a sufficient scale. In addition, they have to be incorporated into various matrices and homogeneously distributed in it. Graphite is inexpensive and available in large quantity. However, it does not readily exfoliate to yield the individual graphene sheets.

It should be noted that carbon nanostructures are promising fillers for polymer nanocomposite materials. Among these fillers, graphene nanoparticles are not the last. A combination of the structural, physics-mechanical, and electrophysical properties of these fillers under their introduction into polymer matrices affords the creation of composite materials possessing improved stress–strain, electro and thermophysical characteristics, and non-combustibility.

Understanding and adapting the properties of new materials on the nanoscale for the desired applications are of the great importance for the fabrication and development of new nanodevices. Given that we are at the beginning of a new 2D era of material science, we should be interested in joining this new field of research, because the chances of success are high when the field is new.

Appendix

GENERALIZED GRADIENT APPROXIMATION FOR EXCHANGE ENERGY

Kon–Sham (KS) created [469] the fundamental basis of the density functional theory [468] for describing the electronic structure of atoms, molecules, and solids. Successful use of DFT involves the search for the exchange-correlation functional that uses the electron density to describe the intricate many-body effects within a single particle formalism. Now available approximations to the exchange-correlation (XC) energy functional allow studying the systems, which are not so small with a reasonable computational effort and quality of outcomes [508]. However, the accuracy in the prediction of structural, thermodynamic, and kinetic properties, etc. with comparatively simple functionals needs to be increased beyond present limits. It is necessary to achieve a reliable method for the description of a wide variety of systems with different characteristics [509].

Some of the issues confronting any attempt at the systematic increase in the accuracy of the XC functional were solved by using the so-called Jacob ladder [510]. The local spin density approximation (LDA) is placed on the first level. Here, the functional is determined solely in terms of the local values of the spin up and spin down electronic densities via the expression for the homogeneous electron gas. The second level consists of functionals that additionally depend on the magnitude of the gradients of the spin up and spin down densities. The functionals take into account the inhomogeneities. Because the form of that dependence is not simply that of the gradient expansion, such functionals are usually considered as generalized gradient approximations. The third level comprises functionals that incorporate the Laplacian of the density and/or the KS kinetic energy density. Through the proposed energy density, one introduces an explicit dependence on the KS orbitals, additional to the one that comes from the expression of the electronic density in terms of these orbitals. On the fourth level, a fraction of the full exact exchange is incorporated. Recall that the XC functional is defined from the KS orbitals through their implicit

dependence on the density. Global and local hybrid functionals correspond to this level. On the fifth level, explicit dependence of the XC functional on the unoccupied KS orbitals is added. The second and third level functionals are said to be of "semi-local" nature (although they are strictly one-point functionals), while the fourth and fifth level functionals have explicitly non-local components.

In the framework of this systematization, the usual expectation is for the accuracy increasing as one climbs the ladder, although, the complexity and computational effort will also increase. However, an interesting aspect is that the actual accuracy limits for a given level are not necessarily stipulated by the current state of the art at that level. Note that the analytical framework by which to assess the ultimately achievable accuracy for some quantity (e.g., bond lengths or atomization energies) are absent. So, the functional developers are forced to explore improvement of existing applied approximations. In this context, the search for better descriptions at the GGA level continues to be a very active research area. Particularly, this is because such functionals provide a good balance between accuracy and computational effort. Interest in GGAs also persists because of the quest for implementation of orbital-free density functional theory [511, 512]. Additionally, the GGA functionals usually are components of the higher-level approximations; so, it is important to achieve a better understanding of their general behavior and the constraints that they could or should satisfy.

We performed the first-principles calculations with the plane-wave ultra-soft pseudopotential by means of GGA with the Perdew–Burke–Ernzerhof (PBE) functional in the SIESTA code [513, 514]. The SIESTA abbreviation comes from the "Spanish Initiative for Electronic Simulations with Thousands of Atoms". In the Appendix below, we show the main aspects of the GGA functionals constraint taking as a starting point the approximation of Perdew, Burke, and Ernzerhof [230]. It is made to analyze the behavior of the reduced density gradient as a function of the density. This can establish some implications it may have in the development of improved GGA functionals.

The exchange energy functional in the generalized gradient approximation usually is expressed (for the spin non-polarized case) in the form

$$E_x[\rho] = \int_{(\rho(\mathbf{r}))} d\mathbf{r}\rho(\mathbf{r})\varepsilon_{x\mathrm{LDA}}[\rho(\mathbf{r})]F(s), \tag{A1}$$

where the integral is taken over the distribution $\rho(\mathbf{r})$ region, the $\varepsilon_{x\mathrm{LDA}}$ energy density in the LDA is described as

$$\varepsilon_{x\mathrm{LDA}}[\rho(\mathbf{r})] = -C_x\rho^{1/3}(\mathbf{r}) = -(3/4)\left(3/\pi\right)^{1/3}\rho^{1/3}(\mathbf{r}), \tag{A2}$$

and the reduced density gradient is defined as

$$s(\boldsymbol{r}) = \left|\nabla\rho(\boldsymbol{r})\right| / \left[2(3\pi^2)^{1/3} \rho^{4/3}(\boldsymbol{r}) \right]. \tag{A3}$$

The enhancement factor $F_x(s)$ describes deviations from the homogeneous electron gas behavior. For PBE, it is written as [230]

$$F_x^{\mathrm{PBE}}(s) = 1 + \kappa - \frac{\kappa}{1 + \frac{\mu s^2}{\kappa}}, \tag{A4}$$

where κ and μ are parameters.

The PBE enhancement factor form (together with the values assigned to the parameters κ and μ) satisfies the following constraints:

(a) Under uniform density scaling, $\rho(\boldsymbol{r}) \to \lambda^3 \rho(\lambda \boldsymbol{r})$ and the exchange energy acts like λ.

(b) From Eq. (4), for $s = 0$, $F_x^{\mathrm{PBE}}(0) = 1$ is put to recover the homogeneous electron gas exchange.

(c) Although written for the spin non-polarized case, the spin-polarized expressions satisfy the spin-scaling relationship

$$E_x[\rho_\uparrow, \rho_\downarrow] = \left(E_x[2\rho_\uparrow] + E_x[2\rho_\downarrow] \right) / 2, \tag{A5}$$

where $\rho_\uparrow$ and $\rho_\downarrow$ are the spin-up and spin-down electron densities.

(d) Being a GGA, the exchange energy and its functional derivative do not diverge for atoms and molecules at the exponential tail of the charge distribution.

(e) The Lieb-Oxford bound [515, 516] establishes the most negative value that the exchange energy may attain for a given electron density, namely,

$$E_x[\rho_\uparrow, \rho_\downarrow] \geq -1.679 \int d\boldsymbol{r} \rho^{4/3}(\boldsymbol{r}) \tag{A6}$$

is satisfied by imposing the condition that the local values of $F_x(s)$ should not grow beyond the value 1.804. Since for the form given by Eq. (A4), the maximum value of $F_x(s)$ is $1 + \kappa$ (the limit as $s \to \infty$); so, one finds that $\kappa = 0.804$.

(f) From Eq. (A4), one has that in the small *s* regime,

$$F_x(s) \to 1 + \mu s^2, \tag{A7}$$

which indicates that μ is directly related to the weight given to the density gradient. At present, the LDA provides a very good description of the linear response of the spin-unpolarized uniform electron gas. Thus, in the PBE functional, μ was set to cancel the second-order gradient contribution to the correlation energy in the high-density limit using the relationship

$$\mu_{\mathrm{PBE}} = \pi^2 \beta / 3, \tag{A8}$$

where according to Ma and Brueckner [517] $\beta = 0.066725$ and, therefore, $\mu_{\mathrm{PBE}} = 0.21951$. The form of the enhancement function given by Eq. (A4) was first proposed by Becke [518]. He determined the values of the parameters empirically on the base of the least squares fit to the Hartree-Fock energies of the noble gas atoms He-Xe. He also used the Hartree-Fock densities to evaluate the integral in Eq. (A1). The values that he found were $\kappa = 0.967$ and $\mu = 0.235$.

The PBE XC functional leads to a reasonable description of a wide variety of properties of molecules and solids. It has become one of the most difficult used approximations in electronic structure calculations. However, several modifications have been proposed all with the objective of improving the calculated values of various sets of properties [519, 520]. A general finding, which emerges from those modifications, is that the magnitude of μ is correlated with the prediction of structural, thermodynamic, and kinetic properties. The smallest non-empirical value μ corresponds to the gradient expansion approximation (GEA) value [521], $\mu_{\mathrm{GEA}} = 10/81 \approx 0.12346$. The largest non-empirical value of μ comes from the imposition of the constraint that (for the hydrogen atom) the exchange energy cancels the Coulomb repulsion energy. The latter constraint leads [520] to the Hartree-Fock value $\mu_x = 0.27583$. Large values μ are better for atomization energies and worse for crystalline lattice constants while low values μ generating the opposite trend. In fact, Zhao and Truhlar [519] also showed that magnitude of the coefficient μ correlates with the behavior of the cohesive energies of solids, reaction barrier heights, and non-hydrogen bond distances in small molecules. It is important to note that, in general, when the value of μ is changed, the value of β is also changed by Eq. (A8), or by influence of other arguments. So, in addition to the exchange energy, the correlation energy also has an impact on this behavior.

In addition to the approximation described above for calculating the exchange energy, we used tolerances within 5.0×10^{-6} eV/atom at full energy for optimizing the geometry. The maximum Hellmann-Feynman force was within 0.01 eV·Å^{-1}, the maximum displacement of the atom did not exceed 5.0×10^{-4} Å, and the maximum stress was within

0.02 GPa. The geometry of all structures was completely optimized. A single silicene cell consisting of 8 atoms and periodic boundary conditions were used to calculate all the properties. The initial coordinates of four Si atoms of the unit cell were shifted to the distance of 0.064 nm perpendicular to the surface, and the remaining Si atoms were on the same (initial) plane. Such a structure of the silicene sheet is close to the surface of the silicene observed on the Ag(111) substrate [432]. In the inverse spatial expansion of the charge density, the cutoff on the grid equal to 2720 eV was used. The Brillouin zone was introduced using a matrix of 20 × 20 × 1 *k*-points in the Monocharst-Pack module. The method of diagonalization was applied to carry out all calculations.

REFERENCES

[1] Kroto, HW; Walton, DRM. *Phil. Trans. R. Soc. A*, 1993, 343, 103–112.

[2] Castro Neto, AH; Guinea, F; Peres, NMR; Novoselov, KS; Geim, AK. *Rev. Mod. Phys.*, 2009, 81, 109–162.

[3] Rechtsman, MC; Zeuner, JM; Tunnermann, A; Nolte, S; Segev, M; Szameit, A. *Nature Photon.*, 2013, 7, 153–158.

[4] Tarruell, L; Greif, D; Uehlinger, T; Jotzu, G; Esslinger, T. *Nature*, 2012, 483, 302–305.

[5] Huang, X; Lai, Y; Hang, ZH; Zheng, H; Chan, C. *Nature Mater.*, 2011, 10, 582–586.

[6] Moitra, P; Yang, Y; Anderson, Z; Kravchenko, II; Briggs, DP; Valentine, J. *Nature Photon.*, 2013, 7, 791–795.

[7] Avouris, P. *Nano Lett.*, 2010, 10, 4285–4294.

[8] Ghosh, S; Sahoo, G; Polaki, SR; Krishna, NG; Kamruddin, M; Mathews, T. *J. Appl. Phys.*, 2017, 122, 214902.

[9] Lehmann, K; Yurchenko, O; Heilemann, A; Vierrath, S; Zielke, L; Thiele, S; Fischer, A; Urban, G. *Carbon*, 2017, 118, 578–587.

[10] Sahoo, G; Ghosh, S; Polaki, SR; Mathews, T; Kamruddin, M. *Nanotechnology*, 2017, 28, 415702.

[11] Banhart, F; Kotakoski, J; Krasheninnikov, AV. *ACS Nano*, 2011, 5, 26–41.

[12] Bertolazzi, S; Brivio, J; Kis, A. *ACS Nano*, 2011, 5, 9703–9709.

[13] Zhao, J; Liu, H; Yu, Z; Quhe, R; Zhou, S; Wang, Y; Liu, CC; Zhong, H; Han, N; Lu J; Yao, Y; Wu, K. *Prog. Mater. Sci.*, 2016, 83, 24–151.

[14] Vogt, P; De Padova, P; Quaresima, C; Avila, J; Frantzeskakis, E; Asensio, MC; Resta, A; Ealet, B; Le Lay, G. *Phys. Rev. Lett*., 2012, 108, 155501.

[15] Lin, CL; Arafune, R; Kawahara, K; Tsukahara, N; Minamitani, E; Kim, Y; Takagi, N; Kawai, M. *Appl. Phys. Express*, 2012, 5, 045802.

[16] Feng, B; Ding, Z; Meng, S; Yao, Y; He, X; Cheng, P; Chen, L; Wu, K. *Nano Lett*., 2012, 12, 3507–3511.

[17] Chen, L; Liu, CC; Feng, B; He, X; Cheng, P; Ding, Z; Meng, S; Yao, Y; Wu, K. *Phys.Rev. Lett*., 2012, 109, 056804.

[18] Chiappe, D; Grazianetti, C; Tallarida, G; Fanciulli, M; Molle, A. *Adv. Mater*., 2012, 24, 5088–5093.

[19] Enriquez, H; Vizzini, S; Kara, A; Lalmi, B; Oughaddou, H. *J. Phys.: Condens. Matter*., 2012, 24, 314211.

[20] Jamgotchian, H; Colignon, Y; Hamzaoui, N; Ealet, B; Hoarau, JY; Aufray, B; Biberian, JP. *J. Phys.: Condens. Matter*., 2012, 24, 172001.

[21] Friedlein, R; Fleurence, A; Ozaki, T; Kawai, H; Wang, Y; Yukiko, YT. *Phys. Rev. Lett*., 2012, 108, 245501.

[22] Aizawa, T; Suehara, S; Otani, S. *J. Phys. Chem*., C 2014, 118, 23049–23057.

[23] Meng, L; Wang, Y; Zhang, L; Du, S; Wu, R; Li, L; Zhang, Y; Li, G; Zhou, H; Hofer, WA; Gao, HJ. *Nano Lett*., 2013, 13, 685–690.

[24] Resta, A; Leoni, T; Barth, C; Ranguis, A; Becker, C; Bruhn, T; Vogt, P; Le Lay, G. *Sci. Rep*., 2013, 3, 2399–2405.

[25] H. Jamgotchian, H; Colignon, Y; Ealet, B; Parditka, B; Hoarau, JY; Girardeaux, C; Aufray, B; Bibérian, JP. *J. Phys.: Conf. Ser*., 2014, 491, 012001.

[26] Grazianetti, C; Chiappe, D; Cinquanta, E; Tallarida, G; Fanciulli, M; Molle, A. *Appl. Surf. Sci*., 2014, 291, 109–112.

[27] Tchalala, MR; Enriquez, H; Yildirim, H; Kara, A; Mayne, AJ; Dujardin, G; Ali, MA; Oughaddou, H. *Appl. Surf. Sci*., 2014, 303, 61–66.

[28] Majzik, Z; Rachid Tchalala, M; Svec, M; Hapala, P; Enriquez, H; Kara, A; Mayne, AJ; Dujardin, G; Jelinek, P; Oughaddou, H. *J. Phys.: Condens. Matter*., 2013, 25, 225301.

[29] Liu, ZL; Wang, MX; Xu, JP; Ge, JF; Lay, GL; Vogt, P; Qian, D; Gao, CL; Liu, C; Jia, JF. *New J. Phys*., 2014, 16, 075006.

[30] Sone, J; Yamagami, T; Aoki, Y; Nakatsuji, K; Hirayama, H. *New J. Phys*., 2014, 16, 095004.

[31] Molle, A; Chiappe, D; Cinquanta, E; Grazianetti, C; Fanciulli, M; Scalise, E; Vanden Broek, B; Houssa, M. *ECS Trans*., 2013, 58, 217–227.

[32] Liu, H; Feng, H; Du, Y; Chen, J; Wu, K; Zhao, J. *2D Mater*., 2016, 3, 025034.

[33] Gao, J; Zhang, J; Liu, H; Zhang, Q; Zhao, J. *Nanoscale*, 2013, 5, 9785–9792.

[34] Shobha, S; Raghvendra Pratap, C; Sumit, S. 2018. "*Free standing layers of silicone like sheets*." Accessed May 25. https://arxiv.org/abs/1511.04726

[35] Raghvendra Pratap, C; Shobha, S; Kumar, V; Pranav Bhagwan, P; Sumit, S. *Materials Research Express*, 2015, 2, 095024.

[36] Takagi, N; Lin, CL; Kawahara, K; Minamitani, E; Tsukahara, N; Kawai, M; Arafune, R. *Prog. Surf. Sci.*, 2015, 90, 1–20.

[37] Zhuang, J; Xu, X; Peleckis, G; Hao, W; Dou, SX; Du, Y. *Adv. Mater*., 2017, 29, 1606716.

[38] Nose, S. *J. Phys.: Condens. Matter.*, 1990, 2, 115–119.
[39] Martyna, GJ. *J. Chem. Phys*., 1994, 101(5), 4177–4189.
[40] Tersoff, J. *Phys. Rev. B: Condens. Matter*., 1988, 37, 6991–7000.
[41] Galashev, AY. *Russ. J. Phys. Chem. B*, 2012, 6, 441–447.
[42] Galashev, AY. *J. Nanopart. Res*., 2014, 16, 2351.
[43] Stuart, SJ; Tutein, AV; Harrison, JA. *J. Chem. Phys*., 2000, 112, 6472–6486.
[44] Rafii-Tabar, H. *Phys. Rep*., 2000, 325, 239–310.
[45] Kutana, A; Giapis, KP. *Nano Lett*., 2006, 6, 656–661.
[46] Munro, LJ; Johnson, JK. *J. Chem. Phys*., 2001, 114, 5545–5551.
[47] Oluwajobi, A; Chen, X. *Int. J. Autom. Comput*., 2011, 8, 326–332.
[48] Kim, YM; Kim, SC. *J. Korean Phys. Soc*., 2002, 40, 293–299.
[49] Arkundato, A; Su'ud, Z; Abdullah, M; Sutrisno, W. *Int. J. Appl. Phys. Math*., 2013, 3, 1–6.
[50] Li, FY; Berry, RS. *J. Phys. Chem*., 1995, 99, 2459–2468.
[51] Galashev, AY. *J. Phys. Chem., C* 2016, 120, 13263−13274.
[52] Chiang, KN; Chou, CY; Wu, CJ; Huang, CJ; Yew, MC. *ICCES*, 2009, 9, 130–141.
[53] Bonechi, A; Moraldi, M. *J. Chem. Phys*., 1998, 109, 5880–5885.
[54] Moore, MC; Kalyanasundaram, N; Freund, JB; Johnson, HT. *Nucl. Instrum. Meth. Phys. Res*., 2004, 225, 241–255.
[55] Smith, R; Harrison, DE; Jr. Garrison, BJ. *Phys. Rev. B*, 1989, 40, 93–101.
[56] Ziegler, JF; Biersack, JP; Littmark, U. *Stopping and Ranges of Ions in Matter*; Pergamon: New York, US, 1985, Vol. 1, pp. 1–321.
[57] Delcorte, A; Garrison, BJ. *J. Phys. Chem. B*, 2000, 104, 6785–6800.
[58] Lamari, FD; Levesque, D. *Carbone*, 2011, 49, 5196–5200.
[59] Lehtinen, O; Kotakoski, J; Krasheninnikov, AV; Tolvanen, A; Nordlund, K; Keinonen, J. *Phys. Rev. B*, 2010, 81, 153401.
[60] Ito, A; Nakamura, H; Takayama, A. *J. Phys. Soc. Jpn.*, 2008, 77, 114602.
[61] Galashev, AE. *J. Surf. Invest.: X-ray, Synchrotron Neutron Tech.*, 2013, 7, 788–796.
[62] Berendsen, HJC; Postma, JPM; van Gunsteren, WF; di Nola, A; Haak, JR. *J. Chem. Phys.*, 1984, 81, 3684–3690.
[63] Galashev, AE. *J. Surf. Invest.: X-ray, Synchrotron Neutron Tech.*, 2016, 10, 15–22.
[64] Davydov, S. Yu. (2012). *Phys. Solid State*, 2012, 54, 875–882.
[65] Jin, ZH; Sheng, HW; Lu, K. *Phys. Rev. B*, 1999, 60, 141–149.
[66] Guerra, GF; Handgraef, JW; Baerends, EJ; Bickelhaupt, FM. *J. Comp. Chem*., 2004, 25, 189–210.
[67] Norman, GE; Stegailov, VV. *JETP*, 2001, 92, 879–886.
[68] Cole, MW; Cresp, VH; Dresselhaus, MS. *J. Phys.: Condens. Mater*., 2010, 22, 334201.
[69] Sondheimer, EH. *Adv. Phys*., 2001, 50, 499–537.
[70] Maksimov, EG; Savrasov, DYu; Savrasov, SYu. *Phys. Usp*., 1997, 40, 337–358.

[71] Reicha, FM; El Hiti, MA; Barna, PB. *J. Mater. Sci.*, 1991, 26, 2007–2014.
[72] Lee, W; Jang, S; Kim, MJ; Myoung, JM. *Nanotechnology*, 2008, 19, 285701.
[73] White, GK; Collocott, SJ. *Phys. Chem. Ref. Data*, 1984, 13, 1251–1257.
[74] Chu, PK; Li, L. *Mater. Chem. Phys.*, 2006, 96, 253–277.
[75] Bundy, FP; Kasper, JS. *J. Chem. Phys.*, 1967, 46, 3437–3446.
[76] Goncharov, AF; Makarenko, IN; Stishov, SM. *Sov. Phys. JETP*, 1989, 69, 380–381.
[77] Hanfland, M; Beister, H; Syassen, K. *Phys. Rev. B*, 1989, 39, 12598–12603.
[78] Utsumi, W; Yagi, T. *Science*, 1991, 252, 1542–1544.
[79] Zhao, YX; Spain, IL. *Phys. Rev. B*, 1989, 40, 993–997.
[80] Yagi, T; Utsumi, W; Yamakata, MA; Kikegawa, T; Shimomura, O. *Phys. Rev. B*, 1992, 46, 6031-6039.
[81] Mao, WL; Mao, HK; Eng, PJ; Trainor, TP; Newville, M; Kao, CC; Heinz, D. L; Shu, J; Meng, Y; Hemley R. J. *Science*, 2003, 302, 425–427.
[82] Ribeiro, FJ; Tangney, P; Louie, SG; Cohen ML. *Phys. Rev. B*, 2005, 72, 214109.
[83] Li, Q; Ma, Y; Oganov, AR; Wang, H; Xu, Y; Cui, T; Mao, HK; Zou G. *Phys. Rev. Lett*., 2009, 102, 175506.
[84] Umemoto, K; Wentzcovitch, RM; Saito, S; Miyake T. *Phys. Rev. Lett.*, 2010, 104, 125504.
[85] Wang, JT; Chen, C; Kawazoe, Y. *Phys. Rev. Lett*., 2011, 106, 075501.
[86] Bundy, FP; Bassett, WA; Weathers, MS; Hemley, RJ; Mao HU; Goncharov, AF. *Carbon*, 1996, 34, 141–153.
[87] Frank, IW; Tanenbaum, DM; van der Zande, AM; McEuen, PL. *J. Vac. Sci. Technol. B*, 2007, 25, 2558–2561.
[88] Lee, C; Wei, X; Kysar, JW; Hone, J. *Science*, 2008, 321, 385–388.
[89] Bhagavantam, S; Bhimasenachar, J. *Proc. R. Soc. Lond. A*, 1946, 187, 381–384.
[90] Hearmon, RFS. *Rev. Mod. Phys.*, 1946, 18, 409–440.
[91] Prince, E; Wooster, WA. *Acta Cryst.*, 1953, 6, 450–454.
[92] McSkimin, HJ; Bond, WL. *Phys. Rev.*, 1957, 105, 116–120.
[93] McSkimin, HJ; Andreatch, P. (Jr.) *J. Appl. Phys.*, 1972, 43, 2944–2948.
[94] Eletskii, AV. *Phys. Usp.*, 2007, 50, 225–261.
[95] Ivanovskii, AL. *Russ. Chem. Rev.*, 1999, 68, 103–118.
[96] Brazhkin, VV. *Phys. Usp.*, 2009, 52 369–376.
[97] Eletskii, AV. *Phys. Usp.*, 2011, 54, 227–258.
[98] Falkovsky, LA. *Phys. Usp.*, 2012, 55, 1140–1145.
[99] Varlamov, AA; Kavokin, AV; Luk'yanchuk, IA; Sharapov, SG. *Phys. Usp.*, 2012, 55, 1146–1151.
[100] Li, Y; Li, H; Zhang, K; Liew, KM. *Carbon*, 2012, 50, 566–576.
[101] Xu, Z; Buehler, MJ. *ACS Nano*, 2010, 4, 3869–3876.
[102] Viculis, LM; Mack, JJ; Kaner, RB. *Science*, 2003, 299, 1361–1362.
[103] Shioyama, H; Akita, T. *Carbon*, 2003, 41, 179–181.

[104] Braga, SF; Coluci, VR; Legoas, SB; Giro, R; Galvao, DS; Baughman RH. *Nano Lett*., 2004, 4, 881–884.
[105] Shi, X; Pugno, NM; Gao, H. *J. Comput. Theor. Nanosci*., 2010, 7, 517–521.
[106] Martins, BVC; Galvao, DS. *Nanotechnology*, 2010, 21, 075710.
[107] Bets, KV; Yakobson, BI. *Nano Res.*, 2009, 2, 161–166.
[108] Chuvilin, A; Bichoutskaia, E; Gimenez-Lopez, MC; Chamberlain, TW; Rance, GA; Kuganathan, N; Biskupek, J; Kaiser, U; Khlobystov, AN. *Nature Mater.*, 2011, 10, 687–690.
[109] Fujihara, M; Miyata, Y; Kitaura, R; Nishimura, Y; Camacho, C; Irle, S; Iizumi, Y; Okazaki, T; Shinohara, H. *J. Phys. Chem. C*, 2012, 116, 15141–15145.
[110] Lim, HE; Miyata, Y; Kitaura, R; Nishimura, Y; Nishimoto, Y; Irle, S; Warner, JH; Kataura, H; Shinohara, H. *Nature Commun.*, 2013, 4, 2548.
[111] Jiang, Y; Li, H; Li, Y; Yu, H; Liew, KM; He, Y; Liu, X. *ACS Nano*, 2011, 5, 2126–2133.
[112] Duan, WH; Wang, Q; Liew, KM; He, XQ. *Carbon*, 2007, 45, 1769–1776.
[113] Coluci, VR; Braga, SF; Baughman, RH., Galvao, DS. *Phys. Rev. B*, 2007, 75, 125404.
[114] Shi, X; Cheng, Y; Pugno, NM; Gao, H. *Small*, 2010, 6, 739–744.
[115] Shi, X; Cheng, Y; Pugno, NM; Gao, H. *Appl. Phys. Lett.*, 2010, 96, 053115.
[116] Li, Y; Li, H; Dong, J. In *Innovative Graphene Technologies: Evaluation and Applications*; edited by Tiwari, A and Balandin, AA; Smithers Rapra Technol: Akron, OH, 2013, Vol. 2, pp. 175–197.
[117] Xie, X; Ju, L; Feng, X; Sun, Y; Zhou, R; Liu, K; Fan, S; Li, Q; Jiang, K. *Nano Lett*., 2009, 9, 2565–2570.
[118] Chen, Y; Lu, J; Gao, Z. *J. Phys. Chem. C*, 2007, 111, 1625–1630.
[119] Zhang, Z; Li, T. *Appl. Phys. Lett.*, 2010, 97, 081909.
[120] Xia, D; Xue, Q; Xie, J; Chen, H; Lv, C; Besenbacher, F; Dong, M. *Small*, 2010, 6, 2010–2019.
[121] Sessi, P; Guest, JR; Bode, M; Guisinger, N. *Nano Lett*., 2009, 9, 4343–4347.
[122] Elias, DC; Nair, RR; Mohiuddin, TMG; Morozov, SV; Blake, P; Halsall, MP; Ferrari, AC; Boukhvalov, DW. *Science*, 2009, 323, 610–613.
[123] Pujari, BS; Gusarov, S; Brett, M; Kovalenko, A. *Phys. Rev. B*, 2011, 84, 041402(R).
[124] Ng, ML; Balog, R; Hornekær, L; Preobrajenski, AB; Vinogradov, NA; Mårtensson, N; Schulte, K. *J. Phys. Chem. C*, 2010, 114(43), 18559–18565.
[125] Zhu, Z; Su, D; Weinberg, G; Schlogl, R. *Nano Lett.*, 2004, 4, 2255–2259.
[126] Jin, W; Fukushima, T; Niki, M; Kosaka, A; Ishii, N; Aida, T. *Proc. Natl. Acad. Sci. USA*, 2005, 102, 10801–10806.
[127] Yu, D; Liu, F. *Nano Lett*., 2007, 7, 3046–3050.
[128] Sidorov, A; Mudd, D; Sumanasekera, G; Ouseph, PJ; Jayanthi, CS; Wu, SY. *Nanotechnology*, 2009, 20, 055611.

[129] Bellido, EP; Seminario, JM. *J. Phys. Chem. C*, 2010, 114, 22472–22477.
[130] Patra, N; Wang, B; Kral, P. *Nano Lett.*, 2009, 9, 3766–3771.
[131] Heath, JR. *ACS Symp. Ser.*, 1992, 481, 1–23.
[132] Hunter, JM; Fye, JL; Roskamp, EJ; Jarrold, MF. *J. Phys. Chem.*, 1994, 98, 1810–1818.
[133] Bunshah, RF; Jou, S; Prakash, S; Doerr, H; Isaacs, L; Wehrsig, A; Yeretzian, C; Cynn, H; Diederich, F. *J. Phys. Chem.*, 1992, 96, 6866–6869.
[134] Chuvilin, A; Kaiser, U; Bichoutskayia, E; Besley, NA; Khlobystov, AN. *Nature Chem.*, 2010, 2, 450–453.
[135] Girit, CO; Meyer, JC; Erni, R; Rossell, MD; Kisielowski, C; Yang, L; Park, CH; Crommie, MF; Cohen, ML; Louie, SG; Zettl, A. *Science*, 2009, 323, 1705–1708.
[136] Jia, X; Hofmann, M; Meunier, V; Sumpter, G; Campos-Delgado, J; Romo-Herrera, JM; Son, H; Hsieh, YP; Reina, A; Kong, J; Terrones, M; Dresselhaus, MS. *Science*, 2009, 323, 1701–1705.
[137] Lebedeva, IV; Knizhnik, AA; Popov, AM; Potapkin, BV. *J. Phys. Chem. C*, 2012, 116, 6572–6584.
[138] Ci, L; Xu, Z; Wang, L; Gao, W; Ding, F; Kelly, KF; Yakobson, BI; Ajayan, PM. *Nano Res.*, 2008, 1, 116–122.
[139] Iskandarov, AM; Umeno, Y; Dmitriev, SV. *Lett. Mater.*, 2011, 1, 143–146.
[140] Zhu, T; Li, J. *Prog. Mater. Sci*., 2010, 55, 710–757.
[141] Li, X; Maute, K; Dunn, ML; Yang, R. *Phys. Rev. B*, 2010, 81, 245318.
[142] Pellegrino, FMD; Angilella, GGN; Pucci, R. *Phys. Rev. B*, 2010, 81, 035411.
[143] Pellegrino, FMD; Angilella, GGN; Pucci, R. In *Graph ITA 2011. Selected Papers from the Workshop on Fundamentals and Applications of Graphene*; edited by Ottaviano, L and Morandi, V; Springer: Berlin, 2012, pp 165–170.
[144] Huang, M; Yan, H; Chen, C; Song, D; Heinz, TF; Hone, J. *Proc. Natl. Acad. Sci. USA*, 2009, 106, 7304–7308.
[145] Pellegrino, FMD; Angilella, GGN; Pucci, R. *Phys. Rev. B*, 2009, 80, 094203.
[146] Kim, KS; Zhao, Y; Jang, H; Lee, SY; Kim, JM; Kim, KS; Ahn, JH; Kim, P; Choi, JY, Hong, BH. *Nature*, 2009, 457, 706–710.
[147] Pellegrino, FMD; Angilella, GGN; Pucci, R. *Phys. Rev. B*, 2010, 82, 115434.
[148] Lu, Q; Huang, R. *Int. J. Appl. Mech*., 2009, 1, 443–468.
[149] Brenner, DW; Shenderova, OA; Harrison, JA; Stuart, SJ; Ni, B; Sinnott, SB. *J. Phys. Condens. Matter*, 2002, 14, 783–802.
[150] Yanovsky, Yu. G; Nikitina, EA; Karnet, Yu. N; Nikitin, SM. *Phys. Mesomech*., 2009, 12, 254–262.
[151] Jin, Y; Yuan, FG. *J. Nanosci. Nanotechnol.*, 2005, 5, 2099–2107.
[152] Brenner, DW. *Phys. Rev. B*, 1990, 42, 9458–9471.
[153] Kudin, KN; Scuseria, GE; Yakobson, BI. *Phys. Rev. B*, 2001, 64, 235406.

[154] Van Lier, G; van Alsenoy, C; van Doren, V; Geerlings, P. *Chem. Phys. Lett*., 2000, 326, 181–185.
[155] Konstantinova, E; Dantas, SO; Barone, PMVB. *Phys. Rev. B*, 2006, 74, 035417.
[156] Tombler, TW; Zhou, C; Alexseyev, L; Kong, J; Dai, H; Liu, L; Jayanthi, CS; Tang, M; Wu, A. Yu. *Nature*, 2000, 405, 769–772.
[157] Jiang, JW; Wang, JS; Li, B. *Phys. Rev. B*, 2009, 80, 113405.
[158] Landau, LD; Lifshitz, EM. *Theory of Elasticity*; Pergamon Press: Oxford, 1986, pp. 1–187.
[159] Krishnan, A; Dujardin, E; Ebbesen, TW; Yianilos, PN; Treacy, MM. *J. Phys. Rev. B*, 1998, 58, 14013.
[160] Blakslee, OL; Proctor, DG; Seldin, EJ; Spebce, GB; Weng, T. *J. Appl. Phys.*, 1970, 41, 3373.
[161] Sanchez-Portal, D; Artacho, E; Soler, JM; Rubio, A; Ordejon, P. *Phys. Rev. B*, 1999, 59, 12678.
[162] Zhang, G; Li, B. *J. Chem. Phys.*, 2005, 123, 114714.
[163] Chang, CW; Fennimore, AM; Afanasiev, A; Okawa, D; Ikuno, T; Garsia, H; Li, D; Majumdar, A; Zettl, A. *Phys. Rev. Lett.*, 2006, 97, 085901.
[164] Galashev, AE; Dubovik, S. Yu. *Phys. Solid State*, 2013, 55, 1976–1983.
[165] Frank, O; Tsoukleri, G; Parthenios, J; Papagelis, K; Riaz, I; Jalil, R; Novoselov, K; Galiotis, K. *ACS Nano*, 2010, 4, 3131–3138.
[166] Schadler, L; Galiotis, C. *Int. Mater. Rev.*, 1995, 40, 116–134.
[167] Novoselov, KS; Geim, AK; Morozov, SV; Jiang, D; Zhang, Y; Dubonosov, SV; Grigorieva, IV; Firsov, AA. *Science*, 2004, 306, 666–669.
[168] Ferrari, AC; Meyer, JC; Scardaci, V; Casiraghi, C; Lazzeri, M; Mauri, F; Piscanec, S; Jiang, D; Novoselov, KS; Roth, S; Geim, AK. *Phys. Rev. Lett.*, 2006, 97, 187401.
[169] Yu, T; Ni, Z; Du, C; You, Y; Wang, Y; Shen, Z. *J. Phys. Chem. C*, 2008, 112, 12602–12605.
[170] Mohiuddin, TMG; Lombardo, A; Nair, RR; Bonetti, A; Savini, G; Jalil, R; Bonini, N; Basko, DM; Galiotis, C; Marzari, N; Novoselov, KS; Geim, AK; Ferrari, AC. *Phys. Rev. B*, 2009, 79, 205433.
[171] Huang, M; Yan, H; Chen, C; Song, D; Heinz, TF; Hone J. *Proc. Natl. Acad. Sci. USA*, 2009, 106, 7304–7308.
[172] Tuinstra, F; Koenig, JL. *J. Chem. Phys.*, 1970, 53, 1126–1130.
[173] Thomsen, C; Reich, S. *Phys. Rev. Lett.*, 2000, 85, 5214–5217.
[174] Piscanec, S; Lazzeri, M; Mauri, F; Ferraru, AC; Robertson, J. *Phys. Rev. Lett.*, 2004, 93, 185503.
[175] Galiotis, C; Batchelder, DN. *J. Mater. Sci. Lett.*, 1988, 7, 545–547.
[176] Zhou, SY; Gweon, GH; Fedorov, AV; First, PN; de Heer, WA; Lee, DH; Guinea, F; Castro Neto, AH; Lanzara, A. *Nature Mater*., 2007, 6, 770–775.
[177] Ribeiro, RM; Peres, NMR. *Phys. Rev. B*, 2008, 78, 075442.

[178] Giovannetti, G; Khomyakov, PA; Brocks, G; Kelly, PJ; van der Brink, J. *Phys. Rev. B*, 2007, 76, 073103.
[179] Ni, ZH; Yu, T; Lu, YH; Wang, YY; Feng, YP; Shen, ZX. *ACS Nano*, 2008, 2, 2301–2305.
[180] Wang, Y; Shao, Y; Matson, DW; Li, J; Lin, Y. *ACS Nano*, 2010, 4, 1790–1798.
[181] Matsunaga, K; Iwamoto, Y. *J. Am. Ceramic Soc*., 2001, 84, 2213–2219.
[182] Tsoukleri, G; Parthenios, J; Papagelis, K; Jalil, R; Ferrari, AC; Geim, AK; Novoselov, KS; Galiotis, C. *Small*, 2009, 5, 2397–2402.
[183] Neek-Amal, M; Peeters, FM. *Appl. Phys. Lett*., 2010, 97, 153118.
[184] Tapaszto, L; Dobric, G; Nemes-Incze, P; Vertesy, G; Lambin, P; Biro, LP. *Phys. Rev. B*, 2008, 78, 233407.
[185] Neubeck, S; Freitag, F; Yang, R; Novoselov, K. *Phys. Status Solidi B*, 2010, 247, 2904–2908.
[186] Kowaki, Y; Harada, A; Shimojo, F; Hoshino, K. *J. Phys. Condens. Matter*, 2009, 21, 064202.
[187] Nordlund, K; Keinonen, J; Mattila, T. *Phys. Rev. Lett*., 1996, 77, 699–702.
[188] Hao, F; Fang, D; Xu, Z. *Appl. Phys. Lett.*, 2011, 99, 041901.
[189] Garaj, S; Hubbard, W; Golovchenko, JA. *Appl. Phys. Lett.*, 2010, 97, 183103.
[190] Krasheninnikov, AV; Banhart, F. *Nature Mater*., 2007, 6, 723–733.
[191] Masrour, R; Bahmad, L; Benyoussef, A; Hamedoun, M; Hlil, EK. *J. Supercond. Nov. Magn.*, 2013, 26, 679–685.
[192] Kogeshima, H; Hibino, H; Nagase, M; Sekine, Y; Yamaguchi, H. *Jpn. J. Appl. Phys*., 2011, 50, 070115.
[193] Galashev, AE; Galasheva, AA. *High Energy Chem*., 2014, 48, 112–116.
[194] Lehtinen, O; Kotakoski, J; Krasheninnikov, AV; Keinonen, J. *Nanotechnology*, 2011, 22, 175306.
[195] Standop, S; Lehtinen, O; Herbig, C; Lewes-Malandrakis, G; Craes, F; Kotakoski, J; Mishely, T; Krasheninnikov, AV; Busse, C. *Nano Lett*., 2013, 13, 1948–1955.
[196] Moliver, SS; Zimagullov, RR; Semenov, AL. *Tech. Phys. Lett*., 2011, 37, 678–673.
[197] Meyer, JC; Kisielowski, C; Erni, R; Rossel, MD; Crommie, MF; Zettl, A. *Nano Lett*., 2008, 8, 3582–3586.
[198] Marton, D; Bu, H; Boyd, KJ; Todorov, SS; Al-Bayati, AH; Rabalais, JW. *Surf. Sci.*, 1995, 326, L489–L493.
[199] Thrower, PA; Mayer, RM. *Phys. Status Solidi A*, 1978, 47, 11–37.
[200] Maeta, H; Iwata, T; Okuda, S. *J. Phys. Soc. Jpn*., 1975, 39, 1558–1565.
[201] Pereira, VM; Guinea, F; Lopes dos Santos, JMB; Peres, NMR; Castro Neto, AH. *Phys. Rev. Lett.*, 2006, 96, 036801.
[202] Pereira, VM; Lopes dos Santos, JMB; Castro Neto, AH. *Phys. Rev. B*, 2008, 77, 115109.
[203] Peres, NMR; Guinea, F; Castro Neto, AH. *Phys. Rev. B*, 2006, 73, 125411.

[204] Xhie, J; Sattler, K; Muller, U; Venkateswaren, N; Raina, G. *Phys. Rev. B*, 1991, 43, 8917–8937.
[205] Ouyang, M; Huang, JL; Lieber, CM. *Phys. Rev. Lett*., 2002, 88, 066804.
[206] Rutter, GM; Crain, JN; Guisinger, NP; Li, T; First, PN; Stroscio, JA. *Science*, 2007, 317, 219–222.
[207] Ahlgren, EH; Kotakoski, J; Krasheninnikov, AV. *Phys. Rev. B*, 2011, 83, 115424.
[208] Miller, JC; Haglund, RF. *Laser Ablation and Desorption*; Academic Press: San Diego, US, 1998, Vol. 30, pp. 1–647.
[209] Wang, H; Wang, Q; Cheng, Y; Li, K; Yao, Y; Zhang, Q; Dong, C; Wang, P; Schwingenschlogl, U; Yang, W; Zhang, X. *Nano Lett*., 2012, 12, 141–144.
[210] Bellido, EP; Seminario, JM. *J. Phys. Chem. C*, 2012, 116, 4044–4049.
[211] Lemme, MC; Bell, DC; Williams, JR; Stern, LA; Baugher, BWH; Jarillo-Herrero, P; Marcus, CM. *ACS Nano*, 2009, 3, 2674–2676.
[212] Bell, DC; Lemme, MC; Stern, LA; Williams, JR; Marcus, CM. *Nanotechnology*, 2009, 20, 455301.
[213] Wang, Y; Huang Y; Song, Y; Zhang, X; Ma, Y; Liang, J; Chen, Y. *Nano Lett*., 2009, 9, 220–224.
[214] Yang, HX; Chshiev, M; Boukhvalov, DW; Waintal, X; Roche, S. *Phys. Rev. B*, 2011, 84, 214404.
[215] Wang, WL; Meng, S; Kaxiras, E. *Nano Lett*., 2008, 8, 241–245.
[216] Zhang, Z; Chen, C; Zeng, XC; Guo, W. *Phys. Rev. B*, 2010, 81, 155428.
[217] Nanda, BRK; Sherafatim, M; Popovich, ZS; Satpathy, S. *New J. Phys*., 2012, 14, 083004.
[218] Ma, Y; Lehtinen, PO; Foster, AS; Nieminen, RM. *New J. Phys*., 2004, 6, 68.
[219] Yazyev, OV; Helm, L. *Phys. Rev. B*, 2007, 75, 125408.
[220] Zhang, Y; Talapatra, S; Kar, S; Vajtai, R; Nayak, SK; Ajayan, PM. *Phys. Rev. Lett*., 2007, 99, 107201.
[221] Yu, D; Lupton, EM; Liu, M; Liu, W; Liu, F. *Nano Res*., 2008, 1, 56–62.
[222] Fujita, M; Wakabayashi, K; Nakada, K. *J. Phys. Soc. Jpn*., 1996, 65, 1920–1923.
[223] Klein, D. *J. Chem. Phys. Lett*., 1994, 217, 261–265.
[224] Jiang, D; Sumpter, BG; Dai, S. *J. Chem. Phys*., 2007, 126, 134701.
[225] Hod, O; Barone, V; Peralta, JE; Scuseria, GE. *Nano Lett*., 2007, 7, 2295–2299.
[226] Wang, Z; Hu, H; Wei, Y; Huang, Q. *Physica B: Cond. Matt*., 2010, 405, 3895–3898.
[227] Rigo, VA; Martins, TB; da Silva, AJR; Fazzio, A; Miwa, RH. *Phys. Rev. B*, 2009, 79, 075435.
[228] Ushhiro M; Uno, K; Fujikawa, T; Sato, Y; Tohji, K; Watari, F; Chun, F; Koike, Y; Asakura, K. *Phys. Rev. B*, 2006, 73, 144103.
[229] Wang, Z; Xiao, J; Li, M. *Appl. Phys. A*, 2013, 110, 235–239.
[230] Perdew, JP; Burke, K; Ernzerhof, M. *Phys. Rev. Lett*., 1996, 77, 3865–3868.
[231] Gunlycke, D; Li, J; Mintmire, W; White, CT. *Appl. Phys. Lett*., 2007, 91, 112108.

[232] Wolf, SA; Awschalom, DD; Buhrman, RA; Daughton, JM; Von Molnar, S; Roukes, ML; Chtchelkanova, AY; Trger, DM. *Science*, 2001, 294, 1488–1495.
[233] Koskinen, P; Hakkinen, H; Huber, B; von Issendorff, B; Moseler, M. *Phys. Rev. Lett*., 2007, 98, 015701.
[234] Koskinen, P; Malola, S; Hakkinen, H. *Phys. Rev. Lett*., 2008, 101, 115502.
[235] Lee, YH; Kim, SG; Tomanek, D. *Phys. Rev. Lett*., 1997, 78, 2393–2396.
[236] Hua, X; Cagin, T; Che, J; Goddard, WA. *Nanotechnology*, 2000, 11, 85–88.
[237] Kobayashi, Y; Fukui, K; Enoki, T; Kusakabe, K. *Phys. Rev. B*, 2006, 73 125415.
[238] Li, X; Wang, X; Zhang, L; Lee, S; Dai, H. *Science*, 2008, 319, 1229.
[239] Gan, Y; Kotakoski, J; Krasheninnikov, AV; Nordlund, K; Banhart, F. *New J. Phys*., 2008, 10, 023022.
[240] Hu, J; Ruan, X; Chen, YP. *Nano Lett*., 2009, 9, 2730–2735.
[241] Nose, S. *J. Chem. Phys*., 1984, 81, 511–519.
[242] Hoover, WG. *Phys. Rev. A*, 1985, 31, 1695–1697.
[243] Savvatimskiy, AI. *Carbon*, 2005, 43, 1115–1142.
[244] Zakharchenko, KV; Fassolino, A; Los, JH; Katsnelson, MI. *J. Phys. Condens. Matter*, 2011, 23, 202202.
[245] Kim, SG; Tomanek, D. *Phys. Rev. Lett*., 1994, 72, 2418–2421.
[246] Zhang, K; Stocks, GM; Zhong, J. *Nanotechnology*, 2007, 18, 285703.
[247] Colonna, F; Los, JH; Fasolino, A; Meijer, E. *J. Phys. Rev. B*, 2009, 80, 134103.
[248] Los, JH; Ghiringhelli, LM; Meijer, EJ; Fasolino, A. *Phys. Rev. B*, 2005, *72*, 214102.
[249] Baichi, M; Chatillon, C; Ducros, G; Froment, K. *J. Nucl. Mater*., 2006, 349, 57–82.
[250] Ghosh, S; Calizo, I; Teweldebrhan, D; Pokatilov, EP; Nika, DL; Balandin, AA; Bao, W; Miao, F; Lau, CN. *Appl. Phys. Lett.*, 2008, 92, 151911.
[251] Hong, X; Posadas, A; Zou, K; Ahn, CH; Zhu, J. *Phys. Rev. Lett.*, 2009, 102, 136808.
[252] Alofi, A; Srivastava, GP. *Phys. Rev. B*, 2013, 87, 115421.
[253] Adamyan, V; Zavalniuk, V. *J. Phys.: Cond. Matt.*, 2012, 24, 415401.
[254] Malekpour, H; Ramnani, P; Srinivasan, S; Balasubramanian, G; Nika, DL; Mulchandani, A; Lakee, RK; Balandin, AA. *Nanoscale*, 2016, 8, 14608–14616.
[255] Park, M; Lee, SC; Kim, YS. *J. Appl. Phys.*, 2013, 114, 053506.
[256] Fthenakis, ZG; Zhu, Z; Tomanek, D. *Phys. Rev. B*, 2012, 86, 125418.
[257] Fugallo, G; Cepellotti, A; Paulatto, L; Lazzeri, M; Marzari, N; Mauri, F. *Nano Lett.*, 2014, 14, 6109–6114.
[258] Hansen, DP; Evans, D. *J. Mol. Phys.*, 1994, 81, 767–779.
[259] Jaćimovski, SK; Bukurov, M; Šetrajčić, JP; Raković, DI. *Superlattices & Microstruct.*, 2015, 88, 330–337.
[260] Berber, S; Kwon, YK; Tomanek, D. *Phys. Rev. Lett.*, 2000, 84, 4613–4616.
[261] Galashev, AE; Rakhmanova, OR. *Rus. J. Phys. Chem. B*, 2014, 8, 893–899.
[262] Peierls, RE. *Helv. Phys. Acta*, 1934, 7, 81– 83.
[263] Landau, LD. *Phys. Z. Sowietunion*, 1937, 11, 26–35.

[264] Rybin, MG; Pozharov, AS; Obraztsova, ED. *Phys. Status Solidi C*, 2010, 7, 2785–2788.

[265] Obraztsov, PA; Rybin, MG; Tyurnina, AV; Garnov, SV; Obraztsova, ED; Obraztsov, AN; Svirko, YP. *Nano Lett.*, 2011, 11, 1540–1545.

[266] Jagannadham, K. *Metall. Mater. Trans. B*, 2012, 43, 316–324.

[267] Krasheninnikov, AV; Lehtinen, PO; Foster, AS; Pyykko, P; Nieminen, RM. *Phys. Rev. Lett.*, 2009, 102, 126807.

[268] Jalili, S; Mochani, C; Akhavan, M; Schofield, J. *Mol. Phys*., 2012, 110, 267–276.

[269] Galashev, AE; Polukhin, VA. *Rus. J. Phys.Chem. A*, 2014, 88, 995–999.

[270] Xu, Z; Buehler, MJ. *J. Phys.: Condens. Matter*., 2010, 22, 485301.

[271] Agrawal, M; Rice, BM; Thompson, DL. *Surf. Sci*., 2002, 515, 21–35.

[272] Zhang, P; Ma, L; Fan, F; Zeng, Z; Peng, C; Loya, PE; Liu, Z; Gong, Y; Zhang, J; Zhang, X. *Nat. Commun*., 2014, 5, 3782.

[273] Gong, L; Kinloch, IA; Young, RJ; Riaz, I; Jalil, R; Novoselov, KS. *Adv. Mater*., 2010, 22, 2694−2697.

[274] Jiang, T; Huang, R; Zhu, Y. *Adv. Funct. Mater*., 2014, 24, 396−402.

[275] Anagnostopoulos, G; Androulidakis, C; Koukaras, EN; Tsoukleri, G; Polyzos, I; Parthenios, J; Papagelis, K; Galiotis, C. *ACS Appl. Mater. Interfaces*, 2015, 7, 4216−4223.

[276] Del Corro, E; Kavan, L; Kalbac, M; Frank, O. *J. Phys. Chem. C*, 2015, 119, 25651−25656.

[277] Na, SR; Wang, X; Piner, RD; Huang, R; Willson, CG; Liechti, KM. *ACS Nano*, 2016, 10, 9616−9625.

[278] Yu, EK; Stewart, DA; Tiwari, S. *Phys. Rev. B: Condens. Matter*., 2008, 77, 195406.

[279] Wander, MCF; Shuford, KL. *J. Phys. Chem. C*, 2010, 114, 20539–20546.

[280] White, GK; Collocott, SJ. *J. Phys. Chem. Ref. Data*, 1984, 13, 1251–1257.

[281] Galashev, AE; Polukhin, VA. *Phys. Solid State*, 2013, 55, 1733–1738.

[282] Li, XS; Cai, W; An, J; Kim, S; Nah, J; Yang, D; Piner R; Velamakanni, A; Jung, I; Tutuc, E; Banerjee, SK; Colombo, L; Ruoff, RS. *Science (Washington)*, 2009, 324, 1312.

[283] Wintterlin, J; Bocquet, ML. *Surf. Sci*., 2009, 603, 1841–1852.

[284] Moors, M; Amara, H; de Bocarme, TV; Bichara, C; Ducastelle, F. *ACS Nano*, 2009, 3, 511–516.

[285] Eizenberg, M; Blakely, JM. *Surf. Sci*., 1979, 82, 228–236.

[286] Portnoi, VK; Leonov, AV; Mudretsova, SN; Fedotov, SA. *Phys. Met. Metallogr.*, 2010, 109, 153–161.

[287] Kwak, J; Chu, JH; Choi, JK; Park, SD; Go, H; Kim, SY; Park, K; Kim, SD; Kim, YW; Yoon, E; Kodambaka, S; Kwon, SY. *Nat. Commun*., 2012, 3, 645.

[288] Galashev, AE; Polukhin, VA. *Phys. Solid State*, 2013, 55, 2368–2373.

[289] Erkoc, S. *Int. J. Mod. Phys. C*, 2000, 11, 1013–1024.

[290] Cagin, T. *Phys. Rev. B: Condens. Matter*., 1999, 59, 3468–3473.
[291] Nayak, SK; Khanna, SN; Rao, BK; Jena, P. *J. Phys. Chem. A*, 1997, 101, 1072–1080.
[292] Shibuta, Y; Elliott, JA. *Chem. Phys. Lett*., 2009, 472, 200–206.
[293] Qi, Y; Cagin, T; Johnson, WL; Goddard, III WA. *J. Chem. Phys*., 2001, 115, 385–394.
[294] Fujita, D; Yoshihara, K. *J. Vac. Sci. Technol. A*, 1994, 12, 2134–2139.
[295] Shelton, JC; Patil, HR; Blakely, JM. *Surf. Sci*., 1974, 43, 493–520.
[296] Reina, A; Thiele, S; Jia, X; Bhaviripudi, S; Dresselhaus, MS; Schaefer, JA; Kong, J. *Nano Res*., 2009, 2, 509–516.
[297] Suzuki, S; Takei, Y; Furukawa K; Hibino, H. *Appl. Phys. Express*, 2011, 4, 065102.
[298] Loomis, J; King, B; Panchapakesan, B. *Appl. Phys. Lett*., 2012, 100, 073108.
[299] Loomis, J; King, B; Burkhead, B; Xu, P; Terentjev, EM; Panchapakesan, B. *Nanotecnology*, 2012, 23, 045501.
[300] Balandin, AA; Ghosh, S; Bao, W; Calizo, I; Teweldebrhan, D; Miao, F; Lau, CN. *Nano Lett*., 2008, 8, 902–907.
[301] Loomis, J; Panchapakesan, B. *Nanotecnology*, 2012, 23, 265203.
[302] Yang, S; Yoon, M; Wang, E; Zhang, Z. *J. Chem. Phys*., 2008, 129, 134707.
[303] Barraza-Lopez, S; Vanevic, M; Kindermann, M; Chou, MY. *Phys. Rev. Lett*., 2010, 104, 076807.
[304] Galashev, AE. *High Temp*., 2014, 52, 633–639.
[305] Galashev, AE. *Phys. Solid State*, 2014, 56, 1048–1053.
[306] Lee, SH; Park, M; Yoh, JJ; Song, H; Jang, EY; Kim, YH; Kang, S; Yoo, YS. *Appl. Phys. Lett*., 2012, 101, 241909.
[307] Wang, L; Travis, JJ; Cavanagh, AS; Liu, X; Koenig, SP; Huang, PY; George, SM; Bunch, JS. *Nano Lett*., 2012, 12, 3706–3710.
[308] Nam, Y; Lindvall, N; Sun, J; Park, YW; Yurgens, A. *Carbon*, 2012, 50, 1987–1992.
[309] Hanaoka, Y; Hinode, K; Takeda, K; Kodama, D. *Mater. Trans*., 2002, 43, 1621–1623.
[310] Cheong, WCD; Zhang, LC. *Nanotechnology*, 2000, 11, 173–180.
[311] Kim, O. *Mol. Simul*., 2005, 31, 115–121.
[312] Galashev, AE. *Tech. Phys*., 2014, 59, 467–473.
[313] Quintana, P; Oliva, AI; Ceh, Q; Corona, JE; Aguilar, M. *Superficies y Vacío*, 1999, 9, 280–282.
[314] Novoselov, KS; McCann, E; Morozov, SV; Falko, VI; Katsnelson, MI; Zeitler, U; Jiang, D; Schedin, F; Geim, AK. *Nat. Phys*., 2006, 2, 177–180.
[315] Stankus, SV; Savchenko, IV; Agadzhanov, ASh; Yatsuk, OS; Zhmurikov, EI. *High Temp*., 2013, 51, 179–182.
[316] Basharin, A. Yu; Lysenko, I. Yu; Turchaninov, MA. *High Temp*., 2012, 50, 464–470.
[317] Meyer, JC; Geim, AK; Katsnelson, MI; Novoselov, KS; Obergfell, D; Roth, S; Girit, C; Zettl, A. *Solid State Commun*., 2007, 143, 101–109.

[318] Gibertini, M; Tomadin, A; Polini, M; Fasolino, A; Katsnelson, MI. *Phys. Rev. B*, 2010, 81, 125437.
[319] Galashev, AE; Rakhmanova, OR. *High. Temp*., 2014, 52, 374–380.
[320] Chekhovskoi, VYa; Peletsky, VE. *High Temp.*, 2011, 49(1), 45–54.
[321] Aboud, S; Sasmaz, E; Wilcox, J. *Main Group Chem.*, 2008, 7, 205−215.
[322] Lim, DH; Wilcox, J. *Environ. Sci. Technol*., 2013, 47, 8515−8522.
[323] Scala, F; Cimino, S. *Chem. Eng. J.*, 2015, 278, 134−139.
[324] Negreira, AS; Wilcox, J. *J. Phys. Chem. C*, 2013, 117, 1761−1772.
[325] Azamat, J; Khataee, A; Joo, SW. *J. Mol. Graphics Modell*., 2014, 53, 112−117.
[326] Li, B; Zhang, Y; Ma, D; Shi, Z; Ma, S. *Nat. Commun.*, 2014, 5, 5537.
[327] Bilewicz, R; Stojek, Z; Kublik, Z. *J. Electroanal. Chem. Interfacial Electrochem.*, 1979, 96, 29−44.
[328] Vassos, BH; Mark, HB. Jr. *J. Electroanal. Chem. Interfacial Electrochem.*, 1967, 13, 1−9.
[329] Awasthi, A; Bhatt, YJ; Garg, SP. *Meas. Sci. Technol.*, 1996, 7, 753−757.
[330] Dujardin, E; Ebbesen, TW; Hiura, H; Tanigaki, K. *Science*, 1994, 265, 1850−1852.
[331] Chen, JY; Kutana, A; Collier, CP; Giapis, KP. *Science*, 2005, 310, 1480−1483.
[332] Galashev, AY. *Mol. Simul*., 2010, 36, 273−282.
[333] Kutana, A; Giapis, KP. *Phys. Rev. B: Condens. Matter Mater. Phys*., 2007, 76, 195444.
[334] Muhammad Bilal Shakoor, MB; Ali, S; Farid, M; Farooq, MA; Tauqeer, HM; Iftikhar, U; Hannan, F; Bharwana, SA. *J. Bio. & Env. Sci.*, 2013, 3(3), 12–20.
[335] Fernandez-Leborans, GH; Yolanda, O. *Ecotoxicol. Environ. Safety*, 2000, 47, 266–267.
[336] Sayari, A; Hamoudi, S; Yang, Y. *Chem. Mater.*, 2005, 17, 212–216.
[337] Li, R; Liu, L; Yang, F. *Chem. Eng. J*., 2013, 229, 460–468.
[338] Kaplow, R; Strong, SL; Averbach, BL. *Phys. Rev*., 1965, 138(5A), 1336-1345.
[339] Bomont, JM; Bretonnet, JL; Gonzalez, DJ; Gonzalez, LE. *Phys. Rev. B*, 2009, 79, 144202.
[340] Galashev, AE; Polukhin, VA. *Russ. J. Phys. Chem. A*, 2015, 89, 1429–1433.
[341] Schwerdtfeger, P; Wesendrup, R; Moyano, GE. *J. Chem. Phys*., 2001, 115, 7401–7412.
[342] Munro, LJ; Johnson, JKJ; Jordan, KD. *Chem. Phys.*, 2001, 114, 5545–5551.
[343] Badyal, YS; Bafile, U; Miyazaki, K; de Schepper, IM; Montfrooij, W. *Phys. Rev. E*, 2003, 68, 061208.
[344] Lobo, VVM; Mills, R. *Electrochim. Acta*, 1982, 27, 969–971.
[345] Epstein, F; Powers, MD. *J. Phys. Chem.*, 1953, 57, 336−341.
[346] Galashev, AY. *Comput. Mater. Sci.*, 2015, 98, 123−128.
[347] Rao, RVG; Murthy, AKK. *Phys. Status Solidi B*, 1974, 66, 703−707.
[348] Galashev, AE. *Colloid J*., 2015, 77, 582–591.

[349] Galashev, AE. *High Temp.*, 2016, 54, 690–697.
[350] Ward, CA; Stanga, D. *Phys. Rev. E: Stat. Phys., Plasmas, Fluids, Relat. Interdiscip. Top*., 2001, 64, 051509.
[351] McGaughey, AJH; Ward, CA. *J. Appl. Phys.*, 2002, 91, 6406−6415.
[352] Lotfi, A; Vrabec, J; Fischer, J. *Int. J. Heat Mass Transfer*, 2014, 73, 303−317.
[353] Kitamura, H. *J. Phys.: Conf. Ser*., 2008, 98, 052010.
[354] Hawaldar, R; Merino, P; Correia, MR; Bdikin, I; Grácio, J; Méndez, J. *Sci. Rep*., 2012, 2, 682.
[355] Siokou, A; Ravani, F; Karakalos, S; Frank, O; Kalbac, M; Galiotis, C. *Appl. Surf. Sci*., 2011, 257, 9785–9790.
[356] Saito, S; Ito, A; Nakamura, H. *Plasma and Fusion Res*., 2010, 5, S2076.
[357] Inui, N; Mochiji, K; Moritani, K. *Nanotechnology*, 2008, 19, 505501.
[358] Krasheninnikov, AV; Nordlund, K. *J. Appl. Phys*., 2010, 107, 071301.
[359] Garcia, H; Castan, H; Duenas, S; Bailon, L; Campabadal, F; Rafi, JM; Tsunoda, I. *Thin Solid Films*, 2013, 534, 482–487.
[360] Ahlgren, E; Kotakoski, J; Lehtinen, O; Krasheninnikov, AV. *Appl. Phys. Lett.*, 2012, 100, 233108.
[361] Luoma, SN. *Sci. Total Environ.*, 1983, 28, 1–22.
[362] Hummers, W; Offeman, R. *J. Am. Chem. Soc*.,1958, 80, 1339.
[363] Choi, YS; Choi, HS. *Bull. Korean. Chem. Soc*., 2003, 24, 222–224.
[364] Zaijan, L; Yuling, Y; Jian, T; Jiaomai, P. *Talanta*, 2003, 60, 123–130.
[365] Kara, D; Alkan, M; Cakir, U. *Turk. J. Chem.*, 2001, 25, 293–303.
[366] Sonawale, SB; Ghalsasi, YV; Argekar, AP. *Anal. Sci.*, 2001, 17, 285–289.
[367] Manzoori, JL; Bavili-Tabrizi, A. *Microchem. J*., 2002, 72, 1–7.
[368] Chen, J; Teo, KC. *Anal. Chim. Acta*, 2001, 450, 215–222.
[369] Yuan, S; Chen, W; Hu, S. *Talanta*, 2004, 64, 922–928.
[370] Gao, H; Zhou, J; Lu, M; Fa, W; Chen, Y. *J. Appl. Phys.*, 2010, 107, 114311.
[371] Ma, D; Yang, Z. *New J. Phys.*, 2011, 13, 123018.
[372] Galashev, AE; Polukhin, VA. *J. Surf. Invest.: X-ray, Synchrotr. Neutron Tech.*, 2014, 8, 1082–1088.
[373] Galashev, AE; Polukhin, VA. *Phys. Met. Metallogr*., 2014, 115, 697–704.
[374] Galashev, AE; Rakhmanova, OR. *Phys. Usp*., 2014, 57, 970–989.
[375] Russo, MF; Jr. Garrison, B. *J. Anal. Chem.*, 2006, 78, 7206–7210.
[376] Russo, MF; Jr. Szakal, C; Kozole, J; Winograd, N; Garrison, B. *J. Anal. Chem.* 2007, 79, 4493–4498.
[377] Smiley, EJ; Winograd, N; Garrison, B. *J. Anal. Chem.*, 2007, 79, 494–499.
[378] Watanabe, Y; Yamaguchi, H; Hashinokuchi, M; Sawabe, K; Maruyama, S; Matsumoto, Y; Shobatake, K. *Chem. Phys. Lett.*, 2005, 413, 331–334
[379] Steckel, JA. *Chem. Phys. Lett*., 2005, 409, 322–330.
[380] Padak, B; Brunetti, M; Lewis, A; Wilcox, J. *Environ. Prog*., 2006, 25, 319–326.

[381] Padak, B; Wilcox, J. *Carbon*, 2007, 47, 2855–2864.
[382] Huggins, FE; Huffman, GP; Dunham, GE; Senior, CL. *Energy Fuels*, 1999, 13, 114–121.
[383] Cao Y; Li, X. *Adsorption*, 2014, 20, 713–727.
[384] Galashev, AE. *Fiz. Mezomekh*., 2014, 17, 67–73.
[385] Galashev, AY; Rakhmanova, OR. *Chin. Phys. B*, 2015, 24, 020701.
[386] Galashev, AE. *Phys. Met. Metallogr*., 2016, 117, 246–253.
[387] Galashev, AE; Polukhin, VA. *Rus. J. Phys. Chem. B*, 2016, 10, 15–22.
[388] Galashev, AE; Rakhmanova, OR. *J. Engineering Phys. Thermophys.*, 2017, 90, 1026–1034.
[389] Galashev, AE; Polukhin, VA. *Rus. Metallurgy (Metally)*, 2016, 2, 124–130.
[390] Galashev, AE; Galasheva, AA. *High Energy Chem*., 2015, 49, 347–351.
[391] Galashev, AE. *Phys. Met. Metallogr*., 2016, 117, 238–245.
[392] Hosseini-Hashemi, S; Sepahi-Boroujeni, A. *Int. J. Solids Struct*., 2017, 109, 93–100.
[393] Yang, L; Tong, L. *Carbon*, 2016, 107, 689–696.
[394] Hill, R; Blenkinsopp, P. *Appl. Surf. Sci*., 2004, 231, 936–939.
[395] Krantzman, KD; Kingsbury, DB; Garrison, BJ. *Nucl. Instrum. Methods. Phys. Res. B*, 2007, 255, 238–241.
[396] Vanin, M; Mortensen, JJ; Kelkkanen, AK; Garcia-Lastra, KS; Thygesen, JM; Jacobsen, KW. *Phys. Rev. B*, 2010, 81, R081408.
[397] Galashev, AE; Galasheva, AA. *High Energy Chem*., 2015, 49, 117–121.
[398] Duval, MC; Soep, B. *Chem. Phys. Lett*., 1987, 141, 225–231.
[399] Novoselov, KS; Geim, AK; Morozov, SV; Jiang, D; Katsnelson, MI; Grigorieva, IV; Dubonos, SV; Firsov, AA. *Nature*, 2005, 438, 197–200.
[400] Huard, B; Sulpizio, JA; Stander, N; Todd, K; Yang, B; Goldhaber– Gordon, D. *Phys. Rev. Lett.*, 2009, 102, 026807.
[401] Krekora, P; Su, Q; Grobe, R. *Phys. Rev. Lett.*, 2004, 92, 040406.
[402] Setare, MR; Jahani, D. *Phys. B*, 2010, 405, 1433–1436.
[403] Allain, PE; Fuchs, JN. *Eur. Phys. J. B*, 2011, 83, 301–317.
[404] Xiao, J; Mei, D; Li, X; Xu, W; Wang, D; Graff, GL; Bennett, WD; Nie, Z; Saraf, LV; Aksay, IA; Liu, J; Zhang, JG. *Nano Lett.*, 2011, 11, 5071–5078.
[405] Pei, QX; Zhang, YW; Shenoy, VB. *Carbon*, 2010, 48, 898–904.
[406] Rangel, E; Vazquez, G; Magana, F; Sansores, E. *J. Mol. Model.*, 2012, 18, 5029–5033.
[407] Gautam, S; Dharamvir, K; Goel, N. *J. Phys. Chem. A*, 2011, 115, 6383–6389.
[408] Ataca, C; Akturk, E; Ciraci, S; Ustunel, H. *Appl. Phys. Lett.*, 2008, 93, 043123.
[409] Kheirabadi, N; Shafiekhani, A. *Phys. E (Amsterdam, Neth.)*, 2013, 47, 309–315.
[410] Tao, Z; Cummings, PT. *Mol. Simul.*, 2007, 33, 1255–1260.
[411] Chan, Y; Hill, JM. *Micro Nano Lett.*, 2010, 5, 247–250.
[412] Galashev, AE; Zaikov, Yu. P. *Rus. J. Electrochem.*, 2015, 51, 867–876.

[413] Galashev, AE; Rakhmanova, OR. *High Temp.*, 2016, 54, 11–19.
[414] Galashev, AE; Zaikov, Yu. P. *Rus. J. Phys. Chem.*, 2015, 89, 2243–2247.
[415] Peng, Q; Wen, X; De, S. *RSC Adv*., 2013, 3, 13772–13781.
[416] Liu, G; Wu, MS; Ouyang, CY; Xu, B. *Europhys. Lett.*, 2012, 99, 17010.
[417] Kaloni, TP; Cheng, YC; Schwingenschlogl, U. *J. Appl. Phys*., 2013, 113, 104305.
[418] Zhao, H. *Phys. Lett. A*, 2012, 376, 3546–3550.
[419] Qin, R; Zhu, W; Zhang, Y; Deng, X. *Nanoscale Res. Lett.*, 2014, 9, 521.
[420] Yang, C; Yu, Z; Lu, P; Liu, Y; Ye, H; Gao, T. *Comput. Mater. Sci*., 2014, 95, 420–428.
[421] Wang, B; Wu, J; Gu, X; Yin, H; Wei, Y; Yang, R; Dresselhaus, M. *Appl. Phys. Lett*., 2014, 104, 081902.
[422] Roman, R; Cranford, SW. *Comput. Mater. Sci.*, 2014, 82, 50–55.
[423] Le, MQ; Nguyen, DT. *Appl. Phys. A*, 2015, 118, 1437–1445.
[424] Wang, Z; Feng, N; Ruan, X. *J. Appl. Phys.*, 2015, 117, 084317.
[425] Muller, K; Krause, FF; Beche, A; Schowalter, M; Galioit, V; Loffler, S; Verbeeck, J; Zweck, J; Schattschneider, P; Rosenauer, A. *Nat. Commun.*, 2014, 5, 5653–5660.
[426] Osbom, TH; Farajian, AA. *J. Phys. Chem. C*, 2012, 116, 22916.
[427] Galashev, AE; Zaikov, Yu. P; Vladykin, RG. *Rus. J. Electrochem.*, 2016, 52, 966–974.
[428] Tersoff, J. *Phys. Rev. B*, 1988, 38, 9902–9905.
[429] Yu, R; Zhai, P; Li, G; Liu, L. *J. Electron. Mater*., 2012, 41, 1465–1469.
[430] Angel, EC; Reparaz, JS; Gomis-Bresco, J; Wagner, MR; Cuffe, J; Graczykowski, B; Shchepetov, A; Jiang, H; Prunnila, M; Ahopelto, J; Alzina, F; Sotomayor Torres, C. M. *Appl. Mater.*, 2014, 2, 012113–012118.
[431] Das, SK; Roy, D; Sengupta, S. *J. Phys. F: Metal. Phys.*, 1977, 7, 5–14.
[432] Kawahara, K; Shirasawa, T; Arafune, R; Lin, CL; Takahashi, T; Kawai, M; Takagi, N. *Surf. Sci.*, 2014, 623, 25–28.
[433] Drissi, LB; Saidi, EH; Bousmina, M; Fassi-Fehri, O. *J. Phys.: Condens. Mater.*, 2012, 24(48), 485502.
[434] Peng, B; Cheng, F; Tao, Z; Chen, J. *J. Chem. Phys.*, 2010, 133, 034701.
[435] Arafune, R; Lin, CL; Kawahara, K; Tsukahara, N; Minamitani, E; Kim, Y; Takagi, N; Kawai, M. *Surf. Sci*., 2013, 608, 297–300.
[436] Galashev, AY; Ivanichkina, KA. *Phys. Lett. A*, 2017, 381, 3079–3083.
[437] Lalmi, B; Oughaddou, H; Enriquez, H; Kara, A; Vizzini, S; Ealet, B; Aufray, B. *Appl. Phys. Lett*., 2010, 97, 223109.
[438] Feng, B; Ding, Z; Meng, S; Yao, Y; He, X; Cheng, P; Chen, L; Wu, K. *Nano Lett*., 2012, 12, 3507–3511.
[439] Du, Y; Zhuang, J; Wang, J; Li, Z; Liu, H; Zhao, J; Xu, X; Feng, H; Chen, L; Wu, K; Wang, X; Dou, SX. *Sci. Adv*., 2016, 2, e1600067.

[440] Le Lay, G; Aufray, B; Leandri, C; Oughaddou, H; Biberian, JP; de Padova, P; Davila, ME; Ealet, B; Kara, A. *Appl. Surf. Sci*., 2009, 256, 524–529.
[441] Gao, JF; Zhang, JF; Liu, HS; Zhang, Q; Zhao, J. *Nanoscale*, 2013, 5, 9785–9792.
[442] Ozcelik, VO; Gurel, HH; Ciraci, S. *Phys. Rev. B: Condens. Matter*, 2013, 88(4), 045440.
[443] Hu, W; Wu, X; Li, Z; Yang, J. *Nanoscale*, 2013, 5, 9062–9066.
[444] Ambrosetti, A; Silvestrelli, PL. *J. Phys. Chem. C*, 2014, 118, 19172–19179.
[445] Berdiyorov, GR; Peeters, FM. *RSC Adv*., 2014, 4, 1133–1137.
[446] Li, S; Wu, Y; Tu, Y; Wang, Y; Jiang, T; Liu, W; Zhao, Y. *Sci. Rep*., 2015, 5, 07881.
[447] Osborn, TH; Farajian, AA. *J. Phys. Chem. C*, 2012, 116, 22916–22920.
[448] Galashev, AE; Ivanichkina, KA; Vorob'ev, AS; Rakhmanova, OR. *Phys. Solid State*, 2017, 59, 1242–1252.
[449] Galashev, AE; Rakhmanova, OR; Zaikov, Yu. P. *Phys. Solid State*, 2016, 58, 1850–1857.
[450] Rakhmanova, OR; Galashev, AE. *Rus. J. Phys. Chem. A*, 2017, 91, 921–925.
[451] Chavez-Castillo, MR; Rodriguez-Meza, MA; Meza-Montes, L. *Rev. Mex. Fis*., 2012, 58, 139–145.
[452] Stillinger, FH; Weber, TA. *Phys. Rev. B: Condens. Matter.*, 1985, 31, 5262–5271.
[453] Galashev, AE; Izmodenov, IA; Novruzov, AN; Novruzova, OA. *Semiconductors*, 2007, 41(2), 190–196.
[454] Galashev, AE; Polukhin, VA; Izmodenov, IA; Rakhmanova, OR. *Glass Phys. Chem.*, 2006, 32(1), 99–105.
[455] Osborn, TH; Farajian, AA. *J. Phys. Chem. C*, 2012, 116, 22916–22920.
[456] Pearse, AJ; Schmitt, TE; Fuller, EJ; El-Gabaly, F; Lin, CF; Gerasopoulos, K; Kozen, AC; Talin, AA; Rubloff, G; Gregorczyk, KE. *Chem. Mater*., 2017, 29(8), 3740–3753.
[457] Skripov, VP; Galashev, AE. *Rus. Chem. Rev*., 1983, 52, 97–116.
[458] Berdiyorov, GR; Peeters, FM. *RSC Adv*., 2014, 4, 1133–1137.
[459] Peng, Q; De, S. *Nanoscale*, 2014, 6, 12071–12079.
[460] Galashev, AE; Ivanichkina, KA. *Rus. J. Phys. Chem. A*, 2017, 91, 2448–2452.
[461] Rasmussen, AA; Jensen, JAD; Horsewell, A; Somers, MAJ. *Electrochim. Acta*, 2001, 47, 67–74.
[462] Shen, YF; Lu, L; Lu, QH; Jin, ZH; Lu, K. *Scripta Materialia*, 2005, 59, 989–994.
[463] Kaloyeros, AE; Eisenbraun, E. *Annu. Rev. Mater. Sci.*, 2000, 30, 363–385.
[464] Furnival, T; Leary, RK; Tyo, EC; Vajda, S; Ramasse, QM; Thomas, JM; Bristowe, PD; Midgley, PA. *Chem. Phys. Lett.*, 2017, 683, 370–374.
[465] Kidambi, PR; Bayer, BC; Blume, R; Wang, ZJ; Baehtz, C; Weatherup, RS; Willinger, MG; Schloegl, R; Hofmann, S. *Nanoletters*, 2013, 13, 4769–4778.
[466] Foiles, SM; Baskes, MI; Daw, MS. *Phys. Rev. B*, 1986, 33, 7983–7991.
[467] Novruzova, OA; Rakhmanova, OR; Galashev, AE. *Rus. J. Phys. Chem. A*, 2007, 81, 1825–1828.

[468] Hohenberg, P; Kohn, W. *Phys. Rev. B*, 1964, 136, 864–871.
[469] Kohn, W; Sham, L. *J. Phys. Rev. A*, 1965, 140, 1133–1138.
[470] Galashev, AE; Rakhmanova, OR; Ivanichkina, KA. *J. Struct. Chem*., 2018, 59(4), 1–7.
[471] Sahin, H; Cahangirov, S; Topsakal, M; Bekaroglu, E; Akturk, E; Senger, RT; Ciraci, S. *Phys. Rev. B*, 2009, 80, 155453.
[472] Politano, A; Chiarello, G. *Nano Res.*, 2015, 8, 1847–1856.
[473] Ru-Ge, Q; Yang, WX; Jin, L. *Chin. Phys. B*, 2015, 24, 088105.
[474] Kahn, H; Ballarini, R; Bellante, JJ; Heuer, AH. *Science*, 2002, 298(8), 1215–1218.
[475] Chang, CA; Siekhaus, WJ. *J. Appl. Phys*., 1975, 46, 3402–3407.
[476] Beaucarne, G; Bourdais, S; Slaoui, A; Poortmans, J. *Appl. Phys. A*, 2004, 79, 469–480.
[477] Shirai, T; Shirasawa, T; Hirahara, T; Fukui, N; Toshio Takahashi, T; Hasegawa, S. *Phys. Rev. B*, 2014, 89, 241403(R).
[478] Ding, Y; Ni, J. *Appl. Phys. Lett.*, 2009, 95, 083115.
[479] Lebegue, S; Eriksson, O. *Phys. Rev. B*, 2009, 79, 115409.
[480] Gao, J; Zhao, J. *Sci. Rep.*, 2012, 2, 861.
[481] Tersoff, J. *Phys. Rev. B Condens. Matter*., 1989, 39, 5566–5568.
[482] Fang, TE; Wu, JH. *Comp. Mater. Sci.*, 2008, 43, 785–790.
[483] Galashev, AY. *J. Chem. Phys.*, 2013, 139, 124303.
[484] Geim, AK; Novoselov, KS. *Nat. Mater.*, 2007, 6, 183–191.
[485] Castro Neto, AH; Guinea, F; Peres, NMR; Novoselov, KS; Geim, AK. *Rev. Mod. Phys.*, 2009, 81, 109–162.
[486] Geim, AK. *Science*, 2009, 324, 1530–1534.
[487] Abergel, DSL; Apalkov, V; Berashevich, J; Ziegler, K; Chakraborty, T. *Adv. in Phys*., 2010, 59, 261–482.
[488] Singh, V; Joung, D; Zhai, L; Das, S; Khondaker, SI; Seal, S. *Prog. in Matter. Sci*., 2011, 56, 1178–1271.
[489] Meyer, JC; Geim, AK; Katsnelson, MI; Novoselov, KS; Booth, TJ; Roth, S. *Nature*, 2007, 446, 60–63.
[490] Kara, A; Enriquez, H; Seitsonen, AP; Lew Yan Voon, LC; Vizzini, S; Aufray, B; Oughaddou, H. *Surf. Sci. Rep*., 2012, 67, 1–18.
[491] Xu, M; Liang, T; Shi, M; Chen, H. *Chem. Rev.*, 2013, 113, 3766–3798.
[492] Chen, L; Liu, CC; Feng, B; He, X; Cheng, P; Ding, Z; Meng, S; Yao, Y; Wu, K. *Phys. Rev. Lett.*, 2012, 109, 056804.
[493] Feng, B; Li, H; Liu, CC; Shao, TN; Cheng, P; Yao, Y; Meng, S; Chen, L; Wu, K. *Acs Nano*, 2013, 7, 9049–9054.
[494] Ni, Z; Liu, Q; Tang, K; Zheng, J; Zhou, J; Qin, R; Gao, Z; Yu, D; Lu, J. *Nano Lett*., 2012, 12, 113–118.
[495] Drummond, ND; Zólyomi, V; Fal'ko, VI. *Phys. Rev. B*, 2012, 85, 075423.

[496] Zandvliet, HJW. *Nano Today*, 2014, 9, 691–694.
[497] Huang, B; Xiang, H; Wei, S. *Phys. Rev. Lett*., 2013, 111, 145502.
[498] Zhuang, J; Xu, X; Du, Y; Wu, K; Chen, L; Hao, W; Wang, J; Yeoh, W; Wang, X; Dou, S. *Phys. Rev. B*, 2015, 91, 161409.
[499] Wang, R; Pi, XD; Ni, Z; Liu, Y; Yang, D. *RSC Adv.*, 2015, 5, 33831–33837.
[500] Du, Y; Zhuang, JC; Liu, HS; Xu, X; Eilers, S; Wu, KH; Peng, C; Zhao, JJ; Pi, XD; See, K; Peleckis, G; Wang, X; Dou, X. *ACS Nano*, 2014, 8, 10019–10025.
[501] Zheng, R; Lin, X; Ni, J. *Appl. Phys. Lett.*, 2014, 105, 092410.
[502] Drissi, LB; Ramadan, FZ. *Physica E*, 2015, 68, 38–41.
[503] Qiu, J; Fu, H; Xu, Y; Oreshkin, A; Shao, T; Li, H; Meng, S; Chen, L; Wu, K. *Phys. Rev. Lett.*, 2015, 114, 126101.
[504] Tao, L; Cinquanta, E; Chiappe, D; Grazianetti, C; Fanciulli, M; Dubey, M; Molle, A; Akinwande, D. *Nat. Nanotechnol*., 2015, 10, 227–231.
[505] Wu, ZS; Ren, WC; Xu, L; Li, F; Cheng, HM. *ACS Nano*, 2011, 5, 5463–5471.
[506] Luo, B; Fang, Y; Wang, B; Zhou, JS; Song, HH; Zhi, L. *J. Energy Environ. Sci.*, 2012, 5, 5226–5230.
[507] Tian, H; Seh, ZW; Yan, K; Fu, Z; Tang, P; Lu, Y; Zhang, R; Legut, D; Cui, Y; Zhang, Q. *Adv. Energy Mater*., 2017, 7, 1602528.
[508] Perdew, JP; Ruzsinszky, A; Tao, JM; Staroverov, VN; Scuseria, GE; Csonka, GI. *J. Chem. Phys*., 2005, 123, 062201.
[509] Cohen, AJ; Mori-Sanchez, P; Yang, WT. *Chem. Rev.*, 2012, 112, 289–320.
[510] Perdew, JP; Schmidt, K. In *Density Functional Theory and its Application to Materials*; edited by Van Doren, VE; Van Alsenoy, C; Geerlings, P; AIP, Melville: New York, US, 2001, pp. 1–250.
[511] Dufty, JW; Trickey, SB. *Phys. Rev. B*, 2011, 84, 125118.
[512] Trickey, SB; Karasiev, VV; Vela, A. *Phys. Rev. B*, 2011, 84, 075146.
[513] Ordejon, P; Artacho, E; Soler, JM. *Phys. Rev. B*, 1996, 53, 10441–10444.
[514] Sanchez-Portal, D; Ordejon, P; Artacho, E; Soler, JM. *Int. J. Quantum. Chem.*, 1997, 65, 453–461.
[515] Lieb, EH; Oxford, S. *Int. J. Quantum Chem.*, 1981, 19, 427–439.
[516] Levy, M; Perdew, JP. *Phys. Rev. B*, 1993, 48, 11638, erratum 1997, *55*, 13321.
[517] Ma, SK; Brueckner, KA. *Phys. Rev.*, 1968, 165, 18–31.
[518] Becke, AD. *J. Chem. Phys*., 1986, 84, 4524.
[519] Zhao, Y; Truhlar, DG. *J. Chem. Phys*., 2008, 128, 184109.
[520] del Campo, M; Gázquez, J; Trickey, JL; Vela, SBA. *J. Chem. Phys*., 2012, 136, 104108.
[521] Antoniewicz, PR; Kleinman, L. *Phys. Rev. B*, 1985, 31, 6779–6781.

ABOUT THE AUTHORS

Alexander Y. Galashev
Doctor Phys.-Math. Sci.
Principal Researcher
Institute of High-Temperature Electrochemistry
of the Ural Branch of the RAS (IHTE UB RAS)
Ekaterinburg, Russia
Email: alexander-galashev@yandex.ru

Dr. Alexander Yevgenyevich Galashev graduated from the Physics and Technology Faculty of the Ural Polytechnic Institute, majoring in "technical physics", graduated the School of the Institute of Thermo-physics of the Ural Branch (UB) of the Russian Academy of Sciences (RAS) in molecular physics. For many years he has been engaged in molecular-dynamic modeling of physic-chemical processes, phase transitions, and investigation of the structure of substances including nano-materials. At present, Dr. Galashev works in the Institute of High Temperature Electrochemistry (IHTE) UB RAS. He is Principal Researcher in the Laboratory of electrode processes. Scientific interests are joined with

computer modeling of electrochemical processes, atomic-molecular concept of the structure of chemical compounds, theoretical studies of physic-chemical properties of low-dimensional structures, and investigation of spent nuclear fuel recovery processes. He has published more than 250 articles in scientific journals. He is author of 4 monographs and 20 chapters in the books written in co-operation with different authors.

Yuri P. Zaikov
Doctor in Chemistry, Professor
Scientific Director of the IHTE UB RAS and the Head of the
Research Department of Electrolysis of the IHTE UB RAS
Institute of High-Temperature Electrochemistry
of the Ural Branch of the RAS, Ekaterinburg, Russia

Dr. Yuri Pavlovich Zaikov, is the Scientific Director of the IHTE UB RAS, the Head of the Research Department of Electrolysis of the IHTE UB RAS, the Head of the Department of Electrochemical Production Technology of the Chemical Technology Institute of the Ural Federal University named after B. N. Yeltsin, Honored Scientist of the Russian Federation.

Scientific interests are joined with investigation of nature and regularities of the processes occurring on the electrodes during the electrolysis of melts, the effect of the electrolyte composition, the electrode material, and the conditions of electrolysis on the polarization. He is co-author of 360 scientific papers (including 24 Inventions and Patents of the Russian Federation and 5 Teaching Aids).

INDEX

C

D

E

F

G

H

I

K

L

M

N

O

P

Q

R

S

T

U

V

W

X

Y

Z